Downloaded from orbit.dtu.dk on: Dec 18, 2017

Technical University of Denmark

Active cooling of a down hole well tractor

Soprani, Stefano; Engelbrecht, Kurt; Bahl, Christian; Nesgaard, Carsten

Publication date:
2016

Document Version
Publisher's PDF, also known as Version of record

Link back to DTU Orbit

Citation (APA):
Soprani, S., Engelbrecht, K., Bahl, C., & Nesgaard, C. (2016). Active cooling of a down hole well tractor. Department of Energy Conversion and Storage, Technical University of Denmark.

DTU Library
Technical Information Center of Denmark

General rights
Copyright and moral rights for the publications made accessible in the public portal are retained by the authors and/or other copyright owners and it is a condition of accessing publications that users recognise and abide by the legal requirements associated with these rights.

- Users may download and print one copy of any publication from the public portal for the purpose of private study or research.
- You may not further distribute the material or use it for any profit-making activity or commercial gain
- You may freely distribute the URL identifying the publication in the public portal

If you believe that this document breaches copyright please contact us providing details, and we will remove access to the work immediately and investigate your claim.

Active cooling of a down hole well tractor

A dissertation submitted in partial fulfillment of the requirements for the degree of

Doctor of Philosophy

Stefano Soprani

Department of Energy Conversion and Storage

Technical University of Denmark

August 31st, 2016

Abstract

Wireline interventions in high temperature wells represent one of today's biggest challenges for the oil and gas industry. The high wellbore temperatures, which can reach 200 °C, drastically reduce the life of the electronic components contained in the wireline downhole tools, which can cause the intervention to fail. Active cooling systems represent a possible solution to the electronics overheating, as they could maintain the sensitive electronics at a tolerable temperature, while operating in hotter environments. This work presents the design, construction and testing of an actively cooled downhole electronics section, which is able to cool the critical electronics below 175 °C while operating at 200 °C. After the investigation of several cooling techniques and the thermal characterization of the studied downhole electronics, thermoelectric coolers were chosen to implement a novel concept of heat management for downhole tools. The chosen design combined active and passive cooling techniques aiming at efficient thermal management, preserving the tool compactness, and avoiding the use of moving parts. Topology optimization was used, in combination with a finite element model of the system, to develop the final design of an actively cooled prototype, which was able to continuously maintain the temperature-sensitive electronics below 170 °C, while operating at 200 °C for more than 200 hours. Effective electrical integration of the cooling system in a wireline downhole tool was also studied, and a power-width-modulation circuit was developed to adapt the downhole power source to a suitable voltage for the thermoelectric cooler. The implementation of the active cooling system was supported by the study of the thermal interaction between the downhole tool and the well environment, which was relevant to define the heat rejection conditions. Given the lack of information from the scientific literature, a downhole sensor that could experimentally quantify the heat transfer rate occurring between the tool and the wellbore was designed and tested. The concept was proved and the sensor calibrated in a laboratory flow loop. Average and maximum mismatches of 3% and 10%, respectively, were found between the measured and predicted heat transfer coefficients, showing good agreement between experimental results and model forecasts.

Resumé (Abstract in Danish)

Kabelbaserede brøndindgreb i højtemperatur brønde er en af de største udfordringer i olie- og gasindustrien i dag. De høje temperaturer nede i hullet, som kan nå op på 200 °C, reducerer levetiden for de elektriske komponenter i de kabelbaserede robot værktøjer indtil nedbrud. En mulig løsning på overophedningen af elektronikken er aktive kølesystemer, idet disse ville kunne holde de følsomme elektronikkomponenter ved tålelige temperaturer imens de opererer i varme omgivelser. Dette arbejde præsenterer design, konstruktion og test af en aktivt kølet down-hole elektroniksektion, som kan køle de kritiske elektriske komponenter til under 175 °C imens den opererer i omgivelser på 200 °C, som nede i en brønd. Efter en undersøgelse af forskellige køleteknikker og den termiske karakterisering af de elektriske komponenter der benyttes i brønden blev det besluttet at benytte termoelektriske kølere. Disse termoelektriske kølere implementerede et nyt koncept til varmestyringen i forhold til tidligere arbejder, således at det valgte design kombinerer både aktive og passive køleteknikker med det mål at opnå en effektiv varmestyrring, samtidig med at bibeholde værktøjets kompakthed og at undgå brugen af bevægelige dele. Det endelige design af prototypen som kunne holde den temperatur følsomme elektronik under 170 °C imens den opererede ved over 200 °C i mere end 200 timer blev udviklet med topologioptimering kombineret med en finite element model. Effektiv elektrisk integration af kølesystemet i down-hole værktøjet blev også studeret og et pulsbredde-modulationskredsløb blev udviklet for at tilpasse down-hole strømforsyningen til en passende spænding til den termoelektriske køler. Implementeringen af det aktive kølesystem blev understøttet af et studie af den termiske vekselvirkning imellem down-hole værktøjet og omgivelserne i brønden, hvilket var relevant for at kunne definere varmeafgivelsen. I mangel af information i den videnskabelige litteratur blev der designer og testet en down-hole sensor der kunne kvantificere varmeoverførselshastigheden imellem værktøjet og brøndboringen eksperimentelt. Konceptet blev bevist og sensoren kalibreret i en laboratorie flow løkke med god overensstemmelse imellem eksperimentelle resultater og modelforudsigelser. De gennemsnitlige og maksimale afvigelser imellem de målte og forudsagte varmeoverføringskoefficienter var på henholdsvis 3% og 10%.

Acknowledgments

In the first place, I would like to express my gratitude to Welltec A/S, the Technical University of Denmark, and the Danish Ministry of Technology and Innovation for funding this industrial Ph.D. program, and giving me the opportunity to work on such an inspiring and stimulating project. It has been three years of continuous challenges which helped me grow both personally and professionally. I had the chance to approach both the academic and the industrial worlds, and to connect with many people who contributed, directly or indirectly, to this work.

I would like to sincerely thank my DTU advisor Kurt Engelbrecht, who guided and supported me through these three years. Your contribution to my education and to this work has been fundamental and I am grateful for having learnt so much from your guidance. I have always appreciated our long and stimulating discussions, which often lasted longer than planned, and the balance with which you helped me face every challenge. I would also like to thank my Welltec advisor Anders Just Nørgaard who, despite the very busy agenda, has always found the time for a productive discussion. Thank you for supporting me with your knowledge about electronics and well interventions, which helped me to transform my ideas into something real and most importantly operational.

Thank you, Christian Bahl and Carsten Nesgaard, for co-supervising this industrial Ph.D. project and providing important and experienced contributions. I would also like to express my gratitude to Niels Falkenberg and Nini Pryds, who first conceived the idea behind this project, and without which this achievement would not have been possible.

I am also grateful for the collaboration with Ole Sigmund, Boyan Lazarov, Jan Haertel and the people from the DTU TopTen group. It has been a pleasure and an honor to work with some of the pioneers of the Topology Optimization method.

I would also like to express my gratitude to all of my colleagues from the DTU EFM section, particularly to Stefano Dall'Olio, Dan Enriksen, and Tian Lei for sharing enthusiastic and never-ending work on the 3D printer, to Jørgen Geyti for the professional support in the lab, to Simone Sanna for always being ready to lend a helping hand, and to Anita Voss for assisting me with a lot of documents and bureaucracy.

I would also like to thank my colleagues from Welltec D&E Electronics, D&E Mechanical, and D&E Completion for the support and the time spent together. In particular, my acknowledgements go to Peter Tønning Munch, Brian Thomsen, Jeppe Hinrichs, Ye Li, Bin Yang, Thomas Gundersen, Jack Kozlowski, Martin Gudtmann, Bo Lyu, Jesper Simonsen, and Jonathan Dam.

A special thanks also to other Ph.D. colleagues Roberto, Andrea C., Federico B., Fabrizio, Federico C., Kristina, Henrique and Andrea I. Thank you all for sharing your experience and for your support during these three years. A big thanks to all my old friends from Torino, especially Andrea, Christian, Carlotta, Stefano, and Federica for always being next to me despite the distance. Finally, I would like to express a special thanks to my parents, Danilo and Daniela, to my family and girlfriend, Alexi, for their love and for always supporting my decisions.

List of publications

Soprani S. , Engelbrecht K. , Nørgaard A. J. Active Cooling and Thermal Management of a Downhole Tool Electronics Section, *Proceedings of the 24th IIR International Congress of Refrigeration*, IIF-IIR, Yokohama, Japan (2015).

Soprani S. , Haertel J. H. K. , Lazarov B. S. , Sigmund O. , Engelbrecht, K. Topology Optimization of an Actively Cooled Electronics Section for Downhole Tools, *Proceedings of COMSOL Conference 2015*, Grenoble, France (2015).

Soprani S. , Haertel J. H. K. , Lazarov B. S. , Sigmund O. , Engelbrecht K. A Design Approach for Integrating Thermoelectric Devices Using Topology Optimization, *Applied Energy*, 176: 49–64 (2016). http://dx.doi.org/10.1016/j.apenergy.2016.05.024

Table of Contents

Abstract i

Resumé (Abstract in Danish) ii

Acknowledgments iii

List of publications v

Table of Contents vi

List of Figures ix

List of Tables xiv

Nomenclature xvi

1. Introduction 1

1.1 Background 1

1.2 Prior works 3

1.3 Welltec A/S and Well Tractor 7

1.4 Research objectives 8

2. Feasibility study 10

2.1 Thermal characterization approach of a wireline tool 10

2.2 Passive cooling 12

2.3 Electronics thermal protection and Dewar flask 14

2.4 Active cooling 15

2.4.1 Vapor compression cycle 18

2.4.2 Thermoelectric cooling 31

2.4.3 Reverse Brayton cycle 45

2.4.4 Magnetic cooling 53

2.4.5 Phase change materials (PCM) 59

2.5 Theoretical feasibility study conclusions 64

3. Thermal modeling of the well tractor electronics 67

3.1 Well tractor electronics section 67

3.2 Well tractor thermal model ... 70
3.3 Experimental results and model validation ... 73
3.4 Thermal characterization conclusions ... 78

4. TEC integration principle and *Prototype mark-1* ... 79

4.1 Thermal management principle ... 79
4.2 Description of Prototype mark-1 ... 81
4.3 Approximation of the cooling load ... 86
4.4 Selection of the assembly technique ... 88
4.5 Selection of the cooler ... 90
4.6 Tests at high temperature ... 92
4.7 Conclusions from the tests on *Prototype mark-1* ... 97

5. Optimization of the system and *Prototype mark-2* ... 98

5.1 Introduction ... 100
5.2 Description of the system ... 101
5.3 Finite element model ... 103
5.3.1 Governing equations ... 103
5.3.2 Boundary conditions ... 104
5.3.3 TEC model ... 105
5.3.4 Topology optimization and SIMP method ... 107
5.4 Results ... 109
5.4.1 Definition of the optimized design concepts ... 109
5.4.2 Comparison of the optimized designs ... 113
5.4.3 Design of the actively cooled electronics section ... 115
5.4.4 Model validation ... 118
5.5 Conclusions from the design and testing of *Prototype mark-2* (part 1) ... 123
5.6 Addendum ... 124
5.6.1 Electrical integration of the system ... 124
5.6.2 TEC degradation ... 132
5.7 Conclusions from the design and testing of *Prototype mark-2* (part 2) ... 134

6. Downhole heat transfer coefficient sensor ... 136

6.1 Background ... 137
6.2 Thermal interaction between tool and well environment ... 138
6.3 Design of the sensor ... 140

6.4 Experimental setup ... 142
6.4.1 Modeling ... 142
6.4.2 Construction ... 145
6.4.3 Working principle ... 148
6.4.4 Results ... 149
6.5 Conclusions from the design and testing of the sensor ... 156
7. Conclusions ... 157
7.1 Suggestions for future work ... 159
References ... 161
APPENDIX A ... 172
A.1 Paper published in the proceedings of the 24th International Conference of Refrigeration 2015. 172
A.2 Poster presented at the 24th International Conference of Refrigeration 2015 ... 181
A.3 Paper published in the proceedings of the COMSOL Conference Grenoble 2015 ... 183
A.4 Paper published in the journal Applied Energy ... 191
APPENDIX B ... 208
B.1 Technical drawings of the manufactured parts for Prototype mark-1 ... 208
B.2 Technical datasheets of the analyzed coolers, displayed in the order Cooler #1, Cooler #2, and Cooler #3 ... 212
APPENDIX C ... 229
C.1 Technical drawings of the manufactured parts for the proof-of-concept heat transfer coefficient sensor and the experimental setup ... 229

List of Figures

Figure 1.1 Schematic representation of a wireline well intervention setup from Jakaboski (2004). 2

Figure 1.2 3D CAD model (a) and photo (b – source www.welltec.com) of a wireline tool electronics section. 3

Figure 1.3 Illustration of a well tractor (source www.welltec.com). 8

Figure 2.1 1D electric analogy of the thermal path between the electronics and the well. 13

Figure 2.2 Schematic representation of a Dewar flask and its main components, from the supplier Mitcoind. (Source http://www.mitcoind.com/heatshield.htm) 14

Figure 2.3 Representation of the thermodynamic integration of an active cooling system into a downhole electronics section. 15

Figure 2.4 Vapor compression system components (left hand side) and ideal cycle on pressure vs. enthalpy diagram (right hand side). 18

Figure 2.5 Schematic of a vapor compression cooling cycle, with preheater. 19

Figure 2.6 Schematic of a two-stage cascade vapor compression cooler. 20

Figure 2.7 Ideal vapor compression cycle on Temperature vs. Entropy. 21

Figure 2.8 Cooling load vs. condenser extension. 25

Figure 2.9 Compressor: 9 cm long, compression ratio = 2.4. (Mongia et al. (2006)) © [2006] IEEE. 26

Figure 2.10 Microchannel evaporator: Cooling load 40W, edge = 5 cm. (Mongia et al. (2006)) © [2006] IEEE. 26

Figure 2.11 Condenser: rejected power around 70 W. 7 x 3 cm. (Mongia et al. (2006)) © [2006] IEEE. 27

Figure 2.12 (a) Integrated mesoscopic cooler circuit of Shannon and co-workers (see Table 2.3), (b) exploded view, and (c) compressor (from Barbosa et al. (2012)). 30

Figure 2.13 Schematic of a thermoelectric refrigerator, composed by a p-n junction (Bennett (1988)). 31

Figure 2.14 Reproduction of the dimensionless figure of merit for several semiconductors vs. temperature from Bennett (1988). 35

Figure 2.15 Thermoelectric unit cooling capacity vs. electric current. 37

Figure 2.16 Thermoelectric unit rejected heat vs. electric current. Optimal operating currents highlighted by a star. 37

Figure 2.17 Thermoelectric unit rejected heat vs. electric current. Optimal operating currents highlighted by a star. 38

Figure 2.18 Number of p-n junctions required to satisfy the cooling load at the optimal operating conditions. 39

Figure 2.19 Rejected heat vs. Cooling load. 39

Figure 2.20 Required electrical power vs. Cooling load. 40

Figure 2.21 Thermoelectric cooler dimensions vs. cooling load. 40

Figure 2.22 Figure of merit vs. Temperature. From Poudel et al. (2008). Reprinted with permission from AAAS. 42

Figure 2.23 Figure of merit vs. Temperature. $Bi_2Te_{2.7-x}Se_{0.3}S_x$ samples. Reproduced from Liu et al. (2012) with permission of The Royal Society of Chemistry 42

Figure 2.24 ΔT vs. Current, at different cooling loads.. 43

Figure 2.25 Voltage vs. Current. 44

Figure 2.26 Schematic of a reverse Brayton cooling cycle. 45

Figure 2.27 Representation of the ideal reverse Brayton cycle on the Temperature vs. Entropy diagram.... 46

Figure 2.28 COP vs. Compression ratio optimization for helium and xenon for operating between 175 °C and 200 °C. 49

Figure 2.29 Cooling load vs. high temperature heat exchanger extension. 51

Figure 2.30 Gd magnetocaloric effect vs. operating temperature, for different magnetic inductions (from Pecharsky et al. (2007)). 53

Figure 2.31 Active Magnetic Regenerative Refrigeration Cycle from Engelbrecht (2004). 54

Figure 2.32 Schematic of the Steyert's regenerative magnetic system. Reproduction from Bennett (1988). 55

Figure 2.33 Gadolinium magnetic entropy change (left) and adiabatic temperature span (right) trends with temperature. Reproduction from El-Hana Bouchekara et al. (2012). 56

Figure 2.34 Curie temperature and magnetic entropy for several ferromagnetic materials (reproduction from Bennett (1988)) 58

Figure 2.35 Length and mass of a PCM based cooling system vs. cooling load, at different downhole residence times. 61

Figure 2.36 Qualitative representation of the temperature trend in time of the electronics in case of passive cooling (dark blue curve), use of a flask (blue curve) and use of a flask + phase change materials (light blue line). 62

Figure 3.1 3D CAD model of the well tractor electronics section 68

Figure 3.2 Power dissipation trend with temperature for the PDs in the electronic groups 2 and 3 (left), and 4 (right). 71

Figure 3.3 Air gap profile between cartridge and housing. 72

Figure 3.4 Cartridge-housing thermal resistance vs. *z* coordinate. 72

Figure 3.5 Schematic representation of the experimental setup used for the thermal characterization of the well tractor electronics. 73

Figure 3.6 Illustration of the placement of the thermocouples within the tool. 74

Figure 3.7 Simulated temperature profile of the well tractor electronics for the validation of the model at ~120 °C 75

Figure 3.8 Simulated temperature profile of the well tractor electronics for the validation of the model at ~150 °C........ 75

Figure 3.9 Simulated temperature profile of the well tractor electronics for the validation of the model at ~170 °C........ 76

Figure 3.10 Comparison between experimental and modeling temperatures of the electronics. Average operating temperature equal of 121.8 °C........ 76

Figure 3.11 Comparison between experimental and modeling temperatures of the electronics. Average operating temperature of 150.7 °C. 77

Figure 3.12 Comparison between experimental and modeling temperatures of the electronics. Average operating temperature of 166.2 °C. 77

Figure 4.1 Well tractor electronic groups 2 and 3. The analogue structure is shown........ 80

Figure 4.2 Thermal integration of the TEC and thermal management principle of the electronic groups 2 and 3. Components involved in the system (a) and main design parameters (b). 81

Figure 4.3 3D model of *Prototype mark-1*. 83

Figure 4.4 Illustration of the thermocouple placements within *Prototype mark-1*........ 84

Figure 4.5 Implementation of the experimental setup. 84

Figure 4.6 Schematic of the experimental setup used for testing *Prototype mark-1*........ 86

Figure 4.7 Estimated cooling load vs. temperature span across the cooler, with linear fit of the experimental data. 87

Figure 4.8 Temperature span across the cooler ΔT_{cooler} vs. coolers feed power for different installation techniques........ 89

Figure 4.9 Temperature span across the cooler ΔT_{cooler} vs. coolers feed power for different coolers in size and cooling action........ 90

Figure 4.10 Estimated COP (left *y*-axis) and estimated cooling load (right y-axis) vs. temperature span across the cooler for different coolers in size and cooling action........ 91

Figure 4.11 Temperature span across the cooler ΔT_{cooler} vs. coolers feed power, at different oven temperatures, for *Prototype mark-1*. 2 x *Cooler #1* were assembled in the tool with thermal grease........ 92

Figure 4.12 Temperature of the HTS electronics vs. coolers feed current, at different oven temperatures, for *Prototype mark-1*. 2 x *Cooler #1* were assembled in the tool with thermal grease........ 93

Figure 4.13 Temperature of the hot plates vs. coolers feed current, at different oven temperatures, for *Prototype mark-1*. 2 x *Cooler #1* were assembled in the tool with thermal grease........ 94

Figure 4.14 Representation of $\Delta T_{HotPlate}$ (red bars) and ΔT_{HTS} (blue bars), at the operating conditions that minimized the HTS electronics temperature, at different oven temperatures T_{oven}. 95

Figure 5.1 Representation of the axial section of the downhole tool (1a, left side); the domain of the optimizable chassis is represented as partially transparent and colored in light blue. Particular of the TEC device (1b, right side). 101

Figure 5.2 Illustration of the simplification process for the TEC model. 105

Figure 5.3 Density field (left) and resulting temperature distribution (right) of the optimized design concepts. 112

Figure 5.4 *R* vs. well fluid convection coefficient, for different TEC feed currents. 113

Figure 5.5 HTS electronics temperature vs. Convection coefficient for three different systems, optimized for h = 10 Wm^{-2}K^{-1} and I_{feed} = 1, 2, 3 A (5a, left side). HTS electronics temperature vs. Convection coefficient for two systems optimized for h = 10, 25 Wm^{-2}K^{-1} and I_{feed} = 4 A (5b, right side). 114

Figure 5.6 HTS electronics temperature vs. TEC feed current of four different designs, optimized for I_{feed} = 1, 2, 3 and 4 A, and h = 50 Wm^{-2}K^{-1} (6a, left side) and 100 Wm^{-2}K^{-1} (6b, right side). 115

Figure 5.7 Illustration of the longitudinal section of the final design. 116

Figure 5.8 Characteristic curve of the finally designed TEC integrated system. 118

Figure 5.9 Illustration of the manufactured components.. 118

Figure 5.10 Schematic of the experimental setup. 119

Figure 5.11 Comparison between experimental data and model prediction.. 120

Figure 5.12 Comparison between experimental and modelling temperatures vs. TEC feed current, at different oven temperatures. 122

Figure 5.13 Experimental trend of ΔT_{cooler} and of HTS electronics temperature vs. feed current and feed voltage. 124

Figure 5.14 Schematic of the circuit to implement the PWM of the 15 V power source. 125

Figure 5.15 Picture of the circuit for modulating the voltage source at 15 V. 126

Figure 5.16 Screen capture from the oscilloscope used for the calibration of the test setup. 126

Figure 5.17 Schematic from LT Spice of the PWM circuit with L-C filter. 128

Figure 5.18 Simulated voltage (green curve – left *y* axis) and current across the cooler (red curve – right *y* axis) until steady state with LT Spice. 128

Figure 5.19 Picture of the PWM system with the integrated L-C filter. Two inductors, 1.94mH each, were connected in parallel to obtain an inductance of 970 μH which is suitable for the application 129

Figure 5.20 Temperature difference across the cooler vs. feed power for the three different TEC feeding solutions: continuous voltage, PWM voltage, and filtered PWM voltage. 130

Figure 5.21 HTS electronics temperature (left) and hot plate temperature (right) vs. cooler feed current for the three different TEC feeding solutions: continuous voltage, PWM voltage, and filtered PWM voltage. 130

Figure 5.22 Results from the degradation test, carried out at 200 °C in the higher convection oven. Trend in time of ΔT_{HTS}, V_{feed}, and ΔT_{HP}. 132

Figure 6.1 Schematic of the ideal interaction between the downhole tool string and the well fluid flow, with velocity *u* and temperature *T*. 139

Figure 6.2 Illustration of the decreasing trend of the local Nusselt number for a simultaneously developing flow in a circular pipe (left), and for a thermally developing flow in an annular geometry (right). 140

Figure 6.3 3D CAD model of the sensor casing with dissipating element (a, b, and c) and section-view of the sensor integrated in a downhole tool (d) 142

Figure 6.4 3D CAD model of the sensor modified for integration in the experimental setup. 143

Figure 6.5 Schematic representation of the thermally developing flow in the sensor section. 144

Figure 6.6 Predicted convection coefficient and flow rate vs. Reynolds number, from Eq. 6.6 and 6.11 145

Figure 6.7 Schematic of the flow loop used for the experimental measurements on the heat transfer coefficient sensor. 145

Figure 6.8 Pictures of the experimental setup: main auxiliary components (a), inlet to the test section (b), main test section (c), and outlet of the test section with DAQ system (d) 147

Figure 6.9 Pictures of the sensor section (a), and of the disassembled sensor (b). 147

Figure 6.10 Implemented PID control for regulating the temperature span between sensor (T_{SENSOR}) and convective fluid (T_{INLET}) to the desired difference $\Delta T_{SetPoint}$. 148

Figure 6.11 LabVIEW interface for the testing and calibration of the sensor. 149

Figure 6.12 Heat transfer coefficient vs. fluid flow rate, without filtering of the heat losses. 150

Figure 6.13 Heat losses from to ambient vs. temperature difference between sensor and ambient. 151

Figure 6.14 Heat transfer coefficient vs. fluid flow rate, with no contribution of heat losses to ambient.. 151

Figure 6.15 Schematic representation of the thermal interaction of the sensor with the setup and the surrounding. 152

Figure 6.16 Heat transfer coefficient vs. fluid flow rate, with the canceled contribution of heat losses. The model prediction is compared to the experimental data points for different $\Delta T_{SetPoint}$. 153

Figure 6.17 Representation of two system transients due to a change in the flow rate from 3 to 2.5 L/min (left) and from 2 to 1.5 L/min. 155

List of Tables

Table 1.1 Design constraints for the integration of the cooling system. 9

Table 2.1 Candidate refrigeration processes. 17

Table 2.2 Resume of the vapor compression cooling cycle; cooling load equal to 50 W. 24

Table 2.3 State of the art of the compact vapor compression cooling cycles from Barbosa et al. (2012) (part 1). 28

Table 2.4 State of the art of the compact vapor compression cooling cycles from Barbosa et al. (2012) (part 2). 29

Table 2.5 Other parameters that characterize the TE unit. 41

Table 2.6 Specifications for TE-127-1.0-0.8 from TE Technology. 43

Table 2.7 Resume of the reverse Brayton cooling cycle with He; cooling load equal to 50 W. 50

Table 2.8 Summary of the regenerative magnetic cooling cycle processes, referring to Figure 2.31. 54

Table 2.9 Curie temperatures for different ferromagnetic materials (source: www.hyperphysics.phy-astr.gsu.edu/hbase/tables/curie) 58

Table 2.10 PCM material properties (source: www.pcmproducts.net). 60

Table 2.11 Feasibility evaluation matrix for the analyzed cooling technologies. 64

Table 2.12 Vapor compression cycles. 64

Table 2.13 Thermoelectric cooling. 65

Table 2.14 Phase-change materials. 65

Table 3.1 Main components of the well tractor electronics section and their geometrical features. 69

Table 3.2 Characterization of the well tractor electronic components. 70

Table 3.3 Experimental temperatures recorded at steady state during the tests on the well tractor electronics. 78

Table 4.1 List of the components used in *Prototype mark-1* and their features. 82

Table 4.2 Summary of the experimental data from the tests of *Prototype mark-1* at high temperature. 96

Table 5.1 List of the components with their dimensions and properties. 103

Table 5.2 Geometric features of the modelled thermoelectric cooler. 107

Table 5.3 Comparison between the performance of the final design (Design) and the optimized systems (Opt). 117

Table 5.4 Temperatures and parameters characterizing both the experimental procedure and the model validation. 120

Table 5.5 Summary of the tests in the higher convection oven at 200 °C. 131

Table 6.1 Summary of the DAQ system. 148

Table 6.2 Summary of the experimental results for the sensor calibration from the tests at $\Delta T_{SetPoint}$ = 5 °C. 154

Table 6.3 Summary of the experimental results for the sensor calibration from the tests at $\Delta T_{SetPoint}$ = 10 °C. 154

Nomenclature

A	Surface area (m^2)
c	specific heat capacity (J/kg-K)
COP	Coefficient of Performance
DAQ	data acquisition
DC	duty cycle
D_h	hydraulic diameter
f	friction coefficient
h	heat transfer coefficient
h_i	enthalpy at the state i (J/kg)
HT	high temperature
$HTNS$	high temperature non-sensitive
HTS	high temperature sensitive
I	electric current (A)
I.D.	Inner diameter
J	electric current density (A/m^2)
k	Thermal conductivity (W/m-K)
L	length (m)
m	mass (kg)
max	maximum
min	minimum
$\mathbf{n}$	surface normal vector
Nu	Nusselt number
O.D.	Outer diameter
p	penalization coefficient
P	power (W)
PCB	printed circuit board
PCM	phase change material
PD	power device
Pe	Peclet number
p_i	pressure at the state i (Pa)
Pr	Prandtl number
PWM	power width modulation
Q	heat flux (W)
R	electrical resistance (Ω)
Re	Reynolds number
R_{th}	thermal resistance (K/W)
s_i	entropy at the state i (J/kg-K)
T	temperature (K)
t	time (s)
TC	thermocouple

TEC	thermoelectric cooler
TEM	thermoelectric module
TIM	thermal interface material
U	thermal transmittance (W/m^2K)
u, v	velocity (m/s)
V	voltage (V)
V_f	volume flow rate (m^3/s)
W	electric power (W)
Z	figure of merit
ZT	dimensionless figure of merit
β	filter steepness parameter
γ , S	Seebeck coefficient (V/K)
η	projection threshold
η_{is}	isentropic efficiency
μ	dynamic viscosity (Pa·s)
ρ	density (kg/m^3)
ρ_{design}	topology optimization design variable
σ	electrical conductivity (S/m)

Subscripts

x	local
m	mean
avg	average
conv	convective
ext	external
int	internal
C	cold
H	hot
c	compression
e	expansion
in	input
cool	cooling
opt	optimal
feed	referred to the electrical feed conditions
ad	adiabatic
lat	latent
ext	external conditions
oven	oven conditions
amb	ambient conditions
exp	experimental
HP	referred to the hot plate
ins	thermal insulation
Al	referred to aluminum
HTS	referred to the high temperature-sensitive electronics
HTNS	referred to the high temperature-non-sensitive electronics

1. Introduction

The worldwide growing energy demand has led the oil and gas industry to drill wells in increasingly harsher reservoirs and downhole environments, increasing the technological challenge related to their construction, maintenance and production. Well interventions in high-temperature (HT) wells, where the temperature can range between 150 °C and 200 °C, represent one of today's biggest challenges for the oil and gas sector. The high downhole temperatures and thermal stresses, to which the intervention tools are exposed, increase the risk of failure and require high temperature tolerant components. The electronic components employed in the well intervention tools (sensors, power converters, data acquisition systems) are particularly sensitive to the high temperatures and, when the maximum operating temperature is exceeded, their life can be drastically reduced until failure. This chapter provides an introduction to well interventions, focusing on high temperature wells and on the challenges related to the electronics overheating that occurs in well intervention tools. A selection of thermal management techniques for downhole electronics is presented and active cooling systems are analyzed as a possible solution.

1.1 Background

Well interventions can be defined as remedial operations that are performed on producing wells with the intention of restoring or increasing production. They can be required in case of reduced production capacity, flow restrictions, sand production, mechanical failure, or to access additional reservoir areas. Typical downhole interventions include the monitoring of the well conditions, as well as component installation (e.g. of valves or pipes), drilling of new well branches, cleaning, and repairing (Sandeep et al. (2003)). Different downhole tools can be employed to carry out the mentioned operations, and several intervention techniques can be adopted in order to deliver the tools down the wellbore.

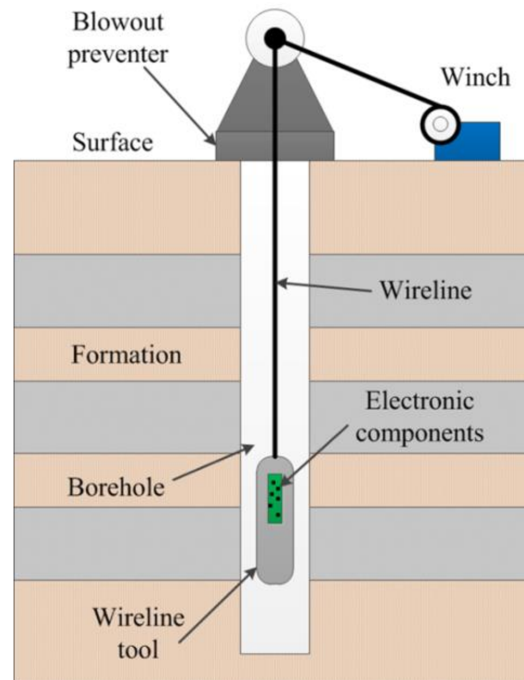

Figure 1.1 Schematic representation of a wireline well intervention setup from Jakaboski (2004).

The *wireline* technique (Figure 1.1) is currently one of the most competitive approaches, as it does not require the use of a conventional workover rig, comprising of a derrick, a rotary table and heavy machinery, and is therefore logistically flexible. Furthermore, it does not require "killing the well" (i.e. counterbalancing the downhole well pressure by injecting fluid in the wellbore), which creates the risk of damaging the reservoir. This becomes an even more significant advantage in the case of subsea and offshore interventions. The wireline technique involves running and pulling tools into and out of the well, by the use of a small diameter solid or braided wire mounted on a powered reel at the surface. This cable is an electric conductor and delivers the feed power to the downhole tools from the surface. Every wireline tool has, therefore, a section that contains electronic components that remotely control the device, transform the feed power or store logging data. Usually, electronic components are installed on a metallic cartridge (also called chassis) that is slid into a cylindrical housing, which in turn protects the inner components from the harsh environment and seals them from the well fluid (Figure 1.2).

The temperature rating of the electronics significantly limits the applicability of this intervention technique and represents a critical aspect for well interventions in HT wells. HT electronic components can be very expensive, much less compact than low-temperature ones, and do not necessarily fit the strict dimensional constraints related to well intervention tools.

Facing an increasing demand of interventions in high temperature wells, active cooling systems and innovative thermal management strategies have been considered as a possible solution to the electronics overheating, and investigated for integration into downhole interventions tools. An active cooling system could maintain the temperature sensitive electronics to tolerable temperatures, while the tool is operating in hotter environments.

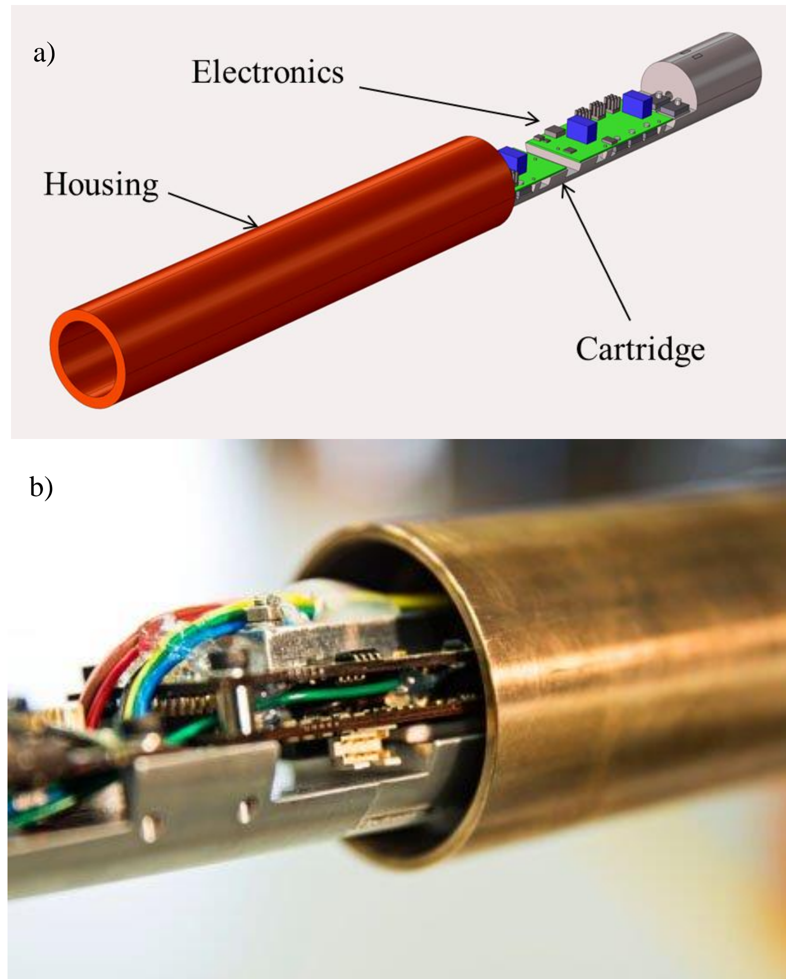

Figure 1.2 3D CAD model (a) and photo (b – source www.welltec.com) of a wireline tool electronics section.

1.2 Prior works

Active cooling and innovative thermal management of downhole electronics has progressively become a dynamic research topic in the oil and gas industry since the 1980s. Bennett (1988) first published a detailed feasibility study regarding active cooling solutions for downhole instrumentation. Eight cooling technologies were analyzed and characterized through thermodynamic and heat transfer equations. Fuel cells were also considered as a potential technology that could be integrated into a downhole tool. The analyzed cooling system aimed at working in a 320 °C environment, while keeping the electronics at maximum 150 °C, with a cooling load of 8 W. Furthermore, the power input was constrained to a maximum 22 W and the COP to a minimum 0.363. Thermo-acoustic refrigeration was chosen as the most suitable cooling technique because of the high COP and the absence of moving parts. Vapor compression and Brayton cycles (with turbine) were also found to be efficient, but required more maintenance and were assessed as more likely to fail due to the moving components. Thermoelectric cooling, absorption cooling, and the Joule-Thompson cycle were discarded in first place because of the low COP, as well as magneto- and electro-caloric devices due to space constraints. No information about the design or the performance of the system is given in the report. The thermo-acoustic downhole refrigerator was then protected by a patent in 1992 (US Pat. No. 5165243), the

description of which revealed more details about the system. An acoustic engine, activated by a heater, generated an acoustic wave in a tube (resonator) filled with helium. The resonator was designed in such a way that a stationary acoustic wave with certain wavelength characteristics was obtained. A stack of fiberglass plates was strategically positioned in the resonator. The helium reacted to the acoustic waves by compressing (heating) and expanding (cooling) in between the fiberglass plates, and created a temperature gradient across the stack between a hot and a cold end. Two heat pipe systems thermally connected the cold end to the electronics and the hot end to the borehole. Two Dewar flask were used to minimize the cooling load. It was claimed the system is able to maintain the electronics at a temperature of 181 °C, absorbing a load of 8 W in a 300 °C well environment, and with a COP equal to 0.18.

Subsequently, Flores (1996) published another work on active cooling systems for wireline oil-exploration tools, where a feasibility study was carried out and a cooling technology was chosen according to its performance, design complexity, maintenance necessity and size. Specific design criteria were reported: the system had to operate up to 200 °C borehole temperature, maintain the sensitive electronics below 125 °C, and absorb a cooling load of 80 W. The tool had to satisfy these criteria for a downhole residence time of a maximum 10 hours and a feed power available of 500 W. Flores was the first to introduce a reference boundary condition for the heat transfer between the tool and the well, assuming a heat transfer coefficient along the housing outer surface of 100 W/m^{2}K. The theoretical study led to the choice of a "once-through" vapor compression cycle, an evaporative cooling system that consists of a cold tank, in thermal contact with the temperature-sensitive electronics, a compressor, and a hot tank, in thermal contact with the well environment. The opportunely pressurized water contained in the cold tank evaporates at the desired temperature and absorbs the cooling load from the electronics; the vapor is compressed and stored in the hot tank, where it condenses again reducing the occupied volume. The electronics and the cold tank are enclosed in a Dewar flask, to reduce the heat leakages from the hot surrounding. A prototype was built and tested. Test results showed a robust performance of the tool, which was able to continuously work in a 200 °C environment and maintain the temperature-sensitive electronics below 122 °C and 114 °C for cooling loads of 50 W and 30 W, respectively. The hot tank was maintained at 204 °C and the COP was estimated around 1. The heat transfer coefficient, between the tool housing and the oven where the tests were carried out, was calculated to be 34 W/m^{2}K, significantly below the one set as a design criterion. One of the critical points highlighted by the author is the choice of the micro-compressor (flow rates in the order of magnitude of 3e-5 m^3/s) and of the motor, which must work in a 200 °C environment. A reciprocating micro-compressor, including a lubrication system and mechanical connections, was designed and built in cast iron for the application. This component significantly contributed to the increase of the tool production cost, which is reported by the author to be around 12 000 USD, 7 000 of which are for the motor. The invention was consequently patented in 1996 (US Pat. No. 5701751 A).

Later, Jakaboski (2004) proposed a different solution where the temperature sensitive electronics were enclosed in a Dewar flask next to a tank of phase change material (PCM). The electronics were thermally interfaced to the PCM thanks to a metallic cold plate and a fluid loop, driven by a small pump. A helical piping system distributed uniformly the excessive heat from the electronics into the PCM bed. The design constrains stated the system had to operate for 24 hours in a 200 °C environment, while maintaining the sensitive electronics below 100 °C, and with a cooling load of 18 W. The cooling system needed to fit a Ø 3 in Dewar flask. The chosen PCM had a transition point, from solid to liquid, of 70 °C and a latent heat density of 311 MJ/m^3. The author highlights how the choice of the material strongly depended on its large latent heat density and relatively high thermal conductivity (18.8 W/m-K), which helps to have a small temperature gradient across the PCM bed and a uniform phase transition. A prototype was built and tested.

The design criteria were fulfilled and the electronics could be maintained below 100 °C for 25 hours in an oven at 200 °C.

Sinha (2010) proposed a thermoelectric adsorption cycle with two stages. The two adsorption beds (zeolites) were connected to an evaporator, in thermal contact with the load, and a condenser, while check valves ensured a proper flow direction. The two beds were heated up and cooled down alternately to respectively release and absorb the coolant (water) and to perform the cooling cycle. A thermoelectric module (TEM) was used for this purpose. The TEM had one plate connected to each of the beds and was fed by an AC square current with low frequency (in the order of magnitude of 0.02-0.03 Hz) so it could pump the heat alternately from one bed to the other. A setup for the proof-of-concept was built and tested, without integration into a downhole tool. A thermal bath maintained the condenser temperature at 190 °C, while the evaporator was cooled to 150 °C with a cooling load of 6 W. The same author presented in Sinha et al. (2011) an alternative solution in which a thermoelectric cooler alone was used to refrigerate some sensitive electronics. The hot side of the thermoelectric cooler rejected the excess heat to the well fluid through a finned copper rod in direct contact with it. The cold plate of the cooler, instead, connected to a finned copper rod immersed into a water tank. A flow loop, powered by a small pump, recirculated the cold water from the tank to a cold plate in contact with the temperature-sensitive electronics. All the components on the cold side of the system were enclosed in a Dewar flask to reduce the cooling load. A prototype was built and tests were carried out in an oven at 140 °C with a cooling load varying from 0 to 8 W. Test results showed the electronics reached steady state at ~140 °C after 8 hours with 8 W of load, ~125 °C after 12 hours with 6 W of load, ~120 °C after 15 hours with 4 W of load, ~110 °C after 15 hours with 2 W of load, and ~100 °C after 15 hours without load. The COP is reported varying from 0.1, at minimum load, to 0.75, for the case with a load of 8 W.

Pennewitz et al. (2012) investigated the suitability of sorbents to operate in harsh conditions and to absorb the vapors coming from an evaporative cooling process. The phase transition from liquid to vapor has a much higher enthalpy change per unit of volume than from solid to liquid. Nevertheless the density of vapors is much lower than for liquids, which creates the problem of handling the resulting vapor downhole. It cannot even be vented off the tool, as the wellbore can reach pressures higher than 1 000 bar. Flores (1996) used the compressor to increase the vapor pressure and make it condense at the wellbore temperature. Sorbents could be a good alternative to replace this expensive component and to avoid moving parts. They would, in fact, adsorb the evaporated fluid, significantly reducing the amount of space required for storage. Pennewitz performs some tests 230 °C with two different types of sorbents and water vapor, which would be suitable for the downhole application. The test results showed the storage capacity of the sorbents is higher if they operate in vacuum, compared to air, and the sorption speed of the desiccant bed needs to be equal or higher than the evaporation speed, which depends in turn on the design criteria and the operating temperatures.

Verma et al. (2012) studied the feasibility of reverse Brayton and vapor compression cycles for active cooling of downhole electronics. Comparing the simulation results for the two systems, the authors highlighted once more the more efficient performance of the vapor compression cycle and chose it for implementation in a wireline formation tester tool. The tool was designed with a triangular chassis divided into four electronics sections, each of which dissipated a maximum of 64 W. The total power dissipation of the tool could range from 30 W to 256 W. The chassis was then inserted into a triangular vacuum flask. In order to prove the concept, the main components of the system were run at room temperature, while the tool was wrapped in a 2.5 kW heating jacket that simulated the high temperature well environment. Instead of a compressor, a pump and a boiler were used to produce water vapor at the desired high temperature and pressure. The vapor was then expanded through an expansion valve and circulated through some channels in

the metallic chassis to absorb the cooling load from the electronics. The wet vapor at the tool outlet was then fully condensed and recirculated through the pump to re-start the cycle. The cooling system, fed with a flow rate of 8 mL/min, was able to maintain the electronics below 150 °C while operating at a cooling load of 160 W and with an outer housing temperature of 200 °C. Tests at 250 °C, with the same flow rate, showed the system could still maintain the electronics below 150 °C with a cooling load of 70 W.

Several thermal management solutions for downhole tool electronics can also be found in patents. The design criteria and the performance of the described devices are usually not publically available, though. A brief summary of the patents is reported below.

Several patents about downhole electronics cooling through thermoelectric modules can be found: US Pat. No. 6134892 , US Pat. No. 5931000, US Pat. No. 5730217, US Pat. No. 5720342, US Pat. No. 5547028, US Pat. No. 4375157. Slightly different setups are presented in these works, but some common features can be found. The cold plate of the Peltier modules is usually connected to the electronics through soft thermally conductive pads, adhesive thermal interface materials or heat pipe systems. The same techniques are used to thermally connect the hot plate of the modules to the borehole. Thermal grease is used to reduce contact thermal resistances. Vacuum flasks and thermally insulating material are used to reduce the cooling load. Spring systems are used to guarantee a good thermal contact between the electronics cartridge and the housing, and an effective thermal path for the excessive heat to be rejected to the wellbore.

Downhole cooling systems adopting the vapor compression technology have also been patented. US Pat. No. 5701751A, which has been previously illustrated, described a "once through" vapor compression solution. The system described in US Pat. No. 5265677 adopts a similar solution to US Pat. No. 5701751A, but uses a piston and a secondary tank filled with the well fluid to pressurize the refrigerant tank. A valve opens and closes, according to a temperature sensor, to expand and regulate the flow from the refrigerant tank, to the evaporator, in thermal contact with the electronics. The exhaust vapor is then collected and stored in a low-pressure dump tank. The integration of a typical vapor compression cycle, comprised of an evaporator, compressor, condenser, and expansion valve is described in US Pat. No. 20120125614A1.

A sorption cooling system was patented in US Pat. No. 6341498. A water reservoir is pressurized and put in close contact with the electronics, so the dissipated heat can be absorbed by the water evaporation process. A valve regulates the pressure in the evaporator and let the exhaust vapor collect in a desiccant bed where it is stored at elevated temperatures. The electronics and the water tank are thermally protected from the wellbore through a vacuum flask lined with phase change material. The desiccant bed is located in a housing, outside the flask, in good thermal contact with the well.

Some innovative thermal protection techniques were also patented. US Pat. No. 6336408 describes a system were an eutectic material (91% tin, 9% zinc), with a phase transition solid-to-liquid temperature at 199 °C, is in thermal contact with some temperature-sensitive electronics in a Dewar flask. The patent claims the system can work in a 260 °C environment for 100 hours, while maintaining the electronics below 200 °C. US Pat. No. 6220346, instead, reports a new thermally insulating pressure housing with smaller heat losses than a vacuum flask. The system is composed of two concentric hollow cylinders, maintained in place by magnetic levitation and separated by vacuum. In this way the thermally conductive paths which exist in a typical vacuum flask are eliminated. Another type of thermally insulating pressure housing is reported in US Pat. No. 5715895. A dual walled pipe encloses the sensitive electronics and is filled with low thermal conductivity granules in the annulus. High pressure inert gas fills the interstitial spaces. The gas pressure

increases with the wellbore temperature and therefore with depth, counterbalancing the increasing well pressure.

Passive cooling techniques for downhole instrumentations have also been patented. US Pat. No. 5554897 describes a convection cooling system for downhole motors based on natural convection. The motor housing is composed of two communicating annular chambers filled with heat transfer fluid. The heat dissipated by the motor is transferred to the heat transfer fluid in the inner cavity; the hotter fluid moves through some strategically designed ports towards the outer chamber by natural convection and is cooled down by lapping the outer chamber walls that are in direct contact with the well fluid. In this case the natural convection enhances the heat rejection to the well. A different approach is presented by US Pat. No. 4407136, where the electronics pressure housing is also divided in an inner and outer chamber. The inner chamber encloses a pump a piping system with small holes that spray liquid refrigerant onto coated electronics and printed circuit boards. The system is pressurized so the refrigerant evaporates absorbing the cooling load at the desired temperature. The vapor is then collected in the outer chamber where exchanges heat with the wellbore and condenses again.

US Pat. No. 4248298 describes another approach, where a heat transfer fluid is pumped into a heat exchanger, in thermal contact with the downhole tool electronics, from the surface. A flexible cabling/piping system, similar to the wireline, connects the tool to the surface instrumentation and provides both electricity and cooling to the tool. The refrigerant is pumped downhole at high pressure and expanded through an expansion valve. A vapor-liquid mixture absorbs the electronics load and turns into exhaust vapor, which is then collected and sent back to the surface through a vacuum pump. The patent claims this technique is able to absorb a cooling load of 44 W an maintain the electronics below 190 °C, while operating in a well bore with temperatures between 250 °C and 375 °C.

Many different solutions have been adopted in the past to provide thermal management for downhole electronics. It can be noticed that the optimal thermal management solution can vary from case to case, depending on the type of electronics, the cooling load, the dimensional constraints, the power availability, the required operating time, and the operating temperature, which all together define the design constraints.

1.3 Welltec A/S and Well Tractor

Welltec A/S is a Danish company, headquartered in Allerød, Denmark, and has co-funded this industrial Ph.D. project in partnership with DTU. Welltec is an international provider of well intervention and completion solutions for the oil and gas industry. Unlike in the automotive, military, and aerospace industries, well intervention companies sell their services to their clients, not their hardware. Welltec, in fact, produces their own robotic tools, trains their personnel on their use, and then sells the entire intervention service to the customer. Welltec’s services range from well logging to perforation, from well cleaning to valve manipulation, from pipe cutting to fishing.

Welltec was founded in 1994 by Jørgen Hallundbæk, current CEO of the company, who first conceived the idea of *well tractor*, which is also the flagship of the company. The well tractor is a wireline robotic tool that is able to convey other intervention devices down the wellbore without using large and expensive equipment like oil rigs. This robotic tool (Figure 1.3) relies on a wheel system, powered from the surface, which is able to drive the tool through the wellbore environment while being remotely controlled by an operator. Additional intervention devices can be mechanically connected to the well tractor, and arranged in a “tool

string", in such a way they can be pulled and driven through the borehole to where the intervention is required. This new technology allowed for the first time to access horizontal well branches and deviated wells (where the inclination of the borehole exceeds 60°) with the wireline technique. As part of the wireline tools, the well tractor contains electronic components and is therefore restricted from operating in high temperature wells by the electronics temperature limitations.

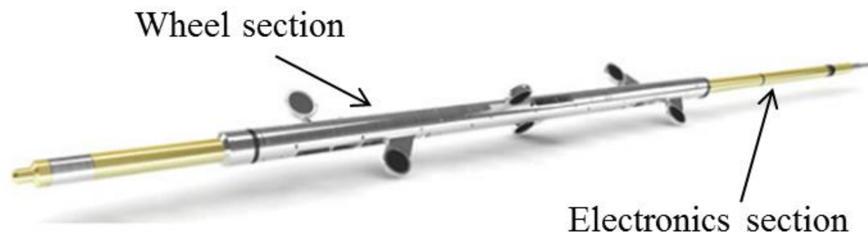

Figure 1.3 Illustration of a well tractor (source www.welltec.com).

1.4 Research objectives

The primary goal of this work is to study, design and implement an active cooling system that can extend the maximum operating temperature of the Welltec's well tractor electronics from 170 °C to 200 °C. The cooling system must fit the tool's dimensions and supply cooling for at least 12 hours of downhole operation. Furthermore, the cooling system needs to be thermally, electrically and mechanically integrated into the system, which means it must be able to work at the design temperature, provide the desired cooling capacity, be fed by the power sources available downhole, and has to withstand the stresses to which the tool is subjected.

While the outer diameter of the well tractor must be maintained in order to fit the same well casing dimensions, there is some freedom in modifying the length of the actively cooled electronics unit. The majority of the works and patents described in Section 1.2 add to the original tool a supplementary unit, where the cooling system is mounted. In this work, the length of the tool is considered very important and the increase in length should be minimized or avoided completely. The compactness of downhole tools is, in fact, a very important parameter for the oil and gas industry. Smaller tools can be more easily conveyed downhole, can fit a larger variety of well casing dimensions, and are more suitable to be driven past restrictions and deviations of the well structure. A lower weight also helps to have a faster logistics and shorter downhole residence times.

No constraints are set on the amount of power that is available downhole, at 15 V. Therefore no COP limitations restrict the choice of the cooling technology, for what concerns feeding the system. However, a low COP could lead to a high heat flux to be rejected to the well environment, which needs to be taken into consideration when evaluating the heat transfer surfaces available and the downhole heat transfer interactions between the tool and the wellbore.

Another parameter which is very important in the oil and gas service industry is the reliability of the well intervention tools. When operating downhole, they can be exposed to extreme and harsh conditions and the risk of failure is an important factor that needs to be minimized. Misruns and failures cause delays in the optimization of the well production, causing in turn financial losses to the customer. For this reason, several tests and strict quality inspections are carried out to assess whether a new tool fulfills the reliability and quality standards. The complexity and the maintenance requirements of the cooling system should be therefore minimized in order to maintain the current reliability of the well tractor.

The design constraints are summarized in Table 1.1.

Table 1.1 Design constraints for the integration of the cooling system.

1) Tool dimensions	I.D. 62 mm
	Length ~970 mm (minimize)
2) Maximum operating temperature	200 °C
3) Maximum electronics temperature	175 °C
4) Downhole power availability	DC @ 15 V
5) Well fluids	Water, oil, gas
6) Electronics power dissipation rate	TBD
7) Downhole residence time	≥ 12 hours
8) Maintenance and complexity	Minimized

Several design constraints need to be taken into account. A feasibility study has to be carried out to define which technologies can fulfill the design criteria and which one is the most suitable. A review of the well tractor electronic components must also be done. HT-sensitive components need to be individuated and the eventual substitution with the corresponding high temperature versions evaluated. The power dissipation of the electronics has to be estimated and the existing well tractor electronics thermally characterized.

Once the power dissipation is defined, a thermal management strategy is required to integrate the cooling system into the tool. It is very important to consider that the thermal design of the actively cooled electronics section affects the cooling load that the refrigeration system needs to absorb. The thermal connections between the electronics and the cooling system, as well as between the cooling system and the wellbore, need to be opportunely designed and the corresponding thermal resistances minimized. The cooling load also needs to be minimized by an opportune use of thermal insulating techniques. Analytical and finite-element modeling can support this design process.

Once a satisfactory design is reached, it has to be implemented into a prototype and tested in the laboratory. A suitable electric integration of the cooling system needs to be provided as well. The performance of the system needs to be analyzed and optimal working settings must be individuated. Advanced optimization techniques could be used to investigate possible improvements of the setup and of the components.

The operation of the cooling system at high temperature could cause degradation of the employed components. For this reason it is also important to investigate how the high temperatures can affect the performance of the system over time.

All these mentioned research approaches and objectives are going to be addressed in the next chapters of this thesis.

2. Feasibility study

This chapter contains an overview of the main thermal management strategies for downhole electronics, with a particular focus on active cooling systems. After an introduction describing the state of the art of thermal management of downhole electronics, represented by the use of passive cooling techniques and vacuum flasks, a detailed analysis of several cooling technologies is presented. Each cooling technology is characterized in terms of performance, compactness and complexity. Theoretical models and data from the literature are used for this purpose. The theoretical feasibility study aims to give an evaluation of the strengths and weaknesses of each system, in relation to their possible integration in the well tractor electronics section.

2.1 Thermal characterization approach of a wireline tool

This section briefly illustrates the theoretical correlations that drive the heat transfer process, with a particular attention to the calculation of thermal resistances for flat layers, convective films and cylindrical tubes.

The equation that correlates the transferred heat flux with the required heat transfer area is reported below; it can be used, once the geometry and the materials properties are known, to calculate the incoming heat flux and the required heat transfer areas:

$$\dot{Q} = UA\Delta T_X \tag{2.1}$$

Where $\dot{Q}$ is the heat flux transferred, U is the overall heat transfer coefficient, A is the reference heat transfer required area, ΔT_X is the temperature difference driving the heat transfer between two bodies. In case of heat transfer between two fluids, or one solid and a fluid, the logarithmic mean temperature difference should be used. In case of heat transfer between two fluids at constant temperatures, or between two solid bodies, ΔT_X becomes a simple temperature difference.

The overall heat transfer coefficient is defined as:

$$U \cdot A = \frac{1}{\sum_{i=1}^{N} R_{th,i}} \tag{2.2}$$

Where $R_{th,i}$ are the thermal resistances of the layer i. Thermal resistances are calculated differently according to the shape of the resistive layer.

- Flat wall:

  $$R_{th,wall} = \frac{1}{k_{wall}} \cdot \frac{t}{A_{wall}} \tag{2.3}$$

  Where k is the thermal conductivity of the material, t thickness of the layer, A_{wall} is the heat transfer surface area.

- Cylindrical vessel/tube:

  $$R_{th,tube} = \frac{ln\left({}^{r_{ext}}/_{r_{int}}\right)}{2\pi\, L\, k_{tube}} \approx \frac{1}{k_{tube}} \cdot \frac{t}{2\pi\, L\, r_m} \tag{2.4}$$

  Where L is the tube length, r_{ext} is the outer tube radius, r_{int} is the inner tube radius, and $r_m = (r_{ext+}r_{int})/2$ is the tube mean radius.

- Convective fluid film:

  $$R_{th,conv} = \frac{1}{h_{conv}A_{film}} \tag{2.5}$$

  Where A_{film} is the surface in contact with the convective film, and h_{conv} is the convective heat transfer coefficient. h_{conv} is calculated with different correlations according to the flow regime: free or forced convection, turbulent or laminar flow.

The heat transfer required area represents one of the fundamental points of the analysis; required surfaces have to meet the space constraints due to the tractor/tool small diameter. The following list reports some possible interventions to reduce the required surface area.

1. Increase the ΔT_X, by varying the design temperatures.

2. Increase U, by bettering the heat transfer in the following ways: reducing the thicknesses and the number of the conducting layers (compatibly with stresses and high pressures), increasing the Reynolds number of flowing fluids (turbulent flows have higher h_{conv}) and using materials with higher thermal conductivity.

3. Reduce the amount of heat that needs to be transferred Q. This could be done by reducing the electronics power dissipation rate (improving electronics efficiency), and decreasing the cooling load or increasing the system efficiency in case of active cooling.

2.2 Passive cooling

"Passive cooling" is a thermal management technique that consists of passively rejecting the excessive electronics heat to the external well environment. It aims at maintaining the component temperatures as close as possible to the one of the well. This technique does not involve systems that require energy inputs and the tool electronics cannot be cooled below the well temperature. A good passive cooling implementation aims at minimizing the thermal resistances between the electronics and the external environment, in order to provide a good thermal path for the heat to be dissipated. Minimizing the thermal resistances means having a low temperature gradient between the electronics and the wellbore fluid; high thermal resistances, instead, lead to an electronics temperature which is much higher than the well fluid one.

The thermal path from the electronics to the external environment consists of the following steps. Every step represents a different thermal resistance.

- *From the electronic component to the component casing:* the heat dissipated by the component is rejected through the component casing. The thermal resistance is given by the shape and material of the component. It is usually given by the manufacturer; it cannot be modified and is generally small compared to the other resistances involved in the system.

- *From the component casing to the tool chassis:* The way the electronic component is mounted on the tool chassis determines the magnitude of the thermal resistance. Components like transistors or diodes, which are directly screwed on the chassis, can be interfaced with ceramic alumina plates, aluminum nitride plates (more performing but also more expensive than the alumina plates), soft thermal silicone sheets, thermal grease or adhesives. The components that are mounted on PCBs are harder to thermally couple in an efficient way to the chassis, although they usually dissipate a smaller amount of heat. FR4 material and the PCB insulating layers are usually bad heat conductors, so the heat is hardly conducted out the PCB. Soft thermal silicone sheets (to be clamped and squeezed between the PCB and the chassis) and thermally conducting circuit boards can be used to reduce the thermal gradient.

- *From the tool chassis to the tool housing:* This step represents one of the biggest thermal resistances for the heat to be rejected to the wellbore. Weak spring/grounding systems, air gaps and thermal insulating layers negatively affect the heat rejection from the chassis to the housing, by increasing the thermal resistance. If not stable, the contact between the chassis and the housing can also change according to the tool orientation due to gravity. A temperature increase of the components, equal 3-4 degrees, was noticed during some tests on the HT Well Tractor, after the running tool was flipped upside down. Strong radial spring systems, screw systems, thermal expansion materials and other mechanical arrangements could be used to give a good stable thermal contact.

- *From the tool housing to the wellbore:* the dissipated power is rejected to the well through three mechanisms such as heat conduction, convection and radiation. The convection is the most relevant mechanism and its contribution is proportional to the speed of the well fluid that laps the housing; oil, and liquids in general, have better convective properties than gases. No passive cooling techniques can control or minimize this thermal resistance, which is a feature of the well fluid only. Nevertheless, it has to be taken into account in the test setups, in order to reproduce realistic test conditions. A good passive cooling design must be able to withstand the expected worst well conditions.

Another important parameter has to be taken into account when designing a passive cooling system: the heat transfer area, through which the heat is rejected. It can be associated in first approximation to the external housing surface. A large heat transfer area reduces the thermal resistance and the temperature gradient between the electronics and the well fluid. The size of this surface is determined by the tool O.D. and length, which are often already constrained by the tool specifications.

Additional devices that are sometimes used in passive cooling configurations are:

- *Heat pipes*: metallic thin cylinders containing a passive fluid loop (no energy input is required) which transports the heat from one pipe end to the other. They can be used to better transport the heat away from the electronics, better spread it around the chassis or thermally connect a heat source to a heat sink. Compared to other thermally conductive materials (Aluminum, copper) used in the thermal management of electronics, they can have an equivalent thermal conductivity that is 10 to 50 times larger.

- *Convective fluid loops*: fluid loops, circulated by a small pump, transfer the excessive heat away from the electronics, towards a heat sink. They can be used with the same purpose of heat pipes, although the regulation is more flexible, as the circulated mass flow rate of liquid can be controlled. On the other hand, it is more complex system and requires an energy input to run a pump; that makes it borderline between passive and active cooling.

In analogy with the electric circuits, the thermal path between the component and the well fluid is illustrated below.

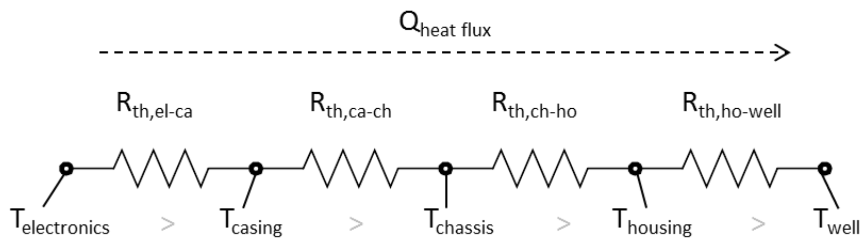

Figure 2.1 1D electric analogy of the thermal path between the electronics and the well. The temperature can be considered analogue to the electric potential, the thermal resistance to the electric resistance and the heat flux to the electric current.

Since the thermal resistances are connected in series, the overall system is very sensitive to the change/growth of every one of them. Even though the chassis-housing thermal resistance is very important for a good heat rejection, the most likely resistance to limit the passive cooling is the housing-well fluid resistance, which can become really high in case of still fluid (in particular of still gas). This shows how a good thermal design of the tool can be affected by external factors, that cannot be controlled, and how important is to take them into account in the test setup.

If the power dissipation rate of the components is known, finite element simulations can be used to model and evaluate the performance of a passive cooling design.

2.3 Electronics thermal protection and Dewar flask

The Dewar flask is an alternative cylindrical housing that is sometimes employed to protect the tool electronics from the high temperature well environment. Two concentric cylindrical shields are soldered and filled with vacuum, so the heat transfer between the outer and inner surfaces is reduced to minimum, by eliminating the conductive and convective heat transfer contributions. Plastic/rubber caps, with holes for electric connections, are used to thermally seal the flask ends. A realistic value of thermal conductance for a Dewar flask is 0.2 W/m^{2}K, compared to the one of a metallic housing which is ~10 000 W/m^{2}K. Differently from the passive cooling technique, the employment of a flask does not require any specific chassis-housing assembly technique.

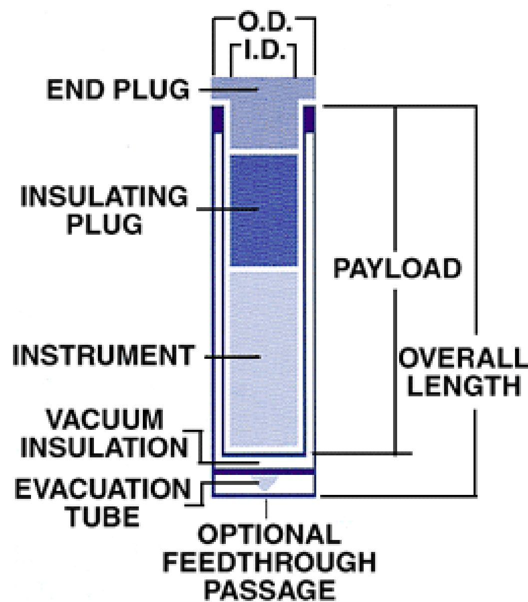

Figure 2.2 Schematic representation of a Dewar flask and its main components, from the supplier Mitcoind. (Source http://www.mitcoind.com/heatshield.htm)

The flask technology is generally used when it is desired to minimize the heat exchange between the components inside the tool and the wellbore environment:

- It can be used in a "passive configuration" whereas the initial surface temperature, at which the tool is assembled (~25 ^{0}C), wants to be preserved by insulating the electronics from the well high temperatures. However, the heat leakages through the flask and the inner power dissipation, which usually has the most relevant impact, contribute to the raise of the electronics temperature in time. The available exposure time to high temperature downhole is inversely proportional to the electronics dissipated power. These two key-parameters are important for the feasibility assessment of such a system, as a longer exposure time can be obtained by enhancing the electronics efficiency. Also, a higher components tolerance to high temperature increases the available exposure time. However, this technique cannot be implemented if the electronics heating rate is large.

- It can be used when an active cooling system is integrated and all the components in the tool section need cooling below well temperature. Using a flask drastically reduces the heat leakages through the housing and reduces the cooling load.

It is important to notice how the employment of a Dewar flask makes the tool design almost independent from the wellbore fluid conditions, while the internal heat generation becomes very relevant. Another significant advantage of using a Dewar flask is that whenever the tool is not running, the raise in temperature of the electronics becomes very slow and is caused by the heat leakages through the flask only.

Lumped properties calculations and finite element simulations can support and evaluate the feasibility of such a system. The dissipated power rate of the electronics has to be known and is crucial for this type of design.

2.4 Active cooling

Active cooling systems are distinguished from passive cooling ones because of the energy input which is required to cool the load. The energy input can be electrical, mechanical, thermal or chemical. Differently than passive cooling techniques, active coolers can maintain the load at or below the temperature of the environment in which they operate.

From a thermodynamic point of view, integrating an active cooling system into a downhole tool means to provide the necessary energy input to the refrigeration system and thermally couple it to the hot and cold reservoirs. Figure 2.3 illustrates the typical thermodynamic diagram for a refrigeration cycle, in case of integration in the electronics section of a downhole tool.

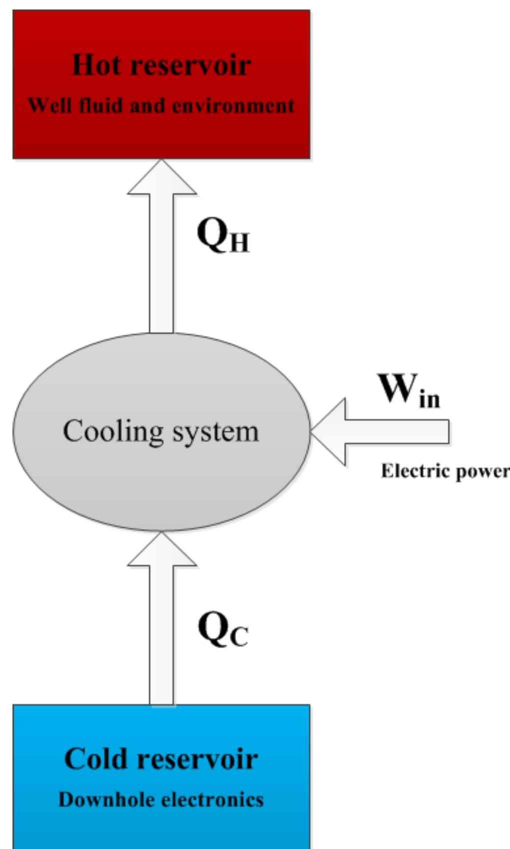

Figure 2.3 Representation of the thermodynamic integration of an active cooling system into a downhole electronics section.

Since the wireline cabling system delivers the feed power to the intervention tools, electric power is available downhole and can be used to feed the cooling system (W_{in}). The cooling system absorbs the cooling load Q_C from the downhole electronics, maintaining it to a lower temperature than the wellbore. The cooling load Q_C is the results of two contributions:

$$Q_C = Q_{C,el} + Q_{C,leaks} \quad (2.6)$$

Where $Q_{C,el}$ is the power dissipation rate of the electronics and $Q_{C,leaks}$ is the heat flux leaking from the hot surrounding to the cooled electronics. Thermal insulation can be employed to reduce this contribution.

The cooling system then pumps the excessive heat Q_H to the well environment. Convection is the dominant heat transfer mechanism that characterizes the thermal interaction between the well environment and the downhole tool, compared to heat conduction and radiation. The well fluid thermophysical properties can therefore influence significantly the heat rejection rate, as well as the well fluid speed around the tool.

According to the first law of thermodynamics, the three energy fluxes need to satisfy the following balance.

$$W_{in} + Q_C = Q_H \quad (2.7)$$

The efficiency of the cooling cycle is estimated through the coefficient of performance (COP), which is defined as follows.

$$COP = \frac{Q_C}{W_{in}} \quad (2.8)$$

The choice of an efficient system is only one of the many requirements the application imposes. Other constraints are influencing the analysis: some of them are the system dimensions, the integration of the device with a harsh environment, the heat management and thermal insulation, the selection of materials.

Among the listed topics heat management is one of the most important. The cooling load to be removed strongly depends on how the system is set and the thermal insulation designed. Large cooling loads require high energetic expenses and wider heat exchanging surfaces. It is important then to use good insulating materials and smart strategies to manage the heat fluxes. It is fundamental to isolate as much as possible the chilled area (electronics, sensors, cameras etc.) in order to minimize the incoming heat flux from outside the housing: Dewar flasks or good insulating materials/foams are some options. The heat rejection to the external environment, instead, has to be characterized by very-low-thermal-impedance materials, in order to minimize the required heat exchanger surface. A short paragraph will be dedicated to these topics.

The first step in a feasibility study involves a systematic search for possible solutions to the problem. In this particular case several cooling technologies are investigated. A list of all the possible solutions is shown below; not all the listed technologies meet the requirements given by the exercise downhole, in terms of size, dimensions, compactness, reliability and effectiveness. Therefore only some of them will be further analyzed, using the theoretical and thermodynamic laws that rule the processes. The study of each cooling technique is organized in three steps: a first part explains the theoretical principles and processes characterizing it; a second part reports the main equations for the modeling of the system, together with some results from theoretical calculations; a third part summarizes information and practical applications from the scientific literature. Since the electronics heating rate is not known yet, and incoming heat flux through the housing strictly depends on the tool design, first-approach calculations are carried out parametrically, keeping the cooling load variable. Cold and hot temperatures of 175 and 200 °C have been chosen.

Table 2.1 Candidate refrigeration processes.

Description	*Energy types involved*	*Process*	*Used refrigerants*
Vapor compression cycle	Thermal - Mechanical	Phase change, vapor expansion	Water, Freon®
Reverse Brayton cycle	Thermal - Mechanical	Isentropic gas expansion	Helium, xenon
Joule-Thompson cycle	Thermal - Mechanical	Isenthalpic gas expansion	Nitrogen
Thermoelectric cooling	Thermal – Electrical	Peltier effect	Bismuth-tellorium, antimony-tellorium alloys
Absorption cooling	Thermal – Chemical	Phase and concentration change	Ammonia-water, LithiumBromide-water
Adsorption cooling	Thermal – Chemical	Adsorption/desorption	Water - Zeolites, silica gel
Magnetocaloric cooling	Thermal – Magnetic	Magnetocaloric effect near Curie point	Gadolinium (at room temperature)
Electrocaloric cooling	Thermal – Electrical	Electrocaloric effect near Curie point	Barium titanate
Thermoacoustic cooling	Thermal – Acoustic	Polytropic gas expansion	Helium
Phase-change materials	Thermal – Chemical	Phase change, latent heat	Salts, paraffins, eutectic alloys

The technologies that will be investigated more in detail are listed below.

- Vapor compression cycle;
- Thermoelectric cooling;
- Reverse Brayton cycle;
- Magnetocaloric cooling;
- Liquid Nitrogen tank.
- Phase Change materials.

Contrary to other technologies, liquid Nitrogen solution is not providing a constant cooling action but extends the operation at high temperatures to a longer time period. Other solutions are excluded from the beginning since they don’t fit the wanted requirements in terms of compactness (absorption and adsorption cooling, thermo-acoustic refrigeration), effectiveness (electrocaloric cooling), and temperature span (Joule-Thompson cycle).

2.4.1 Vapor compression cycle

The vapor compression cycle can be considered one of the most mature and diffused cooling technologies. It is installed in the majority of the domestic fridges and freezers. As it is noticeable in Figure 2.4 the cycle is composed of 4 crucial processes.

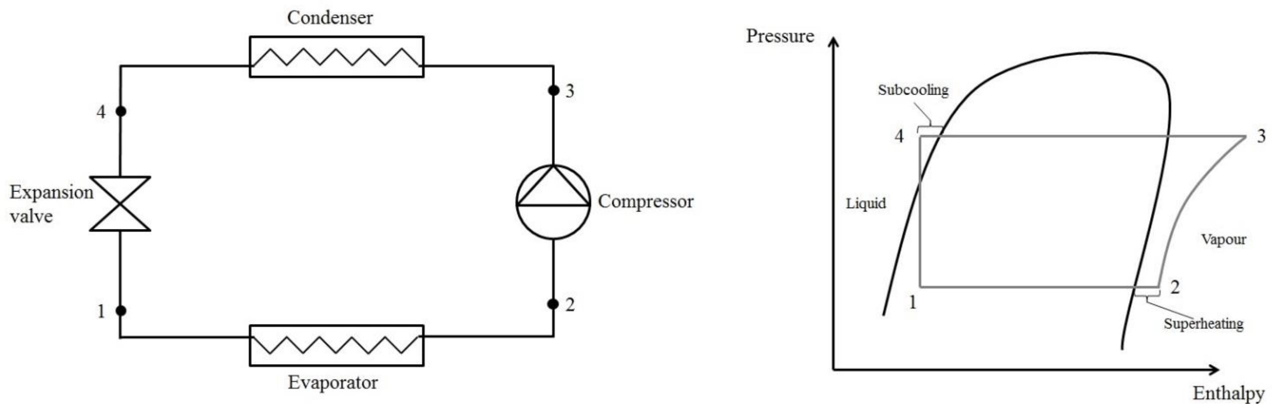

Figure 2.4 Vapor compression system components (left hand side) and ideal cycle on pressure vs. enthalpy diagram (right hand side). The Limit Curve that separates the different phases is reported.

- 1 → 2: isobaric/isothermal evaporation (evaporator)
- 2 → 3: isentropic compression (compressor)
- 3 → 4: isobaric/isothermal condensation (condenser)
- 4 → 1: isenthalpic expansion (throttling valve)

Wet steam at low temperature and pressure (1) absorbs the cooling load in the evaporator, becoming dry saturate steam (2). It is then blown by the compressor and brought to high temperature and pressure (3). The compressor outlet is linked to a condenser in which the steam exchanges heat with the external environment and condenses to saturate liquid at high pressure (4). The saturate liquid is then expanded isenthalpically through a throttling valve. The pressure drop causes a decrease of the temperature and transforms the liquid in wet vapor (1) at low temperature.

Some general artifices to better the reliability and the effectiveness of the cycle can be:

- Superheat the dry steam (2), above the saturation temperature, at the evaporator outlet: it avoids sending wet steam to the compressor and the compressor blades being ruined by water drops.
- Subcool the saturate liquid (3), below the saturation temperature, at the condenser outlet: it increases the specific cooling capacity of the cycle. The expanded wet vapor will be at lower temperature and will be able to receive a higher cooling load.

Both the methods imply an increase of the required heat exchangers area so could not match the downhole employment constraints. Superheating should be minimized, to guarantee the minimum allowable vapor dryness at the compressor inlet. Subcooling should be evaluated instead, as on one hand it would increase the cycle specific cooling power and decrease the evaporator surface area, but on the other hand it would require a larger condenser, which would be in thermal contact with the well fluid.

Currently, the most used refrigerants in industrial and domestic applications are water and Freon®, hydrochlorofluorocarbons with low saturation temperatures. Freon® substances can be employed in cryogenic applications or at room temperature. The most part of them cannot be used at higher temperatures (> 100 °C) because of a low critic temperature. They will therefore not be considered in this analysis.

Water is the main candidate for our application. It is cheap, has a fairly high critic temperature (~ 374 °C) and is nontoxic (contrary to Freon® which have a significant Global Warming Potential, a not negligible Ozone Depletion Potential and can be toxic for humans).

Some other configurations for the vapor compression cycle have also been developed to improve performance, efficiency and temperature spans.

- With a preheater

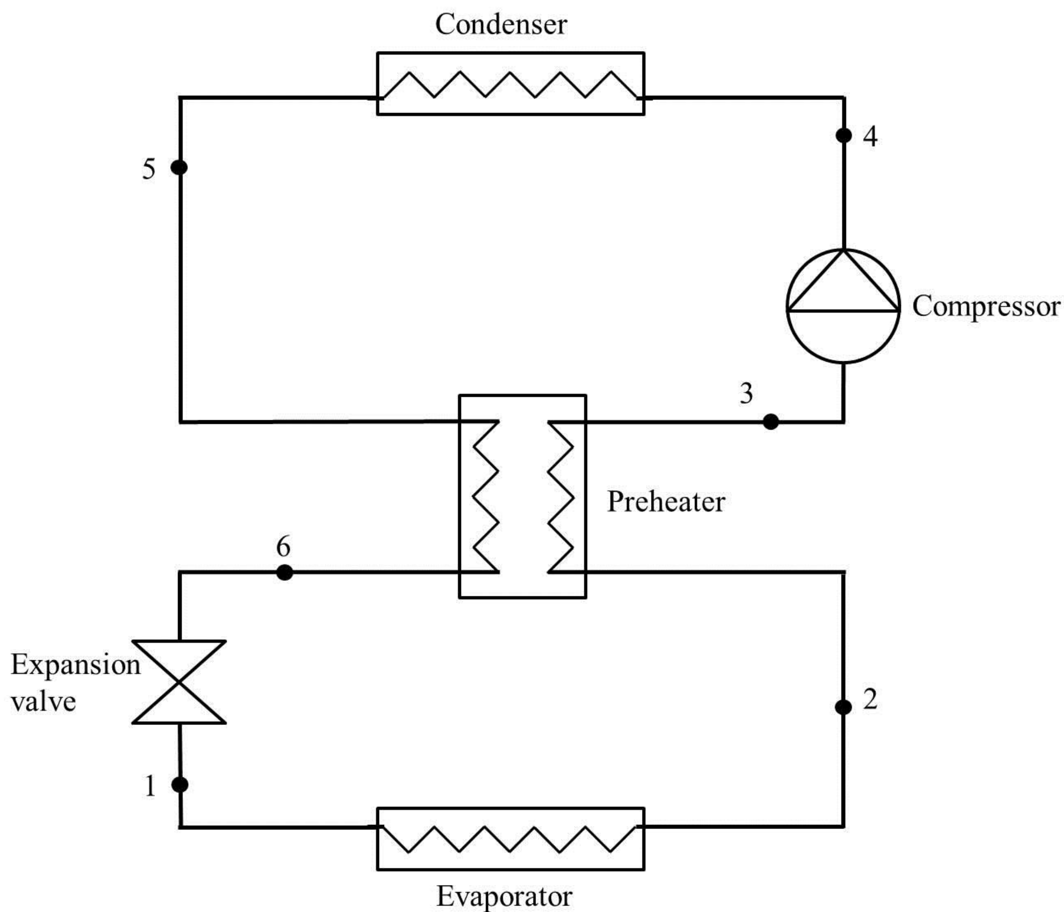

Figure 2.5 Schematic of a vapor compression cooling cycle, with preheater.

A heat exchanger couples the two flows coming out the compressor and the condenser. In this way the superheating and the subcooling are realized while recovering energy. The required heat exchange area towards the external environment is reduced, but a new component is added to the system and the balance benefit-drawbacks (compressing a hotter steam flow requires more power) make the coefficient of performance (COP) slightly decrease.

- Cooling stages in cascade

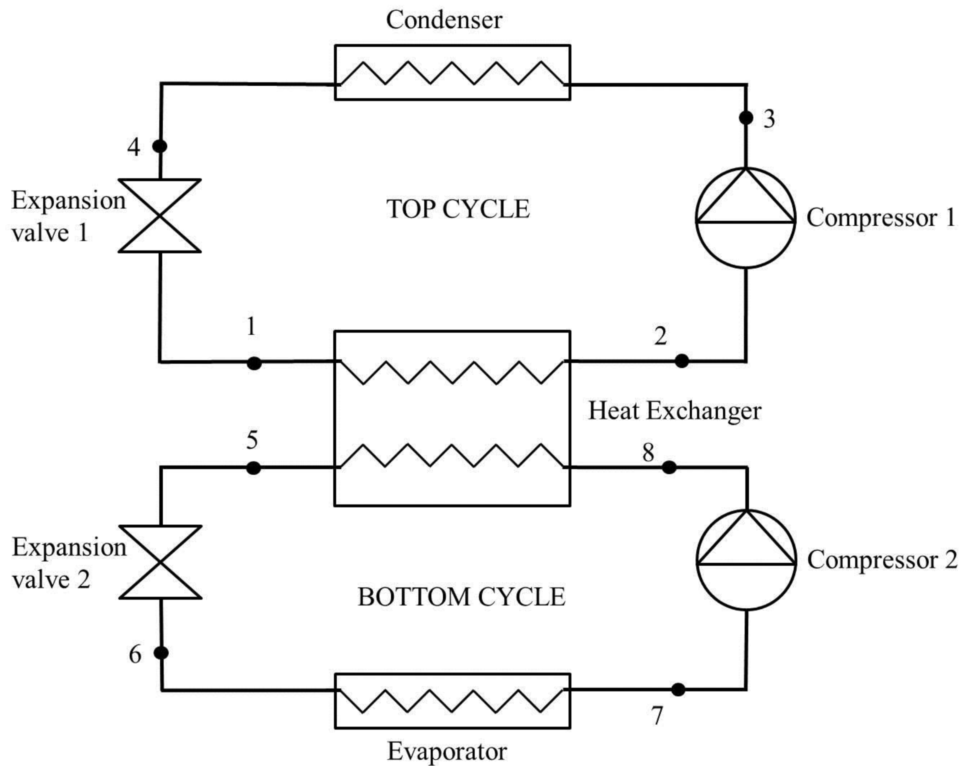

Figure 2.6 Schematic of a two-stage cascade vapor compression cooler.

Compressors and valves are doubled, and a heat exchanger couples the two cycles: the condenser of the bottom cycle exchanges heat with the evaporator of the top one.

This arrangement is useful to minimize the compression ratio and the compression work. It can be employed whenever the temperature difference between the hot and cold reservoirs, thus between the saturation pressures, becomes too high for one compressor only. This solution requires many more components and piping, though and decreases the reliability of the system.

2.4.1.1 Vapor compression cycle - Theory

This paragraph explains the theoretical principles at the base of the single-stage vapor compression cooling process. Thermodynamic laws and diagrams describe the cycle as follows:

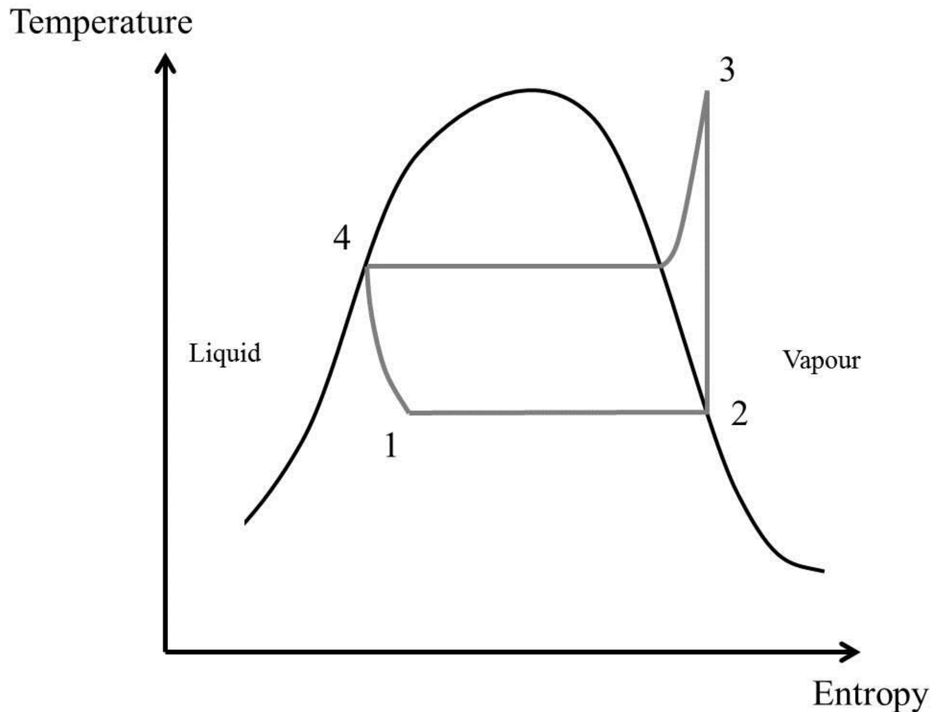

Figure 2.7 Ideal vapor compression cycle on Temperature vs. Entropy. The Limit Curve that separates the different phases is reported.

The thermodynamic state of a refrigerant along the cycle is always defined by two thermodynamic properties (e.g. temperature and pressure). Every transition from state to state is defined as a thermodynamic process. The ideal processes that characterize a one-stage vapor compression system are reported in Figure 2.7. The thermodynamic cycle involves two isobaric, one isenthalpic and one isentropic process.

Thermodynamic quantities can be calculated starting from the saturation pressure at the temperatures T_4 and T_2. They correspond to the temperature at which evaporator and condenser are working, respectively. In the ideal cases they match with the hot and cold reservoir temperatures (respectively T_H and T_C). In reality they are $\Delta T_{eva/cond}$ far from them, depending on the heat transfer characterization.

$$p_4 = p_{sat}(T_H + \Delta T_{cond}) \tag{2.9}$$

$$p_2 = p_{sat}(T_C - \Delta T_{eva}) \tag{2.10}$$

Where p is the pressure, p_{sat} is the saturation pressure. Density, enthalpy, entropy and all other properties in (2) and (4) can be calculated in the same way.

$$p_3 = p_4 + \Delta p_{cond} \tag{2.11}$$

$$p_1 = p_2 + \Delta p_{eva} \tag{2.12}$$

Where $\Delta p_{eva/cond}$ are the pressure losses in the evaporator and in the condenser, respectively. In the ideal case the heat exchange processes are isobaric and $\Delta p_{eva/cond} = 0$. The compression ratio is therefore defined as:

$$\beta = \frac{p_3}{p_2} \tag{2.13}$$

Point (3) can be calculated according to the definition of isentropic process; along the process (2)-(3) the entropy remains constant.

$$s_{3,isentropic} = s_2 \tag{2.14}$$

Knowing two thermodynamic coordinates (p_3, $s_{3,isentropic}$), it is possible to define the isentropic state of the refrigerant at the compressor outlet. This corresponds to an ideal state, though. In the real case compression cannot be isentropic because of the generation of entropy due to irreversibility, losses and frictions. A coefficient $\eta_{is,c}$, called isentropic compression efficiency, defines the ratio between the ideal and the real enthalpy difference across the compressor:

$$\eta_{is,c} = \frac{h_{3,isentropic} - h_2}{h_3 - h_2} \tag{2.15}$$

$\eta_{is,c}$ can assume different values according to the type of compressor (centrifugal, axial, reciprocating, screw) and to its size. Medium-large size centrifugal and axial compressors can reach isentropic efficiencies of 0.85 - 0.90. In our case, in which cooling loads are in the order of magnitude of 10^1-10^2 W, a small refrigerant mass flow rate needs to be treated, with a relatively small compression ratio. Suitable machines are reciprocating and screw compressors, built on a microscopic or mesoscopic scale. They have lower isentropic efficiencies, around 0.44 - 0.70 (Barbosa et al. (2012)) and 0.24-0.40 (Mongia et al. (2006)).

Using this parameter it is possible to evaluate the real refrigerant enthalpy h_3 at the compressor outlet. Knowing (p_3, h_3), all the other thermodynamic properties can be calculated.

Point (1) can be calculated according to the definition of isenthalpic expansion:

$$h_1 = h_4 \tag{2.16}$$

Knowing (p_1, h_1) all other thermodynamic coordinates in (1) can be calculated.

Once all the refrigerant thermodynamic coordinates are defined First Law of Thermodynamics for open systems can be applied to each single component, in order to compute the energetic quantities characterizing the system.

The minimum required refrigerant mass flow rate is given as:

$$\dot{m} = \frac{Q_{load}}{h_2 - h_1} \tag{2.17}$$

Where Q_{load} is the cooling load at the evaporator. The cooling power (assumed equivalent to the cooling load) at the evaporator is then equal to:

$$Q_C = \dot{m}(h_2 - h_1) \tag{2.18}$$

The compression work is equal to:

$$W_c = \dot{m}(h_3 - h_2) \tag{2.19}$$

The heat flux rejected to the external ambient, through the condenser, is equal to:

$$Q_H = \dot{m}(h_3 - h_4) \tag{2.20}$$

These three quantities are linked by the cycle energy balance:

$$Q_H = W_c + Q_C \tag{2.21}$$

The *COP* is generally defined as the ratio between the energetic benefit and expense. In this case it corresponds to the ratio between the cooling and the compression power:

$$COP = \frac{Q_C}{W_C} = \frac{h_2 - h_1}{h_3 - h_2} \tag{2.22}$$

A term of comparison is given by the Carnot efficiency, which is the maximum COP reachable by a cycle operating between temperatures T_H and T_C; it is definite as:

$$COP_{Carnot} = \frac{T_c}{T_H - T_C} \tag{2.23}$$

Temperatures are expressed in Kelvin.

2.4.1.2 Vapor compression cycle - Calculations

The expressions reported in the previous paragraph have been used to carry out some calculations about a vapor compression cycle, operating between 175 °C and 200 °C. The assumptions for the calculations are listed below:

- Refrigerant: water.
- Isobaric heat transfer processes (no pressure drops in the heat exchangers).
- $\Delta T_{overheating}$ = 3 °C , $\Delta T_{subcooling}$ = 0 °C.
- Isentropic compression efficiency $\eta_{c,is}$ = 0.60 ,electro-mechanical efficiency η_0 = 0.97.
- Refrigerant pinch point temperature span, at heat exchangers outlet $\Delta T_{condenser,outlet}$ = 15 °C , $\Delta T_{evaporator,outlet}$ = 5 °C.

Assuming a cooling load of 50 W, refrigerant properties and energetic quantities describing the cycle are shown in the following table.

Table 2.2 Resume of the vapor compression cooling cycle; cooling load equal to 50 W.

Stage	*Pressure (bar)*	*Temperature (°C)*	*Density (kg/m^3)*	*Enthalpy (kJ/kg)*	*Entropy (kJ/kgK)*	*Vapor fraction*
2	7.36	170	3.811	2772	6.707	1
3	21.1	359	7.489	3155	6.707	1
4	21.1	215	846.5	920.6	2.471	0
1	7.36	167	35.60	920.6	2.500	0.1

Pressure ratio	2.9	
Water mass flow rate	2.67E-05	(kg/s)
	0.43	(L/min)
Compression power	10.7	(W)
Rejected thermal power	60.3	(W)

Carnot COP	9.8
Ideal COP	8.1
COP	4.7

Water and steam properties are calculated through a Matlab function called XSteam (XSteam-IAPWS).

The COP is quite high, probably the highest among the analyzed technologies. The vapor mass flow rate is really small and of the same order of magnitude that "mesoscale" compressors treat. To have an idea of the order of magnitude of the heat transfer required area, a parametric study has been done with a variable cooling load. A basic geometry has been considered for the downhole heat exchange, where a piping system is in contact with the housing inner wall. The refrigerant flows inside the tubes and releases the heat to the surrounding, through the inner surface of the cylindrical housing. A convective well fluid flow removes the rejected heat flux, lapping the outer wall of the housing.

Additional assumptions about the heat transfer conditions in the well are needed for the estimation of the condenser length. A convective heat transfer coefficient of 100 W/m^2K (Flores (1996)) is chosen for the well fluid lapping the outer surface of the housing. A convective heat transfer coefficient for the refrigerant condensation process is conservatively assumed equal to 1000 W/m^2K.

.

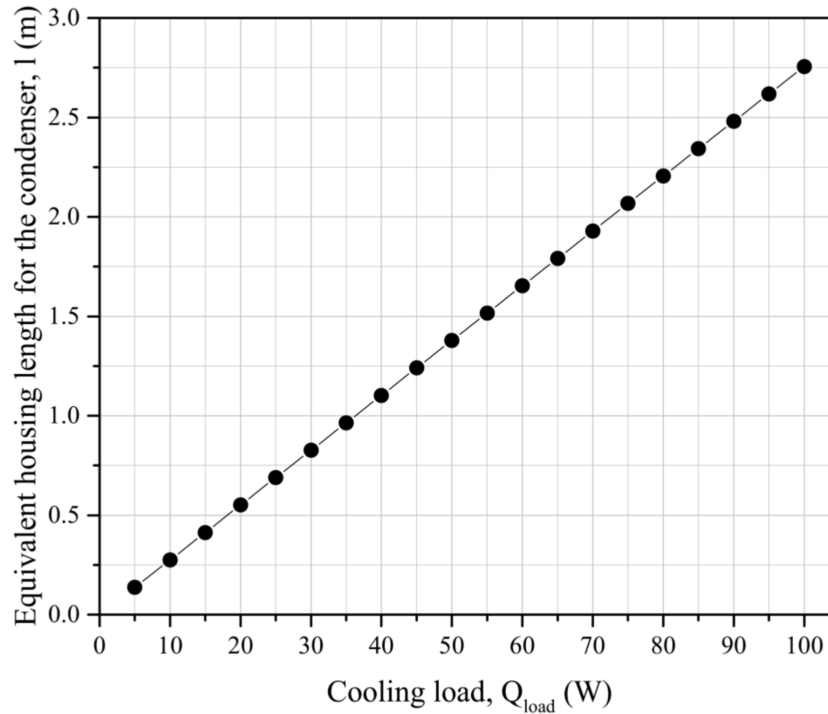

Figure 2.8 Cooling load vs. condenser extension.

On the x-axis the cooling load is varied, while on the y-axis the equivalent required length of the housing is reported. This parameter has been computed as ratio between the required surface and the internal circumference of the housing, assumed to have a diameter of 6 cm.

It is noticeable that the dimensions for the condenser are not negligible compared to the current dimensions of the well tractor electronics section. Only cooling loads below 35 W require a housing shorter than 1m. That means the heat transfer in the condenser has to be bettered in order to reduce the sizes.

An improvement in the heat transfer could be applied by introducing some oil, at the well temperature, inside a shell in which the condenser tubes are immersed. Different geometries for the heat exchangers could be also considered for optimization of the heat transfer, also accounting for the different pressure drops. First approach calculation could be done by using the following expression:

$$\Delta p = f \frac{\rho}{2} \frac{L}{D} v^2 \tag{2.24}$$

Where Δp is the pressure drop due to friction, f is the friction coefficient, ρ is the fluid density, L is the tube length, D is the tube diameter, v is the fluid velocity.

2.4.1.3 Vapor compression cycle - Applications

Some applications of cooling vapor compression cycle for electronics have been found in the literature; it is worth to briefly show them, in order to collect some knowledge about the existing/designed systems.

Mongia et al. (2006) shows a vapor compression cooling cycle for electronics in a laptop. It operates between 50 ^{o}C and 90 ^{o}C, the power to be removed is 50 W. The compressor treats an isobutane mass flow rate equal to 0.26 g/s, from 6.85 bar to 16.4 bar. The evaporator and superheater are composed of heat exchangers with micro-channels, respectively 80 μm and 350 μm wide. The condenser is cooled by an external airflow. Tubes are made copper, with an O.D. of 3.175 mm and an I.D. of 1.65 mm. This work appeared attractive for the studied application because of the small size of the components, shown in the figures below. However, the operating temperature is still far from the one of the downhole tools.

Figure 2.9 Compressor: 9 cm long, compression ratio = 2.4. (Mongia et al. (2006)) © [2006] IEEE.

Figure 2.10 Microchannel evaporator: Cooling load 40W, edge = 5 cm. (Mongia et al. (2006)) © [2006] IEEE.

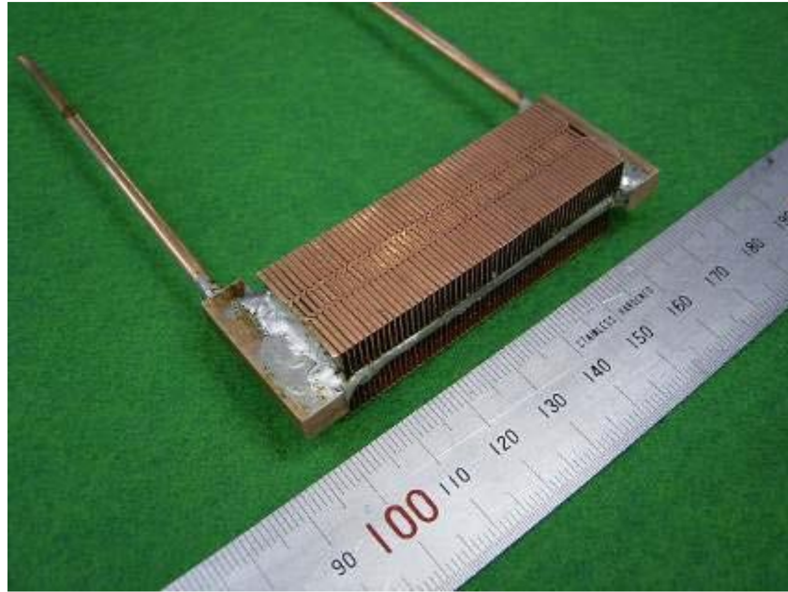

Figure 2.11 Condenser: rejected power around 70 W. 7 x 3 cm. (Mongia et al. (2006)) © [2006] IEEE.

Dimensions like these could be more than suitable for a well tractor. Other than the availability of compact high temperature components, a significant challenge would stand in the heat rejection to the external environment which is not as easy as at room temperature/pressure and with an available airflow. A harsh environment requires thicker layers and more resistant materials, which have worse thermal properties.

Barbosa et al. (2012) make a review of the state of the art of the compact vapor compression cooling cycles reported in the literature. The main points of the analysis are resumed in Table 2.3 and Table 2.4. Cooling powers go from 3 W to 1050 W. Also in these cases temperatures are around ambient temperature or below zero degree Celsius, far from the well operating conditions. However it is worth observing that the most used compressors, for small flow rates and compression ratios, are reprocicating machines. Also rotary, scroll, acoustic or diaphram compressors are employed. Most common expansion devices are, instead, capillary tubes, although needle or thermostatic valves are also commonly used. The majority of the reported cycles use R134a as refrigerant, followed by R507a, R600a or R22. All the reported refrigerants, used for low temperature applications, do not meet the design criteria for operating downhole, as they have critical temperatures below 100 ^{o}C.

Table 2.3 State of the art of the compact vapor compression cooling cycles from Barbosa et al. (2012) (part 1).

	T_{evap} (°C)	T_{cond} (°C)	T_{amb} (°C)	Thermal load/cooling capacity (W)	COP	Flow rate (g/min)	Number of stages	System volume (cm^3)	System mass (kg)	Refrig erant	Refrig erant charge (g)	Compressor type (number)	Condenser type (number)	Evaporator type (number)	Expansion device type (number)	Pressure ratio	Prototype (P) or model (M)?	Main application
Schmidt and Notohardjono [11]	15 to 35	n.d.p. [*1]	n.d.p.	650 to 1050	2 to 3	n.d.p.	1	27 × 27 × 71 [*2]	27 [*2]	R-134a	n.d.p.	DC Rotary (1)	Air-cooled tube-fin (1)	Copper coil, internally enhanced heat sink (2) [*2]	Thermostatic expansion valve (1)	n.d.p.	P	High-performance computer
Shannon [25]	20	50	n.d.p.	3	4 to 6	1.14	1	10 × 10 × 0.25	40 [*3]	R-134a	0.9	Diaphragm double-cavity capacitive (1)	Polymer MC [*4] (1)	Polymer MC (1)	Single orifice (1)	2.4	P,M	Personal cooling
Maveety et al. [26]	5 to 20	n.d.p.	25 to 35	50 to 130	2.2 to 5.8	n.d.p.	1	40.7 × 17.8 × 6.4	n.d.p.	R-134a	n.d.p.	DC Rotary (1)	Air-cooled MC (1)	Copper cold-plate (1)	Capillary tube (1)	3.1 to 3.6	P	2-U rack
Heydari [21]	20	60	n.d.p.	170	3	n.d.p.	1	n.d.p.	n.d.p.	R-134a	n.d.p.	Linear (1)	Compact air-cooled (1)	Cold plate (1)	Capillary tube (1)	n.d.p.	M	High-performance computers
Bash et al. [27]	25	52	22	400 (max)	~ 4 [*5]	n.d.p.	1	~308	n.d.p.	R-134a	n.d.p.	Acoustic (variable capacity)	Air-cooled (1)	Serpentine copper tubes (4—in series)	Capillary tube (1)	2.08	P	5-U computer server
Wadell [28]	-62.6	n.d.p.	25	100	n.d.p.	70	2	241200	n.d.p.	R-134a/R-508b	n.d.p.	AC Reciprocating (2)	Air-cooled (1)	MC (1)	Capillary tube (2)	n.d.p.	P	High-performance desktop computer
Mongia et al. [20]	50	90	50	50	2.25	15.6	1	12 [*6]	n.d.p.	R-600a	n.d.p.	12 V DC Reciprocating	Air-cooled MC (1)	Cold-plate with parallel MC (2—in series)	Needle valve (1—initially), Capillary tube (1—later)	2.3	P	Notebook computer
Agwu Nnanna [29]	4 [*7]	68 [*7]	20	152 to 606	1.2	n.d.p.	1	~26000	n.d.p.	R-134a	n.d.p.	AC Scroll (1)	Compact air-cooled (1)	Copper coil cold-plate (1)	Thermostatic expansion valve (1)	6.1	P	High-end computers
Trutassanawin et al. [23]	21 [*8]	60 [*8]	27 [*8]	121 to 268	2.8 to 4.7	48 to 102	1	n.d.p.	n.d.p.	R-134a	100	DC Rotary	Air-cooled MC (1)	MC (1)	Manual needle valve (1)	1.9 to 3.2	P	Electronics cooling

Table 2.4 State of the art of the compact vapor compression cooling cycles from Barbosa et al. (2012) (part 2).

Chiriac and Chiriac [30]	10	55	n.d.p.	100	4.24	126	1	~755	n.d.p.	R-134a	n.d.p.	Scroll (1)	Air-cooled MC (2)	MC (2)	Capillary tube (2)	3.6	M	High-power electronics
Rao et al. [31]	70 [*9]	n.d.p.	n.d.p.	90 to 180	0.32 to 0.58	n.d.p.	1	n.d.p.	n.d.p.	R-12	n.d.p.	Reciprocating (1)	Air-cooled (1)	n.d.p. (4 —in series)	Capillary tube (1)	n.d.p.	P	High-performance computer
Coggins [32]	-72.3	n.d.p.	21	40 (max)	n.d.p.	n.d.p.	2	60,000	n.d.p.	R-404A/R-508b	360 (R-404A)/ 240 (R-508b)	AC Reciprocating (2)	Air-cooled (1)	MC (1)	Capillary tube (2)	4.72 (high-stage)/ 10.02 (low-stage) [*10]	P	High-performance desktop computer
VapoChill SE (Asetek, Inc.) [36]	-5	n.d.p.	n.d.p.	130	n.d.p.	n.d.p.	1	3537	n.d.p.	R-134a	n.d.p.	AC Reciprocating (1)	Air-cooled (1)	n.d.p.	n.d.p.	n.d.p.	P	High-performance desktop computer
VapoChill XE (Asetek, Inc.) [36]	-4	n.d.p.	n.d.p.	180	n.d.p.	n.d.p.	1	3537	n.d.p.	R-134a	n.d.p.	AC Reciprocating (1)	Air-cooled (1)	n.d.p.	n.d.p.	n.d.p.	P	High-performance desktop computer
VapoChill XE II (Asetek, Inc.) [36]	-18	n.d.p.	n.d.p.	180	n.d.p.	n.d.p.	1	5815	n.d.p.	R-507a	n.d.p.	AC Reciprocating (1)	Air-cooled (1)	n.d.p.	n.d.p.	n.d.p.	P	High-performance desktop computer
VapoChill LS (Asetek, Inc.) [36]	-33	n.d.p.	n.d.p.	200	n.d.p.	n.d.p.	1	7110	n.d.p.	R-507a	n.d.p.	AC Reciprocating (1)	Air-cooled (1)	n.d.p.	n.d.p.	n.d.p.	P	High-performance desktop computer
Deming et al. [33]	n.d.p.	n.d.p.	50	500	2.94	n.d.p.	1	8.8 × 45 × 61	11	n.d.p.	n.d.p.	DC Rotary (1)	n.d.p.	n.d.p.	n.d.p.	n.d.p.	P	Mobile satellite antenna electronics
Ernst and Garimella [34]	22.2 to 26.1	44.2 to 51.5	37.7 to 47.5	120 to 280	5 [*11]	90 to 60	1	31.8 × 27.3 × 15.2	4.46	R-134a	n.d.p.	Reciprocating (1)	Al MC louver-fin (1)	Coiled tube-in-shell heat exchanger (1) [*12]	Thermostatic expansion valve (1)	2.06 [*11]	P	Personal cooling
Wu et al. [35]	7	40	40	300	2.3	n.d.p.	1	26 × 25 × 12	2.85	R-22	100	Wankel rotary (1)	Brazed Al MC (1)	Miniature spiral tube [*12]	Capillary tube (1)	> 3	P	Personal cooling

Note. [*1] n.d.p.: no details provided. [*2] Two systems were used in which one was a backup. [*3] System mass provided by Shannon [25]. In Shannon et al. [36], the reported system mass is 14 g. [*4] MC: microchannel. [*5] At 200 W cooling capacity. [*6] Internal fluid volume only. [*7] At 606 W cooling capacity. [*8] At the maximum cooling capacity. [*9] At 180 W cooling capacity (it is not clear in the paper if this is the external temperature of the evaporator or of the refrigerant). [*10] Under no load. [*11] At 230 W cooling capacity. [*12] Water is the secondary fluid.

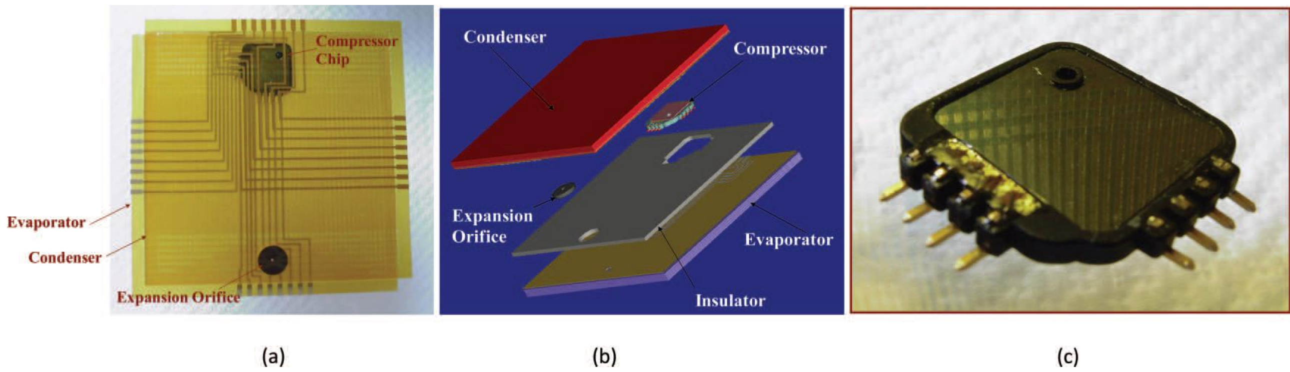

Figure 2.12 (a) Integrated mesoscopic cooler circuit of Shannon and co-workers (see Table 2.3), (b) exploded view, and (c) compressor (Barbosa et al. (2012)).

Figure 2.12, instead, shows a mesoscopic vapor compression circuit for electronics cooling. The active cooler consists of a square patch of approximately 100 mm side and 2.5 mm thickness and has been designed to produce a cooling capacity of 3 W while operating between 20 ˚C (evaporation temperature) and 50 ˚C (condensing temperature) using R-134a. Despite the interesting concept and design, the employed components would not be suitable for operations at high temperature.

Some information about high temperature vapor compression cycles have been written by Bennet (1988) and Flores (1996). Both works aimed to design an active cooling system for downhole applications, as also explained in the introduction. Bennet (1988) seeks for a system operating between 320 °C (hot reservoir) and 150 °C (cold reservoir), with a cooling load of 8 W. Several vapor compression configurations are analyzed: single stage, two stages in cascade and with preheater. The two-stage cycle turns out to be the most efficient one, but also the least compact (with two compressors, three heat exchangers and two valves). Single stage proves to be the most convenient tradeoff, with a COP = 1.087. Operating pressures at evaporator and condenser are respectively 4.6 bar and 106.4 bar, while heat transfer required surfaces are respectively 45 in^2 (0.0290 m^2) and 9.5 in^2 (0.0061 m^2). Tubes are stainless steel ASTM A312 O.D. 1/8 in.

Flores (1996) studies a system that operates between 200 °C (hot reservoir) and 125 °C (cold reservoir), with a cooling load of 50 W. Two vapor compression configurations are taken in account, the single-stage and the once-through solution. COP for the single stage is equal to 4.29, while for the once-through is 3.50. Some information about dimensions are given: single stage cycle has a condenser around 1 m long; once-through solution employs a lower tank (evaporator), with an outer diameter of 6.99 cm and a length of 69.42 cm, and an upper tank (condenser), with an outer diameter of 9.21 cm and a length of 44.43 cm.

2.4.2 Thermoelectric cooling

Thermoelectric coolers exploit the Peltier effect to convert electric current into a cooling action. The direct conversion occurs thanks to the employment of doped semiconductors with particular electro-thermal properties: if crossed by an electric current they can transport a heat flux in the same direction as the current flows, and can generate a temperature gradient.

Figure 2.13 better explains how thermoelectric coolers take advantage of this property.

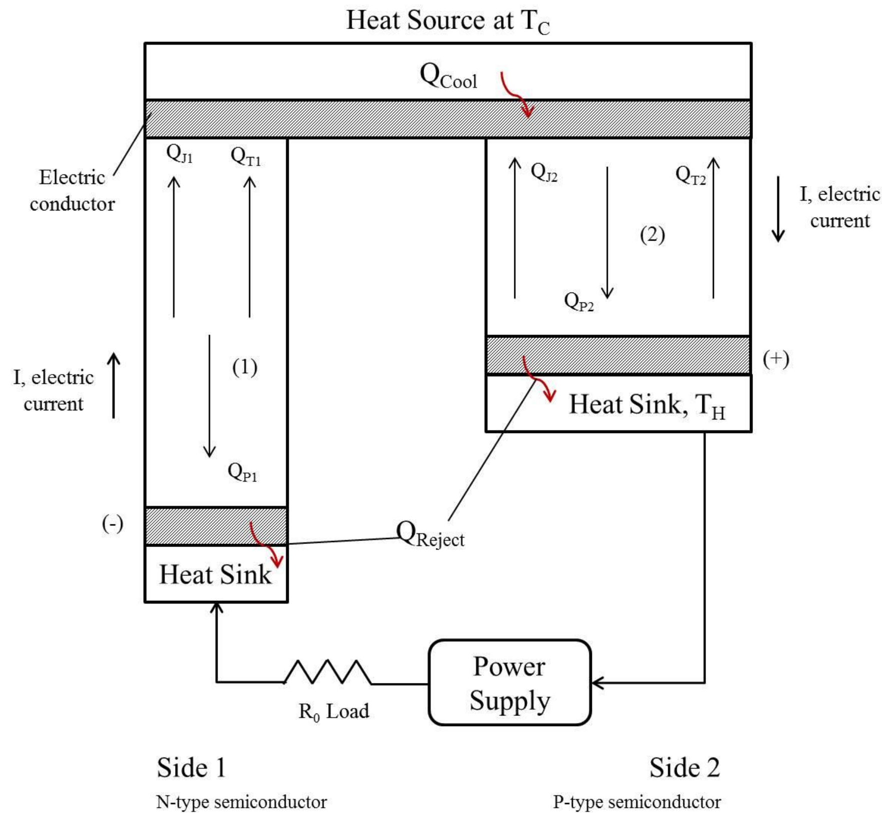

Figure 2.13 Schematic of a thermoelectric refrigerator, composed by a p-n junction (Bennett (1988)).

The basic thermoelectric system is composed of two different semiconductor legs, one n-type and one p-type, with different electron densities. The semiconductor legs are placed parallel to each other and joined with a conducting cooling plate on the cold side. Whenever a voltage is applied to the free ends of the two semiconductors, DC current flows across the junction, causing a temperature difference between the extremes. One cooling plate, on the cold side, absorbs the heat from the load and pumps it to the other side of the device where, where the hot plate and a heat sink are located. The two plates (see Figure 2.13) are usually ceramic.

There are no moving parts and a direct conversion from electric to "cooling" power takes place, limiting the irreversibility generated by mechanical/heat transfer processes (no compressor, no dissipation valve, no flowing fluids); a high irreversibility would affect the efficiency of the device. Furthermore thermoelectric coolers represent a very compact solution since they can be very thin (order of magnitude of millimeters) and

quite short in the other two dimensions (order of magnitude of centimeters). Some of them can also work at relatively high temperature (> 200 °C).

The main drawback of these devices is the high thermal power to be removed from the hot plate. The heat sink has to absorb not only the thermal power coming from the cold plate, but also the electric power dissipated due to the Joule effect, which is even higher than the first one. This phenomenon leads to a very low COP, usually significantly lower than 1. To keep the thermoelectric cooler operating at steady state it is necessary to effectively remove the heat rejected at the hot plate with a heat sink.

Different materials , with different properties, can be employed as semiconductors:

- Bi_2Te_3-Sb_2Te_3 (P)
- Bi_2Te_3-Bi_2Se_3 (N)
- GeTe-AgSbTe (P)
- SnTe-PbTe (N)
- PbTe-1%Na (P)
- PbTe-0.055%PbI_2 (N)

These materials are preferred to have high electrical conductivities to minimize the Joule heating, low thermal conductivities to minimize the heating losses caused by conduction between the plates, and a high Seebeck coefficient to maximize the transported heat flux. The Seebeck coefficient (V/K) is an index of the semiconductor sensitivity to create a voltage when subject to a temperature gradient. The opposite effect is represented by the Peltier coefficient (W/A or J/C), which expresses the heat flux removed by the current unit or the thermal energy removed by the charge unit. Even though the Peltier coefficient describes the cooling potential of a semiconductor, it is usually the Seebeck one to be used for comparisons, since they are directly proportional.

The Seebeck coefficient can be either positive, for p-type semiconductors, or negative, for n-type semiconductors, according to the direction the move heat towards (concord or discord with the current). The overall Seebeck coefficient for a p-n junction is given by the sum of the absolute values of the coefficients.

2.4.2.1 Thermoelectric cooling - Theory

This paragraph will refer to Figure 2.13 to describe and reproduce, with some theoretical correlations, the phenomena occurring in the Peltier cooler. The heat transfer from a cold source to a hot one is just the overall effect of the device, given by several processes and heat fluxes contributions:

- Peltier effect Q_P (W).
- Joule heating Q_J (W).
- Heat conduction Q_T (W) from hot plate to cold plate.

The resulting cooling action Q_{cool} comes from the balance of these three quantities:

$$Q_{cool} = Q_P - Q_J - Q_T \tag{2.25}$$

- The Peltier effect is defined as:

$$Q_P = \gamma\, I\, T_C \tag{2.26}$$

Where γ is the Seebeck coefficient and is computed as the sum of the absolute values of the Seebeck coefficients of the two semiconductors:

$$\gamma = |\gamma_P| + |\gamma_N| \tag{2.27}$$

Where I is the electric current flowing across the device, T_c is the cold plate temperature.

- Joule heating can be calculated as:

$$Q_J = I^2 \left(\frac{l_P}{2\, A_P\, \sigma_P} + \frac{l_N}{2\, A_N\, \sigma_N}\right) \tag{2.28}$$

Where I is the electric current flowing inside the device, l_P and l_N are, respectively the p-type and n-type semiconductor heights, A_P and A_N are the p-type and n-type semiconductor cross sections, and σ_P and σ_N are the p-type and n-type semiconductor electric conductivities. The two terms inside the brackets represent the electric resistances, put in series, of the two semiconductors, which summed give the overall electric resistance R.

- Heat conduction from the cold to the hot plate:

$$Q_T = (T_H - T_C)\left(k_P \frac{A_P}{l_P} + k_N \frac{A_N}{l_N}\right) \tag{2.29}$$

Where T_H and T_C are the hot and cold plate temperatures, l_P and l_N are respectively the p-type and n-type semiconductor height, A_P and A_N are respectively the p-type and n-type semiconductor cross sections, k_P and k_N are respectively the p-type and n-type semiconductor thermal conductivities. The two terms inside the brackets represent the thermal conductivities, in parallel, of the two semiconductors, which summed give the overall thermal conductivity *K*.

The resulting cooling action (W) becomes:

$$Q_{cool} = \gamma\, I\, T_c - \frac{I^2 R}{2} - K(T_H - T_C) \tag{2.30}$$

Q_{cool} depends on the operating temperatures and on the feed current. The thermal power to reject on the hot side is then equal to:

$$Q_h = \gamma\, I\, T_h + \frac{I^2 R}{2} - K(T_H - T_C) \tag{2.31}$$

The voltage applied to the cooler has to generate both the Peltier effect and the electric current:

$$V = \gamma\, (T_H - T_C) + R\, I \tag{2.32}$$

The COP is defined as:

$$COP = \frac{Q_{cool}}{VI} = \frac{\gamma\, I\, T_c - \frac{I^2 R}{2} - K(T_H - T_C)}{\gamma\, I\, (T_H - T_C) + R\, I^2} \tag{2.33}$$

It is possible to optimize the feed current, in order to maximize the cooling effect:

$$\frac{dQ_{cool}}{dI} = 0 \tag{2.34}$$

$$I_{opt} = \frac{\gamma\, T_C}{R} \tag{2.35}$$

$$Q_{cool,max} = \gamma\, I_{opt}\, T_C - \frac{I_{opt}^2 R}{2} - K(T_H - T_C) \tag{2.36}$$

$$COP_{opt} = \frac{\frac{1}{2} Z {T_C}^2 - (T_H - T_C)}{Z\, T_H\, T_C} \tag{2.37}$$

All these calculations are valid for a semiconductor only; if the cooling load is known, the number of couples can be computed as:

$$N = \frac{Q_{load}}{Q_{cool}} \tag{2.38}$$

Semiconductors will be connected electrically in series and thermally in parallel. The electric current will remain the same, the voltage will be *N* times the one for 1 couple, cooling and rejected powers will be multiplied by *N*, ΔT will be kept the same, as well as the COP:

$$COP_N = \frac{N \cdot Q_{cool}}{N \cdot I\, V} = COP \tag{2.39}$$

COP does not depend on the number of semiconductor couples. The maximum allowable thermal resistance of the heat sink can be calculated as follows:

$$R_{th} = \frac{(T_H - T_{heat\, sink})}{Q_h} \tag{2.40}$$

It is necessary to remember, during the design phase, geometric parameters like l_P, l_N and A_P, A_N are very important because not all their values are valid to create a Peltier cooler. Short semiconductor lengths imply low electric resistances but also high heat fluxes due to conduction, from the hot to the cold plate; as well as large cross sections reduce the electric resistance but make the heat conduction grow. There are some threshold values of lengths and areas which set the cooling action to zero and beside which the device just pumps heat from the hot plate to the cold one.

Material choice is very important to have a good Peltier cooler; as already said previously a good semiconductor must have:

- a high Seebeck coefficient γ (V/K) to maximize Peltier effect;
- a low electric resistance R (Ω) to minimize Joule heating;

- a low thermal conductivity K (W/K) to minimize the heat conduction.

These three parameters are combined in one coefficient Z (1/K), which is called Figure of Merit. It expresses, with only one number, the goodness of a semiconductor and is defined as:

$$Z = \frac{\gamma^2}{RK} \tag{2.41}$$

It is still possible to include the operating temperature T in the figure of merit expression, thus obtaining the dimensionless figure of merit ZT. Some graphs about the ZT trend with the temperature are reported below.

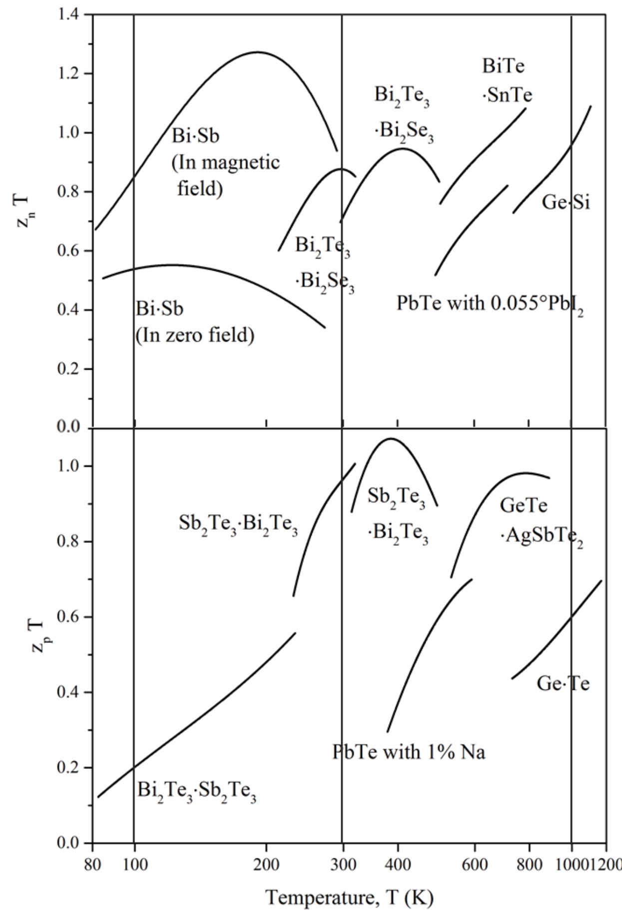

Figure 2.14 Reproduction of the dimensionless figure of merit for several semiconductors vs. temperature from Bennett (1988).

The higher the figure of merit, the better the semiconductor performance becomes. Figure 2.14 shows that Bismuth Telluride - Selenium Telluride and Bismuth Telluride - Antimony Telluride alloys are the best conductors, for this application, in the temperature range 300 - 500 K.

It is also important to define some parameters which are often used to characterize a Peltier cooler and its performances:

- ΔT_{max}: The maximum obtainable temperature difference between the cold and hot side of the thermoelectric elements within the module when I_{max} is applied and there is no heat load applied to the module. This parameter is based on the hot side of the elements within the thermoelectric module being

at 300 K. In reality, it is virtually impossible to remove all sources of heat in order to achieve the true ΔT_{max}. Therefore, the number only serves as a standardized indicator of the cooling capability of a thermoelectric module.

$$\Delta T_{max} = \frac{ZT_C^2}{2} \tag{2.42}$$

- Q_{max}: The heat that a thermoelectric cooler can remove at a zero degree temperature difference, when the hot side of the elements within the thermoelectric module is at 300 K.

$$Q_{max} = \gamma T_C I_{max} - \frac{I_{max}^2 R}{2} \tag{2.43}$$

- I_{max}: The current that produces ΔT_{max} when the hot side of the elements within the thermoelectric module is held at 300 K.

$$I_{max} = \frac{\gamma}{R}(T_H - \Delta T_{\text{max}}) \tag{2.44}$$

- V_{max}: The voltage that is produced at ΔT_{max} when I_{max} is applied and the hot side temperature of the elements within the thermoelectric module is 300 K.

$$V_{max} = \gamma \Delta T_{max} + I_{max} R \tag{2.45}$$

These parameters are called "max", but that does not necessarily mean they are the maximum tolerable quantities for the device. In fact they are referred to one operative condition only.

2.4.2.2 Thermoelectric cooling - Calculations

All the equations reported in the previous paragraph have been implemented and used to calculate the performance of a thermoelectric cooler. Starting from the considerations about Figure 2.14, $Bi_{0.5}Sb_{1.5}Te_3$ has been chosen as p-type semiconductor and $Bi_2Te_{2.7}Se_{0.3}$ as n-type.

Semiconductor properties, depending on temperature, have been taken from Poudel et al. (2008) and Zhu et al. (2007), and fitted into a function. In both papers several samples are examined; for these calculations two semiconductor qualities, for both the p-type and n-type, have been chosen: one corresponding to the state of the art (SOA) standards and one with improved properties, due to innovative treatments. They have been then combined together to examine the two cases, at higher or lower performances. The single semiconductor elements have been assumed to be 1 mm x 1mm x 1mm (height).The thermoelectric cooler operates between 175 ^{o}C and 200 ^{o}C. A ΔT = 5 K has been assumed between the reservoir temperatures and the real operating temperatures. Electric resistance has been majored of 10% to take in account also junctions.

The results of the calculation are reported below. The first three plots show how the cooling power, the rejected heat and the required voltage characterizing the single couple of semiconductors vary with the electric current flowing in the thermoelectric unit. Red and blue lines represent respectively the higher and

lower performance semiconductor case. In Figure 2.15 a maximum can be noticed for the cooling power, it corresponds to the point (I_{opt},$Q_{cool,max}$) explained in the paragraph about thermoelectric cooler theory.

For small electric currents quantities can become negative, that means the driving force is not high enough to move the heat from the cold to the hot plate, and Peltier effect is not balancing Joule heating and thermal conduction.

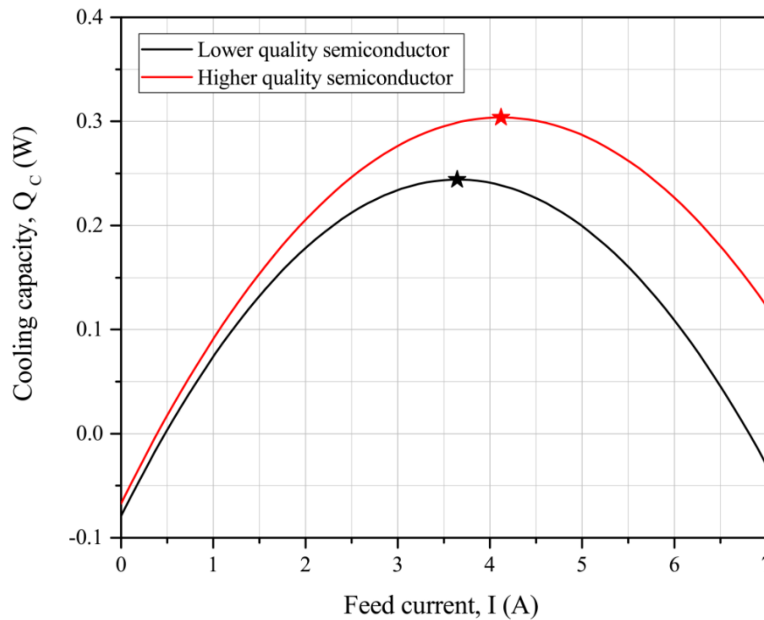

Figure 2.15 Thermoelectric unit cooling capacity vs. electric current. Maximum cooling capacities, corresponding to the optimal operating feed currents, highlighted by a star.

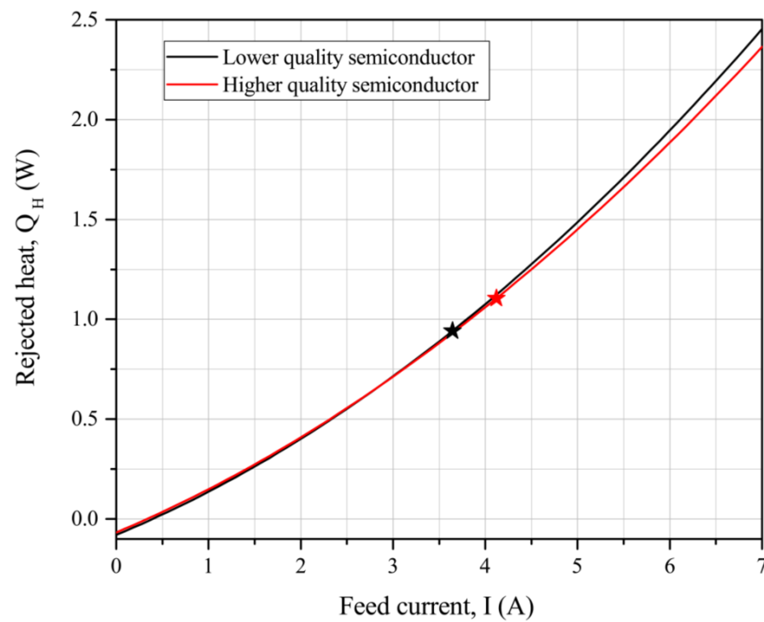

Figure 2.16 Thermoelectric unit rejected heat vs. electric current. Optimal operating currents highlighted by a star.

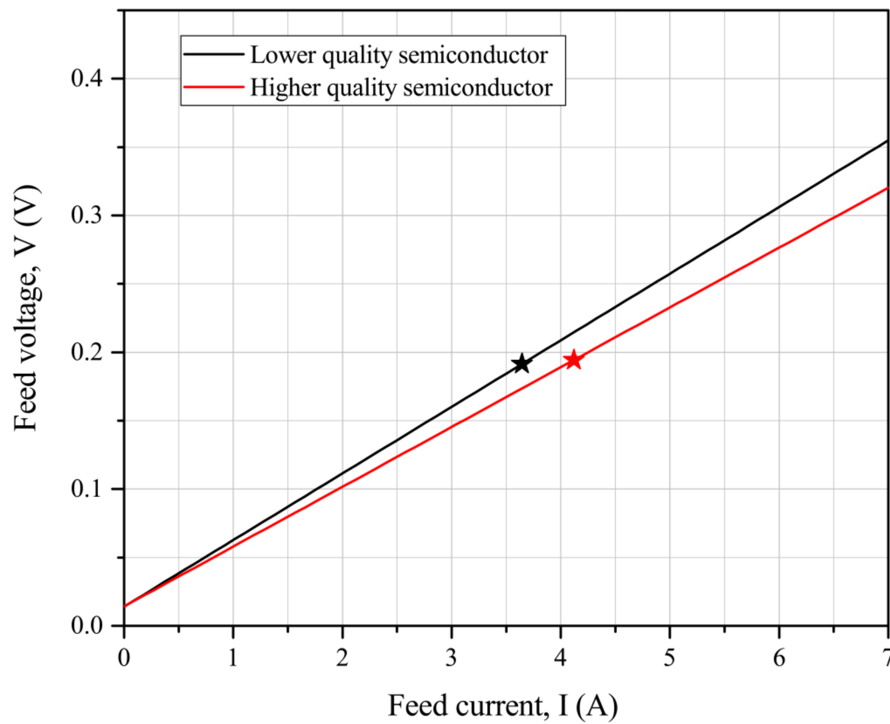

Figure 2.17 Thermoelectric unit rejected heat vs. electric current. Optimal operating currents highlighted by a star.

Operating at the optimal current I_{opt}, respectively 3.6 A and 4.1 A for the lower and higher quality semiconductors, maximizes the cooling action of the thermoelectric unit composed of a single p-n junction, $Q_{cooling,max}$= 0.244 W and 0.304 W. These considerations are valid only for the operating temperatures T_C = 175 °C and T_H = 200 °C. The required number of thermoelectric units (semiconductor couples) is then calculated for every cooling load as the ratio between the actual cooling load and the cooling capacity of a single p-n junction. In the next three plots the performance of a whole thermoelectric module is analyzed, with a variable cooling load.

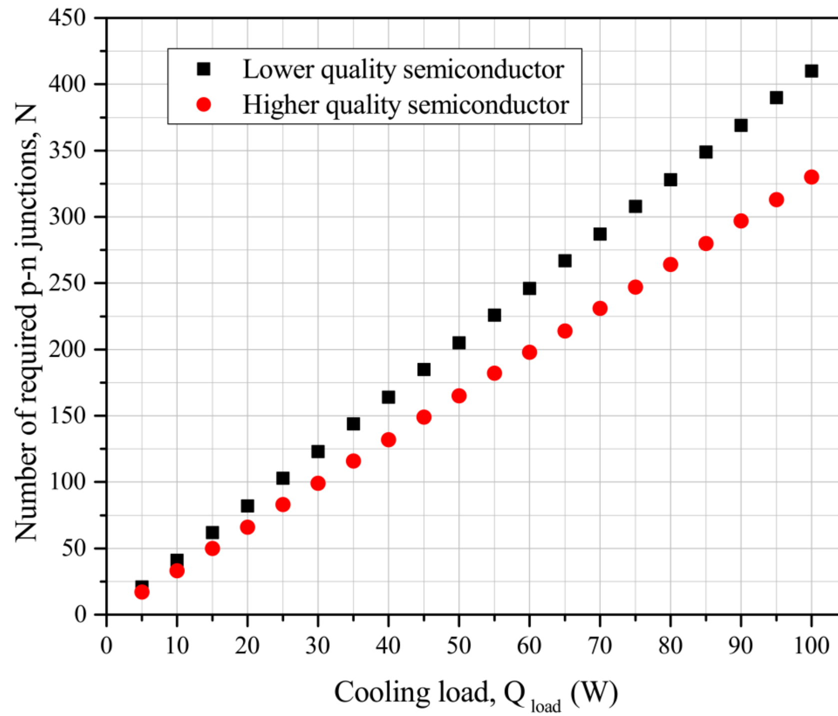

Figure 2.18 Number of p-n junctions required to satisfy the cooling load at the optimal operating conditions.

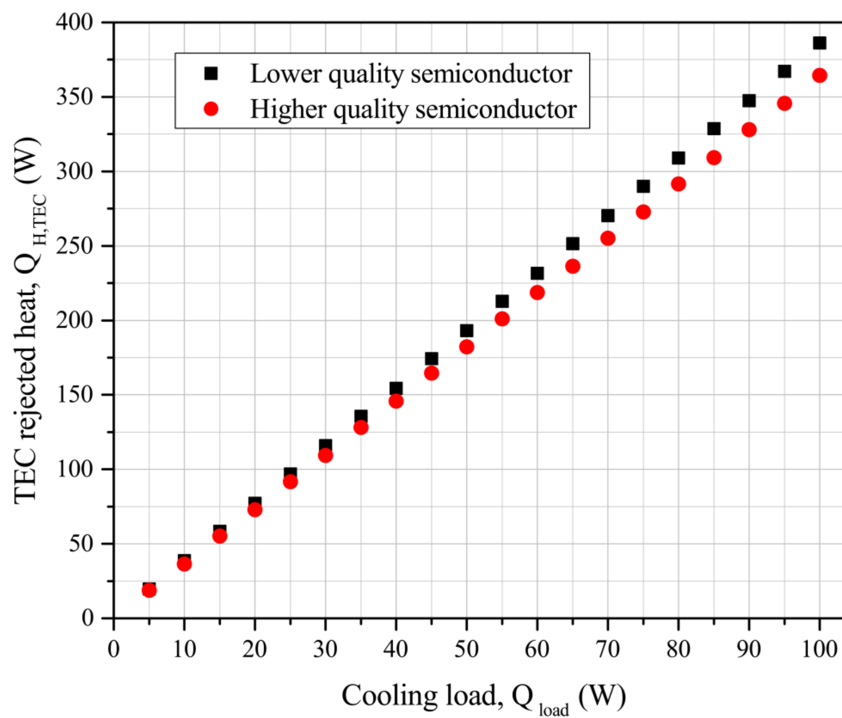

Figure 2.19 Rejected heat vs. Cooling load.

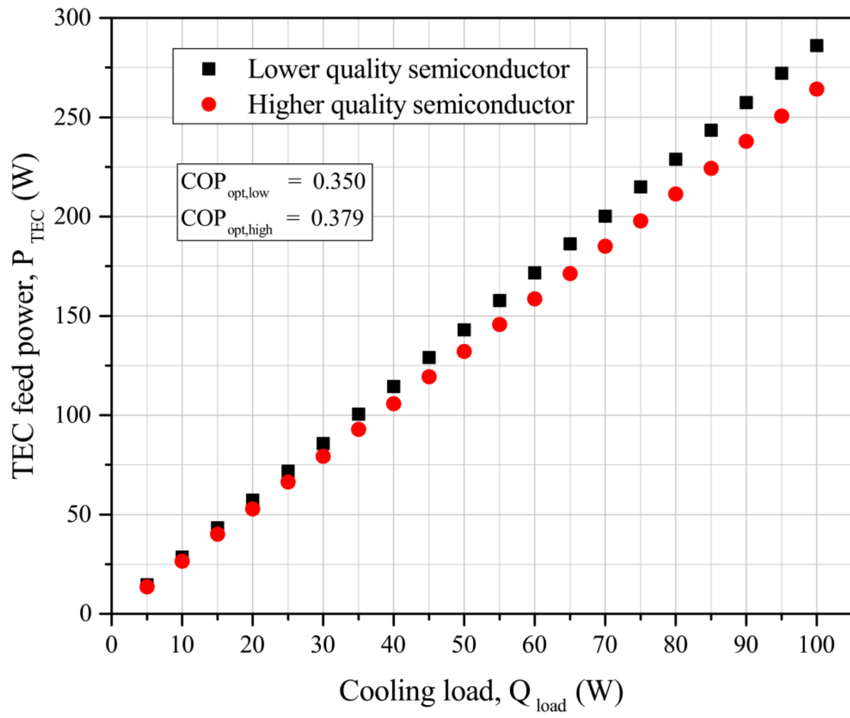

Figure 2.20 Required electrical power vs. Cooling load.

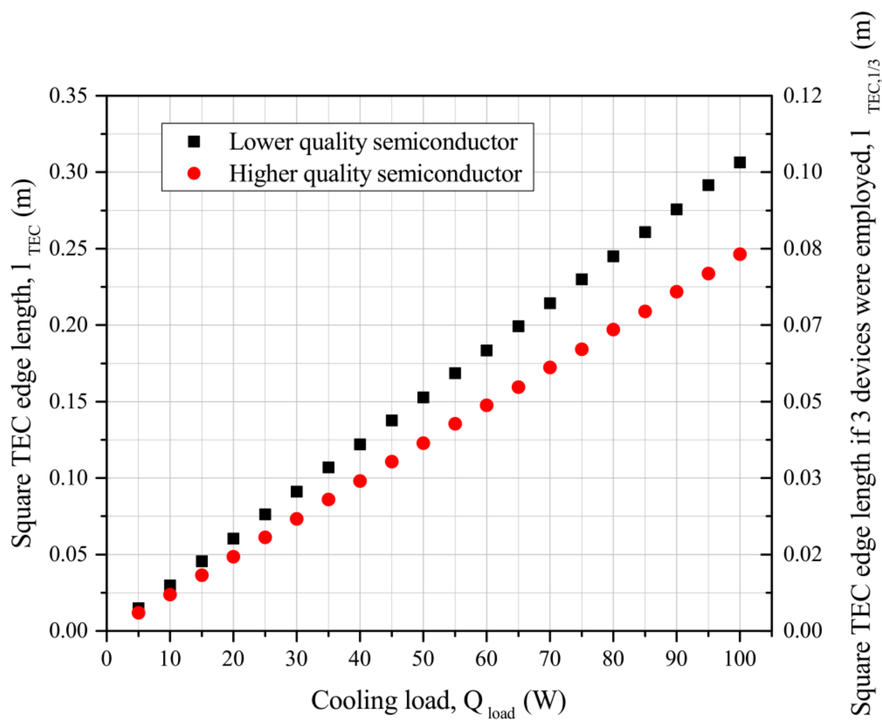

Figure 2.21 Thermoelectric cooler dimensions vs. cooling load.

The difference between the performances of the two semiconductor types is not so significant when analyzing the whole cooler. Absorbed and rejected heat fluxes differ for a few watts, as it can be noticed in Figure 2.19 and 2.20, and the COP_{opt} differ from each other for slightly more than 1%.

As expected the coefficient of performance is very low (below 0.5 in both cases) and the heat flux to be rejected is larger than the vapor compression technology, showing a much lower performance. The convenience of thermoelectric coolers consists of the absence of moving parts, small dimensions and compactness. The difference in size, compared to the vapor compression technology, is shown in Figure 2.21. The thermoelectric unit is assumed to be assembled with 1 mm of distance between every couple of semiconductors. It is also shown how the dimensions of the single thermoelectric cooler could be reduced if the cooling system was assembled in three modules, instead of just one.

The other quantities, previously defined, characterizing the thermoelectric unit are listed in the table below.

Table 2.5 Other parameters that characterize the TE unit.

	Lower performance semiconductors	*Higher performance semiconductors*
ΔT_{max} (K)	157	212
Q_{max} (W)	0.05	0.07
I_{max} (A)	2.64	2.47
V_{max} (V)	0.26	0.22

2.4.2.3 Thermoelectric cooling - Applications

Research about thermoelectric coolers mainly deals with semiconductor improvement; new materials with better conductive properties are researched. In particular new material treatments are analyzed in order to reduce the material's thermal conductivity and to decrease the thermal flux due to pure conduction.

Poudel et al. (2008) try to increase the figure of merit of Bismuth Antimony Telluride (p-type) by modifying the bulk nanostructure and orienting nanocrystals randomly. In this way a significant reduction in thermal conductivity caused by strong phonon scattering by interfaces in the nanostructures has been determined. A peak of 1.4 has been registered for the figure of merit at 100 °C.

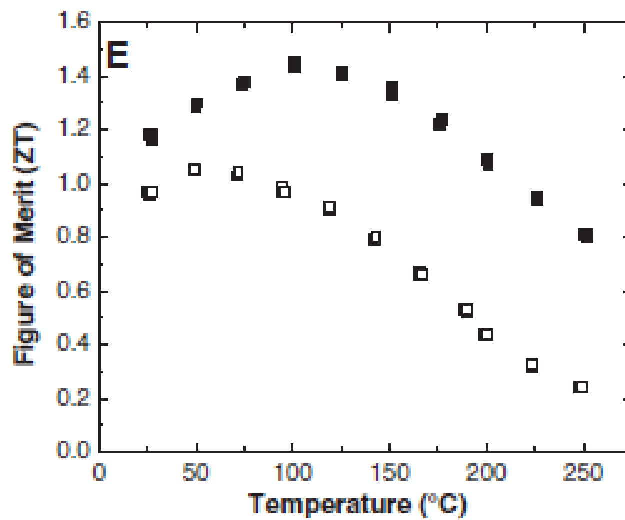

Figure 2.22 Figure of merit vs. Temperature. White squares correspond to the SOA BiSbTe while black ones to the new samples From Poudel et al. (2008). Reprinted with permission from AAAS.

Some similar results and improvements can be found in Zhu et al. (2007). Liu et al. (2012) otherwise, found a way to improve Bi_2Te_3–Bi_2Se_3–Bi_2S_3 (n-type) figure of merit by employing cyclic pressure treatments during the alloy preparation. The increase is now due to the electric conductivity growth and not to the thermal conductivity reduction. Results are not as good as the previous case though.

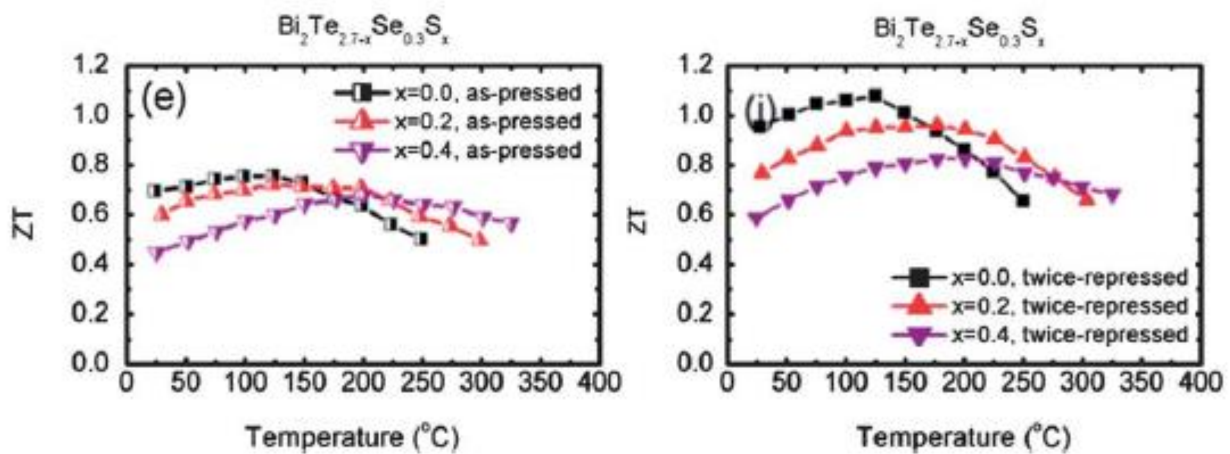

Figure 2.23 Figure of merit vs. Temperature. $Bi_2Te_{2.7-x}Se_{0.3}S_x$ samples. Reproduced from Liu et al. (2012) with permission of The Royal Society of Chemistry.

Other n-type semiconductors improvements are reported in Min et al. (2010). The improvement in performance of thermoelectric modules is an active research topic and new thermoelectric materials are being investigated, as well as new module topologies that can minimize heat leakages and thermal resistances. However thermoelectric cooling has already reached a certain degree of development and thermoelectric modules optimized for high performance or high temperature (200 °C) can be found on the market.

An example of commercial Peltier cooler, with nominal cooling capacity of 56 W, is reported below with the technical characterization.

Table 2.6 Specifications for TE-127-1.0-0.8 from TE Technology.

I_{max} *(A)*	5.8
V_{max} *(V)*	15.7
Q_{max} *(W)*	56
ΔT_{max} *(°C)*	67
Width (mm)	30
Length (mm)	30
Heigth (mm)	3.1

Further details about the design and performance of the TE modules can be found on the data sheets and characteristic curves provided by the supplier, as shown below.

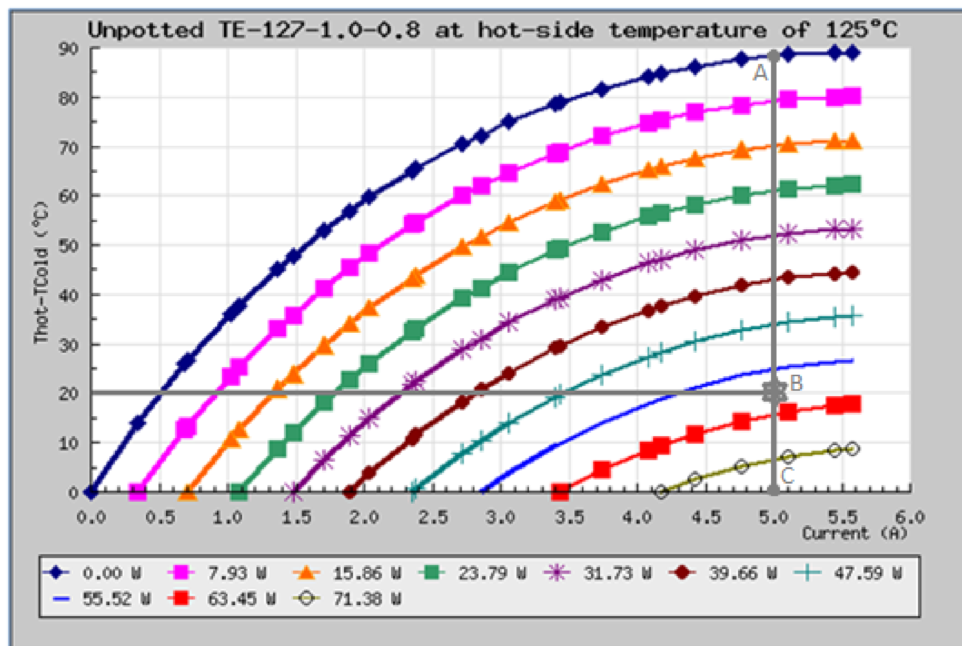

Figure 2.24 ΔT vs. Current, at different cooling loads. Operating point B highlighted by the grey star.

From this graph it is possible to read the required feed current, at given operating conditions: hot side temperature at 125 °C, $\Delta T = 20$°C, cooling load = 60 W. Once the current is known it is possible to read the required voltage from the next graph.

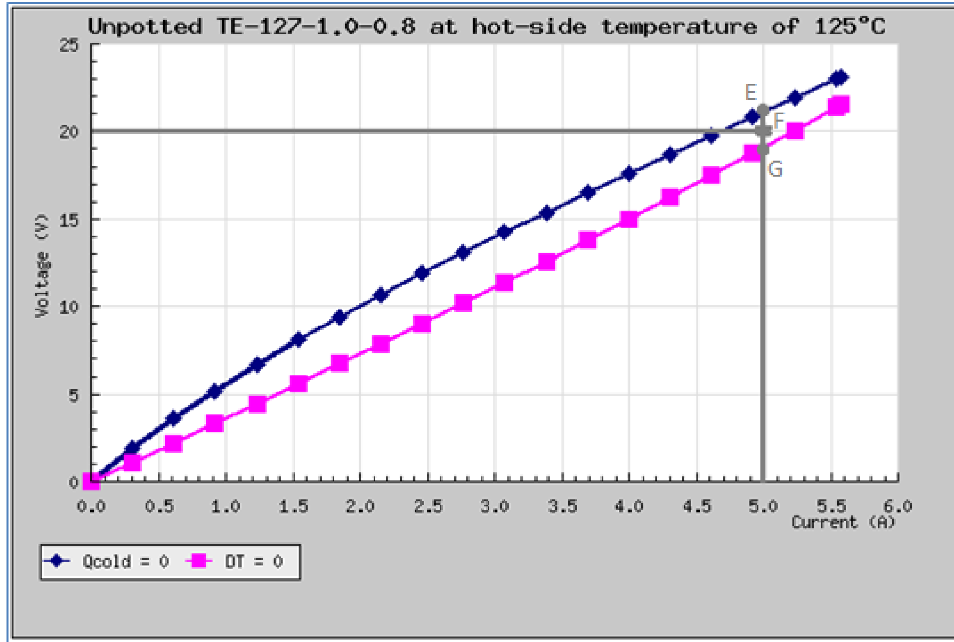

Figure 2.25 Voltage vs. Current. Limit curves for absent cooling load and temperature span equal to zero. Operating point F is highlighted with a grey star.

The placement of the V line can be determined by making the ratio of AB/BC = EF/FG as shown on the graphs above. The result is a required voltage equal to 20 V and a current of 5 A. The feed electric power is equal to 100 W and the COP to 60/100 = 0.6. The wasted heat to be removed from the hot side is equal to 60 + 100 = 160 W.

2.4.3 Reverse Brayton cycle

The reverse Brayton cycle is really similar to the vapor compression one; the four processes characterizing it are almost the same. Nevertheless the employed coolant is a gas and not a two-phase fluid. Condenser and evaporator are substituted with two heat exchangers, respectively at high and low temperature, and only one phase is involved in the circuit. The throttling valve is replaced by an expander that might also recover some mechanical power.

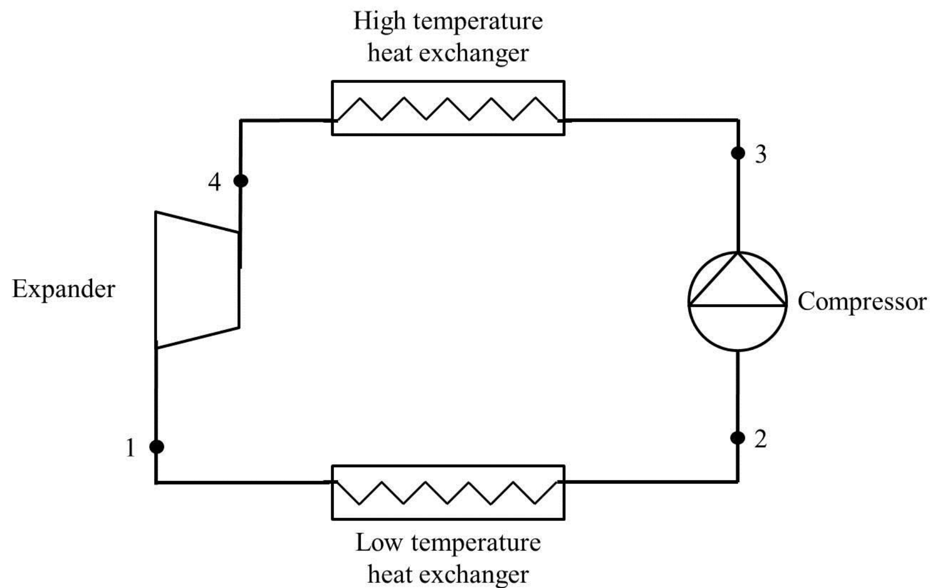

Figure 2.26 Schematic of a reverse Brayton cooling cycle.

The thermodynamic processes are:

- 1 → 2: isobaric/isothermal evaporation (low-temperature heat exchanger)
- 2 → 3: isentropic compression (compressor)
- 3 → 4: isobaric/isothermal condensation (high-temperature heat exchanger)
- 4 → 1: isenthalpic expansion (expander)

The working principle is the same one of the vapor compression cycle. Compared to it, the Brayton cycle is usually less efficient because the heat exchanges are not occurring isothermally; in addition, it requires comparatively larger amounts of gas to be compressed and expanded to produce an equivalent cooling effect, because of a lower density and a lower specific heat capacity.

Coolant gases have to be inert and have a high specific heat ratio (that means good heat transfer properties and lower coolant mass flow rates). Helium is good candidate as refrigerant but also hydrogen, neon, argon, xenon, ammonia, methane, and acetylene could be taken in account. Also air could be an option for its affordability. The most practical circumstances for using an air cycle refrigerator occur if when some power for compression is available from another source, and can be used to decrease the total work input. A qualitative comparison between these candidate refrigerants is provided in *Figure 11* and *Figure 12* from Bennett (1988), where the heat transfer and pressure drop properties of helium, neon, argon, krypton and xenon are compared for laminar and turbulent flow.

Helium appears to be the best candidate for both laminar and turbulent flow applications because it shows the highest heat transfer coefficient and the lowest pressure drops among the studied inert gases. In case of turbulent flow, a mixture He-Xe could also be used in order to obtain a higher heat transfer coefficient. The performance of both helium and xenon in a reverse Brayton cycle is evaluated in the calculation section.

2.4.3.1 Reverse Brayton cycle - Theory

This paragraph explains the theoretical principles at the base of the reverse Brayton cooling process. Thermodynamic laws and diagrams describe the cycle as follows:

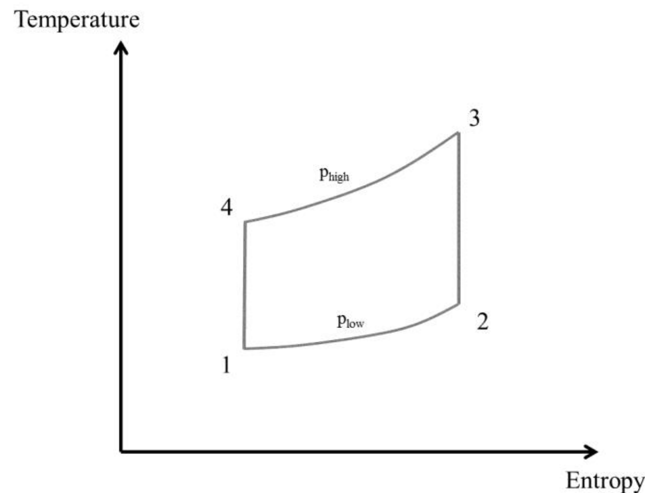

Figure 2.27 Representation of the ideal reverse Brayton cycle on the Temperature vs. Entropy diagram.

In analogy with the analysis of the vapor compression cycle, thermodynamic states and processes of the refrigerant can be individuated along the cycle. The Brayton refrigeration cycle involves two isobaric and two isentropic processes. Differently than the vapor compression cycles, the isobaric heat exchange processes do not occur isothermally.

Cycle thermodynamic steps can be designed starting from the pressure and the temperature at the low-temperature heat exchanger outlet (2).

p_2 is usually set to 1 bar to avoid high pressures, and T_2 can be equal to the cold ambient temperature minus a $\Delta T_{lowT,HE}$ due to irreversibilities.

A compression ratio β has to be defined; the outlet temperature (3) has to be high enough to guarantee a heat rejection to the heat sink. The higher is β and the higher is T_3 and the power to spend in the compressor. Setting β means also setting p_3.

$$p_3 = \beta \, p_2 \qquad (2.46)$$

According to thermodynamic correlations for isentropic compressions:

$$T_{3,is} = \beta^{\frac{\gamma-1}{\gamma}} T_2 \tag{2.47}$$

With temperatures in Kelvin and $\gamma = c_p/c_v$. c_p and c_v are respectively the specific heat capacity at constant pressure and at constant volume of the refrigerant.

Using the isentropic compression efficiency $\eta_{is,c}$, defined as the ratio between the ideal and the real enthalpy difference across the compressor:

$$\eta_{is,c} = \frac{c_p(T_{3,is} - T_2)}{c_p(T_3 - T_2)} \tag{2.48}$$

As already showed for vapor compression cycles, compressors for these applications have low isentropic efficiencies, around 0.44-0.70 (Barbosa et al. (2012)) , 0.24-0.40 (Mongia et al. (2006)). p_4 can be calculated as:

$$p_4 = p_3 - \Delta p_{HT,HE} \tag{2.49}$$

T_4 can be set equal to the temperature of the heat sink plus a $\Delta T_{HT,HE}$ due to the irreversibilities and the heat transfer surface extension. p_1 can be assumed equal to:

$$p_1 = p_2 + \Delta p_{LT,HE} \tag{2.50}$$

$$T_{1,is} = \beta^{\frac{\gamma-1}{\gamma}} T_4 \tag{2.51}$$

Again, using the isentropic expansion efficiency, it is possible to calculate the real temperature in (1). Isentropic expansion efficiency is defined as:

$$\eta_{is,e} = \frac{c_p(T_4 - T_1)}{c_p(T_4 - T_{1,is})} \tag{2.52}$$

Since the gas mass flow rates are small, as well as for the compressor, it is necessary to use micro-turbines and expanders on a mesoscopic scale. That means that $\eta_{is,e}$ can be assumed in the range 50-65% (Qiu et al. (2011)) or 42-68% (Ziviani et al. (2012)), while medium-large size gas turbines can reach isentropic efficiencies of 0.85-0.9.

Once temperature and pressure are known for all the coolant thermodynamic states along the cycle, it is possible to calculate densities with the ideal gas law:

$$\rho = \frac{p}{R^* T} \tag{2.53}$$

Where ρ is the density, p the pressure, and T the temperature.

$$R^* = \frac{R}{PM} \tag{2.54}$$

$R = 8.314472 \frac{J}{mol\,K}$ universal gas constant, PM gas molecular weight.

The minimum required refrigerant mass flow rate is given as:

$$\dot{m} = \frac{Q_{load}}{c_p(T_2 - T_1)} \tag{2.55}$$

Where Q_{load} is the cooling load at the evaporator. The cooling power (assumed to be equivalent to the cooling load) at the evaporator is equal to:

$$Q_C = \dot{m}\, c_p(T_2 - T_1) \tag{2.56}$$

The compression work is equal to:

$$W_c = \dot{m}\, c_p(T_3 - T_2) \tag{2.57}$$

The heat flux rejected to ambient, through the condenser, is equal to:

$$Q_H = \dot{m}\, c_p(T_3 - T_4) \tag{2.58}$$

The mechanical power recovered by the expander can be calculated as:

$$W_e = \dot{m}\, c_p(T_4 - T_1) \tag{2.59}$$

These three quantities are linked by the energy balance:

$$Q_H = W_c - W_e + Q_C \tag{2.60}$$

The coefficient of performance, COP, is computed as:

$$COP = \frac{Q_C}{W_c - W_e} = \frac{c_p(T_2 - T_1)}{[c_p(T_3 - T_2) - c_p(T_4 - T_1)]} \tag{2.61}$$

In the case the expander is just a passive device (valve) and just dissipates energy, the COP becomes like the one for vapor compression cooling.

$$COP = \frac{Q_C}{W_c} = \frac{c_p(T_2 - T_1)}{c_p(T_3 - T_2)} \tag{2.62}$$

As already seen for the vapor compression refrigeration, a term of comparison is given by the Carnot efficiency, which is the maximum COP reachable by a cycle operating between temperatures T_H and T_C; it is definite as:

$$COP_{Carnot} = \frac{T_c}{T_H - T_C} \tag{2.63}$$

Temperatures are expressed in Kelvin.

2.4.3.2 Reverse Brayton cycle - Calculations

The expressions reported in the previous paragraph have been used to carry out some calculations about a reverse Brayton cycle, operating between 175 °C and 200 °C. The assumptions for the calculation are listed below:

- Refrigerant: helium (properties from McCarty (1972)) and xenon (properties from Sifner et al. (1994)).
- Isobaric heat transfer processes (no pressure drops in the heat exchangers).
- Isentropic compression efficiency $\eta_{c,is}$ = 0.60 , Isentropic expansion efficiency $\eta_{c,is}$ = 0.65, electro-mechanical efficiency η_0 = 0.97.
- Refrigerant pinch point temperature span, at heat exchangers outlet $\Delta T_{condenser,outlet}$ = 15 °C , $\Delta T_{evaporator,outlet}$ = 5 °C.
- Compression ratio β assumed according to the optimization reported below.

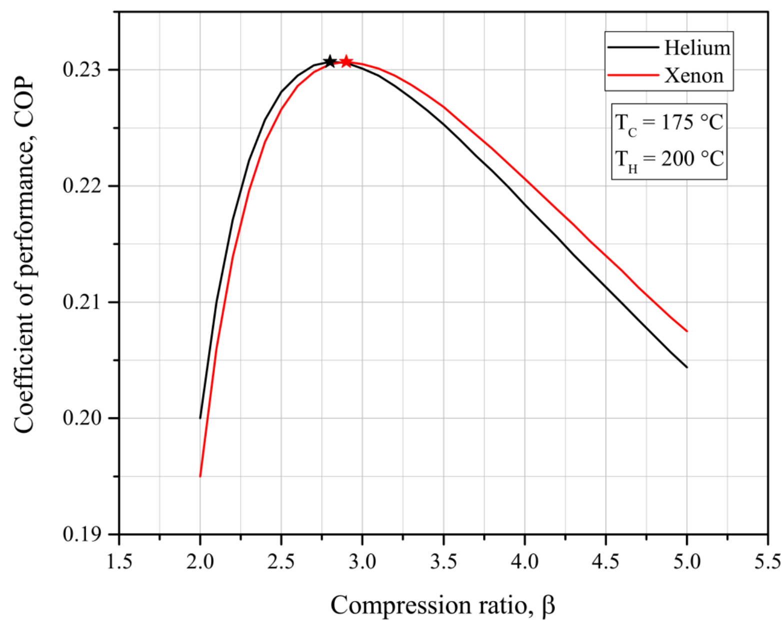

Figure 2.28 COP vs. Compression ratio optimization for helium and xenon for operating between 175 °C and 200 °C.

The maximum COP, in these operating conditions, is reached for β between 2.5 and 3 for both refrigerants. An optimal compression ratio equal to 2.8 is assumed for the calculations. Only the results for helium will be shown since the cycle with xenon performs similarly. Assuming a cooling load of 50 W, refrigerant properties and energetic quantities describing the cycle are shown in the following table.

Table 2.7 Resume of the reverse Brayton cooling cycle with He; cooling load equal to 50 W.

Point	*Pressure (bar)*	*Temperature (°C)*	*Density (kg/m^3)*
2	1	170	0.108
3	2.8	546	0.165
4	2.8	215	0.276
1	1	108	0.126

Pressure ratio	2.8	
Helium flow rate	1.55E-04	(kg/s)
	85.6	(L/min)
Rejected thermal power	267	(W)
Recovered mechanical power (turbine)	86	(W)
Net compression power (turbine)	217	(W)
Net compression power (valve)	303	(W)

Carnot COP	9.85
Ideal COP (turbine)	1.81
Ideal COP (valve)	0.53
COP (turbine)	0.23
COP (valve)	0.17

COPs are much lower than for the vapor compression cycle, also in the case of the mechanical power recovery. Also, the difference with the ideal COP is significant. That is due to the not efficient performance of micro-turbines, which have low isentropic efficiencies. A big amount of power that could be recovered by the expander is otherwise dissipated in frictions and heat. The refrigerant mass flow rate is one order of magnitude bigger than the one for water vapor compression. That is because of a smaller specific heat capacity for gases.

Also in this case, in order to have an idea of the order of magnitude of the heat transfer required areas, a rough parametric study has been done with a variable cooling load, with a laminar flow assumed.

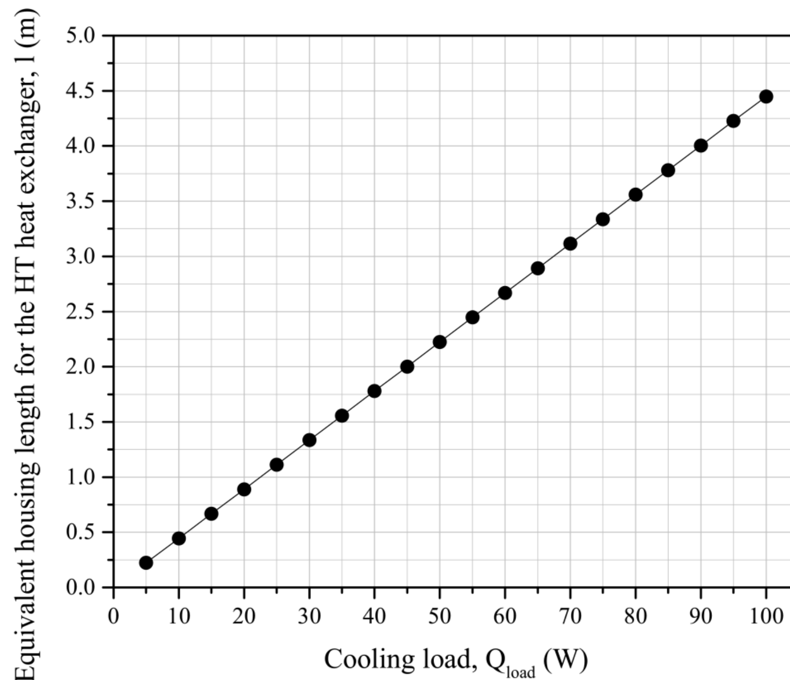

Figure 2.29 Cooling load vs. high temperature heat exchanger extension.

The reverse Brayton cycle can be considered a direct term of comparison with the vapor compression one, since the thermodynamic cycles are, conservatively, very similar. The same considerations done for the condenser of the vapor compression cycle are therefore valid for the reverse Brayton system. With analogue boundary conditions, the required equivalent length for the high temperature heat exchanger has a very similar trend. However, the required heat transfer areas for the Brayton cycle are significantly larger than the ones required by the vapor compression cycle, because of the poorer thermal properties of the refrigerant. Efficiencies are also much higher for vapor compression cycles. These considerations would already exclude the gas refrigeration in favor of the vapor compression.

However, the benefit of the inert gas cycles could lie in the chance of spraying the inert coolant directly on the electronics. This configuration could have one heat exchanger less, and several thermal resistances would be avoided.

2.4.3.3 Reverse Brayton cycle - Applications

Not many applications were found from the literature. Reverse Brayton cycles hardly find a use in common electronics cooling applications, because of the low COP, the presence of moving parts, and the existence of a similar, but much more competitive, technique such as vapor compression cooling. Nevertheless, reverse Brayton cycles have been employed in some space applications for electronics cooling at low temperature. The advantages of this type of technique lie in an extremely low emitted vibration and simplicity of integration with payloads and spacecraft radiating heat rejection systems. The technology was first demonstrated in space in March 2002, when the NICMOS Cryocooler (Swift et al. (2005)) was installed on the Hubble Space Telescope, providing 7 W of cooling at 70 K while using neon as refrigerant and a turbine as expansion device. Zagarola et al. (2009) also developed a two-stage turbo-Brayton cryocooler that uses

neon and one turbine per stage, and was optimized to provide 1.8 W of cooling at 65 K and 12.6 W of cooling at 100 K.

Papers and specific literature have been also useful to retrieve information about the small-size gas turbines. The application that mostly uses this kind of expanders is the ORC system, acronym of Organic Rankine Cycle. These systems are low-temperature thermoelectric plants, for the generation of small amounts of electric power. They use low temperature thermal energy, waste heat or solar collectors, to feed a direct Rankine cycle in which an organic fluid, with a low boiling temperature, is employed. The isentropic expansion efficiency is reported in a review from Ziviani et al. (2012) to be in the range of 0.6 - 0.7 for a pressure ratios above 3.5 and between 0.4 and 0.6 for pressure ratios below 3.5.

2.4.4 Magnetic cooling

Magnetic cooling is probably youngest among the studied cooling techniques, but has shown the potential to compete with more established technologies like vapor compression cycles. It exploits the magnetocaloric effect of ferromagnetic materials to convert a change in magnetic field into a cooling action. The adiabatic magnetization and demagnetization of ferromagnetic materials produce in fact a cyclic and reversible temperature change. This temperature change is maximized around the Curie temperature, where the magnetocaloric effect is maximized because of the material transition from the ferromagnetic to the paramagnetic state.

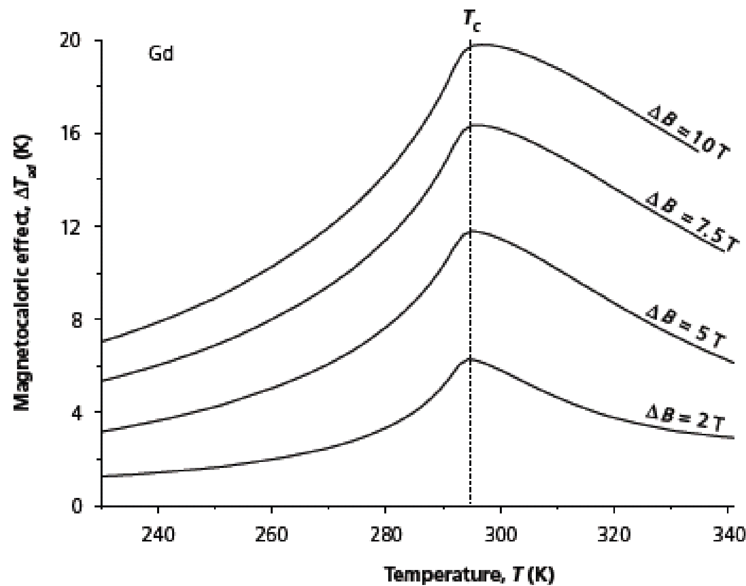

Figure 2.30 Gd magnetocaloric effect vs. operating temperature, for different magnetic inductions (from Pecharsky et al. (2007)).

Figure 2.30 reports an example of magnetocaloric properties for Gadolinium, one of the most suitable ferromagnetic materials for room temperature cooling systems. Gadolinium is widely employed for room temperature applications because it exhibits a Curie temperature of ~293 K, is a pure metal and has a relatively high magnetocaloric effect. Figure 2.30 also shows that the adiabatic temperature differences are not so wide and the energetic expense to induce a ΔT = 20 K is very high (10 T, which requires a superconducting magnet). Most of the currently developed prototypes operate with a magnetic field of 1.5 T, induced by permanent magnets (Kitanovski et al. (2014)) and use regenerative cycles to increase the temperature span.

From the perspective of a cooling cycle, the magnetization and demagnetization processes can be compared, respectively, to the compression and expansion in the vapor compression cycle. The magnetization of the material causes a temperature increase that is proportional to the intensity of the field. The magnetized material can then be cooled down to the ambient temperature, and finally demagnetized. The final temperature of the material is lower than the initial one, and a cooling load can be absorbed, closing the cycle.

Because the change in temperature of the solid refrigerant is low compared to the required temperature span for practical cooling systems, a regenerative cycle is used. A regenerator is employed to periodically receive/release heat from/to a heat transfer fluid. The regenerative material has a porous structure through

which the heat transfer fluid is pumped in an oscillatory counter-flow manner. The four steps characterizing the cycle are illustrated in Figure 2.31 and listed in Table 2.8.

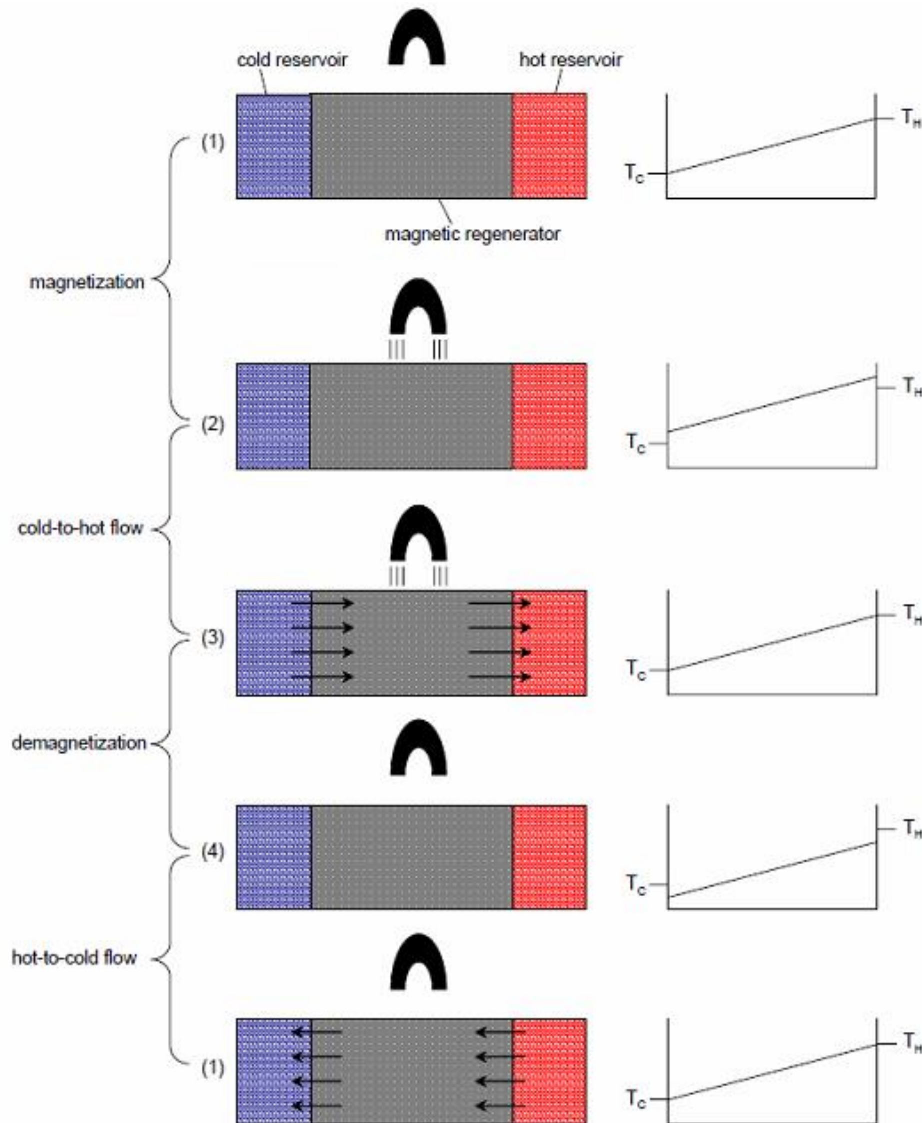

Figure 2.31 Active Magnetic Regenerative Refrigeration Cycle from Engelbrecht (2004).

Table 2.8 Summary of the regenerative magnetic cooling cycle processes, referring to Figure 2.31.

Process	*Refrigerant*	*Heat transfer fluid*
(1-2)	Magnetization	Increasing in temperature / absorbing heat from refrigerant
(2-3)	Magnetized	Releasing heat to heat sink
(2-3)	Demagnetization	Decreasing in temperature / releasing heat to the refrigerant
(1-4)	Demagnetized	Absorbing the cooling load

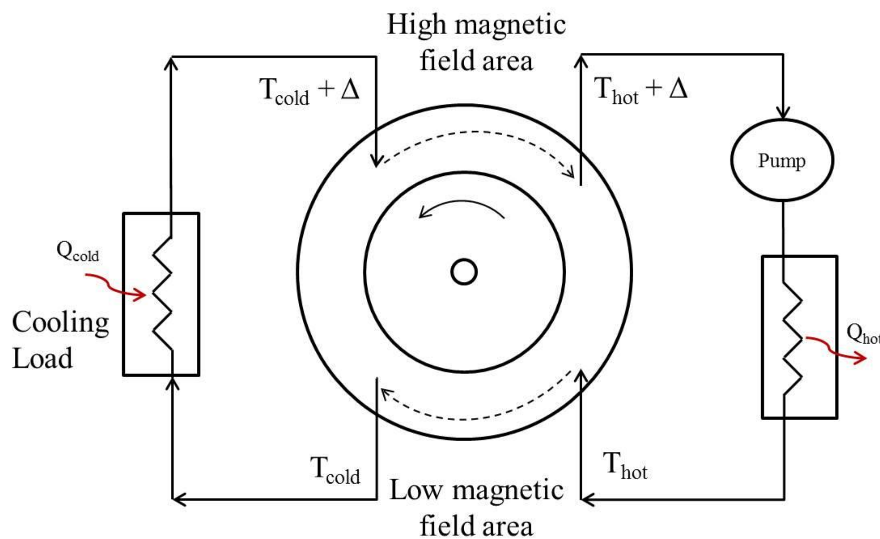

Figure 2.32 Schematic of the Steyert's regenerative magnetic system. Reproduction from Bennett (1988).

The regenerative cycle can be implemented in different system configurations, according to the relative movement between magnets and refrigerant bed (axial or rotating). The Steyert's magnetic system is illustrated in Figure 2.32 as one of the first active magnetic regenerative cycles proposed, in a rotating configuration.

An external ring, containing the ferromagnetic material, is rotated around a magnet which creates one high and one low magnetic field area. A fluid passes through the ferromagnetic material, in the high magnetic induction area, rejecting heat and reaching a higher temperature. A recirculation pump sends it into a heat exchanger where it delivers a heat flux to the external environment. The fluid then passes again through the rotating ring, in the low magnetic induction area, where it is cooled below the initial temperature. It finally refrigerates the cooling load, through a heat exchanger. The cycle is then started again. Water is a good heat transfer fluid for this cycle, although it can corrode many of the magnetocaloric materials in use. Additional fluids can be combined to prevent the corrosion (e.g. ethylene glycol). More than one pole pair can be inserted in the magnet, in order to make the cycle faster and more efficient. In this case the number of fluid circuits must also be increased. Another parameter that influences the performance of the system is the rotation frequency, which determines the size of the absorbed load and the temperature span. The regenerator matrix must be porous to maximize the thermal contact between solid and fluid. Gadolinium, for example, is usually employed in the shape of packed spheres with diameters below 1 mm although many other materials and regenerator geometries have been reported.

2.4.4.1 Materials and applications from the literature

The feasibility assessment for the magnetic cooling technology must start from the evaluation of the material availability for the desired operating temperature range. In particular, a ferromagnetic refrigerant with a Curie temperature in the range 175 °C - 200 °C needs to be found, as well as permanent magnets that can withstand 200 °C.

Important magnetocaloric properties to be considered are the adiabatic temperature difference and the magnetic entropy change. The former, usually indicated with ΔT_{ad} (K), represents the temperature change that the material is adiabatically subject to in case of magnetization/demagnetization, and is proportional to the temperature span that the magnetic cooling system could maintain; the latter, Δs_m (J/kgK), is the entropy change due to the magnetization, and is proportional to the thermal energy that the refrigerant can convert through the active magnetocaloric cycle. As many research works highlight, Gadolinium and its alloys are the most employed magnetocaloric materials for room temperature cooling systems. As previously stated, Gd has a Curie temperature of 293 K and exhibits fairly good magnetocaloric properties (Figure 2.33) with a ΔT_{ad} of 3.3 K and a Δs_m of 3.1 J/kgK, at 1 T (Kitanovski et al. (2014)).

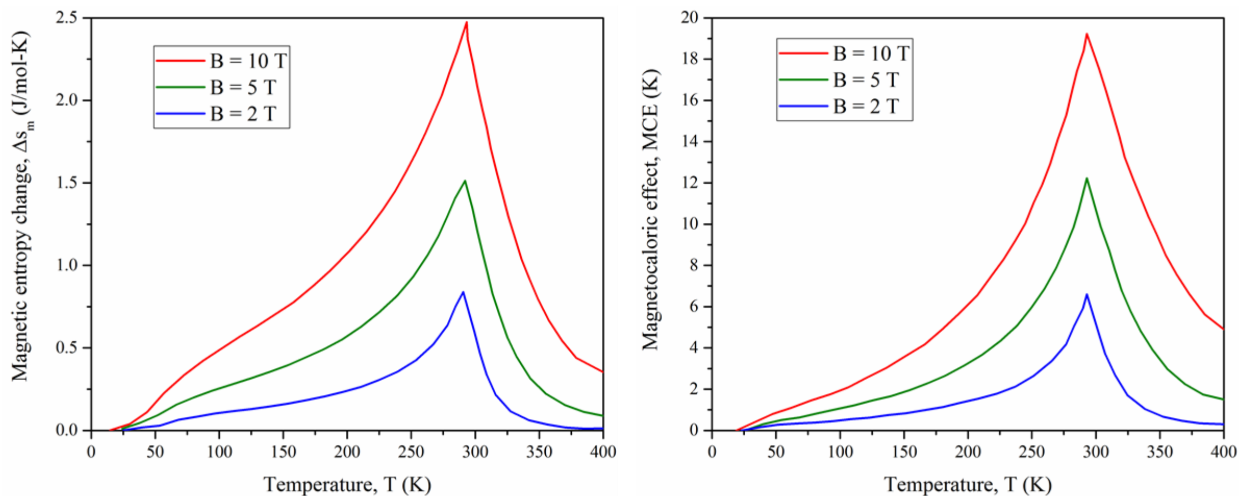

Figure 2.33 Gadolinium magnetic entropy change (left) and adiabatic temperature span (right) trends with temperature. Reproduction from El-Hana Bouchekara et al. (2012).

Other chemical species, like Mn or rare elements (Tb, Dy, Ho, Er), can be combined with Gd to shift the Curie temperature, without drastic changes in the magnetocaloric properties. For instance, Gd - Mn alloys can lower T_C down to 278 K, while the combination between Gd and Tb can generate Curie temperatures in the range from 269 K to 294 K. This turns particularly beneficial when building layered regenerative cycles, where the refrigerant beds are composed of different magnetocaloric materials, with Curie temperatures that follow the steady state temperature profile within the regenerator to maximize the magnetocaloric effect.

La-Fe-Si-based magnetocaloric materials are considered a possible alternative to the expensive Gd-based alloys. Depending on the concentration of the various elements, their Curie temperature can be tuned in the range from 200 K to 340 K. They exhibit a larger magnetic entropy change, compared to Gd, between 5 and 12 J/kgK (with a magnetic field change of 1.6 T), and an adiabatic temperature change (0 → 1.4 T) of 2.8 K (Kitanovski et al. (2014)). The tunable Curie temperature of these materials, their lower cost compared to

Gd, and the possibility of producing them on large industrial scale, make them very attractive for layered active magnetic coolers.

Other studied magnetocaloric materials for magnetic refrigeration are MnAs, and similar compounds, and Manganites. The first exhibit Curie temperatures in the range 150-335 K, while the second in the range 267-370 K (Smith et al. (2012)). They are, however, less attractive than Gd due to the possible toxicity, a high magnetic hysteresis, and lower magnetocaloric properties.

Law et al. (2010) investigated the magnetocaloric effect of $Fe_{80-x}B_{12}Cr_8Gd_x$ compounds. The experimental results show that the T_C of the material can be raised from 350 K to around 410 K by increasing the concentration of Gadolinium. However, the magnetocaloric properties become significantly poorer with the addition of Gd, with a drop in the magnetic entropy change (at 1.1 T) from 1.12 to 0.37 J/kgK. No materials with the Curie temperature above 410 K where investigated from Law et al. Several other research works (Brück et al. (2005), Engelbrecht et al. (2007), Fodeaki et al. (1997), Gschneidner et al. (2005), Pecharsky et al. (2007), Shen et al. (2009)) were consulted to find ferromagnetic materials with a suitable T_C and good magnetocaloric properties. No magnetocaloric materials could be found with a Curie temperature between 448 K and 473 K (Figure 2.34 and Table 2.9). Only FeC was found to have a T_C ~483 K (Bennett (1988)), but no magnetocaloric properties could be retrieved other than the ones summarized in Figure 2.34. By 2014, around 60 active magnetic regenerative prototypes were counted from the scientific literature, evenly split between reciprocating and rotating. The wide majority of the prototypes employed Gadolinium and Gd alloys, while only a small number (8 out 60) used La-Fe-Si-based or Mn-based materials (Kitanovski et al. (2014)). All the mentioned prototypes operated near room temperature.

Also the selection of suitable permanent magnets did not lead to encouraging results. The most commonly employed magnets in magnetic refrigeration are Nd-Fe-B permanent magnets. They exhibit the highest magnet flux density, a high remanence and a relatively high coercivity. However, their high sensitivity to temperature limits their use and their competitive properties to room temperature applications. Nd-Fe-B magnets can be employed in applications up to 230 °C (ndfeb-info), but with a significant drop in the magnetic properties. The required concentration of Neodymium increases significantly with the temperature, exponentially increasing the cost of the magnets. Sm–Co magnets are also competitive solutions, based on rare-earth elements and with similar properties to Nd-Fe-B at high temperature. They are characterized by a lower sensitivity to temperature than Nd-Fe-B and can be employed up to 300-350 °C (ndfeb-info), but are even more expensive than Nd-Fe-B magnets. Other permanent magnets available on the market are based on ceramic materials (ferrites) or on Al-Ni-Co structures. They both have poorer magnetic properties compared, to Nd-Fe-B and Sm-Co, and have not been employed in the magnetic refrigeration field (Kitanovski et al. (2014)).

Since no suitable refrigerant and magnets were found for the downhole operating temperature range, magnetic cooling was excluded from the candidate cooling technologies for downhole applications.

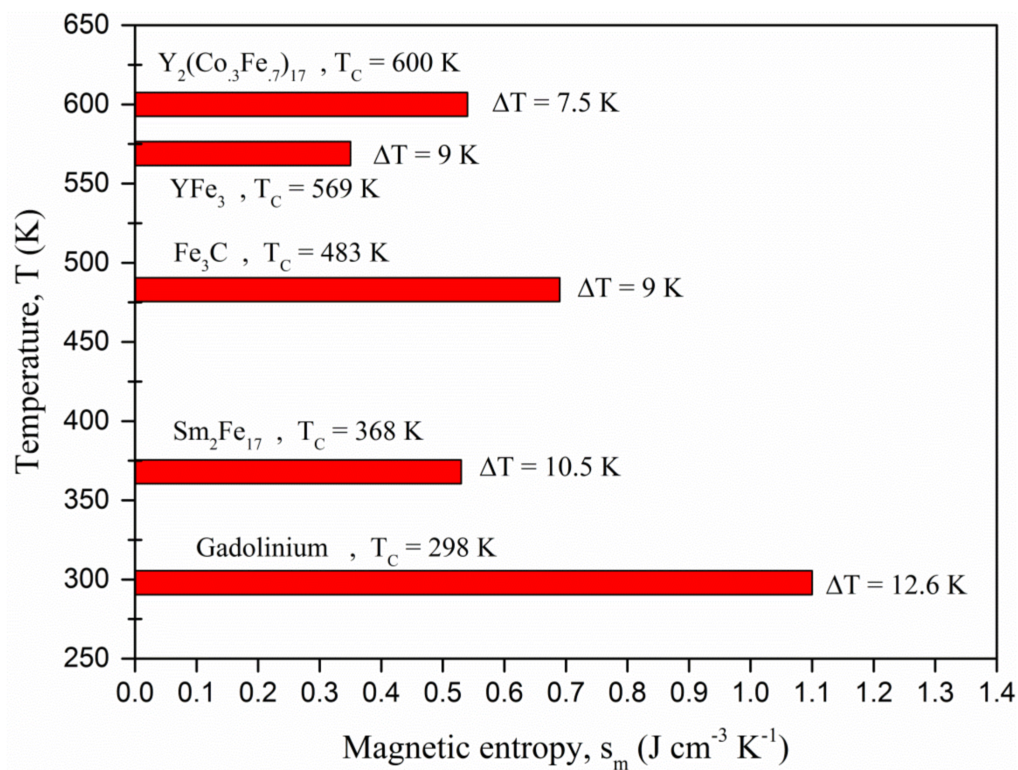

Figure 2.34 Curie temperature and magnetic entropy for several ferromagnetic materials (reproduction from Bennett (1988)).

Table 2.9 Curie temperatures for different ferromagnetic materials (source: **www.**hyperphysics.phy-astr.gsu.edu/hbase/tables/curie)

Material	*Curie temperature (K)*
Fe	1043
Co	1388
Ni	627
Gd	293
Dy	85
$CrBr_3$	37
Au_2MnAl	200
Cu_2MnIn	500
MnAs	318
MnBi	670
$GdCl_3$	2.2
Fe_2B	1015
MnB	578

2.4.5 Phase change materials (PCM)

This category of cooling systems is on the edge between passive and active cooling. It does not require any energy input, but can still cool down the electronics below the well temperature for a limited time period.

PCMs are widely used for storing thermal energy as they are usually characterized by a high latent heat and, if thermally connected to a heat source, they can maintain the load to the phase-change temperature for a certain period of time. Unlike the sensible heat storage method, the latent heat storage method provides much higher storage density, with a smaller temperature difference between storing and releasing heat.

Usually, the phase transition that is considered for energy storage applications and thermal management of electronics is from solid to liquid. That is because the phase transition from liquid to gas, although is usually characterized by a larger latent heat, can generate high pressures inside the storage vessel. The liquid phase has in fact a much higher density than the vapor phase. The change of phase from solid to liquid causes instead a material density change which is much smaller, but that still has to be taken into account to avoid unexpected stresses. PCMs can belong to different material groups and their physical properties depend on the chemical composition (Farid et al. (2004), Xu et al. (2015)).

A comprehensive review of the most investigated PCMs can be found in Cabeza et al. (2011). Several tables list the thermophysical properties of different PCMs used in the literature. *Figure 2* reports the main groups of PCMs on a diagram of melting enthalpy vs. melting temperature and shows their range of operation.

- Eutectic water-salt solutions have melting temperatures between -100 ˚C and 0 ˚C, and melting enthalpies that range between 200 and 300 MJ/m^3.
- Paraffins, fatty acids, and polyethylene glycols have melting points between 0 ˚C and 200 ˚C and melting enthalpies between 100 and 200 MJ/m^3.
- Clathrates, salthydrates, and sugar alchools also have a melting temperature between 0 ˚C and 200 ˚C, but higher melting enthalpies between 200 and 600 MJ/m^3.
- Nitrates and hydroxides have melting temperatures that range between 200 ˚C and 400 ˚C and melting enthalpies between 200 and MJ/m^3.
- Finally, chlorides, carbonates, and fluorides have melting temperatures between 400 ˚C and 800 ˚C, with melting enthalpies from 600 to above 1000 MJ/m^3.

Melting temperature and enthalpy are only two of the main material properties that must be evaluated when selecting a PCM for an energy storage application. A summary of the main thermophysical properties characterizing the behavior of PCM for thermal energy storage is listed below.

- *Phase-change (melting) temperature (°C)*: it is the temperature at which the heat transfer at constant temperature occurs, and at which the load is desired to be maintained. In case of downhole electronics thermal management, it must be as close as possible to the maximum operating temperature of the components, in order not to waste cooling capacity because of the heat leakages through the thermal insulation.
- *Volumetric melting enthalpy (MJ/m^3)*: it is the amount of energy the material is able to absorb at constant temperature, per unit of volume, while changing phase. In case of downhole electronics

thermal management, it is proportional to the time period during which the electronics can be maintained at the material phase-change temperature.

- *Specific heat capacity (kJ/kg-K)*: it is the amount of heat required by a kilogram of PCM to increase its temperature of one Kelvin. It is preferred to have material with high specific heat capacity in order to increase the heat storage capacity outside the phase transition process.
- *Thermal conductivity (W/m-K)*: PCM materials used for thermal storage at or near room temperature usually have a low thermal conductivity, which can cause the creation of hot spots in the heat load. Higher thermal conductivities are preferred in order to have a more uniform heat transfer through the PCM and consequently a more uniform phase change. An opportune heat spreading system needs to be designed.

Additional properties which are desired in a PCM are a high density, chemical stability, low density variation during the phase transition, non-flammability, non-toxicity, and compatibility with a wide range of materials.

2.4.5.1 Phase change materials - Theory

For first approach calculations, the amount of PCM that is required to maintain downhole electronics below a certain temperature, and for a certain period of time, can be computed using the lumped approach.

$$Q_{load}(t_1 - t_0) = m_{PCM}c_{PCM,s}(T_{PC} - T_0) + m_{PCM}c_{PCM,l}(T_C - T_{PC}) + \Delta H_{lat} \quad (2.64)$$

Where Q_{load} is the cooling load, $(t_1 - t_0)$ is the time period in which the tool is able to operate below the desired temperature T_C, m_{PCM} is the required mass of PCM, T_0 is the initial PCM storage temperature, T_{PC} is the phase change temperature, $c_{PCM,s}$ and $c_{PCM,l}$ are the specific heat capacity of the material respectively in the solid and liquid phases, and ΔH_{lat} is the melting enthalpy or latent heat of fusion.

2.4.5.2 Phase change materials - Calculations

Eq. (2.64) has been used to calculate the required amount of PCM and the equivalent storage tank length (inner diameter assumed equal to 5.5 cm) that would be required to maintain some electronics below T_C = 175 °C for 4, 8, and 12 hours. Furthermore, it is assumed that the initial PCM storage temperature T_0 is equal to 20 °C and that the specific heat capacities for the solid and liquid phases are the same.

The external well temperature T_H is not appearing in the equation since it does not influence directly the exercise of this cooling system, like happened with the previously analyzed technologies. T_H is influencing the thermal flux incoming in the tool, hence the cooling load, which in our analysis has been kept variable.

The PCM properties reported in Table 2.10 have been used in the calculations.

Table 2.10 PCM material properties (source: www.pcmproducts.net).

Material	*Melting temperature (°C)*	*Density (kg/m³)*	*Volumetric melting enthalpy (MJ/m³)*	*Specific heat capacity (kJ/kg-K)*
Organic A164	164	1500	435	2.42

The results of the analysis are reported in Figure 2.35.

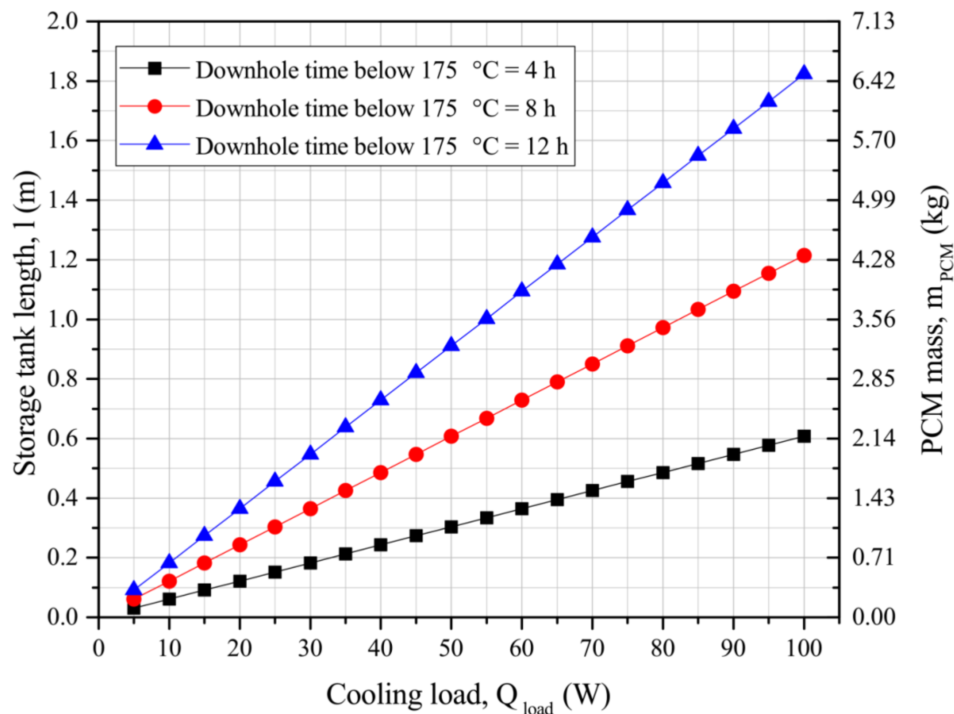

Figure 2.35 Length and mass of a PCM based cooling system vs. cooling load, at different downhole residence times.

These calculations provide a first approach idea of the dimensions of a downhole cooling system based on phase change materials. More detailed analyses should also consider that a heat spreading system (i.e. flow loop, heat pipes, thermally conducting particles, metallic encapsulation of the PCM) would be needed to thermally link the electronics to the heat sink. This heat spreading system would aim to uniformly reject the excessive heat and avoid hot spots in the PCM bed, which would make the change of phase uneven as well as the cooling action. The impact of the heat spreading system dimensions on the availability of space for the PCM storage has to be accounted. A larger heat spreading system would make the heat rejection more uniform, but would also increase the dimensions of the tool and, consequently, the thermal load due the heat leakages. The weight of the system should also be taken into account as it could affect the logistics of the downhole tool.

2.4.5.3 Phase change materials - Applications

Phase change materials are used for many thermal management applications, in different fields.

- They are used for passive heat storage in buildings to decrease the heating loads and provide a higher thermal inertia to the building.
- PCMs are commonly used for electronics thermal management and protection.
- They are used for off-peak power utilization, where the electric energy exceeding the load is converted into heat or cooling.

- PCM can be used in the food industry to maintain product below ambient temperature, when no electric power is available (e.g. transportation).
- They can be employed in the clothing industry to create special clothes with body temperature regulating properties.
- They are also used for medical applications (i.e. transportation of blood, operating tables, hot-cold therapies).

A good example of electronics thermal management through PCMs is reported in Kandasamy et al. (2007). A thermal protection system is designed and an experimental setup is built to simulate the applications of typical portable electronic devices. A package of PCM is built and a flat heater is positioned on a side of the package to simulate the electronics heat load. Tests were carried out for different power dissipation rates and on-off cycle frequencies of the heater. Thirty-one thermocouples monitored the temperature gradient across the PCM bed and an IR camera could capture the temperature evolution of the system through the transparent casing. Results are compared to the model predictions and the influence of the PCM thermal properties, in particular of the low thermal conductivity, is discussed.

The work from Jakaboski (2004) about electronics thermal management through PCMs was described and analyzed in Section 1.2. Building on Jakaboski's work, some further general considerations regarding the use of PCMs in downhole tools are reported next, starting from the qualitative evaluation of their effect on the electronics temperature evolution in time (Figure 2.36).

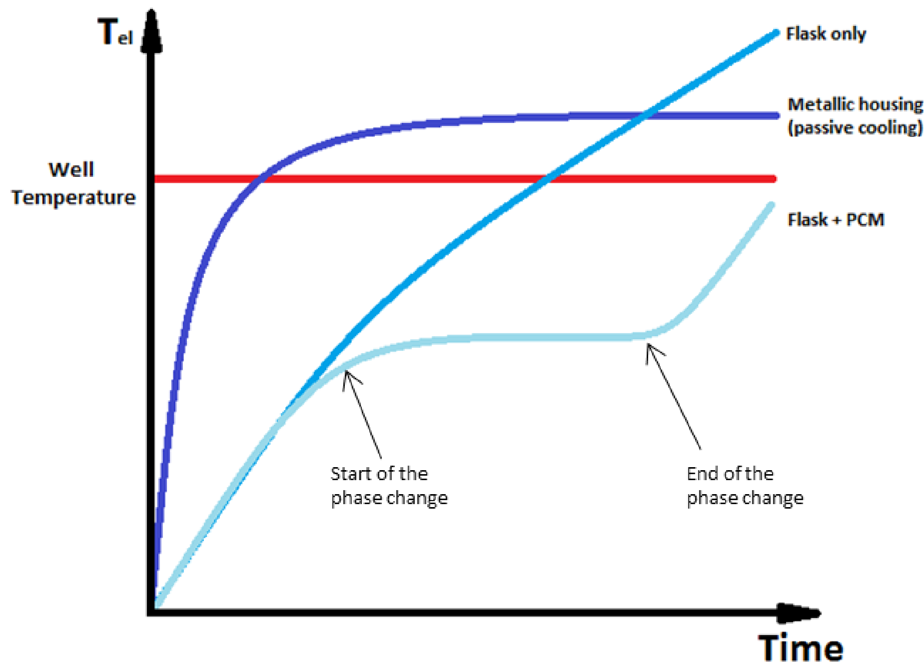

Figure 2.36 Qualitative representation of the temperature trend in time of the electronics in case of passive cooling (dark blue curve), use of a flask (blue curve) and use of a flask + phase change materials (light blue line).

The integration of phase change materials into a downhole tool requires the employment of a Dewar flask. The flask is significantly beneficial for this type of systems, since it minimizes the heat load due to thermal leakages through the housing and significantly increases the available exposure time downhole. Compared to

the use of a Dewar flask only, we can say that phase change materials "can buy some extra exposure time downhole". The extra-time extension is proportional to the electronics efficiency and depends on some important properties of the PCM; these properties become important design parameters for the system.

- No feed power is requested, unless a flow loop is used.
- The performance of the system can be evaluated with the "available exposure time downhole" and the system compactness, instead of the COP.
- The system is approximately independent from the well fluid flow conditions, contrarily to other systems which rely on the heat rejection to the well.
- The required amount of PCM, for a certain exposure time at a certain well temperature, can be calculated in first approximation from the electronics power dissipation rate.
- The melting temperature of the system should be as close as possible to the maximum operating temperature of the electronics. PCM for high temperatures are commercially available.

The type of integration into a downhole tool has to be assessed according to the design constraints and the availability of space inside the device. The electronics could either be mounted directly on a metallic box containing the PCB or be thermally coupled with the PCM, located in an additional tool section, through a heat spreading system. Lumped properties calculations and finite element simulations can support and evaluate the feasibility of such a system.

2.5 Theoretical feasibility study conclusions

In this chapter, the main active cooling technologies currently available have been analyzed in terms of their strengths and weaknesses. Theoretical models and first-approach calculations, supported by a review of the scientific literature, have been used for this purpose. A summary of the findings from such feasibility study is provided in Table 2.11 and further articulated in this section.

Table 2.11 Feasibility evaluation matrix for the analyzed cooling technologies.

* Fair/poor ** Marginal *** Good **** Very good

Technology	*Efficiency*	*Packaging*	*Cost*	*Required development*	*Feasibility*
Vapor compression cycle	****	***	**	**	**
Themoelectric cooler	*	****	****	****	***
Reverse Brayton cycle	*	**	**	**	**
Magnetic cooler	***	*	*	*	*
Phase change materials	/	***	***	***	***

Some of the analyzed technologies have shown objective limitations that prevent them from being integrated into the well tractor electronics section. Magnetic refrigeration, for instance, proved to be not compact enough, and without good refrigerants for the required operating temperature range. The reverse Brayton cycle showed similar features to the vapor compression systems, but exhibited much lower efficiencies and significantly larger required heat transfer areas.

On the other hand, vapor compression cycles, thermoelectric coolers and PCMs represent suitable options for implementation in the well tractor electronics section. The advantages and drawbacks of each of the three technologies are summarized in the three tables below.

Table 2.12 Vapor compression cycles.

Benefits	*Drawbacks*
It can operate with large cooling loads and temperature spans	Not very compact technology (requires a compressor, two heat exchangers and an expansion valve)
High coefficient of performance	The HT(~200 ^{0}C) compressor needs to be designed, since not commercially available
Low power consumption and low heat flux to be rejected to the well	Large development time and costs (HT compressor is the critical component)

The downhole operating time is only limited by the life span of the components	It involves moving parts (compressor) and a fluid loop
	An additional tool section is required for the heat rejection from the coolant to the well
	It requires a suitable power supply for the compressor

Table 2.13 Thermoelectric cooling.

Benefits	*Drawbacks*
Very compact (~ from 10x10x3 to 40x40x4 mm)	Low cooling efficiency (Coefficient of Performance)
The coolers do not have moving parts	High heat fluxes to be rejected to the well
The coolers can be directly integrated into the electronics section, preserving the tool length	Coolers require a suitable power supply
HT Peltier coolers are commercially available (~ 20 - 40 $/piece)	
The downhole operating time is only limited by the life span of the components	

Table 2.14 Phase-change materials.

Benefits	*Drawbacks*
No additional power consumption	PCM need to be coupled with the flask technology
No moving parts	The chassis needs a different design
Heat pipes can interface the electronics with the heat sink given by the PCM	An additional section is required for the storage of the PCM; the length of this section is proportional to the power dissipation rate of the electronics (~0.2-1.5 m)
The electronics thermal profile does not depend on the well fluid flow conditions	The downhole operating time is strictly correlated to the power dissipation rate of the enclosed electronics.
PCMs “buy” an additional operating time downhole, compared to the only use of the Dewar flask	The downhole operating time is strictly correlated to the history of the intervention and to the temperatures at which the tool is exposed.

The development of a reliable HT compressor represents a very critical point for the implementation of the vapor compression cycle. As it has been also reported in the literature, its development requires a significant amount of resources, which makes this technology less attractive for downhole electronics refrigeration. Phase change materials, instead, represent a fairly simple solution to implement in a downhole electronics section. They do not necessarily involve moving parts, can be integrated without any electrical connection, and do not rely on a high heat transfer rate between the tool and the well environment. However they can only guarantee a limited time below the maximum electronics temperature, which is also strictly related to the history of the well intervention and of the temperature exposure. Furthermore, the design of the well tractor electronics section should be re-organized and increased in length.

Considering the compactness of the tool a very important parameter to preserve, thermoelectric coolers represent a more suitable solution. They could be integrated directly in the existing electronics unit, without increasing the existing size of the tool. They also do not have moving parts and can guarantee a theoretically unlimited cooling time period downhole. However, their low COP might lead to large heat fluxes to reject to the well and require some advanced heat dissipation systems to avoid an overheating of the cooling system and of the electronics. The coolers integration scheme and thermal management principle is analyzed in detail and illustrated in the following chapters.

3. Thermal modeling of the well tractor electronics

This chapter aims at introducing the well tractor electronics section, and gives an overview of the tool geometry and electronic components. A particular focus is put on the thermal characterization of the electronics in terms of thermal integration in the tool, power dissipation, and maximum operating temperature. The calculation of the electronics power dissipation rates is crucial for the definition of the cooling load for the active cooling system.

It was first thought to measure this quantity directly, by measuring voltage and current before and after each electronics group and calculating the difference of the powers. However, the complexity of the system and a difference of two orders of magnitude between the power transmitted through the electronics and the actual dissipated power, made this approach very challenging, and therefore the datasheets and the operating conditions of each component have been used to evaluate the electronics power dissipation rates. They were then implemented in a thermal model of the well tractor and validated with experiments.

3.1 Well tractor electronics section

Figure 3.1 shows a detailed 3D model of the well tractor electronics section where the metallic cartridge and the electronic components can be observed. The metallic housing is not included in the main figure for the sake of a clearer representation.

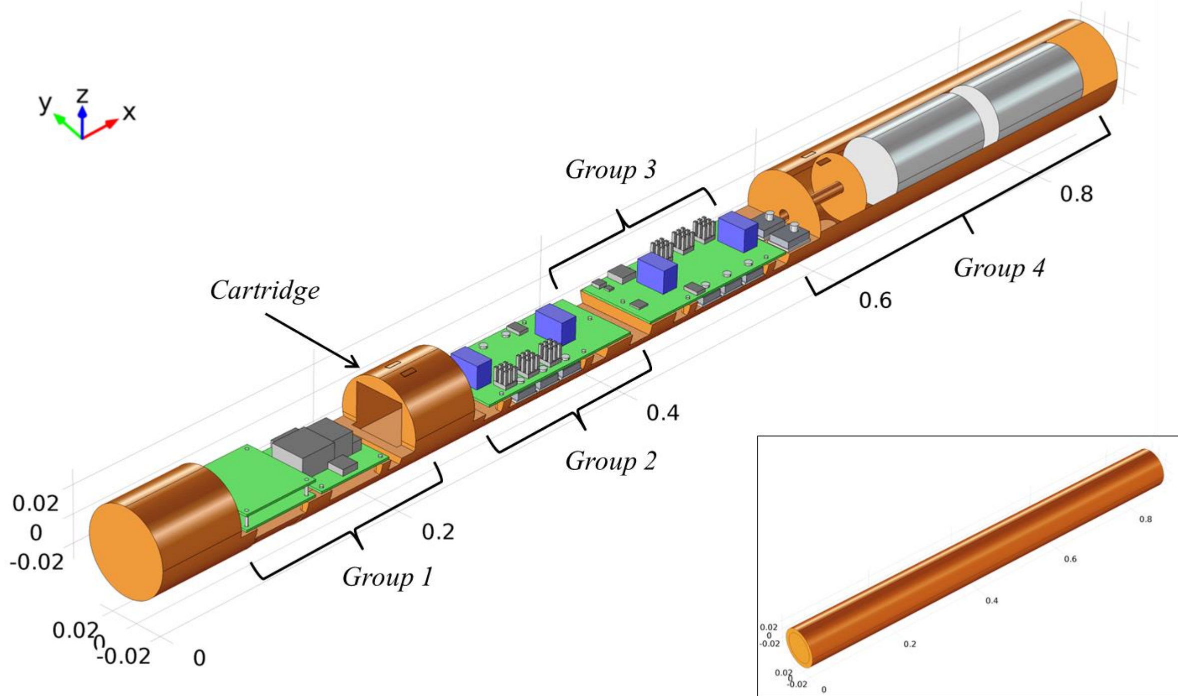

Figure 3.1 3D CAD model of the well tractor electronics section. The main components are illustrated. A surface of the cartridge is hidden to show two of the components from *Group 4*. The complete tool, inclusive of the housing, is shown in the smaller picture. The overall length of the tool is approximately 0.9 m.

The ~0.9 m long metallic cartridge represents the solid and thermally conductive support on which the electronics are installed. Electronic components are either mounted on the cartridge (power devices or PDs) or on printed circuit boards (PCB). The first are interfaced to the metallic support through an alumina plate and some thermal grease; they are characterized by a low thermal resistance to the well, as both the cartridge and the housing are good thermal conductors. The latter are soldered onto a circuit board; they are characterized by a higher thermal resistance towards the well, as the PCB material is usually not a good thermal conductor and the boards are surrounded by air, which acts as an insulator. The electronic components within the tool can be defined as either active or passive, depending on whether or not they dissipate any power during the tool operations. Furthermore, some electronics could be replaced by high-temperature components and others could not because of unavailability from the market, space constraints, or prohibitive costs.

In Figure 3.1, electronics are divided into four different groups, each of them characterized by different tasks, located on different sections of the cartridge, and composed of different components. This grouping approach is useful to assess which are the critical sections that dissipate the most power, where the hot spots are located, and which sections need active cooling. The datasheet of the electronic components was used to estimate their power dissipation rate, according to the reference operating conditions. The operation at "full load" was chosen as a reference condition in order to estimate the maximum dissipated heat flux. The results of this study contribute to the calculation of the cooling load and the dimensioning of the integrated cooling system.

Table 3.1 reports a list of the main components installed in the well tractor electronics section, with their dimensions, while an overview of the well tractor electronics components is reported in Table 3.2.

Table 3.1 Main components of the well tractor electronics section and their geometrical features.

Component	*Material*	*Dimensions*	*Quantity*	*Thermal conductivity (W/m-K)*
Cartridge	Metallic alloy	O.D. 62 mm Length 872 mm	1	105 @ 20 °C 145 @ 200 °C 155 @ 300 °C
Housing	Metallic alloy	O.D. 80 mm I.D. 62 mm Length 872 mm	1	105 @ 20 °C 145 @ 200 °C 155 @ 300 °C
Square PCB	FR4	57 x 57 x 1.6 mm	3	0.3 through-plane 20 in-plane (Graebner et al. (1997))
Long PCB	FR4	126 x 57 x 1.6 mm	3	0.3 through-plane 20 in-plane (Graebner et al. (1997))
Electronic PDs	Semiconductor substrate	20 x 16 x 5 mm	14	130
Cylindrical components	Aluminum alloy	Ø 47 x 87 mm	2	160
Screws	Aluminum alloy	M4 x 12	32	170
Alumina plates	Alumina	21 x 18 x 1 mm	14	27
Passive PCB components	Plastic	Variable	Multiple	0.26
Active PCB components	Semiconductor substrate	Variable	Multiple	130

Table 3.2 Characterization of the well tractor electronic components.

	Component	*Location*	*Estimated power dissipation rate (W)*	*Max. operating temperature (°C)*	*Active or Passive? (A/P)*	*HT version availability ? (Y/N)*
Group 1	PCB	On PCB	1.2 W in total	175	A	Y
Group 2	6 x PD	On cartridge	2.6 W/pc @ 25 °C 3 W/pc @ 125 °C	175	A	Y
	PCB	On PCB	0.7 W in total	175	A	N
Group 3	6 x PD	On cartridge	2.6 W/pc @ 25 °C 3 W/pc @ 125 °C	175	A	Y
	PCB	On PCB	1 W in total	175	A	N
Group 4	1 x PD	On cartridge	0 W	175	P	Y
	1 x PD	On cartridge	4.7 W/pc @ 25 °C 3.8 W/pc @ 150 °C	175	A	Y
	2 x Cylindrical components	On cartridge	0 W	175	P	Y

The total estimated heating rate of the well tractor electronics, at full load, is estimated ~38 W at 25 °C, and ~43 W at 150 °C. The components with the higher heating rates are installed on the cartridge and can be replaced by high temperature ones. Only ~4 W come from the components installed on the PCB, ~2 W of which come from components without HT replacements available.

3.2 Well tractor thermal model

The geometry illustrated in Figure 3.1 was implemented in a finite element model to simulate the heat transfer within the well tractor electronics. The software COMSOL Multiphysics (COMSOL Multiphysics 5.0) was used for this purpose. In order to simulate the heat transfer phenomena and obtain the steady state temperature distribution across the tool, the heat transfer PDE was implemented as governing equation.

$$\nabla \cdot (-k\nabla T) = Q_{source} \tag{3.1}$$

Where k is the material thermal conductivity, T is the temperature and Q_{source} is a volumetric heat source.

Eq. (3.1) was solved over the whole simulated geometry, including the air domain surrounding the components inside the housing. No free convection phenomena were simulated within the air domain, although they would be expected to increase the heat exchange rate between the electronics and the well.

Their contribution to the heat transfer within the tool was considered negligible, compared to the thermal conduction, and not worth the additional computational cost that their implementation would have required.

The materials and the thermal properties reported in Table 3.1 were assigned to each component. The thermal conductivity values for the cartridge and the housing were interpolated with a piecewise cubic Hermite polynomial. The temperature-dependent properties provided by COMSOL, from ASHRAE (1993), were used for the air domain.

A heat source was assigned to every active electronic component, according to the power dissipation rates reported in Table 3.2. While the PCBs were characterized by constant power dissipation, a heating rate that depends on the operating temperature was assigned to the PDs. The data available from the datasheet were interpolated to build a correlation between these two quantities. A linear interpolation was used for PD_2 and PD_3. A decreasing exponential function was used for PD_4, in accordance to the trend of the resistivity of certain semiconductors with temperature (see Figure 3.2). Outside the interpolation range, the power dissipation was conservatively assumed constant.

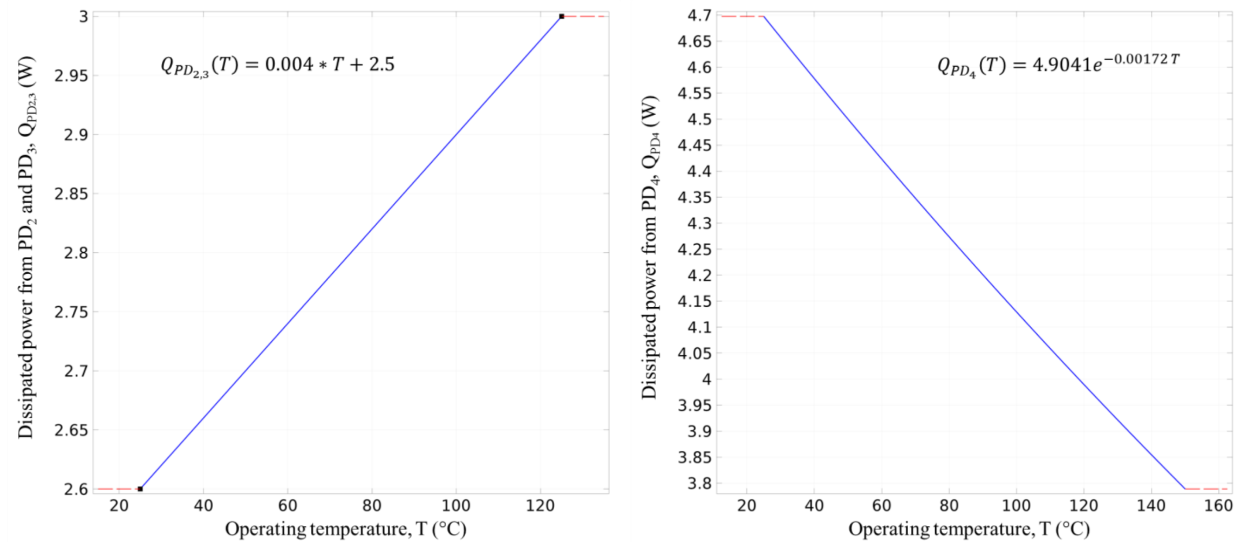

Figure 3.2 Power dissipation trend with temperature for the PDs in the electronic groups 2 and 3 (left), and 4 (right).

While the alumina plates, which are mounted at the interface between the PDs and the cartridge, were included in the simulation as domains, no thermal grease layers were built in the geometry. For this reason an equivalent thermally resistive layer was inserted at the interface between the PDs and the Al_2O_3 plates, as well as between the Al_2O_3 plate and the cartridge. A thermal resistance $R_{th,grease}$ = 2.5e-5 m^2K/W was set, equivalent to a 0.1 mm thick layer of thermal grease with a conductivity of 4 W/m-K.

Additionally, a thermal resistance was set at the interface between the cartridge and the housing. In order to assemble the two cylindrical parts, a certain clearance needs to be maintained, and the air occupying such clearance acts as thermal insulator and introduces an additional thermal resistance. For an effective passive cooling, this air gap should be reduced as much as possible. The housing and the cartridge have been modelled with the same diameter, not to introduce small mesh elements (< 1 mm) that would significantly increase the computational cost. To account for this thermal resistance the profile of the air gap was analytically reproduced, as conceptually shown in Figure 3.3. A profile of the air gap thickness was defined along the coordinate z (refer to Figure 3.1), and implemented in the model as a thermal resistive layer. The

thermal transmittance of the layer was set equal to the thermal conductivity of air and dependent on the operating temperature.

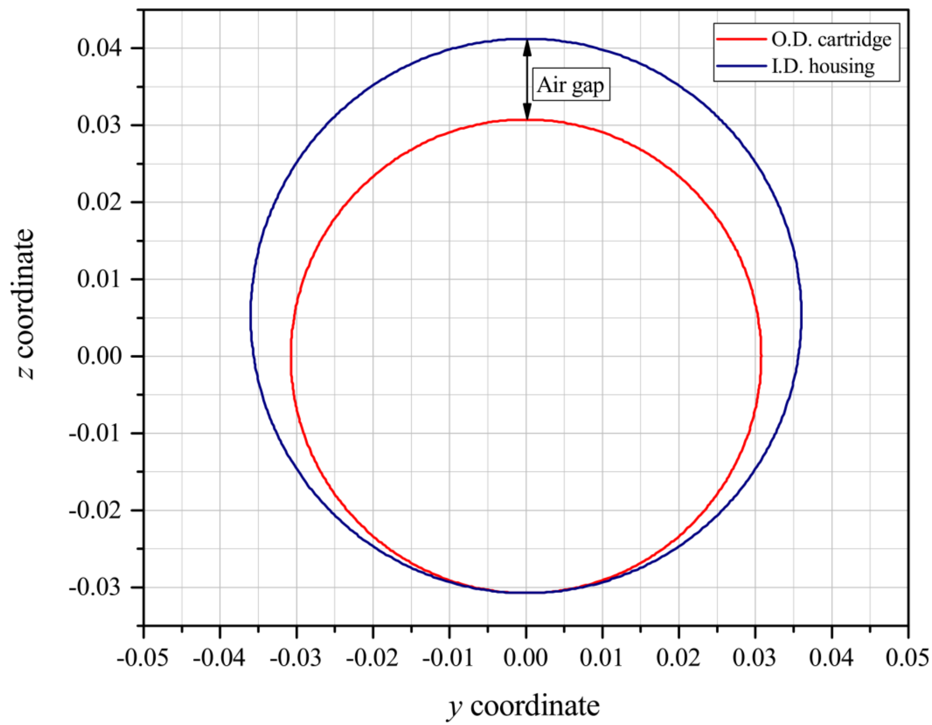

Figure 3.3 Air gap profile between cartridge and housing. The housing I.D. is purposely scaled up to better show the concept.

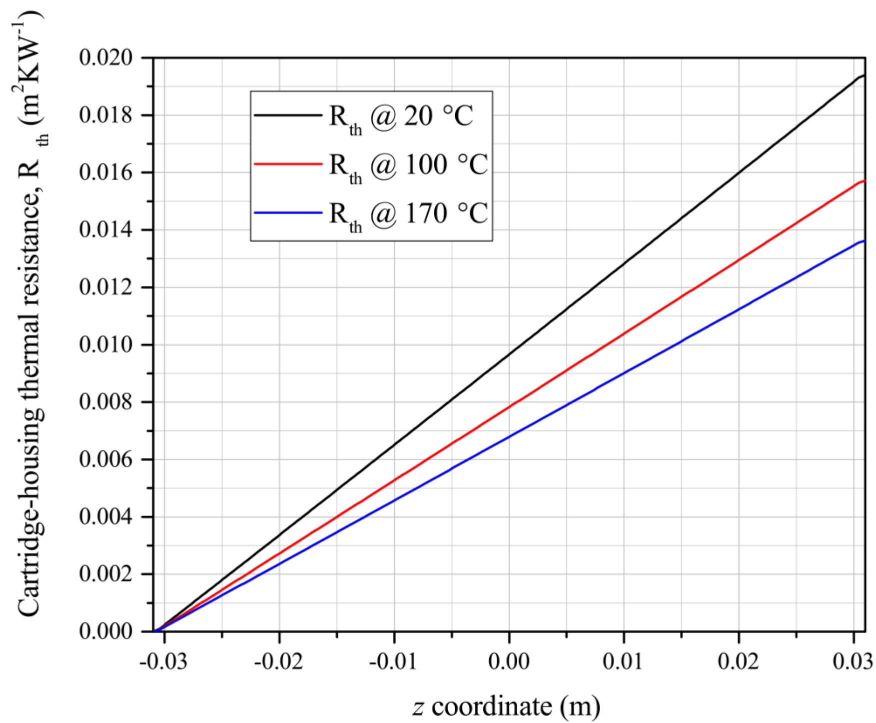

Figure 3.4 Cartridge-housing thermal resistance vs. z coordinate. The z coordinate range goes from $-r_c$ to $+r_c$, where r_c is the radius of the cartridge.

Since the heat transfer within the tool occurs mainly radially (from the electronics to the well fluid), a thermal insulation boundary condition was set at the two ends of the tool:

$$-\boldsymbol{n} \cdot (-k \nabla T) = 0 \tag{3.2}$$

Where $\boldsymbol{n}$ is the surface normal vector. To simulate the thermal interaction between the tool and the well fluid, another type of boundary condition was set on the outer surface of the housing:

$$-\boldsymbol{n} \cdot (-k \nabla T) = h(T - T_{ext}) \tag{3.3}$$

Where T_{ext} is the well fluid temperature and h is the convection heat transfer coefficient that characterizes the interaction between the well fluid and the housing. In case the well fluid flow is very high, or the temperature profile of the outer housing is known, Eq. (3.3) can be replaced by the following expression:

$$T = T_{ext}(x, y, z) \tag{3.4}$$

3.3 Experimental results and model validation

The model predictions were compared to some experimental results, in order to validate the power dissipation calculations for the electronic components. As a reference for the validation process, the steady-state temperature of the main electronic components was compared.

The well tractor electronics section was tested at “full load”, accordingly to the power dissipation calculations. A dry oven with air recirculation was used to test the tractor at the temperatures of ~120 °C, ~150 °C and ~170 °C. Seven thermocouples were used to monitor the temperature of the main components inside the tool and six thermocouples were used to monitor the temperature around the housing. One thermocouple measured the oven temperature. Figure 3.5 shows a schematic representation of the experimental setup and Figure 3.6 shows where the thermocouples were located in the tool.

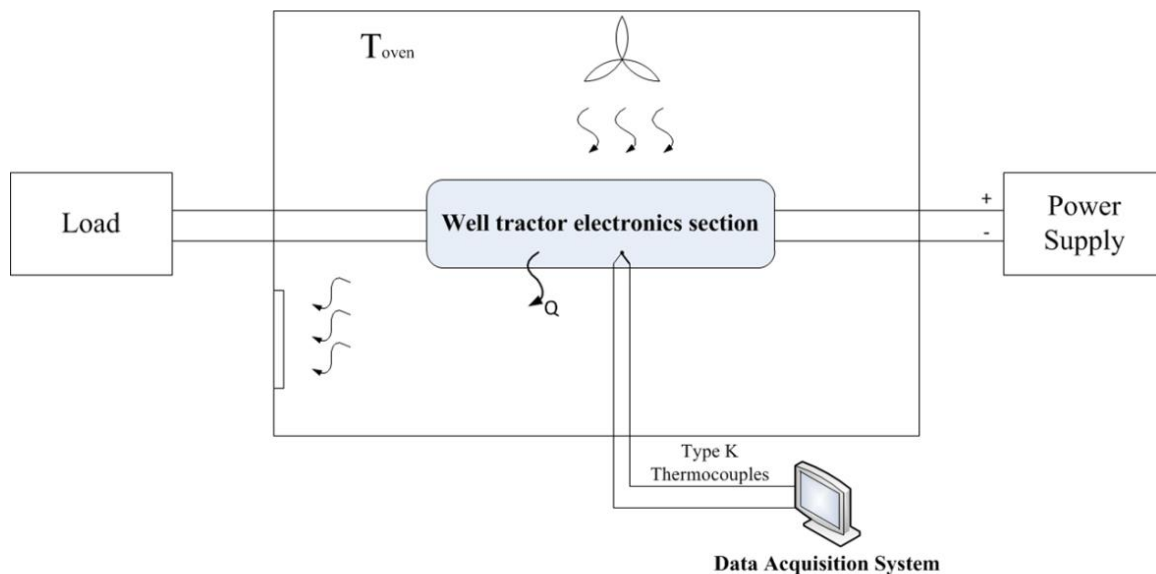

Figure 3.5 Schematic representation of the experimental setup used for the thermal characterization of the well tractor electronics.

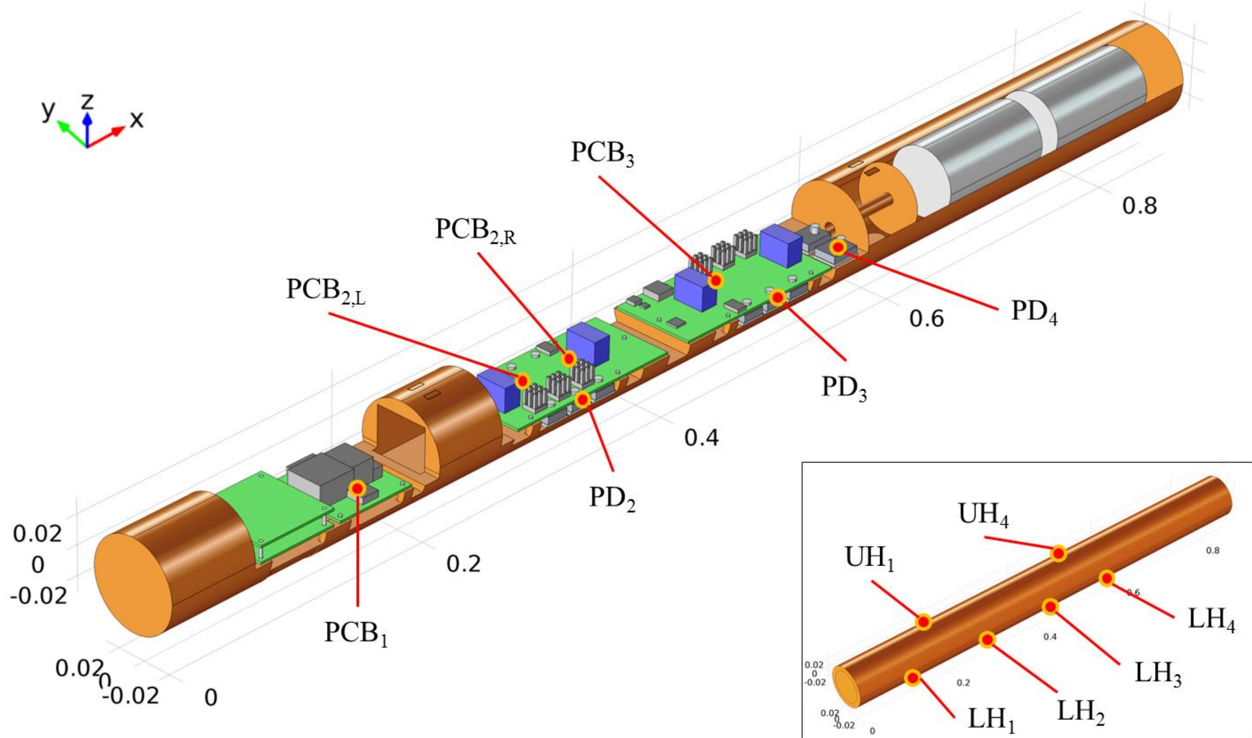

Figure 3.6 Illustration of the placement of the thermocouples within the tool. Thermocouples are labeled according to the component they are monitoring. The labels UH and LH stand for "upper housing" and "lower housing", respectively, and are numbered according to the electronics group they correspond to.

Type-K thermocouples were used to measure the experimental temperatures, which were then compared to the predictions from the model. An accuracy of ± 1.5 °C was used for the thermocouples, according to *IEC 584 Class 1*. Model data points were obtained from the corresponding 1.5 cm^2 square location within the finite-element geometry. Actual measurements were compared with the average temperatures, while lower and higher error bands were introduced according to the model prediction for the maximum and minimum temperatures within the 1.5 cm^2 square.

In order to compare the experimental results to the model predictions, consistent boundary conditions needed to be set according the experimental conditions. Since the convection heat transfer coefficient that describes the thermal interaction between the tool and the airflow in the oven is not known and is complex to predict accurately, a temperature-boundary condition (see Eq. (3.4)) was chosen for these simulations. The housing outer surface was split in 4 zones and a temperature profile corresponding to the experimentally obtained profile was imposed.

Figure 3.7, Figure 3.8, and Figure 3.9 show the simulated temperature distribution across the well tractor electronics at 120 °C, 150 °C, and 170 °C, respectively. Figure 3.10, Figure 3.11, and Figure 3.12 illustrate the comparison between the predicted and measured temperatures. The comparison of the single temperature values is reported in Table 3.3.

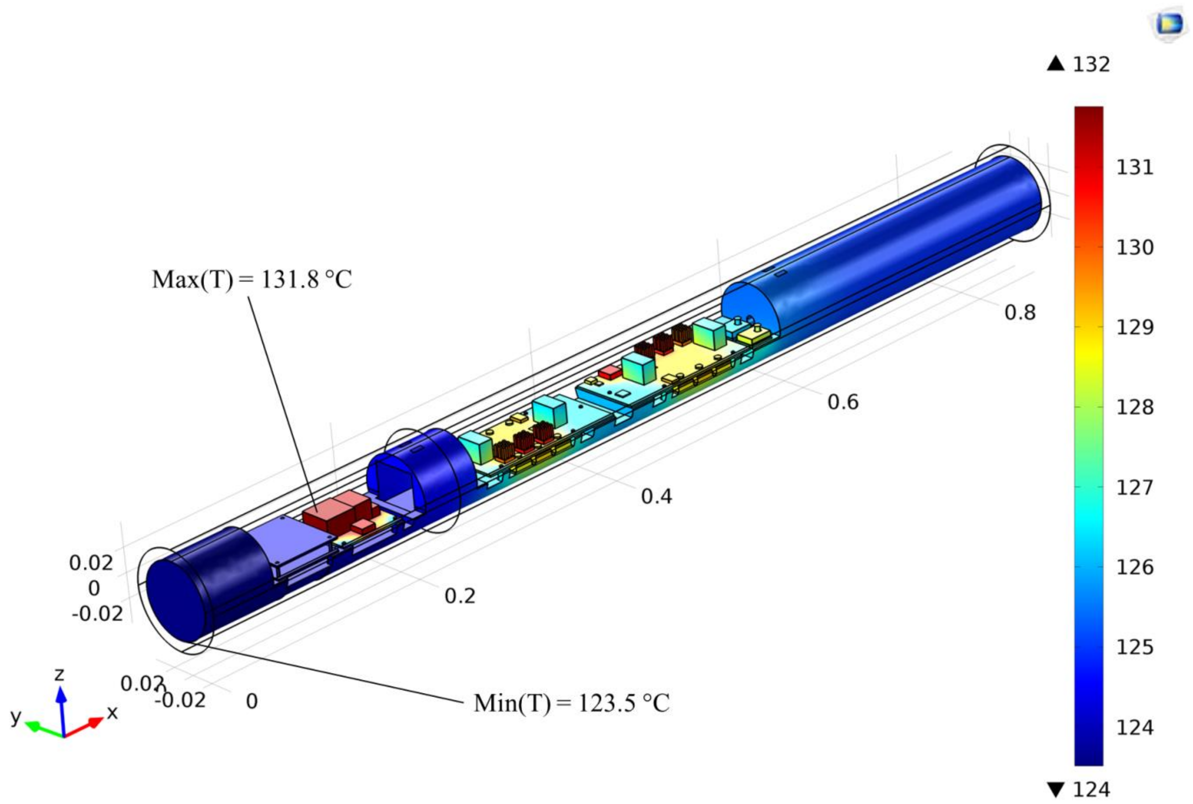

Figure 3.7 Simulated temperature profile of the well tractor electronics for the validation of the model at ~120 °C .

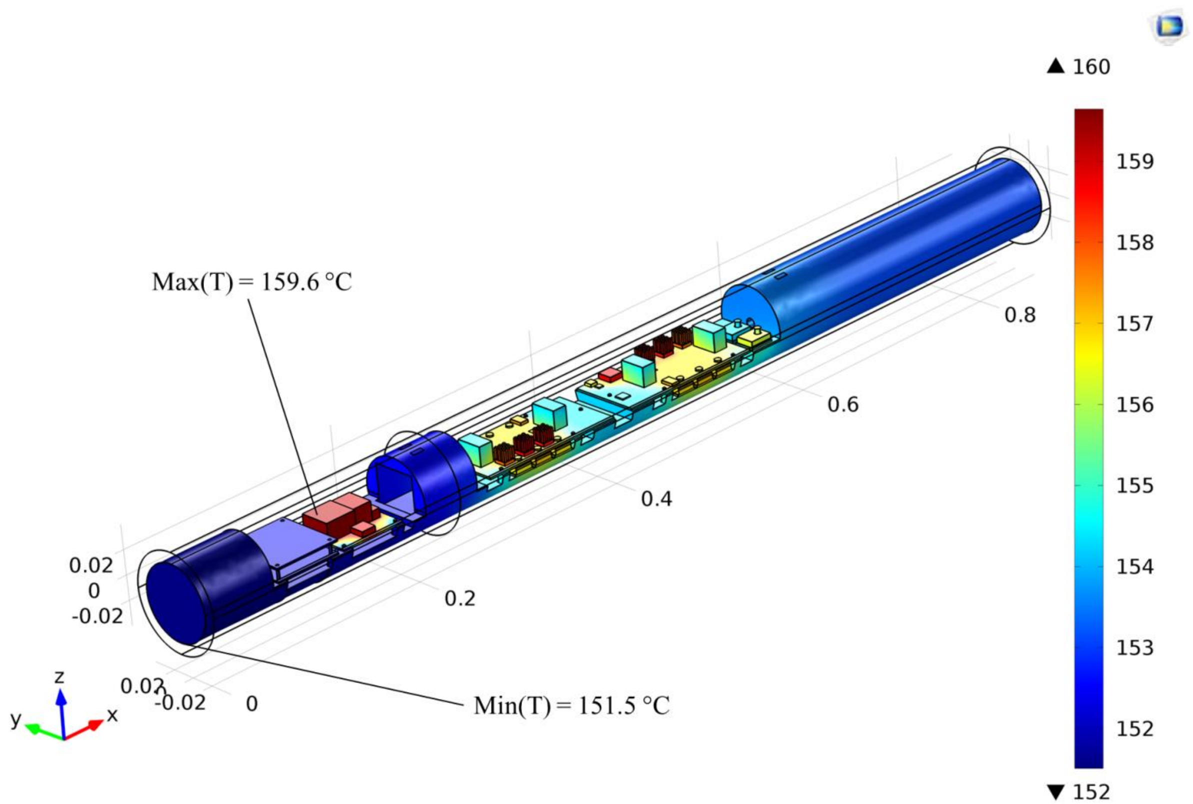

Figure 3.8 Simulated temperature profile of the well tractor electronics for the validation of the model at ~150 °C.

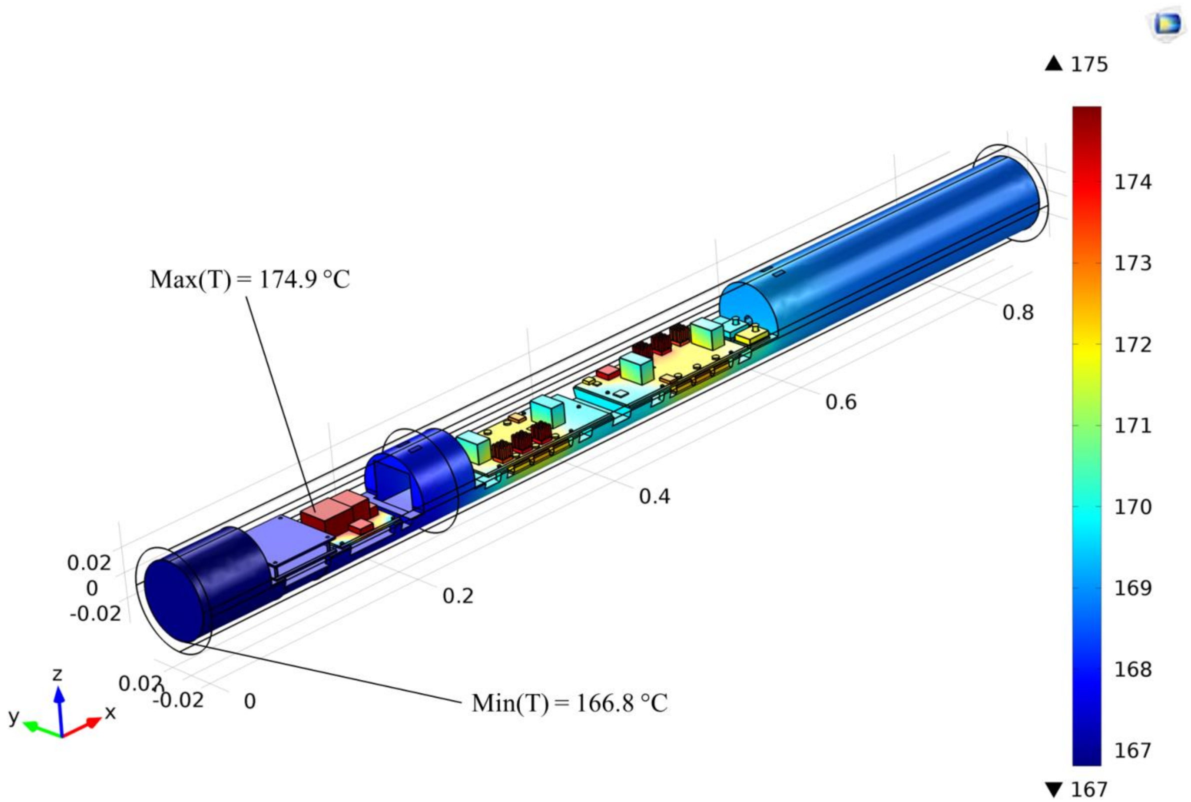

Figure 3.9 Simulated temperature profile of the well tractor electronics for the validation of the model at ~170 °C.

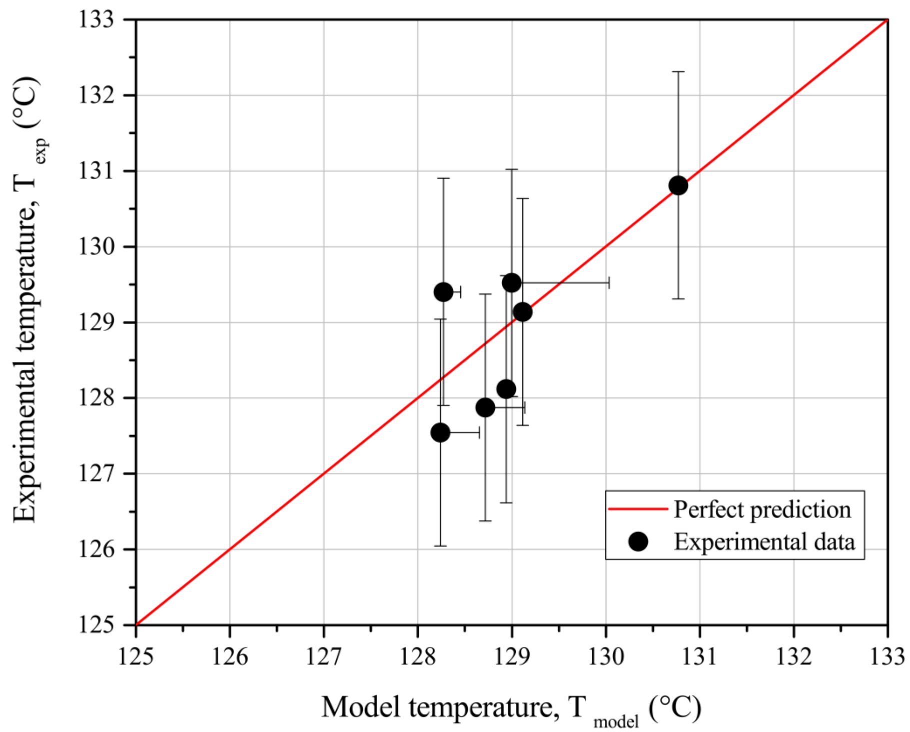

Figure 3.10 Comparison between experimental and modeling temperatures of the electronics. Average operating temperature equal of 121.8 °C.

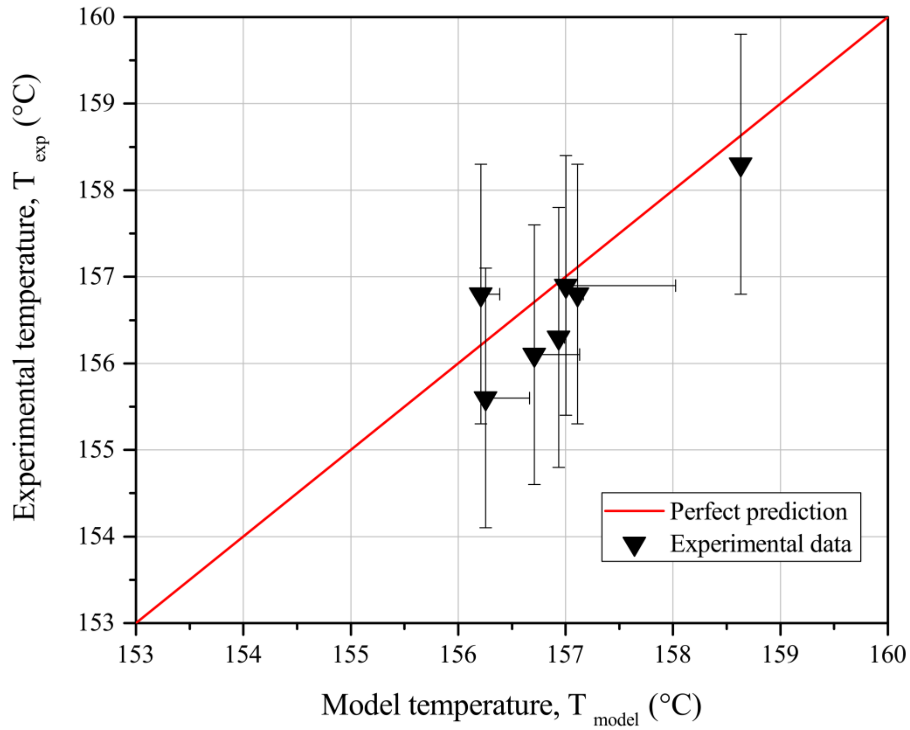

Figure 3.11 Comparison between experimental and modeling temperatures of the electronics. Average operating temperature of 150.7 °C.

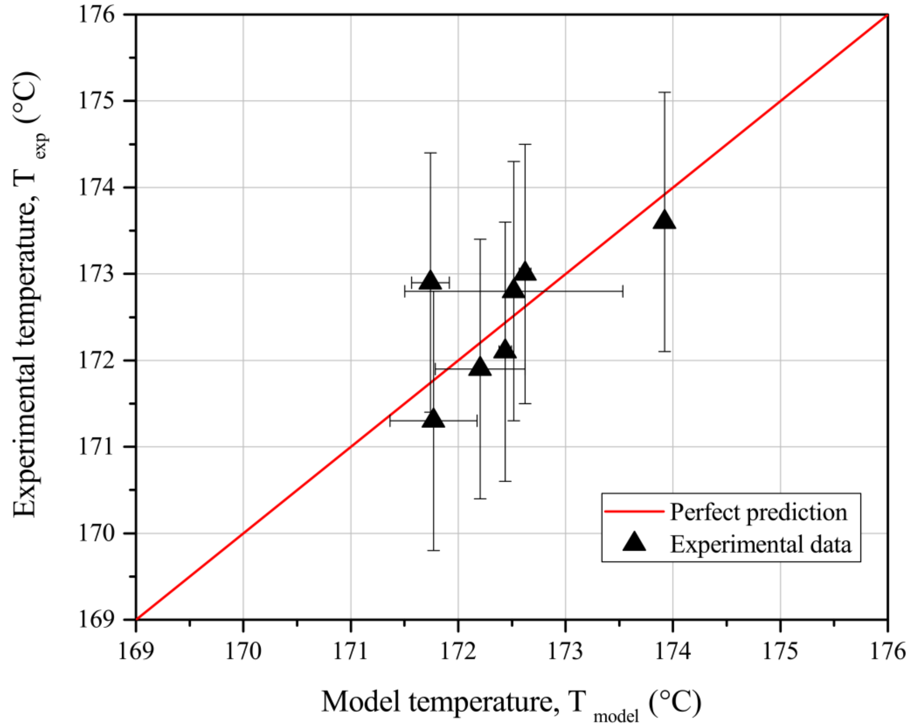

Figure 3.12 Comparison between experimental and modeling temperatures of the electronics. Average operating temperature of 166.2 °C.

Table 3.3 Experimental temperatures recorded at steady state during the tests on the well tractor electronics.

Component	*Temperature (°C)*					
	Exp.	Model	Exp.	Model	Exp.	Model
Oven	121.8		150.7		166.2	
PCB_1	130.8	130.8	158.3	158.6	173.6	173.9
PD_2	128.1	128.9	156.3	156.9	172.1	172.4
$PCB_{2,L}$	127.9	128.7	156.1	156.7	171.9	172.2
$PCB_{2,R}$	127.5	128.2	155.6	156.3	171.3	171.8
PD_3	129.1	129.1	156.8	157.1	173.0	172.6
PCB_3	129.5	129.0	156.9	157.0	172.8	172.5
PD_4	129.4	128.3	156.8	156.2	172.9	171.7
LH_4	125.2		153.3		169.0	
LH_3	125.0		153.1		168.7	
LH_2	124.9		153.2		168.6	
LH_1	123.5		151.5		166.8	
UH_4	124.6		152.4		168.0	
UH_1	123.1		150.8		166.1	

3.4 Thermal characterization conclusions

In this chapter the thermal characterization of the well tractor electronics has been presented. The main components of the electronics section have been illustrated and described. The electronics have been differentiated into different groups and characterized in terms of maximum temperature rating, type of installation, and power dissipation. The power dissipation rates were first estimated through the component datasheets and then validated experimentally. In order to do so, a finite-element model of the well tractor electronics was implemented in the software COMSOL Multiphysics and compared to experimental results. The study confirms a good agreement between the model predictions and the experimental results. A maximum temperature difference between the predicted and measured temperatures of 1.2 °C was found and an average of 0.5 °C. The power dissipation of the well tractor electronics, reported in Table 3.2, has been estimated with a satisfactory degree of accuracy. Furthermore, it was found that only the two PCBs belonging to groups 2 and 3, and dissipating ~2 W in total, need to be actively cooled, while the other components can be replaced by high temperature parts. The next chapter will illustrate how the thermal management principle and the active cooling system have been implemented, accordingly to the findings presented in this chapter.

4. TEC integration principle and *Prototype mark-1*

Building on the analysis of the well tractor electronics, this chapter presents the implementation of the thermoelectric cooling system into the downhole tool. The thermal management strategy is illustrated together with the main characteristics that describe the system. The design of a first proof-of-concept prototype is subsequently developed and illustrated. The construction of what it will be called *Prototype mark-1* for the remainder of this thesis is designed as a simple test setup with which to perform some basic tests and gain experience with the system. The prototype was in fact used to determine which commercial cooler best fits the application and how the Peltier module could be effectively integrated into the tool. Building and testing *Prototype mark-1* has been important to develop a deep understanding of the system and define some guidelines for improvement. Starting from the experience with *Prototype mark-1*, an accurate model of the system has been developed and used for optimization, as it will be shown in chapter 5. Some of the analyses and results illustrated in this chapter have been presented at the *24th International Congress of Refrigeration 2015*, which took place in Yokohama, Japan (Soprani et al (2015a)). The conference paper and the presented poster are attached in the Appendix A.

4.1 Thermal management principle

The analysis of the well tractor electronics showed that the temperature sensitive electronics in groups 2 and 3 need active cooling, while electronics from groups 1 and 4 can be fully replaced by HT components (see Figure 3.1 and Table 3.2). As it can be noticed in Figure 4.1, groups 2 and 3 are structured in the same way, so one thermal management strategy can be developed for both the groups.

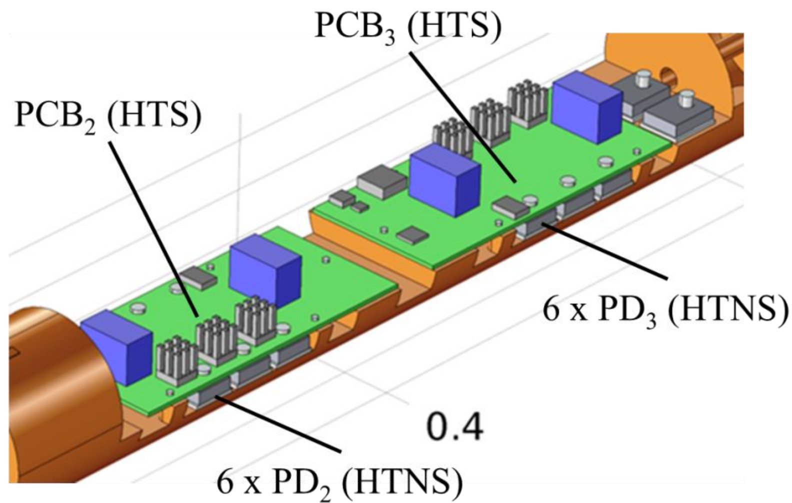

Figure 4.1 Well tractor electronic groups 2 and 3. The analogue structure is shown. Each group contains 6 x power devices (PDs or HTNS), which are high temperature-non sensitive, and 1 x printed circuit board (PCB or HTS), which is high temperature-sensitive.

Specifically, both the PCBs from groups 2 and 3 need to be maintained below 175 °C, and are therefore defined as high temperature-sensitive (HTS) components. The PDs from both groups 2 and 3, instead, can be replaced with high temperature components, and are therefore defined high temperature-non-sensitive (HTNS) components.

In order to deliver the cooling required by the electronics, two thermal management options were considered.

1. Enclose the whole electronics group into a Dewar flask, to minimize the heat leakages, and provide cooling to both the PDs and the PCBs. In this case the cooling load would be equal to the power dissipation rate of the whole electronics (~19 W), plus the much smaller contribution coming from the heat leakages through the flask (~1 W). The design of the well tractor electronics should be revised and additional connections should be designed to couple the Dewar flask to the rest of the tool. Also, an effective technique to reject the excess heat from the hot plate of the cooler to the well should be found. That would likely require the use of additional heat exchangers or heat sinks that would increase the length of the tool.

2. Differentiate the cooling techniques for the PCBs, which would be actively cooled by the TEC and maintained below the operating temperature; and for the PDs, which would be passively cooled by rejecting the heat to the well through the metallic cartridge and housing. In this case, the cooling load would be equal to the PCB power dissipation (~1 W), plus the incoming heat flux through the housing, which is estimated to be lower than 19 W if effective thermal insulation is applied. Furthermore, there would be no need to include an additional tool section, as the excess heat from the cooler could be rejected radially through the metallic housing. In this way the original length of the tool could also be maintained.

The second option shows several advantages for the application, according to the design criteria, and could be implemented in the tool as shown in Figure 4.2.

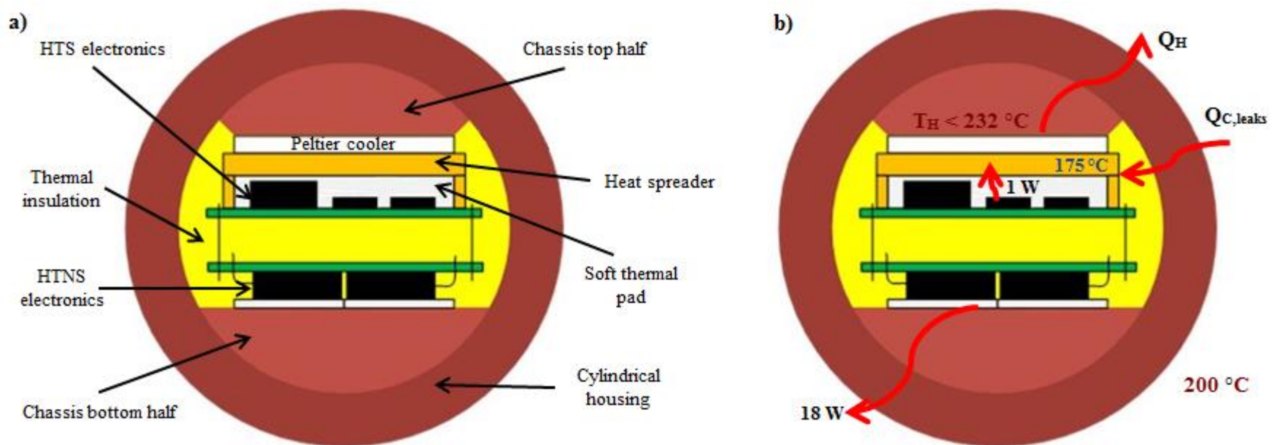

Figure 4.2 Thermal integration of the TEC and thermal management principle of the electronic groups 2 and 3. Components involved in the system (a) and main design parameters (b).

The HTNS electronics are mounted on a bottom chassis and passively cooled, while the HTS electronics are thermally coupled to the cold plate of the Peltier module. A soft thermal pad and a metallic heat spreader are used to provide such thermal interface. The soft thermal pad is able to ensure effective contact over the irregular height on the surface of the PCB, while the heat spreader conducts the heat from the load to the TEC cold plate. The hot plate of the TEC is in thermal contact with the top part of the chassis for the rejection of the excess heat. Both the bottom and top parts of the chassis are in tight contact with the cylindrical housing to minimize the thermal contact resistance. The remaining part of the section is filled with thermal insulation that protects the cooled HTS electronics from the hot surrounding and minimizes the heat leakages.

In accordance to the analysis reported in Chapter 3, the HTNS components dissipate a total of 18 W while the HTS electronics dissipate 1 W. This design aims at a maximum operating well temperature of 200 °C and a corresponding maximum HTS electronics temperature of 175 °C. The hot side of the system is constrained to operate below 232 °C, which corresponds to the melting temperature of the solder employed in the TEC. A reference convection coefficient, which describes the heat transfer in the downhole environment, can be set to 100 W/m^2K (Flores (1996)). However, the design of the unit should aim to minimize the required heat rejection rate.

4.2 Description of *Prototype mark-1*

According to the thermal management principle shown in Figure 4.2, a first lab-prototype, *Prototype mark-1,* was designed and manufactured. An aluminum chassis was designed in two halves, in order to be interfaced with the HTNS electronics on the bottom and with the thermoelectric cooling system on the top. In the top part of the chassis two flat aluminum pads were included to accommodate 2 x TECs. Different installation techniques were tested as reported in Section 4.4. Four pins were installed to secure the two chassis halves close together properly before being slid into a metallic housing. The O.D. of the chassis was designed in a way that a tight contact could be ensured with the housing.

Three different types of HT thermoelectric coolers were bought for testing from different suppliers. They are characterized by a maximum operating temperature of 200 °C and a maximum hot plate temperature of 232 °C.

Test electronics, composed of resistive components, were used to simulate the well tractor electronics: 6 x 10 kΩ resistors were used to reproduce the HTNS components (power devices), and 5 x 33 Ω resistors were installed on a printed circuit board to reproduce the HTS electronics (PCB components).

A soft thermal interface material (TIM), 2 mm thick and with a thermal conductivity of 4.2 W/m-K, was employed to interface the HTS electronics on the PCB to the copper heat spreader, composed of a 2 mm thick copper plate.

Thermally insulating polyimide foam, rated for high temperatures and with a thermal conductivity of 0.046 W/m-K (at 25 °C), was used to fill the unit and protect the cooled zone from the hot surrounding. A 300 mm long metallic housing, with an I.D. of 62 mm and an O.D. of 80 mm, was used to contain the aluminum cartridge and the electronics. More detailed dimensions of the components are listed in Table 4.1 and a 3D model of the system is illustrated in Figure 4.3 and Figure 4.4. Some pictures of the manufactured system are shown in Figure 4.5.

The drawings of the parts and the datasheets of the three different coolers are attached in Appendix B.

Table 4.1 List of the components used in *Prototype mark-1* and their features.

Component	*Dimension*	*Material*	*Additional features*
Metallic housing	O.D. = 80 mm I.D. = 62 mm Length = 300 mm	Metallic alloy	k = 105 W/m-K @ 20 °C k = 145 W/m-K @ 200 °C k = 155 W/m-K @ 300 °C
Top chassis	O.D. = ~ 62 mm Length = 200 mm	Aluminum alloy	k = 138 W/m-K
Bottom chassis	O.D. = ~ 62 mm Length = 200 mm	Aluminum alloy	k = 138 W/m-K
Heat spreader	120 x 41 x 5 mm	Copper	k = 400 W/m- K
Soft thermal interface material (TIM)	115 x 40 x 2 mm	Polymer	k = 4.2 W/m-K Electrically insulating
Peltier coolers	*#1* : 30 x 30 x 3.6 mm (36 W_{max}) #2 : 34 x 30 x 3.3 mm (41 W_{max}) *#3* : 40 x 40 x 3.9 mm (62 W_{max})	Bi_2Te_3 based semiconductors Al_2O_3 plates	Max operating T = 200 °C Max hot plate T = 232 °C

HT thermal insulation	------	Polyimide foam	k = 0.046 W/m-K @ 25 °C
HTNS electronics	6 x 10 kΩ 20 x 16 x 4.8 mm	Thin film resistor	Mounted on bottom chassis Connected in parallel R_{tot} = 1667 Ω
HTS electronics	PCB : 120 x 41 x 1.6 mm 5 x 33 Ω Length = 9.4 mm	Carbon film resistor	Mounted on PCB Connected in series R_{tot} = 166 Ω

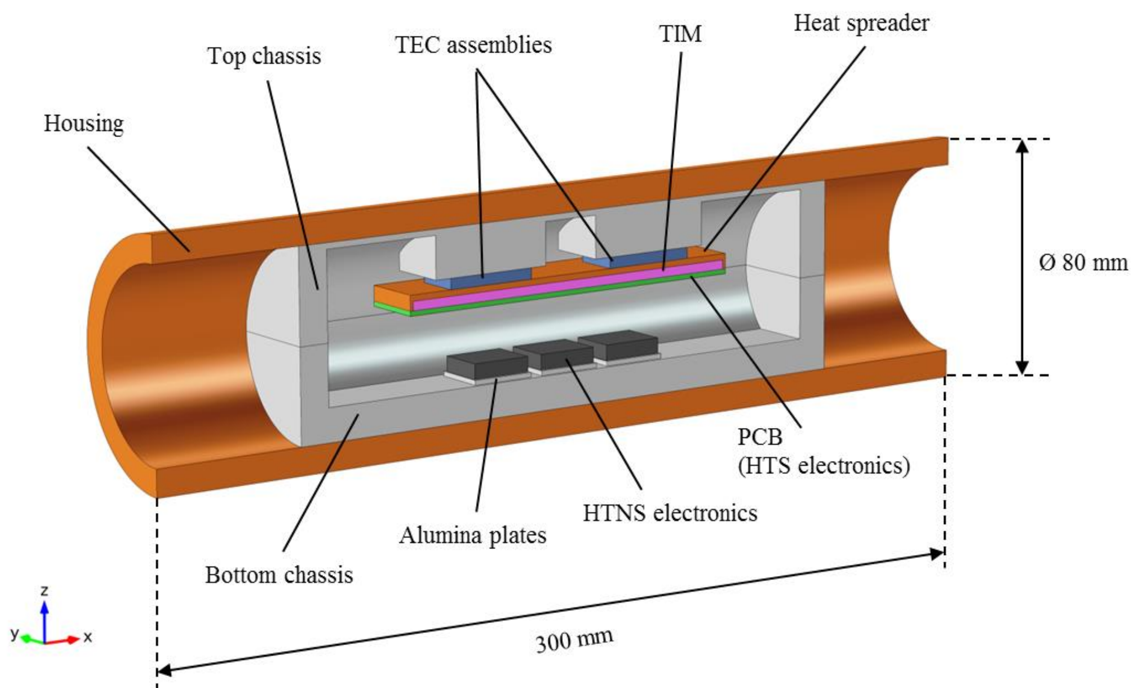

Figure 4.3 3D model of *Prototype mark-1*. The longitudinal section, along the axis of symmetry, is illustrated. The empty space in the unit is filled with thermally insulating foam.

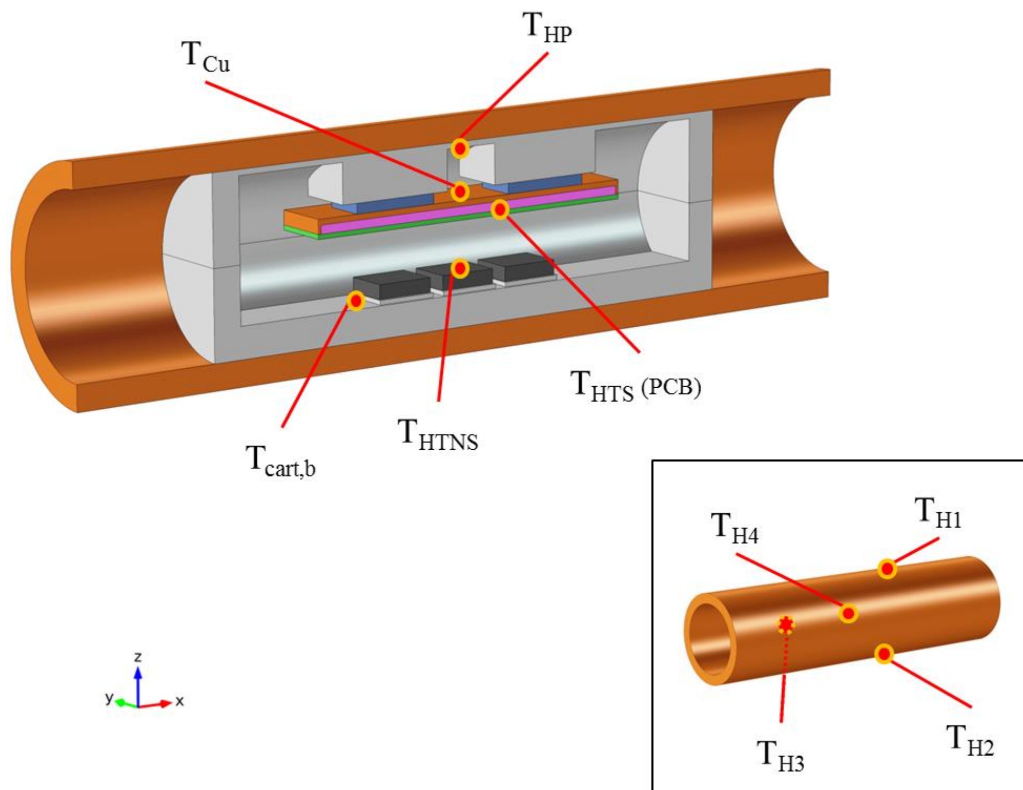

Figure 4.4 Illustration of the thermocouple placements within *Prototype mark-1*. Thermocouples are labeled according to the component they are monitoring.

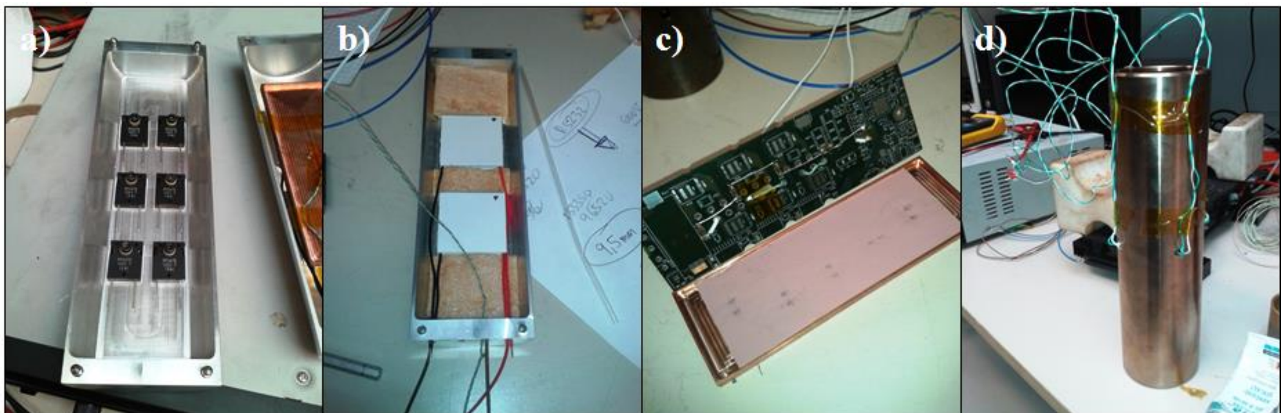

Figure 4.5 Implementation of the experimental setup. Bottom half of the chassis with the HTNS electronics (a), top half of the chassis with two HT thermoelectric coolers and thermal insulating foam (b), HTS electronics installed on a printed circuit board with heat spreader and soft thermal pad (c), cylindrical housing with 4 welded thermocouple wires (d).

The tests on *Prototype mark-1* were carried out in the experimental setup illustrated in Figure 4.6. The tool was tested in a dry ventilated oven, so the operating temperature could be varied. Two power supplies fed the Peltier coolers and the two sets of electronics, respectively. The feed voltage and current to the TECs were monitored by two voltmeters and two current meters, respectively. Nine type-K thermocouples measured the temperature of the following components (see Figure 4.4).

- T_{HTS} measured the temperature of the HTS electronics and was installed in between the PCB and the soft thermal pad.
- T_{HP} measured the temperature of the top half of the cartridge, close to the cooler hot plates.
- T_{Cu} measured the temperature of the copper heat spreader in between the two thermoelectric modules.
- T_{HTNS} was installed on the casing of one test resistor from the HTNS electronics.
- $T_{cart,b}$ measured the temperature on the bottom half of the cartridge, where the HTNS electronics is mounted and passively cooled.
- T_{H1} to T_{H4} measured the temperature along the housing outer surface and were averaged into one mean temperature $T_{housing,avg}$.

The performance of the system was characterized by the temperature span across the coolers ΔT_{cooler} and the feed power P_{feed}.

$$\Delta T_{cooler} = T_{HP} - T_{HTS} \tag{4.1}$$

$$P_{feed} = P_{TEC,1} + P_{TEC,2} = V_{TEC,1} I_{TEC,1} + V_{TEC,2} I_{TEC,2} \tag{4.2}$$

Where T_{HP} is the temperature measured on the aluminum pads of the top cartridge at steady state and approximated with the hot plate temperature, T_{HTS} is the temperature of the HTS electronics, measured on the PCB at steady state, V_{TEC} is the feed DC voltage to the coolers, and I_{TEC} is the current across the coolers.

ΔT_{cooler} was chosen as a figure of merit for the performance of the systems because it is an index of the capability of the cooling system to pump heat from the load to the hot reservoir. Furthermore ΔT_{cooler} is not as sensitive to the oscillations of the heat transfer boundary conditions (oven temperature or recirculated air flow), as the single temperatures T_{HTS} and T_{HP}.

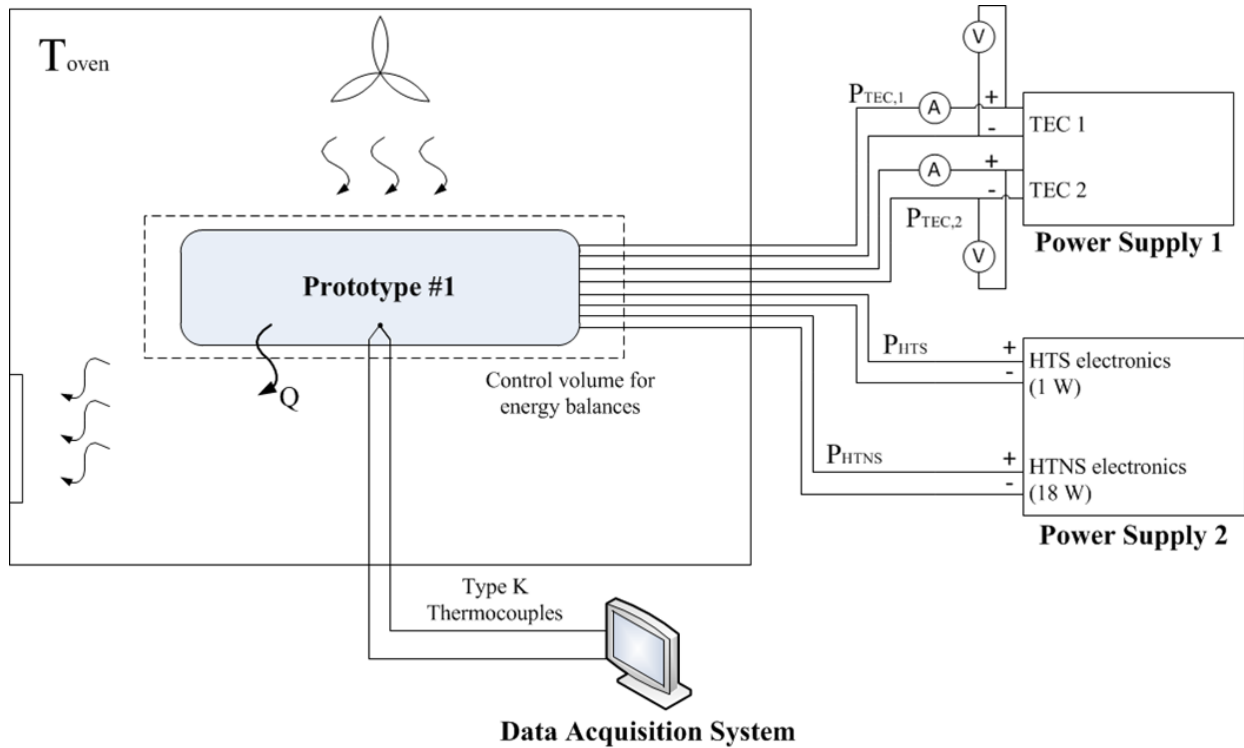

Figure 4.6 Schematic of the experimental setup used for testing *Prototype mark-1*.

4.3 Approximation of the cooling load

A preliminary set of tests were done on the setup to evaluate the cooling load to a first approximation. As previously discussed, the cooling load is given by the sum of the HTS electronics power dissipation ($Q_{C,el}$) plus the contribution of the heat leakages through the thermal insulation ($Q_{C,leaks}$). While the power dissipation from the sensitive electronics has been estimated and set to 1 W, the influence of the incoming heat, which depends on the TECs operating conditions, is still unknown.

Two *Coolers #1* were mounted on the chassis with thermal grease and tested at room temperature. The operating conditions of the system (feed current) were varied and the temperatures within the system (temperature span across the plates) were recorded. The TEC datasheets, attached in Appendix B, were used to compare the experimental results to the characterization given by the supplier, and to estimate the absorbed heat flux for each operating condition. Because the datasheets only characterized the cooler performance at certain hot plate temperatures (30 °C, 50 °C, and 70 °C), linear interpolation was used to make the data comparable to the intermediate experimental conditions. In order to estimate the cooling load through this approach, it was assumed that the temperatures measured on the top chassis (T_{HP}) and on the PCB (T_{HTS}) corresponded to the temperatures of the hot and cold plates, respectively. The approximation was considered accurate enough for the estimation of the cooling load, given the small thermal resistance between the TEC plates and the location of the thermocouples.

Given the dependence of the heat leakages on the temperature span across the cooler, a Q_C vs. ΔT_{cooler} curve was built. Following this approach, it was possible to characterize the overall thermal resistance between the HTS electronics and the hot surrounding.

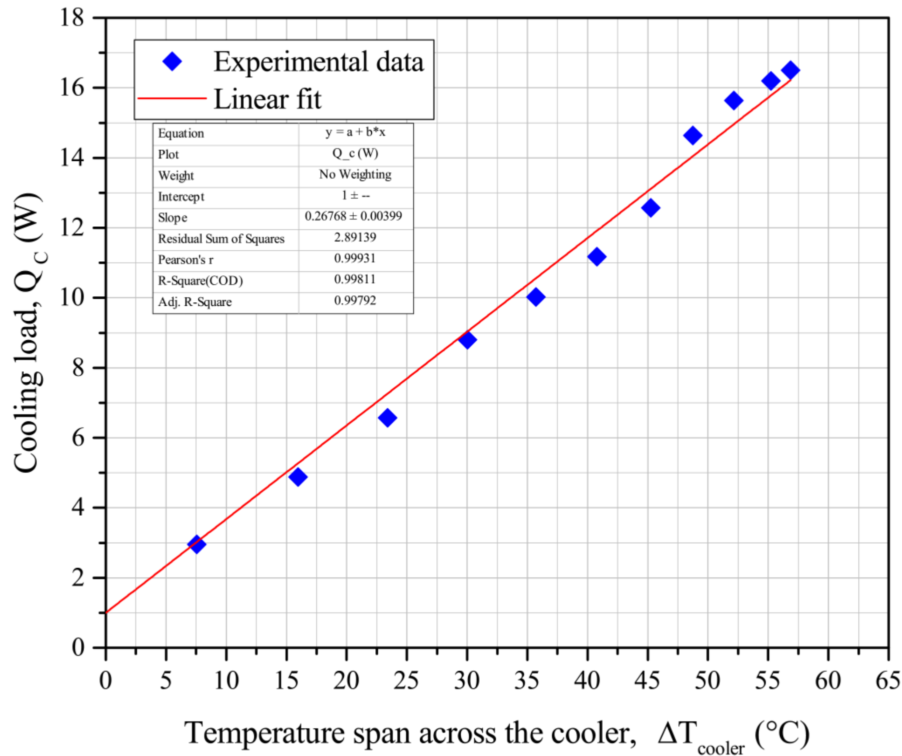

Figure 4.7 Estimated cooling load vs. temperature span across the cooler, with linear fit of the experimental data.

Test results, illustrated in Figure 4.7, show a cooling load that ranges from ~3 W, for a temperature span of ~7.5 °C, to ~16.5 W for a temperature span of ~57 °C. When the temperature span is equal to 0 °C there is still a cooling load of 1W. The linear fit proves to approximate the experimental trend with good accuracy ($R^2 > 0.99$). The equation of the regression line, reported below, illustrates the two contributions to the cooling load Q_C.

$$Q_C = 0.268 \, \frac{\mathrm{W}}{\mathrm{K}} \cdot \Delta T_{cooler} + 1 \, \mathrm{W} \tag{4.3}$$

The intercept, equal to 1 W, represents the component of the cooling load due to the electronics power dissipation. The slope of the line, instead, can be interpreted as the thermal transmittance between the hot side of the system and the HTS electronics that characterizes the contribution of the heat leakages to the cooling load. The slope of the regression line is found to be equal to 0.268 W/K, which corresponds to a thermal transmittance of 3.556 W/m^{2}K, if weighted on the housing outer surface area. Compared to the thermal conductance of a Dewar flask, previously estimated at ~0.02 W/m^{2}K, this thermal insulation solution is much less effective. However, this thermal design allows the direct integration of the cooling system into the well tractor electronics and does not require additional tool sections.

At high temperatures, the cooling load is expected to increase as a consequence of the rise in thermal conductivity of aluminum (chassis), semiconductor material (TECs), and polyimide foam (thermal insulation). Unfortunately, it was not possible to repeat this procedure to estimate the cooling load at high temperatures because of the lack of data from the supplier above 70 °C.

4.4 Selection of the assembly technique

A first tranche of tests was made to assess which technique could be used to mount the TECs in the electronics section. The goal was to ensure a mechanically stable and thermally effective installation that could firmly hold the devices in place, avoid stresses due to thermal expansion, and minimize the thermal resistances at the interface with the TEC plates. The tests aimed at evaluating the temperature span that the cooling system was able to maintain between the hot plate and the PCB, while varying the feed power.

Two coolers of the *type #1* (see Table 4.1) were installed on the aluminum pads of the top chassis with three different assembly techniques, which are described below.

- *Thermal Epoxy:* silver based thermal epoxies were investigated to fix the hot and the cold plates of the coolers to the top chassis and the heat spreader, respectively. The stiffness of the cured epoxy would ensure good mechanical stability and good resistance towards external stresses. Furthermore, the high thermal conductivity of silver based epoxies would introduce a low thermal resistance at the interface with the plates. A two-part thermal epoxy with a thermal conductivity of 7.2 W/m-K and a maximum operating temperature of 260 °C was selected for the application.

- *Adhesive TIM:* soft adhesive thermal pads were investigated as an alternative to the thermal epoxy. They could provide the mechanical connection between the cooler plates and the other components thanks to their adhesive property, and effectively conduct the heat thanks to their good thermal conductivity. Compared to epoxies, adhesive TIMs provide a more flexible mechanical connection, but can absorb the thermal expansion of the components decreasing the stresses on the coolers. An adhesive TIM with a thermal conductivity of 6 W/m-K and a maximum operating temperature of 200 °C was selected for the application.

- *Thermal grease (requires a clamping system):* as a third option, thermal grease was investigated. Thermal grease can provide an effective thermal interface with thermal conductivities in the same order of magnitude of silver epoxies and adhesive TIM. Thermal grease would leave the modules free to expand eliminating the stress due to thermal expansion. However, the use of grease only would not provide any mechanical stability and a clamping system would be needed. Two screws could be installed through the heat spreader and the PCB, and screwed into in the top half of the chassis, in order to put the TECs in slight compression and hold them in place. Thin plastic screws could be used to minimize the heat leakages from the hot chassis to the cooled PCB. Because *Prototype mark-1* was not designed to support a clamping system, thermal grease only was used to test the effectiveness of the thermal interface. Thermal grease with a thermal conductivity of 5 W/m-K and a maximum operating temperature of 180 °C was selected for the application.

Each of the described mounting techniques was tested at room temperature, before and after cycling the setup up to 170 °C in the oven. The test results are shown in Figure 4.8.

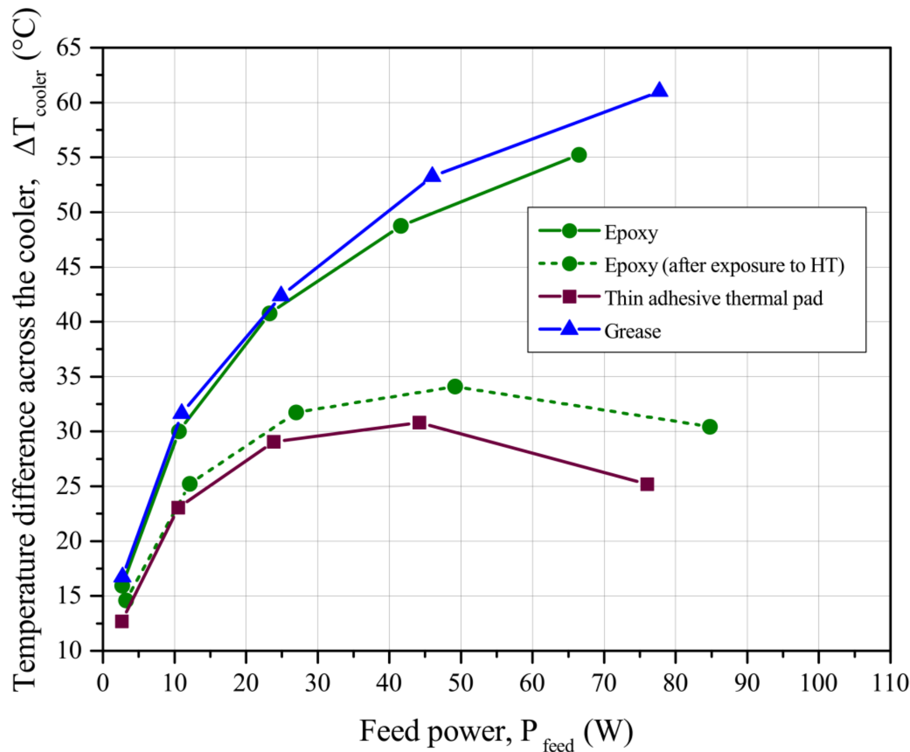

Figure 4.8 Temperature span across the cooler ΔT_{cooler} vs. coolers feed power for different installation techniques.

Thermal epoxy proved to provide a mechanically robust connection and an effective thermal interface, as it can be seen by the increasing trend of ΔT_{cooler} in Figure 4.8. As the second best performing interface material, temperature differences up to 55 °C could be obtained. However, the performance of the system significantly dropped after exposure at high temperature, and only a maximum temperature span of ~34 °C could be reproduced. The issue was investigated and found to be related to thermal expansion.

The alumina plates of the cooler have a coefficient of linear expansion of $8 \cdot 10^{-6}$/°C, which is much lower than the employed thermal epoxy ($41 \cdot 10^{-6}$/°C), and of copper and aluminum ($17 \sim 22 \cdot 10^{-6}$/°C). When exposed to high temperatures, the expansion of the neighboring components likely induced stresses into the alumina plates, causing cracks and affecting the thermal contact with the neighboring components. This hypothesis was confirmed by the measurement of the electrical AC resistance (ACR) of the modules, before and after the exposure to high temperature. Measuring the ACR of a Peltier module can reveal whether any phenomena, in this case thermal expansion, has affected or degraded the electrical configuration of the system, inducing eventually higher heat losses and lower efficiency. At the end of the tests at room temperature, an electrical resistance of ~3 Ω (at 23 °C) was measured for both the modules, while ~9.5 Ω (at 23 °C) was measured after the exposure to high temperature, showing that thermal expansion had modified the electrical connections in the system. The more than tripled electric resistance led to a significantly higher excess heat to be rejected, that in turn increased the heat leakages through the insulation, increased the cooling load, and affected the performance of the system. Further tests at high temperature led to system failure, after which the ACR of the modules was larger than 10 MΩ.

No degradation due to thermal expansion was noticed for the adhesive thermal pad and for the thermal grease, which either absorbed or allowed the thermal expansion of the components. The adhesive pad, however, showed the poorest thermal properties. Unexpectedly, feed powers above ~45 W generated lower

temperature spans than feed powers below ~45 W. The additional Joule losses and transported heat flux, caused by higher feed powers, could not be effectively dissipated because of the poor thermal interface. The ineffective heat rejection led to a higher heat flux leaking into the cooled zone, increasing the cooling load and affecting the system performance. An inhomogeneous adhesion between the soft pad and the other components, or a thermally resistive behavior of the adhesive compound, could have contributed to the poor thermal interface. However, this phenomenon was not further investigated because it is outside the scope of this work.

The thermal grease, which showed the best system performance, was therefore chosen as a thermal interface material for the installation of the TECs. A clamping system, which can guarantee a stable contact and hold the coolers in place, should be included in the next designs of the system.

4.5 Selection of the cooler

The three different types of cooler listed in Table 4.1, which vary in size and cooling capacity, were the object of preliminary tests at room temperature to assess which was the most suitable for the application. Two coolers of each type were mounted in the system and tested. Also for these tests, the performance of the system was evaluated in terms of temperature span across the cooler at different feed powers. The coolers were interfaced to the heat spreader and the top chassis with thermal grease, according to the findings from the previous section. The test results are illustrated below.

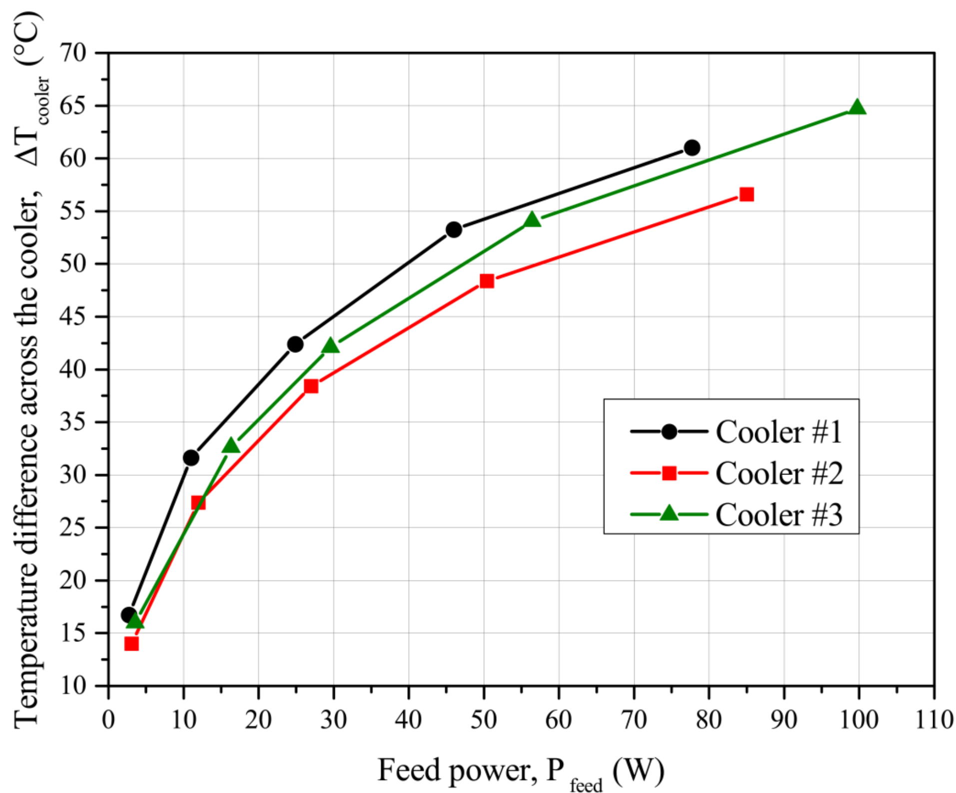

Figure 4.9 Temperature span across the cooler ΔT_{cooler} vs. coolers feed power for different coolers in size and cooling action.

Figure 4.9 shows the comparison between the performances of the three types of cooler. *Cooler #1*, characterized by a maximum cooling power of 36 W, proves to be the best performing type of cooler with a temperature span that ranges from ΔT_{cooler} = 16.7 °C at P_{feed} = 2.8 W, to ΔT_{cooler} = 61.0 °C at P_{feed} = 77.8 W.

Cooler #2, characterized by a maximum cooling power of 41 W, shows the lowest performance, with a temperature span that varies from ΔT_{cooler} = 14.1 °C at P_{feed} = 3.1 W, to ΔT_{cooler} = 56.6 °C at P_{feed} = 84.5 W.

Cooler #3, characterized by a maximum cooling power of 62 W, shows a performance which is very similar to Cooler #1, with a temperature span that ranges from ΔT_{cooler} = 16.6 °C at P_{feed} = 3.7 W, to ΔT_{cooler} = 65.09 °C at P_{feed} = 99.8 W.

Analogue evaluations can be done when looking at the trend of the system COP vs temperature span, illustrated in Figure 4.10. The COP was estimated by calculating the absorbed heat flux through Eq. (4.3), assuming that the thermal resistance from the outer housing to the electronics would not change by using coolers with slightly different dimensions and configurations (from 30x30 to 40x40 mm).

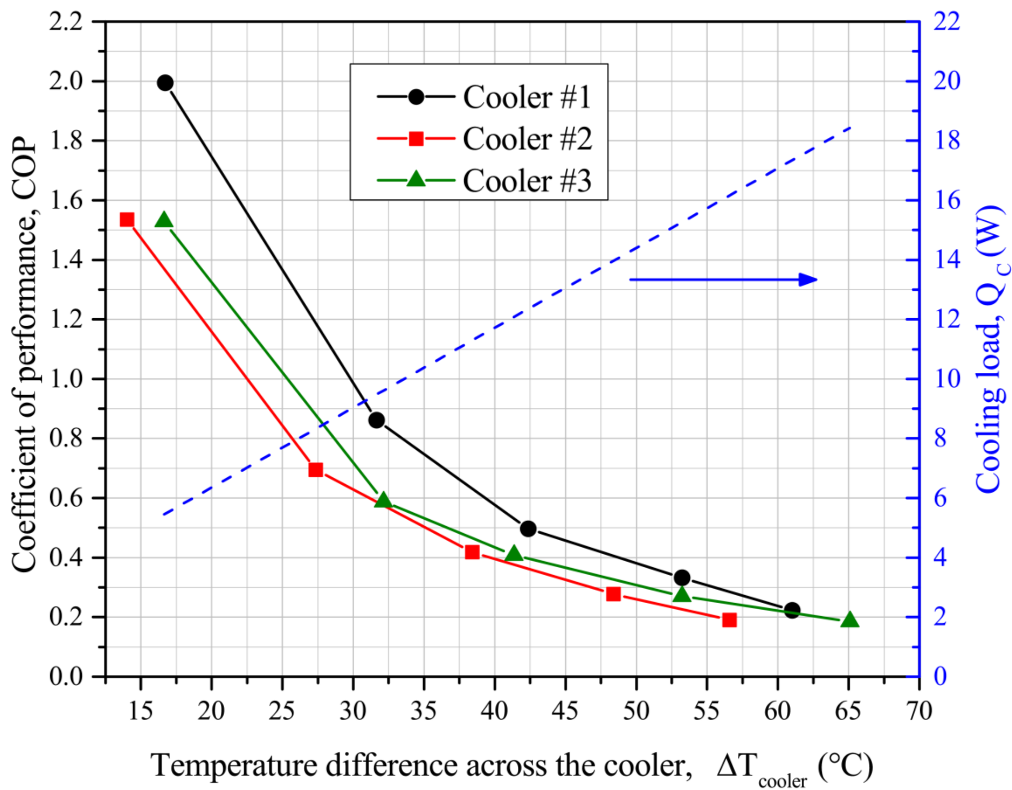

Figure 4.10 Estimated COP (left *y*-axis) and estimated cooling load (right y-axis) vs. temperature span across the cooler for different coolers in size and cooling action. The cooling load at a given ΔT_{cooler} is assumed the same for the three coolers.

As expected, the COPs decrease with the temperature span and the cooling load. The system operates at room temperature between a COP of 2.0 and 0.2. *Cooler #1* proves to be the most efficient in the studied operating range, while *Cooler #2* proves to be the most inefficient. *Cooler #3* operates very similarly to *Cooler #2* at low temperature spans, while has a similar behavior to *Cooler #1* at higher temperature spans.

4.6 Tests at high temperature

Prototype mark-1 was also used to perform some preliminary tests at high temperature. Two *Coolers #1* were mounted in the system with thermal grease, in accordance to the results from the previous sections. The setup shown in Figure 4.6 was also used to perform tests from room temperature to 170 °C. The temperature distribution within the tool was monitored by the thermocouples, which allowed a detailed analysis and understanding of the system.

In order to characterize the heat transfer between the tool and the oven, an experimental value of the convective heat transfer coefficient was calculated. That was possible by computing a balance of the heat fluxes around the control volume illustrated in Figure 4.6, at steady state operation.

$$\bar{h}_{exp} = \frac{(P_{feed} + P_{HTS} + P_{HTNS})}{A_{housing} \cdot (T_{housing,avg} - T_{oven})} \qquad (4.4)$$

Where $\bar{h}_{exp}$ is the average heat transfer coefficient at the tool housing surface; P_{feed}, P_{HTS}, and P_{HTNS} are respectively the electric feed powers of the cooler, of the HTS electronics, and of the HTNS electronics; $A_{housing}$ is the outer surface area of the housing; $T_{housing,avg}$ is the average of the readings from the four thermocouples installed on the outer surface of the housing (see Figure 4.4); and T_{oven} is the measured oven temperature. The test results are illustrated in the figures below and summarized in Table 4.2 at the end of this section.

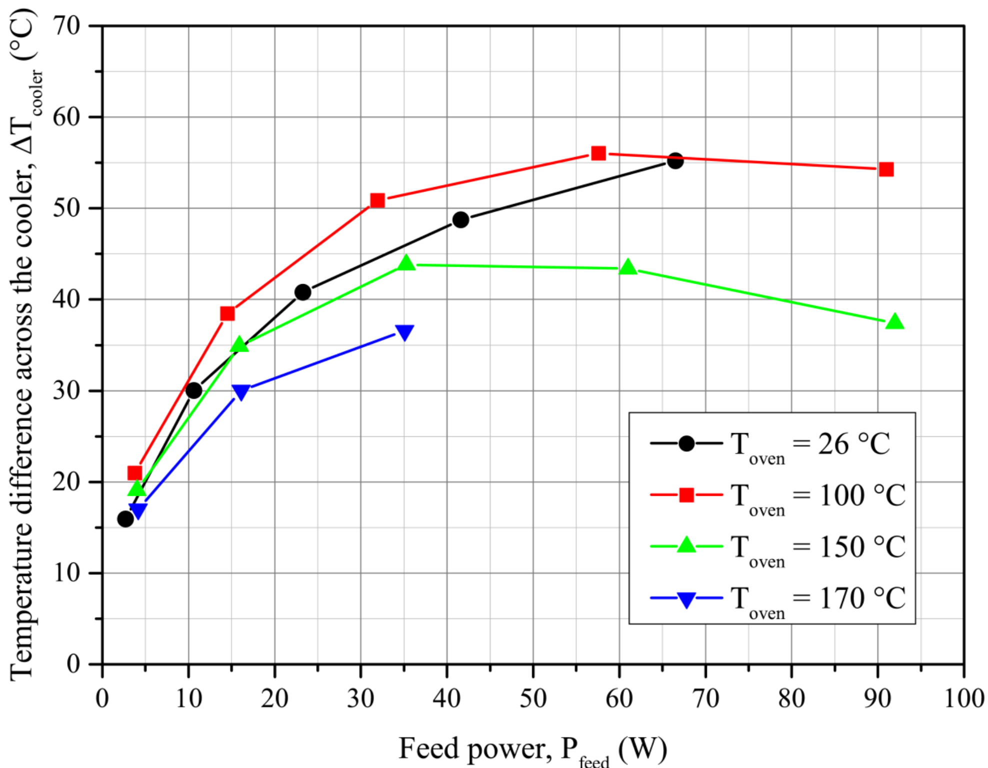

Figure 4.11 Temperature span across the cooler ΔT_{cooler} vs. coolers feed power, at different oven temperatures, for *Prototype mark-1*. 2 x *Cooler #1* were assembled in the tool with thermal grease.

Figure 4.11 reports the trend of the temperature span across the cooler with the feed power. It can be seen the performance of the system varies with the operating temperature because of the dependence of the cooler thermoelectric properties and figure of merit on the operating temperature. The system is able to maintain the largest temperature spans between the hot plates and the HTS electronics at the oven temperatures of 100 °C, with a ~5 °C maximum difference with the trend at room temperature. At 150 °C the system is able to maintain lower temperature spans than at 100 and 26 °C, with a maximum temperature span of ~44 °C at P_{feed} = 35 W. Moving towards even higher temperatures, the performance of the system continues decreasing, as can be seen in the trend at 170 °C oven temperature, where a maximum temperature span of ~36 °C is recorded at 35 W. During the tests at 170 °C the feed power was limited below 40 W in order not to exceed 200 °C on the hot plate of the coolers, reducing the risk of degradation or failure during the preliminary tests.

This behavior results in good agreement with the qualitative trend with temperature of the figure of merit of Bi_2Te_3-based thermoelectric materials, illustrated in Figure 2.22. It can also be noticed that above a certain feed power, which depends on the oven temperature, the temperature span starts decreasing. That can be explained, as for the case in Figure 4.8, with the rise of the Joule losses across the cooler, which can no longer be effectively rejected and leak back to the cooled electronics, reducing the maintained temperature span.

Differently than for the case with degradation for thermal expansion, the increase of the Joule losses is given in this case by the increase of the electrical resistance with temperature. The effect is even accentuated by an increase of the thermal conductivity, which leads to larger thermal conduction losses from plate to plate. The dissipated power from the HTNS electronics, which was estimated and set to 18 W, also contributes to the rise in temperature of the hot side of the system and limits the heat rejection from the hot plates of the coolers.

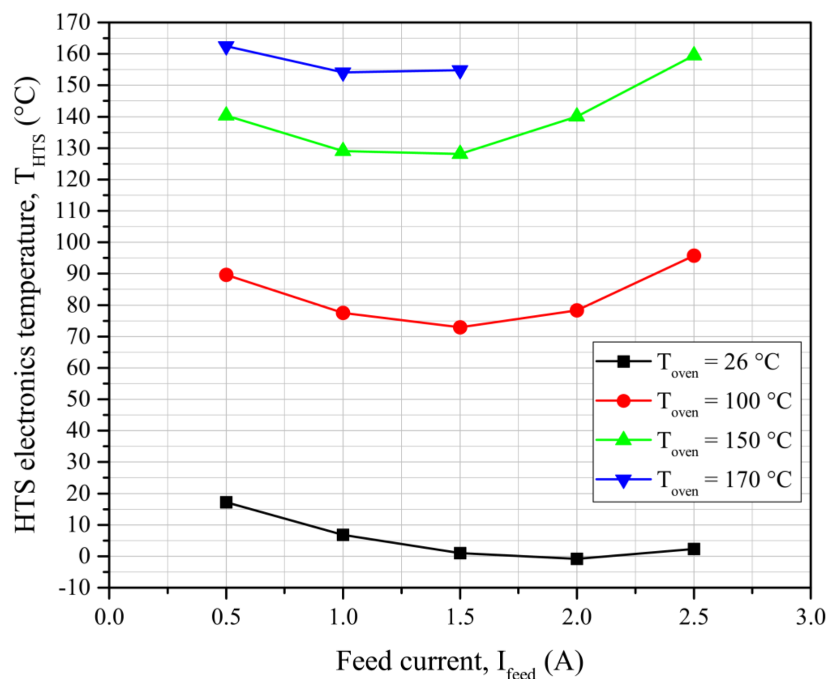

Figure 4.12 Temperature of the HTS electronics vs. coolers feed current, at different oven temperatures, for *Prototype mark-1*. 2 x *Cooler #1* were assembled in the tool with thermal grease.

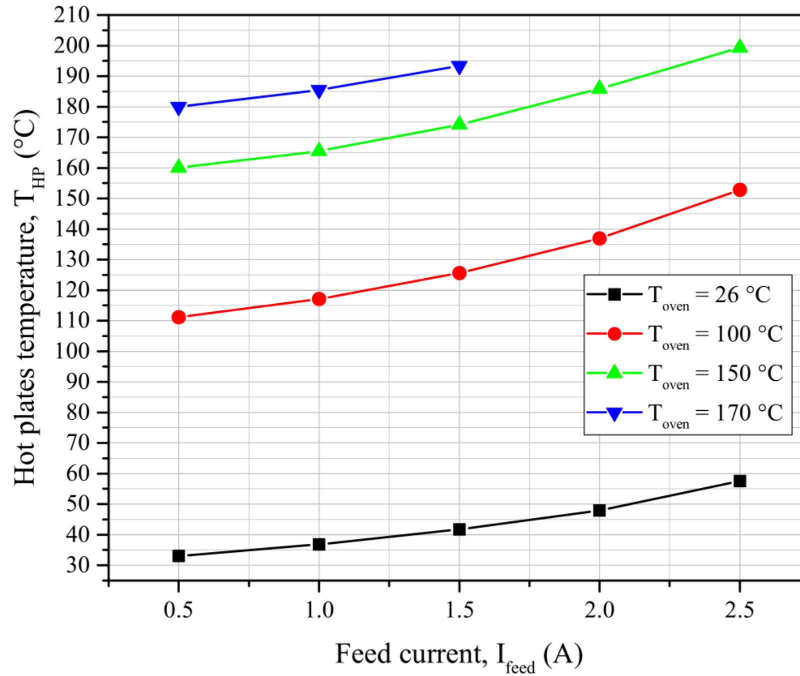

Figure 4.13 Temperature of the hot plates vs. coolers feed current, at different oven temperatures, for *Prototype mark-1*. 2 x *Cooler #1* were assembled in the tool with thermal grease.

Figure 4.12 and Figure 4.13 show the temperature trend of the HTS electronics and of the TEC hot plates, respectively, with the feed current. While the temperature of the hot plates monotonically increases with the feed current, due to the increasing transported flux and Joule losses, the temperature of the cooled electronics reaches a minimum for a certain feed current, which varies with the operating temperature.

This optimal current I_{opt} can be defined as the TEC feed current at which the marginal gain in absorbed heat flux from the cold plate, due to an infinitesimal increase of I_{feed}, becomes smaller than the heat flux that leaks back to the cooled electronics through the insulation. The optimal feed current varies with the operating temperature as a consequence of the change in the thermoelectric properties. The concept of optimal feed current will be further discussed and analyzed in the next chapter.

Since the system was not fed with a continuous range of currents, it was not possible to estimate the value of the optimal currents accurately. However, the concave trend could be clearly observed and the following currents were found to minimize the HTS temperature: 2.5 A at T_{oven} = 26 °C, 2 A at T_{oven} = 100 °C and 150 °C, and 1 A at T_{oven} = 170 °C. The optimal current decreases with the operating temperature as a consequence of the change of the thermoelectric properties and of the increasing Joule losses.

The performance of the system at the estimated optimal feed currents is reported in Figure 4.14. It is shown how the temperature span across the coolers “distributes” below and above the operating temperature. Since the system was tested with an estimated convection coefficient around 30 ~ 40 W/m^{2}K, a forecast was also proposed for operations in a 100 W/m^{2}K environment.

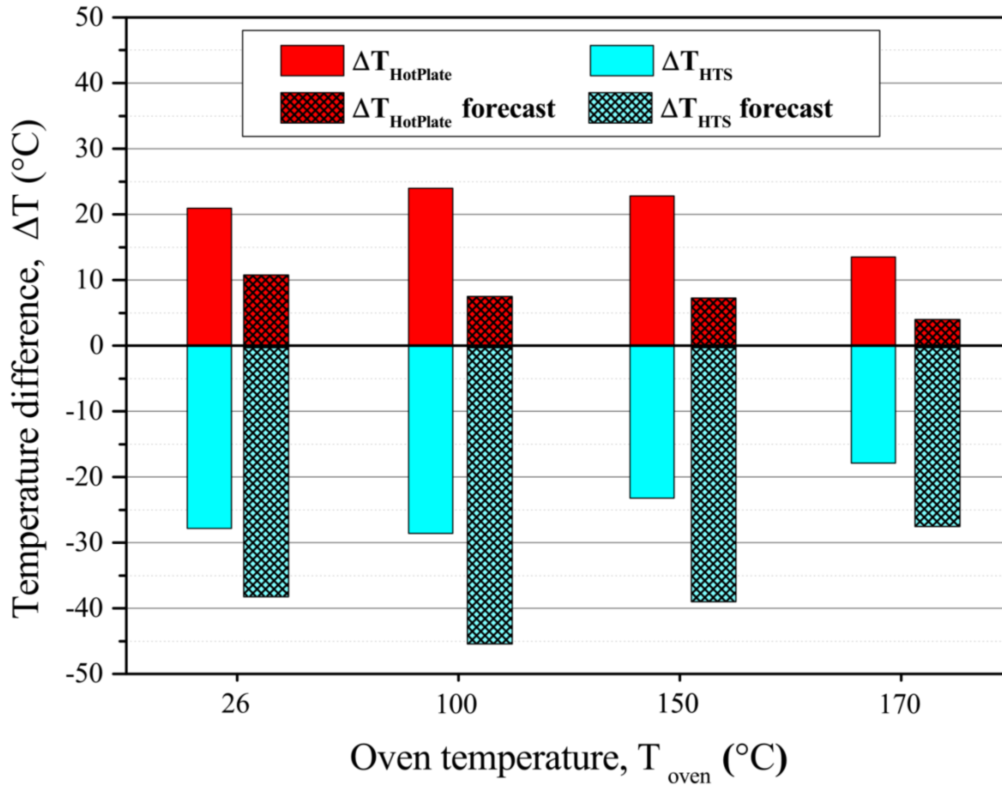

Figure 4.14 Representation of $\Delta T_{HotPlate}$ (red bars) and ΔT_{HTS} (blue bars), at the operating conditions that minimized the HTS electronics temperature, at different oven temperatures T_{oven}. The tests were carried out in air in a ventilated oven, where the convective heat transfer coefficient along the housing surface was estimated ˜ 30 W/m^{2}K. The system behavior was also forecast for an external convection coefficient of 100 W/m^{2}K and represented with dashed bars.

The variables $\Delta T_{HotPlate}$ and ΔT_{HTS} were defined as follows:

$$\Delta T_{HotPlate} = T_{HP} - T_{oven} \tag{4.5}$$

$$\Delta T_{HTS} = T_{HTS} - T_{oven} \tag{4.6}$$

When operating close to the optimal feed currents, the system was able to maintain the HTS electronics at a maximum span of 29 °C below the external temperature, when operating at T_{oven} = 100 °C. As also shown previously, the best performance of the system was observed at 100 °C. Maximum temperature differences below ambient of 28 °C, 23 °C, and 18 °C were obtained respectively for the tests at 26 °C, 150 °C, and 170 °C. The hot side of the system is instead maintained between 13 °C and 24 °C above the oven temperature.

A different scenario appears when evaluating the performance of the system at 100 W/m^{2}K. The enhanced convective heat transfer improves the excess heat rejection, allowing the cold plate to be cooled further below the previously illustrated temperatures. ΔT_{HTS} is predicted to be -38 °C, -45 °C, -39 °C, and -27 °C for operations at 26 °C, 100 °C, 150 °C, and 170 °C. As expected, the hot plate temperature decreases significantly and $\Delta T_{HotPlate}$ ranges now between 4 °C and 11 °C. It is important to notice that the optimal value of feed current changes with the heat rejection conditions, because strictly related to the capability of

the system of dissipating the excessive heat. The values of I_{opt} at h = 100 W/m^{2}K are therefore not the same as the ones at h ~ 30 W/m^{2}K.

The test results at 170 °C already show that *Prototype mark-1* does not satisfy the design criteria (ΔT_{HTS} = 25 °C) in the current setup and operating conditions. However, the tests were characterized by a lower convection heat transfer than the reference value and the forecasts show the cooling integration concept is promising.

Table 4.2 Summary of the experimental data from the tests of *Prototype mark-1* at high temperature. *Experiments at room temperature were carried out with an external fan, which characterized the heat transfer between ambient and tool with a slightly higher convection coefficient compared to the other tests.

T_{oven} (°C)	I_{feed} (A)	V_1 (V)	V_2 (V)	P_{feed} (W)	T_{HTS} (°C)	T_{Cu} (°C)	T_{HP} (°C)	T_{HTNS} (°C)	$T_{cart,b}$ (°C)	$T_{housing,avg}$ (°C)	h_{exp} (W/m^{2}K)	T_{avg} (°C)
25.9	0.5	2.8	2.6	2.7	17.2	17.1	33.1	36.0	33.7	33.3	37.1*	25.1
26.1	1	5.4	5.2	10.6	6.8	7.2	36.8	38.9	36.5	36.5	36.3*	22.0
25.4	1.5	7.9	7.6	23.3	1.0	1.7	41.8	42.5	40.1	40.5	36.2*	21.8
27.0	2	10.6	10.2	41.6	-0.9	0.2	47.9	46.2	43.2	44.8	44.1*	24.1
26.8	2.5	13.6	13	66.5	2.3	3.8	57.5	53.3	49.9	52.7	43.2*	30.7
T_{oven} (°C)	I_{feed} (A)	V_1 (V)	V_2 (V)	P_{feed} (W)	T_{HTS} (°C)	T_{Cu} (°C)	T_{HP} (°C)	T_{HTNS} (°C)	$T_{cart,b}$ (°C)	$T_{housing,avg}$ (°C)	h_{exp} (W/m^{2}K)	T_{avg} (°C)
101.0	0.5	3.8	3.7	3.8	89.7	90.2	111.1	114.3	110.4	111.4	30.0	100.6
101.5	1	7.4	7.1	14.5	77.5	78.6	117.1	119.2	115.2	116.9	29.4	97.9
101.6	1.5	10.8	10.5	32.0	73.0	74.7	125.6	126.2	121.9	124.7	29.3	100.2
101.3	2	14.5	14.3	57.6	78.4	80.9	136.9	135.7	131.1	135.1	30.2	108.9
101.5	2.5	18.3	18.1	91.0	95.8	98.5	152.8	149.5	144.1	149.9	30.2	125.7
T_{oven} (°C)	I_{feed} (A)	V_1 (V)	V_2 (V)	P_{feed} (W)	T_{HTS} (°C)	T_{Cu} (°C)	T_{HP} (°C)	T_{HTNS} (°C)	$T_{cart,b}$ (°C)	$T_{housing,avg}$ (°C)	h_{exp} (W/m^{2}K)	T_{avg} (°C)
151.4	0.5	4.1	4	4.1	140.4	141.0	160.1	163.2	159.2	160.8	33.4	150.6
151.3	1	8	7.9	15.9	129.0	130.6	165.5	167.6	163.5	165.9	32.4	148.1
151.4	1.5	11.8	11.7	35.3	128.2	130.4	174.2	175.0	170.6	174.0	32.2	152.3
151.6	2	15.4	15.1	61.0	140.1	142.6	186.0	185.4	180.3	185.0	32.1	164.3
151.7	2.5	18.6	18.2	92.0	159.6	161.9	199.3	197.3	191.5	197.5	32.3	180.6
T_{oven} (°C)	I_{feed} (A)	V_1 (V)	V_2 (V)	P_{feed} (W)	T_{HTS} (°C)	T_{Cu} (°C)	T_{HP} (°C)	T_{HTNS} (°C)	$T_{cart,b}$ (°C)	$T_{housing,avg}$ (°C)	h_{exp} (W/m^{2}K)	T_{avg} (°C)
171.8	0.5	4.2	4.1	4.2	162.5	163.0	180.0	183.1	179.1	180.8	35.0	171.5
172.0	1	8.2	7.9	16.1	154.1	155.4	185.5	187.7	183.4	186.0	33.9	170.4
172.0	1.5	11.8	11.6	35.1	154.9	156.8	193.3	194.4	189.8	193.3	33.9	175.1

4.7 Conclusions from the tests on *Prototype mark-1*

Prototype mark-1 represents an important step for the progress of the project and proved the concept of the chosen thermal management principle. The preliminary tests on the setup contributed to build a detailed understanding of the system and provided good inputs for further development.

Thermal grease, in combination with a clamping system, proved to be the best approach to interface the TEC with the other components in the system. Thermal epoxy and soft adhesive pads proved, instead, to provide an unstable mechanical connection over the operating temperature range and a poor thermal interface, respectively. Furthermore, the type of *Cooler #1* proved to be the most efficient and best performing, among the tested device pairs. *Cooler #2* proved to be the poorest performing and was excluded by the suitable candidates. *Cooler #3* showed slightly lower temperature spans than *Cooler #1*, with a better performance towards high cooling loads and feed powers. *Cooler #3* could be used in a single-TEC configuration, where only one cooling device is used. Using two TECs helps to better reject the excess heat, but also increases the chances of failure. In this case, having a redundant component does not lower the risk of failure, but increases it. It is enough to have one failed cooler out of the two to compromise the operation of the system. The failed TEC would in fact provide an effective thermal path for the rejected heat to flow back into the electronics, making the cooling action from the functioning TEC in vain. ‘

The preliminary tests provided a first insight into the operation of the system and on the variation of its performance with temperature. The setup was able to maintain the temperature of the sensitive electronics 18 °C below ambient, when operating at 170 °C and with a convection coefficient of ~30 W/m^2K. The tool was predicted to cool the electronics more than 27 °C below ambient, with an operating temperature of 170 °C and a convection coefficient of 100 W/m^2K.

Although *Prototype mark-1* did not meet the design criteria in the current setup, the thermal management concept, supported by the forecasts at higher convection coefficients, appeared promising. The following actions were considered for improvement of the system.

- Review of the existing electronics and efficiency improvement: lowering the power dissipation rate of the HTS and HTNS electronics can reduce the heat rejection temperature and allow cooling the electronics to lower temperatures.

- Modelling of the system: reproducing the heat transfer phenomena that characterize the system can help to individuate and address directions of improvement.

- Application of methods for thermal design optimization: advanced optimization methods can aid in developing optimal thermal design. The minimization of the HTS electronics temperature would be the objective of the optimization.

- Implementation of the clamping method: implementing a screw system that provides a mechanically stable contact between the coolers and the neighboring components can reduce the thermal resistances at the interfaces between them.

All the mentioned actions were performed for the development of *Prototype mark-2*, which is presented in the next chapter.

5. Optimization of the system and *Prototype mark-2*

Building on the knowledge developed from testing *Prototype mark-1*, this chapter presents the improved design and the construction of *Prototype mark-2*. The directions of improvement described in the conclusions from Chapter 4 were investigated to build a second lab-prototype that could meet the design criteria.

- A review of the well tractor electronics was performed to increase the efficiency and lower the heating rate of the tool. More efficient components were selected to replace the power devices and to reduce the heat flux from the HTNS electronics. As previously discussed, lowering the power dissipation from the HTNS components would decrease the heat rejection temperature of the system, and consequently the cooling temperature. The heating rate of the new power devices was estimated to a total of 5 W, with a reduction of 72% compared to the previous electronics. The PCB was re-designed and a more compact layout was obtained. The area in which the HTS components are mounted, and that requires cooling, was reduced from 120 x 41 mm to 7.5 x 38 mm. In this way the heat leakages through the insulation could be lowered by reducing the heat transfer surface area. Furthermore, a more uniform cooling effect could be applied given the smaller size of the PCB. The HTS components were estimated to still dissipate 1 W. The new electronics arrangement was successfully tested up to an oven temperature of 170 °C, given their maximum operating temperature of 175 °C, and the new values of power dissipation were used for the development of *Prototype mark-2*. Due to the reduced dimensions of the system, only one *Cooler #3* was employed, instead of two *Cooler #1*.

- A model of the actively cooled section was implemented in the finite element software COMSOL to simulate the heat transfer within the system, including the thermoelectric heat transport across the cooler.

- The topology optimization method was integrated in the COMSOL model and used to optimize the thermal layout of the two chassis halves. The optimization aimed at defining an optimized topology of the chassis, by optimizing the distribution of thermal insulation and aluminum within the system. The objective of the optimization was to minimize the HTS electronics temperature.
- According to the topology optimization results, *Prototype mark-2* was built and tested at temperatures of 180 °C, 190 °C, and 200 °C. The optimized system included a clamping system that guaranteed a stable and effective thermal contact between the cooler plates and the neighboring components.

The present chapter is, apart from the addendum, published in: Soprani S., Haertel J. H. K., Lazarov B. S., Sigmund O., Engelbrecht K. A design approach for integrating thermoelectric devices using topology optimization, *Applied Energy*, 176: 49–64 (2016). The paper can be found in Appendix A.

5.1 Introduction

Over the past decades, thermoelectric devices (TEDs) have become competitive solutions for waste energy recovery, heat pumping, and cooling applications (Rowe (1995), Bell et al. (2008), He et al. (2015), Tritt et al. (2006), Montecucco et al. (2014)). Advantages of TEDs include compactness, gas-free solid-state operation, lack of moving parts, and long life-span. However, a lower energy conversion efficiency compared to other well established technologies (Hermes et al. (2012)) can limit their application. In order to increase energy conversion efficiency, optimization of thermoelectric devices is an active research topic, both in terms of the thermoelectric materials employed (Dresselhaus et al. (2007), Snyder et al. (2008), Bulusu et al. (2008), Yang et al. (2013)), and the architecture of devices (Abramzon (2007), Heghmanns et al. (2015), Xiao et al. (2012), Takezawa et al. (2012), Chen et al. (2008), Pan et al. (2007)). Additionally, efficient TED operation strongly relies on the integration into the overall energy conversion system (Quan et al. (2013), Taylor et al. (2008), Rezania et al. (2013), Gou et al. (2010), David et al. (2012)). Effective heat transfer at the cold and hot plates, minimization of thermal resistances within the system, and reduction of heat leakages each improves overall efficiency. These features depend on the thermal layout of the integrated system and should be taken into account during the design phase to maximize effectiveness.

Here, we present a novel automated method, using topology optimization, to design thermal interfaces and insulation solutions for a TED to be integrated in a system with design constraints. Topology optimization has not previously been applied to thermoelectric systems, but this technique has great potential as a powerful design tool, as it can be used to optimize the topology of heat sinks, heat exchangers, and to define optimized distributions of thermally conducting and insulating material based on a set of design constraints. We show that the method can be implemented using commercial software, is robust, and is suitable for TED applications that must be packaged in a defined space. The method can be used to optimize a thermoelectric system for a variety of objective functions, such as efficiency, power recovery rate, and temperature span. Contrary to size and shape optimization approaches, topology optimization requires no initial design concept or a priori parametrization (Bendsøe et al. (2004), Sigmund et al. (2013)). This flexibility is especially important in the early design phase, as it saves development time and can yield unintuitive optimized structures. Density-based topology optimization methods are particularly promising, since they consider the systematic distribution of material within a design domain, while aiming to optimize a certain objective function.

Topology optimization was first developed and established for structural mechanics applications and was subsequently applied to various other disciplines (Deaton et al (2014), Dede et al. (2014)). Prior studies on heat transfer using topology optimization have mainly focused on pure 2D heat conduction problems (Bendsøe et al (2004), Li et al. (2004), Gersborg-Hansen et al. (2001)) as well as heat conduction with convective heat transfer to an ambient fluid (Sigmund (2001), Yin et al. (2002), Bruns (2007), Ahn et al. (2010), Iga et al. (2009)). Later works have included the explicit modeling of the fluid flow within the optimization domain in thermo-fluid models with forced convection in 2D (Yoon et al. (2010), McConnell et al. (2012), Marck et al. (2013), Matsumori et al. (2013), Van Oeleven et al. (2014), Lee et al. (2012)) and 3D (Yaji et al. (2015)). More recent applications of the approach have extended models to consider 2D topology optimization of natural convection (Alexandersen et al. (2014)) and radiation as the dominant heat transfer mechanism (Castro et al. (2015)). The design, manufacturing and subsequent experimental testing of optimized forced-convection heat sinks have also been presented (Koga et al. (2013), Dede et al. (2015), Dede et al. (2014)).

Building on previous studies, this work addresses an existing industrial challenge and applies topology optimization to a thermoelectric system for the first time. Here, it is used to design the thermal integration of a thermoelectric cooler (TEC) in a downhole tool for oil well interventions. The space constraints imposed by the application and the clearly defined thermal boundary conditions make this an attractive case for topology optimization (Soprani et al. (2015b)). In the studied application, the TEC maintains a specific group of electronics at a temperature below the outside well temperature to prevent overheating issues that occur when the borehole exceeds the maximum temperature rating of the electronics (175 °C). Topology optimization is used to optimize the distribution of the insulating material, which thermally protects the cooled electronics, and of the conducting material, which aids in rejecting heat from the TEC to the well. The objective of the optimization is to minimize the temperature of the cooled electronics. A more detailed discussion regarding well interventions, active cooling, and thermal management of downhole electronics, is given in Ref. (Bennett (1988), Flores (1996), Jakaboski (2004), Sinha et al. (2011), Pennewitz et al. (2012), Soprani et al. (2015a)).

A model of the thermoelectric device was developed for this application, implemented in a 3D finite element model of the system, and coupled with the optimization algorithm. Temperature dependent properties of the TEC were implemented in order to capture the effects of the real material properties during the optimization process. The topology optimization model was used to optimize the design of the system for different operating conditions and to define the optimal working conditions of the TEC. The improvements in performance for the optimized systems were assessed and used to define a final design of the electronics unit, which is also practical from a manufacturing and assembly standpoint. The defined setup was then manufactured and experimentally tested at different operating conditions, and the results compared to the model predictions.

5.2 Description of the system

This chapter briefly introduces the electronics unit system, its main components and the overall thermal management principle. A 3D model of the longitudinal section of the system is illustrated in Figure 5.1.

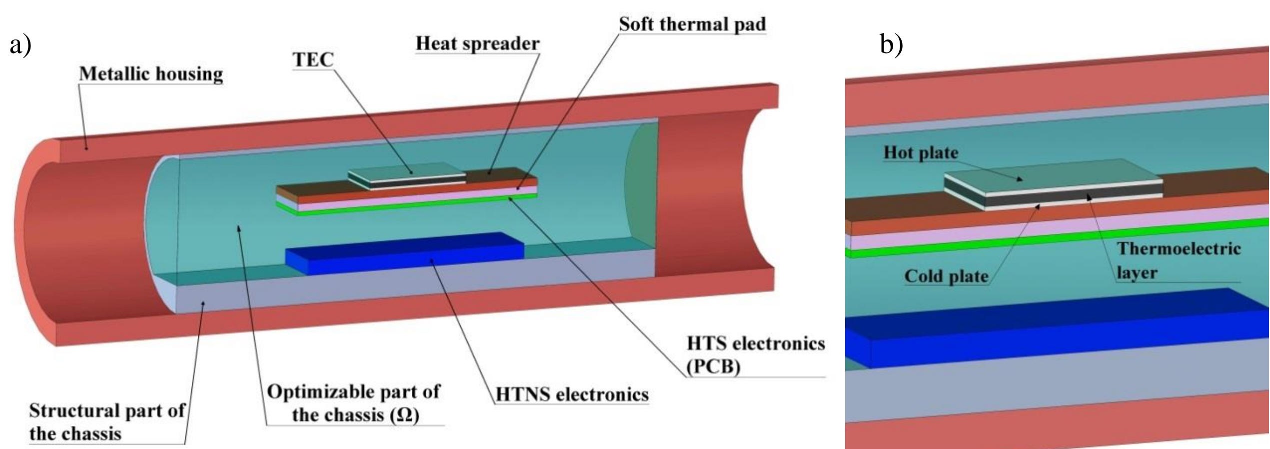

Figure 5.1 Representation of the axial section of the downhole tool (1a, left side); the domain of the optimizable chassis is represented as partially transparent and colored in light blue. Particular of the TEC device (1b, right side).

The analyzed downhole electronics unit is composed of the following parts:

- *Metallic cylindrical housing*: a hollow cylinder that shields and seals the inner components from the harsh well environment.
- *Chassis*: a rigid metallic support used for final assembly, on which the electronics are mounted and slid into the housing. It is divided in a structural part, which mechanically supports the system; and an optimizable part, which surrounds the components within the structural chassis and is the object of the topology optimization.
- *Electronic components*: they can be split into high temperature-sensitive (HTS) and high temperature-non-sensitive (HTNS) components. The former are likely to fail when their operating temperature exceeds 175 °C, the latter can even operate above 200°C. The HTS electronics are mounted on a printed circuit board (PCB) and are characterized by a power dissipation rate of 1 W; the HTNS electronics are mounted directly on the chassis and dissipate an estimated 5 W.

Additional components, used for the integration of the active cooling system into the tool, are:

- *Thermoelectric cooler*: the cooling system is connected to an electric power source and transfers a heat flux from the cold to the hot plate, when an electric current is applied. The TEC cold plate needs to be thermally coupled to the HTS electronics, while the hot plate requires a thermal link to the hot reservoir, represented by the well environment.
- *Metallic heat spreader*: a rigid plate attached to the TEC cold plate that, together with the thermal pad, constitutes the thermal interface between the PCB and the cooler.
- *Soft thermal pad*: a soft silicone sheet, which is inserted between the PCB and the copper plate to create a thermal path between the irregular surface of the PCB and the heat spreader.

The heat management strategy aims at maintaining the HTS electronics at 175 °C or below when the tool is operating in a 200 °C environment. It is based on the passive cooling of the HTNS components, which can withstand high temperatures, and the active cooling of the HTS components through the Peltier module. The PCB is therefore thermally coupled, through the heat spreader and the thermal pad, with the cold plate of the Peltier module so the cooling load can be absorbed by the cooler. The TEC hot plate, in turn, needs to be thermally connected to the chassis; in this way, the excessive heat can flow through the housing and be rejected to the well fluid that laps the outer surface of the housing, through convective heat transfer. A tight mechanical contact is ensured between the structural chassis and the housing, to reduce the contact thermal resistance.

It is important to note that the thermal connection between the TEC hot plate and the chassis, as well as the distribution of insulating material, will be the result of the topology optimization process. The optimization is expected to define an optimized distribution of thermally conducting material and thermal insulation inside the unit, so the refrigerated electronics are properly protected from the hot surroundings and the excessive heat is effectively rejected to the well fluid. These two phenomena both act towards the minimization of the HTS electronics temperature, which is the objective of the optimization. While the optimization is focused on the thermal integration of the TEC, the topology of the TEC module itself is not the object of the optimization. The finite-element model of the TEC is implemented to simulate the performance of a commercial high-temperature module to be integrated into the downhole tool. The freedom to optimize the

electronics unit is limited by three factors: the tool needs to fit a specific well piping size, so its dimensions are constrained to the values reported in Table 5.1; the position and the design of the components inside the system are constrained by the application; the structural part of the chassis cannot be optimized because of its mechanical function.

Table 5.1 List of the components with their dimensions and properties.

Component	*Length (mm)*	*I.D. (mm)*	*O.D. (mm)*	*Thermal conductivity ($Wm^{-1}K^{-1}$)*
Metallic housing	300	62	80	150
Structural chassis	200	58	62	138
Optimizable chassis	200	-	58	(Eq. (5.16))
Component	*Length (mm)*	*Depth (mm)*	*Height (mm)*	*Thermal conductivity ($Wm^{-1}K^{-1}$)*
TEC plates	40	40	0.95 each	27
TEC thermoelectric layer	40	40	2.0	(Eq. (5.8))
Heat spreader	100	40	3.0	400
Soft thermal pad	100	40	3.0	12
HTNS electronics	90	42	6.0	130
HTS electronics (PCB)	100	40	1.6	0.3

5.3 Finite element model

5.3.1 Governing equations

The geometry shown in Figure 5.1 was implemented in the finite element software COMSOL Multiphysics (COMSOL Multiphysics 5.0) and divided in domains, each of them characterized by different material properties and governing equations. In order to simulate the heat transfer within the system, mainly driven by heat conduction, the heat transfer PDE (Eq. (5.1)) was solved in all the domains, except for the thermoelectric material layer.

$$\nabla \cdot (-k\nabla T) = Q_{source} \tag{5.1}$$

where k is the material thermal conductivity, T is the temperature, and Q_{source} is a volumetric heat source. Eq. (5.1) was not applied to the thermoelectric material domain, as the heat transport related to the thermoelectric effect also needed to be taken into account. A modified heat transfer PDE (Eq. (5.2)) was used instead.

$$\nabla \cdot (\boldsymbol{J}S'T - k'\nabla T) = Q'_{JouleHeating} \tag{5.2}$$

where $\boldsymbol{J}$ is the electric current density vector, S' is the material Seebeck coefficient, and $Q'_{JouleHeating}$ is the heat source associated with the Joule heating effect.

5.3.2 Boundary conditions

The boundary conditions were set in order to simulate the operating and external conditions that could occur in a well during a downhole intervention. A convective heat flux was set on the outer surface of the housing, to reproduce the interaction between the well fluid and the tool.

$$-\boldsymbol{n} \cdot (-k\nabla T) = h(T - T_{ext}) \tag{5.3}$$

Furthermore, the tool electronics unit would be assembled in the middle of a tool string, composed of several sections, and the heat transfer with the well is expected to mainly occur radially. For this reason, adiabatic boundaries were set at the two ends of the cylindrical setup.

$$-\boldsymbol{n} \cdot (-k\nabla T) = 0 \tag{5.4}$$

where $\boldsymbol{n}$ is the surface normal vector, T_{ext} is the well fluid temperature and h is the heat transfer convection coefficient. Concerning the interface between the thermoelectric material domain, where Eq. (5.2) is solved, and the rest of the geometry, where Eq. (5.1) is solved, a Dirichlet boundary condition was defined to provide consistency to the temperature distribution. Heat sources were set in the HTNS electronics domain (5 W), and at the interface between the PCB and the soft thermal pad (1 W), to simulate the power dissipation of both electronics modules. Thermal resistances, $R_{th1,2}$ = 2.5e-5 m^2KW^{-1} , were modelled at the interface between the HTNS electronics and the structural chassis, and on the outer boundaries of the TEC hot/cold plates; they simulated the contribution of a 0.1 mm thick layer of thermal grease, with a thermal conductivity of 4 $Wm^{-1}K^{-1}$. An additional thermal resistance, R_{th3} = 1.1e-3 m^2KW^{-1}, was set at the interface between the structural chassis and the housing in order to simulate the contact resistance given by the assembly. The value of this thermal resistance was estimated through the comparison between simulation results and experimental data from thermal tests on an analogue setup.

The operating conditions of the cooler were characterized by the TEC feed current I_{feed}, which represents the electric current which is supplied to the module and is given to the model as an input. The correlation between this parameter and the current density vector $\boldsymbol{J}$ (see Eq. (5.2)) is explained in more detail in the next section.

5.3.3 TEC model

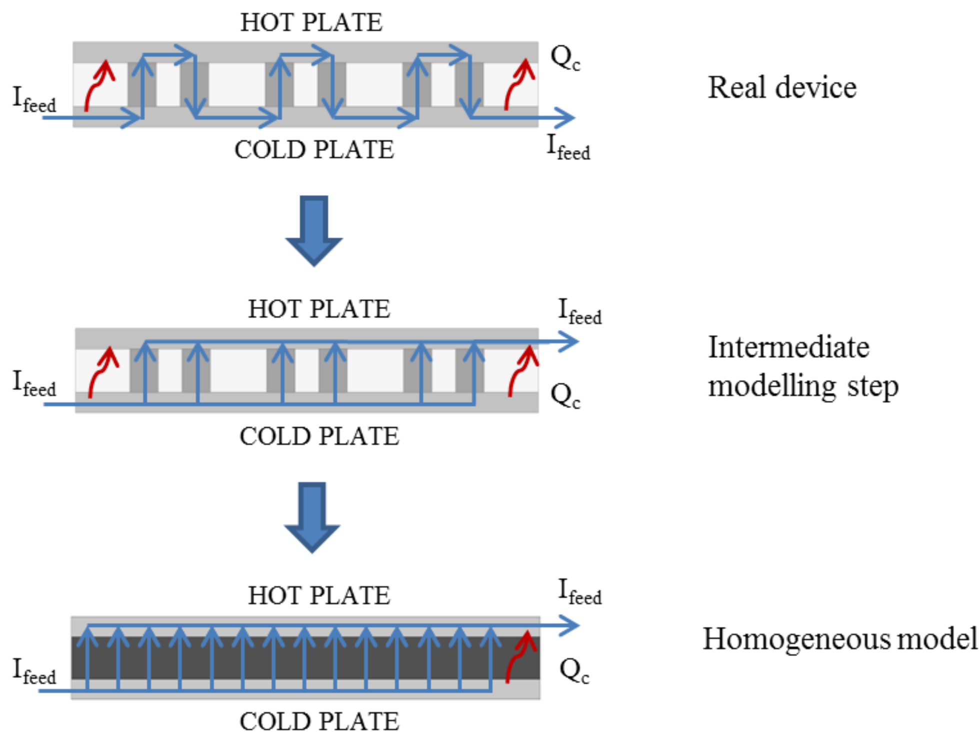

Figure 5.2 Illustration of the simplification process for the TEC model. The longitudinal section and the working principle of the *real device* and of the *homogeneous model* are included. For the sake of a better understanding, an intermediate step of the model development, called *intermediate modelling step*, is also included.

A particular focus was put on the modelling of the thermoelectric cooler. Its main components are two aluminum oxide plates, between which leg pairs of semiconducting material (p-n junctions) are mounted, electrically connected in series, and separated by air. Reproducing the detailed geometry of the module would have drastically increased the complexity and the computational time of the 3D topology optimization model. Therefore a simplified model of the TEC was developed: the intermediate semiconductor layer was modelled as homogeneous and isotropic, and equivalent material properties were weighted on the properties of Bi_2Te_3 and air. In this way, the cooling effect driven by a given TEC feed current could be approximated to the real case, while the geometry could be significantly simplified.

As a consequence of the homogenization process, the electric and thermal transport phenomena could not be differentiated within the Bi_2Te_3 and air domains, and the inhomogeneous temperature gradient across the module could not be reproduced. However, this approximation was considered acceptable as it preserves the average heat fluxes that drive heat transfer in the integrated system.

Figure 5.2 illustrates the steps that were used to develop the homogeneous model and that are explained in the following sub-sections.

5.3.3.1 Effective current density

In the *real device*, the thermoelectric leg pairs are fed in series. The current density through the legs $\boldsymbol{J}$ can be expressed, in good approximation, as the 3D vector $[0 , 0 , \pm J_z]$. The only non-zero contribution is along the

z-axis, perpendicular to the TEC plates, and can be equal to $-J_z$ or $+J_z$**.** The scalar current density can be defined as:

$$J_z = \frac{I_{feed}}{A_{leg}} \tag{5.5}$$

where J_z is the scalar current density along the z-axis, I_{feed} is the TEC feed current and A_{leg} is the cross sectional area of the single thermoelectric leg.

In the *intermediate modelling step*, the thermoelectric legs are all doped p-type and are fed in parallel and the current density vector is now equal to [0 , 0 , + J_z]. Given the parallel configuration, and in order to maintain the same thermoelectric effect in each leg as the *real device*, the TEC feed current becomes *N* times bigger, where *N* is the number of thermoelectric legs installed in the module.

In the *homogeneous model*, there is no distinction between thermoelectric legs and air. The homogeneous layer is supplied by a uniform electric current equal to $N \cdot I_{feed}$, in the positive z-axis direction. A different current density needs to be defined:

$$J_z{}' = \frac{NI_{feed}}{A_{tot}} = \frac{NI_{feed}}{A_{tot}} \cdot \frac{NA_{leg}}{NA_{leg}} = \frac{I_{feed}}{A_{leg}} \cdot \frac{A_{BiTe}}{A_{tot}} = J_z \, x_{BiTe} \tag{5.6}$$

where $J_z{}'$ is the equivalent scalar current density for the homogeneous model, A_{tot} is the total cross sectional area of the thermoelectric module, A_{BiTe} is equal to *N* times A_{leg} and represents the cross sectional area occupied by the thermoelectric legs in the *real device*, and x_{BiTe} is the ratio between A_{BiTe} and A_{tot}. x_{BiTe} is also equal to the volume ratio between bismuth telluride and the total volume of the intermediate layer.

5.3.3.2 Effective Seebeck coefficient

Given the TEC PDE for the homogeneous layer in Eq. (5.2), we want to maintain the same thermoelectric cooling effect ***J'S*** as the *real device*. First, it is assumed that the Seebeck coefficient of the layer does not change with the homogenization process. However, the current density has changed and it can be imposed:

$$J_z{}'S = J_z S' \quad \rightarrow \quad S' = S \, x_{BiTe} \tag{5.7}$$

More intuitively, one could think that the thermoelectric cooling effect is now generated with the same scalar current density J_z as the *real device*, but only by a portion of the layer (x_{BiTe}), ideally occupied by the Bi_2Te_3 legs. Although the cooling effect is maintained to be the same, the homogeneous approximation spreads it equally along the whole layer.

5.3.3.3 Effective thermal conductivity of the layer

The heat transfer within the intermediate layer occurs mainly from a cooler plate to the other, while the temperature gradient along the direction parallel to the plates is expected to be negligible. It is therefore assumed that the effective thermal resistance of the layer is equal to the parallel coupling of the thermal resistances, of air and Bi_2Te_3, between the hot and cold plate.

$$k' = k_{air} \frac{A_{air}}{A_{tot}} + k_{BiTe} \frac{A_{BiTe}}{A_{tot}} = k_{air}(1 - x_{BiTe}) + k_{BiTe} \, x_{BiTe} \tag{5.8}$$

where *k'* is the thermoelectric layer equivalent thermal conductivity for the homogeneous model, and *t* is the thermoelectric layer thickness.

5.3.3.4 Effective electrical conductivity of the layer

In analogy with the effective thermal conductivity calculation, and neglecting the air electrical conductivity:

$$\sigma' = \sigma_{BiTe}\, x_{BiTe} + \sigma_{air}\, x_{air} = \sigma_{BiTe}\, x_{BiTe} \tag{5.9}$$

where *σ'* is the thermoelectric layer equivalent electric conductivity for the homogeneous model. Consequently the Joule heating term can be calculated as:

$$Q'_{JouleHeating} = \frac{x_{Bi2Te3}}{\sigma_{Bi2Te3}}\, \boldsymbol{J} \cdot \boldsymbol{J} = \frac{J_z^2}{\sigma_{Bi2Te3}}\, x_{Bi2Te3} \tag{5.10}$$

Again, the original Joule losses are maintained, but are spread uniformly along the layer because of the homogeneous approximation.

A suitable high-temperature commercial cooler was disassembled and analyzed, so the main geometric features could be measured. They are summarized in Table 5.2.

Table 5.2 Geometric features of the modelled thermoelectric cooler.

Parameter	*Description*	*Value*
h_{TEC}	Total height of the module	3.90 mm
l_{TEC}	Edge length of the module	40.0 mm
h_{Al2O3}	Height of the hot/cold plate	0.95 mm
N	Number of thermoelectric legs	254
h_{Bi2Te3}	Height of the single thermoelectric leg	2.00 mm
l_{Bi2Te3}	Edge length of the single thermoelectric leg	1.30 mm
A_{leg}	Cross sectional area of a thermoelectric leg	1.69e-6 m^2
x_{Bi2Te3}	Volume fraction of semiconductor materials	0.27

The properties of Bismuth Telluride S_{BiTe}, k_{BiTe} and σ_{BiTe} from (Gordon et al. (2002)) were implemented as non-linear functions of temperature. In order to better match the performance of the high-temperature commercial cooler, a linear coefficient was multiplied to the expressions of the Bi_2Te_3 Seebeck coefficient, thermal conductivity, and electrical conductivity. The linear coefficients are the result of a best fit analysis based on experimental data and are respectively equal to S_l=1.30, k_l=0.80, and σ_l=1.15.

5.3.4 Topology optimization and SIMP method

The topology optimization approach was used to assess which distribution of aluminum/thermal insulation inside the electronics unit minimized the temperature of the HTS electronics. Filling the electronics unit with only thermal insulation would maximize the thermal protection of the cooling zone from heat leakages, but would not provide an effective thermal path for the rejected heat to flow to the well environment. The Peltier

module would therefore not be able to work within the cooling design conditions. Filling the electronics unit with aluminum, instead, would enhance the heat rejection process, but would not protect the cooling zone from heat leakages, making the cooling process ineffective. A tradeoff needs to be reached and the Solid Isotropic Material with Penalization (SIMP) method allowed looking for an optimized solution.

The main goal of the SIMP method, as part of the density-based topology optimization approaches, is to achieve a binary design within the optimizable domain, where the design variable can be equal to 0, representing thermal insulation, or to 1, representing aluminum. The topology optimization problem can be stated as follows:

$$minimize: \quad f_{obj}(T, \rho_{design}) = \frac{1}{A_{PCB}} \int_{\Omega_{PCB}} T \, d\Omega_{PCB} \tag{5.11}$$

$$subject\ to: \quad 0 \leq \rho_{design} \leq 1 \tag{5.12}$$

$$\boldsymbol{r}(T, \rho_{design}) = \boldsymbol{0} \tag{5.13}$$

where f_{obj} is the objective function to minimize, equal to the integral average of the temperature distribution along the PCB surface Ω_{PCB}; A_{PCB} is the PCB area surface; ρ_{design} is the design variable that can range between 0 (thermal insulation) and 1 (aluminum), and the distribution of which needs to be optimized; $\boldsymbol{r}(T, \rho_{design})$ is the residual of the state governing equations within the discretized system.

A PDE-based density filter (Lazarov et al. (2011)) was used to smooth the interfaces between aluminum and insulator and to introduce a minimum length scale into the design. The PDE-based filter was used because it can be implemented in the optimization model with little additional effort and it offers a computationally efficient method of density filtering. The PDE that was used for filtering is stated in Eq. (5.14).

$$-r^2 \nabla^2 \tilde{\rho} + \tilde{\rho} = \rho_{design} \tag{5.14}$$

where $\tilde{\rho}$ is the filtered density field and r is a filter parameter, defined as 1.5 times the maximum element size and equal to 3e-3 m. Since density filtering inherently introduces a band of intermediate densities between aluminum and insulator, the filtered design variable field $\tilde{\rho}$ was then projected towards 0 and 1 to obtain a crisp design. For this purpose a smoothed threshold projection (Wang et al. (2011)) was used.

$$\bar{\tilde{\rho_i}} = \frac{\tanh(\beta\eta) + \tanh(\beta(\tilde{\rho_i} - \eta)}{\tanh(\beta\eta) + \tanh(\beta(1 - \eta))} \tag{5.15}$$

where $\bar{\tilde{\rho_i}}$ is the projected density field, η is the projection threshold, equal to 0.5, and β defines the steepness of the projection.

When applying the topology optimization SIMP method, it is not possible to theoretically guarantee the convergence to a global optimum. Nevertheless, it is possible to tune the optimization parameters through the continuation method to ensure that the solution is close to the global optimum (Sigmund et al. (1988)). In this study, using a steep projection at the beginning of the optimization could result in convergence to local minima. Therefore, a continuation approach (Wang et al. (2011)) was used to ramp β, which means that the optimization was started with an almost linear projection ($\beta = 1$) and β was subsequently gradually increased

to steepen the projection function. Thus, one could ensure that the optimization problem is convexified at the beginning of the optimization, while ending up with a crisp design.

The difference of thermal conductivity between aluminum and thermal insulation was accounted by an interpolation function k_{SIMP} that defined the effective thermal conductivity of the optimizable chassis.

$$k_{SIMP} = k_{ins} + (k_{Al} - k_{ins})\bar{\tilde{\rho}}^p \tag{5.16}$$

where k_{SIMP} is the effective thermal conductivity, k_{ins} = 0.17 Wm^{-1}K^{-1} and k_{Al} = 138 Wm^{-1}K^{-1} are respectively the thermal conductivities of the insulator and of the aluminum, $\bar{\tilde{\rho}}$ is the projected design variable, and p is the penalization coefficient. When performing topology optimization for continuous design variables, intermediate regions (areas where the design variable assumes intermediate values between 0 and 1) can appear in the final distribution; these transition zones are not physically meaningful for the analyzed problem and need to be reduced as much as possible. Classically, a penalization coefficient p = 3 is used in topology optimization in combination with an active volume constraint (Sigmund et al. (2013)) to make intermediate regions unattractive with respect to the optimization problem, and to drive the control variable towards either 0 or 1. In this work, no active volume constraint was used, nevertheless a faster convergence was found for p = 3, compared to a linear interpolation (p = 1). Therefore p = 3 was used for the simulations. The globally convergent version of the Method of Moving Asymptotes (GCMMA) (Svanberg (2002)) was finally used to solve the optimization problem; this algorithm is implemented in COMSOL Multiphysics with the solver name *MMA*.

In this study, the structural and design constraints limited the optimization possibilities to the chassis domain only and did not require or allow the optimization of other components (e.g. metallic housing, heat spreader, TEC). However, the topology optimization approach can be used to simultaneously optimize multiple geometrical features by implementing additional interpolation functions for different optimizable domains. This process would increase the non-linearity of the optimization problem, consequentially increasing the computation cost and the risk of converging to local minima. Thus, in these cases, a more careful solution of the problem through the continuation method should be adopted.

5.4 Results

5.4.1 Definition of the optimized design concepts

The model was used to optimize the topology of the electronics unit for different boundary conditions of TEC feed current and well fluid convective heat transfer coefficient. The system was optimized for TEC feed currents I_{feed} = 1, 2, 3 and 4 A, where the maximum feed current stated by the analyzed commercial TEC supplier is 6 A; and for convective heat transfer coefficients h = 10, 25, 50, 100 and 500 Wm^{-2}K^{-1}, in order to reproduce very low, low, and medium well fluid convection regimes. The well temperature T_{ext} was set to 200 °C, as the maximum temperature at which the system is expected to operate.

The optimized structure was found to be a function of the boundary conditions. Various boundary conditions led to different tradeoffs between thermal protection of the cooled electronics and excessive heat rejection from the cooler to the well. The model proved to optimize the unit according to three different design configurations: *Design* 1, where the thermal insulation of the cooled electronics is prioritized; *Design 2*, where the conduction of the excessive heat towards the well is equally important as the thermal protection;

and *Design 3*, where the excessive heat rejection is crucial for the operation of the system. A more detailed illustration of the three design concepts is given in the following paragraphs.

Low feed currents and high well fluid convection coefficients led to an optimized system (*Design 1* concept), where only an aluminum pad links the cooler hot plate to the structural chassis and provides a thermal path for the excessive heat to be dissipated radially. The remaining volume of the unit is filled with thermal insulation (Figure 5.3a, Figure 5.3b, Figure 5.3c, and Figure 5.3d). In this case the thermal protection of the electronics is prioritized, as the heat rejection from the cooler to the well is not challenging. Low currents generate small Joule losses across the cooler and the high convection coefficients provide an effective heat rejection towards the well. The length of the aluminum plate increases when the TEC feed current grows and when the external convection coefficient decreases, so the heat can be better spread through the structural chassis and housing, towards the well.

When the feed current is increased and the well fluid convection coefficient lowered, the optimized system (*Design 2* concept) aims at better spreading the excessive heat, coming from the cooler hot plate, around the structural chassis and housing. A better distribution of the heat enhances, in fact, the heat exchange with the well, limits the temperature gradients due to the thermal resistances, and reduces the heat backflow to the cooled electronics. This is done by adding an aluminum layer, around the structural chassis, that spreads the heat not only radially, but also along the longitudinal direction of the tool (Figure 5.3e and Figure 5.3f). A thermally insulating layer still protects the cooled components from the hot surroundings. The thickness of the aluminum layer grows when the feed current, and the Joule losses, increase or when the well fluid convection coefficient decreases.

A third type of optimized design (*Design 3* concept) appeared for I_{feed} = 4 A and h = 10 $Wm^{-2}K^{-1}$, which respectively correspond to the highest feed current and the lowest convection coefficient that were simulated. In this case the power dissipation rate, due to Joule heating, proves to be much higher than the capability of the well fluid to remove heat through the convective mechanism. The generated heat flux increases the HTS electronics temperature above the well temperature, making active cooling infeasible at these operating conditions. The optimization process hence strongly prioritizes the heat rejection by creating a thermal path between the PCB and the well fluid, while two thin insulating layers protect the electronics from the cooler hot plate and from the HTNS electronics (Figure 5.3g and Figure 5.3h).

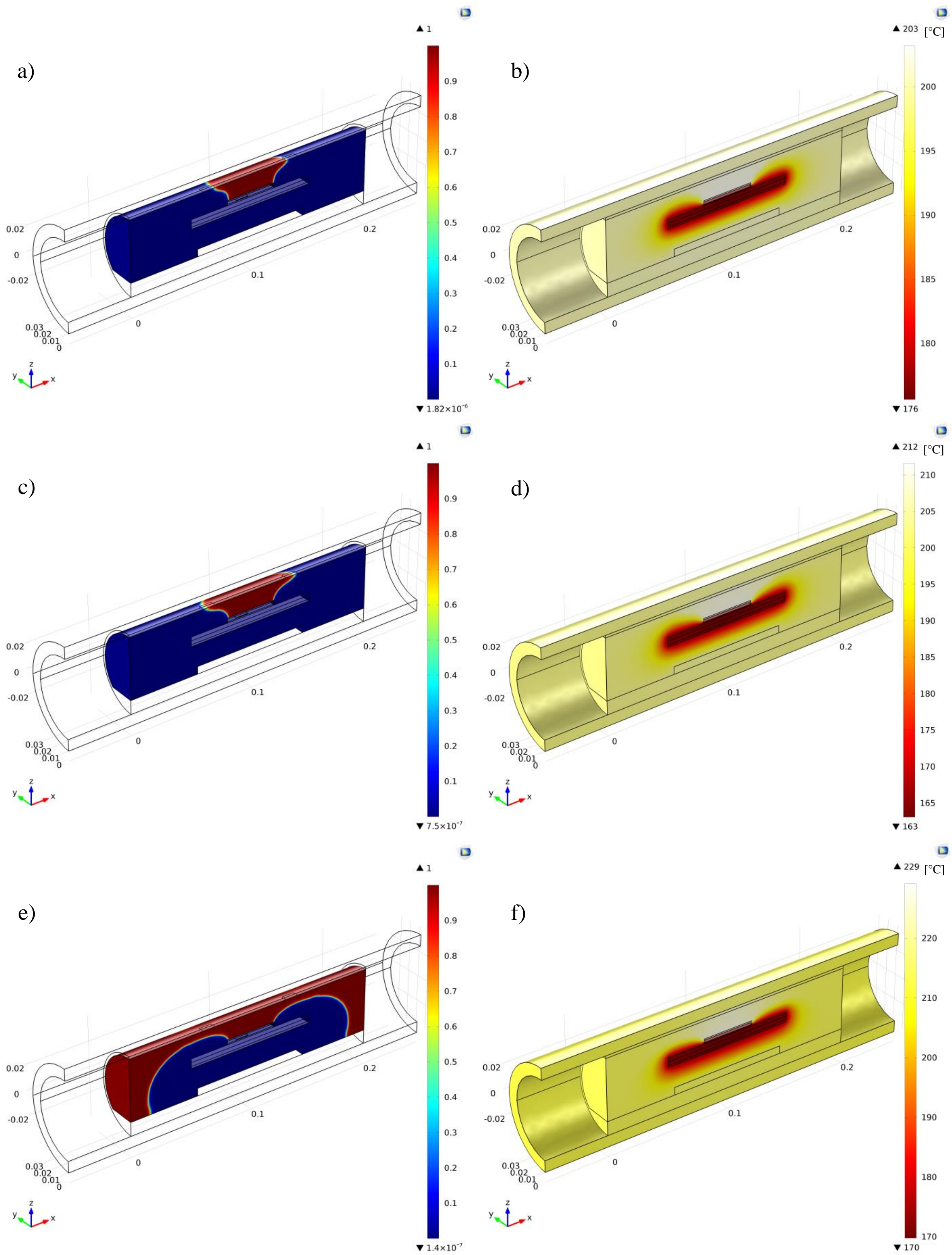
a)
b)
c)
d)
e)
f)
[°C]
▲ 203
▼ 176
▲ 212
▼ 163
▲ 229
▼ 170
▲ 1
▼ 1.82×10⁻⁶
▼ 7.5×10⁻⁷
▼ 1.4×10⁻⁷

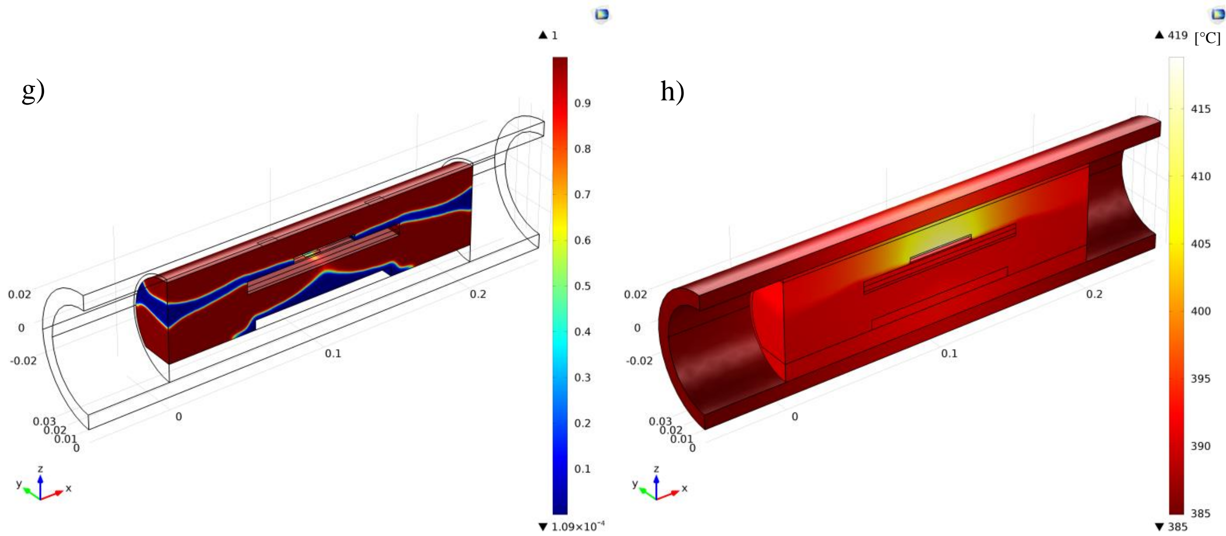

Figure 5.3 Density field (left) and resulting temperature distribution (right) of the optimized *Design 1* concept at I_{feed} = 1 A / h = 500 Wm^{-2}K^{-1} (a, b), and at I_{feed} = 2 A / h = 100 Wm^{-2}K^{-1} (c, d); of the optimized *Design 2* concept at I_{feed} = 3A / h = 50 W/m^{-2}K^{-1} (e, f), and of the optimized *Design 3* concept at I_{feed} = 4 A / h = 10 Wm^{-2}K^{-1} (g, h). The density fields illustrate the different distributions of aluminum (red) and thermal insulation (blue), for the four optimized systems.

The balance between thermal protection of the cooled electronics and rejection of the excessive heat is reached differently for each set of boundary conditions and with different aluminum-thermal insulation ratios. Computing the volume percentage of employed aluminum, over the total optimizable volume, helps to have a clearer picture of the optimized designs trend with the boundary conditions. That can be calculated with the following expression:

$$R = \frac{1}{V_{\Omega}} \int_{\Omega} \bar{\tilde{\rho}} \, d\Omega \qquad (5.17)$$

where V_{Ω} is the volume of the optimizable domain and $\bar{\tilde{\rho}}$ is the projected design variable.

The amount of employed aluminum decreases with the convection coefficient and increases with the feed current (Figure 5.4); more in general, more aluminum is employed when a better heat rejection to the well is needed.

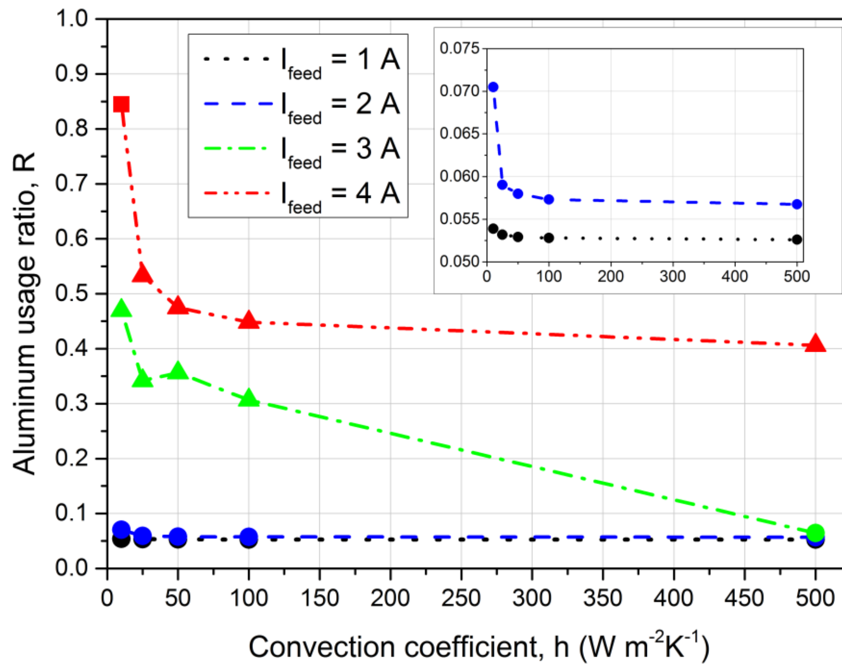

Figure 5.4 *R* vs. well fluid convection coefficient, for different TEC feed currents. The three different symbols correspond to the three obtained design configurations: ● = *Design 1*, ▲ = *Design 2*, ■ = *Design 3*.

5.4.2 Comparison of the optimized designs

Defining the categories of the optimized topologies is only the first step towards the selection of a final design for the actively cooled electronics unit. The performance of the optimized designs, at conditions they were not optimized for, is also an important feature to take into account. Furthermore, a cross-validation between the resulting topologies can be used to check for convergence to local minima. It can be detected if an optimized design does not show the best performance at the boundary condition it was optimized for.

A first sensitivity analysis was carried out to evaluate how the performance of an optimized system would change at different well fluid convection regimes. The electronics section was first optimized for a certain value of feed current and well fluid convection; the optimized design was then simulated at different values of convection coefficient, maintaining the TEC feed current constant. The resulting performances were compared as illustrated in Figure 5.5. The performance of the system was evaluated in terms of HTS electronics average temperature, computed through the objective function reported in Eq. (5.11).

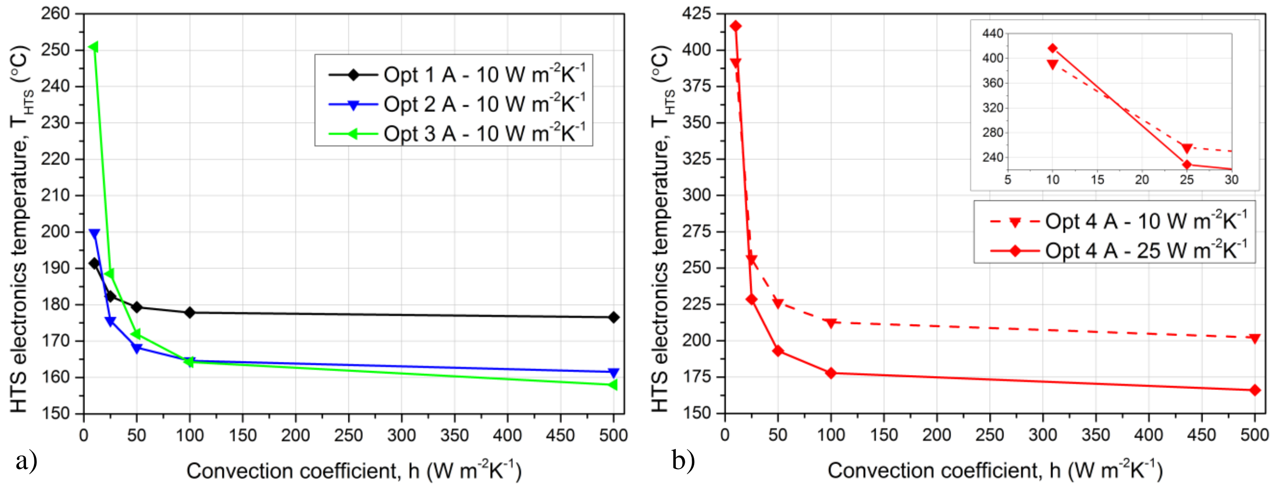

Figure 5.5 HTS electronics temperature vs. Convection coefficient for three different systems, optimized for h = 10 Wm^{-2}K^{-1} and I_{feed} = 1, 2, 3 A (5a, left side). HTS electronics temperature vs. Convection coefficient for two systems optimized for h = 10, 25 Wm^{-2}K^{-1} and I_{feed} = 4 A (5b, right side).

Figure 5.5a reports the performance trend with h of the systems optimized for h = 10 Wm^{-2}K^{-1} and I_{feed} = 1, 2, and 3A. As forecast, the HTS electronics is maintained colder at higher h values, when the heat rejection to the well is enhanced. Furthermore, higher feed currents are able to keep the electronics colder only if the well fluid is able to absorb the additional excessive heat, generated by the higher Joule losses. The lowest T_{HTS}, at a certain convection regime, is given by the system that was optimized for it.

Unexpectedly, it was found that the systems optimized for the same feed current operate very closely to each other, independently on the value of h they were optimized for. The performance trends of the systems optimized for I_{feed} = 1, 2 and 3A, and h > 10 Wm^{-2}K^{-1}, would in fact overlap with the corresponding three curves illustrated in Figure 5.5a. A maximum mismatch of only 0.05 °C, 0.01 °C, and 1.47 °C was found between the performance trends of the systems optimized for I_{feed} = 1, 2, and 3 A, respectively. This analysis proved that the optimization process is not significantly sensitive to the considered well fluid convection range. In other words, the length of the aluminum pad, which characterizes the *Design 1* concept, as well as the thickness of the aluminum layer, which characterizes the *Design 2* concept, do not significantly affect the performance of the optimized systems between 1A and 3 A.

On the contrary, not all the topologies optimized for 4 A have a similar behavior. As Figure 5.5b shows, the system optimized for 4 A and 10 Wm^{-2}K^{-1} (*Design 3* concept) maintains the electronics at a significantly lower temperature at low convection coefficients, compared to the one optimized for 4 A and 25 Wm^{-2}K^{-1}. However, above 25 Wm^{2}K^{-1} the system optimized for 4 A and 25 Wm^{-2}K^{-1} (*Design 2* concept) is able to maintain the HTS electronics down to a 37 °C lower temperature. In analogy with the previous cases, the other designs optimized for 4 A and h > 25 Wm^{-2}K^{-1} were found to operate similarly to the case optimized for 4 A and h = 25 Wm^{-2}K^{-1}, with a maximum mismatch between the performance trends of 6.67 °C.

In an analogue way, the sensitivity of the optimized topologies to the TEC feed current was studied. The electronics unit was initially optimized for a certain value of well fluid convection coefficient and of TEC feed current; the resulting optimized design was then simulated at different values of feed current, while maintaining the value of h constant.

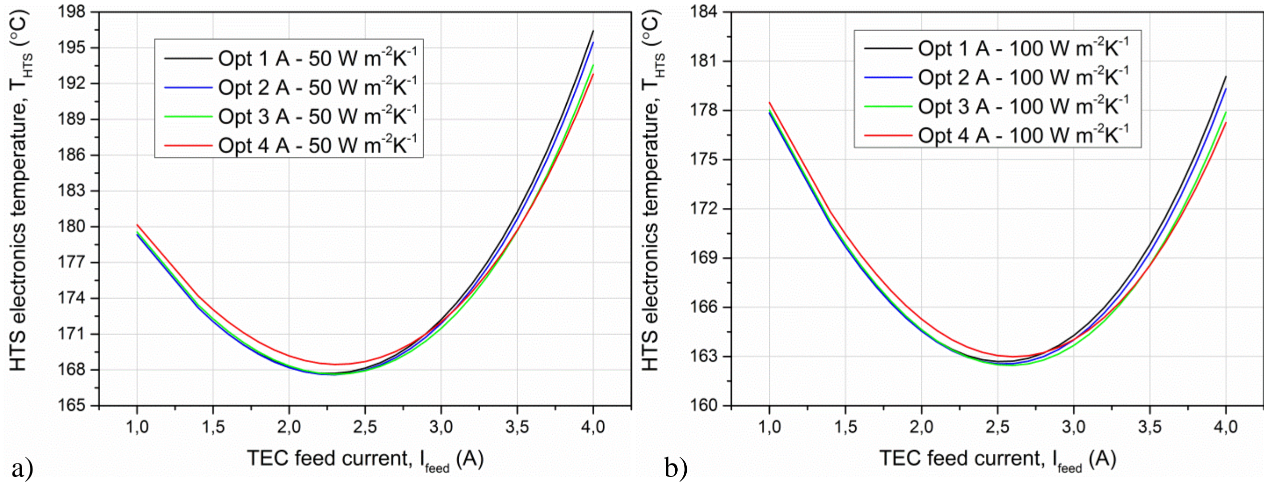

Figure 5.6 HTS electronics temperature vs. TEC feed current of four different designs, optimized for I_{feed} = 1, 2, 3 and 4 A, and h = 50 Wm^{-2}K^{-1} (6a, left side) and 100 Wm^{-2}K^{-1} (6b, right side).

Figure 5.6 shows that the optimization process is more sensitive to the feed current than to the external convection coefficient. The mismatch between the curves is now larger and can go up to several degrees Celsius. As expected, the lowest T_{HTS}, at a certain TEC feed current, is given by the system that was optimized for it.

An optimal feed current I_{opt}, which minimizes the HTS electronics temperature, can be individuated. Increasing the TEC feed current enhances the thermoelectric effect and the heat transport from the cold to the hot plate. However, that makes the Joule losses within the module larger, in turn causing a larger excessive heat flux that needs to be rejected to the wellbore, and a higher heat backflow to the HTS electronics through the thermal insulation. The optimal current I_{opt} can be defined as the TEC feed current at which the marginal gain in absorbed heat flux from the cold plate, due to an infinitesimal increase of the TEC feed current, becomes smaller than the heat flux that leaks back to the cooled electronics through the insulation. I_{opt} varies slightly for each optimized design, and depends mainly on h.

I_{opt} is equal to ~1.2 A for h = 10 Wm^{-2}K^{-1}, to ~1.9 A for h = 25 Wm^{-2}K^{-1}, to ~2.3 A for h = 50 Wm^{-2}K^{-1}, to ~2.6 A for h = 100 Wm^{-2}K^{-1}, and to ~2.9 A for h = 500 Wm^{-2}K^{-1}. With respect to the considered operations at non-optimal current, working at I_{opt} can reduce the electronics temperature by a maximum ~244 °C at h = 10 Wm^{-2}K^{-1}, ~59 °C at h = 25 Wm^{-2}K^{-1}, ~29 °C at h = 50 Wm^{-2}K^{-1}, ~17 °C at h = 100 Wm^{-2}K^{-1}, and ~20 °C at h = 500 Wm^{-2}K^{-1}. The designs that prove to maintain the HTS electronics at the lowest temperature, around the optimal current, are the ones optimized for 2 A and 3 A.

5.4.3 Design of the actively cooled electronics section

The results from the topology optimization study were used to define the final design of the actively cooled electronics unit (Figure 5.7); practical assembly constraints were also taken into account. The heat transfer analysis of the system revealed that the ideal operating condition for the device to work is a combination of high TEC feed current, that guarantees a strong cooling effect, and a high well fluid convection regime, which guarantees an effective removal of the excessive heat. Unfortunately the well fluid convection regime can vary significantly in operation, and therefore the tool needs to be designed for the worst-case design convection coefficient, which was set to 25 Wm^{-2}K^{-1}. *Design 3* can be immediately discarded from the

suitable topologies, as it was optimized for a convection regime that is outside the design conditions and for a TEC feed current that is far from the optimal ones. As mentioned previously, the optimal feed current for $h = 25$ Wm^{-2}K^{-1} is ~1.9 A; the optimized design for these conditions corresponds to the *Design 1* concept (see Figure 5.4). However, *Design 2* proved to have a very similar performance around the optimal feed current (see Figure 5.6), which means that there is some freedom in the design of the aluminum pad and/or layer. The lower mass of aluminum that characterizes *Design 1* would make the tool lighter, though, which is preferable from a logistic and operational point of view. Furthermore, the aluminum pad, which provides the radial thermal path from the cooler hot plate to the structural chassis, proved to be the fundamental feature for effective operation of the system: an aluminum pad was therefore implemented in the final design. No aluminum layer was included, except for two walls, 10 mm thick, at the two ends of the chassis: they provide mechanical stability, an additional thermal path to better spread the heat in the case of a poor heat rejection rate, and are suitable for the installation of pins for the assembly of the system. The chassis would be in fact split into a top half, where the cooling system and the PCB are installed, and a bottom half, on which the HTNS electronics are mounted. Two smaller pads, with threaded holes, were designed in the top part of the chassis: they support a plastic screw system that clamps the cooler between the heat spreader and the chassis, while ensuring effective thermal contacts. The remaining volume was filled with thermal insulation, for thermal protection of the cooled electronics.

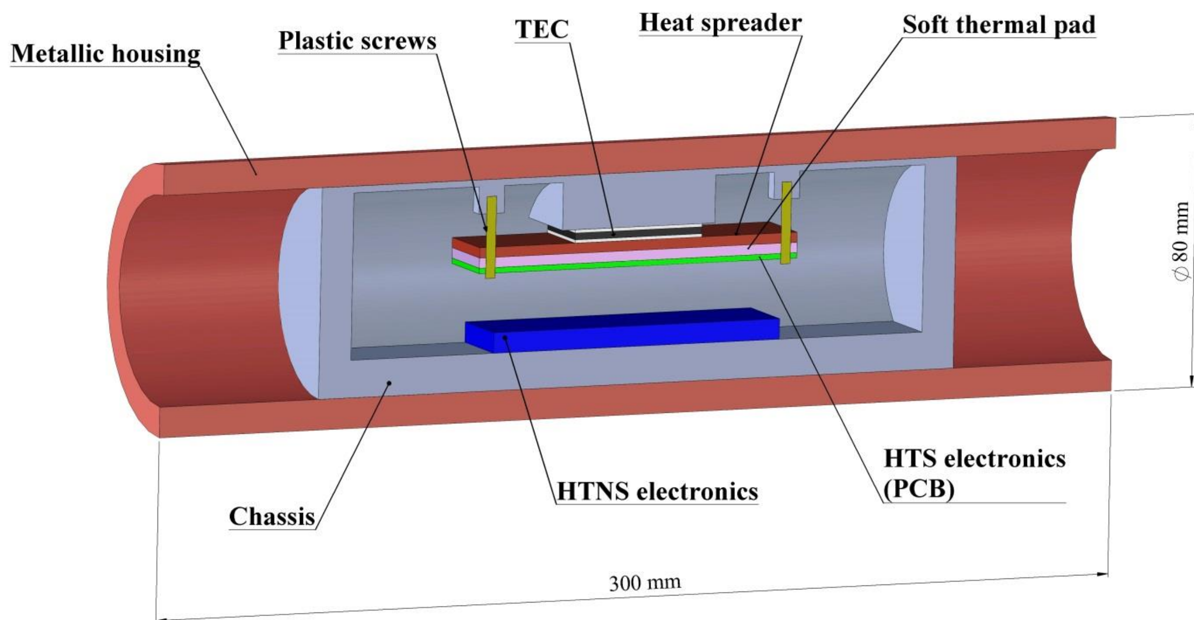

Figure 5.7 Illustration of the longitudinal section of the final design. The thermoelectric cooler is clamped between the aluminum pad and the heat spreader through two plastic screws (in yellow). The remaining volume within the chassis is filled with thermal insulation.

Simulations showed the chosen design operates very similarly to the optimized systems (Table 5.3). The difference in HTS electronics temperature is very small when operating at 1 A or 2 A, as the final design is very similar to the *Design 1* concept. The HTS electronics are in fact maintained maximum 0.11 °C above the optimized case. When operating at 3 A and 4 A, the mismatch becomes larger, since the *Design 2* concept would perform better at higher feed currents. However, when operating at 3 A, the HTS components are always maintained less than 1 °C above the optimized system. The mismatch becomes larger than 1 °C

for operations at 4 A; that can be considered irrelevant, since I_{feed} = 4 A is far from the observed optimal TEC settings and the system would always aim at operating between 2 A and 3 A, close to the optimal conditions. Table 5.3 also shows the final system fulfills the design conditions and the electronics can be maintained below 175 °C for every well fluid convection regime, as far as a control system can regulate the TEC feed current around the optimal one. The only exception occurs for the case at h = 25 Wm^{-2}K^{-1}, where the heat rejection is very poor and the electronics can only be maintained between at an average temperature of 175 °C and 176 °C; this result is still considered acceptable given the small mismatch.

Table 5.3 Comparison between the performance of the final design (Design) and the optimized systems (Opt). $\Delta T = T_{HTS,desig} - T_{HTS,Opt}$.

h (Wm^{-2}K^{-1})	*Opt - 1A* T_{HTS} (°C)	*Design - 1A* T_{HTS} (°C)	ΔT (°C)
25	182.31	182.41	0.10
50	179.32	179.43	0.11
100	177.83	177.94	0.11
500	176.56	176.67	0.11
h (Wm^{-2}K^{-1})	*Opt - 2A* T_{HTS} (°C)	*Design - 2A* T_{HTS} (°C)	ΔT (°C)
25	175.63	175.68	0.05
50	168.18	168.23	0.05
100	164.54	164.57	0.03
500	161.46	161.48	0.02
h (Wm^{-2}K^{-1})	*Opt - 3A* T_{HTS} (°C)	*Design - 3A* T_{HTS} (°C)	ΔT (°C)
25	188.22	188.93	0.71
50	171.48	171.87	0.39
100	163.68	163.90	0.22
500	157.12	157.35	0.23
h (Wm^{-2}K^{-1})	*Opt - 4A* T_{HTS} (°C)	*Design - 4A* T_{HTS} (°C)	ΔT (°C)
25	228.62	233.59	4.97
50	192.79	195.71	2.92
100	177.25	179.29	2.04
500	165.23	166.37	1.14

In order to have a clearer overview of the operation of the final design, a characteristic curve that displays the HTS average temperature as a function of the TEC feed current and of the well fluid convection coefficient is illustrated in Figure 5.8. As already observed in the previous analyses, the performance of the system is enhanced when high well fluid convection regimes occur. At high TEC feed currents the performance of the system is more sensitive to the convection coefficient than at low I_{feed}, as it can be noticed from the curve slopes on the h-T_{HTS} plane. On the I_{feed}-T_{HTS} plane, instead, it can be observed the HTS electronics temperature reaches a minimum at I_{opt}, which varies for different conditions of well fluid

convection. The I_{opt} front is highlighted with red line. The optimal operating current changes more rapidly with h at low convection regimes, where the excessive heat rejection is crucial, and engages a flatter trend while the convection coefficient grows.

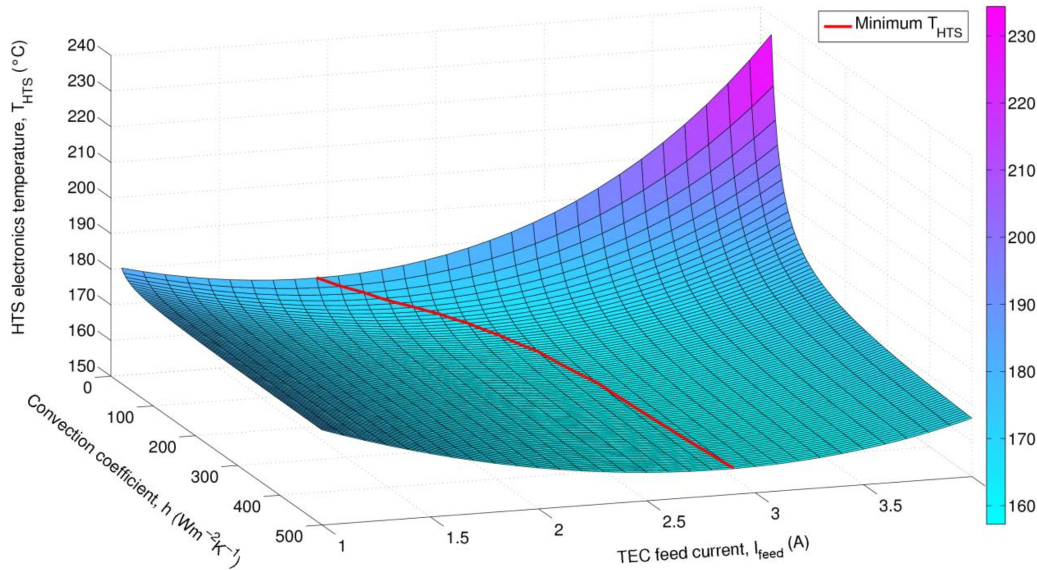

Figure 5.8 Characteristic curve of the finally designed TEC integrated system. The plot reports the simulated performance of the cooling system, in a 200 °C environment, as HTS electronics temperature vs. convection coefficient and TEC feed current. The minimum HTS electronics temperature, for each operating condition, is highlighted by a red line. The color bar expresses the HTS electronics temperature in degrees Celsius.

5.4.4 Model validation

The system illustrated in Figure 5.7 was manufactured and assembled as shown in Figure 5.9. Thermal grease was used to interface the heating components to the chassis, lead wires were installed to feed the two sets of electronics through external power supplies, and type-K thermocouples were installed to monitor the temperature profile within the tool.

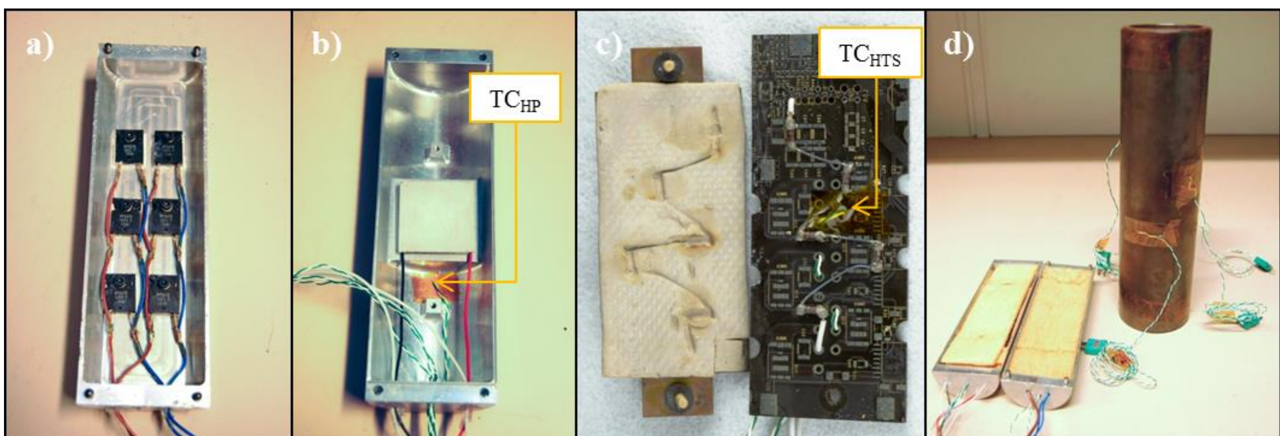

Figure 5.9 Illustration of the manufactured components. Six resistors were installed on the chassis bottom half to reproduce the HTNS electronics (a).The TEC was located in the chassis top half, with two threaded holes for implementing the clamping system;

the thermocouple TC_{HP} measured the temperature on the hot side of the TEC(b). Five resistors were soldered onto the PCB, to simulate the HTS electronics, and coupled with the soft thermal pad and the heat spreader (c); the thermocouple TC_{HTS} measured the temperature of the PCB. The two halves of the chassis were finally filled with thermally insulating foam and inserted into the metallic housing; the temperature of the housing was monitored by four thermocouples (d).

The assembled tool was tested in a dry and ventilated hot environment, where a fan recirculated air at the set-point temperature T_{oven}. *Power Supply 1* provided the electric power to the TEC, while a voltmeter and a current meter measured the feed voltage and current, respectively. *Power Supply 2* provided the feed power to the test electronics. A *Data Acquisition System* monitored and recorded the temperature distribution within the tool. The schematic of the experimental setup is reported in Figure 5.10.

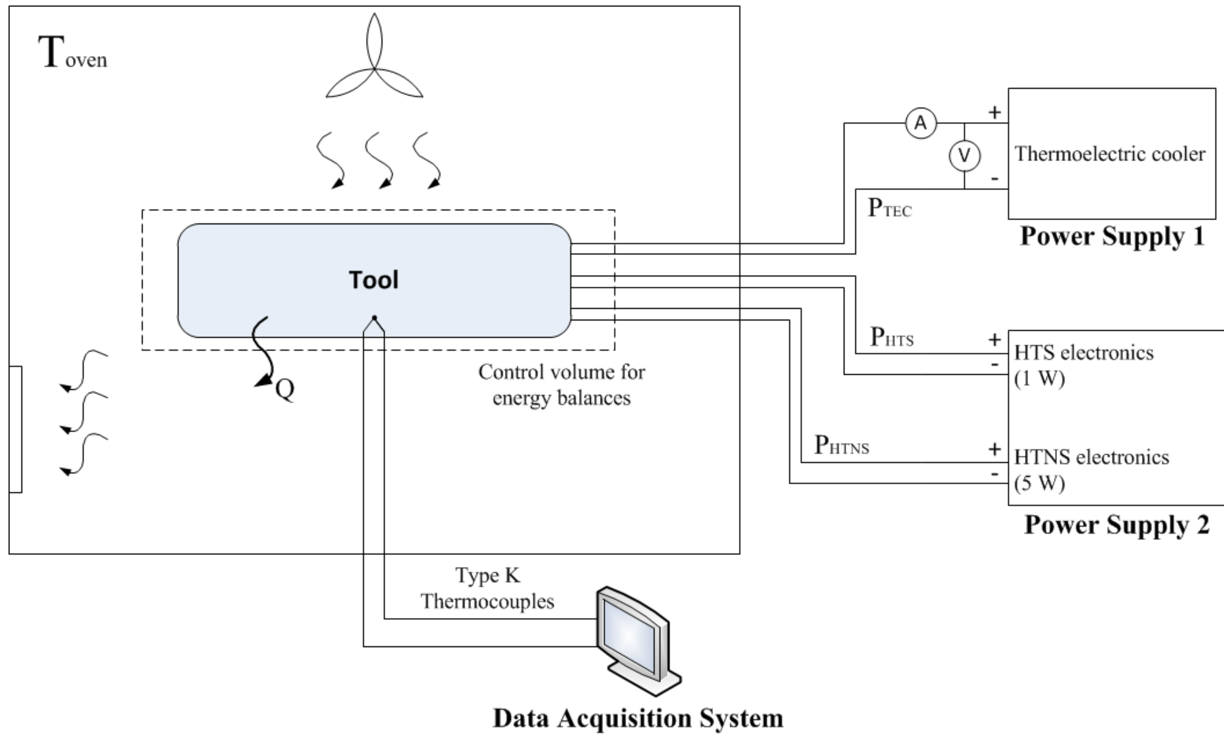

Figure 5.10 Schematic of the experimental setup. The main components characterizing the experimental validation of the model are illustrated.

Two different ovens, in size and air flow capacity, were used to test the tool at 180 °C, 190 °C, and 200 °C. For every oven temperature, the TEC feed current was varied between 1 A and 4 A, and the steady state temperature distribution across the tool was recorded. Furthermore, each test was characterized by the calculation of the average heat transfer coefficient $\bar{h}_{exp}$, which described the heat transfer, mainly driven by convection, occurring at the steady state between the tool housing and the oven environment. Eq. (5.18) was calculated from the balance of the energy fluxes through the control volume shown in Figure 5.10, and was used for this purpose. The term $\bar{h}_{exp}$ provides the reference boundary condition for the model validation process.

$$\bar{h}_{exp} = \frac{(P_{TEC} + P_{HTS} + P_{HTNS})}{A_{housing} \cdot (\bar{T}_{housing} - T_{oven})} \tag{5.18}$$

where $\bar{h}_{exp}$ is the average heat transfer coefficient at the tool housing surface; P_{TEC}, P_{HTS}, and P_{HTNS} are respectively the electric feed powers of the cooler, of the HTS electronics, and of the HTNS electronics; $A_{housing}$ is the outer surface area of the housing; $\bar{T}_{housing}$ is the average of the readings from the four thermocouples installed on the outer surface of the housing (see Figure 5.9d); and T_{oven} is the measured oven temperature.

The experimental temperatures were measured with type-K thermocouples and compared with the predictions from the model. An accuracy of ± 1.5 °C was used for the thermocouples, according to *IEC 584 Class 1*. Model data points were obtained from the corresponding 1 cm^2 square location within the finite-element geometry; actual measurements were compared with the average temperatures, while lower and higher error bands were introduced according to the model prediction for the maximum and minimum temperatures within the 1 cm^2 square.

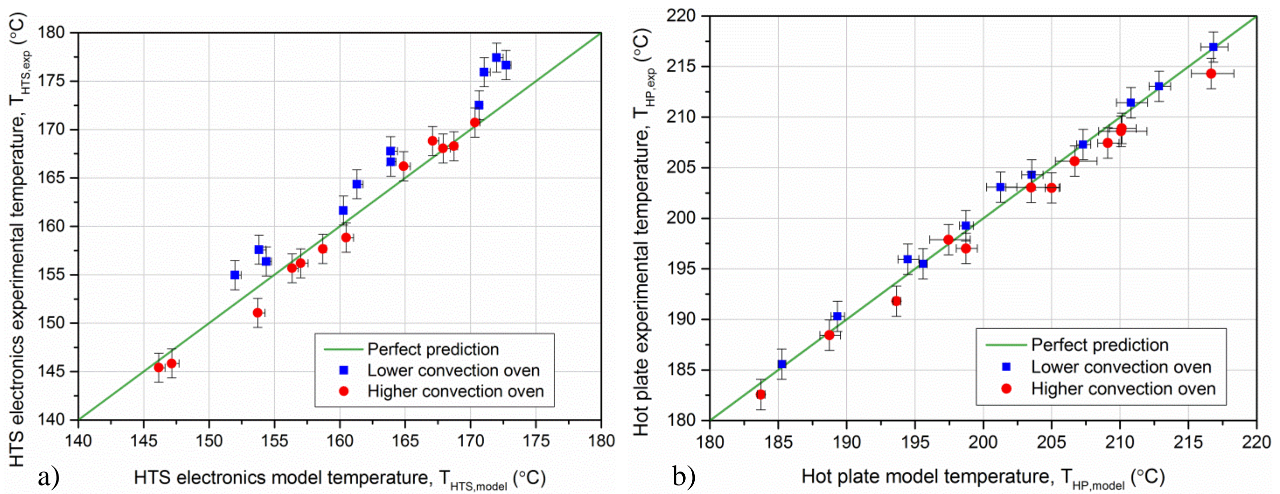

Figure 5.11 Comparison between experimental data and model prediction. HTS electronics temperatures are reported on the left (a) and hot plate temperatures are reported on the right (b). Results from all the tests from both the ovens are illustrated, and compared to the perfect prediction scenario.

Figure 5.11 shows the comparison between the experimental and the model temperatures, from the TEC hot plate (probe shown Figure 5.9b) and HTS electronics (probe shown in Figure 5.9c), which represent the most relevant temperatures for the system operation.

Table 5.4 Temperatures and parameters characterizing both the experimental procedure and the model validation. The first three columns define the boundary conditions of each test, while the last four columns summarize the TEC hot plate (HP) and HTS electronics temperatures, at stationary operations.

	T_{oven} (°C)	I_{feed} (A)	$\bar{h}_{exp}$ (Wm^{-2}K^{-1})	$T_{HTS,model}$ (°C)	$T_{HTS,exp}$ (°C)	$T_{HP,model}$ (°C)	$T_{HP,exp}$ (°C)
Lower convection oven	180.4	1.0	35.1	160.3	161.6	185.3	185.6
	180.7	1.5	30.9	154.4	156.4	189.3	190.3
	180.5	2.0	29.1	152.0	155.0	194.5	196.0
	180.3	2.5	28.2	153.8	157.6	201.3	203.1

	T_{oven} (°C)	I_{feed} (A)	$\bar{h}_{exp}$ ($Wm^{-2}K^{-1}$)	$T_{HTS,model}$ (°C)	$T_{HTS,exp}$ (°C)	$T_{HP,model}$ (°C)	$T_{HP,exp}$ (°C)
	190.8	1.0	36.8	170.7	172.5	195.6	195.5
	189.9	1.5	31.0	163.9	166.7	198.7	199.3
	190.1	2.0	31.1	161.3	164.4	203.5	204.3
	190.6	2.5	30.3	163.9	167.8	210.8	211.4
	199.3	1.5	35.6	172.7	176.7	207.3	207.3
	199.5	2.0	32.3	171.0	175.9	212.9	213.0
	199.7	2.3	31.7	172.0	177.4	216.8	216.9
Higher convection oven	180.7	1.0	65.7	158.7	157.7	183.7	182.6
	181.0	2.0	62.4	146.2	145.4	188.7	188.4
	180.7	3.0	57.7	147.1	145.8	197.5	197.9
	181.1	3.5	59.0	153.7	151.1	203.5	203.1
	190.8	1.0	72.9	168.7	168.3	193.6	191.8
	191.0	2.0	64.8	156.4	155.7	198.7	197.0
	190.2	3.0	60.8	157.0	156.2	206.7	205.7
	190.8	3.3	61.1	160.5	158.8	210.1	208.6
	200.4	1.5	75.9	170.3	170.7	205.0	203.0
	201.8	2.0	73.4	167.1	168.8	209.1	207.4
	200.3	2.3	66.3	164.9	166.2	210.1	208.9
	200.1	3.0	62.6	167.9	168.1	216.7	214.3

As indicated in Figure 5.11, experimental data and model forecasts revealed a good match, and proved the model can reproduce the performance of the real system with a good degree of accuracy. Figure 5.11a shows the majority of the data points for the HTS electronics temperature are close to the perfect prediction. Points from the tests at lower convection show a slightly worse match with the model, which predicts slightly lower HTS electronics temperatures. Based on the thermocouple readings and visual inspection of the system, no degradation at the cold side of the TEC was observed after the tests. No visible breakdown of the thermal interface material, which is rated for a maximum operating temperature of 200 °C, or change in the thermal resistances were detected. The mismatch in the model results can be attributed to the degradation of the TEC itself, which occurred in the ~50 hours of testing at high temperature in the higher convection oven, which were carried out first chronologically. The degradation of the module consists of a decrease in the thermoelectric effect and was detected as a drop in the temperature span across the TEC and a decrease of the TEC feed voltage at constant current (Barako et al. (2012)). The lower heat transport between the plates could therefore have led to higher experimental HTS electronics temperatures. The effects of the degradation are also accentuated when operating in low convection environments and high feed currents.

Figure 5.11b, instead, shows a very good match between experiments and model predictions for the hot plate temperatures, both for the lower and higher convection scenarios. The previously described behavior can also be observed in Figure 5.12, where a comparison between model and experiments is reported as a function of the TEC feed current. Experimental results show a good agreement with the model predictions

and are able to reproduce the forecast trends with I_{feed}. Furthermore, the experimental data confirm the presence of an optimal operating current I_{opt}, as described in the section 4.3, and the trend is reproduced by the model. Although Figure 5.12c shows a slightly larger mismatch between predictions and experiments, for the lower convection scenario, the convex trend and the value of I_{opt} are reproduced with good approximation. The observed I_{opt} values varied with the outer fluid convection regime, confirming the behavior predicted by the model. As expected and previously shown, lower electronics temperatures were obtained in the higher convection scenario.

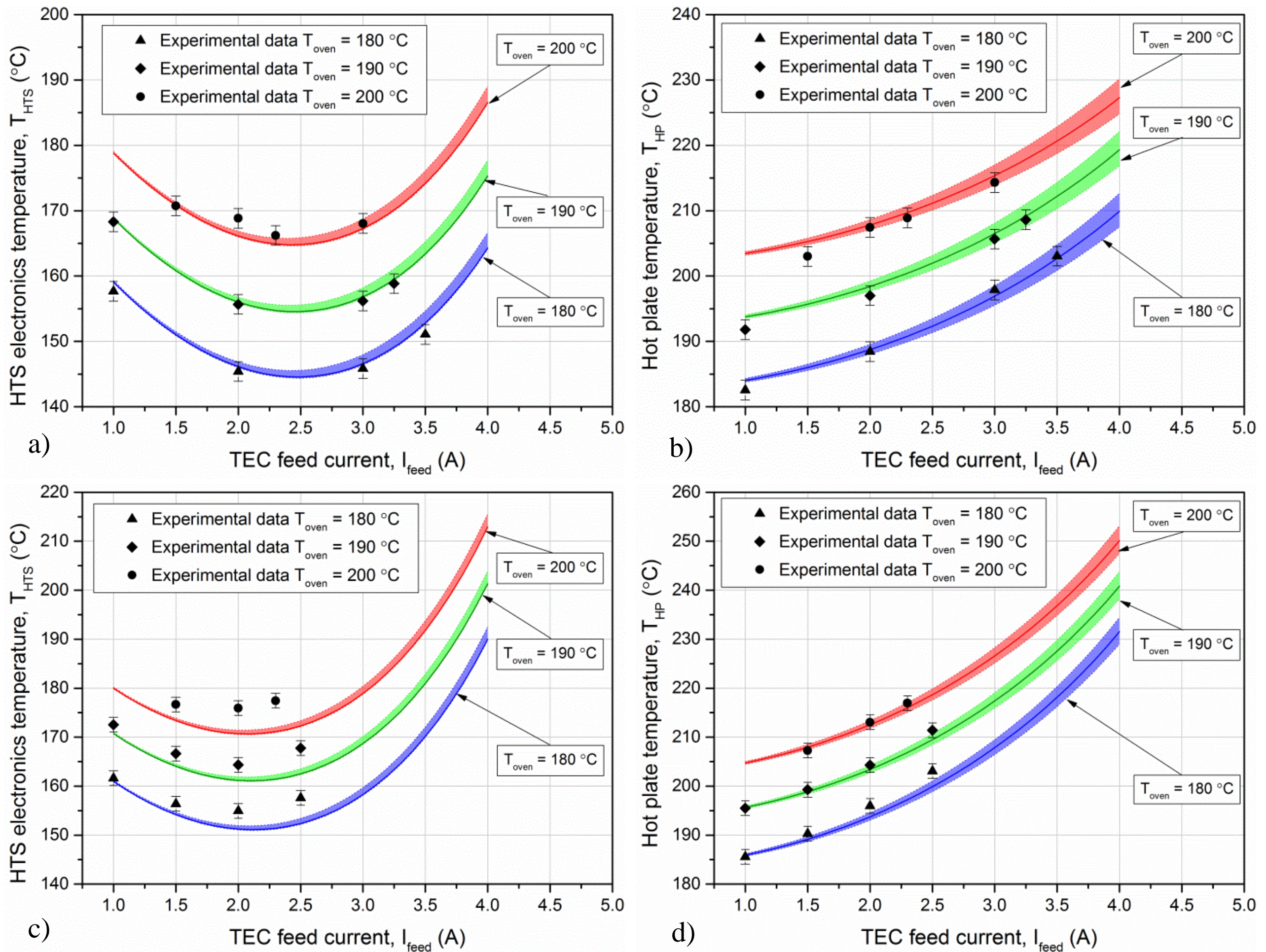

Figure 5.12 Comparison between experimental and modelling temperatures vs. TEC feed current, at different oven temperatures. The two figures on the top (a, b) report respectively the HTS electronics and the hot plate temperatures trends vs. TEC feed current, for the higher convection oven. The two figures on the bottom (c, d) report respectively the HTS electronics and the hot plate temperatures vs. TEC feed current, for the lower convection oven. The colored lines show the trends predicted by the model, defined by the maximum and minimum temperatures from the 1cm^2-square model probe. The single points represent the experimental data.

5.5 Conclusions from the design and testing of *Prototype mark-2* (part 1)

This work presented and demonstrated a method of integrating a TEC into a system with specific design constraints, using topology optimization combined with a 3D finite element model of the system. This technique allows efficient integration of TECs by optimizing how they interact thermally with their surroundings, and is suitable for any TED application where the module must be mounted in a fixed volume. As a specific application, the optimization method was used to aid in the design of an actively cooled electronics unit for a downhole oil well intervention tool, and to optimize the integration setup of a commercial thermoelectric cooler. The geometry to be optimized and the problem-related governing equations were implemented in COMSOL Multiphysics, together with the SIMP topology optimization approach. The model was used to optimize the distribution of aluminum and thermally insulating material within the unit, so the temperature-sensitive electronics could be maintained at a minimum temperature. The system was optimized for several well conditions and for the TEC feed current, and different design concepts were generated and analyzed. When heat rejection was critical (high TEC feed currents and low convection regimes) the mass of aluminum increased for better conduction out of the tool to the well; when the heat rejection was not critical (low TEC feed currents and high convection regimes) the thermal protection of the cooled electronics was prioritized, and the use of aluminum was significantly lower than the previous cases in favor of the thermal insulator. Optimized systems were found to cool the electronics down to a temperature 37 °C colder than before optimization. Furthermore, the optimization process proved to be not significantly sensitive to the convection range, but highly sensitive to the operating current of the TEC. An optimal operating current, which minimizes the temperature of the HTS components and depends on the well fluid convection regime, was found. This analysis highlighted the importance of a control system that would always seek the best operating conditions for the cooler.

Topology optimization was used to implement the final design of the electronics unit, which simulations predicted to perform very closely to the optimized systems. The final design was manufactured and tested in an experimental setup, at different operating conditions. Model predictions reproduced experimental results with good agreement, replicated the predicted optimal feed currents, and demonstrated the effectiveness of the design method. Topology optimization was shown to be a powerful design tool that can be combined with a TED model to yield optimized designs for thermoelectric integrated systems.

5.6 Addendum

The analysis and the optimization presented in the previous sections led to the construction of *Prototype mark-2*, which was successfully tested and satisfactorily met the design criteria. *Prototype mark-2* was able to cool the electronics below ~175 °C when operating at 200 °C, even in the case of poor convective heat transfer (h_{exp} ~ 30 W/m^{2}K). Furthermore, the hot side of the system was maintained at a tolerable temperature both for the cooler and the HTNS electronics. *Prototype mark-2* definitely proved the thermal integration concept.

However, during the tests, the cooling system was fed by external power supplies with a variable DC voltage. Once installed into the well tractor, the cooling system would be connected to the downhole power source fixed at 15 V DC. A feed voltage of 15 V is not suitable for the cooler in every operating condition, so a way to adapt V_{feed} to a suitable range of values needed to be defined.

Also, the cooler degradation that was noticed in the HT tests of *Prototype mark-2* (Section 5.4.4), required further investigation to assess whether it could affect the reliability of the system during a single well intervention. The investigation of these topics is addressed in the next two sections of the addendum.

5.6.1 Electrical integration of the system

Once integrated into the well tractor, the thermoelectric cooling system would be coupled to a 15 V DC source. However 15 V would generate a current that is above the rated value of the employed TEC, both at room temperature and at 200 °C, when the resistance of thermoelectric material increases, which is far from the optimal one (see Figure 5.13). Furthermore, in case of poor convection, the high currents could generate heat rejection issues and not enough cooling for the electronics.

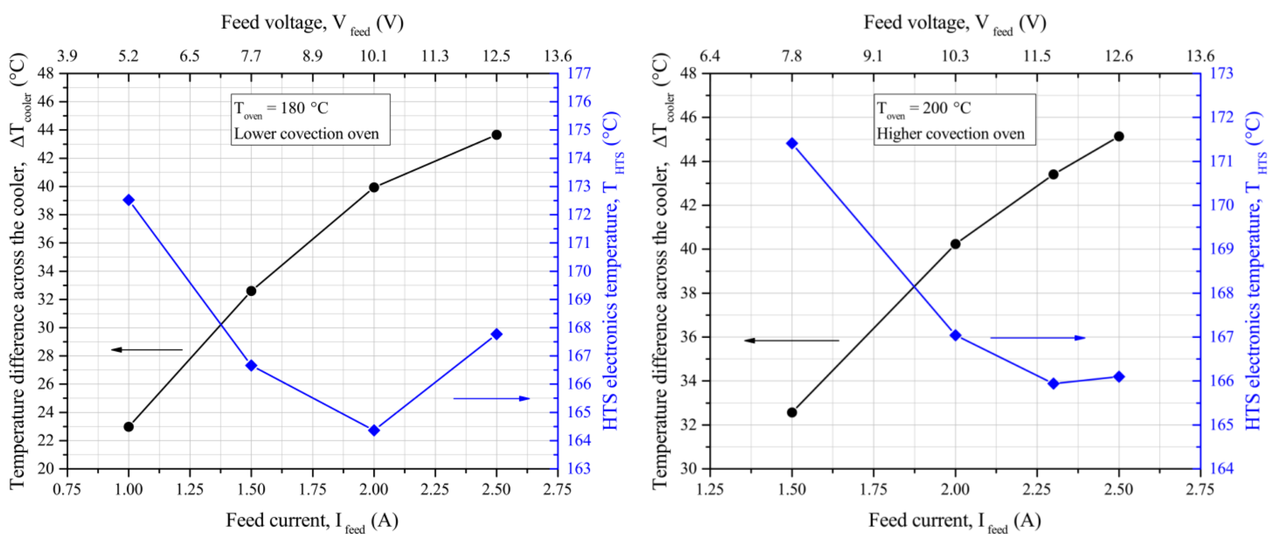

Figure 5.13 Experimental trend of ΔT_{cooler} and of HTS electronics temperature vs. feed current and feed voltage. Tests of *Prototype mark-2* at 180 °C in the lower convection oven (left) and at 200 °C in the higher convection oven (right).

It is important, for an effective operation of the system, that the feed voltage can be varied below 15 V. Furthermore, having a variable and controllable feed voltage to the cooler would allow seeking for the optimal operating conditions that minimize the temperature of the HTS electronics, for each operating

temperature and convection regime. In order to achieve this result, the Power Width Modulation (PWM) technique was studied and implemented in the feeding system of the cooler.

5.6.1.1 Implementation of the PWM technique

PWM is a modulation technique that allows the control of the power supplied to an electrical device. The average value of voltage and current fed to the load is controlled by switching between supply and load, on and off at a fast rate. The longer the switch is on compared to the off periods, the higher the total power supplied to the load. There can be defined a *switching frequency* as the frequency with which the system is turned on; such frequency has to be much higher than what would affect the load and the resultant waveform perceived by the load must be as smooth as possible. The inverse of the switching frequency is defined as *switching period*, while the switching period fraction in which the system is maintained on is defined as *duty cycle*.

To implement the PWM modulation technique, a transistor was used according to the scheme shown in Figure 5.14. The transistor "opens" and "closes" the circuit whenever a voltage of 10 V and -5 V, respectively, is applied between the *gate* (G) and the *source* (S). A signal generator was used to generate a square wave, with a certain frequency, between -5 V and 10 V (Figure 5.16) that could drive the transistor. The same configuration could be used in the well tractor where the transistor could be driven by a microprocessor, which also controls the cooling system.

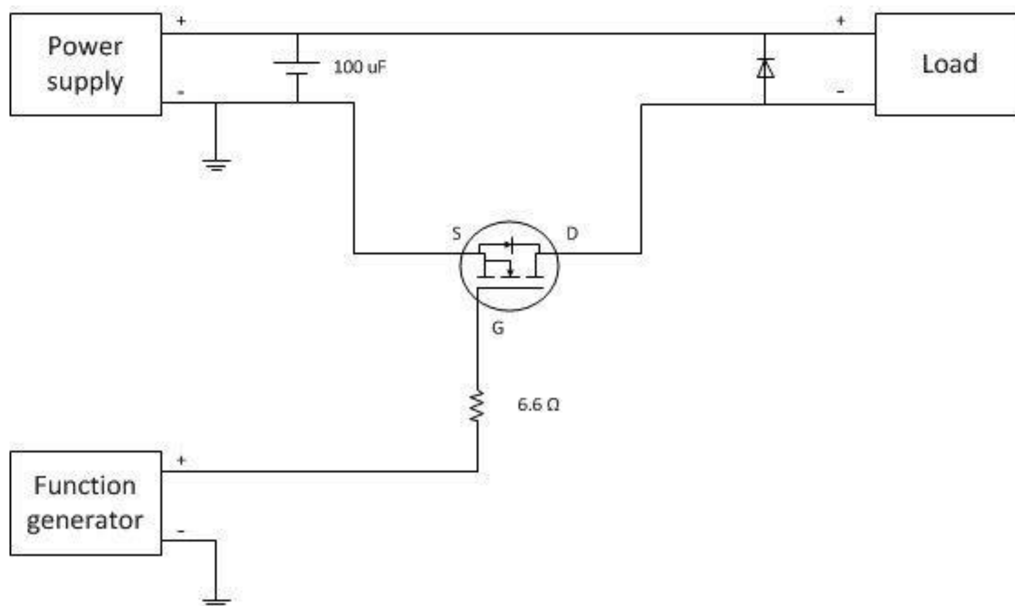

Figure 5.14 Schematic of the circuit to implement the PWM of the 15 V power source.

A 100 µF capacitor and a diode were used to absorb the voltage variations during the transients and ensure proper operation of the system. A small resistor (6.6 Ω) was mounted between the signal generator and the gate of the transistor to limit the transient current peaks that could damage the signal generator.

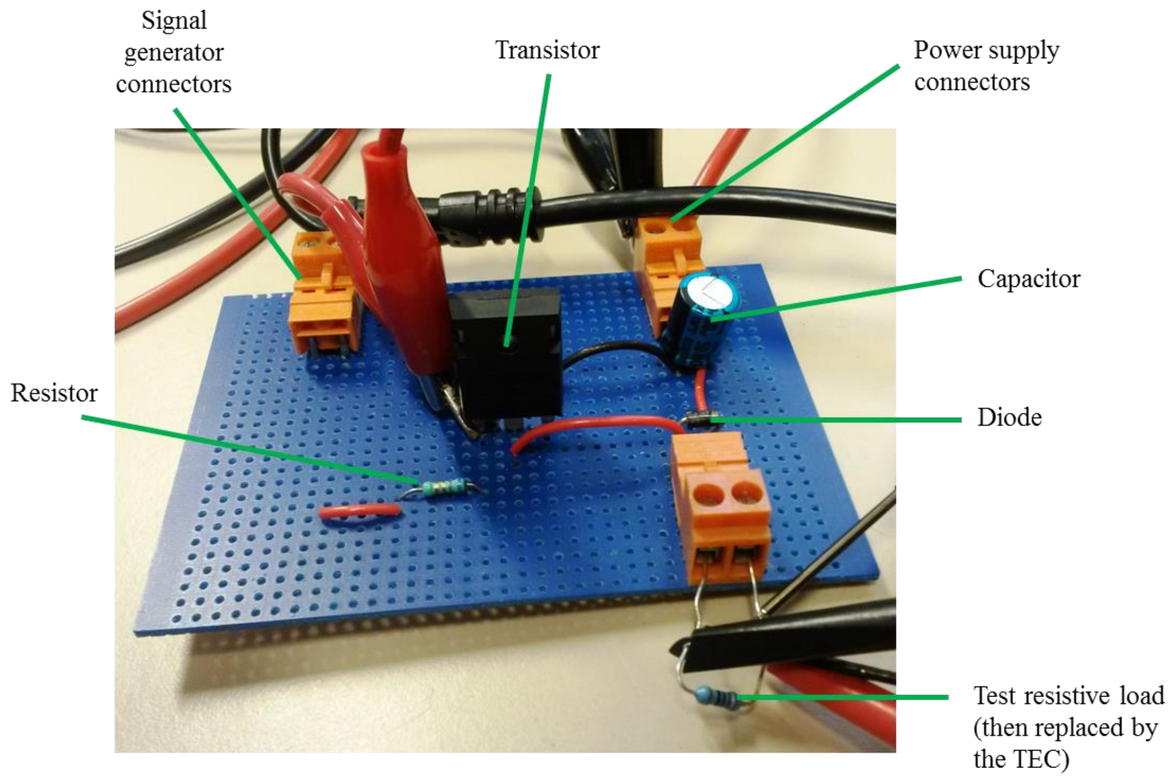

Figure 5.15 Picture of the circuit for modulating the voltage source at 15 V.

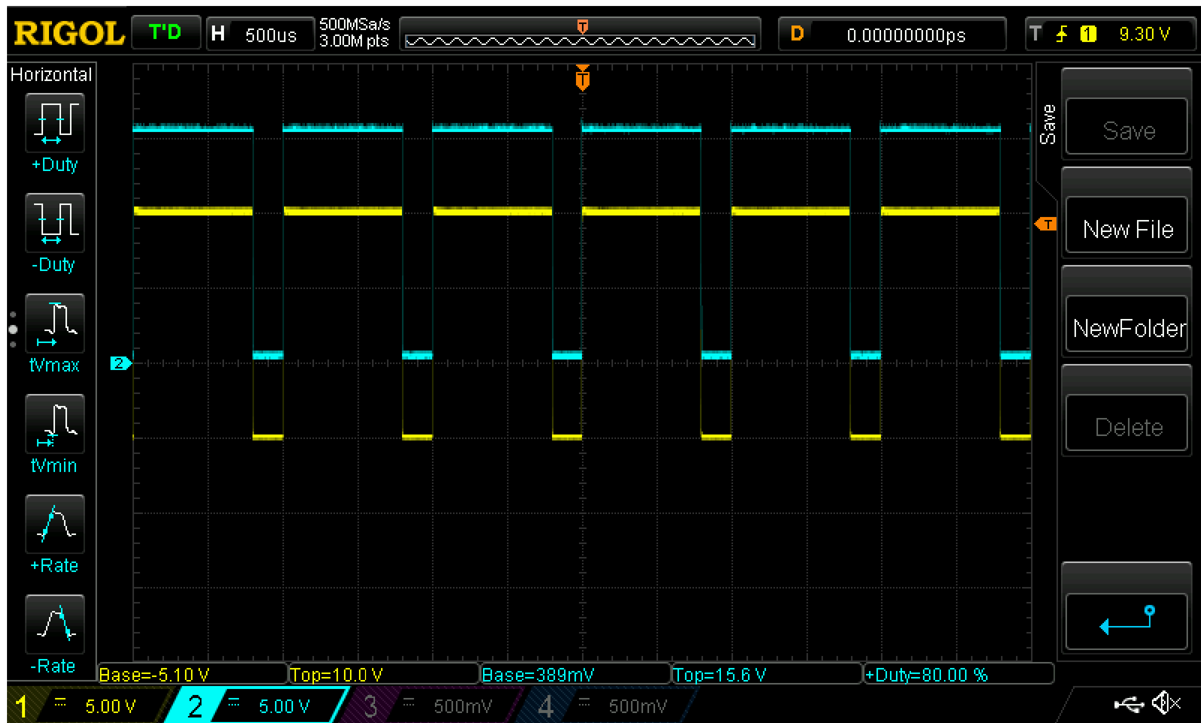

Figure 5.16 Screen capture from the oscilloscope used for the calibration of the test setup. The square wave in yellow, which varies from -5 V to 10 V, represents the signal that drives the transistor. The square wave in blue represents the modulation of the 15V voltage source, across the test resistor. An 80% duty cycle is set for this picture. The switching frequency is 1 kHz.

The resulting voltage across the load V_{avg} can be calculated as the product between the voltage source V_{source} and the duty cycle DC ($0 < DC < 1$) with which the transistor is switched. The average current across the load I_{avg} can also be calculated in the same way as V_{avg}.

$$V_{avg} = V_{source} \cdot DC$$
$$I_{avg} = I_{source} \cdot DC \tag{5.19}$$

However, although the average current from the PWM can be approximated to the continuous one through Eq. (5.19), the Joule losses across the load are not equivalent, and are higher than $R{\cdot}I_{avg}^2$ as shown in Eq. (5.20).

$$Q_{Joule} = R \cdot I_{source}^2 \cdot DC = R \cdot \frac{I_{avg}^2}{DC} \qquad \geq \qquad R \cdot I_{avg}^2 \tag{5.20}$$

Eq. (5.20) shows the Joule losses given by an average PWM current are higher or equal ($DC = 1$) to the Joule losses generated by the equivalent DC current. The difference between the Joule losses in the PWM and continuous cases becomes smaller and smaller while the duty cycle approaches unity. Despite the cooling action generated by I_{avg} is the same as the case with a DC current, the higher Joule losses significantly affect the performance of the system.

A way to reduce the Joule losses when using PWM is to flatten the square waveform of the feed voltage, which oscillates between 0 V to V_{source}, at the desired average value. In this way the electric current induced in the cooler would also be flat, without the peaks that cause higher losses. This can be achieved by implementing an L-C filter in the PWM circuit. Such a system was preliminarily designed and simulated on LT Spice (LT Spice IV) (Figure 5.17 and Figure 5.18), and subsequently implemented in the lab setup (Figure 5.19).

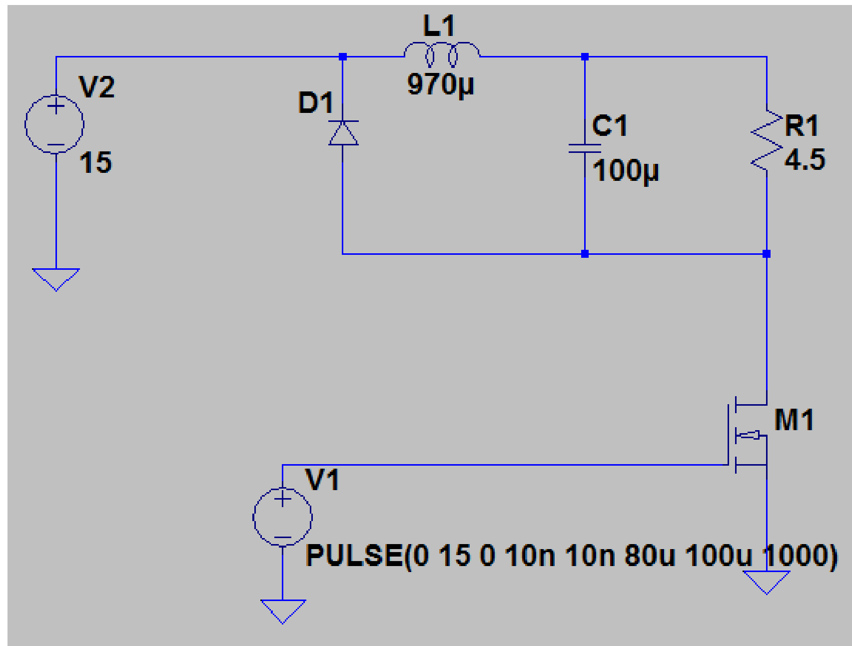

Figure 5.17 Schematic from LT Spice of the PWM circuit with L-C filter.

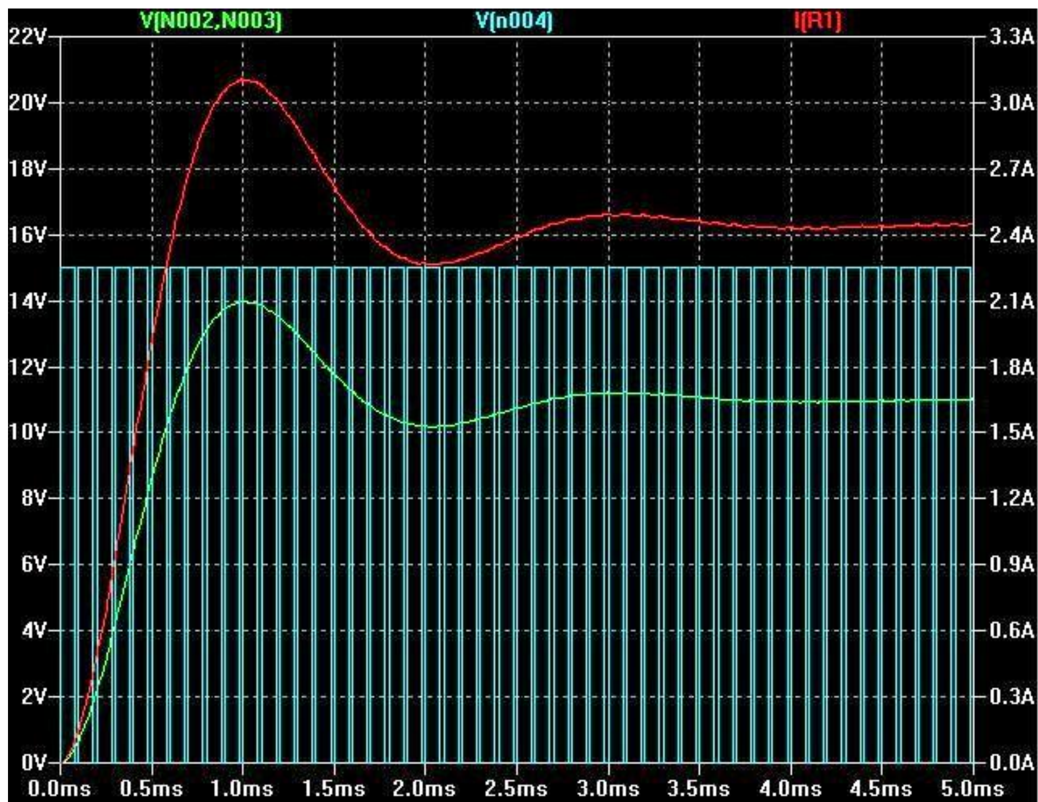

Figure 5.18 Simulated voltage (green curve – left *y* axis) and current across the cooler (red curve – right *y* axis) until steady state with LT Spice. The light blue square wave (left *y* axis) represents the modulated voltage without filtering. The PWM system was simulated with an inductor of 970 μH, a capacitor 100 μF, an operating frequency of 10 kHz, a voltage source of 15 V, a duty cycle

of 80%, and a resistive load of 4.5 Ω.

The circuit illustrated in Figure 5.17 was modelled in LT Spice. A parametric study over the operating frequency, size of the inductor, and size of the capacitor was performed and a satisfactory output was obtained for a frequency of 10 kHz, an inductance of 970 μH and a capacity of 100 μF. The trend of the voltage at steady state is no longer a square wave, as shown in Figure 5.18, but is a flattened curve with oscillations, in the order of magnitude of millivolts, around the desired value. In Figure 5.18, a duty cycle of 80 % is simulated and a stable output voltage of ~11 V is obtained, compared to the theoretical of 0.8·15 = 12 V. The mismatch is due to the simulated losses in the circuit due to conduction and switch losses in the transistor. Consequently to the flattened trend of the voltage, also the current across the load has a constant trend at steady state and does not follow a square trend anymore.

Given the satisfactory voltage output trend, this solution was tested in the feeding system of the TEC. The experimental results are illustrated in the next section, in comparison with the reference results at continuous voltage and the results from the basic PWM system.

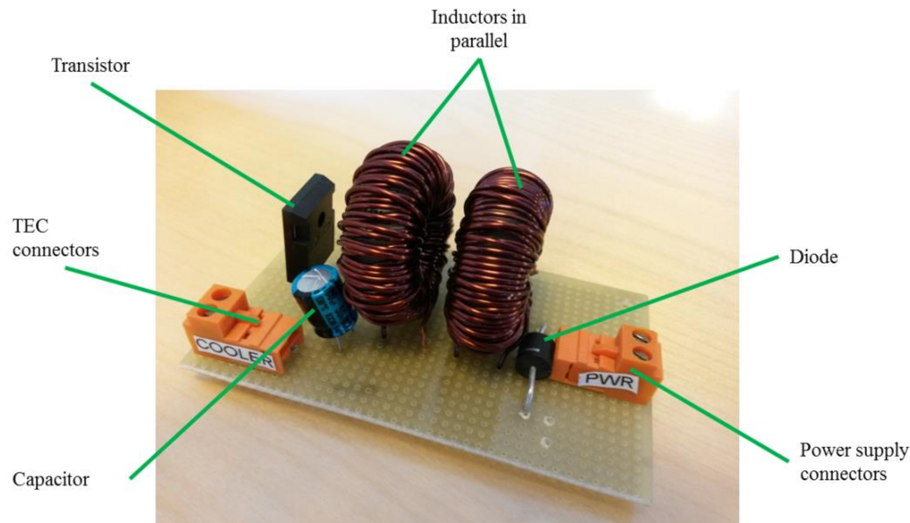

Figure 5.19 Picture of the PWM system with the integrated L-C filter. Two inductors, 1.94mH each, were connected in parallel to obtain an inductance of 970 μH which is suitable for the application. No connectors for the signal generator were installed in this circuit and the transistor was driven through some cables connecting directly the signal generator to the device pins.

5.6.1.2 Test results with PWM

Tests were conducted in the higher convection oven at 200 °C. Figure 5.20 shows the trend of the temperature span across the cooler with the TEC feed power, while Figure 5.21 shows how the HTS electronics and the hot plate temperatures change with the feed current. The three different feeding solutions are compared. The results are also summarized in Table 5.5 at the end of the section.

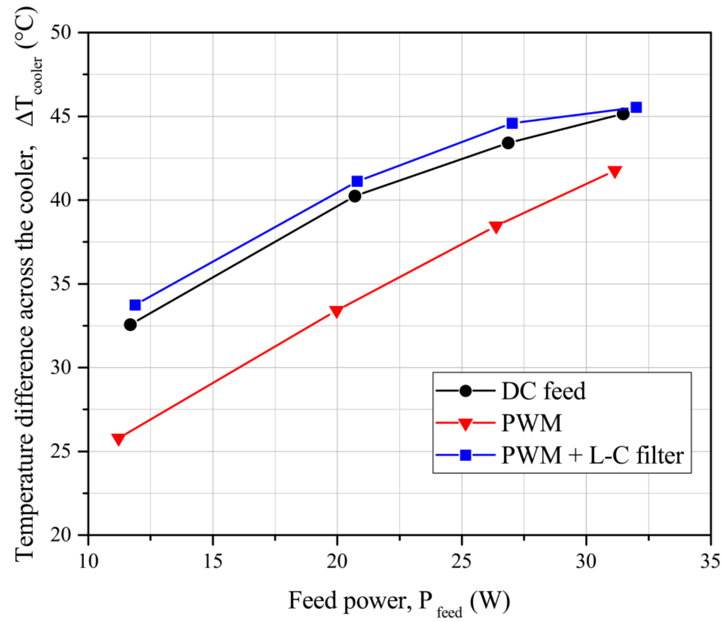

Figure 5.20 Temperature difference across the cooler vs. feed power for the three different TEC feeding solutions: continuous voltage, PWM voltage, and filtered PWM voltage.

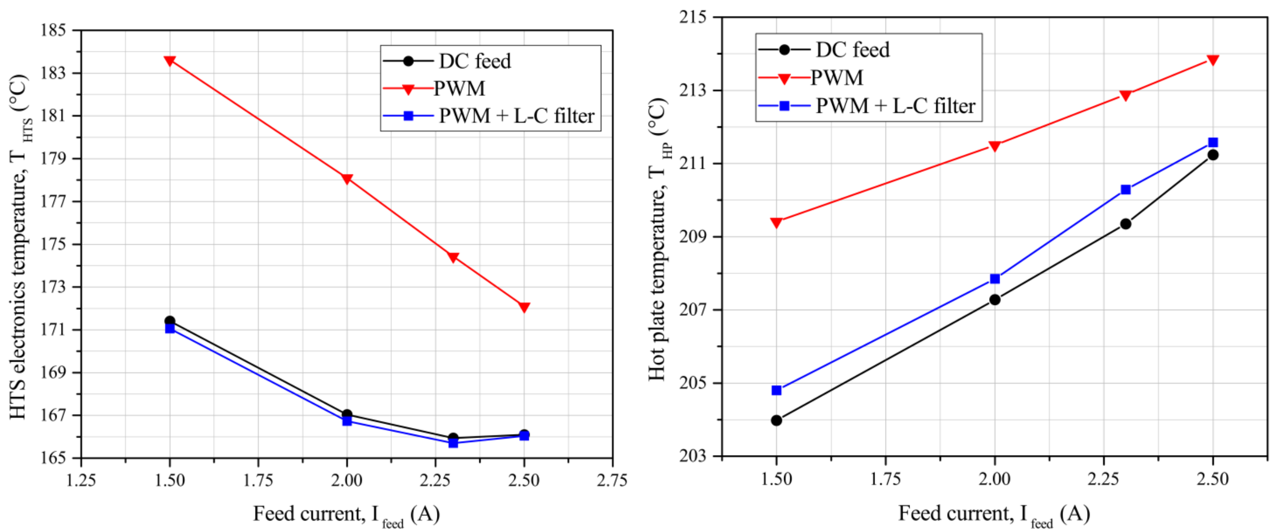

Figure 5.21 HTS electronics temperature (left) and hot plate temperature (right) vs. cooler feed current for the three different TEC feeding solutions: continuous voltage, PWM voltage, and filtered PWM voltage.

The test results show that the implementation of the basic PWM method is not enough to obtain as efficient TEC performance as the case with DC feed currents. The increased Joule losses compromised the temperature span that the cooler is able to maintain and a mismatch, which varies between ~4 °C and ~7 °C, was observed between the curves. The difference in performance with the reference DC case becomes smaller and smaller as the duty cycle approaches unity. With a duty cycle of one, the Joule losses are theoretically equal for the two configurations and the two systems are expected to perform in the same way. The inefficient operation leads to significantly higher HTS electronics and hot plate temperatures (Figure **5.21**).

The introduction of the L-C filter shows a significant improvement in the cooling system performance. The thermoelectric cooler is able to replicate very similar HTS electronics temperatures (Figure 5.21) to the reference DC case, and slightly larger temperature spans (Figure 5.20). The difference in the temperature spans is explained by the higher hot plate temperatures (Figure 5.21), caused by the small oscillations of the feed current around the set point and by the additional losses introduced by the new components. Again, the difference in performance between the systems becomes smaller and smaller as the duty cycle grows towards 1. The PWM with L-C filter proved to be an efficient and suitable solution for electrical integration of the TEC into the well tractor.

Table 5.5 Summary of the tests in the higher convection oven at 200 °C.

	I_{feed} (A)	V_{source} (V)	Duty cycle (%)	V_{feed} (V)	P_{feed} (W)	P_{loss} (W)	T_{oven} (°C)	T_{HTS} (°C)	$T_{HTS,ext}$ (°C)	T_{HP} (°C)	ΔT_{cooler} (°C)
DC feed	1.5	7.8	/	7.8	11.7	0	200.0	171.4	171.8	204.0	32.6
	2.0	10.4	/	10.4	20.7	0	200.2	167.0	167.6	207.3	40.2
	2.3	11.7	/	11.7	26.9	0	200.1	165.9	166.6	209.4	43.4
	2.5	12.6	/	12.6	31.5	0	199.9	166.1	166.7	211.2	45.1
	I_{feed} (A)	V_{source} (V)	Duty cycle (%)	V_{feed} (V)	P_{feed} (W)	P_{loss} (W)	T_{oven} (°C)	T_{HTS} (°C)	$T_{HTS,ext}$ (°C)	T_{HP} (°C)	ΔT_{cooler} (°C)
PWM 1 kHz	1.5	15.0	47.7	7.5	11.2	0.2	199.8	183.6	184.6	209.4	25.8
	2.0	15.0	66.5	10.0	20.0	0.4	200.7	178.1	179.1	211.5	33.4
	2.3	14.9	78.4	11.5	26.4	0.5	200.5	174.4	175.5	212.9	38.5
	2.5	15.0	86.3	12.5	31.2	0.6	200.6	172.1	173.3	213.9	41.8
	I_{feed} (A)	V_{source} (V)	Duty cycle (%)	V_{feed} (V)	P_{feed} (W)	P_{loss} (W)	T_{oven} (°C)	T_{HTS} (°C)	$T_{HTS,ext}$ (°C)	T_{HP} (°C)	ΔT_{cooler} (°C)
PWM + L-C filter 10kHz	1.5	14.9	60.0	7.9	11.9	0.5	199.2	171.1	171.9	204.8	33.7
	2.0	15.0	76.0	10.4	20.8	0.7	199.2	166.7	167.7	207.9	41.1
	2.3	15.0	85.6	11.8	27.0	0.9	199.2	165.7	166.7	210.3	44.6
	2.5	15.1	92.0	12.8	32.0	1.0	199.6	166.0	167.1	211.6	45.5

5.6.2 TEC degradation

After experiencing degradation of the thermoelectric cooler during the tests at high temperature, reported in Section 5.4.4, the effects of the exposure to high temperature were further investigated. A new thermoelectric cooler was installed in *Prototype mark-2* and the tool was tested in the higher convection oven at 200 °C for 200 hours. The goal of the test was to quantify the degradation rate of the cooler and to assess whether such degradation could be critical during the design downhole residence time (≥ 12 hours). The trend of the ΔT_{HTS} and of the feed voltage were monitored during the tests, while maintaining the feed current at the optimal value of 2.3 A. The test results are shown in Figure 5.22.

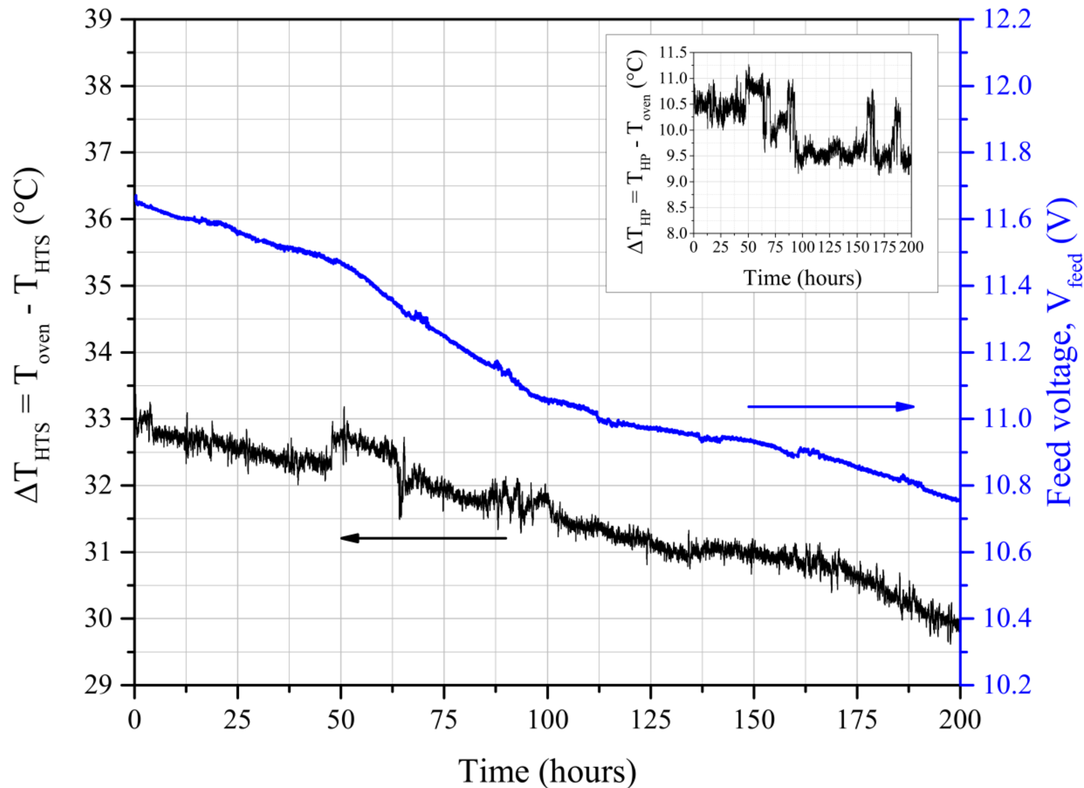

Figure 5.22 Results from the degradation test, carried out at 200 °C in the higher convection oven. Trend in time of ΔT_{HTS}, V_{feed}, and ΔT_{HP}.

A decrease of the cooling performance in time was noticed by the increase of the HTS electronics temperature of 3 °C in 200 hours. ΔT_{HTS} varied in fact from 33 °C to 30 °C, which means the HTS electronics increased from ~167 °C to ~170 °C. While the feed current was maintained constant at 2.3 A, a drop of the feed voltage was detected from ~11.7 V to ~10.7 V. Only a slight change in the hot plate temperature was detected: ΔT_{HP} decreased by ~1 °C over 200 hours, but kept oscillating around a value of 10 °C.

Different mechanisms could have contributed to the drop in performance of a TEC (Barako et al (2012)):

- *Inter-diffusion between thermoelectric material, solder, and copper connectors*. This phenomenon is driven by the charge transport at the interface between the semiconductor legs and the thin copper electric connectors. The process is accelerated by high temperature operation and high current, and increases the electrical contact resistance of the module. This contribution leads to an increase of the module resistance. (Allred et al (1988), Moores et al (1999))

- *Thermal expansion*. When an application involves large temperature changes or thermal cycling, thermoelectric modules should not be installed using stiff connections. Unless the thermal coefficients of expansion of all system components are similar, rigid bonding combined with temperature cycling often results in early module failure due to the induced thermal stresses. This phenomenon can generate cracks within the system and electrical connections, with a raise in the overall electrical resistance. (Click et al (1978))
- *Change in the chemical composition*. Sublimation of Tellurium (more volatile than Bismuth), oxidation of the thermoelectric legs, and reactions in corrosive environments can change the chemical composition of the TE material when operating at high temperatures. This change in the chemical composition results in a change of the thermoelectric properties and thus a drop in the Seebeck coefficient. This contribution leads to a decrease of the cooling effect at a given current, and a drop in the absorbed voltage required by the feed current (see Eq. (2.32)). (Lee et al. (2010), Brostow et al (2012))

It is reasonable to assume that no degradation from thermal expansion occurred in the 200 hour test. As opposed to what was previously experienced (Section 4.4), no increase of the ACR resistance was found after the tests. It was measured that ACR (24.3 °C) = 2.253 Ω before the tests, and ACR (24.3 °C) = 2.139 Ω after the tests. The ACR decreased by 0.114 Ω, probably due to the change in the chemical composition of the thermoelectric material. Tellurium, which tends to evaporate more easily, has in fact a much higher electric resistivity than Bismuth. This effect likely overcame the less impacting increase of the electric contact resistances due to molecular inter-diffusion.

The drop in the feed voltage observed during the tests can be partially motivated by this change in the electrical resistance. However, the main contribution to the decrease of the feed voltage is expected to come from the reduction of the Seebeck coefficient of the thermoelectric material, which also explains the drop in the HTS temperature. A further confirmation of this phenomenon can be found in the trend of ΔT_{HP}, which slightly decreases in time because of the reduced transported heat flux and Joule losses.

It was possible to quantify the degradation in terms of cooling loss per hour (°C/hour) and voltage drop per hour (V/hour) by approximating the trend in time of the studied variables to linear ($R^2 > 0.95$).

$$\Delta T_{HTS,fit} = -0.014\ \frac{°C}{hour} \cdot t + 33.014\ °C \tag{5.21}$$

$$V_{feed,fit} = -0.0048 \frac{V}{hour} \cdot t + 11.6386\ V \tag{5.22}$$

$$\Delta T_{cooler,fit} = -0.020 \frac{°C}{hour} \cdot t + 43.647\ °C \tag{5.23}$$

Where t is the time in hours. Based on the linear fit approximation, a TEC performance degradation of 0.014 °C/hour was found, corresponding to a drop of the feed voltage of 4.78 mV/hour. The temperature span across the cooler was found to decrease with a rate of 0.020 °C/hour. These values are related to the test conditions of temperature, convection regime, and feed current and the effect of degradation would be accentuated at lower convection regimes. The values obtained in these tests are slightly higher than those experienced by Moores et al. (1999) who tested a commercial HT TEC for 1500 hours, at 173 °C and with a

feed current of 1 A. A degradation rate of 0.006 °C/hour was found for ΔT_{cooler} and of 0.67 mV/hour for the feed voltage. The higher degradation rates found in this work could be due to the harsher test conditions at 200 °C and with a feed current of 2.3 A.

The results from the degradation tests could be considered successful and proved that the performance of the cooling system is almost not affected over a time period of 12 hours. After 200 hours of operation at 200 °C, with a medium-low convection regime (~60 W/m^{2}K), the cooling system could still maintain a temperature span between the plates of ~39 °C, and maintain the HTS electronics ~30 °C below the oven temperature.

5.7 Conclusions from the design and testing of *Prototype mark-2* (part 2)

This chapter described the design, construction and testing of *Prototype mark-2*. Starting from the results of the analysis and the testing of *Prototype mark-1*, several modifications were done to the setup in order to improve the cooling system performance and meet the design criteria.

A revision of the well tractor electronics was performed and the total power dissipation of the analyzed components was reduced from 19 W to 6 W. This significantly lowered the excess heat flux to be rejected from the tool and the heat rejection temperature, improving the performance of the cooling system.

Successively, a finite-element model of the tool was implemented in COMSOL Multiphysics and coupled with a topology optimization algorithm. The thermal layout of the actively cooled electronics unit was optimized and an optimized distribution of thermally conducting material, represented by the aluminum chassis, and thermal insulation, represented by the HT polyimide foam, was sought for the design operating conditions. The optimization developed a new design for the chassis that could effectively integrate the TEC and minimize the HTS electronics temperature. The final design was manufactured and tested, showing good agreement with the model forecasts, and supporting topology optimization as a powerful design tool. *Prototype mark-2* was able to maintain the electronics at 166 °C and 176 °C when operating at 200 °C with convective heat transfer coefficients of ~60W/m^{2}K and ~30 W/m^{2}K, respectively. The hot side of the system was always maintained at a tolerable temperature for the TEC and the HTNS components, and never exceeding 212 °C. The design criteria were satisfied and the tool could always maintain the electronics at tolerable temperatures.

After successfully proving the thermal management concept, the electrical integration of the TEC into the well tractor was investigated. The downhole DC voltage source at 15 V needed to be modulated and adapted to suitable voltage ranges for the cooler. A power width modulation system was built with a signal generator and a transistor, to regulate the voltage across the cooler by controlling the duty cycle of the modulated signal. The basic PWM system proved to be not efficient enough for the application due to the introduced additional losses in the TEC that affected its performance. An L-C filter was therefore integrated into the PWM circuit to stabilize the voltage across the cooler at the desired value and cancel the additional Joule losses. The filtered PWM system was successfully tested and the results from the tests at DC feed conditions could be reproduced.

Finally, the degradation of the thermoelectric cooling system at high temperatures was investigated. *Prototype mark-2* was run for 200 hours in a ventilated oven at 200 °C, at the optimal feed current of 2.3 A. A drop of the temperature span across the cooler of 0.020 °C/hour was recorded, while the HTS temperature increased with a rate of 0.014 °C/hour. A drop of the feed voltage equal to 4.8 mV/hour was also recorded,

indicating a change in the thermoelectric material properties due to the exposure to high temperature. These results could be considered successful since the effects of the degradation proved to be negligible over the target HT exposure time of 12 hours.

6. Downhole heat transfer coefficient sensor

The development process that successfully led to the construction of *Prototype mark-2* has been presented in the previous chapters. As for the design of cooling systems for general applications, several quantities that characterized the heat transfer within and outside the electronics unit (cold and hot reservoir temperatures, cooling load, thermal resistances, and heat transfer areas) were studied to achieve an effective design.

However, a big challenge was encountered in the definition of the heat rejection conditions to the well. More specifically, it was complex to quantify the heat transfer coefficient that described the thermal interaction between the tool and the wellbore, also given the lack of scientific literature. Contrary to general cooling applications, the heat rejection rate to the hot reservoir could not be designed and optimized, but depended on several features of the operating environment (well dimensions, well fluid composition and phases, temperature, pressure, flow rate, and type of performed well intervention). Such a heat transfer coefficient is, in fact, defined by a large number of variables and is complex to estimate, as it also varies with the depth of the well.

This parameter is not only relevant for the design of an active cooling system, but also provides important information about the temperature evolution of the passively cooled components. Having a better knowledge of the heat transfer occurring downhole can help to improve the risk management related to electronics overheating failures and predict more accurately the temperature trend of the electronics and the tractor as a whole.

This chapter presents the design and construction of a proof-of-concept sensor that could be integrated in a diagnostic downhole tool to measure the heat transfer coefficient that characterizes the thermal interaction between the tool and the well environment. The data acquired by the sensor could be employed in two different ways.

- "*In real-time*": coupled with the active cooling system, the sensor could provide the input for regulating the feed current of the TEC around the optimal point, which mainly varies with the heat transfer conditions (see Section 5.4.4).

- "*Post-acquisition*": a database could be built by measuring the downhole heat transfer coefficient for different wells, fluids, depths and well intervention types. Such a database could be used both for the thermal design of new tools, to predict the electronics temperatures during the job-planning phase, and to mitigate the risk of electronics overheating. Furthermore, the sensor could be used to detect heat transfer anomalies such as bubbles, infiltrations or lateral well branches.

6.1 Background

When operating in a wellbore, a downhole tool thermally interacts with the well environment in different ways. The power dissipation from the embedded electronics increases the temperature of the tool, which exchanges heat with the well environment through conduction, convection, and radiation. As previously discussed, convection is the dominant heat transfer mechanism that drives the heat dissipation which can be approximated by the convective heat transfer coefficient h. This coefficient describes the heat flux exchanged per unit of tool housing area, and per degree of temperature difference.

The scientific literature does not contain much information about the heat transfer dynamics occurring between downhole tools and the well environment. The majority of the articles that study the heat transfer in oil and gas wells analyze the thermal interaction between the well fluid, the well casing, and the formation (Hasan et al. (2012)) to predict the temperature profile of the well, and uses correlations for single-phase fully developed flow (Santoyo et al. (2003), Keller et al. (1973)). Furthermore, many of these studies are limited to particular well operations, for instance, well drilling (Santoyo et al. (2003)) or cementing (Beirute (1991)). A comprehensive study of the wellbore heat transfer mechanisms is reported by Zhou (2013), although the values for convective heat transfer coefficients are, again, reported for specific operating conditions and did not consider the interaction with well intervention tools. These models developed in the literature require an enormous amount of inputs related to the well geometry and fluid composition, which are often unknown to the oil and gas service companies. Among the studies on downhole active cooling presented in Chapter 1, only Flores (1996) proposed an analysis of the downhole heat transfer boundary conditions. A model was developed to describe the thermal interaction between the moving downhole tool and the well fluid in case of plug, laminar and Bingham-Plastic flow. The well fluid was modelled as a mixture of water, oil, barite, and clay. Among the different analyzed scenarios, a minimum convection coefficient of 100 W/m^2K was estimated and set as design boundary condition. Further calculations were made for the case of a stationary tool, neglecting free convection and assuming zero velocity of the tool and the well fluid. Only pure conduction through the well fluid was considered and a heat transfer coefficient of 7 W/m^2K was estimated. The actively cooled tool was finally dimensioned for non-stationary applications, with a design heat transfer coefficient of 100 W/m^2K. Sinha el al. (2010) also considered and discussed this parameter. They first assumed a convection coefficient equal to ~4.4 W/m^2K to model the heat transfer between a finned copper bar, coupled to the hot side of the Peltier cooler, and air. However, the experimental results, obtained by testing the tool in a ventilated oven, found better agreement with the model predictions for a convection coefficient of ~50 W/m^2K.

The lack of information from the literature, and the complexity related to accurate modeling, support the development of a sensor that can experimentally measure the downhole heat transfer coefficient and does not rely on any well fluid or borehole properties.

6.2 Thermal interaction between tool and well environment

Before presenting the design and the development of the sensor, it is opportune to better characterize the heat transfer dynamics that occur between the downhole tool and the well environment. The main mechanism that drives the heat transfer in the borehole is the heat convection, while conduction and radiation can be considered negligible for the considered operating conditions. The heat transfer coefficient can therefore be approximated to the well fluid convection coefficient. As previously discussed the convection coefficient depends on a large number of parameters, among which:

- The well fluid thermophysical properties: density, thermal conductivity, and dynamic viscosity are some of the well fluid properties that influence the convective heat transfer.

- The flow regime: In case of single-phase flow, depending on the Reynolds number (Eq. (6.1)), the flow regime can be laminar, transitional, or turbulent. In case of multiphase flow, several other flow regimes can occur depending on the balance and speed of the phases.

$$Re = \frac{\rho u D}{\mu} \tag{6.1}$$

  Where *Re* is the Reynolds number, ρ is the well fluid density, u is the well fluid average speed, D is the geometry characteristic length, and μ is the fluid dynamic viscosity.

- The type of the flow: starting from some inlet conditions, the velocity and temperature profiles vary with the flow direction, and develop towards an asymptotic distribution. Depending on the development state of the velocity and temperature profiles, the fluid flow can be classified fully developed, hydro-dynamically developing, thermally developing, or simultaneously developing.

- The geometry of the system: the shape of the cross section of the pipe affects the convective heat transfer with the pipe walls. Different convection coefficients can be observed for analogue fluid flows in circular, rectangular, or annular pipe geometries.

- The boundary conditions: the convection coefficient can have different values depending on the heat transfer boundary conditions at the pipe walls. Two of the most studied cases in the literature are for the heat transfer at constant heat flux and at constant temperature.

While the thermophysical properties of the well fluid are complicated to estimate and vary from well to well, or even with the well depth, the type of flow and its developing conditions can be approximated to some reference conditions classified in the literature (Kacaç et al. (1987)), like shown in Figure 6.1.

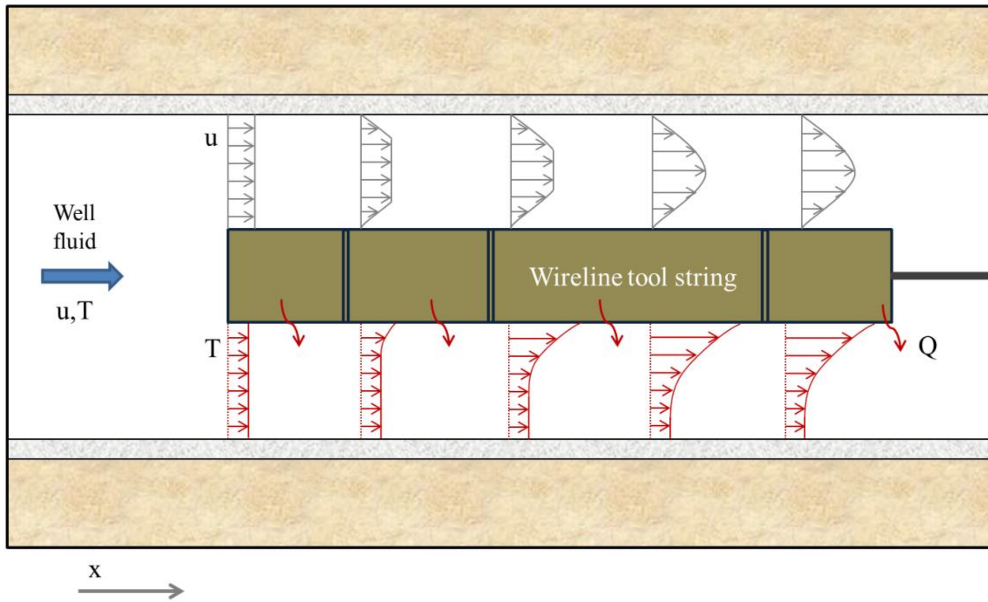

Figure 6.1 Schematic of the ideal interaction between the downhole tool string and the well fluid flow, with velocity u and temperature T. The qualitative development of the velocity and temperature profiles is illustrated, with the assumption that the tool string dissipates a uniform heat flux Q and the well fluid is single-phase. The illustrated velocity profile resumes more of a laminar flow parabolic distribution. In case of turbulent flow, the u profile is described by a flatter curve that still evolves towards a hydro-dynamically developed state.

In order to simplify the problem, the well fluid flow around the tool can be classified as (i) single-phase, (ii) simultaneously developing, (iii) in annular geometry,(iv) with a constant-heat flux boundary condition, and (v) either laminar, transitional or turbulent.

It is possible to find correlations in the scientific literature that describe the heat transfer for the described case. They express the Nusselt number (Eq. (6.2)) as a function of the position along the x-axis (see Figure **6.1**) and of the geometric features of the flow. In the case of developing flow, the convection coefficient varies, in fact, along the length of the tool (see Figure 6.2). It then stabilizes around an asymptotic value when the velocity and temperature profiles fully develop. The same behavior is observed for the different pipe geometries and flow regimes.

$$Nu_x = \frac{h_x D}{k} \tag{6.2}$$

$$Nu_m = \frac{1}{x}\int_0^x Nu_x dx = \frac{h_m D}{k} \tag{6.3}$$

Where Nu is the Nusselt number, h is the convective heat transfer coefficient, D is geometry characteristic length, and k is the fluid thermal conductivity. The subscripts x and m mean that the Nusselt number and the heat transfer coefficient can be either evaluated locally (x) or averaged over a certain length (m).

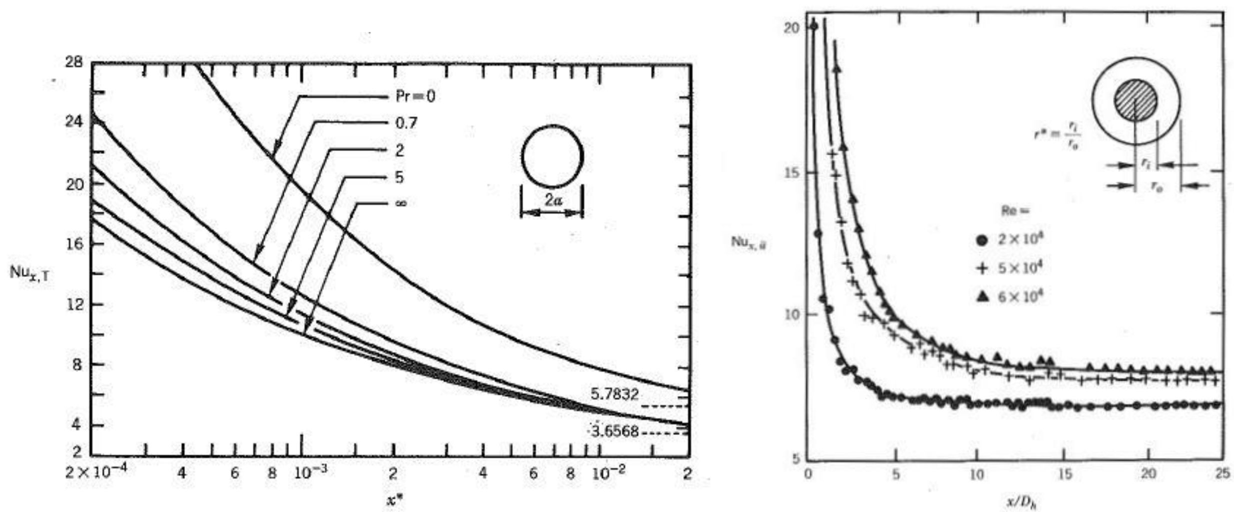

Figure 6.2 Illustration of the decreasing trend of the local Nusselt number for a simultaneously developing flow in a circular pipe (left), and for a thermally developing flow in an annular geometry (right). The Nusselt number depends on the Reynolds and Prandtl numbers. Graphs from Kacaç et al. (1987).

In the real application, the thermal interaction between the tool string and the well environment is significantly different from the ideal case from Figure 6.1. The tool orientation and position in the wellbore continuously change and the well fluid can be composed of several phases. The size of the tool string can vary and additional geometric features (e.g. well tractor wheels) can disrupt the development of the velocity profile. Furthermore, the power dissipation along the tool is not uniform and different tool sections can influence the temperature profile of the well fluid in different ways. It is therefore very complex to forecast the heat transfer coefficient between tool and well environment. The great advantage of having a sensor that experimentally measures such a quantity is that none of the aforementioned information is needed. Given the variability of the heat transfer coefficient along the tool string profile, more than one sensor could be installed to locally measure the downhole heat transfer coefficient and reconstruct its trend along the tool string length.

6.3 Design of the sensor

The average heat transfer coefficient h over a certain surface can be expressed according to its general definition (Kakaç et al. (1987)) reported in Eq. (6.4).

$$h_{def} = \frac{Q}{A \cdot (T_{surf} - T_{ext})} \tag{6.4}$$

Where Q is the rejected heat flux through the surface A exposed to the well fluid, T_{surf} is the average temperature of the surface, and T_{ext} is the well fluid bulk mean temperature. The heat transfer coefficient h_{def} can be experimentally obtained by measuring the temperature difference between the surface and the lapping fluid when dissipating a certain amount of heat Q through a surface A. The sensor should therefore have a surface A in contact with the well fluid, through which a controlled amount of power Q is dissipated. Furthermore, the sensor should be able to measure both the temperature of the surface and of the well fluid.

This configuration could be achieved by mounting a dissipating element into a metallic casing, which is then installed on a downhole tool and put in contact with the well fluid. The dissipating element, fed by a controlled power source, would dissipate heat through the surface of the casing and a temperature sensor could measure the heat rejection temperature. The casing that interfaces the dissipating element to the well should be designed with highly conductive material, so the inner surface temperature can be approximated to the outer one. The well fluid bulk temperature could be measured, instead, by a shielded temperature sensor or by another diagnostic tool used by Welltec for this purpose. The control and data acquisition systems could be integrated in the inner part of the tool.

A preliminary analysis of the system showed that the design of the sensor should:

- Aim at a maximum operating temperature of 200 °C.
- Not interfere, either thermally or electrically, with any other device in the downhole tool. The power dissipated through the sensor should therefore not affect the operating temperature of the other components.
- Not disrupt the hydro-dynamic development of the flow (fit the profile of the tool) and affect the fluid temperature distribution the least possible (not too high power dissipation rates).
- Minimize the heat losses to the surrounding to have an accurate estimation of the heat transfer coefficient and not to affect the temperature of other components.
- Minimize the temperature gradient between the surface exposed to the well fluid and the heat source.
- Minimize the response time to measure h and detect possible anomalies in real time. This implies minimizing the sensor thermal mass and heat dissipation surface area.
- Fit, together with the data acquisition system, a tool housing with O.D. 80 mm and I.D. of 62 mm.

Furthermore, two operating approaches for the sensor were individuated:

1) Dissipate a fixed heat flux → calculate the heat transfer coefficient by measuring the variable temperature difference between the well fluid and the sensor.

2) Set a $\Delta T_{SetPoint}$ → calculate the heat transfer coefficient by regulating the dissipated heat flux so the temperature difference between well fluid and sensor is maintained at $\Delta T_{SetPoint}$.

The implementation of approach (1) appears to be less complex and does not require any automated control of the power dissipation. Nevertheless, high power dissipation rates are required to maintain a significant temperature difference and a good resolution of the measurements at high convection regimes. This high heating rate can generate high sensor temperatures in case of poor convection, which can damage the sensor and the neighboring components. Approach (2), instead, regulates the dissipation rate to maintain the temperature difference $(T_{surf} - T_{ext})$ constant and in an acceptable range. It therefore requires a lower dissipation rate. Maintaining a constant temperature difference between the sensor and the well fluid also decreases significantly the response time as the thermal mass of the sensor is maintained at constant temperature and is subject to much shorter temperature transients than for Approach (1).

The analysis of the system led to the sensor design illustrated in Figure 6.3.

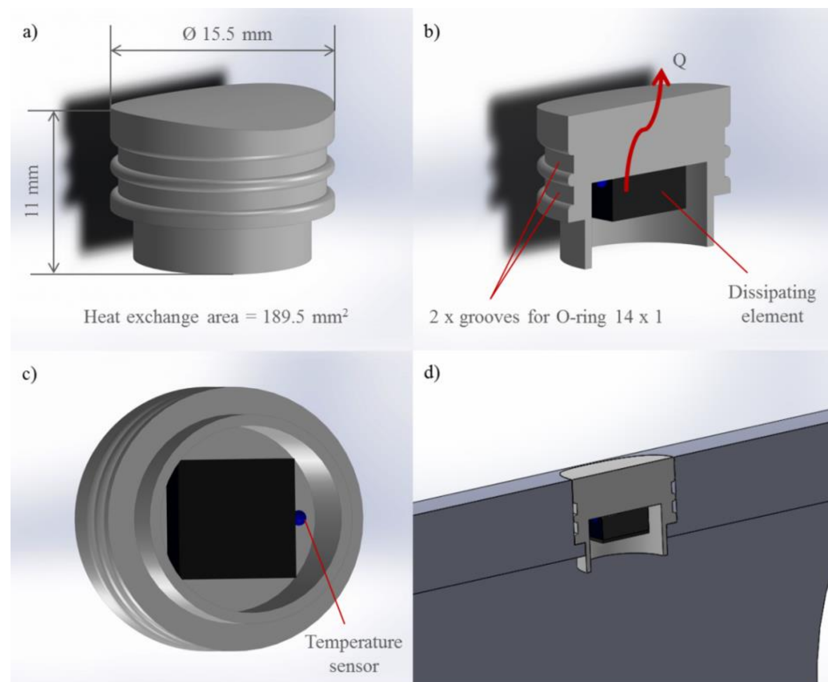

Figure 6.3 3D CAD model of the sensor casing with dissipating element (a, b, and c) and section-view of the sensor integrated in a downhole tool (d).

The sensor is composed of a hollow metallic casing which hosts the dissipating element and the temperature sensor. The dissipating element is mounted on a 5 mm thick surface that conducts the rejected heat towards the well fluid. When the sensor is assembled in the downhole tool, two O-rings seal the inner side from fluid invasion. The inner part of the tool could host the feeding and data acquisition systems (DAQ). In order to test the concept and the design of the sensor, an experimental setup was designed with room temperature components. The goal of the experimental setup was to reproduce a known type of flow, for which the convection coefficient could be predicted with correlations from the literature. The experimental measurements from the sensor could then be compared to the predictions and the sensor could be calibrated. The design of the experimental flow loop is presented in the next section.

6.4 Experimental setup

The design of the flow loop aimed at reproducing known convective heat transfer conditions that could be modelled and compared with the experimental measurements. Since the sensor was conceived to detect poor heat rejection conditions, a low range of convection coefficients needed to be reproduced. Laminar flow was chosen to reproduce a range from 0 to 1000 W/m^{2}K.

6.4.1 Modeling

A tube with circular cross section was chosen as reference geometry and a solution of water-glycol 10% vol as heat transfer fluid. The type of flow that the setup aimed at reproducing is a thermally developing flow. A straight tube section needed to be installed before the sensor to let the flow develop hydro-dynamically. The flow would then start developing thermally when lapping the sensor. The geometry of the sensor was slightly

modified to be interfaced with the fluid flow, as shown in Figure 6.4. The sensor head was adapted to the circular profile of the pipe to not disrupt the flow velocity profile and a plate was designed at the bottom of the casing to install the sensor in the setup. A sensor section was designed to mount the device with four screws.

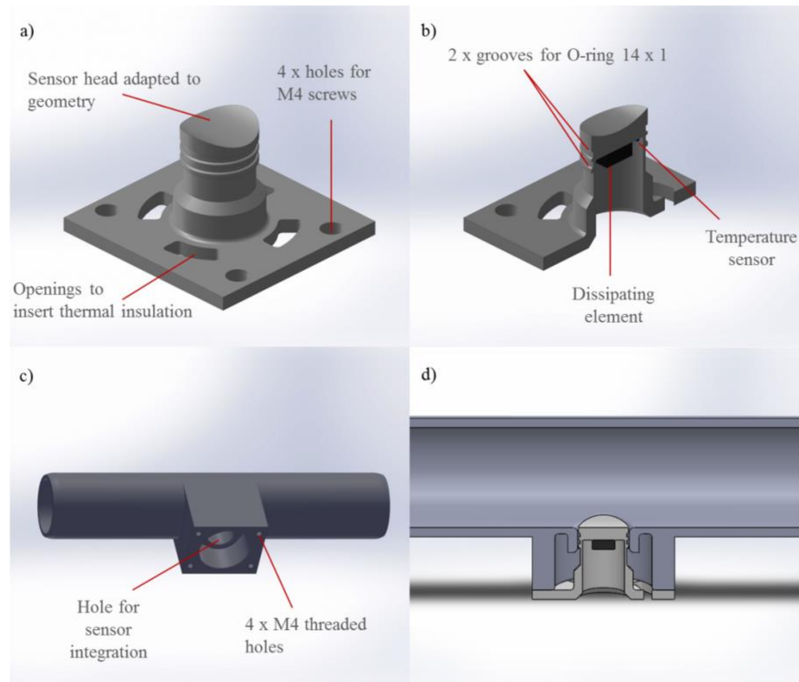

Figure 6.4 3D CAD model of the sensor modified for integration in the experimental setup. Modified sensor casing with dissipating element (a and b), pipe section hosting the sensor (c), and section-view of the sensor integrated in the pipe section (d).

The software Engineering Equation Solver (EES) (EES 2016) was used to build a model of the system and to retrieve the thermophysical properties of the heat transfer fluid. The model was initially used to perform a parametric study and to find suitable dimensions for the pipe, which could reproduce the desired range of convection coefficients. Eq. (6.5) and (6.6), from Kakaç et al. (1987), were used to calculate the convective heat transfer coefficient for the thermally developing flow in the circular pipe. The equations calculate the local and average Nusselt number for the constant temperature boundary condition, in analogy with the experimental conditions.

$$Nu_{x,T} = \begin{cases} 1.077 \cdot x^{*-\frac{1}{3}} - 0.7 & for\ x^* \leq 0.01 \\ 3.657 + 6.874 \cdot (10^3 \cdot x^*)^{-0.488} e^{-57.2 \cdot x^*} & for\ x^* > 0.01 \end{cases} \tag{6.5}$$

$$Nu_{m,T} = \begin{cases} 1.615 \cdot x^{*-\frac{1}{3}} - 0.7 & for\ x^* \leq 0.005 \\ 1.615 \cdot x^{*-\frac{1}{3}} - 0.2 & for\ 0.005 < x^* < 0.03 \\ 3.657 + (0.0499/x^*) & for\ x^* \geq 0.03 \end{cases} \tag{6.6}$$

Where $Nu_{x,T}$ and $Nu_{m,T}$ are respectively the local and mean Nusselt numbers, calculated for the constant temperature boundary condition (T). $x*$ is the dimensionless axial coordinate for the thermal entrance region and is defined as:

$$x^* = \frac{x}{D_h \cdot Pe} \tag{6.7}$$

Where x is the axial coordinate along the pipe where Nu is calculated, D_h is the hydraulic diameter corresponding to the I.D. of the pipe, and Pe is the Peclet number, defined as the product of the Reynolds (Eq. (6.1)) and Prandtl numbers:

$$Pe = Re \cdot Pr \tag{6.8}$$

$$Pr = \frac{c_p \cdot \mu}{k} \tag{6.9}$$

Where Pr is the Prandtl number, c_p is the specific heat capacity at constant pressure of the fluid, and k is the fluid thermal conductivity.

In order to calculate the length of the required straight entrance section Eq. (6.10) from Kakaç et al. (1987) was used:

$$L_{entrance} = 0.056 \cdot Re \cdot D_h \qquad for\ Re \leq 2300 \tag{6.10}$$

The fluid flow rate was calculated as:

$$V_f = u \cdot \frac{\pi D_h^2}{4} \tag{6.11}$$

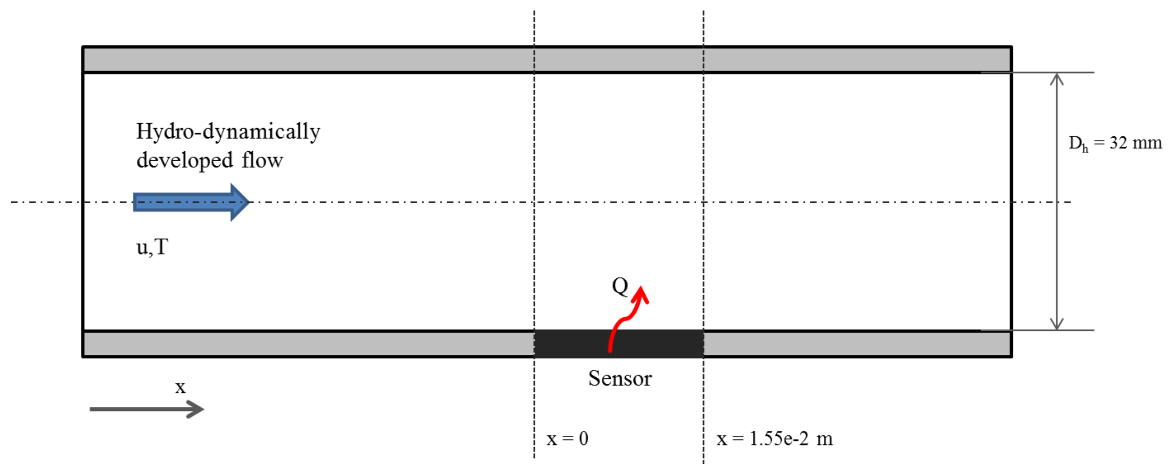

Figure 6.5 Schematic representation of the thermally developing flow in the sensor section. The main design dimensions, which were used in the EES model to determine the average convection coefficient over the sensor, are illustrated.

The model wad used to perform a parametric study over the diameter of the circular pipe D_h. Simulations were run to calculate the trend of the heat transfer coefficient and of the required entrance length over the laminar range of Reynolds numbers $0 < Re < 2300$. The heat transfer fluid flow rate was also monitored. A value of $x = 1.55\text{e-}2$ m was used, as shown in Figure 6.5, to calculate the average convection coefficient over the sensor surface.

It was found that for lower pipe diameters the convection coefficient grows faster with the Reynolds number, and the measurable range of convection coefficients is wider over the laminar regime. Additionally, the entrance length was found to decrease with the pipe diameter, as well as the required heat transfer flow rate. A tradeoff between pipe dimensions, measurable h range, and required volume flow rates was reached choosing a diameter of 32 mm. A maximum entrance length of ~4 m for Re = 2300 was obtained. The use of a flow straightener could be considered to reduce this length in the practical implementation of the setup. The predicted trend of the calculated variables is shown in Figure 6.6 and represented the reference predictions to compare with the data measured by the sensor.

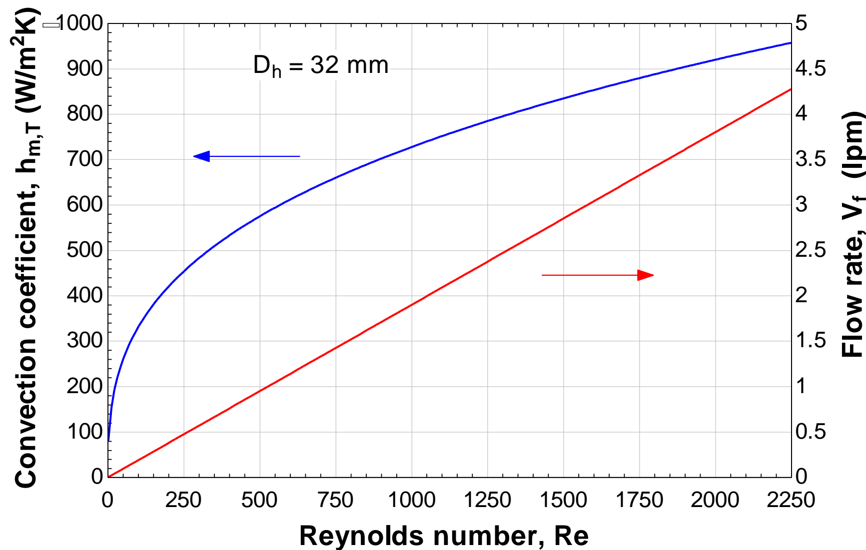

Figure 6.6 Predicted convection coefficient and flow rate vs. Reynolds number, from Eq. (6.6) and (6.11).

6.4.2 Construction

In order to reproduce the modelled heat transfer conditions, the flow loop shown in Figure 6.7 was built.

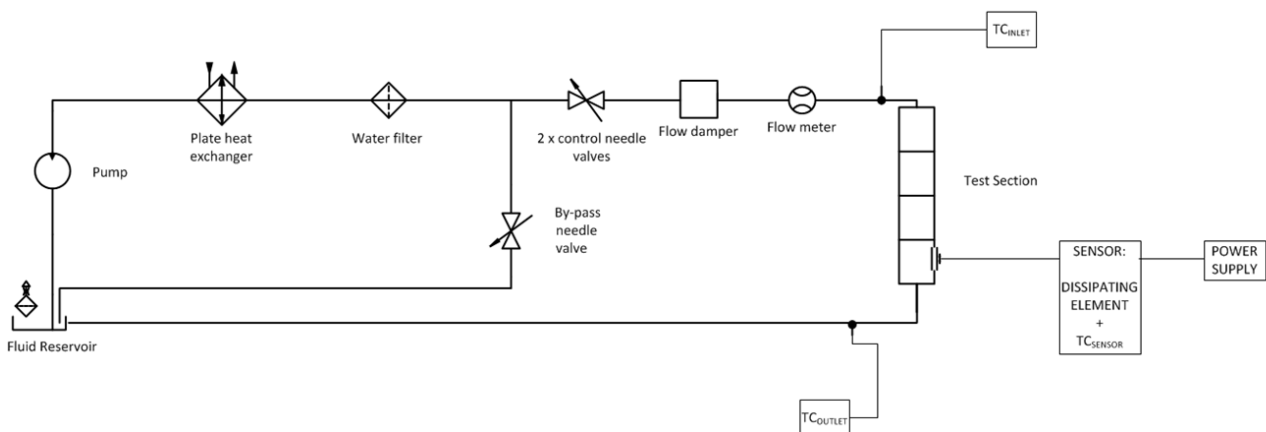

Figure 6.7 Schematic of the flow loop used for the experimental measurements on the heat transfer coefficient sensor.

A fluid reservoir contains a solution at 10%vol of water-ethylene glycol at ambient pressure. A pump recirculates the heat transfer fluid from the storage tank, through the flow loop and the sensor section. Plastic tubing is used to connect the main components of the setup. A plate heat exchanger couples to a chiller is adopted to absorb the pump work and maintain the fluid temperature constant at the pump outlet. A filter is used to remove particles from the fluid. A by-pass line and a needle valve are used to regulate the flow through the main test section, while two needle valves adjust the flow on the main test line. A flow damper absorbs the pressure waves caused by the pump, stabilizing the flow rate. A flow meter and a thermocouple measure the fluid flow rate and temperature, respectively, at the inlet of the main test section.

The test section is designed with an I.D. of D_h = 32 mm, as stated in the previous paragraphs. A POM inlet adapter (Figure 6.8), which receives the flow from the rubber hose and conveys it into a 2 m long plexiglas straight pipe. At the end of the 2 m long pipe the sensor section is connected (Figure 6.9), where the sensor itself is mounted. The sensor section was fabricated in POM, while the sensor casing was manufactured in aluminum for the good heat transfer properties. At the end of the sensor section, a plastic collector receives the flow and leads it back to the storage tank through a tube. At the end of the test section, another thermocouple measures the fluid temperature. Before the interaction with the sensor, a straight pipe section of ~2.5 m is provided for the development of the velocity profile. A gradually enlarging inlet section and a honeycomb flow straightener are used to decrease the required entrance length. The four piping components of the test section (inlet adapter, 2m plexiglas pipe, sensor section, and outlet adapter) are connected to each other through some custom designed couplings which seal the pipe ends together, and prevent them from moving apart.

An 8.2 x 7.3 x 3.6 mm surface-mounted (SM) power resistor of 220 Ω was used as dissipating element in the sensor. The resistor was glued to the inner side of the sensor with a thin layer of thermal epoxy (k = 7.2 W/m-K) and connected to a power supply. A type-E thermocouple was also located next to the resistor with the same epoxy to monitor the temperature of the dissipating surface. The technical drawings of the inlet and outlet sections, sensor section, sensor, and couplings are reported in Appendix C. Some pictures of the flow loop are shown in Figure 6.8 and Figure 6.9.

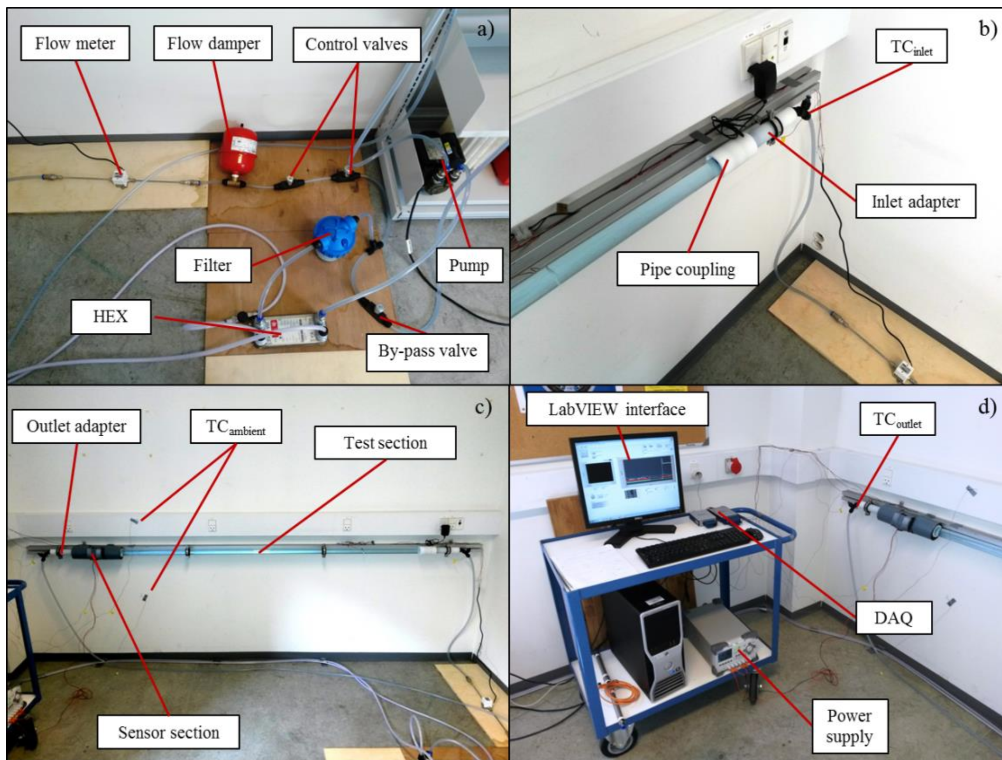

Figure 6.8 Pictures of the experimental setup: main auxiliary components (a), inlet to the test section (b), main test section (c), and outlet of the test section with DAQ system (d).

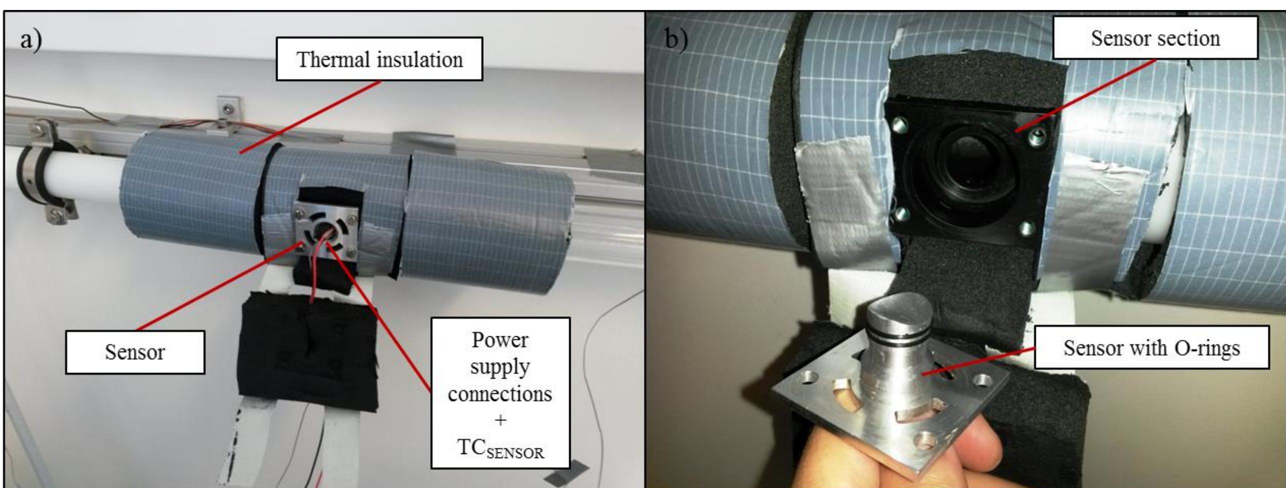

Figure 6.9 Pictures of the sensor section (a), and of the disassembled sensor (b).

A data acquisition system was set up through National Instruments' equipment and interfaced to the laboratory computer with the software LabVIEW (LabVIEW 2015). The quantities that are monitored through the DAQ are listed below.

Table 6.1 Summary of the DAQ system.

Quantity	*Instrument*	*Acquisition*
Flow rate through the test section	Turbine flow meter 1: 0.05 – 0.5 L/min Vortex flow meter 2: 0.5 – 10 L/min	NI 9203 - 4-20 mA input.
Inlet temperature	Type-E thermocouple	NI 9212 - ±78 mV input
Sensor temperature	Type-E thermocouple	
Outlet temperature	Type-E thermocouple	
Ambient temperature	2 x Type-E thermocouples	
Feed voltage to the sensor	Power supply (3 channels: 30 – 30 – 5 V)	Rigol DP832

6.4.3 Working principle

A LabVIEW interface was developed to acquire, display and record the measured quantities. In accordance with the chosen approach (2) (see section 6.3), a PID control was implemented in LabVIEW according to the working principle shown in Figure 6.10.

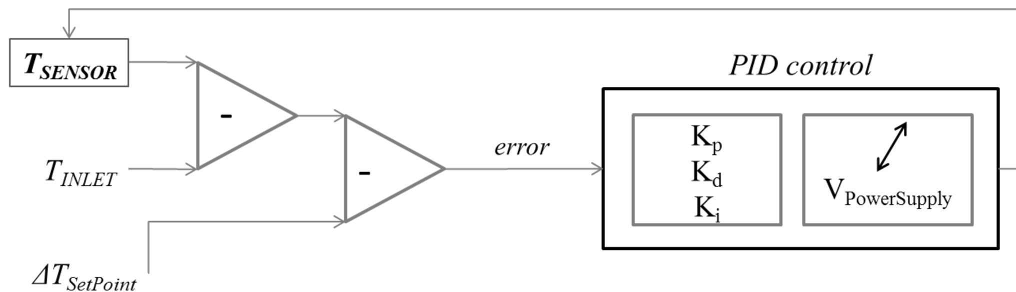

Figure 6.10 Implemented PID control for regulating the temperature span between sensor (T_{SENSOR}) and convective fluid (T_{INLET}) to the desired difference $\Delta T_{SetPoint}$.

The PID control loop aimed at adjusting the voltage and the power across the dissipating element, so the temperature span between the sensor (T_{SENSOR}) and the convective fluid (T_{INLET}) could be regulated at the set point $\Delta T_{SetPoint}$. The communication with the power supply was also built through a LabVIEW interface. K_p, K_d, and K_i are the proportional, derivative and integral gains of the control loop, respectively.

The heat transfer coefficient measured by the sensor was then calculated as:

$$h = \frac{Q}{A_{SENSOR} \cdot (T_{SENSOR} - T_{INLET})} \tag{6.12}$$

Where Q is the power rejected from the dissipating element to the well fluid. It is expectable that part of the dissipated power leaks to ambient or to the neighboring components. Q is therefore different than $V_{PowerSupply} \cdot I_{PowerSupply}$, and assuming otherwise would mean to overestimate h. The effect of the heat leakages was removed from the calculations as shown in the next sections.

6.4.4 Results

The tests were run for $\Delta T_{SetPoint}$ = 5, 10, 15, and 20 °C to investigate which could provide the best accuracy, fastest response and highest resolution. The setup from Figure 6.7 was used to perform the experimental measurements and calibrate the sensor. Several flow rates were set through the flow loop for each different $\Delta T_{SetPoint}$. Once the system reached the steady state, the measurement of the heat transfer coefficient was recorded and correlated to the flow rate. A calibration procedure that could be reproduced on the downhole tool was sought. The LabVIEW interface used for the experiments is illustrated in Figure 6.11.

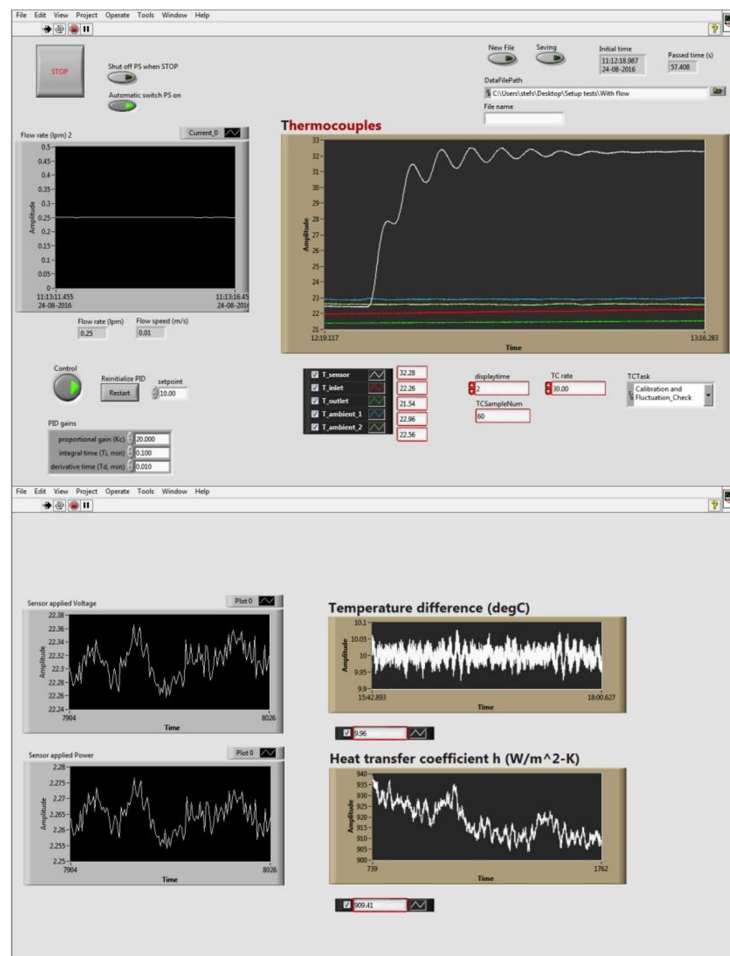

Figure 6.11 LabVIEW interface for the testing and calibration of the sensor. The PID control satisfactorily proved to maintain the temperature difference between the sensor and the inlet conditions at $\Delta T_{SetPoint} \pm 0.05$ °C.

6.4.4.1 First measurements

A first round of experiments was conducted and the heat transfer coefficient was calculated from Eq. (6.12), assuming Q equal to the total power dissipation of the resistive elements. The test results were compared to the predicted results from the EES model, as shown in Figure 6.12.

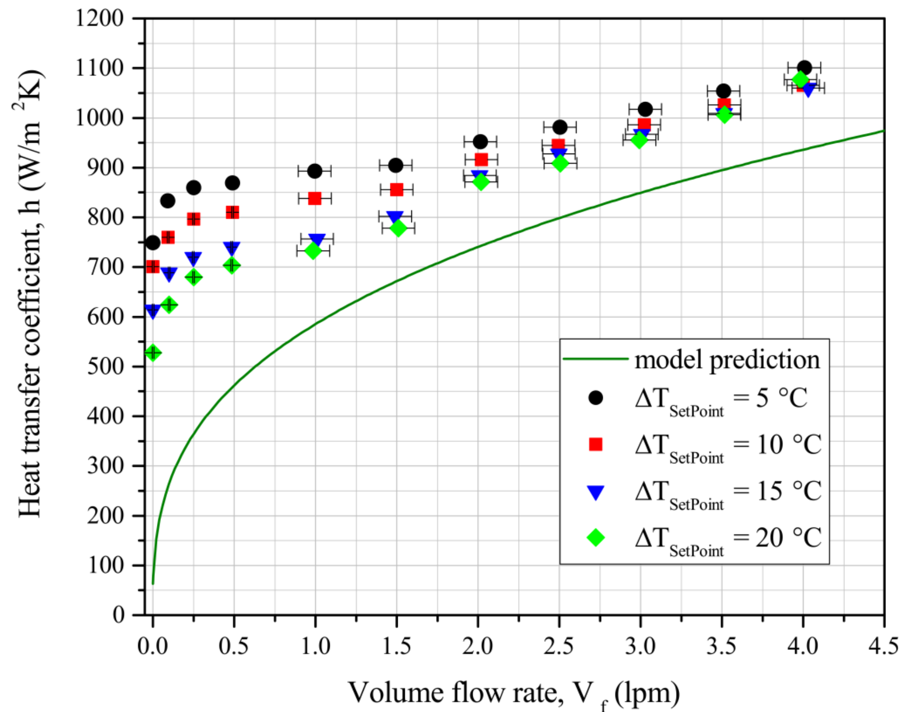

Figure 6.12 Heat transfer coefficient vs. fluid flow rate, without filtering of the heat losses. The model prediction is compared to the experimental data points for different $\Delta T_{SetPoint}$.

As expected, the heat transfer coefficient was overestimated compared to the model predictions. Part of the dissipated power likely leaked to the ambient or to the fluid through alternative thermal paths. The mismatch with the model prediction is higher for higher $\Delta T_{SetPoint}$ and lower volume flow rates. When maintaining a higher temperature difference with the fluid temperature, as well as with ambient, the heat losses from the sensor become also higher and more impacting on the measurements. When operating at low flow rates, instead, the thermal resistance between the dissipating element and the fluid becomes higher and the heat losses increase. In order to improve the accuracy of the sensor, the heat leakages need to be compensated, as shown in the next sections.

6.4.4.2 Step 1 - Compensation for the ambient losses

A series of tests were carried out to characterize and the heat leakages to ambient through the thermal insulation. Thermal insulation was applied on the dissipating surface of the sensor and the test section was emptied of the heat transfer fluid to also insulate the inner side of the pipe. In this way, the only heat sink for the power dissipated in the sensor was the ambient and the heat losses could be characterized. The ambient losses were therefore calculated by running the sensor and correlating the obtained temperature difference with ambient with the used feed power (Figure 6.13).

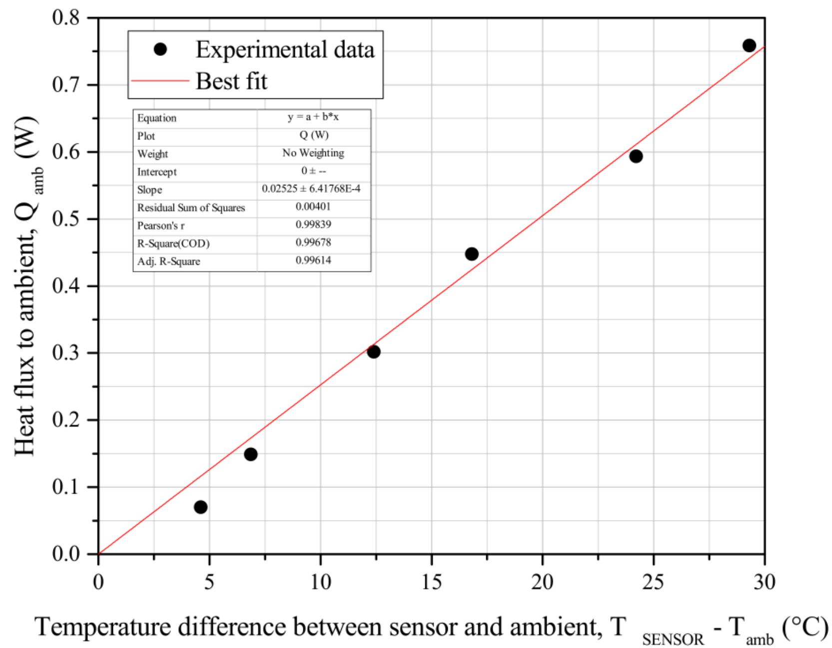

Figure 6.13 Heat losses from to ambient vs. temperature difference between sensor and ambient.

The heat losses to ambient were characterized as 0.0253 (W/K) times the temperature difference between the sensor and the ambient. Such losses were subtracted in the definition of Q, and the heat transfer coefficient computed again.

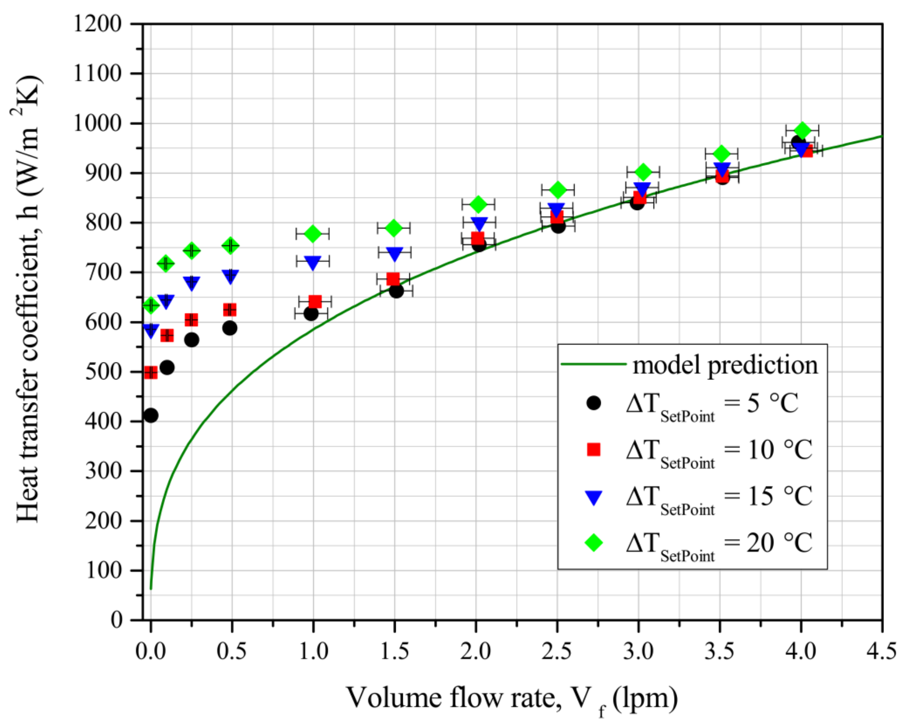

Figure 6.14 Heat transfer coefficient vs. fluid flow rate, with no contribution of heat losses to ambient. The model prediction is compared to the experimental data points for different $\Delta T_{SetPoint}$.

Compensating for the contribution of the losses to ambient led to a better accuracy of the measurements. For $\Delta T_{SetPoint}$ of 5 °C and 10 °C, the experimental data points agreed very well (max error of 6%) with the model for flow rates above 1 L/min. For flow rates below 1 L/min, the mismatch remained significantly large. As previously discussed, lower flow rates correspond to higher thermal resistances between the sensor dissipating surface and the fluid, so part of the dissipated heat is more likely to leak through the casing and the surrounding components. Such leakages needed further investigation and are elaborated in the next section. $\Delta T_{SetPoint}$ of 15 °C and 20 °C led to less accurate measurements also at high flow rates, and were therefore excluded from the next analysis.

6.4.4.3 Step 2 - Compensation for other convective losses

Figure 6.15 shows more in detail the thermal interaction between the sensor and the setup, as well as the distribution of the heat fluxes.

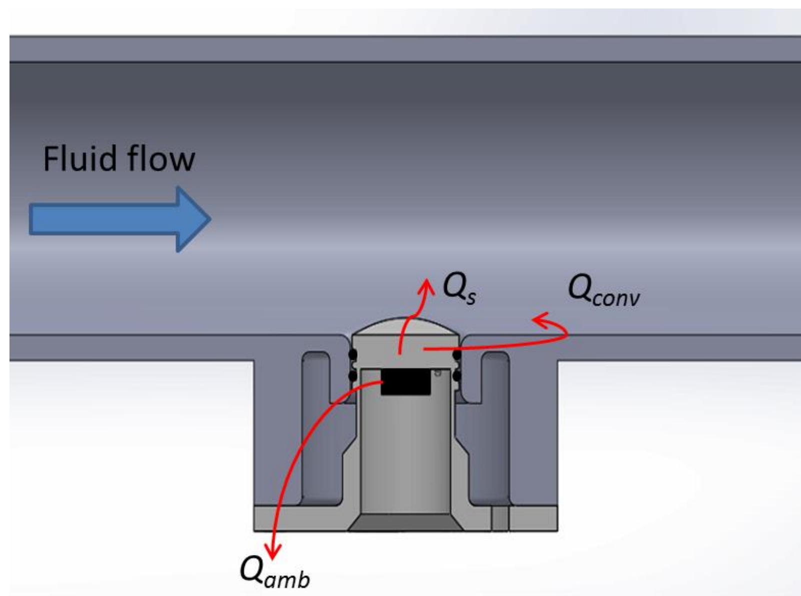

Figure 6.15 Schematic representation of the thermal interaction of the sensor with the setup and the surrounding.

The dissipated power in the sensor can be split in three different contributions: Q_s is the heat flux exchanged with the fluid through the surface of the sensor designed for the thermal interaction; Q_{amb} is the part of the dissipated power which is lost to ambient through the insulation; and Q_{conv} is the heat flux leaked through the sensor casing, but still absorbed by the convective fluid. The impact of Q_{conv} on the measurements is higher at low flow rates, as discussed before, and still needs to be taken into account.

The values of Q_{conv} and the corrected heat transfer coefficients were found by comparing the different values of h, obtained for $\Delta T_{SetPoint}$ = 5 °C and 10 °C, which should result the same in absence of losses. The following energy balance equations were implemented in EES, together with the experimental results, to calculate the contribution of Q_{conv} and exclude it from the calculation of h.

$$Q_s = Q_{PowerSupply} - Q_{amb} - Q_{conv} \tag{6.13}$$

$$h = \frac{V_{PowerSupply} \cdot I_{PowerSupply} - 0.0253 \cdot (T_{SENSOR} - T_{INLET}) - Q_{conv}}{A_{SENSOR} \cdot (T_{SENSOR} - T_{INLET})} \quad (6.14)$$

Where h and Q_{conv} are the unknowns. Eq. (6.14) was implemented for the experimental results, below 1 L/min, from the tests at $\Delta T_{SetPoint}$ = 5 °C and 10 °C. Additional boundary conditions were added to state (i) the equality of the convection coefficients calculated, at the same flow rates, for $\Delta T_{SetPoint}$ = 5 °C and 10 °C (Eq. (6.15)); and (ii) the analogy of the convection losses to the correlations for natural convection over horizontal plates (Kitamura et al. (1995)) (Eq. (6.16)). This second boundary condition was chosen because of the higher impact of convective losses at stationary or very slow flow regimes. Other correlations could be sought for better accuracies and improvement of the results.

$$h|_{\Delta T_{SetPoint}=10} = h|_{\Delta T_{SetPoint}=5} \quad (6.15)$$

$$\frac{Q_{conv}}{A \cdot (T_{SENSOR} - T_{INLET})} = k(T_{SENSOR} - T_{INLET})^{0.32} \quad (6.16)$$

The system of 5 equations and 5 unknowns was implemented and solved in EES. The results of the calculation are shown in Figure 6.16.

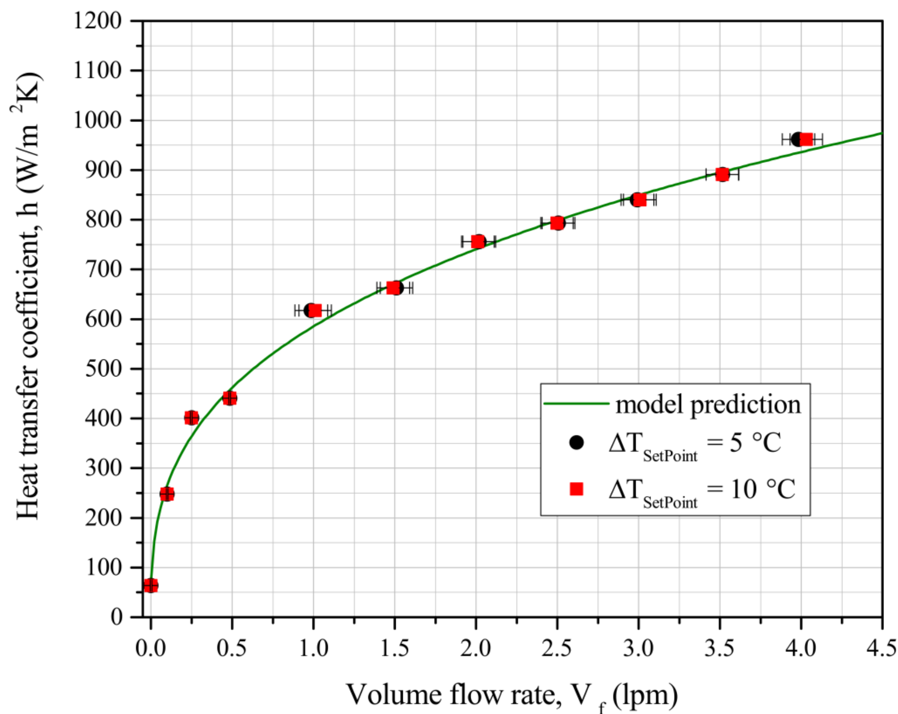

Figure 6.16 Heat transfer coefficient vs. fluid flow rate, with the canceled contribution of heat losses. The model prediction is compared to the experimental data points for different $\Delta T_{SetPoint}$.

The two steps for filtering the influence of the heat leakages led to a more accurate calibration of the system. The experimental results finally reproduced the model predictions very well, with an average and maximum errors of ~3% and ~10%, respectively, for both the cases at $\Delta T_{SetPoint}$ = 5 °C and 10 °C.

6.4.4.4 Resolution and response time

Table 6.2 Summary of the experimental results for the sensor calibration from the tests at $\Delta T_{SetPoint}$ = 5 °C.

V_f (L/min)	h_{EES} (W/m^2K)	h (W/m^2K)	error (%)	Required Power (W)	Voltage reading (V)
0.00	63.2	63.6	0.01	0.53	10.9
0.10	265.1	248.2	0.06	0.71	12.4
0.25	364.2	401.4	0.10	0.73	12.7
0.48	427.4	440.6	0.03	0.75	12.8
0.99	582.5	617.1	0.06	0.79	13.1
1.51	673.1	662.5	0.02	0.84	13.5
2.02	742.9	755.8	0.02	0.94	14.3
2.51	799.3	793.2	0.01	0.99	14.7
2.99	848.6	839.9	0.01	1.04	15.0
3.52	896.1	890.9	0.01	1.09	15.4
3.98	934.7	961.3	0.03	1.18	16.0
	Average resolution (mV per W/m^2K)	6.6			

Table 6.3 Summary of the experimental results for the sensor calibration from the tests at $\Delta T_{SetPoint}$ = 10 °C.

V_f (L/min)	h_{EES} (W/m^2K)	h (W/m^2K)	error (%)	Required Power (W)	Voltage reading (V)
0.00	63.2	63.6	0.01	1.35	17.2
0.10	265.2	248.2	0.06	1.52	18.1
0.25	363.5	401.4	0.10	1.57	18.5
0.48	457.0	440.6	0.04	1.62	18.8
1.01	587.2	640.8	0.09	1.64	19.0
1.49	670.2	686.6	0.02	1.77	19.7
2.01	741.9	768.6	0.04	1.92	20.5
2.50	798.3	811.9	0.02	2.00	20.9
3.01	850.1	851.2	0.00	2.09	21.4
3.51	896.0	893.7	0.00	2.18	21.9
4.03	938.5	944.7	0.01	2.30	22.5
	Average resolution (mV per W/m^2K)	8.7			

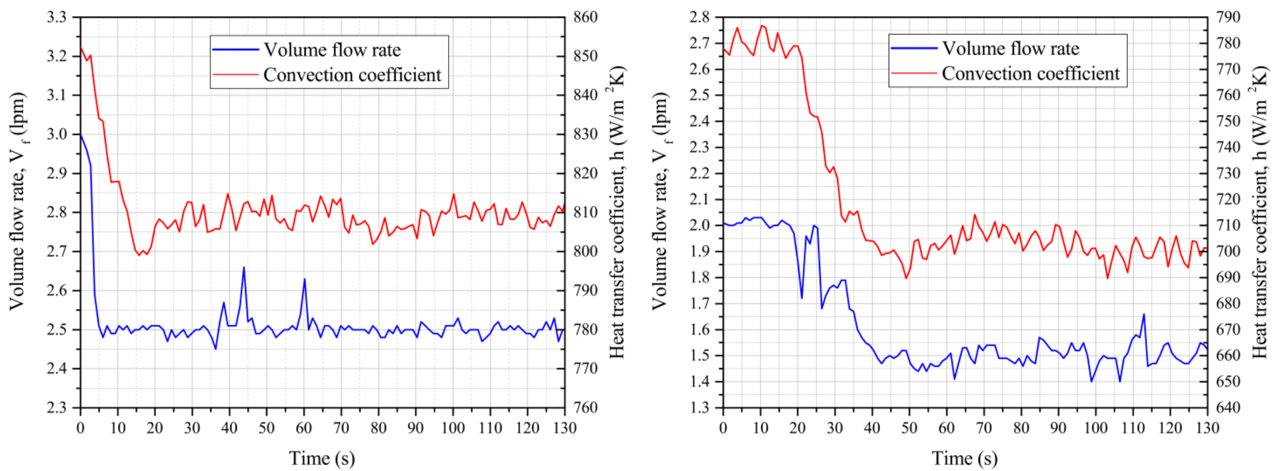

Figure 6.17 Representation of two system transients due to a change in the flow rate from 3 to 2.5 L/min (left) and from 2 to 1.5 L/min. The change in flow rate corresponded to a change in the fluid speed of ~1cm/s. Operations at a $\Delta T_{SetPoint}$ = 10 °C. A first estimation of the response time was done around 11 seconds for both cases.

Table 6.2 and Table 6.3 summarize the final results for the sensor calibration over the measurement range at $\Delta T_{SetPoint}$ = 5 °C and 10 °C, respectively. The average resolution characterizing the measurement is expressed for the two cases in millivolts per measured W/m^{2}K. A higher resolution was found for the approach at a $\Delta T_{SetPoint}$ = 10 °C, compared to the case at $\Delta T_{SetPoint}$ = 5 °C. That is due to the to the higher voltage increment required to measure different convective coefficients.

In other words, we could say that higher temperature differences of set point provide better resolution of the measurements. However, the accuracy becomes worse as it could be observed in Figure 6.12 and Figure **6.14**, due to the higher heat losses. A tradeoff needs to be reached. The choice of the resistance of the dissipating element also affects the resolution of the voltage readings, whereas a higher resistance gives a better resolution. Nevertheless, the choice of the dissipating element must still be compatible with the available downhole power source.

Although the observed response time in Figure 6.17 is promising, further tests should be conducted to acquire additional data and broaden the evaluation. A response time of the sensor of ~11 s was estimated for a decrease of the fluid speed of 1cm/s, which can be considered a sudden and significant velocity change for a well fluid in a borehole.

6.5 Conclusions from the design and testing of the sensor

This chapter presented the design and the proof of concept of a sensor for measuring the heat transfer coefficient between the tool and the downhole environment. An experimental flow loop was designed to create known convective heat transfer conditions and compare the experimental measurements to known correlations from the literature. A procedure for calibrating the sensor, which could also be applied to a sensor installed into a downhole tool, was developed and consisted of: (i) the implementation of a PID control that could regulate the temperature span between the dissipating surface of the sensor and the convective fluid, (ii) the estimation of the heat transfer losses to ambient, (iii) the comparison between measurements at different $\Delta T_{SetPoint}$, and (iv) the elimination of additional convective losses.

Good agreement between the model predictions and the final experimental measurements, with an average error of ~3% and maximum error of ~10%, were obtained for $\Delta T_{SetPoint}$ of 5 °C and 10 °C. A higher resolution, equal to 8.7 mV per W/m^{2}K was found for $\Delta T_{SetPoint}$ = 5 °C, compared to 6.6 mV per W/m^{2}K for $\Delta T_{SetrPoint}$ = 10 °C. A promising response time of ~11 s for 1 cm/s velocity change was also observed.

The response time and the resolution of the sensor are expected to change not only with its thermal mass, but also with the thermal mass and thermal conductivity of the surrounding components because of the heat leakages. The response time and the resolution of the sensor could differ in case of integration in a downhole tool and should be analyzed again. The sensor would in fact be integrated into a metallic, and not plastic, frame and would exhibit larger heat leakages. Further analyses should also study more in detail the dependence of the heat leakages on the well fluid flow regime; tests on a different heat transfer fluid (air), energy balance equations and finite element modeling could support this study.

Also, the implementation of a thermally insulating system around the sensor would be more complex in a downhole environment, given the harsher conditions. However, the reduced mass of the sensor, and the smaller area of the casing in contact with other components, should benefit its accuracy. The calibration of the sensor could still follow an analogue procedure to the one described for the proof of concept, but should also consider that only the convective heat losses would now affect the system.

Further development should also consider the selection of the electronic components required by the integration in a downhole tool, starting from the micro-controller responsible for the control loop and the data acquisition system. A suitable temperature sensor should be selected for the measurement of the well temperature, or an opportune interface with the existing well-temperature tool should be developed. Finally, given the small dimensions and the modular configuration, more than one sensor could be installed in one tool string. Several sensors, measuring the heat transfer coefficient locally, would help to characterize the heat transfer profile along the whole tool string.

7. Conclusions

This thesis presented the analysis and implementation of active cooling techniques for thermal management of the downhole tool electronics. Specifically, this work focused on the design of an active cooler that could maintain the Welltec well tractor electronics at a tolerable temperature of 175 °C, while operating at 200 °C.

The relevance of active cooling systems as a possible solution to the overheating of downhole electronics was highlighted in Chapter 1, together with an overview of the currently employed thermal management techniques and prior works on downhole active cooling systems.

A feasibility study was then presented in Chapter 2, where the main cooling technologies were investigated for integration in a downhole tool. Important requirements for the cooling technology were individuated in compactness, compatibility with the tool dimensions and thermal layout, reliability, integrability with the power sources available downhole, and suitability to work in the desired high temperature range. Theoretical calculations and prior works from the scientific literature were used to evaluate these features. Thermoelectric coolers proved to be the most suitable option for the analyzed case because of their compactness, absence of moving parts, integrability to the well tractor electric system, and suitability for high temperature operation. Vapor compression cycles and phase change materials proved to be also attractive solutions, but some critical aspects, such as the development of a high temperature micro compressor and the requirement of additional tool sections, discouraged their implementation.

In order to define an effective integration strategy for the TEC, a review of the downhole electronics was carried out as presented in Chapter 3. A thermal model of the well tractor electronics section was implemented in COMSOL Multiphysics and validated through experimental testing. A total power dissipation of ~43 W at 150 °C was estimated for the well tractor electronics. Furthermore, the electronic components were distinguished into high temperature sensitive and non-sensitive. The first dissipated ~2W and needed active cooling to operate at 200 °C; the latter dissipated ~41 W and could be passively cooled when running at 200 °C.

The thermal characterization of the well tractor led to the integration scheme presented in Chapter 4. The temperature sensitive electronics were coupled to the cold plate of the thermoelectric cooling system thorough a soft thermal pad and a heat spreader. The excess heat could be rejected radially to the well through the metallic chassis and housing. The temperature non-sensitive components were, instead, mounted on the chassis and passively cooled. In this way, the length of the well tractor could be preserved, without any additional tool section required. Compared to the analyzed prior works, this represented an innovative result. The thermal management concept was implemented, using test electronics and two TECs, in *Prototype mark-1*, which was used for some preliminary tests up to 170 °C. The testing of *Prototype mark-1* led to the choice of a clamping system, supported by thermal grease, to effectively install the TEC into the downhole tool. This assembly technique proved to provide effective mechanical stability and heat transfer. Furthermore, *Prototype mark-1* was used to evaluate the performance of three different commercial thermoelectric modules, selected for operation at high temperature, and to choose the best performing one. The tests of *Prototype mark-1* at 170 °C did not meet the design criteria as they could only maintain the electronics 18 °C below the operating temperature, compared to the 25 °C required by the application. However, the tests were carried out in a dry ventilated oven with poor heat rejection conditions (convective heat transfer coefficient ~30 W/m^2K), compared to the ones expected downhole. Forecasts at a heat rejection rate of 100 W/m^2K proved that the thermal integration concept was promising and worth further development.

The design of the first lab-prototype was therefore reviewed for improvement and led to the design of *Prototype mark-2*, presented in Chapter 5. The improvement of the electronics efficiency, which contributed to a reduction of the power dissipation of ~72%, proved to be very beneficial for the system. The heat rejection temperature could in fact be reduced, as well as the cooling load temperature. The new design of *Prototype mark-2* was supported by the topology optimization approach, which was implemented in a COMSOL-MATLAB environment, and coupled with a finite element model of the system. Topology optimization proved to be a powerful design tool for effective integration of thermoelectric devices. The testing of *Prototype mark-2* showed significant improvements compared to the previous version. The HT sensitive electronics could be maintained ~33 °C and ~25 °C below the operating temperature of 200 °C, with heat rejection rates of ~30 W/m^2K and ~60 W/m^2K, respectively. The testing of *Prototype mark-2* met the design criteria even below the design heat rejection conditions of 100 W/m^2K. The temperatures of the TEC hot plate and of the passively cooled electronics were maintained in a tolerable range around 210 °C. Furthermore, it was found that the temperature of the cooled electronics could be minimized by an optimal feed current, which mainly depends on the heat rejection rate. Slight degradation of the cooler performance was noticed after cycling the TEC at high temperatures. Further tests at 200 °C, and with a feed current of 2.3 A, showed an increase of the electronics temperature of 0.014 °C/hour and a drop in the absorbed voltage of 4.2 mV/hour. The degree of degradation of the cooler was assessed as irrelevant for the system performance over the design downhole exposure time of ~12 hours. Furthermore, the combination between a PWM circuit and an L-C filter was adopted to adapt the 15 V downhole power source to a suitable voltage range for the TEC. The L-C filter proved to be crucial for the system efficiency, as it could dampen the oscillations of the output voltage and current. Such oscillations were in fact found to increase the losses within the TEC and the temperature of the cooled electronics up to 13 °C higher than with a DC feed voltage. The combination between PWM and L-C filter satisfactorily reproduced the results obtained with a DC feed voltage.

Finally, given the uncertainty of the downhole heat rejection conditions, a sensor for direct measurements of the downhole heat transfer coefficient between the tool and the well was designed. An experimental flow

loop was built to test the sensor, measure heat transfer coefficients between 0 and 1000 W/m^{2}K, and compare the results to known correlations from the literature. The accuracy of the sensor proved to be significantly affected by the heat losses from the dissipating element to the surrounding. A calibration procedure for the sensor, which could filter out the effect of the heat leakages, and also be applied to the integration in a downhole tool, was finally developed. The final measurements showed an average mismatch with the predicted trend of ~3% and a maximum error of ~10%. An average resolution of 8.7 mV per W/m^{2}K was obtained. The resolution could be improved by increasing the resistance of the dissipating element or $\Delta T_{SetPoint}$. In the first case, the sensor would not lose any accuracy, but should still be compatible with the voltage of the downhole power source. In the second case, the accuracy of the sensor would be lowered and a different calibration procedure should be developed. Preliminary tests also showed a response time of the sensor of ~11 s for a change of the fluid speed of 1 cm/s.

7.1 Suggestions for future work

For what concerns the implementation of active cooling techniques into downhole tools, the following future work is suggested:

- Mechanical testing of the thermoelectric module is suggested to evaluate whether any kind of well intervention could induce critical stresses on the TEC.
- A spring system should be implemented to make the assembling process of chassis and housing easier, and reduce the thermal resistance between chassis and housing by increasing the contact force between them.
- A control loop that aims at the optimal TEC feed conditions should be developed and tested at different heat rejection conditions.
- Since the review of the electronics significantly lowered the power dissipation of the electronics, an alternative configuration with a Dewar flask coupled and an active cooler could be considered.
- In connection to the use of vacuum flasks, phase change materials could also be further investigated. They could either provide an additional heat sink in case of poor heat rejection, or supply the whole required cooling capacity.

For what concerns the development of the downhole heat transfer sensor, the following future work is suggested:

- Repeat the tests with other heat transfer fluids (e.g. air) to make the calibration procedure more robust and further investigate the influence of the heat losses.
- Support the calculation of the heat losses by modelling the system.
- Perform additional tests to better characterize the response time of the sensor.
- Start testing the sensor in a downhole tool and adapt the calibration procedure to a different geometry.

- Select a suitable microprocessor for automating the PID control in a downhole tool and develop the interface (PWM is a suitable option for regulating the power across the sensor).
- Select suitable components for the data acquisition (e.g. ADC converter) in order to evaluate the final resolution and accuracy of the measurements.
- Perform further tests aimed at detecting downhole heat transfer anomalies such as bubbles, or singularities, such as intersections between well branches.

References

Abramzon B.. Numerical Optimization of the Thermoelectric Cooling Devices, *Journal of Electronic Packaging*, 129(3): 339-347 (2007). http://dx.doi.org/10.1115/1.2753959

Ahn S. H. , Cho S. Level Set-based Topological Shape Optimization of Heat Conduction Problems Considering Design-dependent Convection Boundary, *Numerical Heat Transfer, Part B*, 58(5): 304-322 (2010). http://dx.doi.org/10.1080/10407790.2010.522869

Alexandersen J. , Aage N. , Andreasen C.S. , Sigmund O. Topology Optimisation for Natural Convection Problems, *International Journal for Numerical Methods in Fluids*, 76(10): 699-721 (2014). http://dx.doi.org/10.1002/fld.3954

Allred D.D., Van Nguyen, O. Accelerated Life Test For Thermoelectric Junctions: Solder Element Interactions, *Proceedings of the 7th International Conference on Thermoelectric Energy Conversion*, 137-140 Arlington TX, USA (1988).

ASHRAE Handbook of Fundamentals, *American Society of Heating, Refrigerating and Air Conditioning Engineers*, 1993.

Barako M.T. , Park W, Marconnet A.M. , Asheghi M. , Goodson K.E. Thermal Cycling, Mechanical Degradation, and the Effective Figure of Merit of a Thermoelectric Module, *Journal of Electronic Materials*, 42(3): 372–381 (2012). http://dx.doi.org/10.1007/s11664-012-2366-1

Barbosa J. R. , Ribeiro G. B. , de Oliveira P. A. A State-of-the-Art Review of Compact Vapor Compression Refrigeration Systems and Their Applications, *Heat Transfer Engineering*, 33(4-5): 356–374 (2012). http://dx.doi.org/10.1080/01457632.2012.613275

Barclay J. A. , Stewart W. F. , Overton W. C. Jr. , Steyert W. A. Magnetic Refrigeration for 4-10 K Applications, *Los Alamos National Laboratory report LA-UR-84-540*, 1983. http://dx.doi.org/10.2172/920237

Beirute R.M. A Circulating and Shut-in Well-Temperature-Profile Simulator. *Journal of Petroleum Technology*, 43(9): 1140–1146 (1991). http://dx.doi.org/10.2118/17591-pa

Bell L. E. Cooling, Heating, Generating Power, and Recovering Waste Heat with Thermoelectric Systems, *Science*, 321(5895): 1457-1461 (2008). http://dx.doi.org/10.1126/science.1158899

Bendsøe M. P. , Sigmund O. Topology Optimization: Theory, Methods, and Applications, *Springer Verlag*, Berlin Heidelberg (2004). http://dx.doi.org/10.1007/978-3-662-05086-6

Bennett G. A. Active Cooling for Downhole Instrumentation: Preliminary Analysis and System Selection, *Los Alamos National Laboratory*, Mexico (1988). http://dx.doi.org/10.2172/5360643

Brostow W. , Datashvili T. , Hagg Lobland H. E. , Hilbig T. , Su L. , Vinado C. , White J. Bismuth telluride-based thermoelectric materials: Coatings as protection against thermal cycling effects, *Journal of Materials Research*, 27(22): 2930–2936 (2012). http://dx.doi.org/10.1557/jmr.2012.335.

Brück E. , Ilyn M. , Tishin A.M. , Tegus O. Magnetocaloric Effects in $MnFeP_{1-x}As_x$-based Compounds, *Journal of Magnetism and Magnetic Materials*, 290-291: 8–13 (2005). http://dx.doi.org/10.1016/j.jmmm.2004.11.152

Bruns T. E. Topology Optimization of Convection-dominated, Steady-state Heat Transfer Problems, *International Journal of Heat and Mass Transfer*, 50(15): 2859-2873 (2007). http://dx.doi.org/10.1016/j.ijheatmasstransfer.2007.01.039

Bulusu A. , Walker D. G. Review of Electronic Transport Models for Thermoelectric Materials, *Superlattices and Mictrostuctures*, 44(1): 1-36 (2008). http://dx.doi.org/10.1016/j.spmi.2008.02.008

Cabeza L. F. , Castell A. , Barreneche C. , de Gracia A. , Fernandez A. I. Materials used as PCM in thermal energy storage in buildings: A review. *Renewable and Sustainable Energy Reviews*, 15(3), 1675–1695 (2011). http://dx.doi.org/10.1016/j.rser.2010.11.018

Castro D. A. , Kiyono C. Y. , Silva E. C. N. Design of Radiative Enclosures by Using Topology Optimization, *International Journal of Heat and Mass Transfer*, 88: 880-890 (2015). http://dx.doi.org/10.1016/j.ijheatmasstransfer.2015.04.077

Chen L. , Li J. , Sun F. Performance Optimization for a Two-stage Thermoelectric Heat-pump with Internal and External Irreversibilities, *Applied Energy*, 85(7): 641–9 (2008). http://dx.doi.org/10.1016/j.apenergy.2007.10.005

Click P. B. , Marlow R. Reliability and Failure Modes of Thermoelectric Heat Pumps, *Proceedings of the 2nd International Conference on Thermoelectric Energy Conversion*, 115-120, Arlington TX, USA (1978).

COMSOL Multiphysics 5.0, COMSOL AB, Stockholm, Sweden.

David B. , Ramousse J. , Luo L. Optimization of Thermoelectric Heat Pumps by Operating Condition Management and Heat Exchanger Design, *Energy Conversion and Management*, 60: 125-133 (2012). http://dx.doi.org/10.1016/j.enconman.2012.02.007

Deaton J. D. , Grandhi R. V. A Survey of Structural and Multidisciplinary Continuum Topology Optimization: Post 2000, *Structural and Multidisciplinary Optimization*, 49(1): 1-38 (2014). http://dx.doi.org/10.1007/s00158-013-0956-z

Dede E. M. , Joshi S. N. , Zhou F. Topology Optimization, Additive Layer Manufacturing, and Experimental Testing of an Air-Cooled Heat Sink, *Journal of Mechanical Design*, 137(11): 111702 (2015). http://dx.doi.org/10.1115/1.4030989

Dede E. M. Single-phase Microchannel Cold Plate for Hybrid Vehicle Electronics, *2014 Semiconductor Thermal Measurement and Management Symposium (SEMI-THERM)*, (2014). http://dx.doi.org/10.1109/semi-therm.2014.6892227

Dede E.M. , Lee J., Nomura T. Multiphysics Simulation: Electromechanical System Simulation and Optimization Studies. *Springer London*, Heidelberg New York Dordrecht (2014). http://dx.doi.org/10.1007/978-1-4471-5640-6_5

Dresselhaus M. S. , Chen G. , Tang M. Y. , Yang R. , Lee H., Wang D. , Ren Z. , Fleurial J.P. , Gogna P. New Directions for Low-Dimensional Thermoelectric Materials, *Advanced Materials*, 19(8): 1043-1053 (2007). http://dx.doi.org/10.1002/adma.200600527

EES 2016, Engineering Equation Solver, F-Chart Software.

El-Hana Bouchekara H. R. , Nahas M. Magnetic Refrigeration Technology at Room Temperature. *Trends in Electromagnetism - From Fundamentals to Applications*, 2012. http://dx.doi.org/10.5772/33789

Engelbrecht K. A Numerical Model of an Active Magnetic Regenerator Refrigeration System. *M.Sc. thesis*, University Of Wisconsin-Madison, USA (2004).

Engelbrecht K. L. , Nellis G. F. , Klein S. A., Zimm C. B. Recent Developments in Room Temperature Active Magnetic Regenerative Refrigeration. *HVAC&R Research*, 13(4):.525–542 (2007). http://dx.doi.org/10.1080/10789669.2007.10390970

Farid M. M. , Khudhair A. M. , Razack S. A. K. , Al-Hallaj S. A Review on Phase Change Energy Storage: Materials and Applications, *Energy Conversion and Management,* 45(9-10): 1597–1615 (2004). http://dx.doi.org/10.1016/j.enconman.2003.09.015

Flores A. G. Active Cooling for Electronics in a Wireline Oil-Exploration Tool, *Ph.D. Thesis*, M.I.T., USA (1996).

Foldeaki M. , Schnelle W. , Gmelin E. , Benard P. , Koszegi B. , Giguere A. , Chahine R. , Bose, T. K. Comparison of magnetocaloric properties from magnetic and thermal measurements, *Journal of Applied Physics*, 82(1): 309 (1997). http://dx.doi.org/10.1063/1.365813

Gersborg-Hansen A. , Sigmund O. , Haber R. B. Topology Optimization of Channel Flow Problems, *Structural and Multidisciplinary Optimization*, 30(3): 181-192 (2005). http://dx.doi.org/10.1007/s00158-004-0508-7

Gordon J. M. , Ng K. C. , Chua H. T. , Chakraborty A. The Electro-adsorption Chiller: a Miniaturized Cooling Cycle with Applications to Micro-electronics, *International Journal of Refrigeration*, 25(8): 1025–1033 (2002). http://dx.doi.org/10.1016/s0140-7007(02)00026-9

Gou X. , Xiao H. , Yang S. Modeling, Experimental Study and Optimization on Low-temperature Waste Heat Thermoelectric Generator System, *Applied Energy*, 87(10): 3131-3136 (2010). http://dx.doi.org/10.1016/j.apenergy.2010.02.013

Graebner J. E. , Azar K. Thermal Conductivity Measurements in Printed Wiring Boards, *Journal of Heat Transfer*, 119(3): 401 - 405 (1997). http://dx.doi.org/10.1115/1.2824111

Gschneidner Jr K. A. , Pecharsky V. K. , Tsokol A. O. Recent Developments in Magnetocaloric Materials. *Reports on Progress in Physics*, 68(6): 1479–1539. http://dx.doi.org/10.1088/0034-4885/68/6/r04

Hasan A.R. , Kabir C.S. Wellbore Heat-transfer Modeling and Applications, *Journal of Petroleum Science and Engineering*, 86-87: 127–136 (2012). http://dx.doi.org/10.1016/j.petrol.2012.03.021

He W. , Zhang G. , Zhang X. , Ji J. , Li G. , Zhao X. Recent Development and Application of Thermoelectric Generator, *Applied Energy*, 143: 1-25 (2015). http://dx.doi.org/10.1016/j.apenergy.2014.12.075

Heghmanns, A. , Beitelschmidt M. Parameter Optimization of Thermoelectric Modules Using a Genetic Algorithm, *Appl Energy*, 155: 447-454 (2015). http://dx.doi.org/10.1016/j.apenergy.2015.06.034

Hermes C. J. L. , Barbosa Jr. J. R. Thermodynamic Comparison of Peltier, Stirling, and Compression Portable Coolers, *Applied Energy*, 91(1): 51-58 (2012). http://dx.doi.org/10.1016/j.apenergy.2011.08.043

Iga A. , Nishiwaki S., Izui K., Yoshimura M. Topology Optimization for Thermal Conductors Considering Design-dependent Effects, Including Heat Conduction and Convection, *International Journal of Heat and Mass Transfer*, 52(11): 2721-2732 (2009). http://dx.doi.org/10.1016/j.ijheatmasstransfer.2008.12.013

Jakaboski J. C. Innovative Thermal Management of Electronics in Oil Well Logging, *M.Sc. thesis*, Georgia Institute of Technology USA (2004).

Kakaç S. , R.K. Shah , W. Aung. Handbook of Single-Phase Convective Heat Transfer. *Wiley* 1987.

Kandasamy R. , Wang X.-Q. , Mujumdar A. S. Application of Phase Change Materials in Thermal Management of Electronics, *Applied Thermal Engineering*, 27(17-18): 2822–2832 (2007). http://dx.doi.org/10.1016/j.applthermaleng.2006.12.013.

Keller H.H. , Couch E.J. , Berry P.M. Temperature Distribution in Circulating Mud Columns. *Society of Petroleum Engineers Journal*, 13(1): 23–30 (1973). http://dx.doi.org/10.2118/3605-pa

Kitamura K. , Kimura F. Heat Transfer and Fluid Flow of Natural Convection Adjacent to Upward-Facing Horizontal Plates, *International Journal of Heat and Mass Transfer,* 38(17): 3149–3159 (1995). http://dx.doi.org/10.1016/0017-9310(95)00066-i

Kitanovski A. , Tušek J. , Tomc U. , Plaznik U. , Ožbolt M. , Poredoš A. Magnetocaloric Energy Conversion: From Theory to Applications. *Springer London* (2014).

Koga A. A. , Lopes E. C. C. , Villa Nova H. F. , de Lima C. R. , Silva E. C. N. Development of Heat Sink Device by Using Topology Optimization, *International Journal of Heat and Mass Transfer*, 64: 759-772 (2013). http://dx.doi.org/10.1016/j.ijheatmasstransfer.2013.05.007

LabVIEW 2015, National Instruments.

Law J.Y. , Ramanujan R.V. , Franco V. Tunable Curie Temperatures in Gd Alloyed Fe–B–Cr Magnetocaloric Materials. *Journal of Alloys and Compounds*, 508(1): pp.14–19 (2010). http://dx.doi.org/10.1016/j.jallcom.2010.08.049

Lazarov B. S. , Sigmund O. Filters in Topology Optimization Based on Helmholtz-Type Differential Equations, *International Journal of Numerical Methods in Engineering* 86(6): 765-781 (2011). http://dx.doi.org/10.1002/nme.3072

Lee J. , Berger A. , Cagnon L. , Gösele U. , Nielsch K. , Lee J. Disproportionation of thermoelectric bismuth telluride nanowires as a result of the annealing process, *Physical Chemistry Chemical Physics*, 12(46): 15247 (2010). http://dx.doi.org/10.1039/c0cp00749h

Lee J. , Nomura T. , Dede E.M. Heat Flow Control in Thermo-magnetic Convective Systems Using Engineered Magnetic Fields, *Applied Physics Letters,* 101, 123507 (2012). http://dx.doi.org/10.1063/1.4754119

Li Q. , Steven G. P. , Xie Y. M. , Querin O. M. Evolutionary Topology Optimization for Temperature Reduction of Heat Conducting Fields, *International Journal of Heat and Mass Transfer*, 47(23): 5071-5083 (2004). http://dx.doi.org/10.1016/j.ijheatmasstransfer.2004.06.010

Liu W. , Lukas K. C. , McEnaney K. , Lee S. , Zhang Q. , Opeil C. P. , Chen G. , Ren Z. Studies on the Bi_2Te_3–Bi_2Se_3–Bi_2S_3 System for Mid-temperature Thermoelectric Energy Conversion, *Energy & Environmental Science*, 6(2): 552–60 (2012). http://dx.doi.org/10.1039/c2ee23549h

LT Spice IV software, Linear Technology 2016.

Marck G. , Nemer M. , Harion J.L. Topology Optimization of Heat and Mass Transfer Problems: Laminar Flow, *Numerical Heat Transfer, Part B*, 63(6): 508-539 (2013). http://dx.doi.org/10.1080/10407790.2013.772001

Matsumori T. , Kondoh T. , Kawamoto A. , Nomura T. Topology Optimization for Fluid-Thermal Interaction Problems Under Constant Input Power, *Structural and Multidisciplinary Optimization*, 47(4): 571-581 (2013). http://dx.doi.org/10.1007/s00158-013-0887-8

McCarty R. D. Thermodynamic Properties of Helium 4 from 2 to 1500 K at Pressures to 10^8 Pa, *National Institute of Standards and Technology (NIST)*, 1972. http://dx.doi.org/10.6028/nbs.tn.631

McConnell C. , Pingen G. Multi-layer, Pseudo 3D Thermal Topology Optimization of Heat Sinks, *Proceedings of the ASME 2012 International Mechanical Engineering Congress*, Houston, USA (2012). http://dx.doi.org/10.1115/imece2012-93093

Min Y. , Roh J. W. , Yang H. , Park M. , Kim S. I. , Hwang S. , Lee S. M, Lee K. H. , Jeong U. Surfactant-Free Scalable Synthesis of Bi_2Te_3 and Bi_2Se_3 Nanoflakes and Enhanced Thermoelectric Properties of Their Nanocomposites, *Advanced Materials*, 25(10): 1425–1429 (2013). http://dx.doi.org/10.1002/adma.201203764

Mongia R. , Masahiro K. , Distefano E. , Barry J. , Chen W. , Izenson M. , Possamai, F. , Zimmermann A. , Mochizuki M. Small Scale Refrigeration System for Electronics Cooling Within a Notebook Computer, *Proceedings of the 10th Intersociety Conference on Phenomena in Electronics Systems ITHERM 2006 (IEEE)*, 2006. http://dx.doi.org/10.1109/itherm.2006.1645421

Montecucco, A. , Knox A. R. Accurate Simulation Of Thermoelectric Power Generating Systems, *Applied Energy*, 118(20): 166-172 (2014). http://dx.doi.org/10.1016/j.apenergy.2013.12.028

Moores K.A. , Joshi Y.K. , Miller G. Performance Assessment of Thermoelectric Coolers for Use in High Temperature Electronics Applications, *Proceedings of the 18th International Conference on Thermoelectrics* (1999). http://dx.doi.org/10.1109/ict.1999.843328.

ndfeb-info: http://www.ndfeb-info.com/temperature_ratings.aspx

Pan Y. , Lin B. , Chen J. Performance Analysis and Parametric Optimal Design of an Irreversible Multi-couple Thermoelectric Refrigerator under Various Operating Conditions, *Applied Energy*, 84(9): 882-892 (2007),. http://dx.doi.org/10.1016/j.apenergy.2007.02.008

Pecharsky V. K. , Gschneidner K. A. Advanced Materials for Magnetic Cooling , *Handbook of Magnetism and Advanced Magnetic Materials* (2007). http://dx.doi.org/10.1002/9780470022184.hmm417

Pennewitz E. , Kruspeb T. , Jungb S. , Schillinga M. Evaluation of Sorbents at Elevated Temperatures for Downhole Application, *Chemical Engineering Transactions*, 29: 1543-1548 (2012). http://dx.doi.org/10.3303/CET1229258

Poudel B. , Hao Q. , Ma Y. , Lan Y. , Minnich A. , Yu B. , Yan X. , Wang D. , Muto A. , Vashaee D. , Chen X. , Liu J. , Dresselhaus M. S. , Chen G. , Ren Z. , High-Thermoelectric Performance of Nanostructured

Bismuth Antimony Telluride Bulk Alloys, *Science,* 320(5876): 634–638 (2008). http://dx.doi.org/10.1126/science.1156446

Qiu G. , Liu H. , Riffat S. Expanders for Micro-CHP Systems with Organic Rankine Cycle, *Applied Thermal Engineering* , 31(16): 3301–3307 (2011). http://dx.doi.org/10.1016/j.applthermaleng.2011.06.008

Quan R. , Tang X. , Quan S. , Huang L. A Novel Optimization Method for the Electric Topology of Thermoelectric Modules Used in an Automobile Exhaust Thermoelectric Generator, *Journal of Electronic Materials*, 42(7): 1469-1475 (2013). http://dx.doi.org/10.1007/s11664-012-2291-3

Rezania A. , Yazawa K. , Rosendahl L. A. , Shakouri A. Co-optimized Design of Microchannel Heat Exchangers and Thermoelectric Generators, *International Journal of Thermal Science*, 72: 73-81 (2013). http://dx.doi.org/10.1016/j.ijthermalsci.2013.05.002

Rowe D. M. Handbook of Thermoelectrics. *CRC Press Boca Raton*, London (1995). http://dx.doi.org/10.1201/9781420049718

Sandeep K. , DeWalt B. , Headworth C. Well Intervention Using Rigless Techniques, *Proceedings of Offshore Technology Conference,* Houston, OTC 15177:1 – 13 (2003). http://dx.doi.org/10.4043/15177-ms

Santoyo E. , Garcia A. , Espinosa G. , Santoyo-Gutiérrez S. , González-Partida E. Convective Heat-transfer Coefficients of non-Newtonian Geothermal Drilling Fluids, *Journal of Geochemical Exploration*, 78-79: 249–255 (2003). http://dx.doi.org/10.1016/s0375-6742(03)00146-8

Shen B. G. , Sun J. R. , Hu F.X. , Zhang H.W. , Cheng Z.H. Recent Progress in Exploring Magnetocaloric Materials, *Advanced Materials*, 21(45): 4545–4564 (2009). http://dx.doi.org/10.1002/adma.200901072

Sifner O. , Klomfar J. Thermodynamic Properties of Xenon from the Triple Point to 800 K with Pressures up to 350 MPa, *Journal of Physical and Chemical Reference Data* , 23(1) : 63 (1994). http://dx.doi.org/10.1063/1.555956

Sigmund O. , Maute K. Topology Optimization Approaches, *Structural and Multidisciplinary Optimization*, 48(6): 1031-1055 (2013). http://dx.doi.org/10.1007/s00158-013-0978-6

Sigmund O. , Petersson J. Numerical Instabilities in Topology Optimization: A Survey on Procedures Dealing with Checkerboards, Mesh-dependencies and Local Minima, *Structural and Multidisciplinary Optimization*, 16(1): 68–75 (1998). http://dx.doi.org/10.1007/bf01214002

Sigmund O. Design of Multiphysics Actuators Using Topology Optimization-Part I: One Material Structures, *Computer Methods in Applied Mechanics and Engineering*, 190(49): 6577-6604 (2001). http://dx.doi.org/10.1016/s0045-7825(01)00251-1

Sinha A. , Joshi Y. K. Downhole Electronics Cooling Using a Thermoelectric Device and Heat Exchanger Arrangement, *Journal of Electronic Packaging*, 133(4): 041005-1 - 041005-12 (2011). http://dx.doi.org/10.1115/1.4005290

Sinha A. An adsorption based cooling solution for electronics used in thermally harsh environments, *Ph.D. thesis*, Georgia Institute of Technology, USA (2010).

Smith A. , Bahl C. R. H. , Bjørk R. , Engelbrecht K. , Nielsen K.K. , Pryds N. Materials Challenges for High Performance Magnetocaloric Refrigeration Devices, *Advanced Energy Materials*, 2(11): 1288–1318 (2012). http://dx.doi.org/10.1002/aenm.201200167

Snyder G. J. , Toberer E. S. Complex Thermoelectric Materials, *Nature Materials*, 7(2): 105-114 (2008). http://dx.doi.org/10.1038/nmat2090

Soprani S. , Engelbrecht K. , Nørgaard A. J. Active Cooling and Thermal Management of a Downhole Tool Electronics Section, *Proceedings of the 24th IIR International Congress of Refrigeration*, IIF-IIR, Yokohama, Japan (2015a).

Soprani S. , Haertel J. H. K. , Lazarov B. S. , Sigmund O. , Engelbrecht, K. Topology Optimization of an Actively Cooled Electronics Section for Downhole Tools. *Proceedings of COMSOL Conference 2015*, Grenoble, France (2015b).

Soprani S. , Haertel J. H. K. , Lazarov B. S. , Sigmund O. , Engelbrecht K. A Design Approach for Integrating Thermoelectric Devices using Topology Optimization, *Applied Energy*, 176: 49–64 (2016). http://dx.doi.org/10.1016/j.apenergy.2016.05.024

Svanberg K. A Class of Globally Convergent Optimization Methods Based on Conservative Convex Separable Approximations, *SIAM Journal on Optimization*, 12(2): 555-573 (2002). http://dx.doi.org/10.1137/s1052623499362822

Swift W. L. , McCormack J. A. , Zagarola M. V. , Dolan F. X. , Sixsmith H. The NICMOS Turbo-Brayton Cryocooler - Two Years in Orbit, *Cryocoolers 13*, 633–639 (2005). http://dx.doi.org/10.1007/0-387-27533-9_79

Takezawa A. , Kitamura M. Geometrical Design of Thermoelectric Generators Based on Topology Optimization, *International Journal of Numerical Methods in Engineering* 90(11): 1363-1392 (2012). http://dx.doi.org/10.1002/nme.3375

Taylor R. A. , Solbrekken G. L. Comprehensive System-Level Optimization of Thermoelectric Devices for Electronic Cooling Applications, *IEEE Transactions on Components and Packaging Technologies*, 31(1): 23-31 (2008). http://dx.doi.org/10.1109/tcapt.2007.906333

Tritt, T. M. , Subramanian M. A. Thermoelectric Materials, Phenomena, and Applications: A Bird's Eye View, *MRS Bulletin*, 31(3): 188-198 (2006). http://dx.doi.org/10.1557/mrs2006.44

US Pat. No. 20120125614 A1, Verma S. , Brisson J. G, Stabinski E. L, Elias Q. K. , Method for active cooling of downhole tools using the vapor compression cycle, 2012.

US Pat. No. 4248298, Lamers M. D. , Martelli V. P. , Well logging evaporative thermal protection system, 1981.

US Pat. No. 4375157, Boesen G. F. , Downhole thermoelectric refrigerator, 1983.

US Pat. No. 4407136, De Kanter S. , Downhole tool cooling system, 1983.

US Pat. No. 5165243, Bennett G. A. , 1992.

US Pat. No. 5265677, Schultz R. L. , Refrigerant-cooled downhole tool and method, 1992.

US Pat. No. 5547028 A Owens S. , Bouldin B. , Downhole system for extending the life span of electronic components, 1996.

US Pat. No. 5554897 A, Martin F. S. , Bearden J. L. , Downhole motor cooling and protection system, 1996.

US Pat. No. 5701751 A, Flores A. G. , Apparatus and method for actively cooling instrumentation in a high temperature environment, 1996.

US Pat. No. 5720342, Owens S. , Bouldin B. , Elliott G. , Integrated converter for extending the life span of electronic components, 1998.

US Pat. No. 5730217, Owens S. , Bouldin B. , Elliott G. , Vacuum insulated converter for extending the life span of electronic components, 1998.

US Pat. No. 5931000, Turner W. E. , Seppa R. , Turner W. E. , Cooled electrical system for use downhole, 1999.

US Pat. No. 6134892, Turner W. E. , Seppa R. , Turner W. E. , Sallwasser A. J. , Cooled electrical system for use downhole, 2000.

US Pat. No. 6220346, Gissler R. W. , Thermal insulation vessel, 2001.

US Pat. No. 6336408, Parrott R. A. , Song H. , Chen K.-C. , Cooling system for downhole tools, 2002.

US Pat. No. 6341498, DiFoggio R. , Downhole sorption cooling of electronics in wireline logging and monitoring while drilling, 2002.

US Pat. No. 5715895, Champness E. , Champness A. T. , Downhole drilling tool cooling system.

Van Oevelen T. , Baelmans M. Numerical Topology Optimization of Heat Sinks, *Proceedings of the 15th International Heat Transfer Conference*: 10-15 (2014). http://dx.doi.org/10.1615/ihtc15.opt.009168

Verma S. , Elias Q. Thermal Management of Electronics Used in Downhole Tools, *SPE Annual Technical Conference and Exhibition* (2012). http://dx.doi.org/10.2118/159737-ms

Wang F. , Lazarov B. S. , Sigmund O. On Projection Methods, Convergence and Robust Formulations in Topology Optimization, *Structural and Multidisciplinary Optimization*, 43(6): 767-784 (2011). http://dx.doi.org/10.1007/s00158-010-0602-y

Xiao J. , Yang T. , Li P. , Zhai P. , Zhang Q. Themal Design and Management for Performance Optimization of Solar Thermoelectric Generator, *Applied Energy*, 93(20): 33-38 (2012). http://dx.doi.org/10.1016/j.apenergy.2011.06.006

XSteam, by Magnus Holmgren, www.x-eng.com. Water and steam properties are computed according to IAPWS IF-97.

Xu B. , Li P. , Chan C. Application of Phase Change Materials for Thermal Energy Storage in Concentrated Solar Thermal Power Plants: A Review to Recent Developments, *Applied Energy*, 160: 286-307 (2015). http://dx.doi.org/10.1016/j.apenergy.2015.09.016.

Yaji K. , Yamada T. Koga Kubo S. , Izui K. , Nishiwaki S. A Topology Optimization Method for a Coupled Thermal–Fluid Problem Using Level Set Boundary Expressions, *International Journal of Heat and Mass Transfer*, 81: 878-888. (2015). http://dx.doi.org/10.1016/j.ijheatmasstransfer.2014.11.005

Yang Y. , Ma F. Y. , Lei C. H. , Liu Y. Y. , Li J. Y. Is Thermoelectric Conversion Efficiency of a Composite Bounded by its Constituents? , *Applied Physics Letters*, 102(5): 053905 (2013). http://dx.doi.org/10.1063/1.4791684

Yin L. , Ananthasuresh G. K. A Novel Topology Design Scheme for the Multi-physics Problems of Electro-thermally Actuated Compliant Micromechanisms, *Sensors and Actuators A*, 97: 599-609 (2002). http://dx.doi.org/10.1016/s0924-4247(01)00853-6

Yoon G.H. Topological Design of Heat Dissipating Structure with Forced Convective Heat Transfer, *Journal of Mechanical Science and Technology*, 24(6): 1225-1233 (2010). http://dx.doi.org/10.1007/s12206-010-0328-1

Zagarola M. V. , Breedlove J. J. , Kirkconnell C. S. , Russo J. T. , Chiang T. Demonstration of a Two-Stage Turbo - Brayton Cryocooler for Space Applications, *Cryocoolers 15*, 461 – 469 (2009).

Zhou F. Research on Heat Transfer in Geothermal Wellbore and Surroundings, Technischen Universität Berlin, *M.Sc. Thesis* (2013).

Zhu T.J. , Cao Y.Q. , Yan F. , Zhao X. B. Nanostructuring and Thermoelectric Properties of Semiconductor Tellurides. *Proceedings of the 26th International Conference on Thermoelectrics (IEEE)*, 2007. http://dx.doi.org/10.1109/ict.2007.4569410

Ziviani D. , Beyene A. , Venturini M. Development and Validation of an Advanced Simulation Model for ORC-based Systems, *Energy, Parts A and B. ASME International*, 2012. http://dx.doi.org/10.1115/imece2012-85734

APPENDIX A

A.1 Paper published in the proceedings of the 24th International Conference of Refrigeration 2015, in Yokohama, Japan

Soprani S. , Engelbrecht K. , Nørgaard A. J. Active Cooling and Thermal Management of a Downhole Tool Electronics Section, *Proceedings of the 24th IIR International Congress of Refrigeration*, IIF-IIR, Yokohama, Japan (2015).

ACTIVE COOLING AND THERMAL MANAGEMENT OF A DOWNHOLE TOOL ELECTRONICS SECTION

Stefano SOPRANI[*], Kurt ENGELBRECHT[*], Anders Just NØRGAARD
[*] Department of Energy Conversion and Storage, Technical University of Denmark, Frederiksborgvej 399, DK-4000 Roskilde, Denmark
stefs@dtu.dk

ABSTRACT

High Temperature (HT) wellbores represent one of today's biggest challenges for the oil and gas industry. The majority of well intervention wireline tools contain temperature sensitive electronics that are not able to withstand the high temperatures of HT wellbores (> 150 °C), for an extended period of time. This work presents the design and construction of an actively cooled laboratory prototype, which is able to operate at temperatures which are higher than the temperature limit of the electronics. A different concept of heat management, compared to prior works, is presented: the design combines active and passive cooling techniques, aiming at an efficient thermal management, preserving the tool compactness and avoiding the use of moving parts. Thermoelectric coolers were used to transfer the dissipated heat from the temperature-sensitive electronics to the external environment. Thermal contact resistances were minimized and thermally insulating foam protected the refrigerated microenvironment from the hot surroundings.

1. INTRODUCTION

Sandeep *et al.*(2003) defined well interventions as remedial operations that are performed on producing wells, with the intention of restoring or increasing production. Well interventions may be necessary because of flow restrictions, sand production, mechanical failure, changes in reservoir characteristics, or to access additional reservoir areas. Typical downhole applications that are performed during the interventions include monitoring of the well conditions, as well as installations (e.g. of valves or pipes), drilling of new well branches, cleaning, and repairing. Different downhole tools can be employed to carry out the mentioned operations and several intervention techniques can be adopted in order to deliver the tools down the wellbore.

The *electric wireline* intervention technique involves running and pulling tools and equipment into and out of the well, by the use of a continuous length, small diameter solid or braided wire mounted on a powered reel at the surface. This cable is an electric conductor and delivers the feed power to the downhole tools from the surface; every wireline tool has, therefore, a section that contains electronic components and circuits that remotely control the tool, transform the feed power or store logging data. The enclosed electronics dictate one of the main limits of the electric wireline technique, which is represented by the exposure of the downhole tools to high temperatures. High Temperature wells, where the temperature ranges from 150 °C to 200 °C, represent one of today's biggest challenges for wireline interventions, since most of the currently employed electronics are rated for lower temperatures. Active cooling systems are a possible solution to the electronics overheating, as they would maintain the critical components at a temperature below the external environment. This type of solution has been investigated in several works in the literature, which faced different integration constraints, cooling loads, operating temperatures and adopted different cooling technologies.

Bennett (1988) performed a theoretical analysis of the suitable cooling technologies for a downhole application, defining respectively an acoustic cycle, a two-stage vapor compression cycle and a reverse Brayton cycle as the best options. Flores (1996) performed a similar analysis and implemented his results into a once-through vapor compression cooler for a downhole exploration tool. Jakaboski (2004) first carried out a review of the prior

works and patents and then studied the integration of a phase change material tank into a downhole tool string, in order to maintain the electronics at a lower temperature than the borehole. Sinha and Joshi (2011) investigated, instead, the use of thermoelectric devices for thermal management of downhole electronics, reporting the test results of a lab-prototype. Pennewitz *et al.* (2012) evaluated the feasibility of sorption cooling for downhole electronics in the geothermal sector.

Some common features among the mentioned works are the employment of Dewar flasks for thermal insulation of the cooled electronics from the external environment, the use of convective fluids and heat exchangers, and the necessity of adding to the tool string a section containing the cooling system. This work aims at presenting the design and the implementation of a different heat management concept, which involves both active and passive cooling, aims at preserving the original compactness of the tool and does not require the use of a Dewar flask.

2. APPROACH AND METHOD

The desired active cooling and thermal management systems have to satisfy certain design criteria:

- Absorb the cooling load and keep the temperature of the high temperature-sensitive electronics below 175 °C.
- Provide cooling for an unlimited time period.
- Be able to operate in up to 200 °C borehole temperatures.
- Fit a cylindrical housing with an inner diameter of 60 mm.
- Require less than 1 kW of feed power.
- Preserve the original length of the tool (no additional sections).
- Minimize the thermal resistances between different materials.

Electronic components of an existing downhole tool were considered for the implementation of the cooling system and of the thermal management. The main components of the section are a metallic cylindrical housing, with an inner diameter of 60 mm, a metallic chassis, on top of which the electronic components are mounted and then inserted into the housing. The electronic components can be distinguished between high temperature-sensitive (HTS) and high temperature-non-sensitive (HTNS). The HTS components were mounted on a printed circuit board (PCB) and were estimated to dissipate 1 W at maximum load; HTNS components were mounted directly on the chassis and were expected to dissipate 18 W at maximum load.

The main cooling techniques were screened and their suitability to the application evaluated according to the design criteria listed above. The result of the feasibility study is summarized in Table 1.

Table 1. Feasibility study summary. *fair/poor,**marginal, ***good, ****very good, / not available.

Technology	Efficiency	Packaging	Cost	Feasibility
Vapor compression cycle	****	***	**	**
Thermoelectric (Peltier) cooling	*	****	****	***
Reverse Brayton cycle	*	**	**	**
Magnetic cooling	***	*	*	*
Liquid Nitrogen/Phase Change materials	/	***	**	***

The thermoelectric cooling technique was chosen to be implemented as it is very compact, cheap, and does not have any moving parts. It is less efficient than competing technologies, though, and might generate some heat rejection issues, as discussed in the next sections.

Figure 1 shows the thermal management principle that was implemented in the experimental setup.

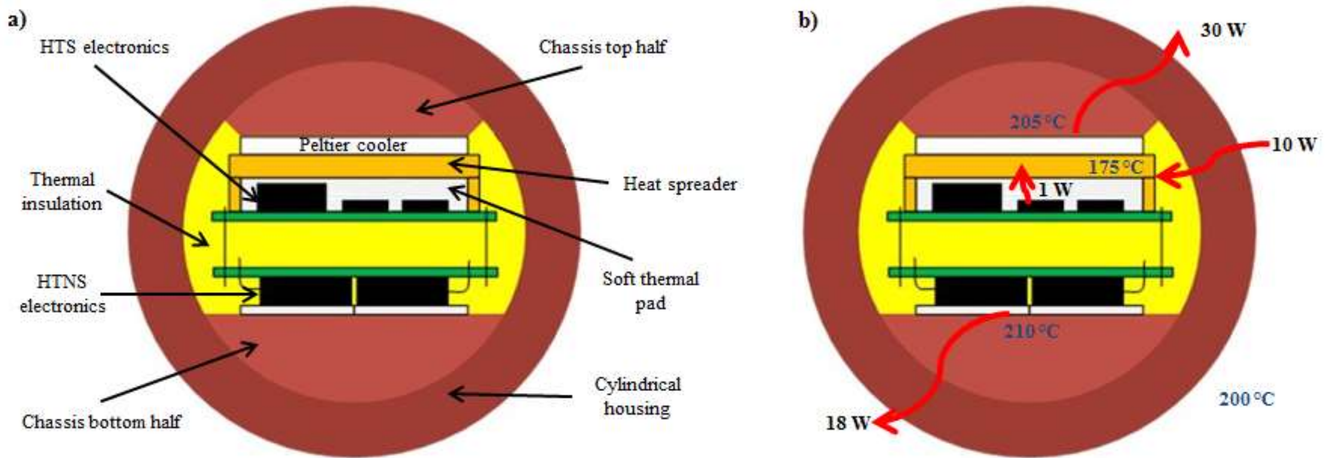

Figure 1. Illustration of the thermal management principle for the actively cooled electronic unit. A representation of the cross section of the tool shows the main components (a) and the design parameters that characterize the system (b).

The HTNS electronics are mounted on the bottom half of the chassis, so the dissipated power can be passively rejected to the surroundings, through the chassis itself and through the tool housing. Some electric wires connect the HTNS components to the high temperature-sensitive ones, which are soldered on a printed circuit board and thermally coupled with the cold plate of the thermoelectric cooler (TEC). The interface between the HTS components and the cold plate is composed of a soft thermally conducting silicone pad and a metallic heat spreader. The hot plate of the cooler is, instead, attached to the top half of the chassis. Both the top and the bottom halves of the chassis are in tight contact with the cylindrical housing, so the thermal resistance is minimized. The housing outer surface is in contact with the external fluid in the borehole and experiences forced convection. The remaining volume of the unit is filled with thermal insulating foam. No Dewar flask is employed, so the generated heat can be rejected directly through the housing and the original length of the tool is maintained.

This design aims at a maximum operating well temperature of 200 °C, a maximum cooler hot plate temperature of 205-210 °C, a maximum HTS electronics temperature of 175 °C and a maximum HTNS electronics temperature of 210 °C. From a first approach estimation, the heat fluxes that characterize the system are 18 W dissipated by the passively cooled components, 1 W dissipated by the HTS components, 10 W of heat conduction through the housing and 30 W rejected by the cooler hot plate (assuming a TEC coefficient of performance equal to 0.5).

3. IMPLEMENTATION OF THE EXPERIMENTAL SETUP

The previously described system was implemented in an experimental setup. The two halves of the chassis were manufactured; both the HTS and the HTNS electronics were simulated by resistive components and respectively installed on the bottom chassis and on the printed circuit board; two high temperature thermoelectric coolers were assembled between the top chassis and the metallic heat spreader. Thermally insulating polyimide foam was used to insulate the cooled electronics from the hot surroundings. The temperatures of the main components were monitored by thermocouples.

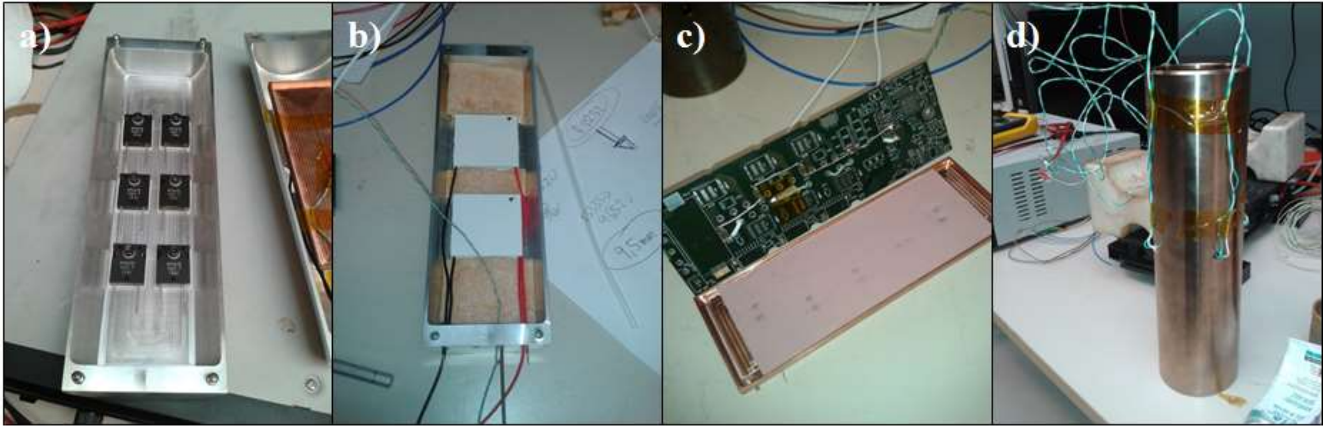

Figure 2. Implementation of the experimental setup. Bottom half of the chassis with the HTNS electronics (a), top half of the chassis with two HT thermoelectric coolers and thermal insulating foam (b), HTS electronics installed on a printed circuit board with heat spreader and soft thermal pad (c), cylindrical housing with welded thermocouple wires (d).

Three different assembly techniques have been investigated for testing the thermal interface between the hot and cold plates of the cooler and, respectively, the top chassis and the heat spreader. The performance of the system was evaluated as proportional to the temperature difference (ΔT_{cooler}) the cooler could maintain, at steady state, between the HTS electronics and the cooler hot plate. The three assembly techniques comprise the use of:

- thermal conductive epoxy;
- adhesive soft thin thermal pads;
- a spring system with thermal grease (clamping method).

The clamping method proved to be the best performing technique as can be seen in Figure 3(a). The coolers were spread with thermal grease on the plates and then “clamped” between the heat spreader and the top chassis, with two plastic screws. On the other side, epoxy guaranteed a good thermal connection, but caused a degradation of the cooler when cycled at high temperature; the adhesive thermal pad absorbed the stresses due to the thermal expansion, but did not perform well from a thermal standpoint. Several candidate coolers from different manufacturers and in different sizes were also tested in the setup, in order to obtain the best performance of the system. The criterion for the choice of the cooler type is the same used for the choice of the assembling technique. *Coolers #1* and *#3* proved to be the best performing in our system, as can be notice in Figure 3(b).

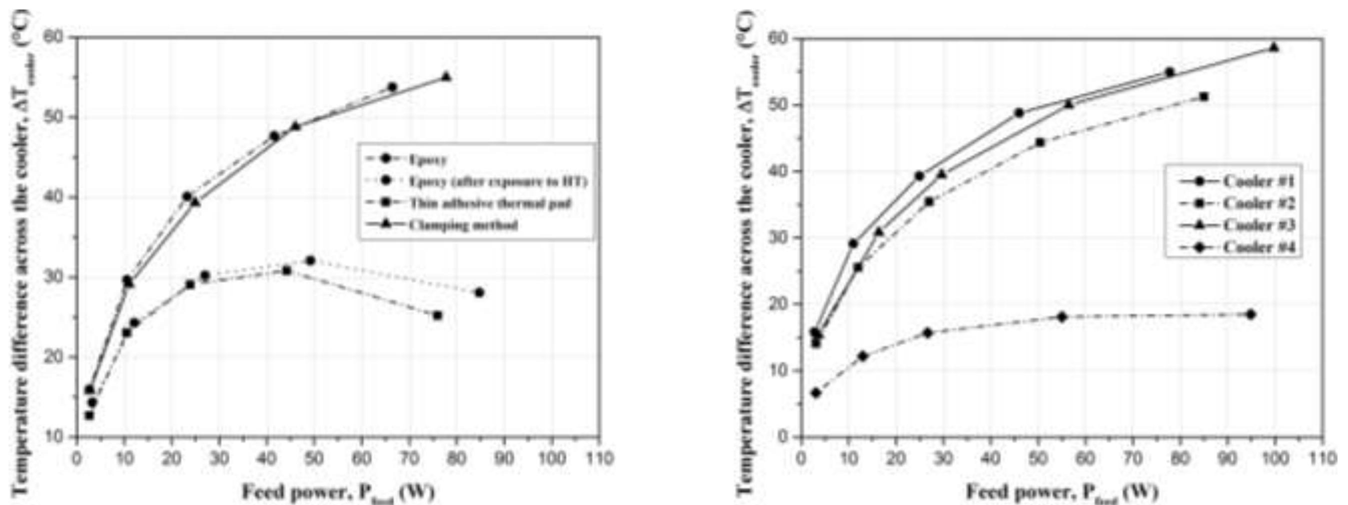

Figure 3. Temperature span across the cooler ΔT_{cooler} vs coolers feed power. Test of the different assembling techniques (left) and of the different cooler types and sizes (right). Tests were carried out at room temperature.

The main components of the system and their dimensions are listed in Table 2.

Table 2. List of the main components with their dimensions.

Component	Dimension
Metallic housing	O.D. = 80 mm I.D. = 60 mm Length = 300 mm
Top chassis	O.D. = ˜ 60 mm Length = 200 mm
Bottom chassis	O.D. = ˜ 60 mm Length = 200 mm
Heat spreader	120 mm x 41 mm x 3 mm
Soft thermal pad	115 mm x 40 mm x 2 mm
Peltier cooler	*#1* : 30 mm x 30 mm x 3.6 mm / *#3* : 40 mm x 40 mm x 3.9 mm

4. TEST RESULTS

Based on the setup test, it was decided to use two *Cooler #1* assembled with thermal grease with a clamp. The coolers were installed between the top chassis and the heat spreader with the clamping method. The two halves of the chassis were coupled and inserted into the housing. Power supplies were used to feed the test electronics and the coolers. A ventilated furnace was used in order to reproduce a dry borehole environment and characterize the performance of the system at different temperatures 25 °C, 100 °C, 150 °C and 170 °C. Three main parameters were considered to evaluate the performance of the system at steady state, and were evaluated at different operating conditions and temperatures:

$$\Delta T_{cooler} = T_{HotPlate} - T_{PCB} \quad (1)$$

$$\Delta T_{HotPlate} = T_{HotPlate} - T_{ext} \quad (2)$$

$$\Delta T_{PCB} = T_{PCB} - T_{ext} \quad (3)$$

Where:

$T_{HotPlate}$ is the temperature of the cooler hot plate [°C], T_{PCB} is the temperature of the HTS electronics on the PCB and T_{ext} is the oven temperature. ΔT_{cooler} (Eq. 1) proves the capability of the system to maintain the electronics to a lower temperature than the hot plate. A low $\Delta T_{HotPlate}$ (Eq. 2) is an indicator of a good heat rejection to the external environment. ΔT_{PCB} (Eq. 3) is usually negative; a low value of ΔT_{PCB} is an indicator of a good insulation and a good overall system performance, as the HTS electronics is cooled far below the oven temperature.

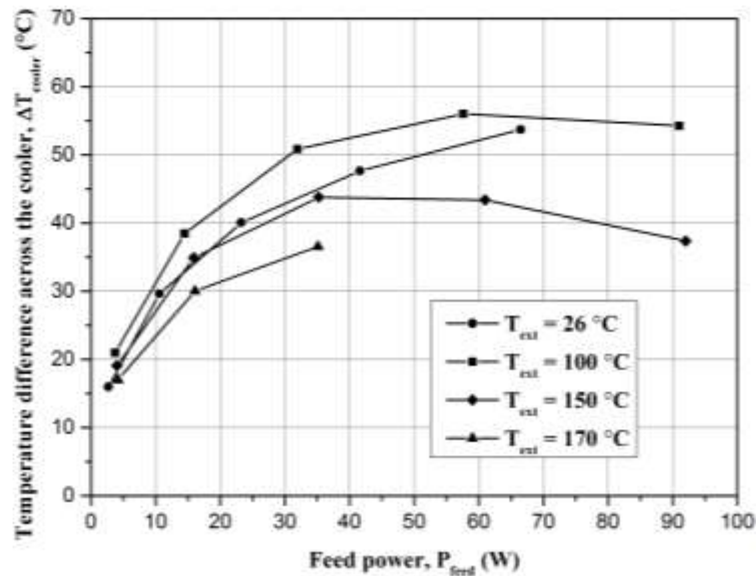

Figure 4. Temperature span across the cooler ΔT_{cooler} vs. cooler feed power, at different oven temperatures.

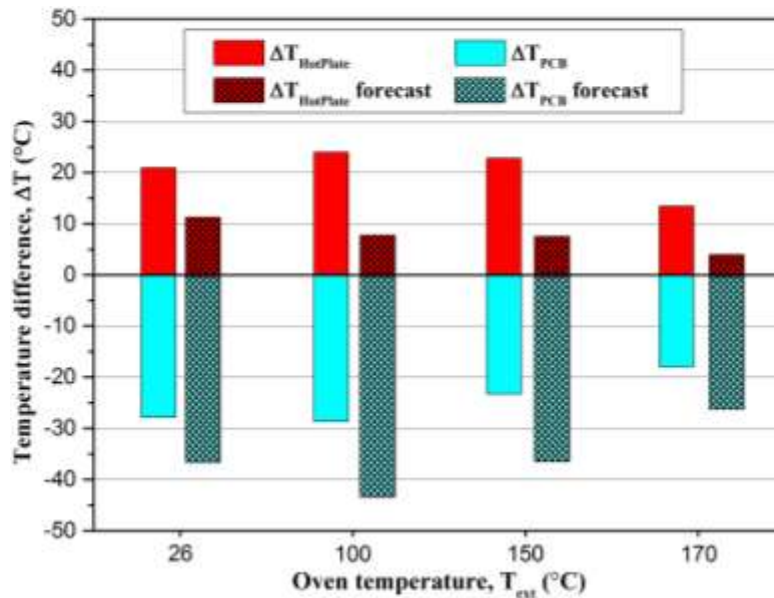

Figure 5. Representation of $\Delta T_{HotPlate}$ (red bar) and ΔT_{PCB} (blue bar), at the operating conditions that minimized the HTS electronics temperature, at different oven temperatures T_{ext}. The tests were carried out in air in a ventilated furnace, where the convective heat transfer coefficient along the housing surface was estimated ˜ 30 W/(m^{2}K). The system behavior was also forecast for an external convective coefficient of 100 W/(m^{2}K) and represented with dashed bars.

The performance of the system strongly depends on the operating temperature, as can be noticed in Figure 4. The largest temperature span between the PCB and the cooler hot plates is obtained around 100 °C oven temperature. Bismuth Telluride, the semiconductor material generating the thermoelectric cooling effect, has in fact a peak of its thermoelectric properties (i.e. figure of merit) around 100 °C. Above 100 °C the performance of the system decreases again and the HTS electronics temperature increases (see Figure 5). At T_{ext} = 100 °C the HTS electronics is maintained 28 °C below ambient; while at T_{ext} = 170 °C it is only 18 °C colder than ambient. With an increased outside convection coefficient (100 W/(m^{2}K)) the HTS electronics would be cooled 43°C and 26°C below ambient, for T_{ext} respectively equal to 100 °C and 170 °C.

Tests results also revealed that the power dissipated by the HTNS electronics significantly increases the temperature of the chassis and of the coolers' hot plate; if the coolers' hot side temperature rises, the temperature of the cold plate and of the HTS components subsequently increases; that is because the temperature span the coolers are able to maintain between the plates (ΔT_{cooler}) remains approximately constant (at a given feed power). In other words, an increase in the coolers hot side temperature "shifts" the temperature difference between the plates upwards, towards hotter temperatures.

Therefore, reducing the hot plate temperature could be an effective way to improve the cooling of the HTS electronics and to keep the coolers far below their maximum operating temperature. That could be done by reducing the power dissipated by the passively cooled components or by improving the heat rejection to the external environment, which is mainly driven by convection in the wellbore and cannot be controlled in a downhole environment.

4.1 Implementation of the real tool electronics

The original downhole tool electronics were then reviewed and optimized; the main components were replaced with more efficient ones so the dissipated power from the HTNS electronics was reduced to one fourth of the original value, around 5 W. The same heat management principles were applied to the new setup, which aimed at actively cooling the new, optimized, electronics. Only one *Cooler #3* was used in the new setup, which preserved the same main components and dimensions of the previous setup. The tool was then tested in a larger furnace at the temperatures 100 °C, 125 °C, 150 °C and 180 °C.

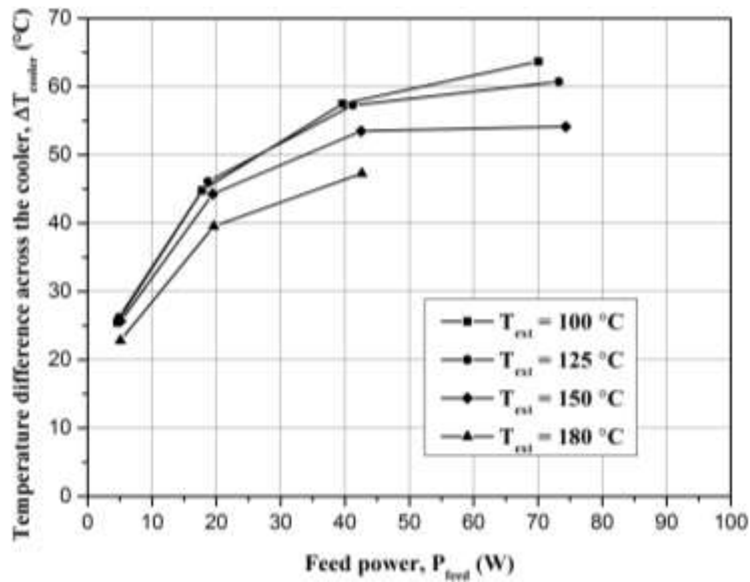

Figure 6. Temperature span across the cooler ΔT_{cooler} vs. cooler feed power at different oven temperatures.

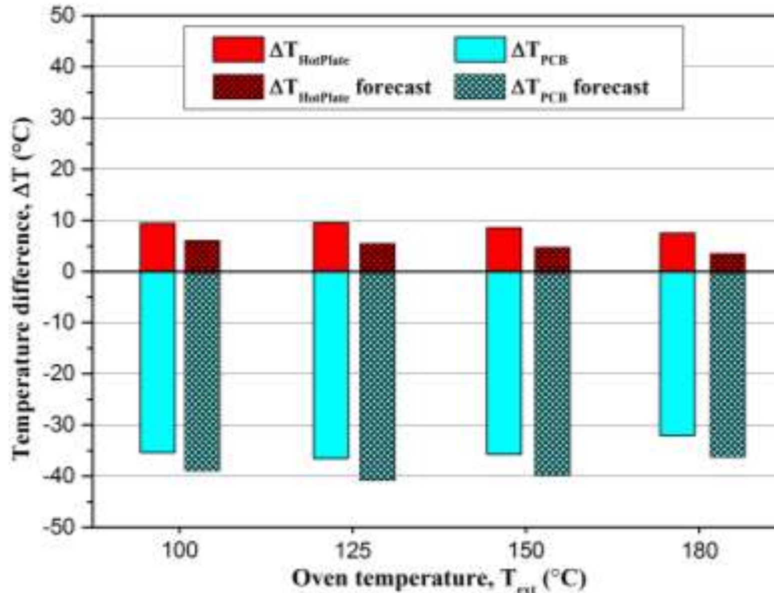

Figure 7. Representation of $\Delta T_{HotPlate}$ (red bar) and ΔT_{PCB} (blue bar), at the operating conditions that minimized the HTS electronics temperature, at different oven temperatures T_{ext}. The tests were carried out in a ventilated furnace, where the convective heat transfer coefficient along the housing surface was estimated ˜ 45 W/(m^{2}K). The system behavior was also forecast for an external convective coefficient of 100 W/(m^{2}K) and represented with dashed bars.

The capability of the cooling system of maintaining a temperature differential between the HTS electronics and the coolers hot plate is enhanced by the use of one *Cooler #3*; Figure 6 shows in fact higher values of ΔT_{cooler}, compared to Figure 4, at a given feed power and oven temperature. Figure 7 shows, instead, how the system performance is improved by the increased efficiency of the HTNS electronics. The cooler hot plate temperature is significantly lower compared to the previous setup; consequently the HTS electronics are maintained at a lower temperature: 35 °C and 32 °C colder than the oven temperatures 100 °C and 180 °C. The dependence of the system performance on the external convection is also reduced since the heat that needs to be rejected is lower. The difference between measured temperatures differences and those forecast with an external convective coefficient of 100 W/(m^{2}K) is much lower than seen in Fig. 5 and is only 3 – 4 °C of cooling in this case.

5. CONCLUSIONS

This work presented the design and implementation of an active cooling system into a downhole tool electronics section. Thermoelectric coolers were chosen among the possible cooling technologies in order to fulfill the main design criteria. The tool length and compactness were preserved, no Dewar flasks were used, no moving parts were introduced and the thermal resistances were minimized.

The thermal management principle was first demonstrated with resistors to simulate the actual electronics. The most suitable assembly technique and types of thermoelectric coolers for the application were investigated and successively applied, and the system was tested at different oven temperatures. The test results proved the heat rejection to the external environment can be a critical design parameter.

The real tool electronics were reviewed and improved in efficiency; the new optimized electronics were then implemented in a new actively cooled setup, with the same features of the previous one. The new test results showed a significant enhancement in performance, thanks to an improvement in the heat rejection mechanism, and are encouraging for operations in a 200 °C environment. A better management of the thermal expansion issues and a further development of the new electronics will improve the performance of the system. More tests, at higher temperatures, will be carried out.

The setup was tested for 60 hours at high temperature (between 150 °C and 200 °C) and a stable and constant cooling performance was delivered within the design criteria. After the 60 hours a degradation of the cooler was noticed, so the temperature span was reduced by ~2 °C. This result is promising if we consider well interventions on wireline rarely require more than 24 continuous hours downhole; furthermore the cheap price of commercial HT thermoelectric coolers allows a frequent replacement of the degraded parts, when deemed necessary. The degradation of the cooling system can be evaluated by measuring anomalous temperature differentials across the cooler and by measuring the AC electric resistance of the thermoelectric module, which would increase as the performance decreases.

6. REFERENCES

Bennett G.A. 1988, Active Cooling for Downhole Instrumentation: Preliminary Analysis and System Selection, *Los Alamos National Laboratory*, Mexico.

Flores A.G. 1996, Active Cooling for Electronics in a Wireline Oil-Exploration Tool, *Ph.D. thesis*, M.I.T., USA.

Jakaboski J.C. 2004, Innovative Thermal Management of Electronics in Oil Well Logging, *M.Sc. thesis*, Georgia Institute of Technology USA.

Pennewitz E. , Kruspeb T. , Jungb S. , Schillinga M. 2012, Evaluation of Sorbents at Elevated Temperatures for Downhole Application, *Chem. Eng. Trans.,* 29: 1543-1548.

Sandeep K. , DeWalt B. , Headworth C. 2003, Well Intervention Using Rigless Techniques, *Proceedings of Offshore Technology Conference,* Houston, OTC 15177:1 – 13.

Sinha A. , Joshi Y.K. 2011, Downhole Electronics Cooling Using a Thermoelectric Device and Heat Exchanger Arrangement, *J. Electron. Packaging*, 133(4): 041005-1 - 041005-12.

A.2 Poster presented at the 24th International Conference of Refrigeration 2015, in Yokohama, Japan

Active Cooling and Heat Management of a Downhole Tool Electronics Section

Stefano Soprani[1], Kurt Engelbrecht[1], Anders J. Nørgaard[2]

[1]Department of Energy Conversion and Storage, Technical University of Denmark – Frederiksborgvej 399, DK-4000 Roskilde – Denmark
[2]Welltec A/S – Gydevang 25, DK-3450 Allerød - Denmark

Introduction

- Downhole interventions in *high-temperature wells* (150 ^{0}C < T < 200 ^{0}C) represent one of today's biggest challenges for the oil and gas industry, because of the temperature limits of the electronics that are employed in the robotic intervention tools [1].
- *Active cooling systems* could maintain the electronics at a tolerable temperature (175 ^{0}C), when the tool is operating in hotter environments up to 200 ^{0}C [2, 3].
- **The scope of this poster is to report the integration process of a thermoelectric cooler (TEC) into a downhole tool electronics section and its performance.**

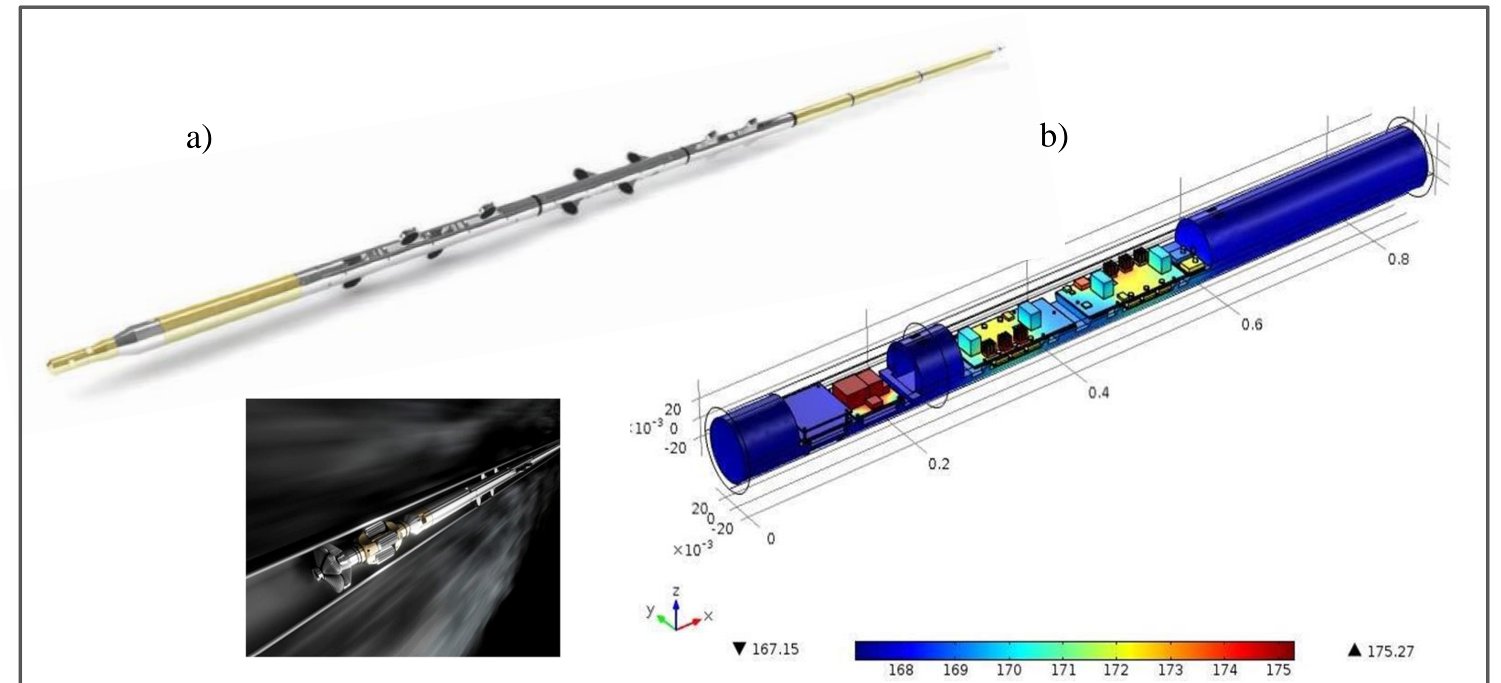

Figure 1. Illustration of a downhole tool (a) and COMSOL [4] simulation of the electronics overheating, at 167 ^{0}C well temperature (b).

Heat management strategy

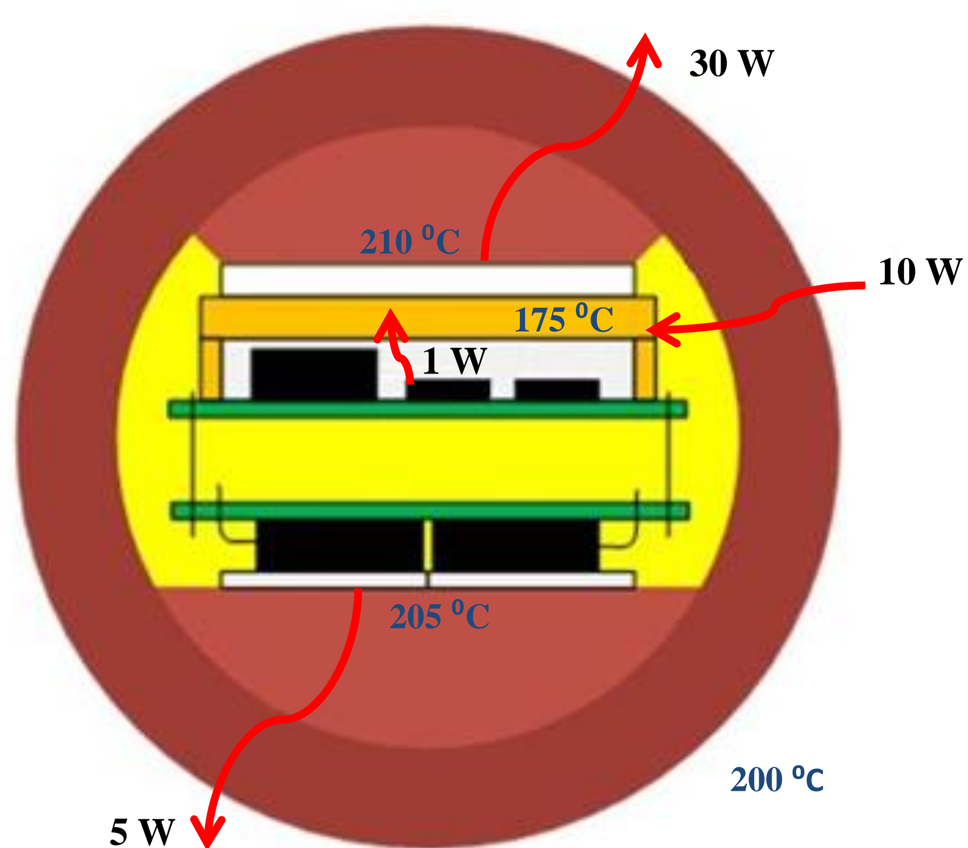

Figure 2. Downhole electronics unit cross section; schematic integration of the cooling technology. Heat fluxes and design temperatures are reported.

- High temperature-sensitive (HTS) electronics were mounted on a printed circuit board and actively cooled.
- High temperature-non sensitive (HTNS) electronics were mounted on a metallic cartridge and passively cooled.
- Thermal insulation protects the cooled components.
- **The thermoelectric cooler absorbs the load from the HTS electronics and rejects the excessive heat to the well reservoir, through the tool housing.**

Setup design

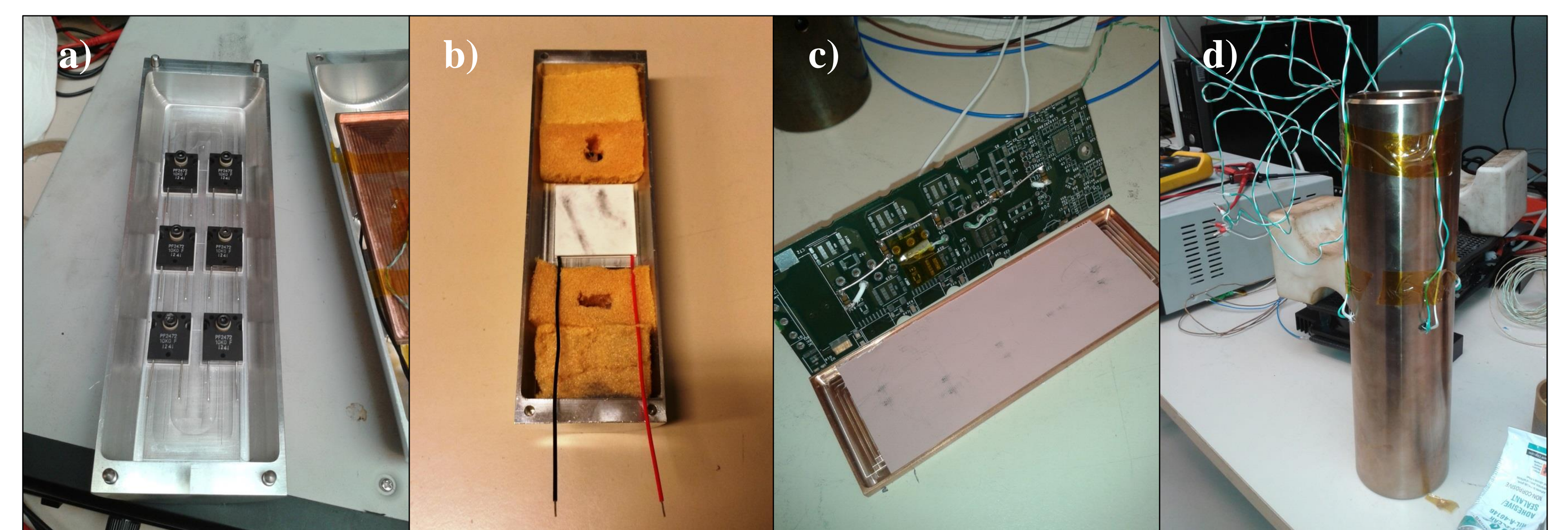

Figure 3. Experimental setup with test electronics. HTNS electronics installed on the bottom half of the cartridge (a). TEC and thermal insulation on the top part of the cartridge (b). HTS electronics on PCB, soft thermal pad and heat spreader (c). Tool housing (d).

- A soft thermal pad and a metallic heat spreader were used to interface the HTS electronics with the cooler cold plate.
- **Thermal grease and a clamping system were used to integrate the cooler into the setup.**

Characterization and test results

- **An optimal feed current/power minimizes the HTS electronics temperature.** It is a function of the well fluid temperature and convection regime.

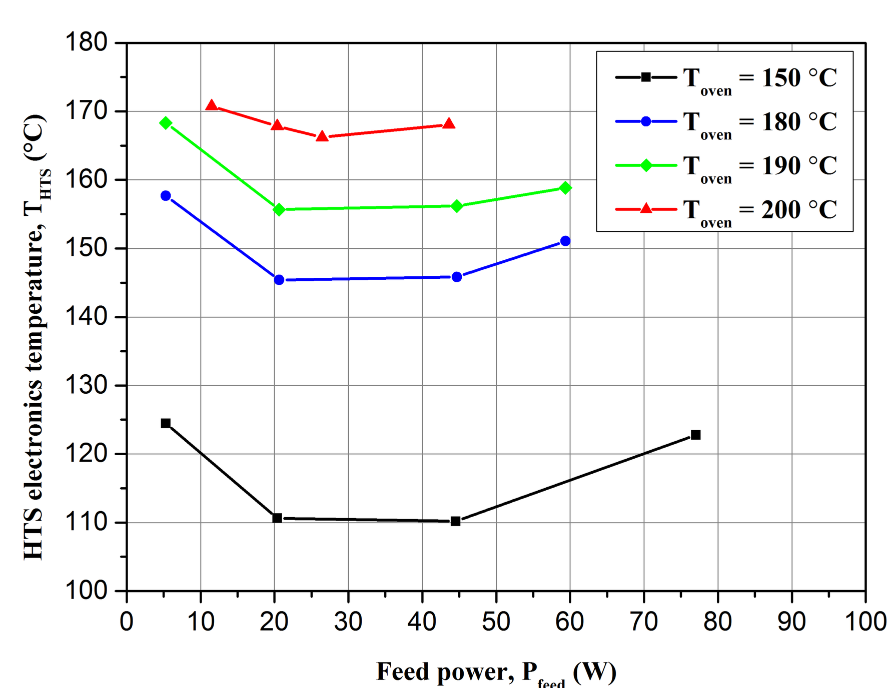

Figure 4. HTS electronics temperature as a function of the TEC feed power at different operating temperatures. Tests were carried out in a furnace that reproduced a dry forced-convection environment.

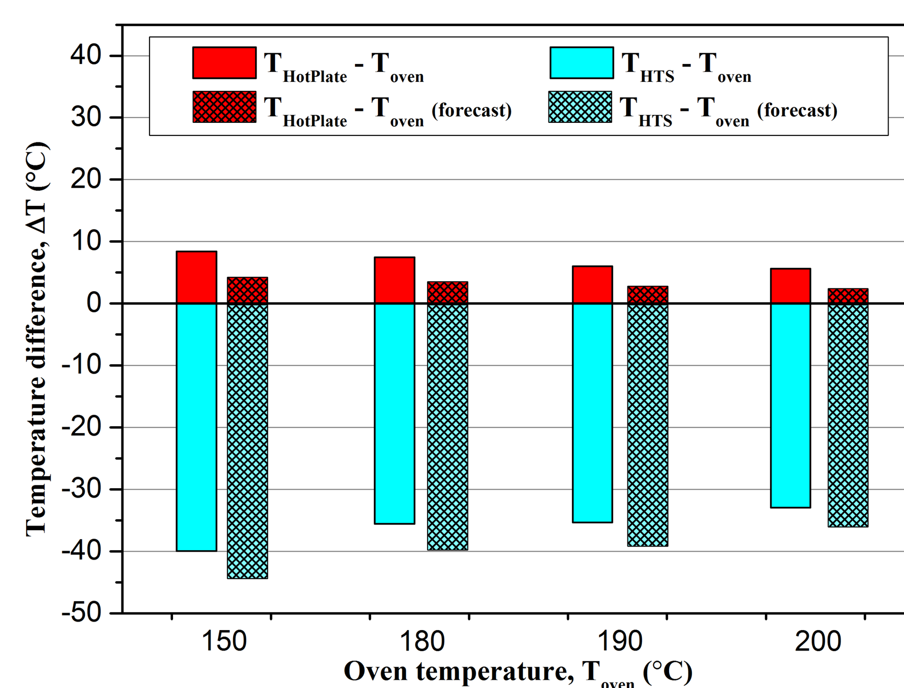

Figure 5. Temperature differentials between the oven and, respectively, the cooler hot plate (red bars) and HTS electronics (blue bars), when operating at optimal feed current, with an estimated forced convective coefficient of ~ 60 Wm^{-2}K^{-1}. A forecast was made for an external convective coefficient of 500 Wm^{-2}K^{-1} (dashed bars).

Reliability test

- The setup was tested at 200 ^{0}C in a dry forced-convection environment, for 75 hours (the equivalent of ~ 5 well interventions).
- The system degradation was estimated at ~ 0.03 ^{0}C/hour and ~ 4.4 mV/hour.

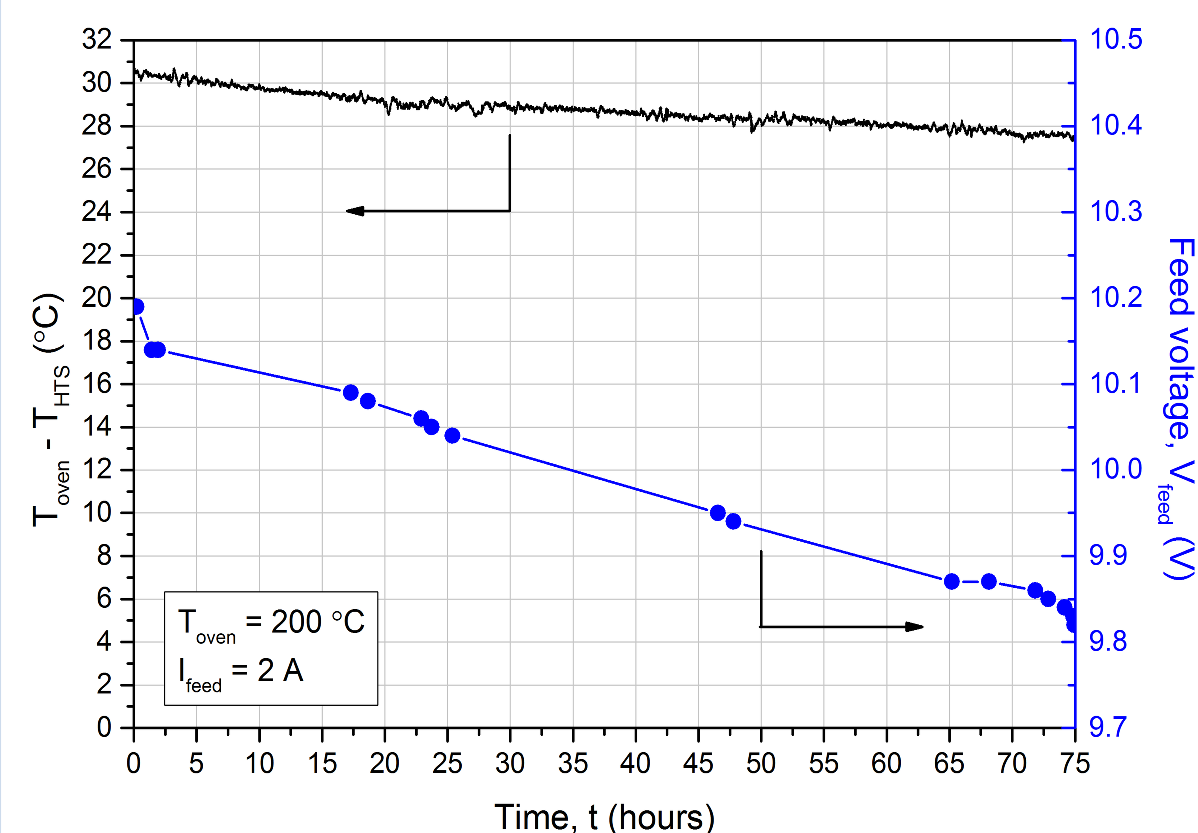

- The cooler degradation is caused by a change in the semiconductor properties, enhanced by the exposure to high temperature.
- **The HTS electronics were always maintained below 175 ^{0}C.**

Figure 6. Evaluation of the cooler degradation: trend in time of the temperature differential between the oven and the HTS electronics (left vertical axis) and of the feed voltage, given a feed current of 2 A (right vertical axis).

Acknowledgements

- The setup was built in Welltec A/S and tested with Welltec's facilities.
- This work is partially financed by the Danish Agency for Science, Technology and Innovation (FI), as it is part of an Industrial Ph.D. project.
- The authors would like to show their gratitude to Christian Bahl (Department of Energy Conversion and Storage, Technical University of Denmark) for constructive meetings and discussions.

References

[1] K.P. Seymour, R. MacAndrew, "Design, Drilling, and Testing of a Deviated HTHP Exploration Well in the North Sea", Society of Petroleum Engineers 9, 244 - 248 (1994).

[2] Aaron G. Flores. "Active cooling for electronics in a wireline oil-exploration tool". Ph.D. thesis, M.I.T. Boston, USA. (1996).

[3] G.A. Bennett. "Active cooling for downhole instrumentation: preliminary analysis and system selection". Master thesis, Los Alamos National Laboratory, Mexico (1988).

[4] COMSOL Multiphysics 4.3b.

DTU Energy Conversion
Department of Energy Conversion and Storage

Corresponding author e-mail: stefs@dtu.dk

A.3 Paper published in the proceedings of the COMSOL Conference 2015, in Grenoble France

Soprani S. , Haertel J. H. K. , Lazarov B. S. , Sigmund O. , Engelbrecht, K. Topology Optimization of an Actively Cooled Electronics Section for Downhole Tools, *Proceedings of COMSOL Conference 2015*, Grenoble, France (2015).

Topology Optimization of an Actively Cooled Electronics Section for Downhole Tools

S. Soprani*[1], J. H. K. Haertel[1], B. S. Lazarov[2], O. Sigmund[2], K. Engelbrecht[1],
[1] Department of Energy Conversion and Storage - Technical University of Denmark, [2]Department of Mechanical Engineering - Technical University of Denmark.
* Frederiksborgvej 399 - Building 778, 4000 Roskilde, Denmark, stefs@dtu.dk

Abstract: Active cooling systems represent a possible solution to the electronics overheating that occurs in wireline downhole tools operating in high temperature oil and gas wells. A Peltier cooler was chosen to maintain the downhole electronics to a tolerable temperature, but its integration into the downhole electronics unit proved to be challenging, because of the space constraints and the proximity of the cooling zone (electronics) to the heat sink (well fluid). The topology optimization approach was therefore chosen to optimize the thermal design of the actively cooled electronics section and the SIMP (Solid Isotropic Material with Penalization) method was implemented in COMSOL Multiphysics. Several optimized designs were obtained for different operating conditions and their sensitivity to the change in the boundary conditions was evaluated. A final design for the electronics unit was selected, according to the topology optimization results and assembly constraints, and compared to the optimized cases.

Keywords: Topology optimization, SIMP, Electronics cooling.

1. Introduction

Well interventions are remedial operations that are performed in oil and gas wells in order to restore or increase the production. The *electric wireline* well intervention technique relies on the usage of a cabling technology that connects the downhole tools to the surface equipment and, thanks to the integration of electronic components into the downhole devices, allows the operator to remotely control the tool during the operation. However, the application of the wireline technique in high temperature wells, where the temperature can range between 150 °C and 200 °C, is often restricted by the electronics temperature limit, which is currently set to 175 °C for the majority of the employed components available on the market.

Active cooling systems represent a possible solution to the electronics overheating [1] as they could extend the application of the wireline tools to a wider range of high temperature wells. The high-temperature sensitive electronics would be maintained below the well temperature, while the well fluid would be used as a heat sink for the cooler excessive heat. A thermoelectric cooler (TEC) was chosen to fulfill this task [2], because of its compactness and lack of moving parts; on the other hand its low efficiency (COP) might generate issues due to excessive heat rejection at the hot end in the case of low convection regimes in the oil well.. It is therefore very important to define an effective thermal design of the electronics unit that provides a good thermal path to reject the excessive heat to the well, protects the cooled electronics from the hot surroundings and minimizes the heat leakages. The limited availability of space in the downhole tool and the proximity between the cooling load and the heat sink make this task challenging.

The topology optimization approach was adopted in order to define an optimized distribution of the thermal conductive material and thermal insulation, so the high-temperature sensitive components' temperature could be minimized. The geometry of the electronics unit was modelled in COMSOL Multiphysics and the topology optimization SIMP (Solid Isotropic Material with Penalization) method [3] was implemented. A density filter was applied in order to avoid mesh-dependent solutions, and coupled with a projection function, in order to obtain a better resolution of the design variable distribution that defines the optimized distribution of thermally conductive material and thermal insulation.

2. System integration overview

The downhole tool electronics unit (Figure 1) is composed of two main structural components: a 200 mm long cylindrical *chassis* (O.D. 60 mm), on which the electronic components are installed,

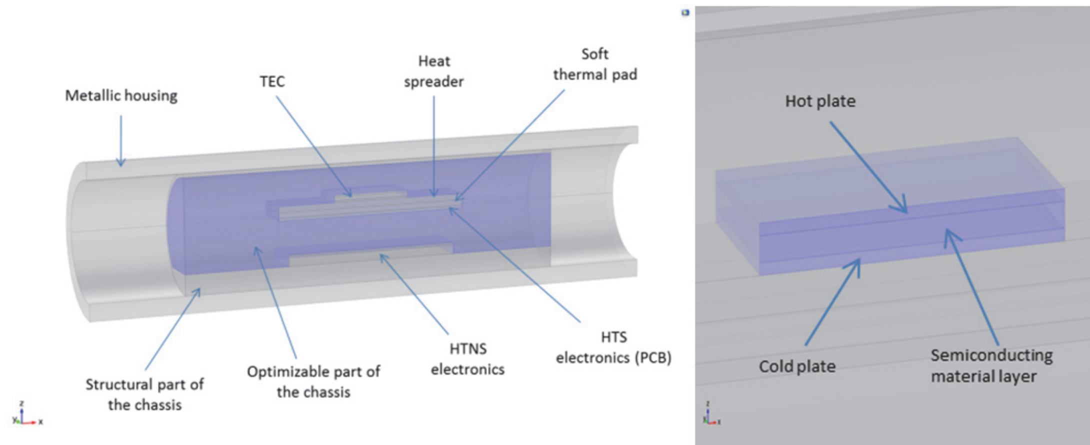

Figure 1. COMSOL Multiphysics representation of the longitudinal section of the downhole tool (left side) and particular of the TEC device with the two plates and the semiconducting material layer highlighted in blue (right side).

and a 300 mm long metallic *housing* (O.D. 80 mm, I.D. 60 mm), which encloses the chassis and the electronics, protecting and sealing them from the outer well fluid at high pressure. The chassis, in turn, is divided into a "*structural*" part made of aluminum, that provides mechanical stability to the system, and an "*optimizable*" part, that will be the object of the topology optimization.

Furthermore, the electronic components can be distinguished into *high temperature-non sensitive (HTNS)* and *high temperature-sensitive (HTS)* components. The first dissipate 5 W, are mounted directly on the chassis and are passively cooled; the latter dissipate 1 W, are installed on a printed circuit board (PCB) and are actively cooled with the TEC. The TEC cold plate is thermally coupled with the HTS electronics through a copper *heat spreader* and a *soft thermal pad*. On the other side, the TEC hot plate needs to be thermally connected to the well fluid through a heat sink that the topology optimization solver is asked to optimize. The design of the system aims at maintaining the HTS electronics below 175 °C, when operating in a 200 °C well environment.

3. Governing equations

The heat transfer within the system is mainly driven by heat conduction, so the heat transfer PDE (Eq. 1) was implemented in the COMSOL model through the Heat Transfer module.

$$\nabla(-k\nabla T) = Q_{source} \tag{1}$$

Where k ($Wm^{-1}K^{-1}$) is the material thermal conductivity, T (K) is the temperature and Q_{source} (Wm^{-3}) is a volumetric heat source.

A modified heat transfer equation, that accounted for the thermoelectric effect, was implemented in the TEC semiconductor domain, in between the TEC hot and cold plates, through the Coefficient Form PDE module.

$$\nabla(\boldsymbol{J}ST - k\nabla T) = Q_{JouleHeating} \tag{2}$$

Where $\boldsymbol{J}$ (Am^{-2}) is the electric current density vector, S (VK^{-1}) is the material Seebeck coefficient, $Q_{JouleHeating}$ (Wm^{-3}) is the heat source associated to the Joule effect. The layer between the TEC hot and cold plates (Figure 1), in reality, is composed of leg pairs of semiconductor material (Bi_2Te_3) separated by air; in order to reduce the geometry complexity this layer was modelled as isotropic and homogeneous, and its properties were weighted based on the volumes of Bi_2Te_3 and air (Eq. 3, 4, 5). Equations from Gordon et al. [4] were used to characterize the behavior of Bi_2Te_3, while the COMSOL material library was used for the air properties. The equations were combined through linear coefficients in order to match a commercial Peltier cooler performance that was evaluated in terms of hot and cold plate temperatures at different cooling loads and operating temperatures.

$$S = S_1(-2.025e-9T^2 + 1.42e-6T + -4.49e-5) \tag{3}$$

$$k = k_1(2.91e-5T^2 - 0.019T + 4.81) + +k_2\, k_{air}(T) \tag{4}$$

$$\sigma = \sigma_1(4.35e.8T - 2.754e - 6)^{-1} \quad (5)$$

$$Q_{JouleHeating} = 0.268\, \sigma^{-1} \boldsymbol{J} \cdot \boldsymbol{J} \quad (6)$$

Where $k_{air}(T)$ ($Wm^{-1}K^{-1}$) is the thermal conductivity of air as a function of temperature from the COMSOL material library; $S_1 = 0.349$, $k_1 = 0.215$, $k_2=0.732$ and $\sigma_1 = 0.309$ are linear coefficients. At the two ends of the electronics unit, an adiabatic boundary condition was set. A convective heat flux, simulating the well fluid interaction with the housing surface, was imposed by setting the external well fluid temperature T_{fl} and heat transfer convective coefficient h. The partial differential equations (1) and (2) were then interfaced through a Dirichlet boundary condition that matched the temperatures at the interface. Heat sources were set in the HTNS electronics domain (5W) and at the interface between the PCB and the soft thermal pad (1 W), to simulate the electronics power dissipation. According to empirical estimations, thermal contact resistances were simulated by setting a thin resistive layer at the interface between the structural chassis and the housing ($R_{th1} = 1.1e\text{-}3$ m^2KW^{-1}), between the HTNS electronics and the structural chassis (R_{th2} = 2.5e-5 m^2KW^{-1}), and between the TEC plates and the structural chassis/heat spreader (R_{th3} = 2.5e-5 m^2KW^{-1}). R_{th1} was estimated through the comparison between simulation results and experimental data from thermal tests on the structural chassis. R_{th2} and R_{th3} instead, simulated a 0.1 mm thick layer of thermal grease, with a thermal conductivity of 4 $Wm^{-1}K^{-1}$. Another relevant boundary condition was set for the TEC feed current I_{feed} and used to characterize the cooler operating state.

4. Topology optimization implementation

The topology optimization problem can be stated as follows:

minimize:

$$f_{obj}(T, \rho_{design}) = \frac{1}{A_{PCB}} \int_{\Omega_{PCB}} T \, d\Omega_{PCB} \quad (7)$$

constraints:

$$0 \leq \rho_{design} \leq 1 \quad (8)$$

$$0 \leq \int_{\Omega} \rho_{design} d\Omega \leq \gamma V_{\Omega} \quad (9)$$

$$0 \leq \gamma \leq 1 \quad (10)$$

$$\boldsymbol{r}(T, \rho_{design}) = \boldsymbol{0} \quad (11)$$

Where f_{obj} is the objective function to be minimized, defined as the integral average of the temperature distribution along the PCB surface Ω_{PCB}; A_{PCB} is the PCB area surface (m^2), ρ_{design} is the design variable that can range between 0 (thermal insulation) and 1 (aluminum), and whose distribution needs to be optimized; γ is the fraction of the optimizable domain V_Ω that sets the constraint on the maximum volume that can be occupied by aluminum; $\boldsymbol{r}(T, \rho_{design})$ is the residual of the discretized system of the state equations reported in section 3.

The topology optimization problem was implemented in COMSOL through the Optimization module: ρ_{design} was defined and bounded as a c*ontrol variable field*, while the volume constraint was set with an *integral inequality constraint*. A density filter [5] was applied to the design variable, in order to make the solution independent from the mesh size (Eq. 12), and implemented in COMSOL through the Coefficient Form PDE module:

$$-r^2 \nabla^2 \tilde{\rho} + \tilde{\rho} = \rho_{design} \quad (12)$$

Where r is a filter parameter and is equal to 1.5 times the maximum mesh element length in the optimizable domain. $\tilde{\rho}$ was then projected in order to obtain a sharper transition zone between aluminum and insulator in the optimized topology [6]; Eq. 13 was used.

$$\bar{\tilde{\rho}} = \frac{tanh(\beta\eta) + tanh(\beta(\tilde{\rho} - \eta))}{tanh(\beta\eta) + tanh(\beta(1 - \eta))} \quad (13)$$

η = 0.5 ensured a good convergence of the solution; β was ramped from 1 to 8, using the continuation approach, as suggested by Wang et al. [7]. The thermal properties of the optimizable domain were then calculated through the projected design variable, with an interpolation function that defined the thermal conductivity.

$$k_\Omega = k_{ins} + (k_{Al} - k_{ins})\bar{\tilde{\rho}}^p \quad (14)$$

Where k_Ω ($Wm^{-1}K^{-1}$) is the domain effective thermal conductivity, k_{ins} = 0.17 $Wm^{-1}K^{-1}$ and k_{Al}= 138 $Wm^{-1}K^{-1}$ are respectively the thermal conductivities of the thermal insulation and of the considered aluminum alloy, and p = 3 [7] is the penalization coefficient.

The problem was solved through the optimization solver MMA (Method of Moving Asymptotes), embedded in COMSOL.

5. Results

The model was simulated for a well temperature of 200 °C and different conditions of well fluid convection regimes h and TEC feed current I_{feed}, so the design could be optimized for different operating conditions.

The system was optimized for I_{feed} of 1, 2, 3 and 4 A, according to the modelled commercial cooler specifications, and for h of 25, 50, 100 and 500 $Wm^{-2}K^{-1}$, in order to reproduce low, medium-low and medium well fluid convection regimes. h = 25 $Wm^{-2}K^{-1}$ is defined as the worst case design condition, while for h > 500 $Wm^{-2}K^{-1}$ the design of the unit is expected not to be critical anymore. The optimization of the system balanced the use of aluminum and thermal insulation in different ways at different boundary conditions; a tradeoff between thermal protection of the cooled electronics and heat rejection of the excessive heat was always reached and two main design concepts were individuated.

Low TEC feed currents and high values of convective coefficients led to an optimized design (*Design 1*) where an aluminum pad connects the cooler hot plate to the structural chassis, so the excessive heat can be rejected radially through the housing to the well (Figure 2). Low I_{feed} (low ohmic losses across the cooler) and high h values make the heat rejection process not critical, so the thermal protection of the cooled electronics is prioritized and the use of aluminum is limited to provide a radial heat sink. The length of the aluminum pad increases when the feed current grows or the heat transfer convective coefficient decreases.

High TEC feed currents and low values of convective coefficients, on the other side, led to a design (*Design 2*) where the heat rejection becomes more problematic than in the previous case. An aluminum layer is now attached to the structural chassis (Figure 3). This layer does not only provide a radial path for the excessive heat to be rejected to the well, but also spreads it along the longitudinal direction of the tool; a better distribution of the heat enhances the heat exchange with the well fluid and minimizes the heat backflow to the cooled electronics. Thermal insulation still protects the cooled electronics from the HTNS components and the hot surroundings. The thickness of the layer increases with I_{feed} and when h decreases.

The balance between materials can be evaluated, for different boundary conditions, through the ratio of used aluminum over the optimizable volume (Figure 4).

$$R = \frac{1}{V_\Omega}\int_\Omega \bar{\tilde{\rho}}\, d\Omega \qquad (15)$$

Where R is the aluminum usage ratio and V_Ω is the optimizable domain volume (m^3). In order to have a good overview of the system behavior, the sensitivity of the optimized designs to operations at different boundary conditions was assessed. The performance of the system was evaluated in terms of temperature at which the HTS electronics could be maintained.

The electronics section was initially optimized for a certain value of feed current and well fluid convective coefficient; the resulting

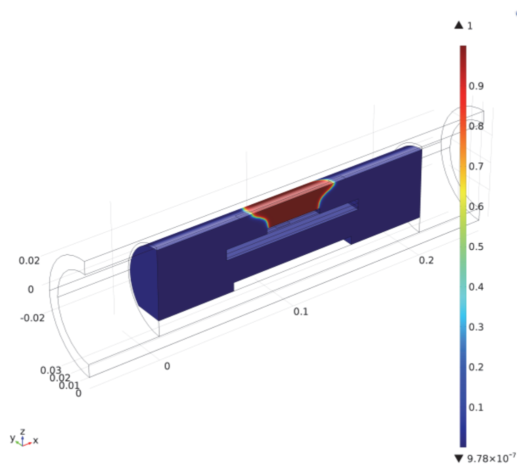

Figure 2. $\bar{\tilde{\rho}}$ distribution for the *Design 1* concept. System optimized for I_{feed} = 1 A and h = 100 $Wm^{-2}K^{-1}$.

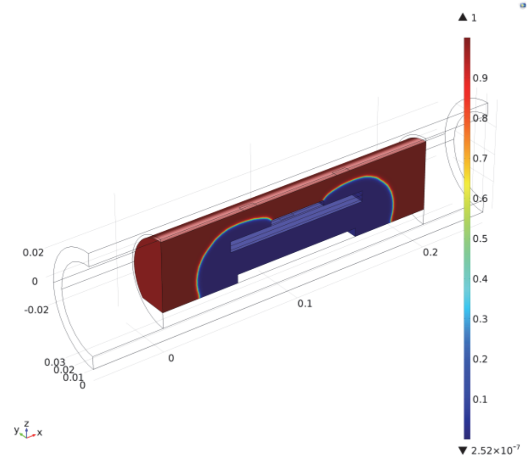

Figure 3. $\bar{\tilde{\rho}}$ distribution for the *Design 2* concept. System optimized for I_{feed} = 4 A and h = 50 $Wm^{-2}K^{-1}$.

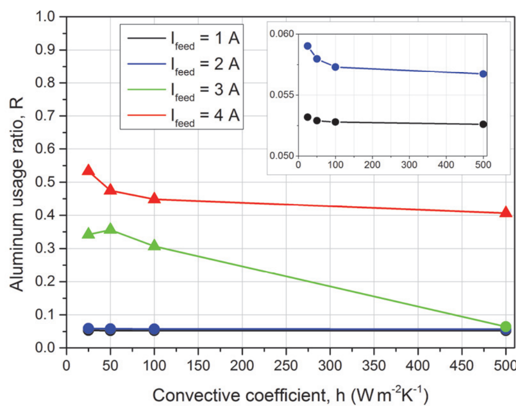

Figure 4. R vs. well fluid convective coefficient, for different TEC feed currents. Different symbols refer to the different optimized design concepts.
● = Design 1, ▲ = Design 2.

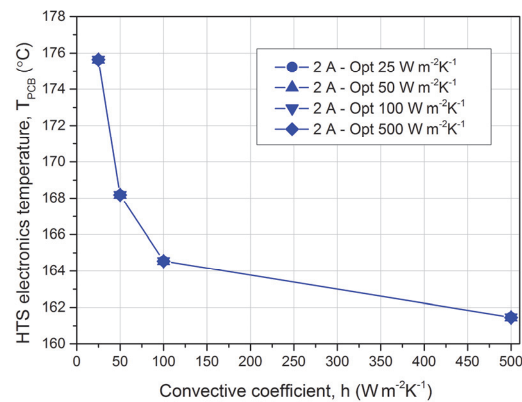

Figure 5. HTS electronics temperature vs. well fluid convective coefficient for four different systems, optimized for I_{feed} = 2 A and h = 25, 50, 100 and 500 Wm^{-2}K^{-1}.

design was then simulated, maintaining the TEC feed current constant, at different values of well fluid convective coefficients. Figure 5 reports the performance of the optimized designs versus the well fluid convective coefficient: each of the five illustrated curves refers to a system optimized for I_{feed} = 2 A and a different value of h. It can be noticed the five curves overlap and the performance of the systems is very similar, despite they were optimized for different h values. A maximum temperature mismatch of 0.05 °C between the curves was found. The same behavior was obtained with the optimizations with the other feed currents. For I_{feed} = 1 A the maximum mismatch between the curves is equal to 0.005 °C, for I_{feed} = 3 A is equal to 0.88 °C and for I_{feed} = 4 A is equal to 0.88 °C. We can conclude the optimization of the electronics unit, at a given feed current is not significantly sensitive to the well fluid convective coefficients in the considered range; in other words, the performance of the optimized systems, at a given feed current, is not significantly sensitive to the length/thickness of the optimized aluminum pad/layer and can be considered robust.

The same approach was used to evaluate the sensitivity of the optimized designs to the TEC feed current, at a given convective coefficient. The electronics section was first optimized for a certain value of feed current and well fluid convection; the resulting design was then simulated, maintaining the convection regime constant, at different values of operating current. Figure 6 shows the optimization process is more sensitive to the feed current as the mismatch between the curves can go up to several degrees Celsius. An optimal feed current I_{opt} that minimizes the HTS electronics temperature can be individuated. It can be defined as the TEC feed current at which the marginal gain in absorbed heat flux, due to an infinitesimal increase of the TEC feed current, becomes lower than the heat flux that leaks through the insulation. I_{opt} is slightly different for each optimized design, but mainly depends on h and on the well fluid capability of absorbing the excessive heat. I_{opt} is equal to ~1.9 A for h = 25 Wm^{-2}K^{-1}, to ~2.3 A for h = 50 Wm^{-2}K^{-1}, to ~2.6 A for h = 100 Wm^{-2}K^{-1} and to ~2.9 A for h = 500 Wm^{-2}K^{-1}. The designs that best operate around the optimal current are the ones optimized for 2 A and 3 A.

The topology optimization results, together with the knowledge of the practical assembly constraints, were used to define the final design for the actively cooled downhole electronics unit (Figure 7). *Design 1* proved to be as well performing as *Design 2* around the optimal current, but with a lower employment of aluminum and therefore with a lower weight. The aluminum pad that provided the thermal path from the cooler hot plate to the structural chassis proved to be crucial. An aluminum pad, 41x41 mm was therefore implemented in the final design, illustrated in Figure 7. No aluminum layer was included, except for 2 walls, 10 mm thick, at each end of the chassis. They provide mechanical stability, an additional

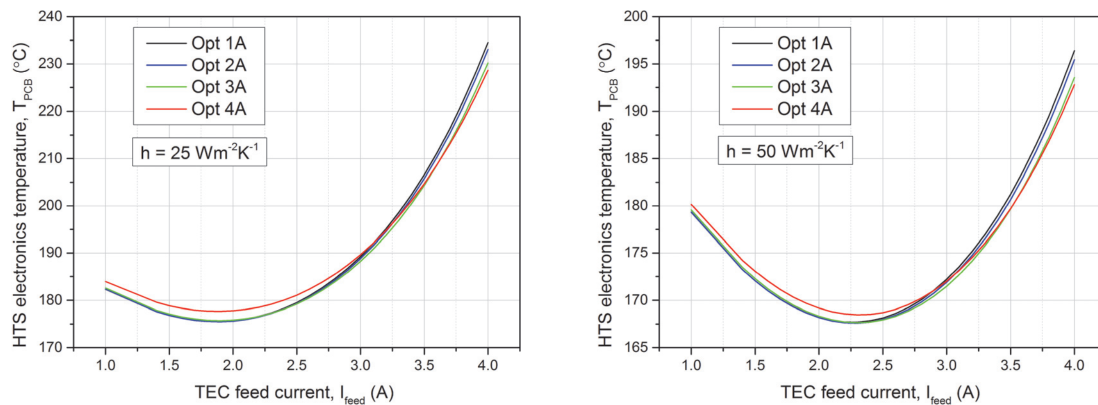

Figure 6. HTS electronics temperature vs. TEC feed current for four different systems, optimized for I_{feed} = 1, 2, 3 and 4 A, and h = 25 Wm^{-2}K^{-1} (left side) and 50 Wm^{-2}K^{-1} (right side).

thermal path for the heat to better spread in case of low heat rejection rate, and are suitable for the installation of pins for the assembly of the system. The chassis would be in fact split in a bottom half, were the HTNS electronics are installed, and a top half, where the cooling system is installed. The two halves would then be coupled and held in place by four pins (not reported in Figure 7). Two smaller pads, 8x8 mm, with threaded holes, were also designed in the top part of the chassis in order to clamp the cooler in between the heat spreader and the chassis itself, through a plastic screw system. The rest of the domain is filled with thermal insulation.

Simulations proved the chosen design operates very closely to the optimized systems performance (Table 1). The difference in HTS electronics temperature is very small when operating at 1 or 2 A, as the chosen design is very similar to the *Design 1* concept: the electronics is maintained maximum 0.09 K above the HTS electronics temperature in the optimized case. When operating at 3 and 4 A the mismatch becomes higher, since the *Design 2* concept would work better at high feed currents. However, the HTS components are always maintained less than 1 K above the optimized case for operations at 3 A. The mismatches are larger than 1 K for I_{feed} = 4 A, but can be

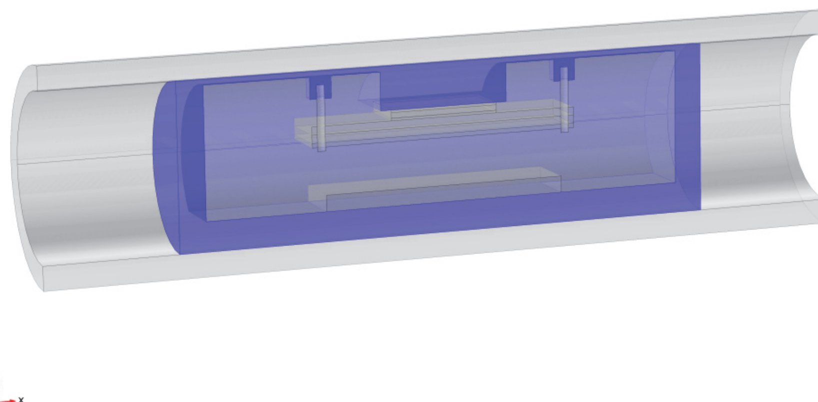

Figure 7. COMSOL Multiphysics illustration of the longitudinal section of the final design. The designed aluminum chassis is highlighted in blue.

considered irrelevant; a feed current of 4 A is far from the observed optimal feed currents and the system would always aim to operate close to the optimal conditions, between 2 and 3 A.

Table 1. Comparison between the performance of the optimized systems (Opt) and final chosen design (Design). $\Delta T = T_{HTS,design} - T_{HTS,Opt}$.

h (*Wm*$^{-2}$*K*$^{-1}$)	*Opt - 1A* T_{HTS} (°C)	*Design - 1A* T_{HTS} (°C)	ΔT (K)
25	182.31	181.95	0.10
50	179.32	178.97	0.11
100	177.83	177.47	0.11
500	176.56	176.21	0.11
h (*Wm*$^{-2}$*K*$^{-1}$)	*Opt - 2A* T_{HTS} (°C)	*Design - 2A* T_{HTS} (°C)	ΔT (K)
25	175.63	175.68	0.05
50	168.18	168.23	0.05
100	164.54	164.57	0.04
500	161.46	161.48	0.03
h (*Wm*$^{-2}$*K*$^{-1}$)	*Opt - 3A* T_{HTS} (°C)	*Design - 3A* T_{HTS} (°C)	ΔT (K)
25	188.22	188.93	0.71
50	171.48	171.87	0.39
100	163.68	163.90	0.22
500	157.12	157.35	0.23
h (*Wm*$^{-2}$*K*$^{-1}$)	*Opt - 4A* T_{HTS} (°C)	*Design - 4A* T_{HTS} (°C)	ΔT (K)
25	228.62	233.59	4.97
50	192.79	195.71	2.92
100	177.25	179.29	2.04
500	165.23	166.37	1.14

6. Conclusions

The distribution of thermally conductive material and thermal insulation was optimized within an actively cooled electronics unit for downhole tools. The heat transfer mechanisms were modelled in COMSOL Multiphysics and the topology optimization SIMP method was implemented. Diverse design concepts were obtained for different boundary conditions. The analysis of the resulting designs supported the development of a final unit, whose performance was compared to the optimized cases. An acceptable deviation between them was assessed and the importance of controlling the operating conditions close to the optimal TEC feed current was underlined.

7. Acknowledgments

S. Soprani and K. Engelbrecht would like to show their gratitude to the Danish Ministry of Technology and Innovation and to Welltec A/S for partially funding this work. The authors would also like to acknowledge the TopTEN project, sponsored through the Sapere Aude Program of the Danish Council for Independent Research (DFF–4005-00320), for supporting this study.

8. References

[1] A.G. Flores. Active Cooling for Electronics in a Wireline Oil-Exploration Tool, *Ph.D. thesis*, M.I.T., USA (1996).

[2] S. Soprani, K. Engelbrecht, A.J. Nørgaard. Active Cooling and Thermal Management of a Downhole Tool Electronics Section, *Proceedings of the 24th IIR International Congress of Refrigeration*, Yokohama, Japan (2015).

[3] E.M. Dede, J. Lee, T. Nomura. Multiphysics simulation: electromechanical system applications and optimization, *Springer London* (2014).

[4] J.M. Gordon, K.C. Ngc, H.T. Chuac, A. Chakrabortyc, The electro-adsorption chiller: a miniaturized cooling cycle with applications to micro-electronics, *International Journal of Refrigeration,* 25 (8): 1025–1033 (2002).

[5] B. S. Lazarov, O. Sigmund. Filters in Topology Optimization Based on Helmholtz-Type Differential Equations, *International Journal for Numerical Methods in Engineering*, 86 (6): 765-781 (2011).

[6] F. Wang, B. S. Lazarov, O. Sigmund. On Projection Methods, Convergence and Robust Formulations in Topology Optimization, *Structural and Multidisciplinary Optimization*, 43 (6): 767-784 (2011).

[7] O. Sigmund, K. Maute. Topology Optimization Approaches, *Structural and Multidisciplinary Optimization*, 48 (6): 1031-1055 (2013).

A.4 Paper published in the journal Applied Energy

Soprani S. , Haertel J. H. K. , Lazarov B. S. , Sigmund O. , Engelbrecht K. A Design Approach for Integrating Thermoelectric Devices Using Topology Optimization, *Applied Energy*, 176: 49–64 (2016). http://dx.doi.org/10.1016/j.apenergy.2016.05.024

Applied Energy 176 (2016) 49–64

Contents lists available at ScienceDirect

Applied Energy

journal homepage: www.elsevier.com/locate/apenergy

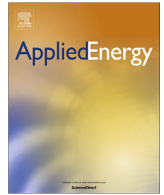

A design approach for integrating thermoelectric devices using topology optimization

S. Soprani [a,*], J.H.K. Haertel [a], B.S. Lazarov [b], O. Sigmund [b], K. Engelbrecht [a]

[a] Department of Energy Conversion and Storage, Technical University of Denmark, Denmark
[b] Department of Mechanical Engineering, Technical University of Denmark, Denmark

HIGHLIGHTS

- The integration of a thermoelectric (TE) cooler into a robotic tool is optimized.
- Topology optimization is suggested as design tool for TE integrated systems.
- A 3D optimization technique using temperature dependent TE properties is presented.
- The sensitivity of the optimization process to the boundary conditions is studied.
- A working prototype is constructed and compared to the model results.

ARTICLE INFO

Article history:
Received 5 February 2016
Received in revised form 29 April 2016
Accepted 2 May 2016

Keywords:
Topology optimization
Thermoelectric devices
Thermoelectric cooling
System integration
Thermal management
Downhole electronics cooling

ABSTRACT

Efficient operation of thermoelectric devices strongly relies on the thermal integration into the energy conversion system in which they operate. Effective thermal integration reduces the temperature differences between the thermoelectric module and its thermal reservoirs, allowing the system to operate more efficiently. This work proposes and experimentally demonstrates a topology optimization approach as a design tool for efficient integration of thermoelectric modules into systems with specific design constraints. The approach allows thermal layout optimization of thermoelectric systems for different operating conditions and objective functions, such as temperature span, efficiency, and power recovery rate. As a specific application, the integration of a thermoelectric cooler into the electronics section of a downhole oil well intervention tool is investigated, with the objective of minimizing the temperature of the cooled electronics. Several challenges are addressed: ensuring effective heat transfer from the load, minimizing the thermal resistances within the integrated system, maximizing the thermal protection of the cooled zone, and enhancing the conduction of the rejected heat to the oil well. The design method incorporates temperature dependent properties of the thermoelectric device and other materials. The 3D topology optimization model developed in this work was used to design a thermoelectric system, complete with insulation and heat sink, that was produced and tested. Good agreement between experimental results and model forecasts was obtained and the system was able to maintain the load at more than 33 K below the oil well temperature. Results of this study support topology optimization as a powerful design tool for thermal design of thermoelectric systems.

© 2016 Elsevier Ltd. All rights reserved.

1. Introduction

Over the past decades, thermoelectric devices (TEDs) have become competitive solutions for waste energy recovery, heat pumping, and cooling applications [1–5]. Advantages of TEDs include compactness, gas-free solid-state operation, lack of moving parts, and long life-span. However, a lower energy conversion efficiency compared to other well established technologies [6] can limit their application. In order to increase energy conversion efficiency, optimization of thermoelectric devices is an active research topic, both in terms of the thermoelectric materials employed [7–10], and the architecture of devices [11–16]. Additionally, efficient TED operation strongly relies on the integration into the overall energy conversion system [17–21]. Effective heat transfer at the cold and hot plates, minimization of thermal resistances within the system, and reduction of heat leakages each

* Corresponding author at: Frederiksborgvej 399, Building 778, 4000 Roskilde, Denmark.
E-mail address: stefs@dtu.dk (S. Soprani).

http://dx.doi.org/10.1016/j.apenergy.2016.05.024
0306-2619/© 2016 Elsevier Ltd. All rights reserved.

improves overall efficiency. These features depend on the thermal layout of the integrated system and should be taken into account during the design phase to maximize effectiveness.

Here, we present a novel automated method, using topology optimization, to design thermal interfaces and insulation solutions for a TED to be integrated in a system with design constraints. Topology optimization has not previously been applied to thermoelectric systems, but this technique has great potential as a powerful design tool, as it can be used to optimize the topology of heat sinks, heat exchangers, and to define optimized distributions of thermally conducting and insulating material based on a set of design constraints. We show that the method can be implemented using commercial software, is robust, and is suitable for TED applications that must be packaged in a defined space. The method can be used to optimize a thermoelectric system for a variety of objective functions, such as efficiency, power recovery rate, and temperature span. Contrary to size and shape optimization approaches, topology optimization requires no initial design concept or a priori parametrization [22,23]. This flexibility is especially important in the early design phase, as it saves development time and can yield unintuitive optimized structures. Density-based topology optimization methods are particularly promising, since they consider the systematic distribution of material within a design domain, while aiming to optimize a certain objective function.

Topology optimization was first developed and established for structural mechanics applications and was subsequently applied to various other disciplines [24,25]. Prior studies on heat transfer using topology optimization have mainly focused on pure 2D heat conduction problems [22,26,27] as well as heat conduction with convective heat transfer to an ambient fluid [28–32]. Later works have included the explicit modeling of the fluid flow within the optimization domain in thermo-fluid models with forced convection in 2D [33–38] and 3D [39]. More recent applications of the approach have extended models to consider 2D topology optimization of natural convection [40] and radiation as the dominant heat transfer mechanism [41]. The design, manufacturing and subsequent experimental testing of optimized forced-convection heat sinks have also been presented [42–44].

Building on previous studies, this work addresses an existing industrial challenge and applies topology optimization to a thermoelectric system for the first time. Here, it is used to design the thermal integration of a thermoelectric cooler (TEC) in a downhole tool for oil well interventions. The space constraints imposed by the application and the clearly defined thermal boundary conditions make this an attractive case for topology optimization [45]. In the studied application, the TEC maintains a specific group of electronics at a temperature below the outside well temperature to prevent overheating issues that occur when the borehole exceeds the maximum temperature rating of the electronics (175 °C). Topology optimization is used to optimize the distribution of the insulating material, which thermally protects the cooled electronics, and of the conducting material, which aids in rejecting heat from the TEC to the well. The objective of the optimization is to minimize the temperature of the cooled electronics. A more detailed discussion regarding well interventions, active cooling, and thermal management of downhole electronics, is given in Refs. [46–51].

A model of the thermoelectric device was developed for this application, implemented in a 3D finite element model of the system, and coupled with the optimization algorithm. Temperature dependent properties of the TEC were implemented in order to capture the effects of the real material properties during the optimization process. The topology optimization model was used to optimize the design of the system for different operating conditions and to define the optimal working conditions of the TEC. The improvements in performance for the optimized systems were assessed and used to define a final design of the electronics unit, which is also practical from a manufacturing and assembly standpoint. The defined setup was then manufactured and experimentally tested at different operating conditions, and the results compared to the model predictions.

2. Description of the system

This chapter briefly introduces the electronics unit system, its main components and the overall thermal management principle. A 3D model of the longitudinal section of the system is illustrated in Fig. 1.

The analyzed downhole electronics unit is composed of the following parts:

- *Metallic cylindrical housing:* a hollow cylinder that shields and seals the inner components from the harsh well environment.
- *Chassis:* a rigid metallic support used for final assembly, on which the electronics are mounted and slid into the housing. It is divided in a structural part, which mechanically supports the system; and an optimizable part, which surrounds the components within the structural chassis and is the object of the topology optimization.
- *Electronic components:* they can be split into high temperature-sensitive (HTS) and high temperature-non-sensitive (HTNS) components. The former are likely to fail when their operating temperature exceeds 175 °C, the latter can even operate above 200 °C. The HTS electronics are mounted on a printed circuit board (PCB) and are characterized by a power dissipation rate of 1 W; the HTNS electronics are mounted directly on the chassis and dissipate an estimated 5 W.

Additional components, used for the integration of the active cooling system into the tool, are:

- *Thermoelectric cooler:* the cooling system is connected to an electric power source and transfers a heat flux from the cold to the hot plate, when an electric current is applied. The TEC cold plate needs to be thermally coupled to the HTS electronics, while the hot plate requires a thermal link to the hot reservoir, represented by the well environment.
- *Metallic heat spreader:* a rigid plate attached to the TEC cold plate that, together with the thermal pad, constitutes the thermal interface between the PCB and the cooler.
- *Soft thermal pad:* a soft silicone sheet, which is inserted between the PCB and the copper plate to create a thermal path between the irregular surface of the PCB and the heat spreader.

The heat management strategy aims at maintaining the HTS electronics at 175 °C or below when the tool is operating in a 200 °C environment. It is based on the passive cooling of the HTNS components, which can withstand high temperatures, and the active cooling of the HTS components through the Peltier module. The PCB is therefore thermally coupled, through the heat spreader and the thermal pad, with the cold plate of the Peltier module so the cooling load can be absorbed by the cooler. The TEC hot plate, in turn, needs to be thermally connected to the chassis; in this way, the excessive heat can flow through the housing and be rejected to the well fluid that laps the outer surface of the housing, through convective heat transfer. A tight mechanical contact is ensured between the structural chassis and the housing, to reduce the contact thermal resistance.

It is important to note that the thermal connection between the TEC hot plate and the chassis, as well as the distribution of

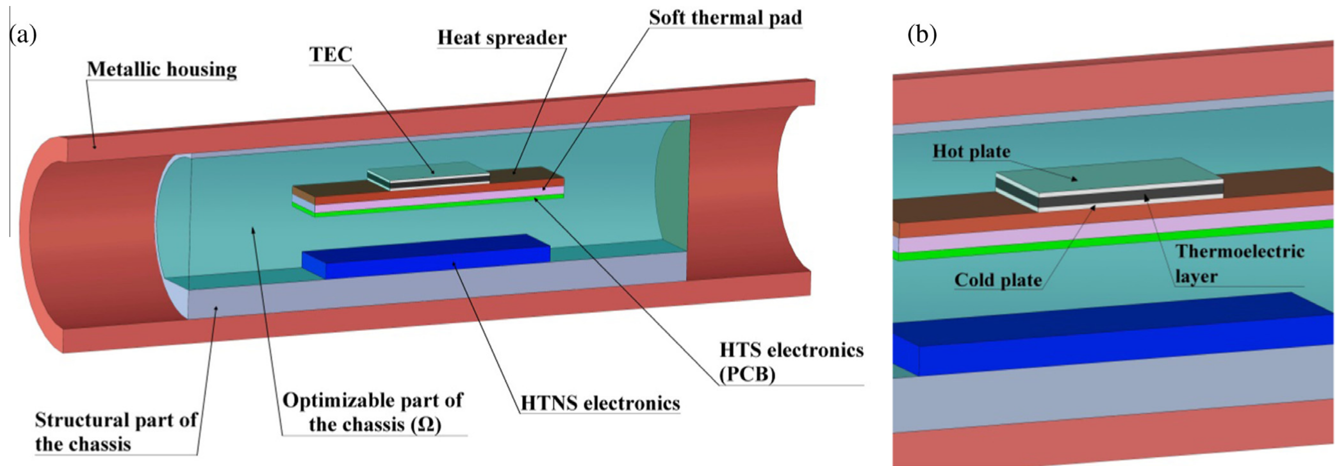

Fig. 1. Representation of the longitudinal section of the downhole tool (1a); the domain of the optimizable chassis is represented as partially transparent and colored in light blue. Particular of the TEC device (1b). (For interpretation of the references to color in this figure legend, the reader is referred to the web version of this article.)

insulating material, will be the result of the topology optimization process. The optimization is expected to define an optimized distribution of thermally conducting material and thermal insulation inside the unit, so the refrigerated electronics are properly protected from the hot surroundings and the excessive heat is effectively rejected to the well fluid. These two phenomena both act towards the minimization of the HTS electronics temperature, which is the objective of the optimization. While the optimization is focused on the thermal integration of the TEC, the topology of the TEC module itself is not the object of the optimization. The finite-element model of the TEC is implemented to simulate the performance of a commercial high-temperature module to be integrated into the downhole tool. The freedom to optimize the electronics unit is limited by three factors: the tool needs to fit a specific well piping size, so its dimensions are constrained to the values reported in Table 1; the position and the design of the components inside the system are constrained by the application; the structural part of the chassis cannot be optimized because of its mechanical function.

3. Finite element model

3.1. Governing equations

The geometry shown in Fig. 1 was implemented in the finite element software COMSOL Multiphysics [52] and divided in domains, each of them characterized by different material properties and governing equations. In order to simulate the heat transfer within the system, mainly driven by heat conduction, the heat transfer PDE (Eq. (1)) was solved in all the domains, except for the thermoelectric material layer.

$$\nabla(-k\nabla T) = Q_{source} \tag{1}$$

where k is the material thermal conductivity, T is the temperature, and Q_{source} is a volumetric heat source. Eq. (1) was not applied to the thermoelectric material domain, as the heat transport related to the thermoelectric effect also needed to be taken into account. A modified heat transfer PDE (Eq. (2)) was used instead.

$$\nabla(\boldsymbol{J}S'T - k'\nabla T) = Q'_{JouleHeating} \tag{2}$$

where $\boldsymbol{J}$ is the electric current density vector, S' is the material Seebeck coefficient, and $Q'_{JouleHeating}$ is the heat source associated with the Joule heating effect.

3.2. Boundary conditions

The boundary conditions were set in order to simulate the operating and external conditions that could occur in a well during a downhole intervention. A convective heat flux was set on the outer surface of the housing, to reproduce the interaction between the well fluid and the tool.

$$-\boldsymbol{n}\cdot(-k\nabla T) = h(T - T_{ext}) \tag{3}$$

Furthermore, the tool electronics unit would be assembled in the middle of a tool string, composed of several sections, and the heat transfer with the well is expected to mainly occur radially. For this reason, adiabatic boundaries were set at the two ends of the cylindrical setup.

$$-\boldsymbol{n}\cdot(-k\nabla T) = 0 \tag{4}$$

where $\boldsymbol{n}$ is the surface normal vector, T_{ext} is the well fluid temperature and h is the heat transfer convection coefficient. Concerning

Table 1
List of the components with their dimensions and properties.

Component	Length (mm)	I.D. (mm)	O.D. (mm)	Thermal conductivity (W m^{-1} K^{-1})
Metallic housing	300	62	80	150
Structural chassis	200	58	62	138
Optimizable chassis	200	–	58	Eq. (16)
Component	**Length (mm)**	**Depth (mm)**	**Height (mm)**	**Thermal conductivity (W m^{-1} K^{-1})**
TEC plates	40	40	0.95 each	27
TEC thermoelectric layer	40	40	2.0	Eq. (8)
Heat spreader	100	40	3.0	400
Soft thermal pad	100	40	3.0	12
HTNS electronics	90	42	6.0	130
HTS electronics (PCB)	100	40	1.6	0.3

the interface between the thermoelectric material domain, where Eq. (2) is solved, and the rest of the geometry, where Eq. (1) is solved, a Dirichlet boundary condition was defined to provide consistency to the temperature distribution. Heat sources were set in the HTNS electronics domain (5 W), and at the interface between the PCB and the soft thermal pad (1 W), to simulate the power dissipation of both electronics modules. Thermal resistances, $R_{th1,2} = 2.5e{-}5\ \mathrm{m^2\,K\,W^{-1}}$, were modeled at the interface between the HTNS electronics and the structural chassis, and on the outer boundaries of the TEC hot/cold plates; they simulated the contribution of a 0.1 mm thick layer of thermal grease, with a thermal conductivity of $4\ \mathrm{W\,m^{-1}\,K^{-1}}$. An additional thermal resistance, $R_{th3} = 1.1e3\ \mathrm{m^2\,K\,W^{-1}}$, was set at the interface between the structural chassis and the housing in order to simulate the contact resistance given by the assembly. The value of this thermal resistance was estimated through the comparison between simulation results and experimental data from thermal tests on an analogue setup.

The operating conditions of the cooler were characterized by the TEC feed current I_{feed}, which represents the electric current which is supplied to the module and is given to the model as an input. The correlation between this parameter and the current density vector $\boldsymbol{J}$ (see Eq. (2)) is explained in more detail in the next section.

3.3. TEC model

A particular focus was put on the modeling of the thermoelectric cooler. Its main components are two aluminum oxide plates, between which leg pairs of semiconducting material (p–n junctions) are mounted, electrically connected in series, and separated by air. Reproducing the detailed geometry of the module would have drastically increased the complexity and the computational time of the 3D topology optimization model. Therefore a simplified model of the TEC was developed: the intermediate semiconductor layer was modeled as homogeneous and isotropic, and equivalent material properties were weighted on the properties of Bi_2Te_3 and air. In this way, the cooling effect driven by a given TEC feed current could be approximated to the real case, while the geometry could be significantly simplified.

As a consequence of the homogenization process, the electric and thermal transport phenomena could not be differentiated within the Bi_2Te_3 and air domains, and the inhomogeneous temperature gradient across the module could not be reproduced. However, this approximation was considered acceptable as it preserves the average heat fluxes that drive heat transfer in the integrated system.

Fig. 2 illustrates the steps that were used to develop the homogeneous model and that are explained in the following subsections.

3.3.1. Effective current density

In the *real device*, the thermoelectric leg pairs are fed in series. The current density through the legs $\boldsymbol{J}$ can be expressed, in good approximation, as the 3D vector $[0, 0, \pm J_z]$. The only non-zero contribution is along the *z*-axis, perpendicular to the TEC plates, and can be equal to $-J_z$ or $+J_z$. The scalar current density can be defined as:

$$J_z = \frac{I_{feed}}{A_{leg}} \tag{5}$$

where J_z is the scalar current density along the *z*-axis, I_{feed} is the TEC feed current and A_{leg} is the cross sectional area of the single thermoelectric leg.

In the *intermediate modeling step*, the thermoelectric legs are all doped p-type and are fed in parallel. The current density vector is now equal to $[0, 0, +J_z]$. Given the parallel configuration, and in order to maintain the same thermoelectric effect in each leg as the *real device*, the TEC feed current becomes *N* times bigger, where *N* is the number of thermoelectric legs installed in the module.

In the *homogeneous model*, there is no distinction between thermoelectric legs and air. The homogeneous layer is supplied by a

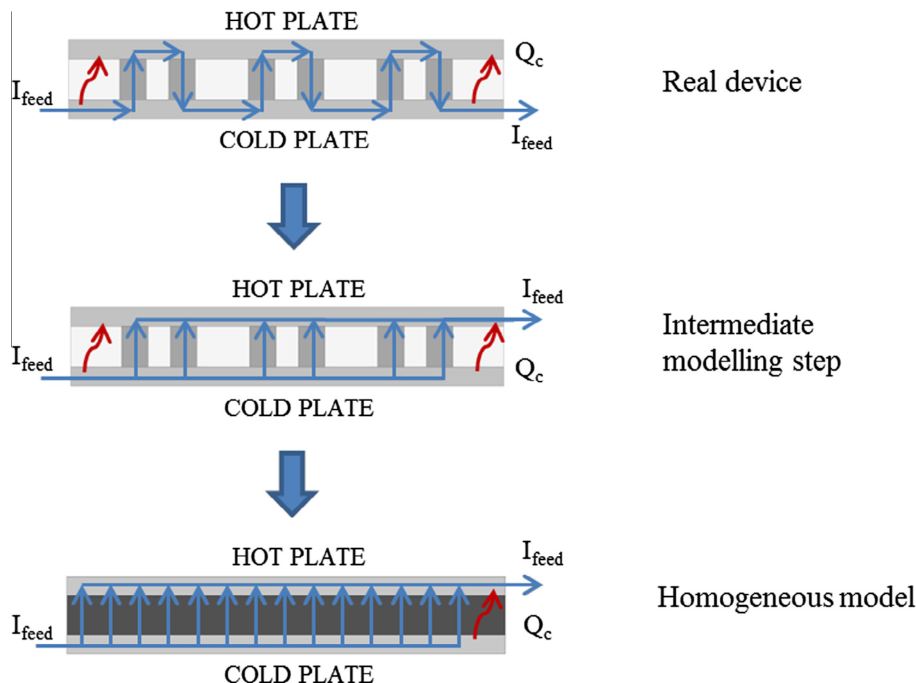

Fig. 2. Illustration of the simplification process for the TEC model. The longitudinal section and the working principle of the *real device* and of the *homogeneous model* are included. For the sake of a better understanding, an intermediate step of the model development, called *intermediate modelling step*, is also included.

uniform electric current equal to $N \cdot I_{feed}$, in the positive z-axis direction. A different current density needs to be defined:

$$J_z' = \frac{NI_{feed}}{A_{tot}} = \frac{NI_{feed}}{A_{tot}} \cdot \frac{NA_{leg}}{NA_{leg}} = \frac{I_{feed}}{A_{leg}} \cdot \frac{A_{\text{BiTe}}}{A_{tot}} = J_z x_{\text{BiTe}} \tag{6}$$

where J_z' is the equivalent scalar current density for the homogeneous model, A_{tot} is the total cross sectional area of the thermoelectric module, A_{BiTe} is equal to N times A_{leg} and represents the cross sectional area occupied by the thermoelectric legs in the *real device*, and x_{BiTe} is the ratio between A_{BiTe} and A_{tot}. x_{BiTe} is also equal to the volume ratio between bismuth telluride and the total volume of the intermediate layer.

3.3.2. Effective Seebeck coefficient

Given the TEC PDE for the homogeneous layer in Eq. (2), we want to maintain the same thermoelectric cooling effect $\boldsymbol{J}S$ as the *real device*. First, it is assumed that the Seebeck coefficient of the layer does not change with the homogenization process. However, the current density has changed and it can be imposed:

$$J_z'S = J_zS' \rightarrow S' = Sx_{\text{BiTe}} \tag{7}$$

More intuitively, one could think that the thermoelectric cooling effect is now generated with the same scalar current density J_z as the *real device*, but only by a portion of the layer (x_{BiTe}), ideally occupied by the Bi_2Te_3 legs. Although the cooling effect is maintained to be the same, the homogeneous approximation spreads it equally along the whole layer.

3.3.3. Effective thermal conductivity of the layer

The heat transfer within the intermediate layer occurs mainly from a cooler plate to the other, while the temperature gradient along the direction parallel to the plates is expected to be negligible. It is therefore assumed that the effective thermal resistance of the layer is equal to the parallel coupling of the thermal resistances, of air and Bi_2Te_3, between the hot and cold plate.

$$k' = k_{air}\frac{A_{air}}{A_{tot}} + k_{\text{BiTe}}\frac{A_{\text{BiTe}}}{A_{tot}} = k_{air}(1 - x_{\text{BiTe}}) + k_{\text{BiTe}}x_{\text{BiTe}} \tag{8}$$

where k' is the thermoelectric layer equivalent thermal conductivity for the homogeneous model, and t is the thermoelectric layer thickness.

3.3.4. Effective electrical conductivity of the layer

In analogy with the effective thermal conductivity calculation, and neglecting the air electrical conductivity:

$$\sigma' = \sigma_{\text{BiTe}}x_{\text{BiTe}} + \sigma_{air}x_{air} = \sigma_{\text{BiTe}}x_{\text{BiTe}} \tag{9}$$

where σ' is the thermoelectric layer equivalent electric conductivity for the homogeneous model. Consequently the Joule heating term can be calculated as:

$$Q'_{JouleHeating} = \frac{x_{Bi_2Te_3}}{\sigma_{Bi_2Te_3}}\boldsymbol{J} \cdot \boldsymbol{J} = \frac{J_z^2}{\sigma_{Bi_2Te_3}}x_{Bi_2Te_3} \tag{10}$$

Again, the original Joule losses are maintained, but are spread uniformly along the layer because of the homogeneous approximation.

A suitable high-temperature commercial cooler was disassembled and analyzed, so the main geometric features could be measured. They are summarized in Table 2.

The properties of Bismuth Telluride S_{BiTe}, k_{BiTe} and σ_{BiTe} from [53] were implemented as non-linear functions of temperature. In order to better match the performance of the high-temperature commercial cooler, a linear coefficient was multiplied to the expressions of the Bi_2Te_3 Seebeck coefficient, thermal conductivity, and electrical conductivity. The linear coefficients are the result of a best fit analysis based on experimental data and are respectively equal to $S_1 = 1.30$, $k_1 = 0.80$, and $\sigma_1 = 1.15$.

Table 2
Geometric features of the modelled thermoelectric cooler.

Parameter	Description	Value
h_{TEC}	Total height of the module	3.90 mm
l_{TEC}	Edge length of the module	40.0 mm
$h_{Al_2O_3}$	Height of the hot/cold plate	0.95 mm
N	Number of thermoelectric legs	254
$h_{Bi_2Te_3}$	Height of the single thermoelectric leg	2.00 mm
$l_{Bi_2Te_3}$	Edge length of the single thermoelectric leg	1.30 mm
A_{leg}	Cross sectional area of a thermoelectric leg	1.69e−6 m^2
$x_{Bi_2Te_3}$	Volume fraction of semiconductor materials	0.27

3.4. Topology optimization and SIMP method

The topology optimization approach was used to assess which distribution of aluminum/thermal insulation inside the electronics unit minimized the temperature of the HTS electronics. Filling the electronics unit with only thermal insulation would maximize the thermal protection of the cooling zone from heat leakages, but would not provide an effective thermal path for the rejected heat to flow to the well environment. The Peltier module would therefore not be able to work within the cooling design conditions. Filling the electronics unit with aluminum, instead, would enhance the heat rejection process, but would not protect the cooling zone from heat leakages, making the cooling process ineffective. A tradeoff needs to be reached and the Solid Isotropic Material with Penalization (SIMP) method allowed looking for an optimized solution.

The main goal of the SIMP method, as part of the density-based topology optimization approaches, is to achieve a binary design within the optimizable domain, where the design variable can be equal to 0, representing thermal insulation, or to 1, representing aluminum. The topology optimization problem can be stated as follows:

$$minimize: f_{obj}(T, \rho_{design}) = \frac{1}{A_{PCB}}\int_{\Omega_{PCB}} T d\Omega_{PCB} \tag{11}$$

$$subject\ to: 0 \leqslant \rho_{design} \leqslant 1 \tag{12}$$

$$\boldsymbol{r}(T, \rho_{design}) = 0 \tag{13}$$

where f_{obj} is the objective function to minimize, equal to the integral average of the temperature distribution along the PCB surface Ω_{PCB}; A_{PCB} is the PCB area surface; ρ_{design} is the design variable that can range between 0 (thermal insulation) and 1 (aluminum), and the distribution of which needs to be optimized; $\boldsymbol{r}$ (T, ρ_{design}) is the residual of the state governing equations within the discretized system.

A PDE-based density filter [54] was used to smooth the interfaces between aluminum and insulator and to introduce a minimum length scale into the design. The PDE-based filter was used because it can be implemented in the optimization model with little additional effort and it offers a computationally efficient method of density filtering. The PDE that was used for filtering is stated in Eq. (14).

$$-r^2\nabla^2\tilde{\rho} + \tilde{\rho} = \rho_{design} \tag{14}$$

where $\tilde{\rho}$ is the filtered density field and r is a filter parameter, defined as 1.5 times the maximum element size and equal to 3e−3 m. Since density filtering inherently introduces a band of intermediate densities between aluminum and insulator, the

filtered design variable field $\tilde{\rho}$ was then projected towards 0 and 1 to obtain a crisp design. For this purpose a smoothed threshold projection [55] was used.

$$\bar{\tilde{\rho}}_i = \frac{\tanh(\beta\eta) + \tanh(\beta(\tilde{\rho}_i - \eta)}{\tanh(\beta\eta) + \tanh(\beta(1 - \eta))} \quad (15)$$

where $\tilde{\rho}_i$ is the projected density field, η is the projection threshold, equal to 0.5, and β defines the steepness of the projection.

When applying the topology optimization SIMP method, it is not possible to theoretically guarantee the convergence to a global optimum. Nevertheless, it is possible to tune the optimization parameters through the continuation method to ensure that the solution is close to the global optimum [56]. In this study, using a steep projection at the beginning of the optimization could result in convergence to local minima. Therefore, a continuation approach [55] was used to ramp β, which means that the optimization was started with an almost linear projection ($\beta = 1$) and β was subsequently gradually increased to steepen the projection function. Thus, one could ensure that the optimization problem is convexified at the beginning of the optimization, while ending up with a crisp design.

The difference of thermal conductivity between aluminum and thermal insulation was accounted by an interpolation function k_{SIMP} that defined the effective thermal conductivity of the optimizable chassis.

$$k_{SIMP} = k_{ins} + (k_{Al} - k_{ins})\bar{\tilde{\rho}}^p \quad (16)$$

where k_{SIMP} is the effective thermal conductivity, $k_{ins} = 0.17$ W m^{-1} K^{-1} and $k_{Al} = 138$ W m^{-1} K^{-1} are respectively the thermal conductivities of the insulator and of the aluminum, $\bar{\tilde{\rho}}$ is the projected design variable, and p is the penalization coefficient. When performing topology optimization for continuous design variables, intermediate regions (areas where the design variable assumes intermediate values between 0 and 1) can appear in the final distribution; these transition zones are not physically meaningful for the analyzed problem and need to be reduced as much as possible. Classically, a penalization coefficient $p = 3$ is used in topology optimization in combination with an active volume constraint [30] to make intermediate regions unattractive with respect to the optimization problem, and to drive the control variable towards either 0 or 1. In this work, no active volume constraint was used, nevertheless a faster convergence was found for $p = 3$, compared to a linear interpolation ($p = 1$). Therefore $p = 3$ was used for the simulations. The globally convergent version of the Method of Moving Asymptotes (GCMMA) [57] was finally used to solve the optimization problem; this algorithm is implemented in COMSOL Multiphysics [52] with the solver name *MMA*.

In this study, the structural and design constraints limited the optimization possibilities to the chassis domain only and did not require or allow the optimization of other components (e.g. metallic housing, heat spreader, TEC). However, the topology optimization approach can be used to simultaneously optimize multiple geometrical features by implementing additional interpolation functions for different optimizable domains. This process would increase the non-linearity of the optimization problem, consequentially increasing the computation cost and the risk of converging to local minima. Thus, in these cases, a more careful solution of the problem through the continuation method should be adopted.

4. Results

4.1. Definition of the optimized design concepts

The model was used to optimize the topology of the electronics unit for different boundary conditions of TEC feed current and well fluid convective heat transfer coefficient. The system was optimized for TEC feed currents $I_{feed} = 1$, 2, 3 and 4 A, where the maximum feed current stated by the analyzed commercial TEC supplier is 6 A; and for convective heat transfer coefficients $h = 10$, 25, 50, 100 and 500 W m^{-2} K^{-1}, in order to reproduce very low, low, and medium well fluid convection regimes. The well temperature T_{ext} was set to 200 °C, as the maximum temperature at which the system is expected to operate.

The optimized structure was found to be a function of the boundary conditions. Various boundary conditions led to different tradeoffs between thermal protection of the cooled electronics and excessive heat rejection from the cooler to the well. The model proved to optimize the unit according to three different design configurations: *Design* 1, where the thermal insulation of the cooled electronics is prioritized; *Design* 2, where the conduction of the excessive heat towards the well is equally important as the thermal protection; and *Design* 3, where the excessive heat rejection is crucial for the operation of the system. A more detailed illustration of the three design concepts is given in the following paragraphs.

Low feed currents and high well fluid convection coefficients led to an optimized system (*Design* 1 concept), where only an aluminum pad links the cooler hot plate to the structural chassis and provides a thermal path for the excessive heat to be dissipated radially. The remaining volume of the unit is filled with thermal insulation (Fig. 3a–d). In this case the thermal protection of the electronics is prioritized, as the heat rejection from the cooler to the well is not challenging. Low currents generate small Joule losses across the cooler and the high convection coefficients provide an effective heat rejection towards the well. The length of the aluminum plate increases when the TEC feed current grows and when the external convection coefficient decreases, so the heat can be better spread through the structural chassis and housing, towards the well.

When the feed current is increased and the well fluid convection coefficient lowered, the optimized system (*Design* 2 concept) aims at better spreading the excessive heat, coming from the cooler hot plate, around the structural chassis and housing. A better distribution of the heat enhances, in fact, the heat exchange with the well, limits the temperature gradients due to the thermal resistances, and reduces the heat backflow to the cooled electronics. This is done by adding an aluminum layer, around the structural chassis, that spreads the heat not only radially, but also along the longitudinal direction of the tool (Fig. 3e and f). A thermally insulating layer still protects the cooled components from the hot surroundings. The thickness of the aluminum layer grows when the feed current, and the Joule losses, increase or when the well fluid convection coefficient decreases.

A third type of optimized design (*Design* 3 concept) appeared for $I_{feed} = 4$ A and $h = 10$ W m^{-2} K^{-1}, which respectively correspond to the highest feed current and the lowest convection coefficient that were simulated. In this case the power dissipation rate, due to Joule heating, proves to be much higher than the capability of the well fluid to remove heat through the convective mechanism. The generated heat flux increases the HTS electronics temperature above the well temperature, making active cooling infeasible at these operating conditions. The optimization process hence strongly prioritizes the heat rejection by creating a thermal path between the PCB and the well fluid, while two thin insulating layers protect the electronics from the cooler hot plate and from the HTNS electronics (Fig. 3g and h).

The balance between thermal protection of the cooled electronics and rejection of the excessive heat is reached differently for each set of boundary conditions and with different aluminum-thermal insulation ratios. Computing the volume percentage of employed aluminum, over the total optimizable volume, helps to

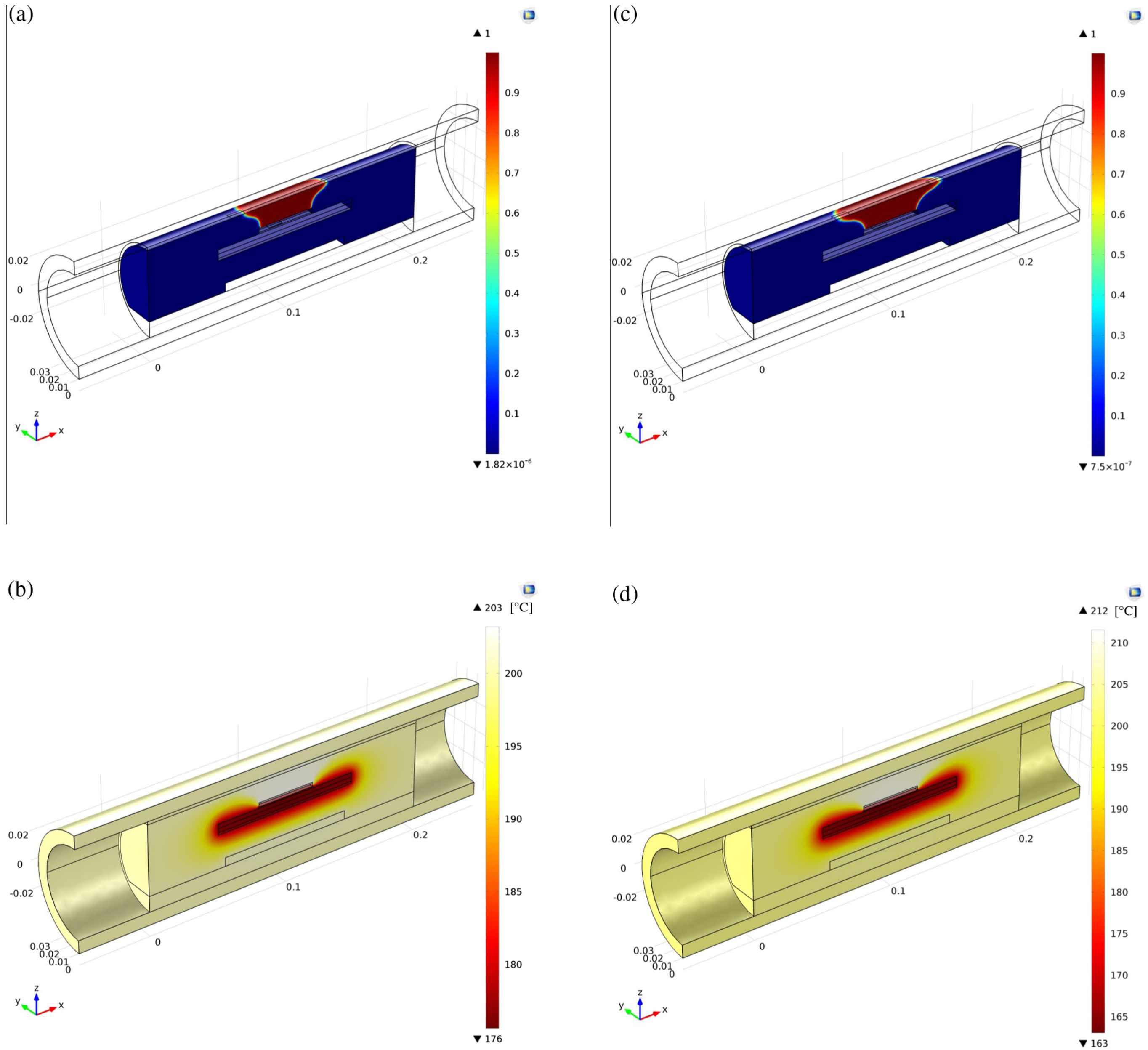

Fig. 3. Density field and resulting temperature distribution of the optimized *Design* 1 concept at I_{feed} = 1 A/h = 500 W m^{-2} K^{-1} (a and b), and at I_{feed} = 2 A/h = 100 W m^{-2} K^{-1} (c and d); of the optimized *Design* 2 concept at I_{feed} = 3 A/h = 50 W m^{-2} K^{-1} (e and f), and of the optimized *Design* 3 concept at I_{feed} = 4 A/h = 10 W m^{-2} K^{-1} (g and h). The density fields illustrate the different distributions of aluminum (red) and thermal insulation (blue), for the four optimized systems. (For interpretation of the references to color in this figure legend, the reader is referred to the web version of this article.)

Fig. 3 (*continued*)

have a clearer picture of the optimized designs trend with the boundary conditions. That can be calculated with the following expression:

$$R = \frac{1}{V_\Omega}\int_\Omega \bar{\bar{\rho}}\, d\Omega \quad (17)$$

where V_Ω is the volume of the optimizable domain and $\bar{\bar{\rho}}$ is the projected design variable.

The amount of employed aluminum decreases with the convection coefficient and increases with the feed current (Fig. 4); more in general, more aluminum is employed when a better heat rejection to the well is needed.

4.2. Comparison of the optimized designs

Defining the categories of the optimized topologies is only the first step towards the selection of a final design for the actively cooled electronics unit. The performance of the optimized designs, at conditions they were not optimized for, is also an important feature to take into account. Furthermore, a cross-validation between the resulting topologies can be used to check for convergence to local minima. It can be detected if an optimized design does not show the best performance at the boundary condition it was optimized for.

A first sensitivity analysis was carried out to evaluate how the performance of an optimized system would change at different well fluid convection regimes. The electronics section was first optimized for a certain value of feed current and well fluid convection; the optimized design was then simulated at different values of convection coefficient, maintaining the TEC feed current constant. The resulting performances were compared as illustrated

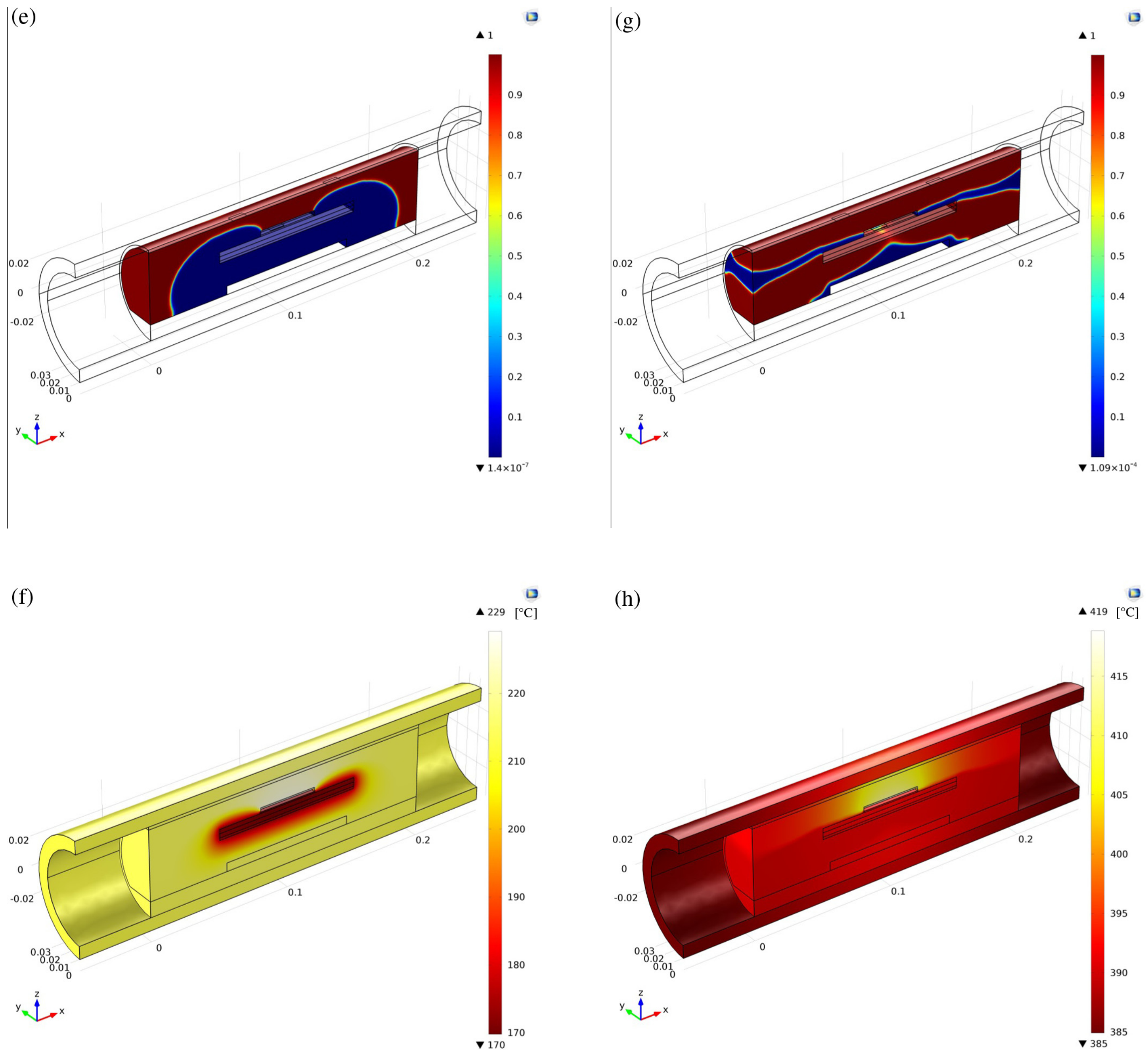

Fig. 3 (*continued*)

Fig. 3 (*continued*)

in Fig. 5. The performance of the system was evaluated in terms of HTS electronics average temperature, computed through the objective function reported in Eq. (11).

Fig. 5a reports the performance trend with h of the systems optimized for $h = 10\ \mathrm{W\,m^{-2}\,K^{-1}}$ and $I_{feed} = 1$, 2, and 3 A. As forecast, the HTS electronics is maintained colder at higher h values, when the heat rejection to the well is enhanced. Furthermore, higher feed currents are able to keep the electronics colder only if the well fluid is able to absorb the additional excessive heat, generated by the higher Joule losses. The lowest T_{HTS}, at a certain convection regime, is given by the system that was optimized for it.

Unexpectedly, it was found that the systems optimized for the same feed current operate very closely to each other, independently on the value of h they were optimized for. The performance trends of the systems optimized for $I_{feed} = 1$, 2 and 3 A, and $h > 10\ \mathrm{W\,m^{-2}\,K^{-1}}$, would in fact overlap with the corresponding three curves illustrated in Fig 5a. A maximum mismatch of only 0.05 °C, 0.01 °C, and 1.47 °C was found between the performance trends of the systems optimized for $I_{feed} = 1$, 2, and 3 A, respectively. This analysis proved that the optimization process is not significantly sensitive to the considered well fluid convection range. In other words, the length of the aluminum pad, which characterizes the *Design* 1 concept, as well as the thickness of the aluminum layer, which characterizes the *Design* 2 concept, do not significantly affect the performance of the optimized systems between 1 A and 3 A.

On the contrary, not all the topologies optimized for 4 A have a similar behavior. As Fig. 5b shows, the system optimized for 4 A and $10\ \mathrm{W\,m^{-2}\,K^{-1}}$ (*Design* 3 concept) maintains the electronics at a significantly lower temperature at low convection coefficients, compared to the one optimized for 4 A and $25\ \mathrm{W\,m^{-2}\,K^{-1}}$. However, above $25\ \mathrm{W\,m^{-2}\,K^{-1}}$ the system optimized for 4 A and $25\ \mathrm{W\,m^{-2}\,K^{-1}}$ (*Design* 2 concept) is able to maintain the HTS electronics down to a 37 °C lower temperature. In analogy with the previous cases, the other designs optimized for 4 A and $h > 25\ \mathrm{W\,m^{-2}\,K^{-1}}$ were found to operate similarly to the case

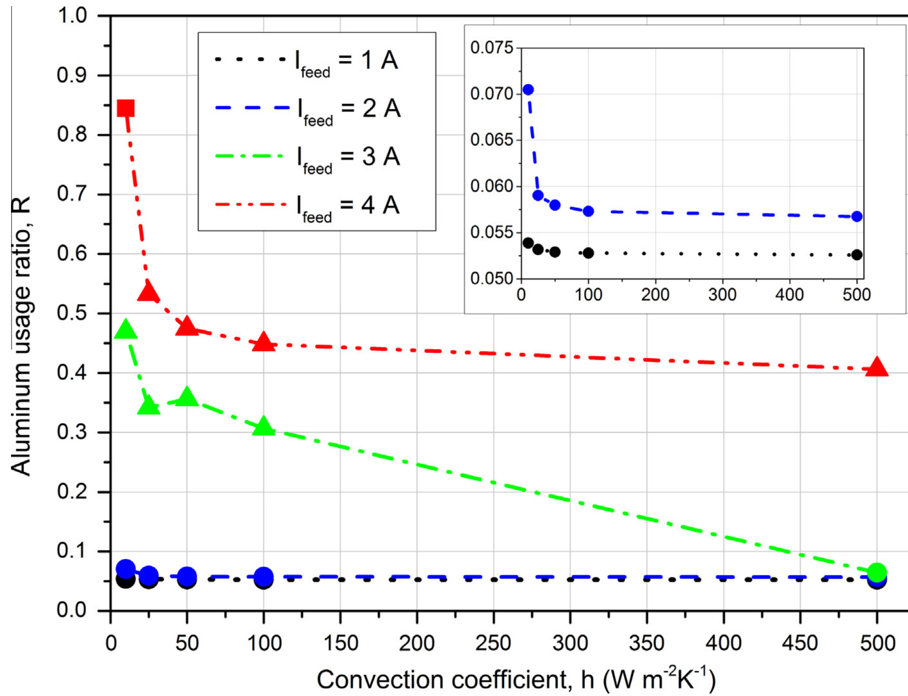

Fig. 4. *R* vs. well fluid convection coefficient, for different TEC feed currents. The three different symbols correspond to the three obtained design configurations: ● = *Design* 1, ▲ = *Design* 2, ■ = *Design* 3.

optimized for 4 A and $h = 25\ \text{W m}^{-2}\,\text{K}^{-1}$, with a maximum mismatch between the performance trends of 6.67 °C.

In an analogue way, the sensitivity of the optimized topologies to the TEC feed current was studied. The electronics unit was initially optimized for a certain value of well fluid convection coefficient and of TEC feed current; the resulting optimized design was then simulated at different values of feed current, while maintaining the value of h constant.

Fig. 6 shows that the optimization process is more sensitive to the feed current than to the external convection coefficient. The mismatch between the curves is now larger and can go up to several degrees Celsius. As expected, the lowest T_{HTS}, at a certain TEC feed current, is given by the system that was optimized for it.

An optimal feed current I_{opt}, which minimizes the HTS electronics temperature, can be individuated. Increasing the TEC feed current enhances the thermoelectric effect and the heat transport from the cold to the hot plate. However, that makes the Joule losses within the module larger, in turn causing a larger excessive heat flux that needs to be rejected to the wellbore, and a higher heat backflow to the HTS electronics through the thermal insulation. The optimal current I_{opt} can be defined as the TEC feed current at which the marginal gain in absorbed heat flux from the cold plate, due to an infinitesimal increase of the TEC feed current, becomes smaller than the heat flux that leaks back to the cooled electronics through the insulation. I_{opt} varies slightly for each optimized design, and depends mainly on h.

I_{opt} is equal to ~1.2 A for $h = 10\ \text{Wm}^{2}\,\text{K}^{-1}$, to ~1.9 A for $h = 25\ \text{W m}^{-2}\,\text{K}^{-1}$, to ~2.3 A for $h = 50\ \text{W m}^{-2}\,\text{K}^{-1}$, to ~2.6 A for $h = 100\ \text{W m}^{-2}\,\text{K}^{-1}$, and to ~2.9 A for $h = 500\ \text{W m}^{-2}\,\text{K}^{-1}$. With respect to the considered operations at non-optimal current, working at I_{opt} can reduce the electronics temperature by a maximum ~244 °C at $h = 10\ \text{W m}^{-2}\,\text{K}^{-1}$, ~59 °C at $h = 25\ \text{W m}^{-2}\,\text{K}^{-1}$, ~29 °C at $h = 50\ \text{W m}^{-2}\,\text{K}^{-1}$, ~17 °C at $h = 100\ \text{W m}^{-2}\,\text{K}^{-1}$, and ~20 °C at $h = 500\ \text{W m}^{-2}\,\text{K}^{-1}$. The designs that prove to maintain the HTS electronics at the lowest temperature, around the optimal current, are the ones optimized for 2 A and 3 A.

4.3. Design of the actively cooled electronics section

The results from the topology optimization study were used to define the final design of the actively cooled electronics unit (Fig. 7); practical assembly constraints were also taken into account. The heat transfer analysis of the system revealed that the ideal operating condition for the device to work is a combination of high TEC feed current, that guarantees a strong cooling effect, and a high well fluid convection regime, which guarantees an effective removal of the excessive heat. Unfortunately the well fluid convection regime can vary significantly in operation, and therefore the tool needs to be designed for the worst-case design convection coefficient, which was set to $25\ \text{W m}^{-2}\,\text{K}^{-1}$. *Design* 3 can be immediately discarded from the suitable topologies, as it was optimized for a convection regime that is outside the design conditions and for a TEC feed current that is far from the optimal ones. As mentioned previously, the optimal feed current for $h = 25\ \text{W m}^{-2}\,\text{K}^{-1}$ is ~1.9 A; the optimized design for these conditions corresponds to the *Design* 1 concept (see Fig. 4). However, *Design* 2 proved to have a very similar performance around the optimal feed current (see Fig. 6), which means that there is some freedom in the design of the aluminum pad and/or layer. The lower mass of aluminum that characterizes *Design* 1 would make the tool lighter, though, which is preferable from a logistic and operational point of view. Furthermore, the aluminum pad, which provides the radial thermal path from the cooler hot plate to the structural chassis, proved to be the fundamental feature for effective operation of the system: an aluminum pad was therefore implemented in the final design. No aluminum layer was included, except for two walls, 10 mm thick, at the two ends of the chassis: they provide mechanical stability, an additional thermal path to better spread the heat in the case of a poor heat rejection rate, and are suitable for the installation of pins for the assembly of the system. The chassis would be in fact split into a top half, where the cooling system and the PCB are installed, and a bottom half, on which the HTNS electronics are mounted. Two smaller pads, with

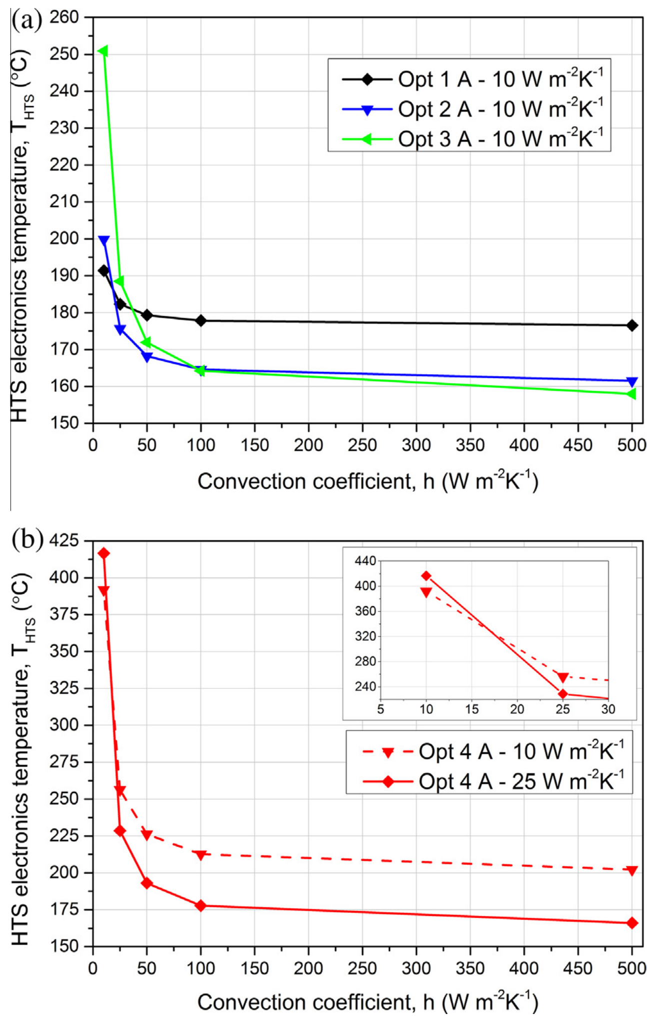

Fig. 5. HTS electronics temperature vs. Convection coefficient for three different systems, optimized for $h = 10\ \mathrm{W\ m^{-2}\ K^{-1}}$ and $I_{feed} = 1, 2, 3$ A (a). HTS electronics temperature vs. Convection coefficient for two systems optimized for $h = 10$, $25\ \mathrm{W\ m^{-2}\ K^{-1}}$ and $I_{feed} = 4$ A (b).

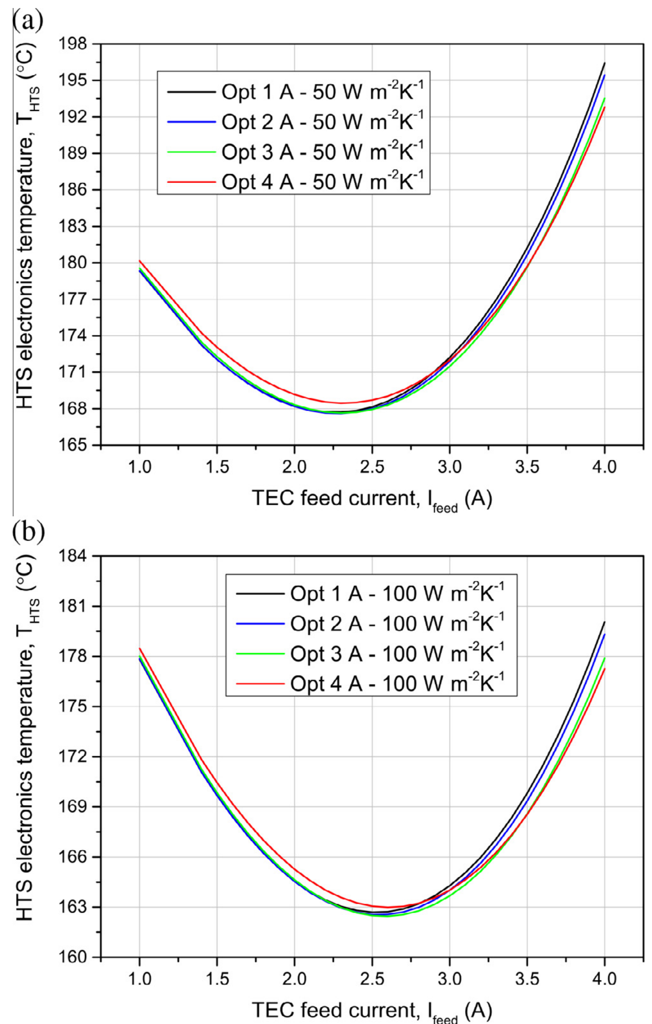

Fig. 6. HTS electronics temperature vs. TEC feed current for four different designs, optimized for $I_{feed} = 1, 2, 3$ and 4 A, and $h = 50\ \mathrm{W\ m^{-2}\ K^{-1}}$ (a) and $100\ \mathrm{W\ m^{-2}\ K^{-1}}$ (b).

threaded holes, were designed in the top part of the chassis: they support a plastic screw system that clamps the cooler between the heat spreader and the chassis, while ensuring effective thermal contacts. The remaining volume was filled with thermal insulation, for thermal protection of the cooled electronics.

Simulations showed the chosen design operates very similarly to the optimized systems (Table 3). The difference in HTS electronics temperature is very small when operating at 1 A or 2 A, as the final design is very similar to the *Design* 1 concept. The HTS electronics are in fact maintained maximum 0.11 °C above the optimized case. When operating at 3 A and 4 A, the mismatch becomes larger, since the *Design* 2 concept would perform better at higher feed currents. However, when operating at 3 A, the HTS components are always maintained less than 1 °C above the optimized system. The mismatch becomes larger than 1 °C for operations at 4 A; that can be considered irrelevant, since $I_{feed} = 4$ A is far from the observed optimal TEC settings and the system would always aim at operating between 2 A and 3 A, close to the optimal conditions.

Table 3 also shows the final system fulfills the design conditions and the electronics can be maintained below 175 °C for every well fluid convection regime, as far as a control system can regulate the TEC feed current around the optimal one. The only exception occurs for the case at $h = 25\ \mathrm{W\ m^{-2}\ K^{-1}}$, where the heat rejection is very poor and the electronics can only be maintained between at an average temperature of 175 °C and 176 °C; this result is still considered acceptable given the small mismatch.

In order to have a clearer overview of the operation of the final design, a characteristic curve that displays the HTS average temperature as a function of the TEC feed current and of the well fluid convection coefficient is illustrated in Fig. 8. As already observed in the previous analyses, the performance of the system is enhanced when high well fluid convection regimes occur. At high TEC feed currents the performance of the system is more sensitive to the convection coefficient than at low I_{feed}, as it can be noticed from the curve slopes on the h-T_{HTS} plane. On the I_{feed}–T_{HTS} plane, instead, it can be observed the HTS electronics temperature reaches a minimum at I_{opt}, which varies for different conditions of well fluid convection. The I_{opt} front is highlighted with red line. The optimal operating current changes more rapidly with h at low convection regimes, where the excessive heat rejection is crucial, and engages a flatter trend while the convection coefficient grows.

4.4. Model validation

The system illustrated in Fig. 7 was manufactured and assembled as shown in Fig. 9. Thermal grease was used to interface the heating components to the chassis, lead wires were installed to

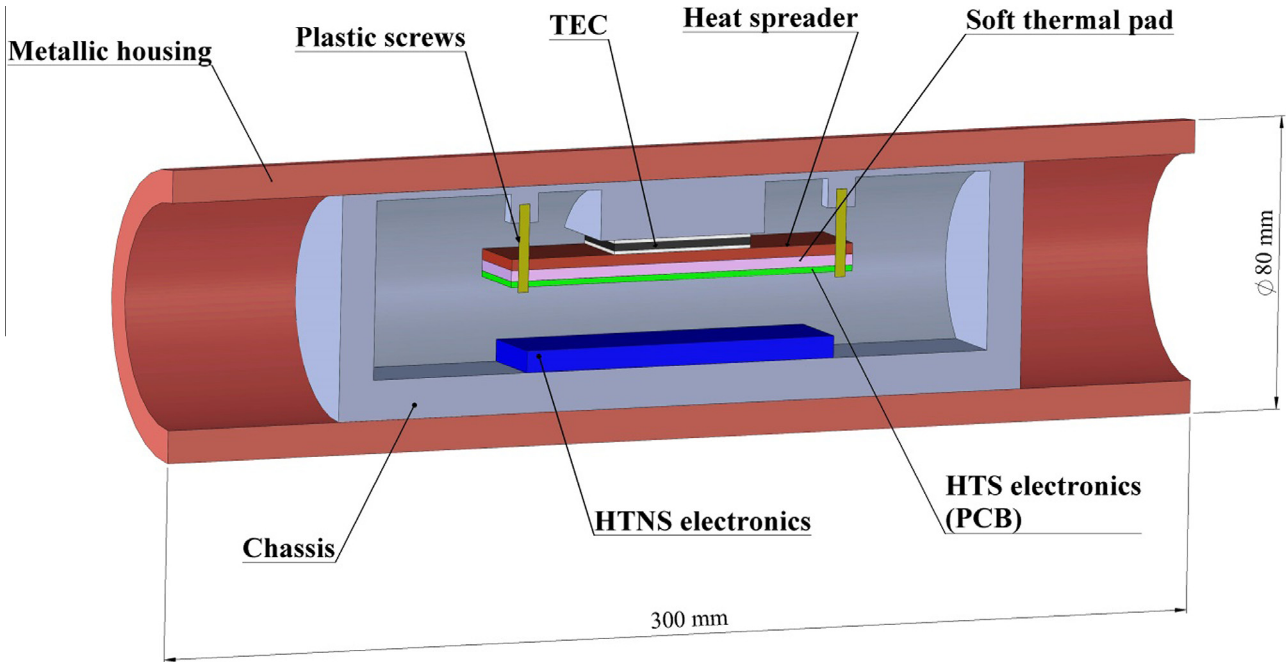

Fig. 7. Illustration of the longitudinal section of the final design. The thermoelectric cooler is clamped between the aluminum pad and the heat spreader through two plastic screws. The remaining volume within the chassis is filled with thermal insulation.

Table 3
Comparison between the performance of the final design (Design) and the optimized systems (Opt). $\Delta T = T_{HTS,design}\ T_{HTS,Opt}$.

h (W m^{-2} K^{-1})	*Opt – 1 A* T_{HTS} (°C)	*Design – 1 A* T_{HTS} (°C)	ΔT (°C)
25	182.31	182.41	0.10
50	179.32	179.43	0.11
100	177.83	177.94	0.11
500	176.56	176.67	0.11
	Opt – 2 A T_{HTS} (°C)	*Design – 2 A* T_{HTS} (°C)	
25	175.63	175.68	0.05
50	168.18	168.23	0.05
100	164.54	164.57	0.03
500	161.46	161.48	0.02
	Opt – 3 A T_{HTS} (°C)	*Design – 3 A* T_{HTS} (°C)	
25	188.22	188.93	0.71
50	171.48	171.87	0.39
100	163.68	163.90	0.22
500	157.12	157.35	0.23
	Opt – 4 A T_{HTS} (°C)	*Design – 4 A* T_{HTS} (°C)	
25	228.62	233.59	4.97
50	192.79	195.71	2.92
100	177.25	179.29	2.04
500	165.23	166.37	1.14

feed the two sets of electronics through external power supplies, and type-K thermocouples were installed to monitor the temperature profile within the tool.

The assembled tool was tested in a dry and ventilated hot environment, where a fan recirculated air at the set-point temperature T_{oven}. *Power Supply* 1 provided the electric power to the TEC, while a voltmeter and a current meter measured the feed voltage and current, respectively. *Power Supply* 2 provided the feed power to the test electronics. A *Data Acquisition System* monitored and recorded the temperature distribution within the tool. The schematic of the experimental setup is reported in Fig. 10.

Two different ovens, in size and air flow capacity, were used to test the tool at 180 °C, 190 °C, and 200 °C. For every oven temperature, the TEC feed current was varied between 1 A and 4 A, and the steady state temperature distribution across the tool was recorded. Furthermore, each test was characterized by the calculation of the average heat transfer coefficient $\bar{h}_{exp}$, which described the heat transfer, mainly driven by convection, occurring at the steady state between the tool housing and the oven environment. Eq (18) was calculated from the balance of the energy fluxes through the control volume shown in Fig. 10, and was used for this purpose. The term $\bar{h}_{exp}$ provides the reference boundary condition for the model validation process.

$$\bar{h}_{exp} = \frac{(P_{TEC} + P_{HTS} + P_{HTNS})}{A_{housing} \cdot (\bar{T}_{housing} - T_{oven})} \tag{18}$$

where $\bar{h}_{exp}$ is the average heat transfer coefficient at the tool housing surface; P_{TEC}, P_{HTS}, and P_{HTNS} are respectively the electric feed powers of the cooler, of the HTS electronics, and of the HTNS electronics; $A_{housing}$ is the outer surface area of the housing; $\bar{T}_{housing}$ is the average of the readings from the four thermocouples installed on the outer surface of the housing (see Fig. 9d); and T_{oven} is the measured oven temperature.

The experimental temperatures were measured with type-K thermocouples and compared with the predictions from the model (see Table 4). An accuracy of ±1.5 °C was used for the thermocouples, according to *IEC 584 Class* 1. Model data points were obtained from the corresponding 1 cm^2 square location within the finite-element geometry; actual measurements were compared with the average temperatures, while lower and higher error bands were introduced according to the model prediction for the maximum and minimum temperatures within the 1 cm^2 square.

Fig. 11 shows the comparison between the experimental and the model temperatures, from the TEC hot plate (probe shown Fig. 9b) and HTS electronics (probe shown in Fig. 9c), which represent the most relevant temperatures for the system operation.

As indicated in Fig. 11, experimental data and model forecasts revealed a good match, and proved the model can reproduce the performance of the real system with a good degree of accuracy. Fig. 11a shows the majority of the data points for the HTS electronics temperature are close to the perfect prediction. Points from the tests at lower convection show a slightly worse match with the

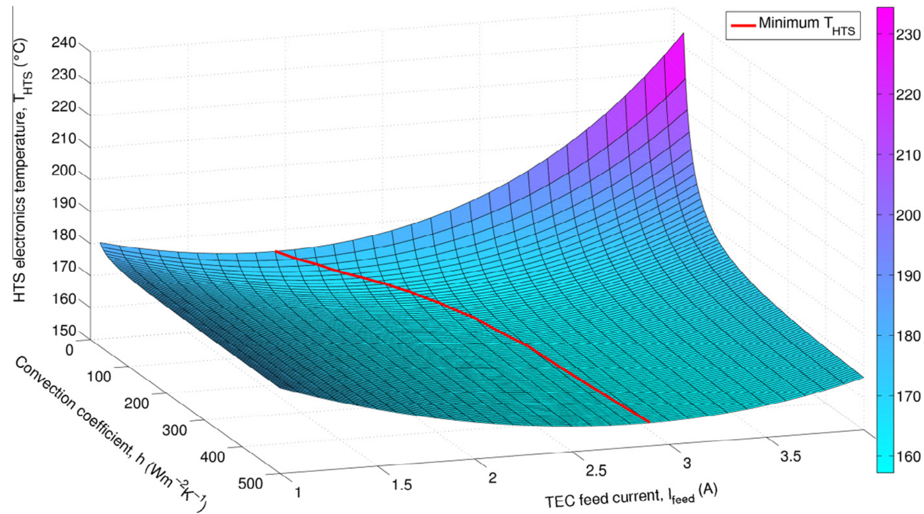

Fig. 8. Characteristic curve of the finally designed TEC integrated system. The plot reports the simulated performance of the cooling system, in a 200 °C environment, as HTS electronics temperature vs. convection coefficient and TEC feed current. The minimum HTS electronics temperature, for each operating condition, is highlighted by a red line. The color bar expresses the HTS electronics temperature in degrees Celsius. (For interpretation of the references to color in this figure legend, the reader is referred to the web version of this article.)

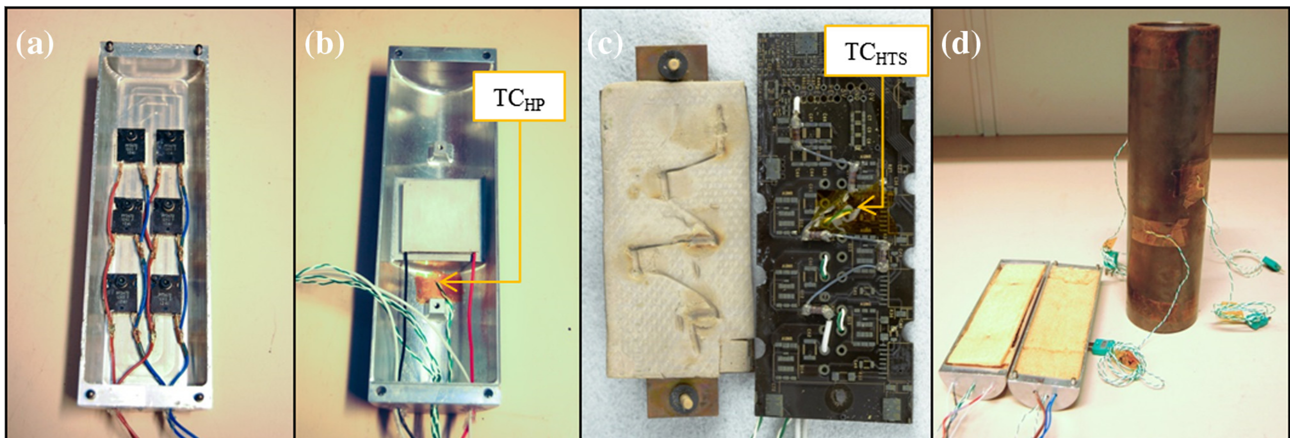

Fig. 9. Illustration of the manufactured components. Six resistors were installed on the chassis bottom half to reproduce the HTNS electronics (a).The TEC was located in the chassis top half, with two threaded holes for implementing the clamping system; the thermocouple TC_{HP} measured the temperature on the hot side of the TEC (b). Five resistors were soldered onto the PCB, to simulate the HTS electronics, and coupled with the soft thermal pad and the heat spreader (c); the thermocouple TC_{HTS} measured the temperature of the PCB. The two halves of the chassis were finally filled with thermally insulating foam and inserted into the metallic housing; the temperature of the housing was monitored by four thermocouples (d).

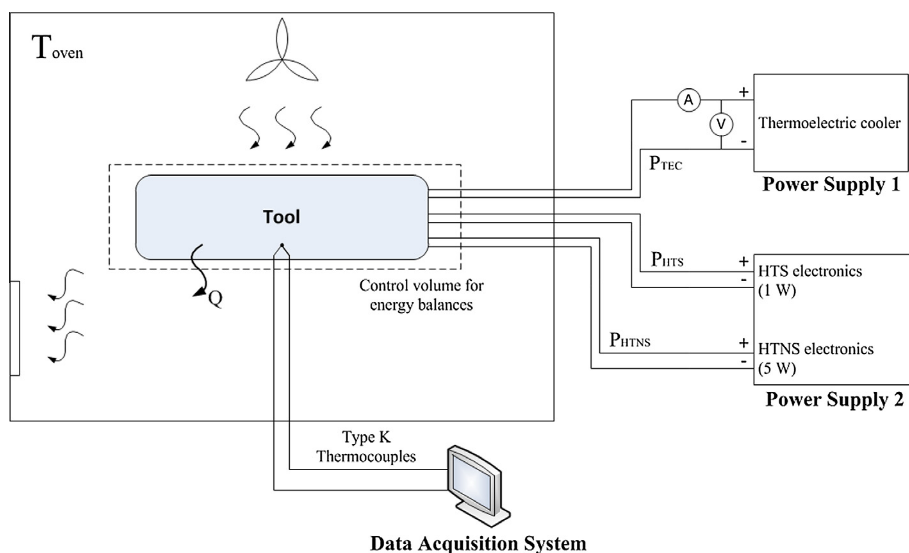

Fig. 10. Schematic of the experimental setup. The main components characterizing the experimental validation of the model are illustrated.

Table 4
Temperatures and parameters characterizing both the experimental procedure and the model validation. The first three columns define the boundary conditions of each test, while the last four columns summarize the TEC hot plate (HP) and HTS electronics temperatures, at stationary operations.

T_{oven} (°C)	I_{feed} (A)	$\bar{h}_{exp}$ (W m^{-2} K^{-1})	$T_{HTS,model}$ (°C)	$T_{HTS,exp}$ (°C)	$T_{HP,model}$ (°C)	$T_{HP,exp}$ (°C)
Lower convection oven						
180.4	1.0	35.1	160.3	161.6	185.3	185.6
180.7	1.5	30.9	154.4	156.4	189.3	190.3
180.5	2.0	29.1	152.0	155.0	194.5	196.0
180.3	2.5	28.2	153.8	157.6	201.3	203.1
190.8	1.0	36.8	170.7	172.5	195.6	195.5
189.9	1.5	31.0	163.9	166.7	198.7	199.3
190.1	2.0	31.1	161.3	164.4	203.5	204.3
190.6	2.5	30.3	163.9	167.8	210.8	211.4
199.3	1.5	35.6	172.7	176.7	207.3	207.3
199.5	2.0	32.3	171.0	175.9	212.9	213.0
199.7	2.3	31.7	172.0	177.4	216.8	216.9
Higher convection oven						
180.7	1.0	65.7	158.7	157.7	183.7	182.6
181.0	2.0	62.4	146.2	145.4	188.7	188.4
180.7	3.0	57.7	147.1	145.8	197.5	197.9
181.1	3.5	59.0	153.7	151.1	203.5	203.1
190.8	1.0	72.9	168.7	168.3	193.6	191.8
191.0	2.0	64.8	156.4	155.7	198.7	197.0
190.2	3.0	60.8	157.0	156.2	206.7	205.7
190.8	3.3	61.1	160.5	158.8	210.1	208.6
200.4	1.5	75.9	170.3	170.7	205.0	203.0
201.8	2.0	73.4	167.1	168.8	209.1	207.4
200.3	2.3	66.3	164.9	166.2	210.1	208.9
200.1	3.0	62.6	167.9	168.1	216.7	214.3

model, which predicts slightly lower HTS electronics temperatures. Based on the thermocouple readings and visual inspection of the system, no degradation at the cold side of the TEC was observed after the tests. No visible breakdown of the thermal interface material, which is rated for a maximum operating temperature of 200 °C, or change in the thermal resistances were detected. The mismatch in the model results can be attributed to the degradation of the TEC itself, which occurred in the ~50 h of testing at high temperature in the higher convection oven, which were carried out first chronologically. The degradation of the module consists of a decrease in the thermoelectric effect and was detected as a drop in the temperature span across the TEC and a decrease of the TEC feed voltage at constant current [58]. The lower heat transport between the plates could therefore have led to higher experimental HTS electronics temperatures. The effects of the degradation are also accentuated when operating in low convection environments and high feed currents.

Fig. 11b, instead, shows a very good match between experiments and model predictions for the hot plate temperatures, both for the lower and higher convection scenarios.

The previously described behavior can also be observed in Fig. 12, where a comparison between model and experiments is reported as a function of the TEC feed current. Experimental results show a good agreement with the model predictions and are able to reproduce the forecast trends with I_{feed}. Furthermore, the experimental data confirm the presence of an optimal operating current I_{opt}, as described in the Section 4.3, and the trend is reproduced by the model. Although Fig. 12c shows a slightly larger mismatch between predictions and experiments, for the lower convection scenario, the convex trend and the value of I_{opt} are reproduced with good approximation. The observed I_{opt} values varied with the outer fluid convection regime, confirming the behavior predicted by the model. As expected and previously shown, lower electronics temperatures were obtained in the higher convection scenario.

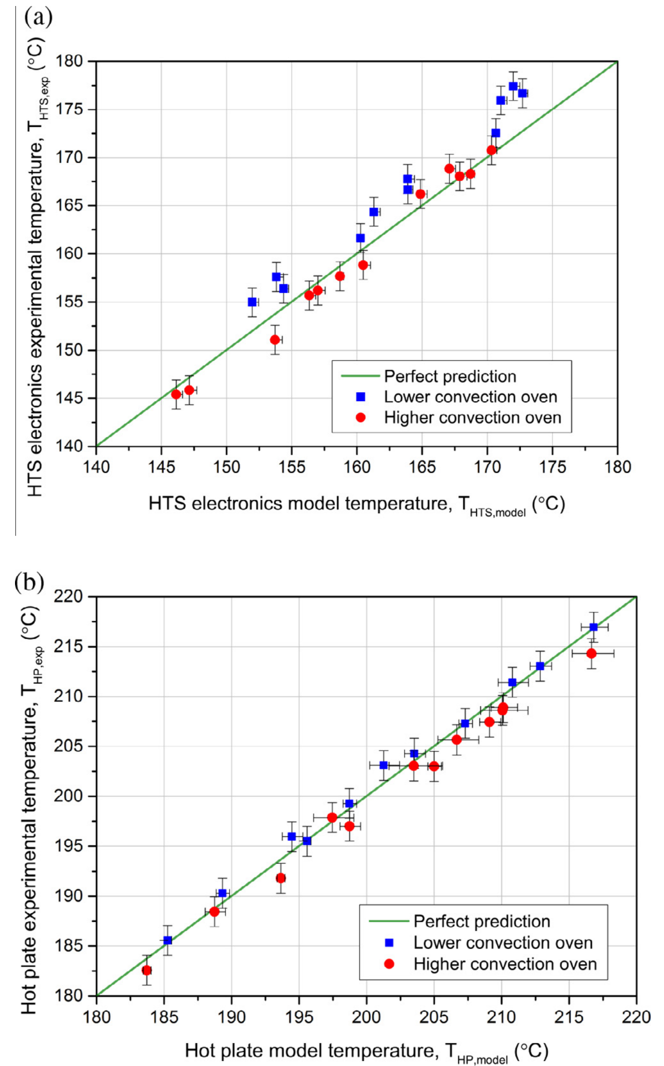

Fig. 11. Comparison between experimental data and model prediction. HTS electronics temperatures are reported in figure (a) and hot plate temperatures are reported in figure (b). Results from all the tests from both the ovens are illustrated, and compared to the perfect prediction scenario.

5. Conclusions

This work presented and demonstrated a method of integrating a TEC into a system with specific design constraints, using topology optimization combined with a 3D finite element model of the system. This technique allows efficient integration of TECs by optimizing how they interact thermally with their surroundings, and is suitable for any TED application where the module must be mounted in a fixed volume. As a specific application, the optimization method was used to aid in the design of an actively cooled electronics unit for a downhole oil well intervention tool, and to optimize the integration setup of a commercial thermoelectric cooler. The geometry to be optimized and the problem-related governing equations were implemented in COMSOL Multiphysics, together with the SIMP topology optimization approach. The model was used to optimize the distribution of aluminum and thermally insulating material within the unit, so the temperature-sensitive electronics could be maintained at a minimum temperature. The system was optimized for several well conditions and for the TEC feed current, and different design concepts

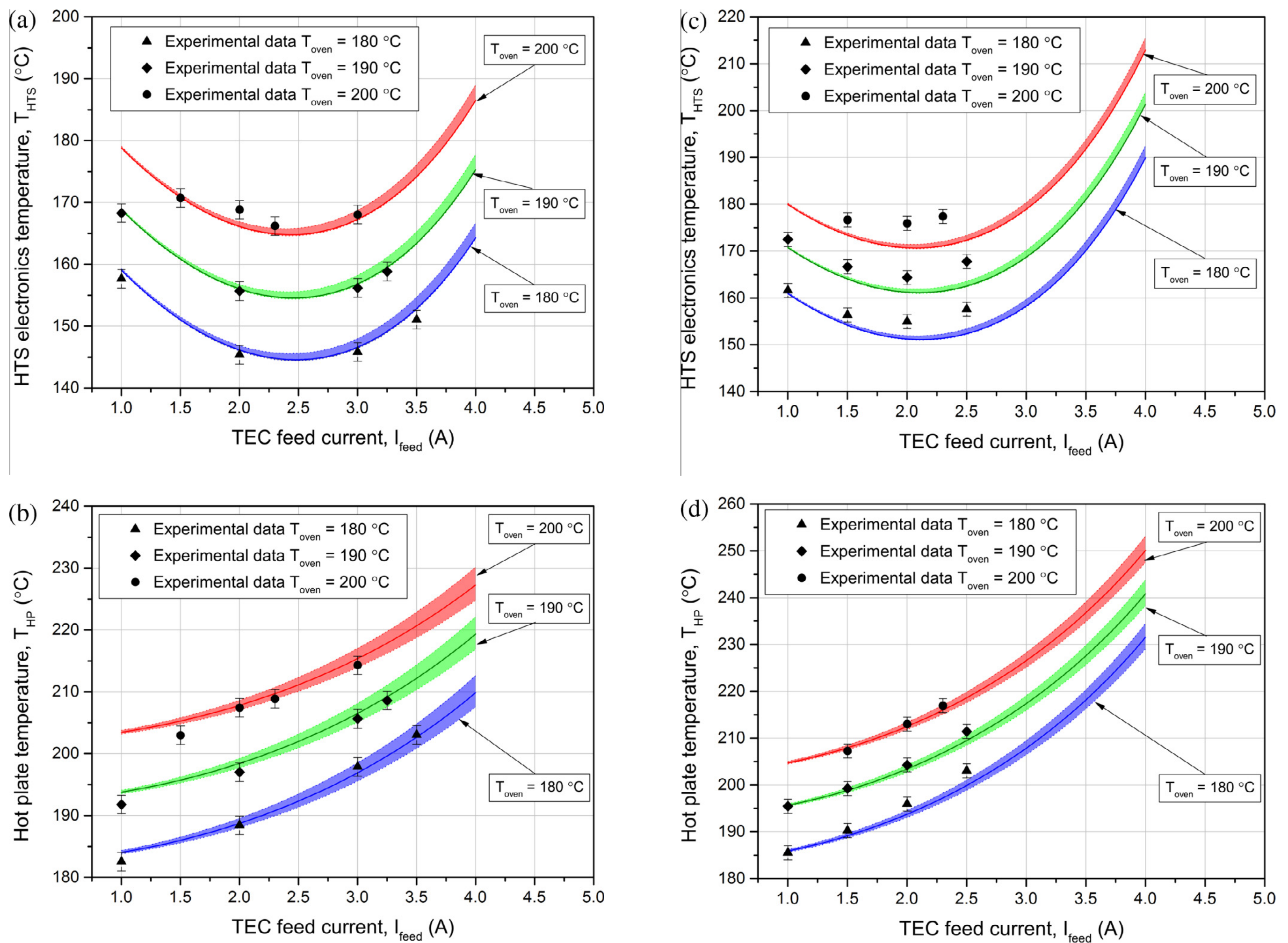

Fig. 12. Comparison between experimental and modeling temperatures vs. TEC feed current, at different oven temperatures. Figures (a) and (b) report respectively the HTS electronics and the hot plate temperatures trends vs. TEC feed current, for the higher convection oven. Figures (c) and (d) report respectively the HTS electronics and the hot plate temperatures vs. TEC feed current, for the lower convection oven. The colored lines show the trends predicted by the model, defined by the maximum and minimum temperatures from the 1 cm^2-square model probe. The single points represent the experimental data. (For interpretation of the references to color in this figure legend, the reader is referred to the web version of this article.)

Fig. 12 (*continued*)

were generated and analyzed. When heat rejection was critical (high TEC feed currents and low convection regimes) the mass of aluminum increased for better conduction out of the tool to the well; when the heat rejection was not critical (low TEC feed currents and high convection regimes) the thermal protection of the cooled electronics was prioritized, and the use of aluminum was significantly lower than the previous cases in favor of the thermal insulator. Optimized systems were found to cool the electronics down to a temperature 37 °C colder than before optimization. Furthermore, the optimization process proved to be not significantly sensitive to the convection range, but highly sensitive to the operating current of the TEC. An optimal operating current, which minimizes the temperature of the HTS components and depends on the well fluid convection regime, was found. This analysis highlighted the importance of a control system that would always seek the best operating conditions for the cooler.

Topology optimization was used to implement the final design of the electronics unit, which simulations predicted to perform very closely to the optimized systems. The final design was manufactured and tested in an experimental setup, at different operating conditions. Model predictions reproduced experimental results with good agreement, replicated the predicted optimal feed currents, and demonstrated the effectiveness of the design method. Topology optimization was shown to be a powerful design tool that can be combined with a TED model to yield optimized designs for thermoelectric integrated systems.

Acknowledgements

S. Soprani and K. Engelbrecht would like to show their gratitude to the Danish Ministry of Technology and Innovation (contract 1355-00051B) and to Welltec A/S for partially funding this work. The authors would also like to acknowledge the TopTEN project, sponsored through the Sapere Aude Program of the Danish Council for Independent Research (DFF–4005-00320), for supporting this study.

Appendix A. Supplementary material

Supplementary data associated with this article can be found, in the online version, at http://dx.doi.org/10.1016/j.apenergy.2016.05.024.

References

[1] Rowe DM. Handbook of thermoelectrics. London: CRC Press Boca Raton; 1995. http://dx.doi.org/10.1201/9781420049718.

[2] Bell LE. Cooling, heating, generating power, and recovering waste heat with thermoelectric systems. Science 2008;321(5895):1457–61. http://dx.doi.org/10.1126/science.1158899.

[3] He W, Zhang G, Zhang X, Ji J, Li G, Zhao X. Recent development and application of thermoelectric generator. Appl Energy 2015;143:1–25. http://dx.doi.org/10.1016/j.apenergy.2014.12.075.

[4] Tritt TM, Subramanian MA. Thermoelectric materials, phenomena, and applications: a bird's eye view. MRS Bull 2006;31(3):188–98. http://dx.doi.org/10.1557/mrs2006.44.

[5] Montecucco A, Knox AR. Accurate simulation of thermoelectric power generating systems. Appl Energy 2014;118(20):166–72. http://dx.doi.org/10.1016/j.apenergy.2013.12.028.

[6] Hermes CJL, Barbosa Jr JR. Thermodynamic comparison of Peltier, stirling, and compression portable coolers. Appl Energy 2012;91(1):51–8. http://dx.doi.org/10.1016/j.apenergy.2011.08.043.

[7] Dresselhaus MS, Chen G, Tang MY, Yang R, Lee H, Wang D, et al. New directions for low-dimensional thermoelectric materials. Adv Mater 2007;19(8):1043–53. http://dx.doi.org/10.1002/adma.200600527.

[8] Snyder GJ, Toberer ES. Complex thermoelectric materials. Nat Mater 2008;7(2):105–14. http://dx.doi.org/10.1038/nmat2090.

[9] Bulusu A, Walker DG. Review of electronic transport models for thermoelectric materials. Superlatt Mictrostuct 2008;44(1):1–36. http://dx.doi.org/10.1016/j.spmi.2008.02.008.

[10] Yang Y, Ma FY, Lei CH, Liu YY, Li JY. Is thermoelectric conversion efficiency of a composite bounded by its constituents? Appl Phys Lett 2013;102(5):053905. http://dx.doi.org/10.1063/1.4791684.

[11] Abramzon B. Numerical optimization of the thermoelectric cooling devices. J Electron Packag 2007;129(3):339–47. http://dx.doi.org/10.1115/1.2753959.

[12] Heghmanns A, Beitelschmidt M. Parameter optimization of thermoelectric modules using a genetic algorithm. Appl Energy 2015;155:447–54. http://dx.doi.org/10.1016/j.apenergy.2015.06.034.

[13] Xiao J, Yang T, Li P, Zhai P, Zhang Q. Thermal design and management for performance optimization of solar thermoelectric generator. Appl Energy 2012;93(20):33–8. http://dx.doi.org/10.1016/j.apenergy.2011.06.006.

[14] Takezawa A, Kitamura M. Geometrical design of thermoelectric generators based on topology optimization. Int J Numer Methods Eng 2012;90(11):1363–92. http://dx.doi.org/10.1002/nme.3375.

[15] Chen L, Li J, Sun F. Performance optimization for a two-stage thermoelectric heat-pump with internal and external irreversibilities. Appl Energy 2008;85(7):641–9. http://dx.doi.org/10.1016/j.apenergy.2007.10.005.

[16] Pan Y, Lin B, Chen J. Performance analysis and parametric optimal design of an irreversible multi-couple thermoelectric refrigerator under various operating conditions. Appl Energy 2007;84(9):882–92. http://dx.doi.org/10.1016/j.apenergy.2007.02.008.

[17] Quan R, Tang X, Quan S, Huang L. A novel optimization method for the electric topology of thermoelectric modules used in an automobile exhaust thermoelectric generator. J Electron Mater 2013;42(7):1469–75. http://dx.doi.org/10.1007/s11664-012-2291-3.

[18] Taylor RA, Solbrekken GL. Comprehensive system-level optimization of thermoelectric devices for electronic cooling applications. IEEE Trans Compon Packag Technol 2008;31(1):23–31. http://dx.doi.org/10.1109/tcapt.2007.906333.

[19] Rezania A, Yazawa K, Rosendahl LA, Shakouri A. Co-optimized design of microchannel heat exchangers and thermoelectric generators. Int J Therm Sci 2013;72:73–81. http://dx.doi.org/10.1016/j.ijthermalsci.2013.05.002.

[20] Gou X, Xiao H, Yang S. Modeling experimental study and optimization on low-temperature waste heat thermoelectric generator system. Appl Energy 2010;87(10):3131–6. http://dx.doi.org/10.1016/j.apenergy.2010.02.013.

[21] David B, Ramousse J, Luo L. Optimization of thermoelectric heat pumps by operating condition management and heat exchanger design. Energy Convers Manage 2012;60:125–33. http://dx.doi.org/10.1016/j.enconman.2012.02.007.

[22] Bendsøe MP, Sigmund O. Topology optimization: theory, methods and applications. Berlin Heidelberg: Springer Verlag; 2004. http://dx.doi.org/10.1007/978-3-662-05086-6.

[23] Sigmund O, Maute K. Topology optimization approaches. Struct Multidiscip Optim 2013;48(6):1031–55. http://dx.doi.org/10.1007/s00158-013-0978-6.

[24] Deaton JD, Grandhi RV. A survey of structural and multidisciplinary continuum topology optimization: post 2000. Struct Multidiscip Optim 2014;49(1):1–38. http://dx.doi.org/10.1007/s00158-013-0956-z.

[25] Dede EM, Lee J, Nomura T. Multiphysics simulation: electromechanical system simulation and optimization studies. London, Heidelberg New York Dordrecht: Springer; 2014. http://dx.doi.org/10.1007/978-1-4471-5640-6_5.

[26] Li Q, Steven GP, Xie YM, Querin OM. Evolutionary topology optimization for temperature reduction of heat conducting fields. Int J Heat Mass Transfer 2004;47(23):5071–83. http://dx.doi.org/10.1016/j.ijheatmasstransfer.2004.06.010.

[27] Gersborg-Hansen A, Sigmund O, Haber RB. Topology optimization of channel flow problems. Struct Multidiscip Optim 2005;30(3):181–92. http://dx.doi.org/10.1007/s00158-004-0508-7.

[28] Sigmund O. Design of multiphysics actuators using topology optimization-Part I: One material structures. Comput Methods Appl Mech Eng 2001;190(49):6577–604. http://dx.doi.org/10.1016/s0045-7825(01)00251-1.

[29] Yin L, Ananthasuresh GK. A novel topology design scheme for the multi-physics problems of electro-thermally actuated compliant micromechanisms. Sens Actuators A 2002;97:599–609. http://dx.doi.org/10.1016/s0924-4247(01)00853-6.

[30] Bruns TE. Topology optimization of convection-dominated, steady-state heat transfer problems. Int J Heat Mass Transfer 2007;50(15):2859–73. http://dx.doi.org/10.1016/j.ijheatmasstransfer.2007.01.039.

[31] Ahn SH, Cho S. Level set-based topological shape optimization of heat conduction problems considering design-dependent convection boundary. Numer Heat Transfer, Part B 2010;58(5):304–22. http://dx.doi.org/10.1080/10407790.2010.522869.

[32] Iga A, Nishiwaki S, Izui K, Yoshimura M. Topology optimization for thermal conductors considering design-dependent effects, including heat conduction and convection. Int J Heat Mass Transfer 2009;52(11):2721–32. http://dx.doi.org/10.1016/j.ijheatmasstransfer.2008.12.013.

[33] Yoon GH. Topological design of heat dissipating structure with forced convective heat transfer. J Mech Sci Technol 2010;24(6):1225–33. http://dx.doi.org/10.1007/s12206-010-0328-1.

[34] McConnell C, Pingen G. Multi-layer, Pseudo 3D thermal topology optimization of heat sinks. In: Proceedings of the ASME 2012 international mechanical engineering congress, Houston, USA; 2012. http://dx.doi.org/10.1115/imece2012-93093.

[35] Marck G, Nemer M, Harion JL. Topology optimization of heat and mass transfer problems: laminar flow. Numer Heat Transfer, Part B 2013;63(6):508–39. http://dx.doi.org/10.1080/10407790.2013.772001.

[36] Matsumori T, Kondoh T, Kawamoto A, Nomura T. Topology optimization for fluid–thermal interaction problems under constant input power. Struct Multidiscip Optim 2013;47(4):571–81. http://dx.doi.org/10.1007/s00158-013-0887-8.

[37] Van Oevelen T, Baelmans M. Numerical topology optimization of heat sinks. In: Proceedings of the 15th international heat transfer conference; 10–15 2014. http://dx.doi.org/10.1615/ihtc15.opt.009168.

[38] Lee J, Nomura T, Dede EM. Heat flow control in thermo-magnetic convective systems using engineered magnetic fields. Appl Phys Lett 2012;101:123507. http://dx.doi.org/10.1063/1.4754119.

[39] Yaji K, Yamada T, Kubo S, Izui K, Nishiwaki S. A topology optimization method for a coupled thermal-fluid problem using level set boundary expressions. Int J Heat Mass Transfer 2015;81:878–88. http://dx.doi.org/10.1016/j.ijheatmasstransfer.2014.11.005.

[40] Alexandersen J, Aage N, Andreasen CS, Sigmund O. Topology optimisation for natural convection problems. Int J Numer Methods Fluids 2014;76(10):699–721. http://dx.doi.org/10.1002/fld.3954.

[41] Castro DA, Kiyono CY, Silva ECN. Design of radiative enclosures by using topology optimization. Int J Heat Mass Transfer 2015;88:880–90. http://dx.doi.org/10.1016/j.ijheatmasstransfer.2015.04.077.

[42] Koga AA, Lopes ECC, Villa Nova H, de Lima CR, Silva E CN. Development of heat sink device by using topology optimization. Int J Heat Mass Transfer 2013;64:759–72. http://dx.doi.org/10.1016/j.ijheatmasstransfer.2013.05.007.

[43] Dede EM, Joshi SN, Zhou F. Topology optimization, additive layer manufacturing, and experimental testing of an air-cooled heat sink. J Mech Des 2015;137(11):111702. http://dx.doi.org/10.1115/1.4030989.

[44] Dede EM. Single-phase microchannel cold plate for hybrid vehicle electronics. Semicond Therm Meas Manage Symp (SEMI-THERM) 2014. http://dx.doi.org/10.1109/semi-therm.2014.6892227.

[45] Soprani S, Haertel JHK, Lazarov BS, Sigmund O, Engelbrecht K. Topology optimization of an actively cooled electronics section for downhole tools. In: Proceedings COMSOL conference 2015, Grenoble, France; 2015.

[46] Bennett GA. Active cooling for downhole instrumentation: preliminary analysis and system selection. Mexico: Los Alamos National Laboratory; 1988.

[47] Flores AG. Active cooling for electronics in a wireline oil-exploration tool Ph.D. Thesis. USA: M.I.T; 1996.

[48] Sinha A, Joshi YK. Downhole electronics cooling using a thermoelectric device and heat exchanger arrangement. J Electron Packag 2011;133(4). http://dx.doi.org/10.1115/1.4005290. 041005-1–041005-12.

[49] Jakaboski JC. Innovative thermal management of electronics in oil well logging. M.Sc. thesis. Georgia Institute of Technology USA; 2004.

[50] Pennewitz E, Kruspeb T, Jungb S, Schillinga M. Evaluation of sorbents at elevated temperatures for downhole application. Chem Eng Trans 2012;29:1543–8. http://dx.doi.org/10.3303/CET1229258.

[51] Soprani S, Engelbrecht K, Nørgaard AJ. Active cooling and thermal management of a downhole tool electronics section. In: Proceedings of the 24th IIR international congress of refrigeration, IIF-IIR, Yokohama, Japan; 2015.

[52] COMSOL Multiphysics 5.0.

[53] Gordon JM, Ng KC, Chua HT, Chakraborty A. The electro-adsorption chiller: a miniaturized cooling cycle with applications to micro-electronics. Int J Refrig 2002;25(8):1025–33. http://dx.doi.org/10.1016/s0140-7007(02)00026-9.

[54] Lazarov BS, Sigmund O. Filters in topology optimization based on helmholtz-type differential equations. Int J Numer Methods Eng 2011;86(6):765–81. http://dx.doi.org/10.1002/nme.3072.

[55] Wang F, Lazarov BS, Sigmund O. On projection methods, convergence and robust formulations in topology optimization. Struct Multidiscip Optim 2011;43(6):767–84. http://dx.doi.org/10.1007/s00158-010-0602-y.
[56] Sigmund O, Petersson J. Numerical instabilities in topology optimization: a survey on procedures dealing with checkerboards, mesh-dependencies and local minima. Struct Optim 1998;16(1):68–75. http://dx.doi.org/10.1007/bf01214002.
[57] Svanberg K. A class of globally convergent optimization methods based on conservative convex separable approximations. SIAM J Optim 2002;12 (2):555–73. http://dx.doi.org/10.1137/s1052623499362822.
[58] Barako MT, Park W, Marconnet AM, Asheghi M, Goodson KE. Thermal cycling, mechanical degradation, and the effective figure of merit of a thermoelectric module. J Electron Mater 2012;42(3):372–81.

APPENDIX B

B.1 Technical drawings of the manufactured parts for *Prototype mark-1*

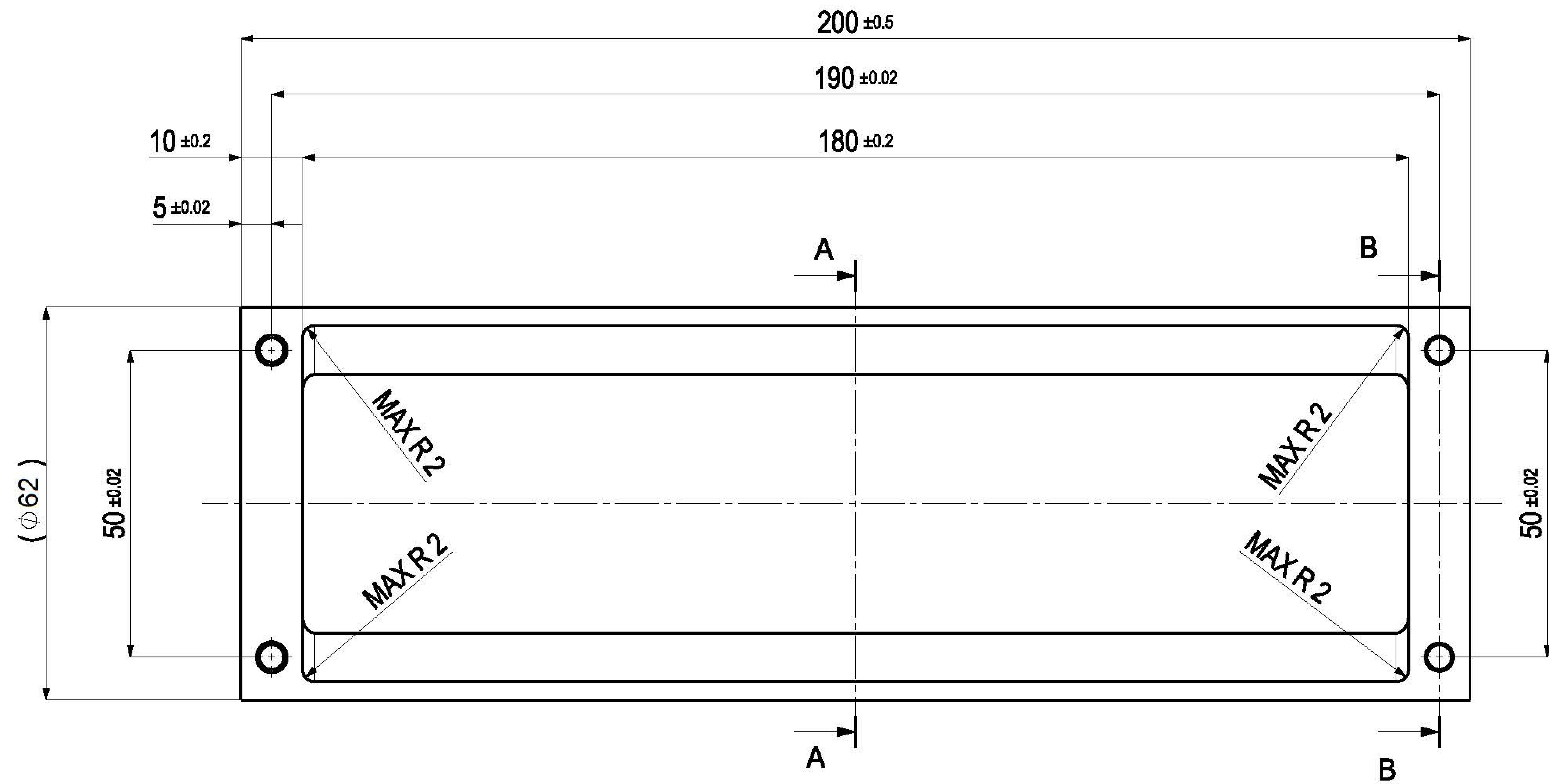

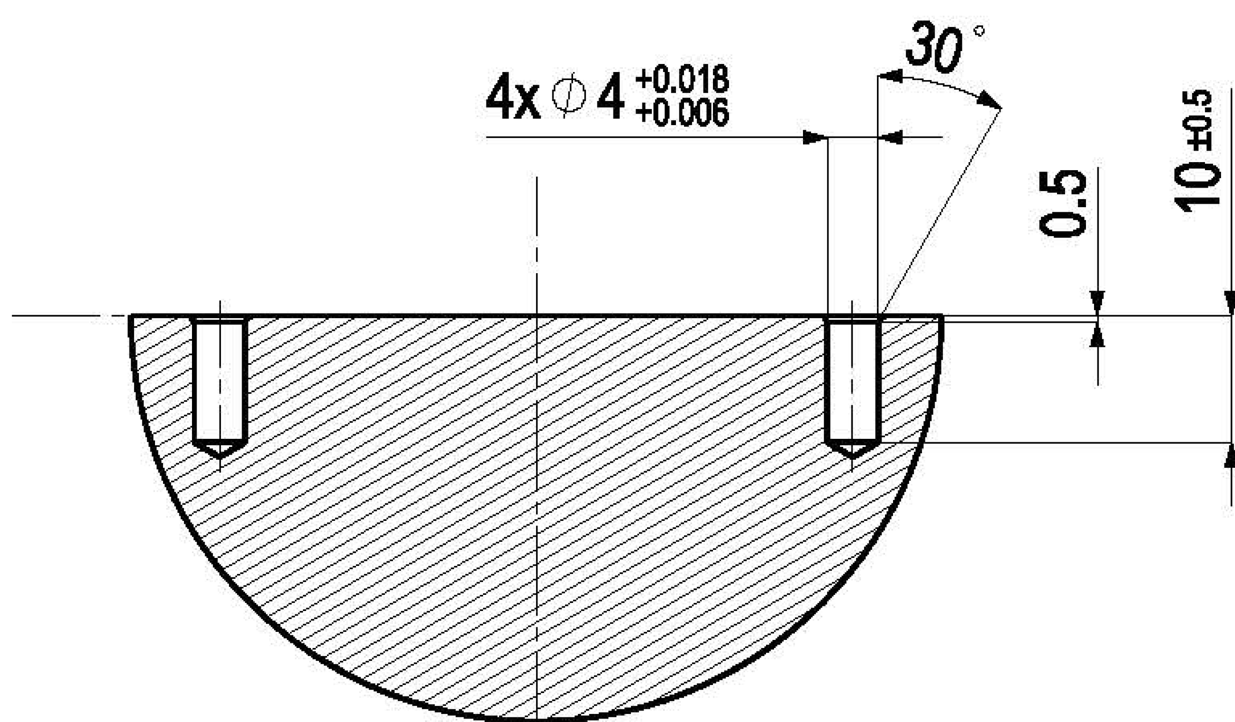

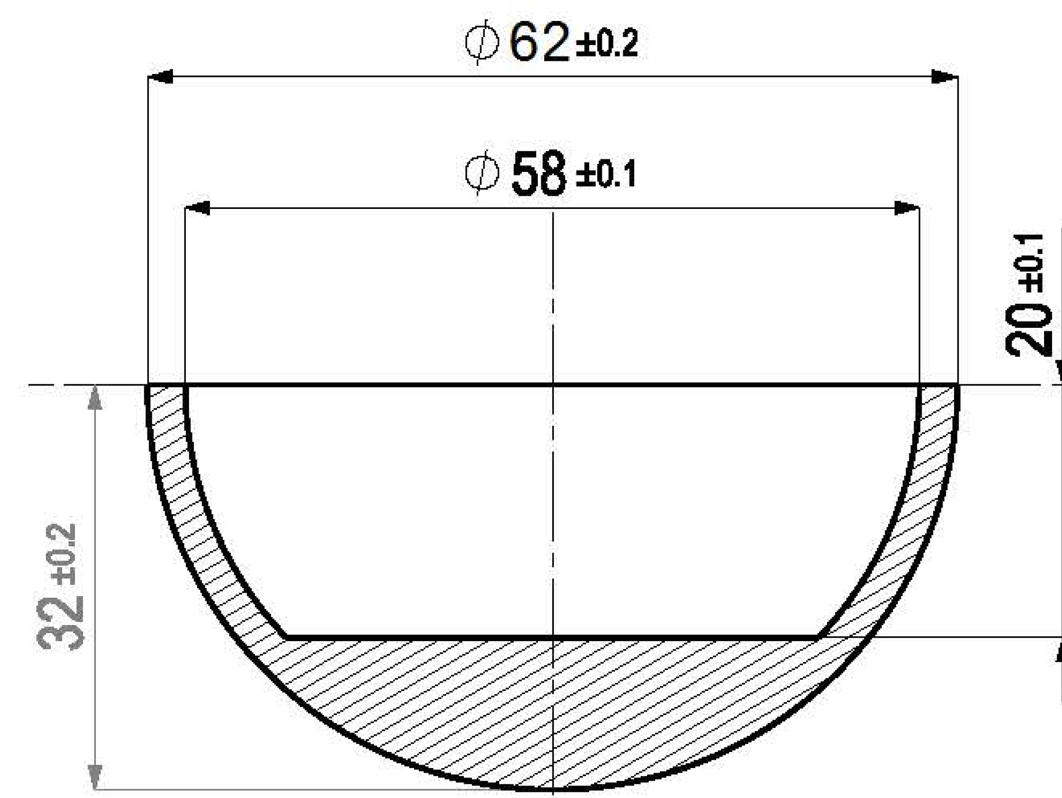

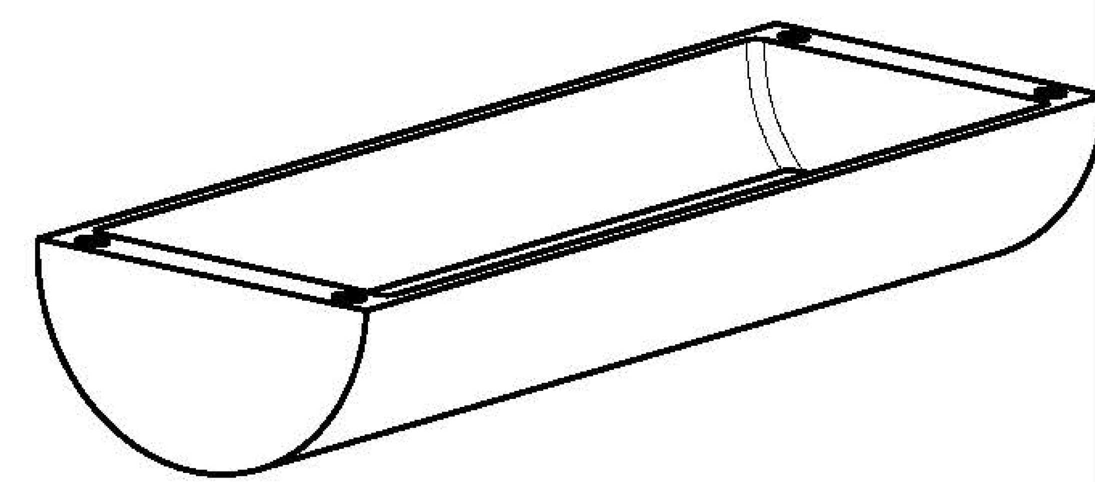

Material:	Mass (kg.):	Engineer	
Aluminum alloy		Drawn By	
		Revised By	

Description:	IPL.:	Page:	Format:	Scale:
Bottom Chassis			A3	1:1
	Drawing No.:			Rev.:

200 ±0.5
190 ±0.02
180 ±0.2
10 ±0.2
5 ±0.02
A
MAX R 2
MAX R 2
MAX R 2
MAX R 2
50 ±0.02
50 ±0.02
B
B
(41.1)
D
D
A
49.5 ±0.05
41 ±0.1
19 ±0.1
41 ±0.1

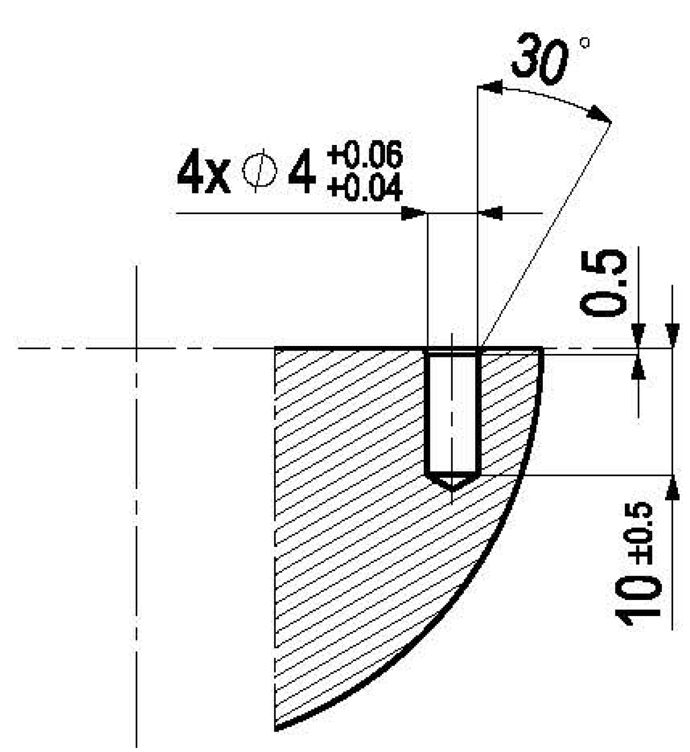

Section view D-D

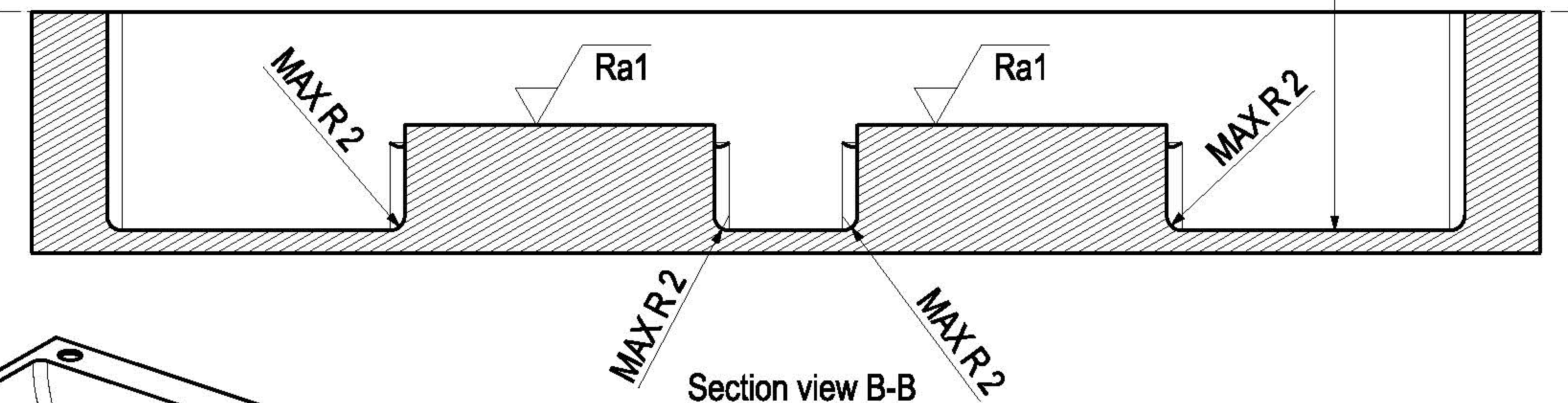

Section view B-B

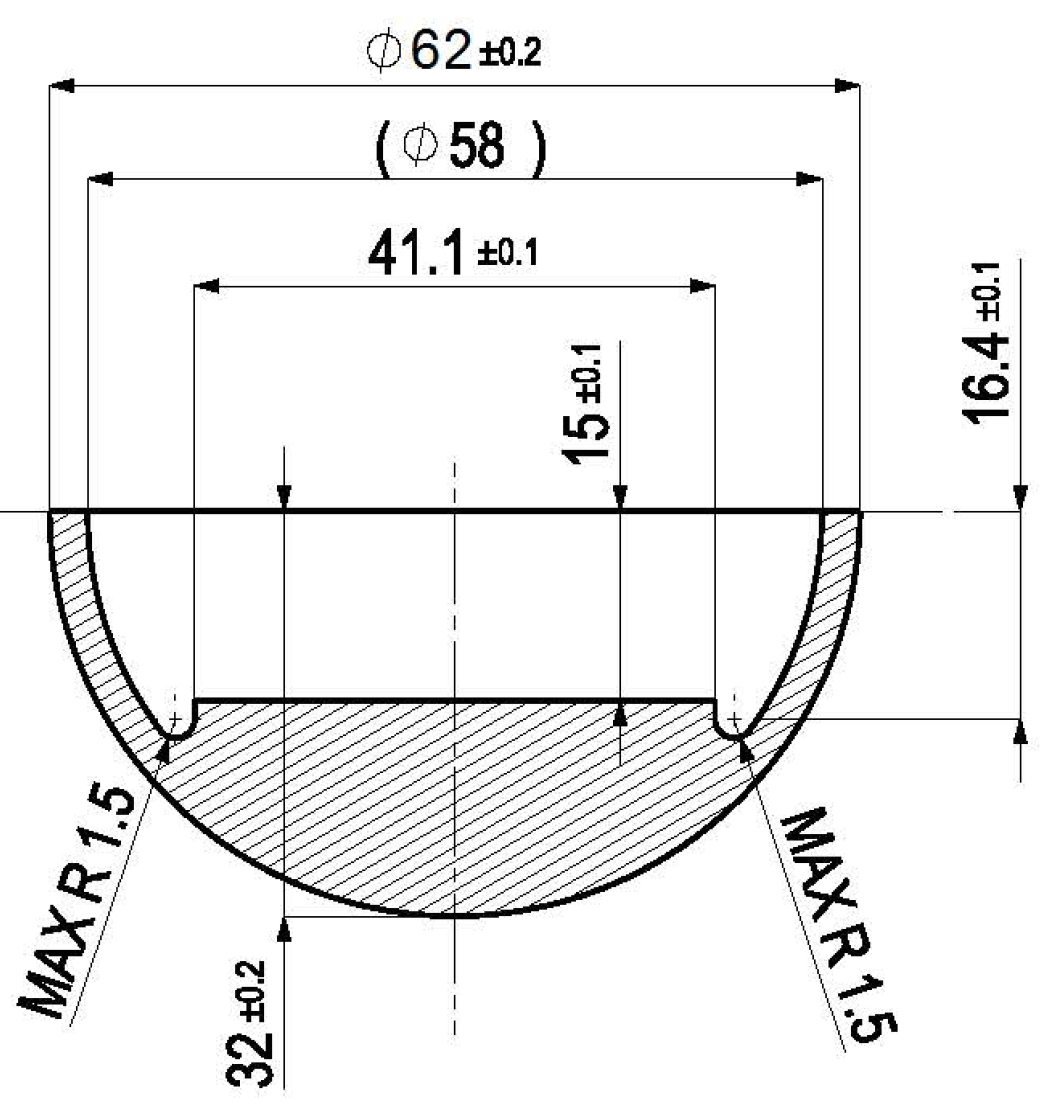

Section view A-A

Material:	Mass (kg.):	Engineer		Date:
Aluminum alloy		Drawn By		
		Revised By		

Description:	IPL.:	Page:	Format:	Scale:
Top chassis			A3	1:1
	Drawing No.:			Rev.:

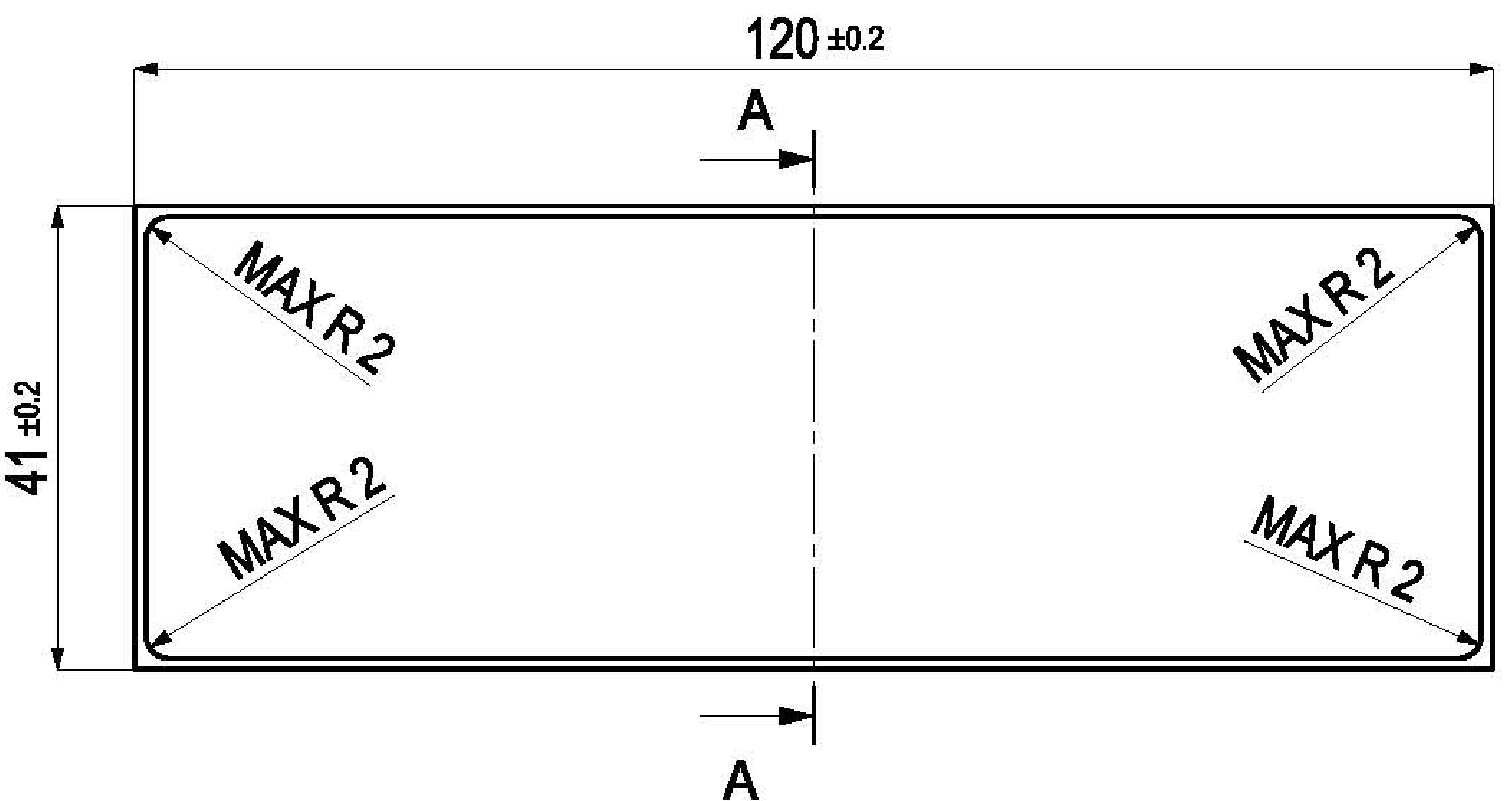

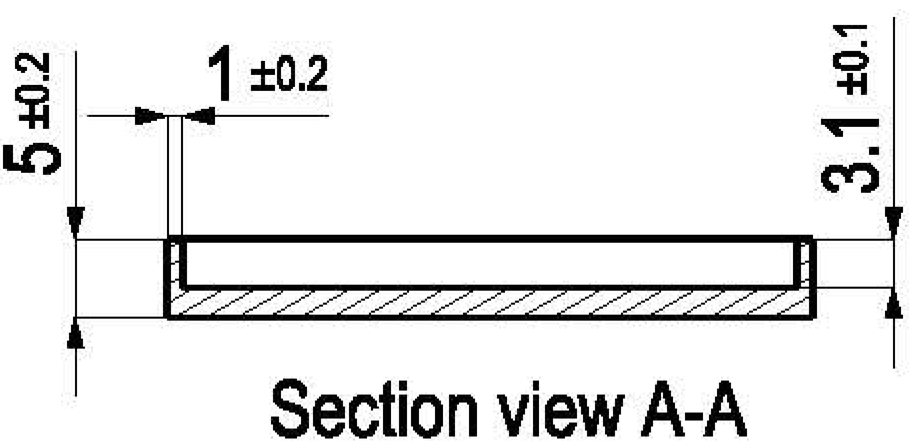

Section view A-A

Material:	Mass (kg.):	Engineer		Date:
Copper		Drawn By		
		Revised By		

Description:	IPL.:	Page:	Format:	Scale:
Heat spreader			A4	1:1
	Drawing No.:			Rev.:

B.2 Technical datasheets of the analyzed coolers, displayed in the order *Cooler #1*, *Cooler #2*, and *Cooler #3*

VT-127-1.0-1.3-71 Thermoelectric Module (Peltier Module) Specifications		Material Specifications (27 °C hot side temperature)	Material Specifications (50 °C hot side temperature)
	Vmax (V)	16.1	17.9
	Imax (A)	3.9	3.9
	Qmax (W)	36.0	39.5
	DTmax (°C)	71	80
	Operation/storage temperature	-40 °C to +200 °C	

Module *material* specifications are nominal values based on the hot-side temperature indicated. Thermoelectric material parameter tolerance is +/-10%.

In no case should the module temperature be allowed to exceed its maximum operation/storage temperature.

Please review all product and technical information, *Thermoelectric Module Mounting Procedure*, parameter definitions, FAQ's, and ordering information posted on our website before purchasing or using this product.

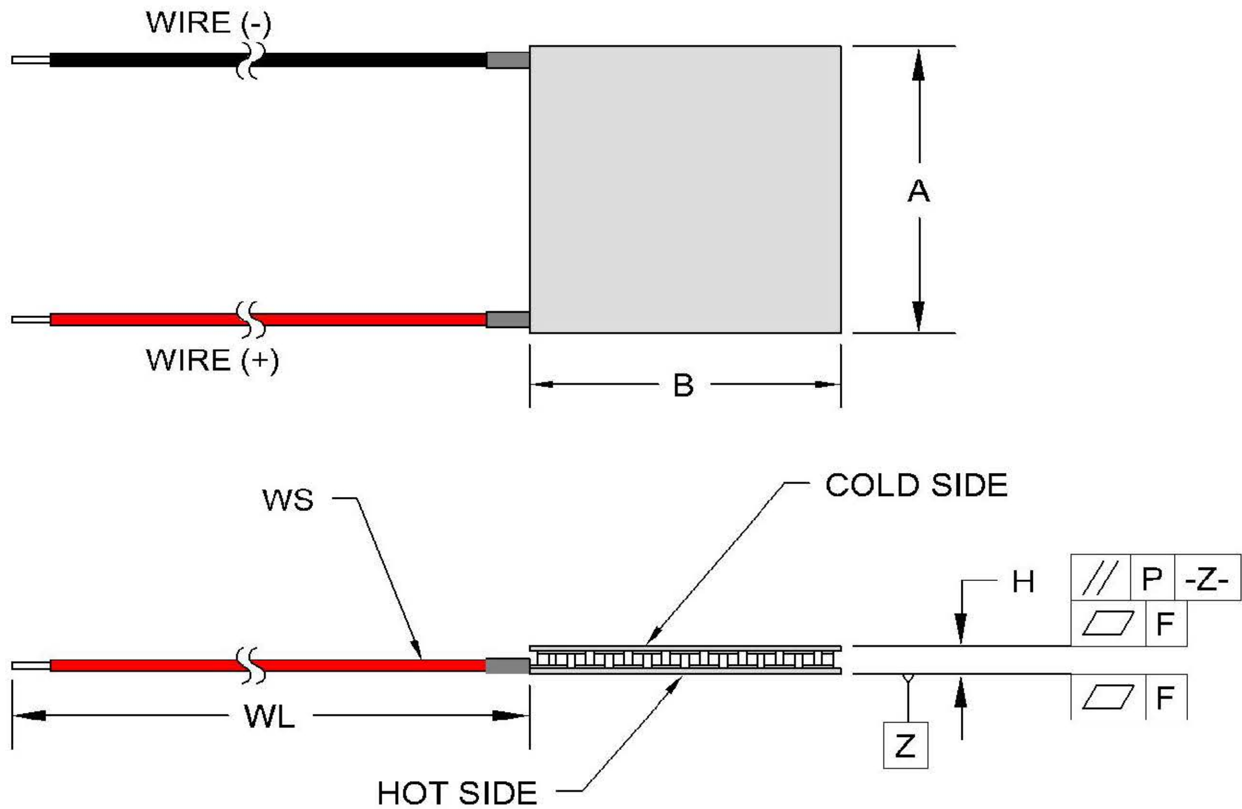

Width, A (mm)	30 +0.5/-0.2
Width, B (mm)	30 +0.5/-0.2
Height, H (mm)	3.6 ±0.05
Flatness, F (mm)	0.02
Parallelism, P (mm)	0.03
Wire Size, WS (mm²)	0.2
Wire Length, WL (mm)	120

Optional Features and Notes:

Add "P" to part number for sealing module with epoxy potting.

Maximum operating/storage temperature with potting is 150 °C

Performance graphs include thermal resistance of substrates.

RoHS Compliant

1590 Keane Drive, Traverse City, MI, 49696-8257 USA
PH: 231-929-3966 FAX: 231-929-4163 email: cool@tetech.com

© 2010 TE Technology, Inc.

1590 Keane Drive, Traverse City, MI, 49696-8257 USA
PH: 231-929-3966 FAX: 231-929-4163 email: cool@tetech.com

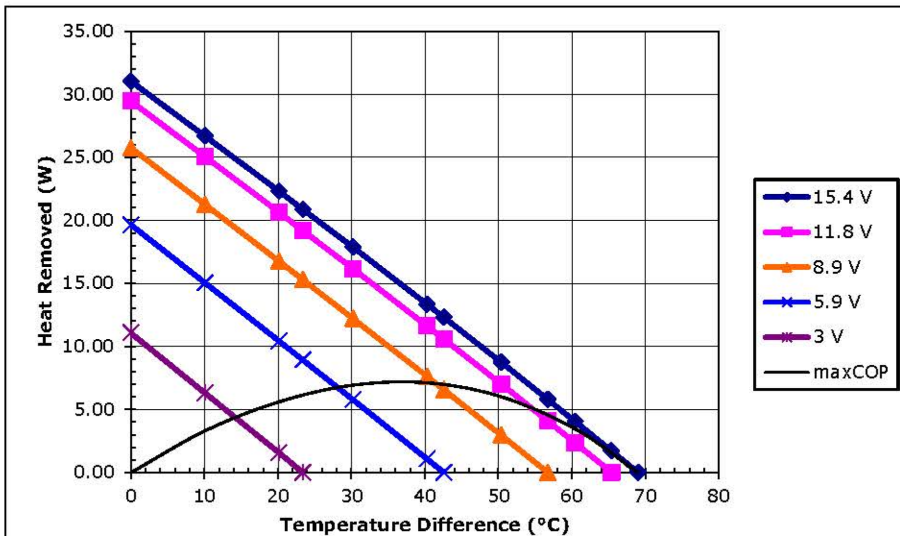

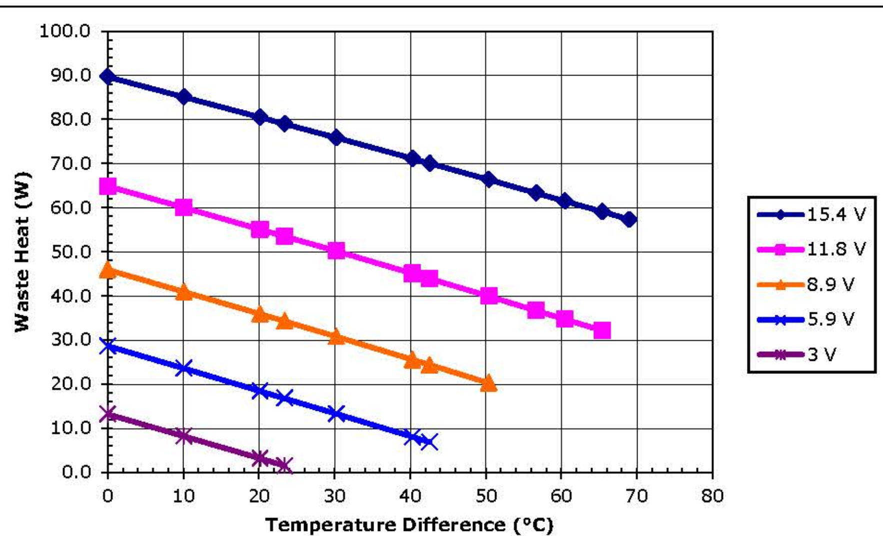

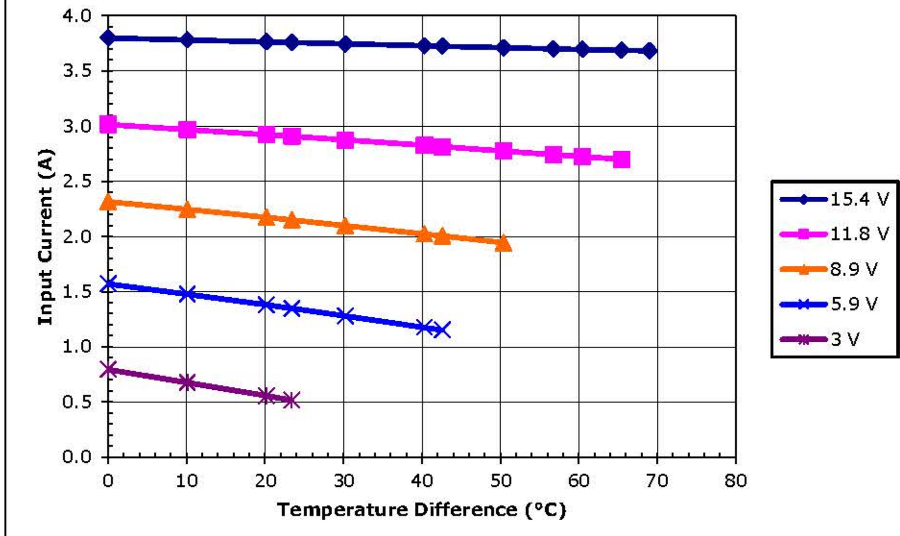

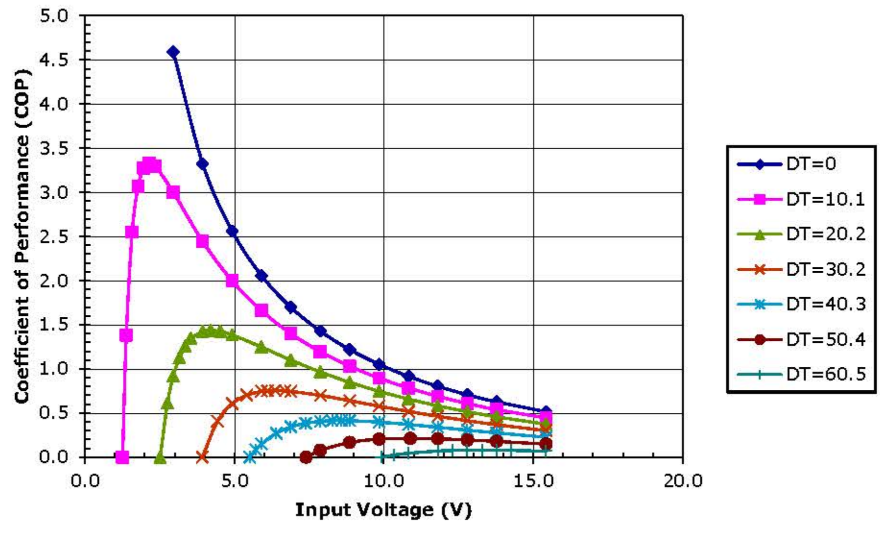

Unpotted VT-127-1.0-1.3-71 at a hot-side temperature of 30 °C

© 2010 TE Technology, Inc.

1590 Keane Drive, Traverse City, MI, 49696-8257 USA
PH: 231-929-3966 FAX: 231-929-4163 email: cool@tetech.com

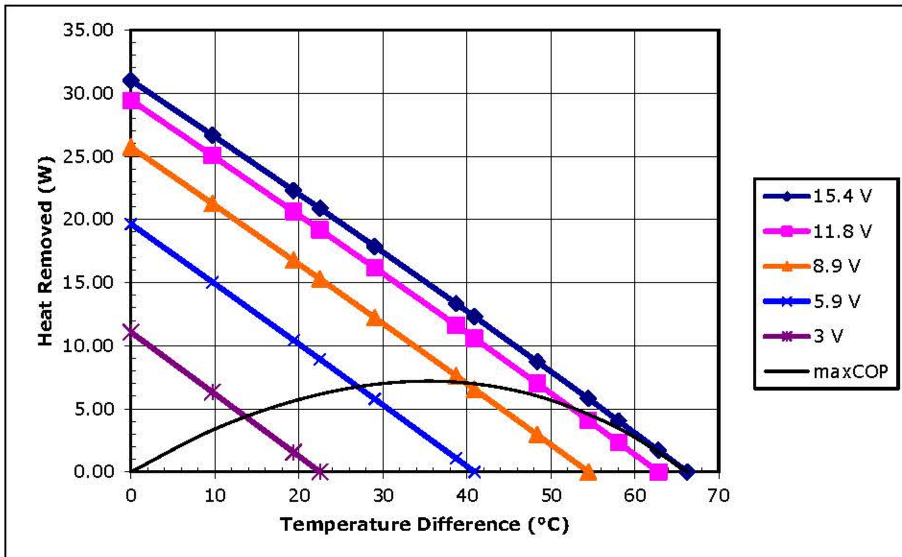

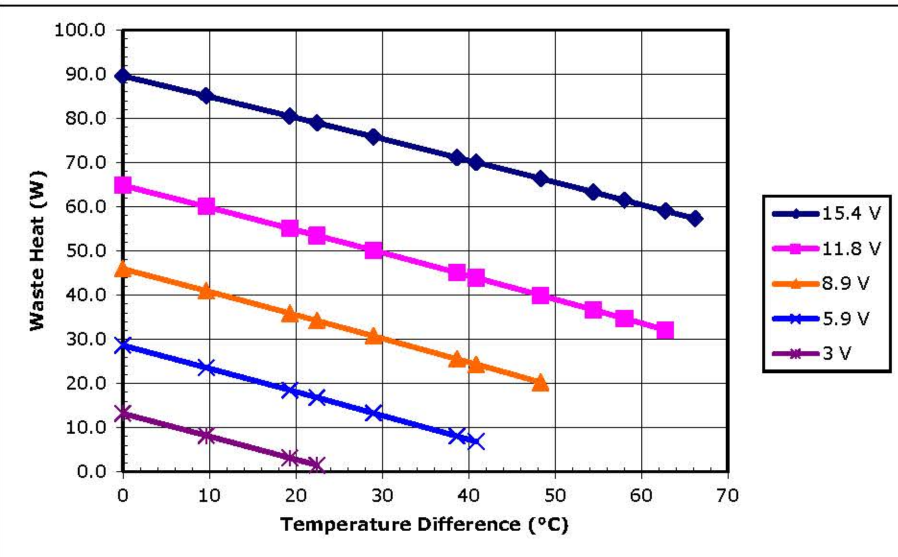

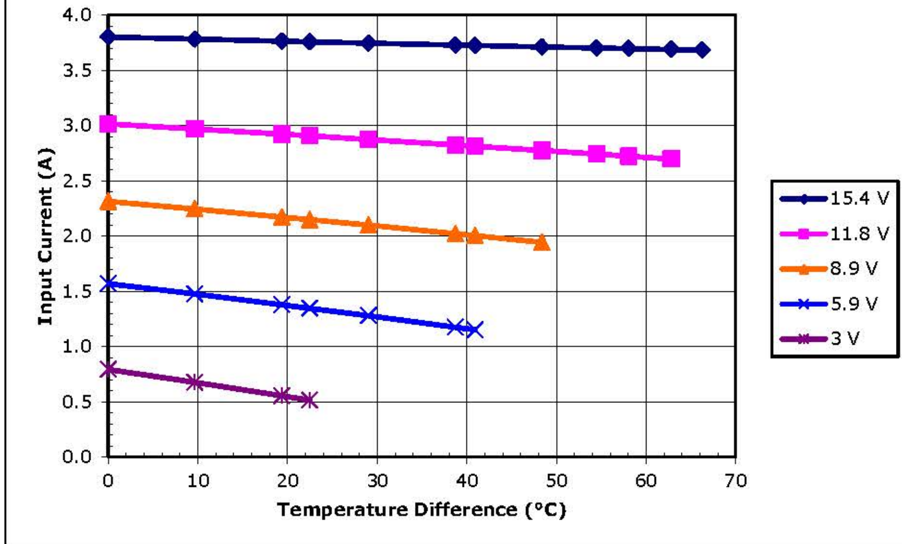

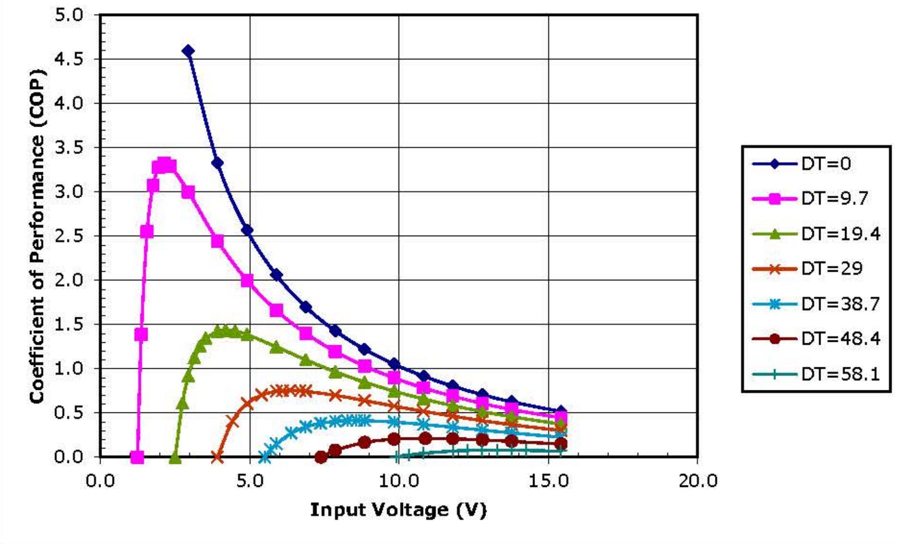

Potted VT-127-1.0-1.3-71 at a hot-side temperature of 30 °C

© 2010 TE Technology, Inc.

1590 Keane Drive, Traverse City, MI, 49696-8257 USA
PH: 231-929-3966 FAX: 231-929-4163 email: cool@tetech.com

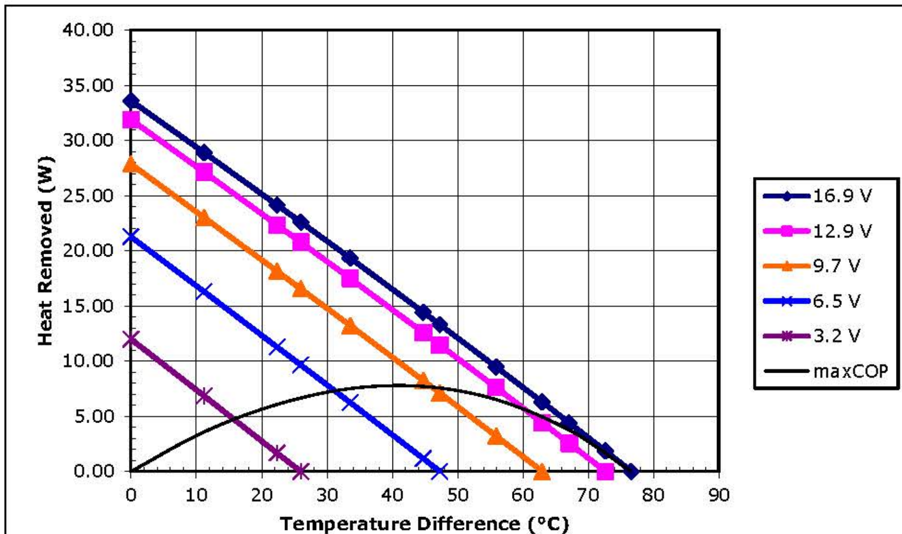

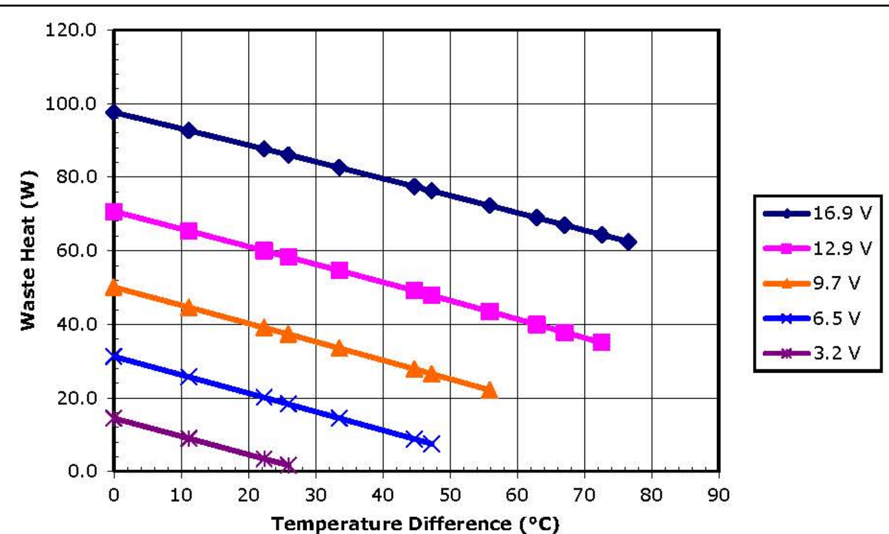

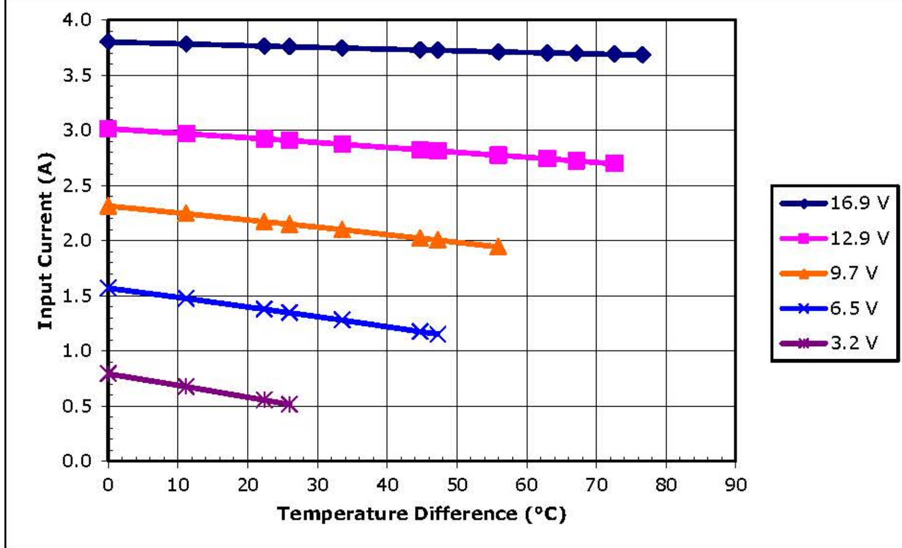

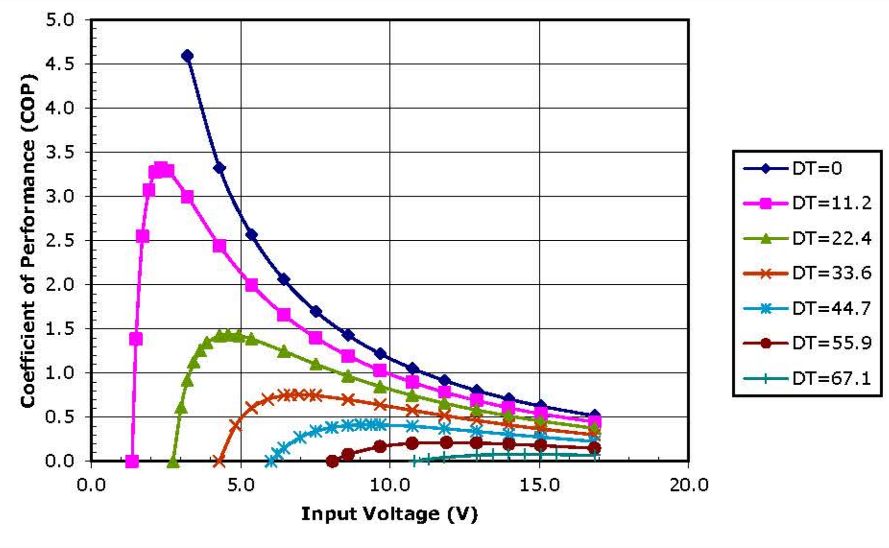

Unpotted VT-127-1.0-1.3-71 at a hot-side temperature of 50 °C

© 2010 TE Technology, Inc.

1590 Keane Drive, Traverse City, MI, 49696-8257 USA
PH: 231-929-3966 FAX: 231-929-4163 email: cool@tetech.com

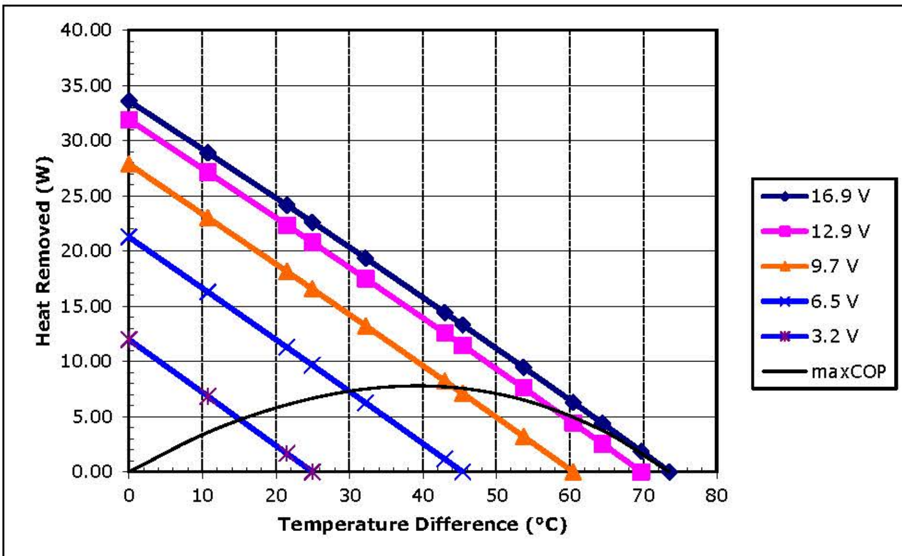

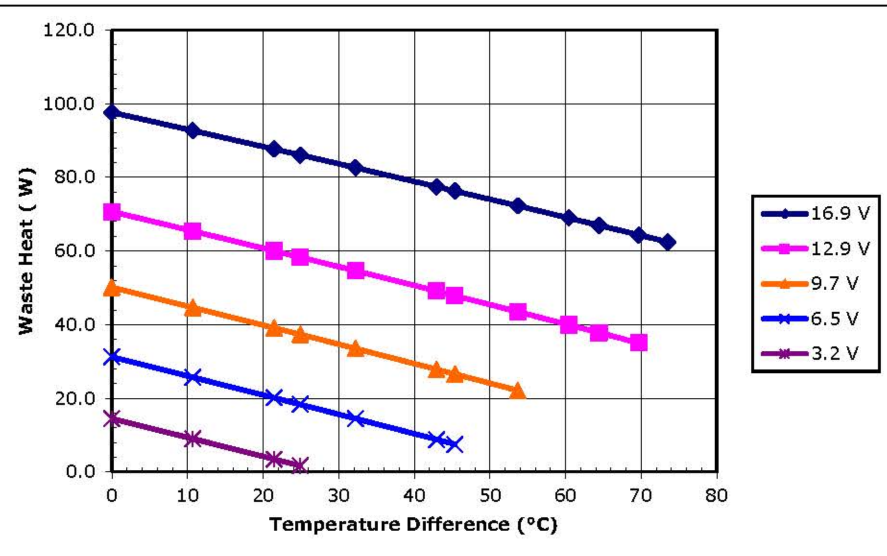

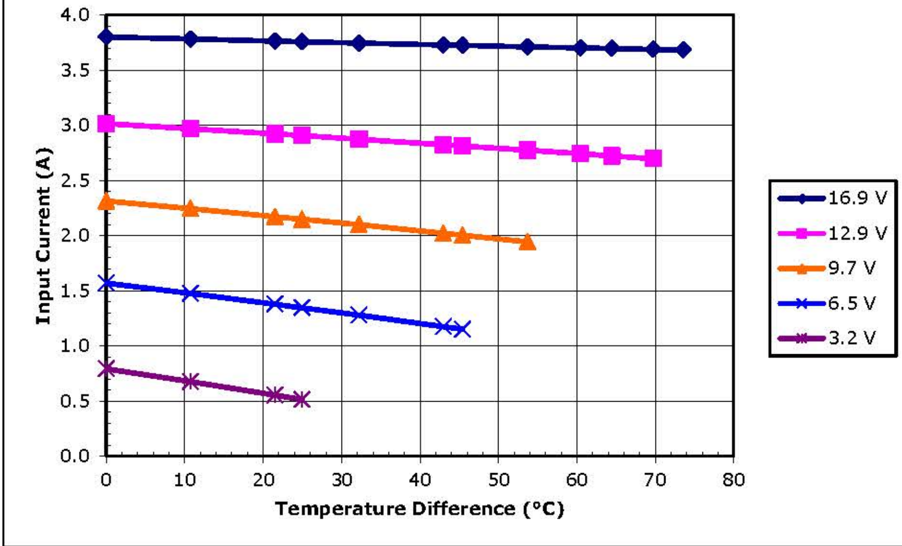

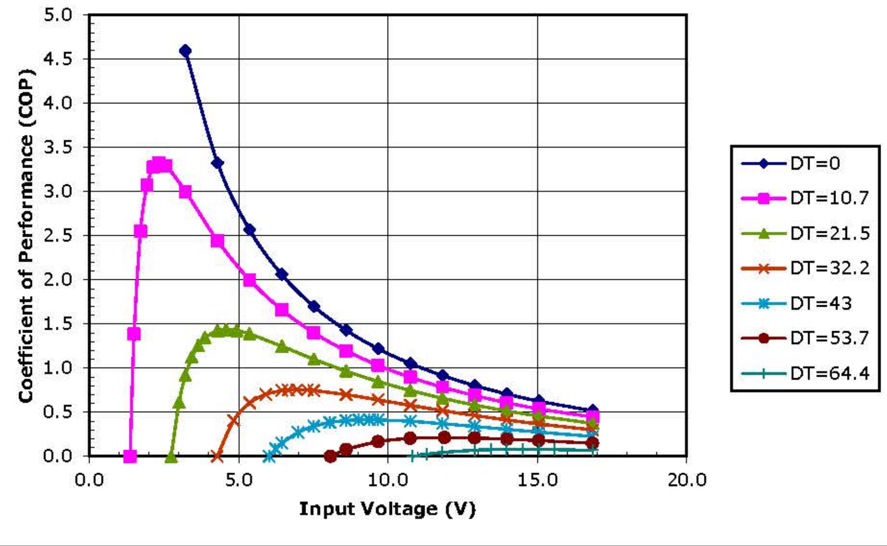

Potted VT-127-1.0-1.3-71 at a hot-side temperature of 50 °C

© 2010 TE Technology, Inc.

1590 Keane Drive, Traverse City, MI, 49696-8257 USA
PH: 231-929-3966 FAX: 231-929-4163 email: cool@tetech.com

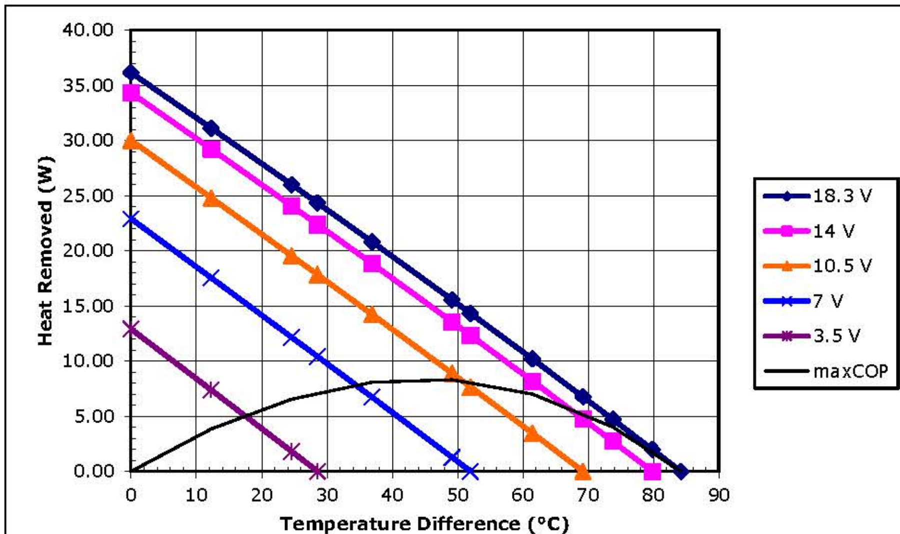

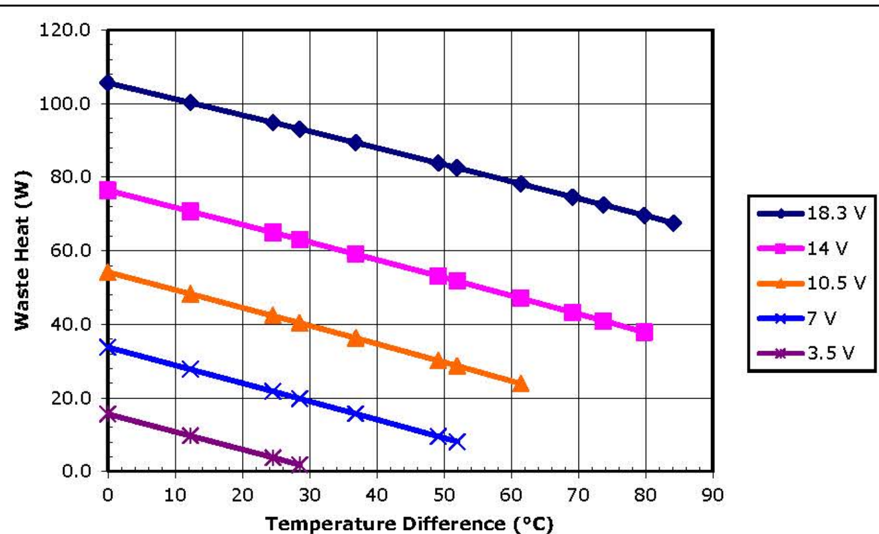

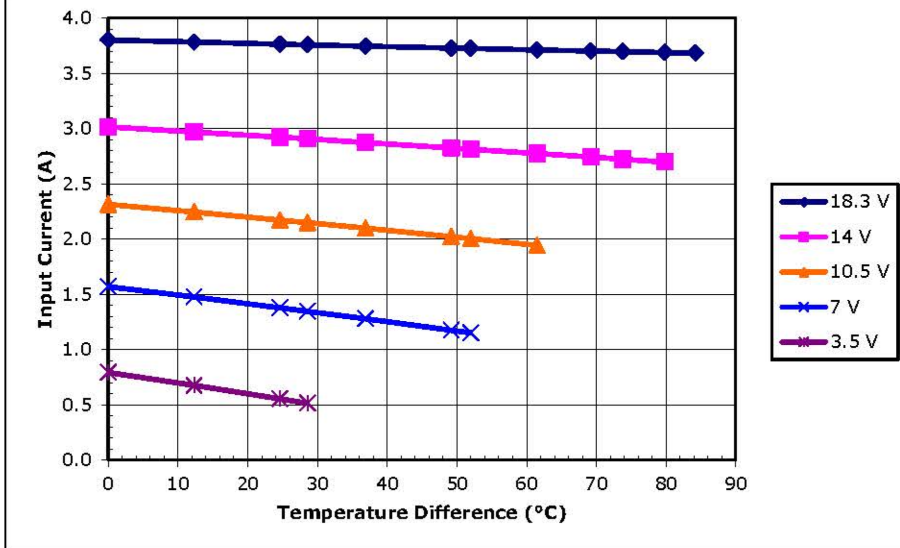

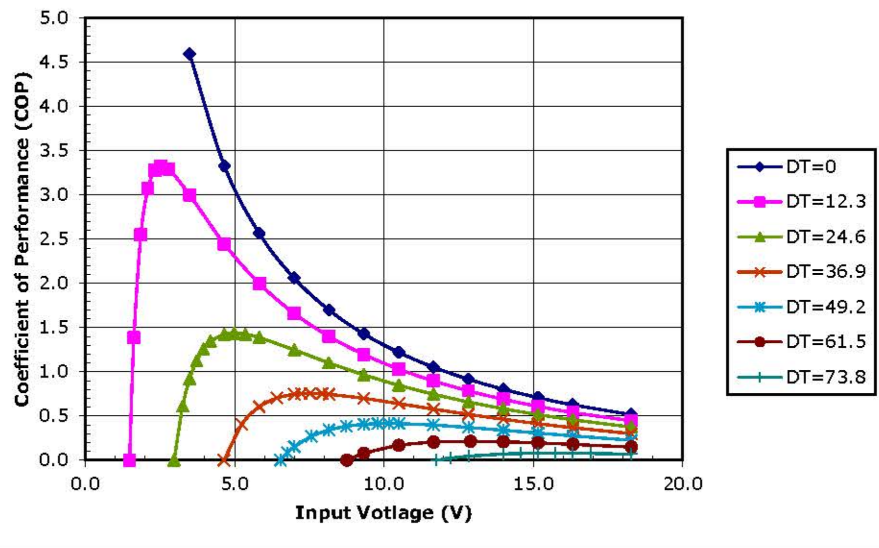

Unpotted VT-127-1.0-1.3-71 at a hot-side temperature of 70 °C

© 2010 TE Technology, Inc.

1590 Keane Drive, Traverse City, MI, 49696-8257 USA
PH: 231-929-3966 FAX: 231-929-4163 email: cool@tetech.com

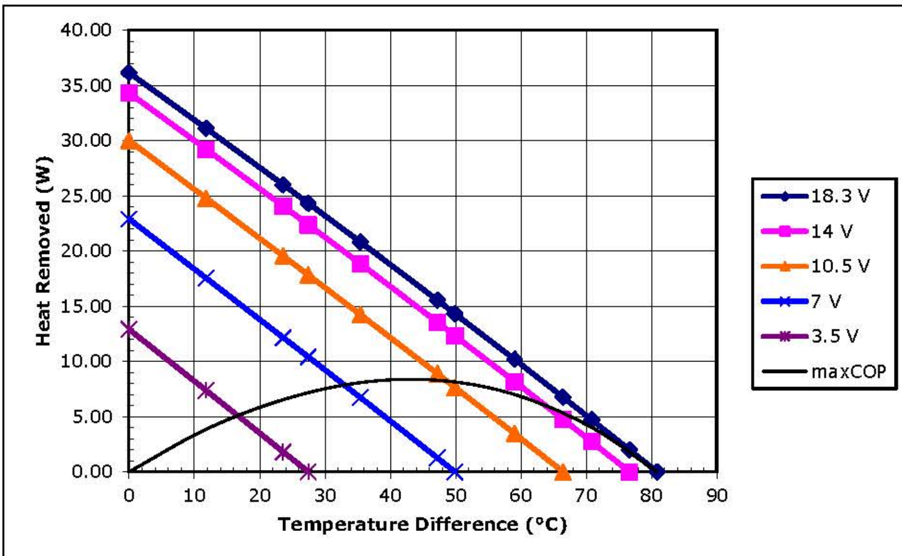

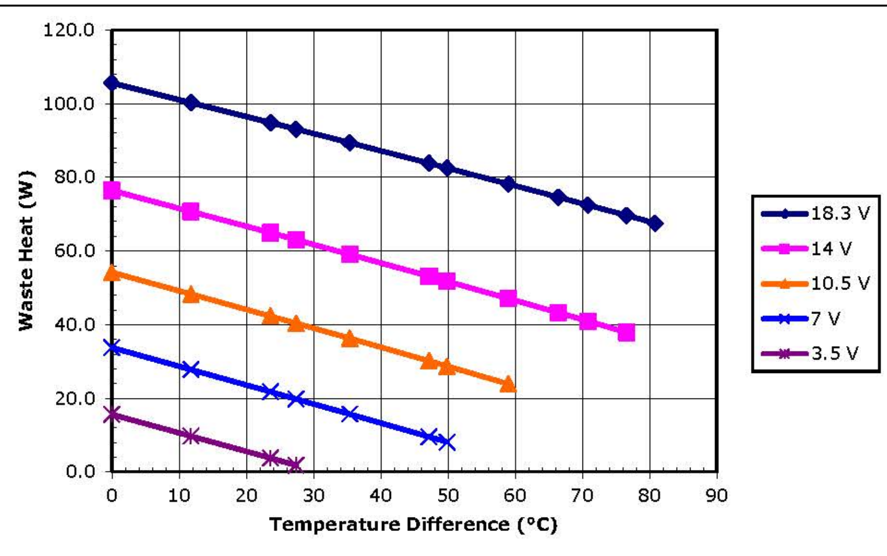

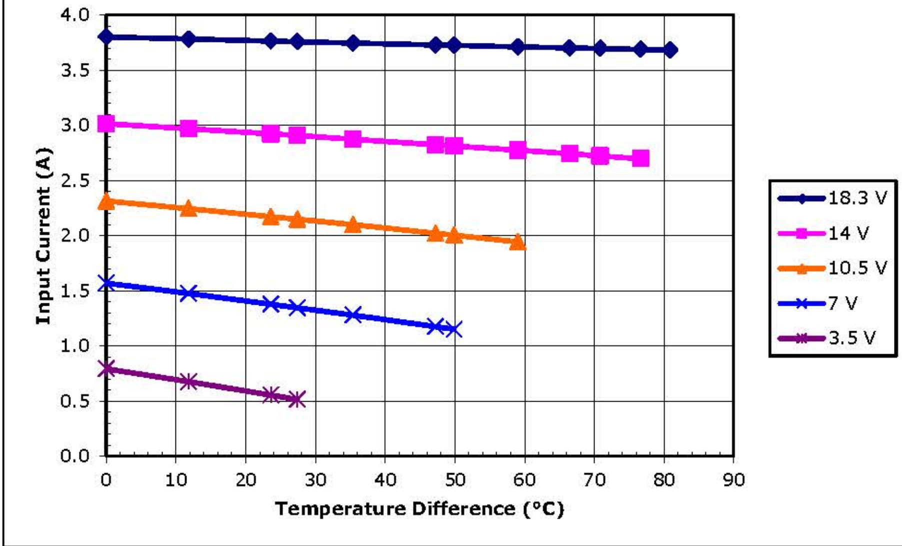

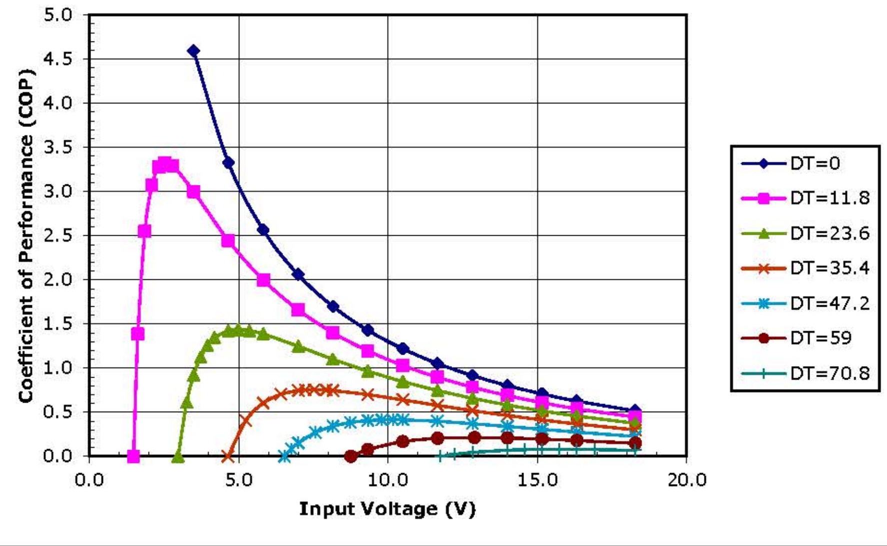

Potted VT-127-1.0-1.3-71 at a hot-side temperature of 70 °C

© 2010 TE Technology, Inc.

Innovative **Technology** for a **Connected** World

ThermaTEC™ Series HT8,7,F2,3030
Thermoelectric Modules

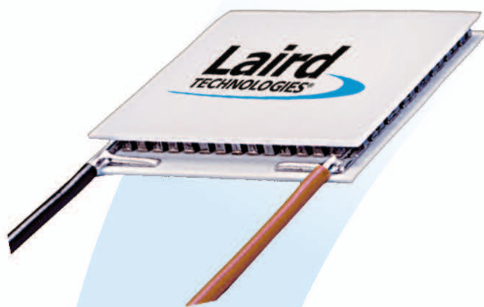

The ThermaTEC™ Series of thermoelectric modules (TEMs) are designed to operate under cycling conditions or high temperature applications.

This product line is available in multiple configurations and is ideal for applications that require both heating and cooling mode (reverse polarity) or power generation. Assembled with proprietary solder construction, Bismuth Telluride semiconductor material and thermally conductive Aluminum Oxide ceramics, the ThermaTEC™ Series is designed for higher current and larger heat-pumping applications.

FEATURES

- Thermal Cycling Durability
- Power Cycling Reliability
- Precise Temperature Control
- Strong Lead Attachment
- RoHS Compliant
- Continuous Operation at High Temperatures

APPLICATIONS

- Analytical Instrumentation
- PCR Cyclers
- Thermal Test Sockets
- Electronic Enclosure Cooling
- Chillers (Liquid Cooling)
- Power Generation

PERFORMANCE SPECIFICATIONS		
Hot Side Temperature (°C)	25°C	50°C
Qmax (Watts)	40.7	45.5
Delta Tmax (°C)	63	75
Imax (Amps)	8.5	8.7
Vmax (Volts)	8.1	9.2
Module Resistance (Ohms)	0.88	0.99

SUFFIX	THICKNESS (PRIOR TO TINNING)	FLATNESS & PARALLELISM	HOT FACE	COLD FACE	Lead Length
11	0.131″± 0.005″	0.002″ / 0.0035″	Lapped	Lapped	6.0
TA	0.131″± 0.001″	0.001″ / 0.001″	Lapped	Lapped	6.0″
TB	0.131″± 0.0005″	0.0005″ / 0.0005″	Lapped	Lapped	6.0″

SEALING OPTION

SUFFIX	SEALANT	COLOR	TEMP RANGE	DESCRIPTION
R	RTV	White	-60 to 204 °C	Non-corrosive, silicone adhesive sealant
E	Epoxy	Black	-55 to 150 °C	Low density syntactic foam epoxy encapsulant

global solutions: **local** support ™

Americas: +1 888.246.9050
Europe: +46.31.420530
Asia: +86.755.2714.1166

clv.customerpos@lairdtech.com
www.lairdtech.com

Laird TECHNOLOGIES

Innovative Technology for a Connected World

ThermaTEC™ Series HT8,7,F2,3030
Thermoelectric Modules

Performance Curves at Th = 25°C

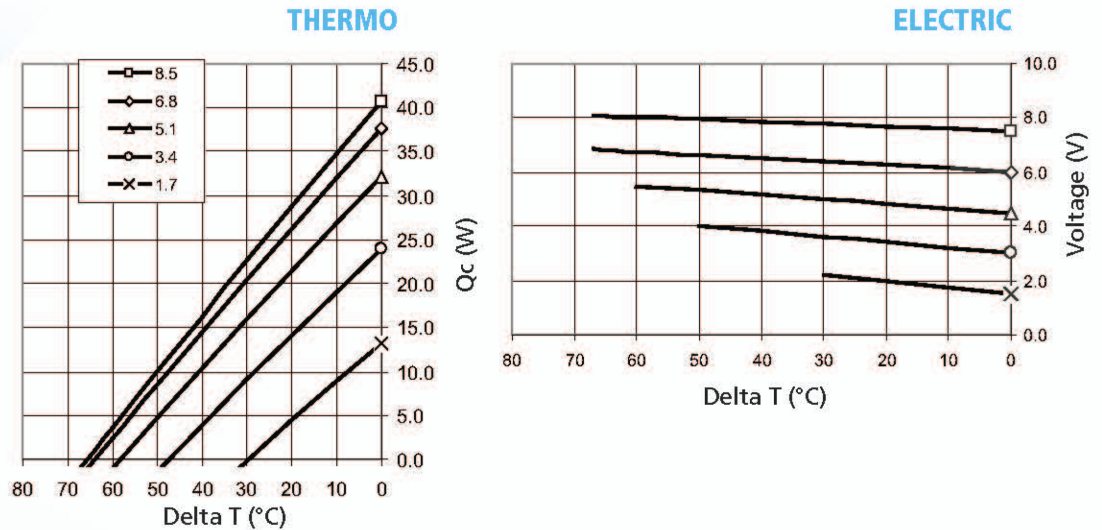

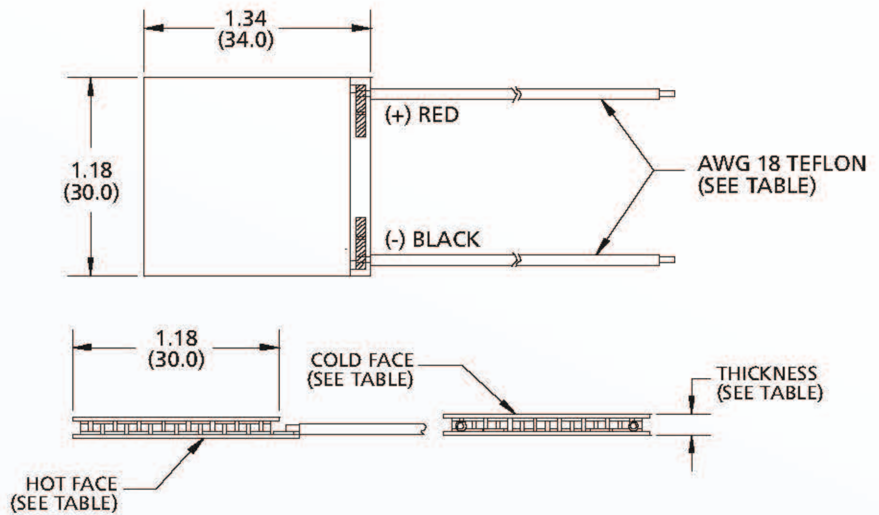

Ceramic Material: Alumina (Al_2O_3)
Solder Construction: 271°C, Proprietary

OPERATING TIPS

- Max Operating Temperature: 175°C
- Do not exceed Imax or Vmax when operating module
- Reference assembly guidelines for recommended installation

THR-DS-HT8,7,F2,3030 0509

Any information furnished by Laird Technologies and its agents is believed to be accurate and reliable. Responsibility for the use and application of Laird Technologies materials rests with the end user since Laird Technologies and its agents cannot be aware of all potential uses. Laird Technologies makes no warranties as to the fitness, merchantability, or suitability of any Laird Technologies materials or products for any specific or general uses. Laird Technologies shall not be liable for incidental or consequential damages of any kind. All Laird Technologies products are sold pursuant to the Laird Technologies terms and conditions of sale in effect from time to time, a copy of which will be furnished upon request. For further information please visit our website at www.lairdtech.com Alternatively contact: sales@lairdtech.com. Bluetooth® is a trademark owned by Bluetooth SIG, Inc., USA and licensed to Laird Technologies.

® 2008 All Rights Reserved. Laird Technologies is a registered trademark of Laird Technologies, Inc.

VT-127-1.4-1.5-72 Thermoelectric Module (Peltier Module) Specifications		Material Specifications (27 °C hot side temperature)	Material Specifications (50 °C hot side temperature)
	Vmax (V)	16.3	18.1
	Imax (A)	6.1	6.1
	Qmax (W)	62.0	68.0
	DTmax (°C)	72	81
	Operation/storage temperature	-40 °C to +200 °C	

Module *material* specifications are nominal values based on the hot-side temperature indicated. Thermoelectric material parameter tolerance is +/-10%.

In no case should the module temperature be allowed to exceed its maximum operation/storage temperature.

Please review all product and technical information, *Thermoelectric Module Mounting Procedure,* parameter definitions, FAQ's, and ordering information posted on our website before purchasing or using this product.

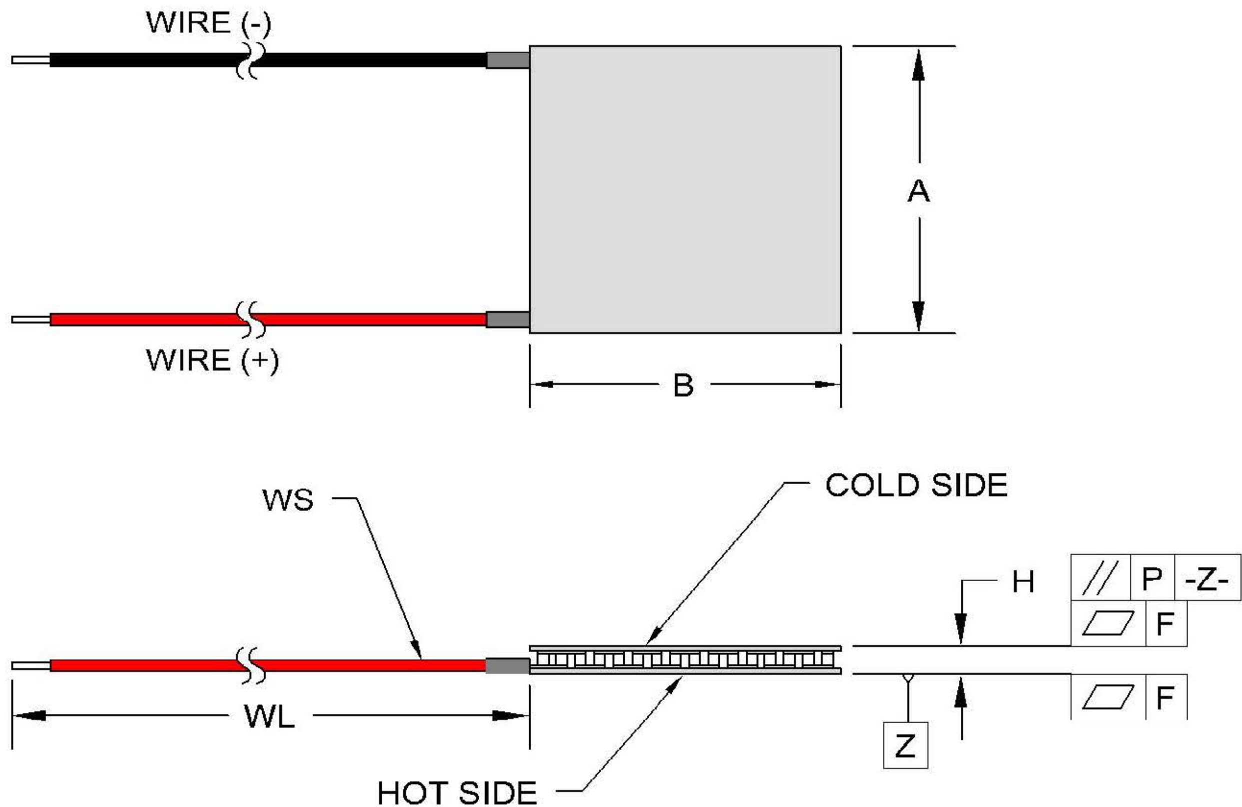

Width, A (mm)	40 +0.5/-0.2
Width, B (mm)	40 +0.5/-0.2
Height, H (mm)	3.9 ±0.05
Flatness, F (mm)	0.02
Parallelism, P (mm)	0.03
Wire Size, WS (mm²)	0.34
Wire Length, WL (mm)	120

Optional Features and Notes:

Add "P" to part number for sealing module with epoxy potting.

Maximum operating/storage temperature with potting is 150 °C

Performance graphs include thermal resistance of substrates.

RoHS Compliant

1590 Keane Drive, Traverse City, MI, 49696-8257 USA
PH: 231-929-3966 FAX: 231-929-4163 email: cool@tetech.com

 © 2010 TE Technology, Inc.

1590 Keane Drive, Traverse City, MI, 49696-8257 USA
PH: 231-929-3966 FAX: 231-929-4163 email: cool@tetech.com

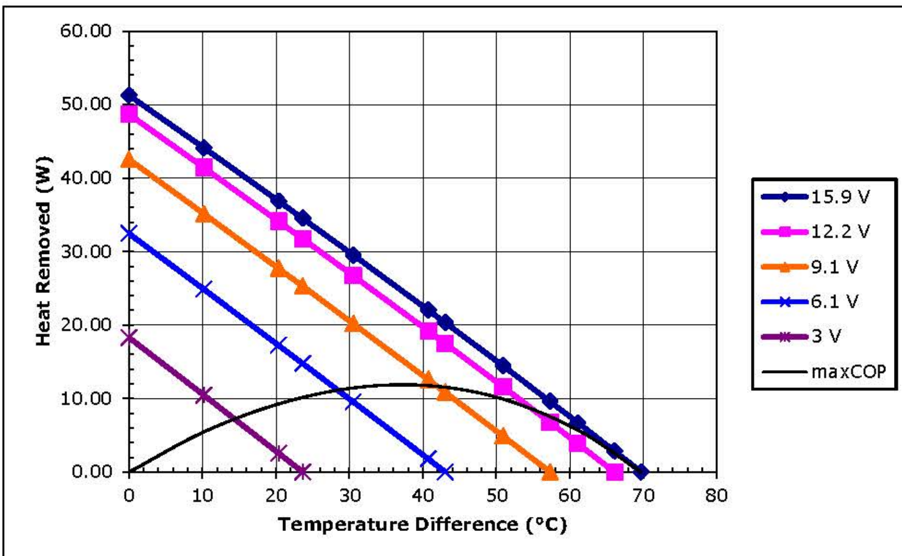

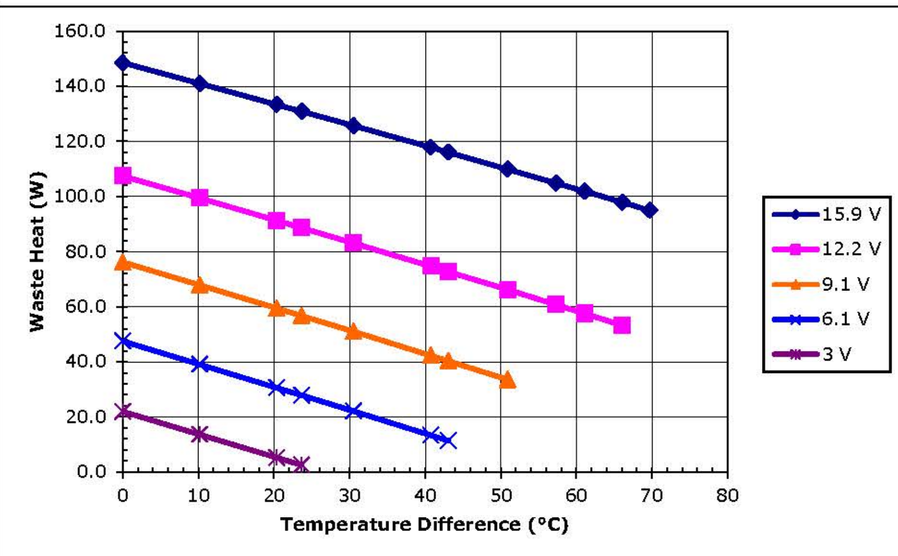

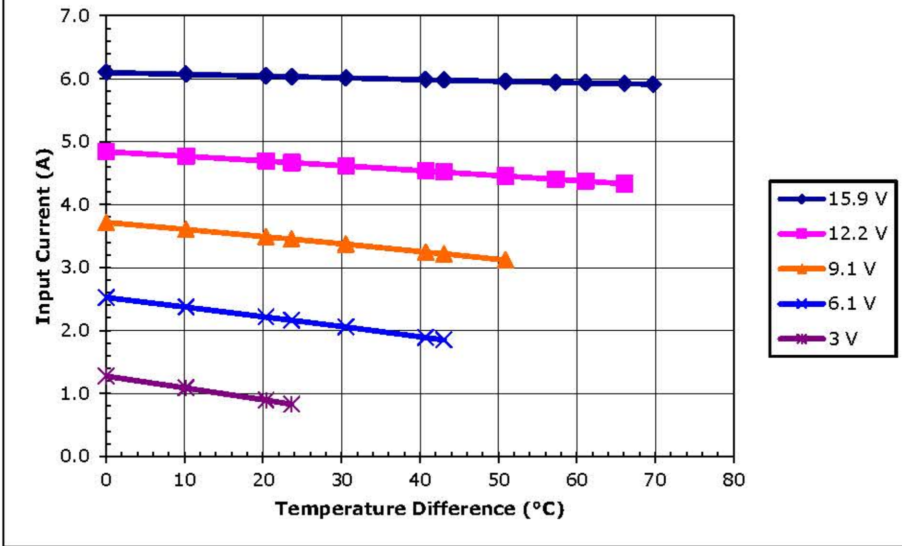

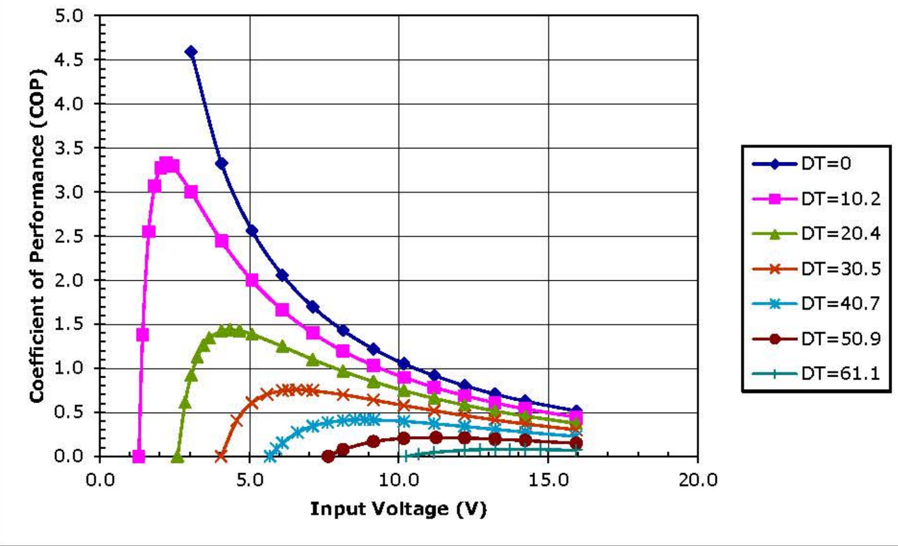

Unpotted VT-127-1.4-1.5-72 at a hot-side temperature of 30 °C

© 2010 TE Technology, Inc.

1590 Keane Drive, Traverse City, MI, 49696-8257 USA
PH: 231-929-3966 FAX: 231-929-4163 email: cool@tetech.com

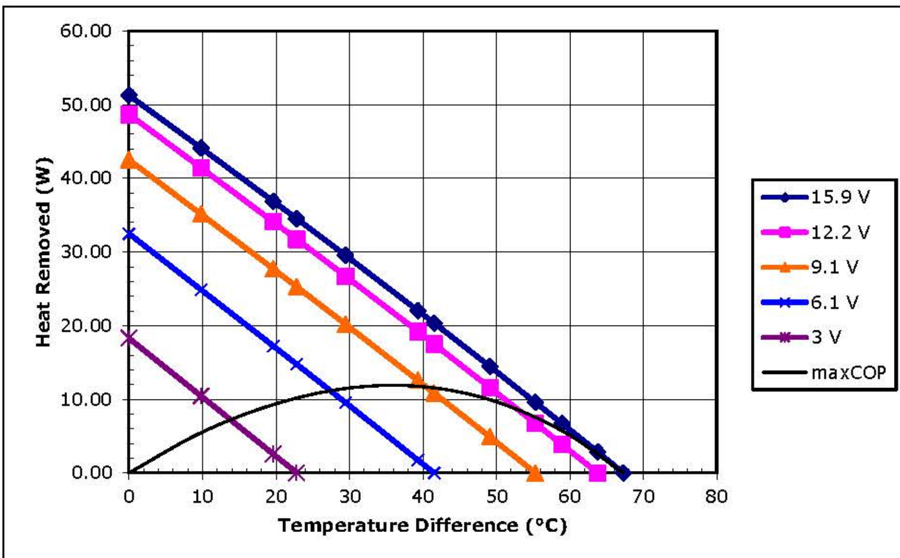

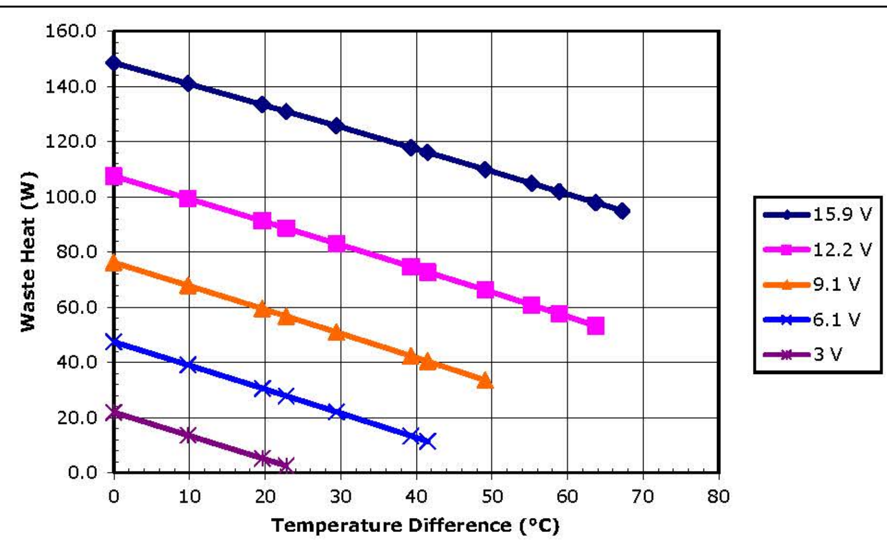

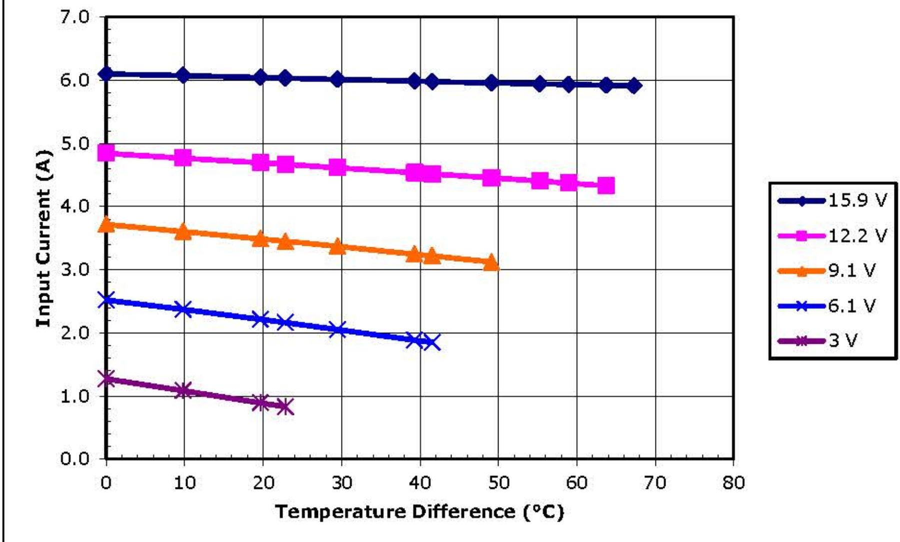

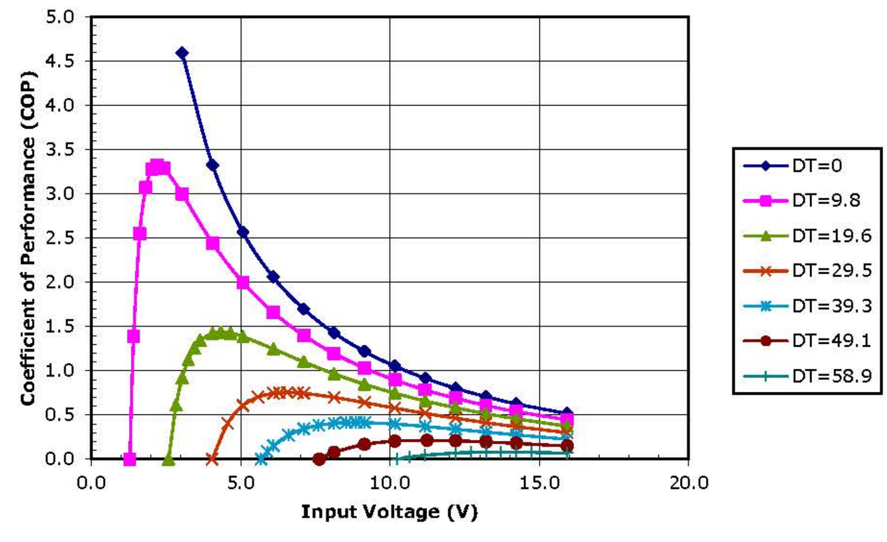

Potted VT-127-1.4-1.5-72 at a hot-side temperature of 30 °C

© 2010 TE Technology, Inc.

1590 Keane Drive, Traverse City, MI, 49696-8257 USA
PH: 231-929-3966 FAX: 231-929-4163 email: cool@tetech.com

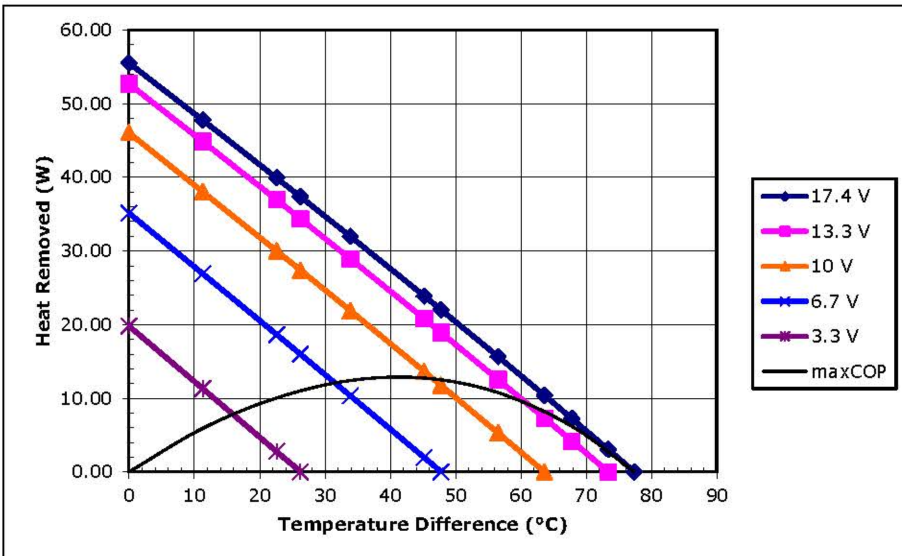

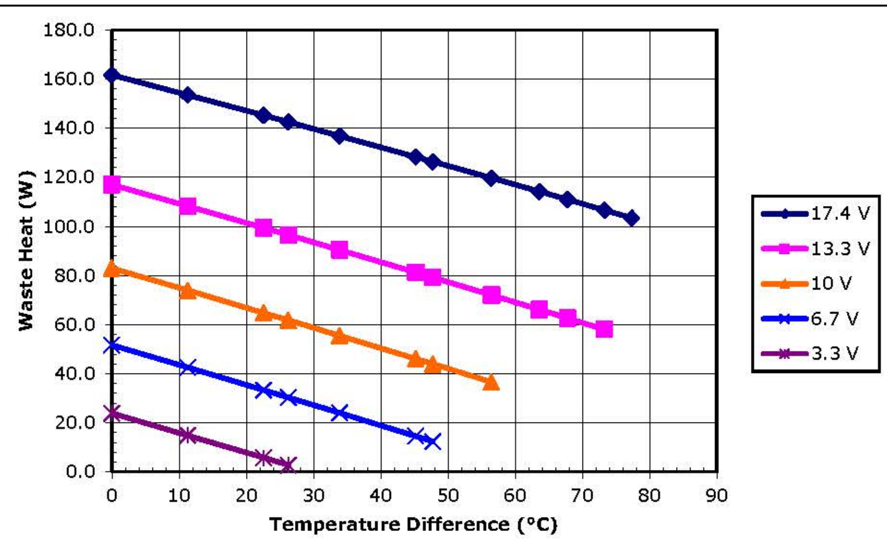

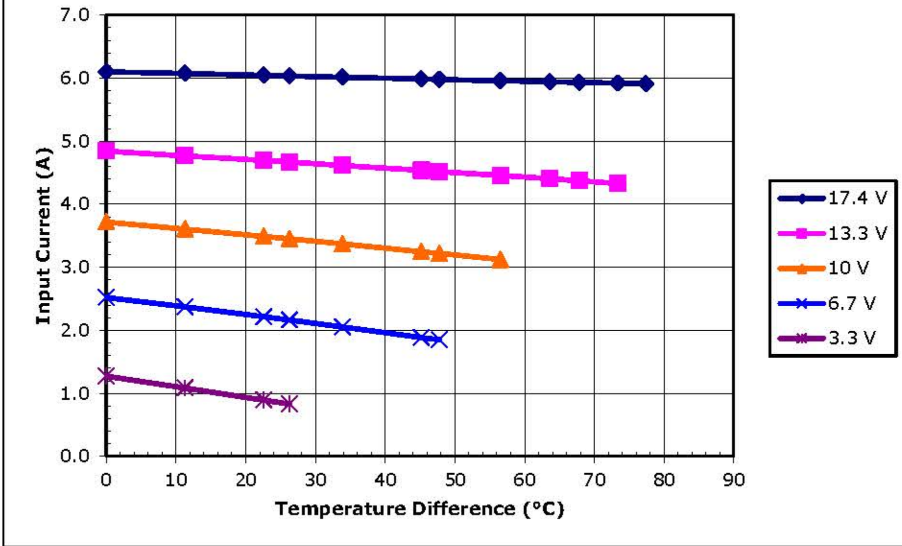

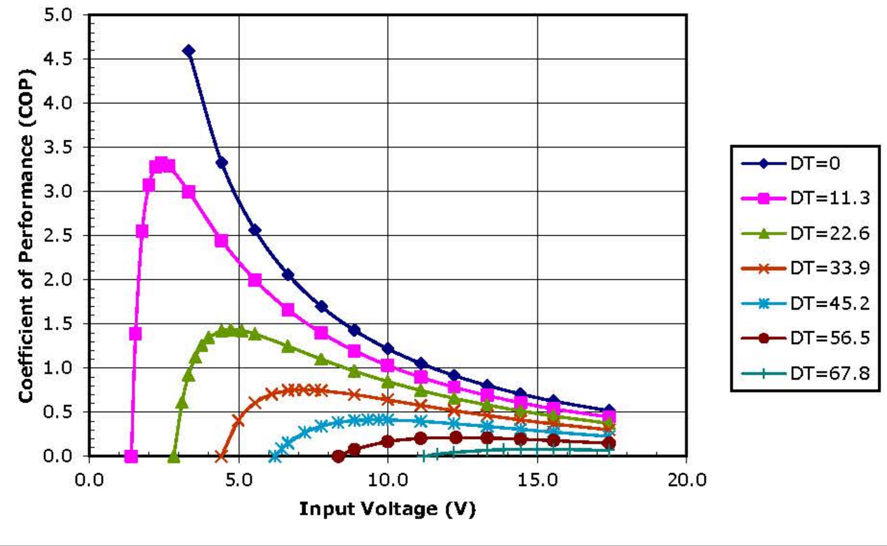

Unpotted VT-127-1.4-1.5-72 at a hot-side temperature of 50 °C

© 2010 TE Technology, Inc.

TE TECHNOLOGY, INC.
1590 Keane Drive, Traverse City, MI, 49696-8257 USA
PH: 231-929-3966 FAX: 231-929-4163 email: cool@tetech.com

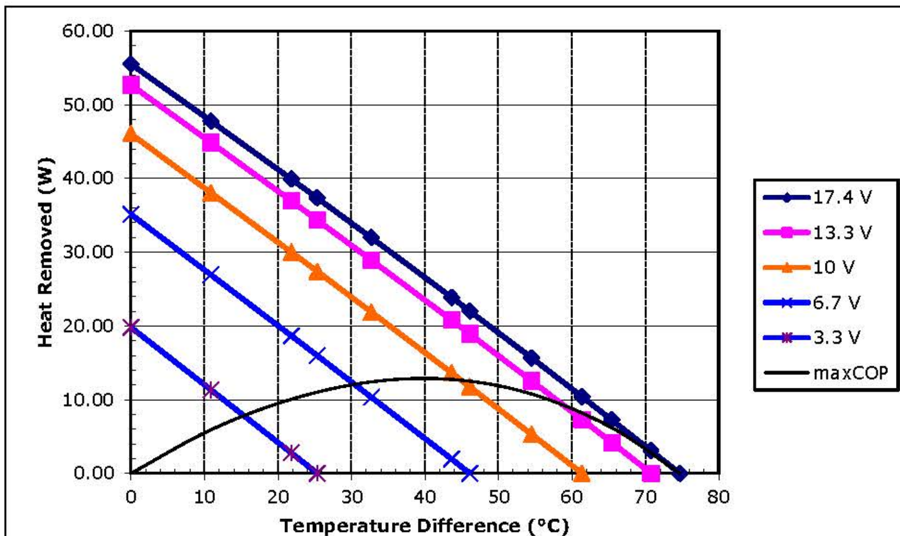

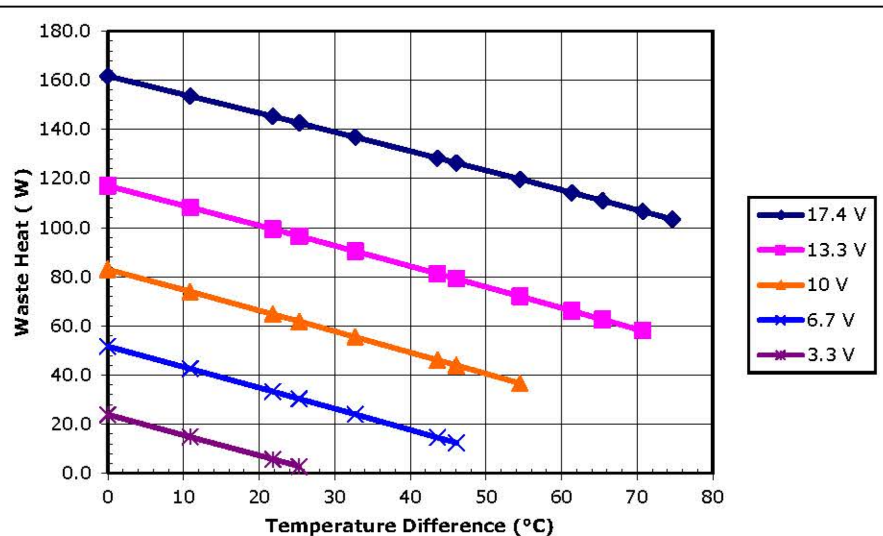

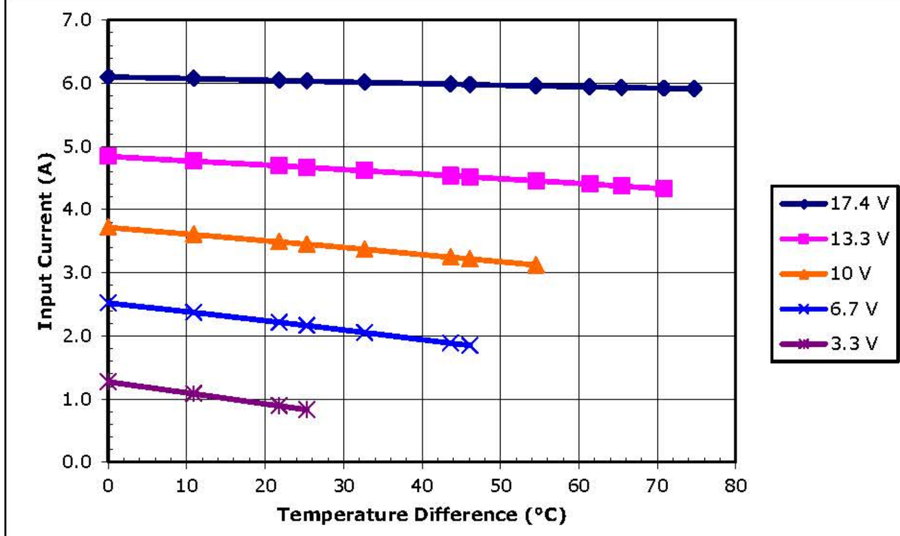

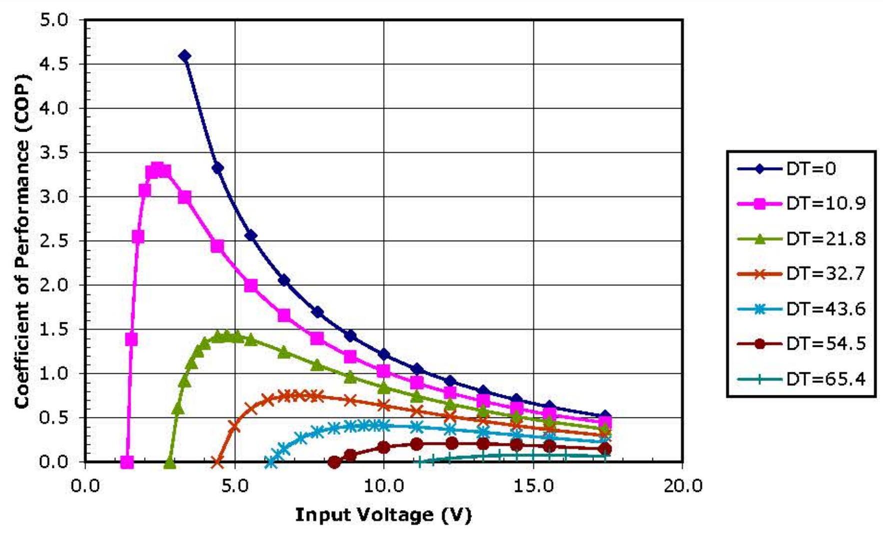

Potted VT-127-1.4-1.5-72 at a hot-side temperature of 50 °C

© 2010 TE Technology, Inc.

1590 Keane Drive, Traverse City, MI, 49696-8257 USA
PH: 231-929-3966 FAX: 231-929-4163 email: cool@tetech.com

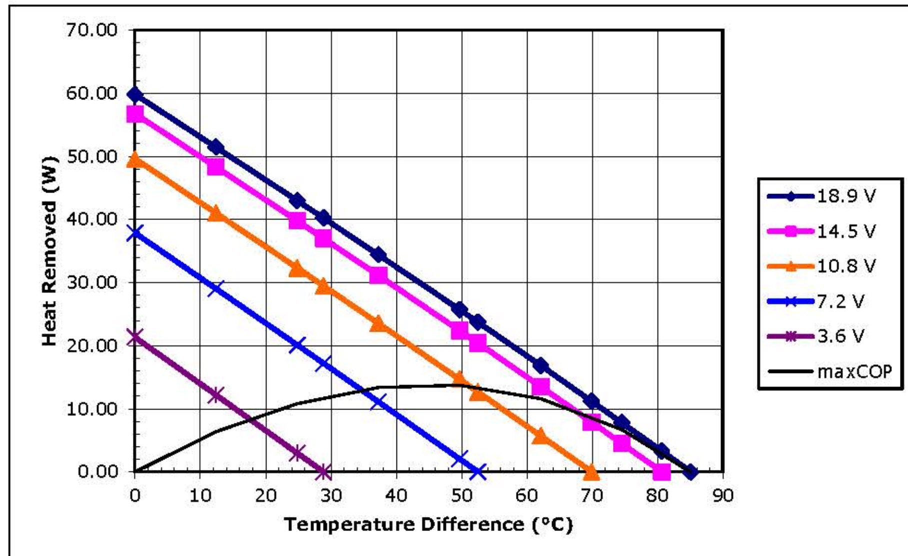

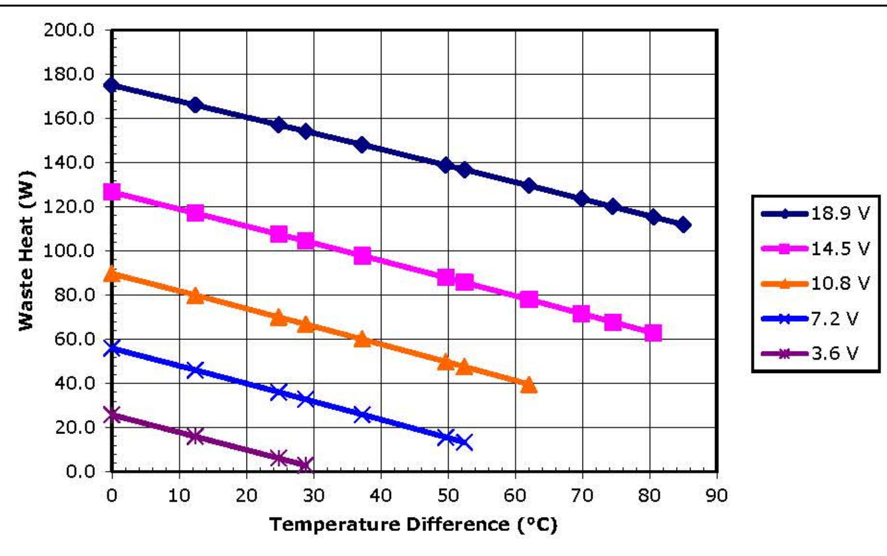

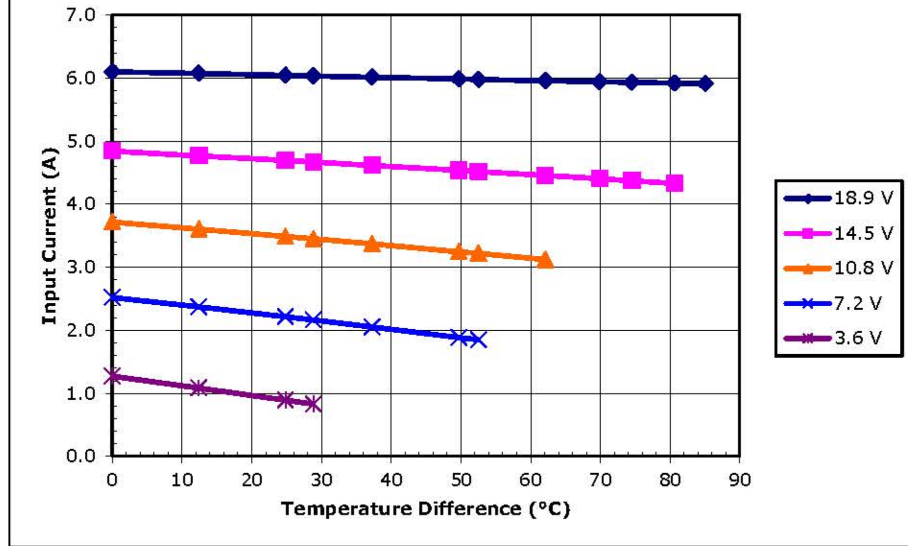

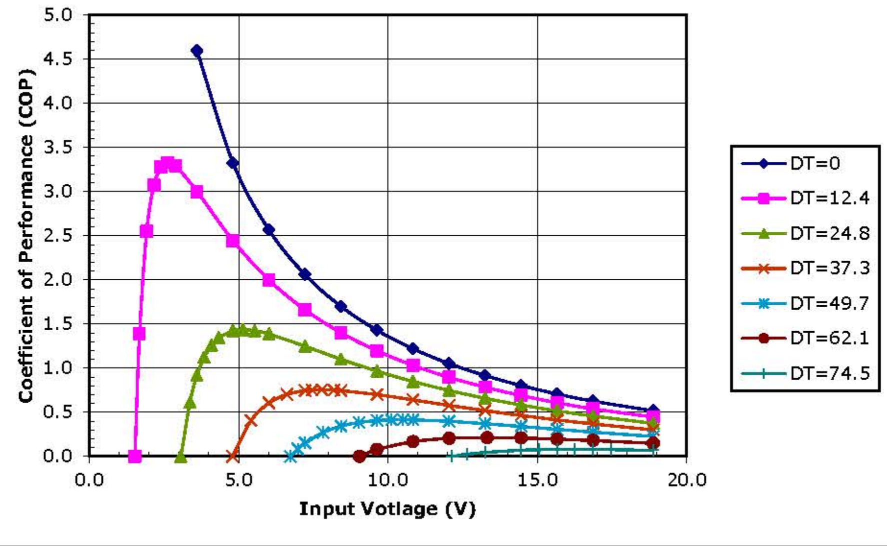

Unpotted VT-127-1.4-1.5-72 at a hot-side temperature of 70 °C

© 2010 TE Technology, Inc.

1590 Keane Drive, Traverse City, MI, 49696-8257 USA
PH: 231-929-3966 FAX: 231-929-4163 email: cool@tetech.com

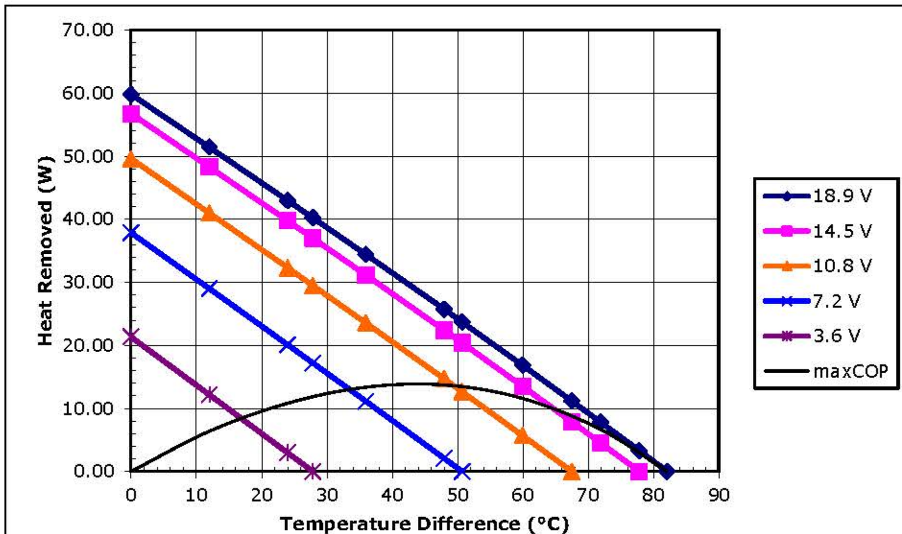

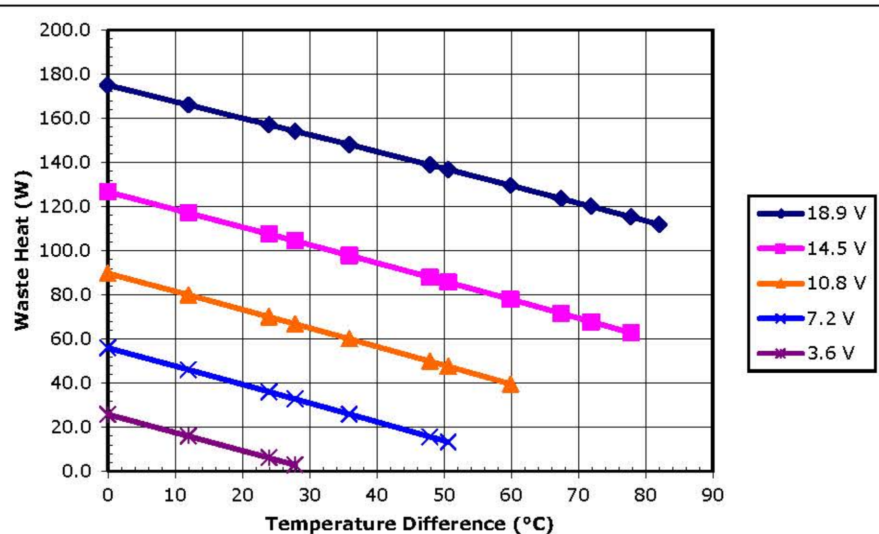

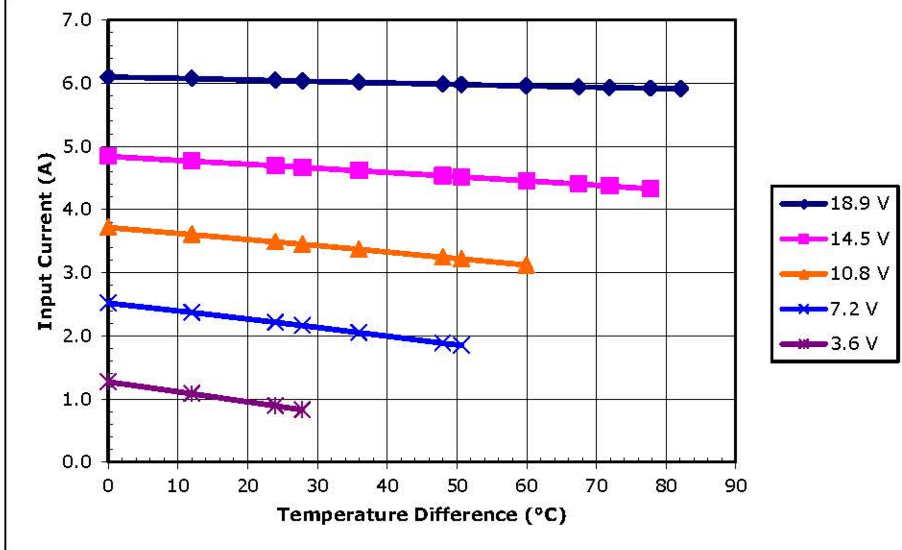

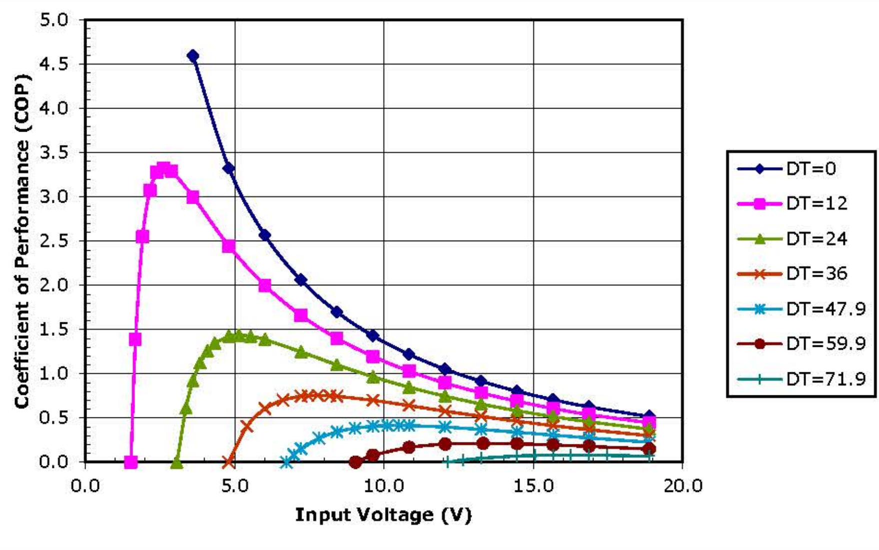

Potted VT-127-1.4-1.5-72 at a hot-side temperature of 70 °C

© 2010 TE Technology, Inc.

APPENDIX C

C.1 Technical drawings of the manufactured parts for the proof-of-concept heat transfer coefficient sensor and the experimental setup

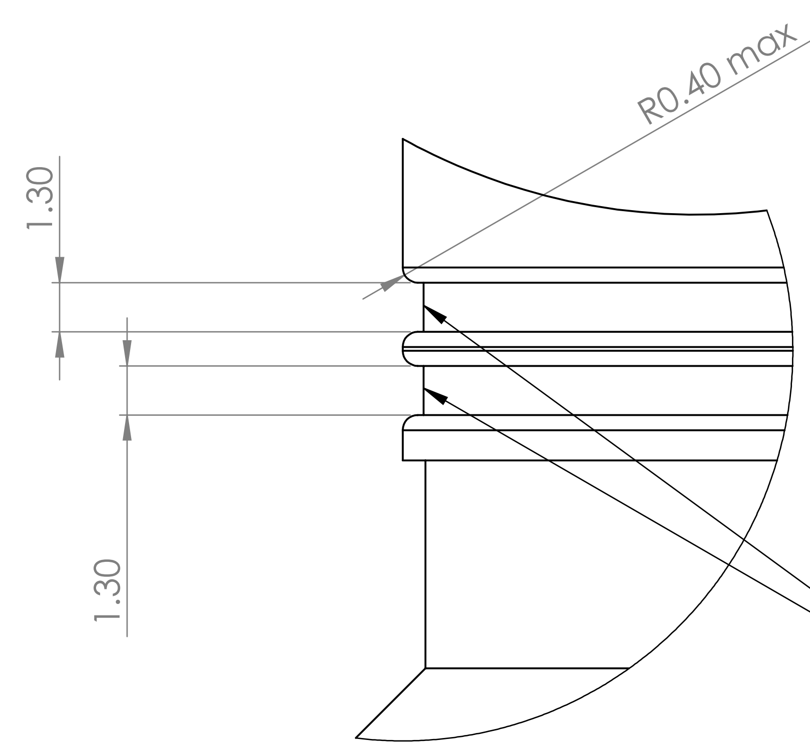

DETAIL C
SCALE 5 : 1

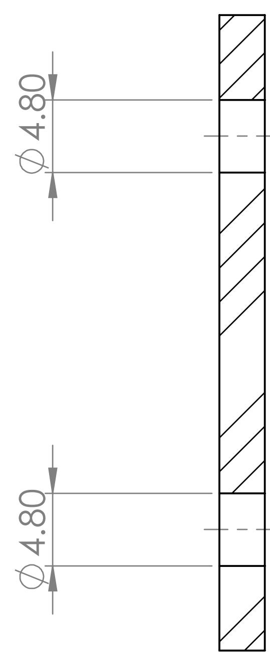

SECTION B-B

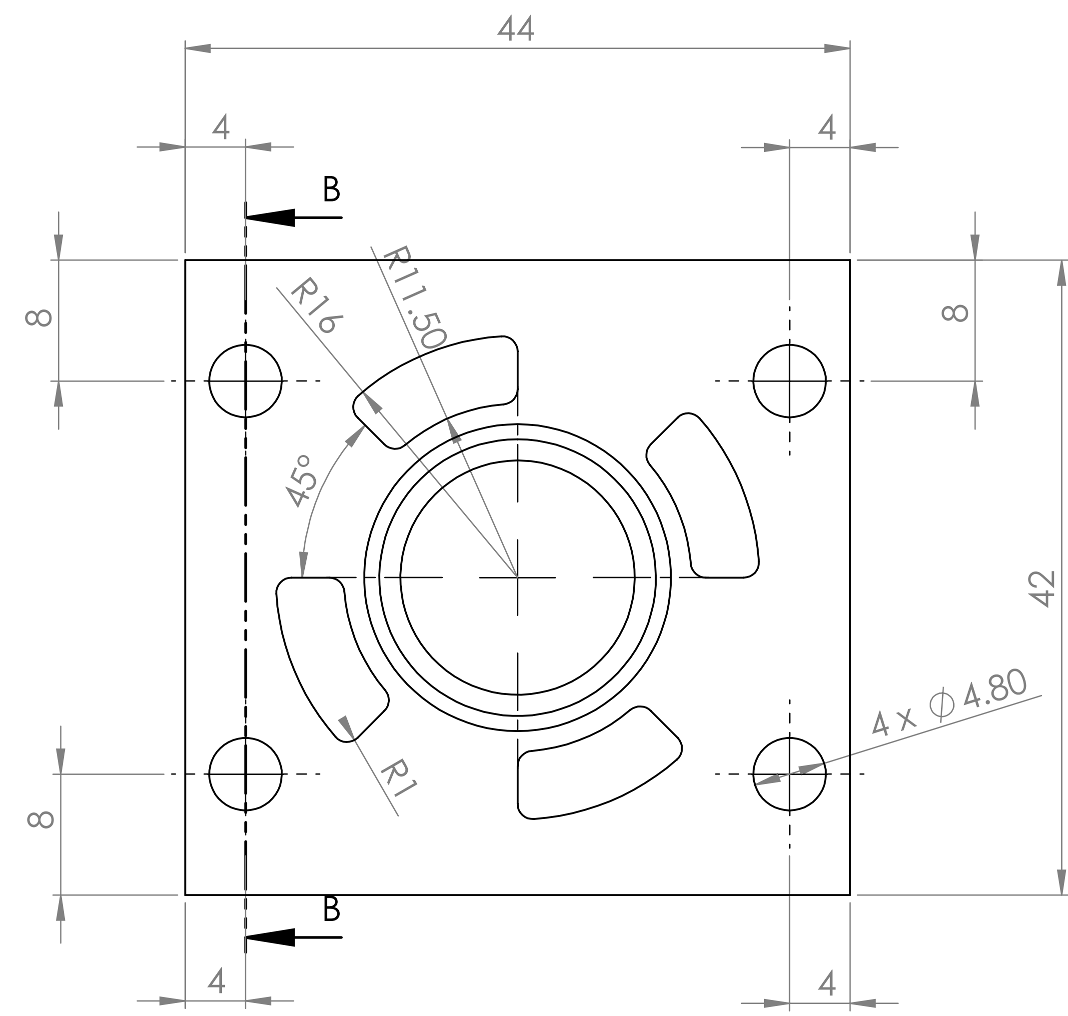

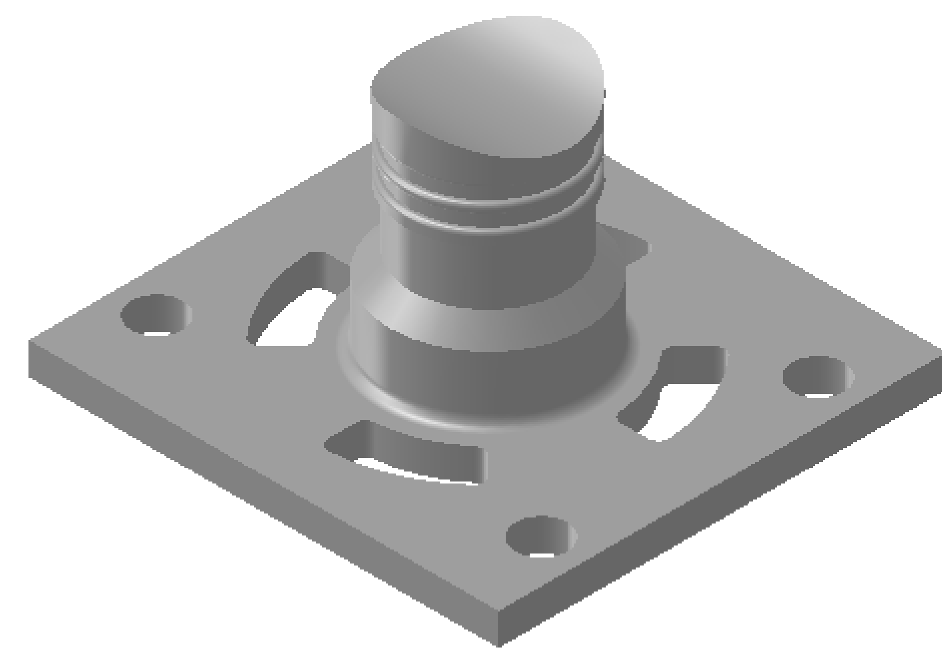

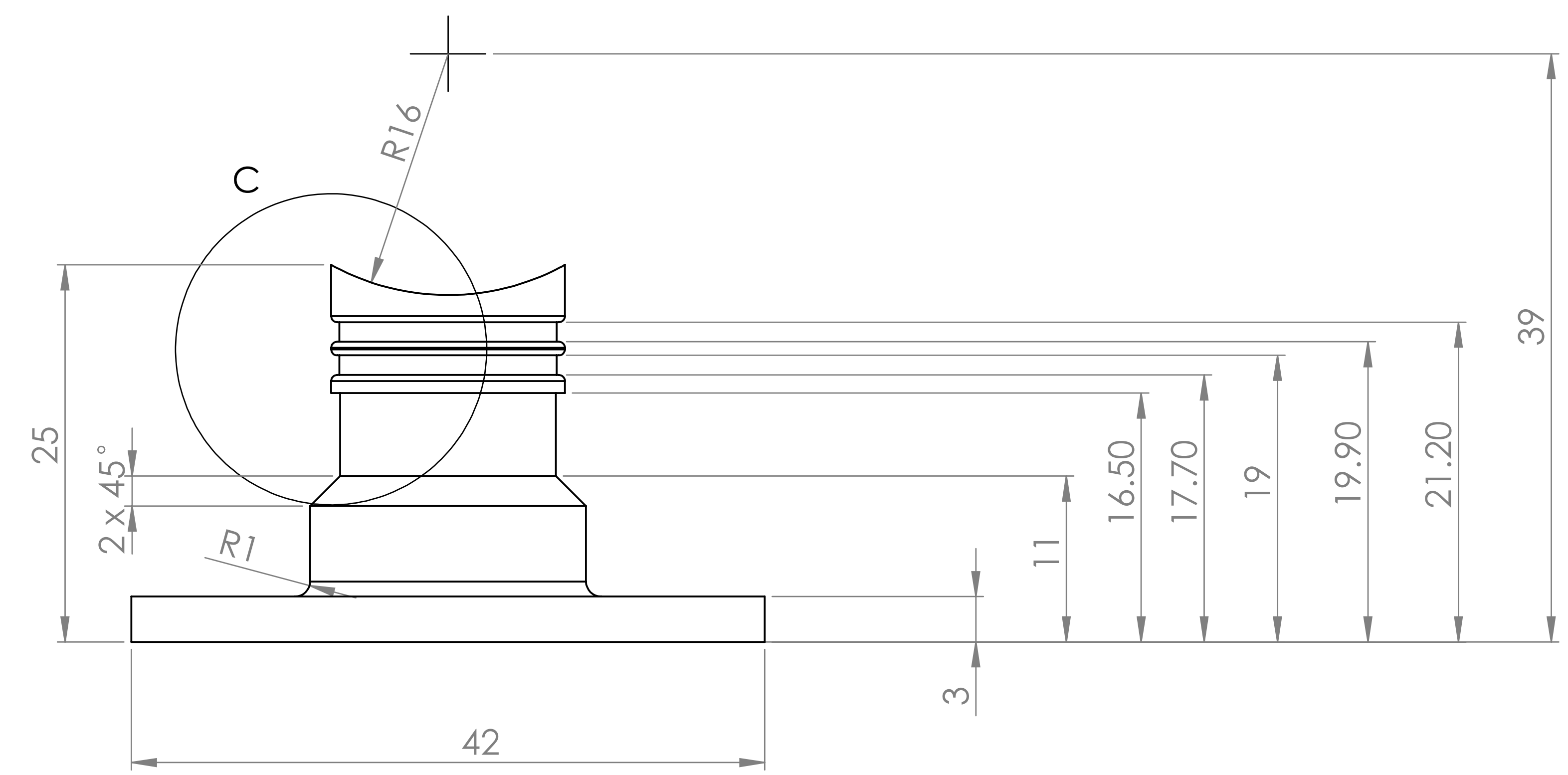

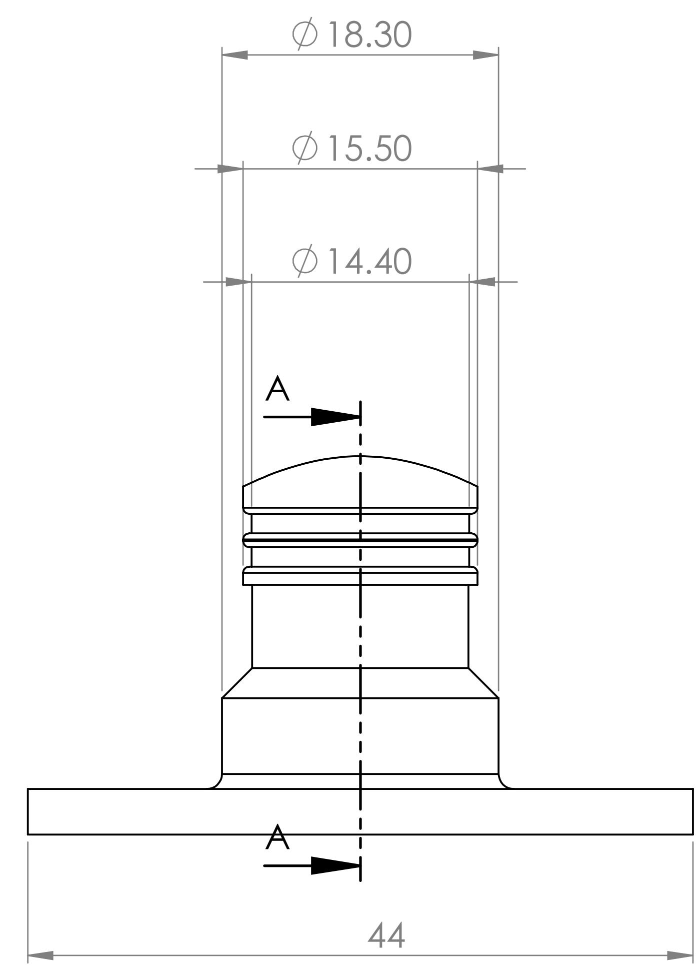

∅13
19
2 x 45°

SECTION A-A

UNLESS OTHERWISE SPECIFIED:
DIMENSIONS ARE IN MILLIMETERS
SURFACE FINISH:
TOLERANCES:
LINEAR:
ANGULAR:

FINISH:

DEBURR AND BREAK SHARP EDGES

DO NOT SCALE DRAWING

REVISION

	NAME	SIGNATURE	DATE
DRAWN			
CHK'D			
APPV'D			
MFG			
Q.A			

Stefano Soprani stefs@dtu.dk

TITLE:

Sensor casing

MATERIAL:
Aluminum

DWG NO.

A2

WEIGHT:

SCALE: 2:1

SHEET 1 OF 1

SOLIDWORKS Student Edition.
For Academic Use Only.

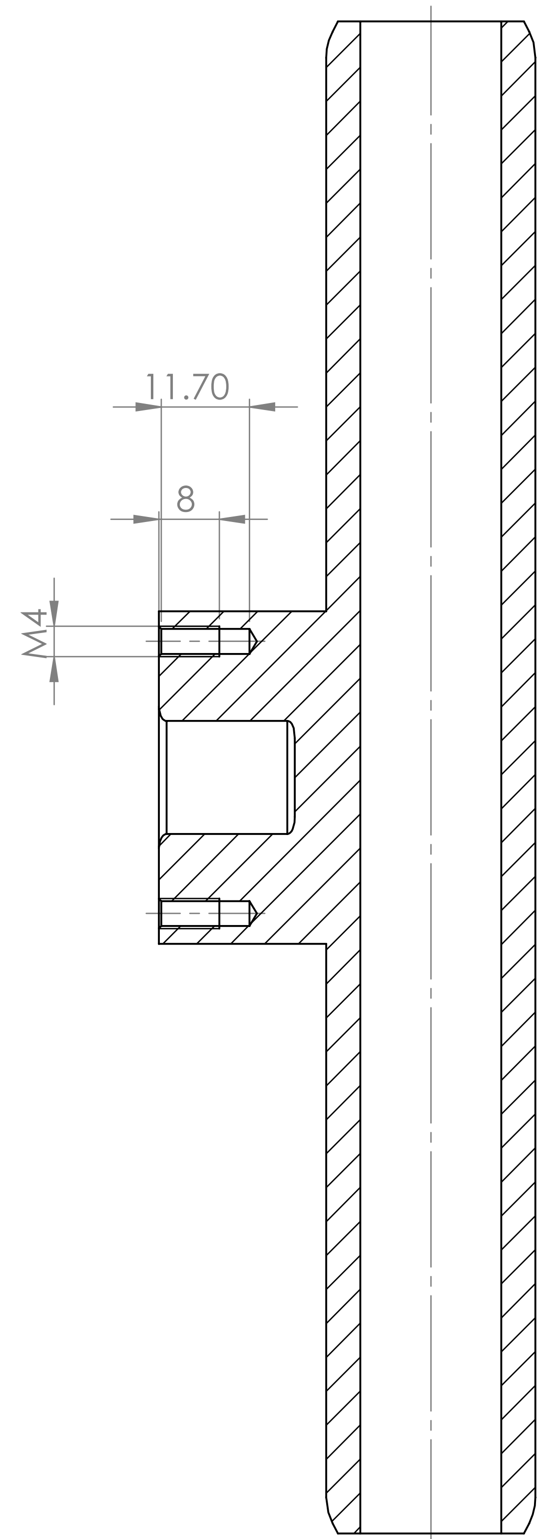

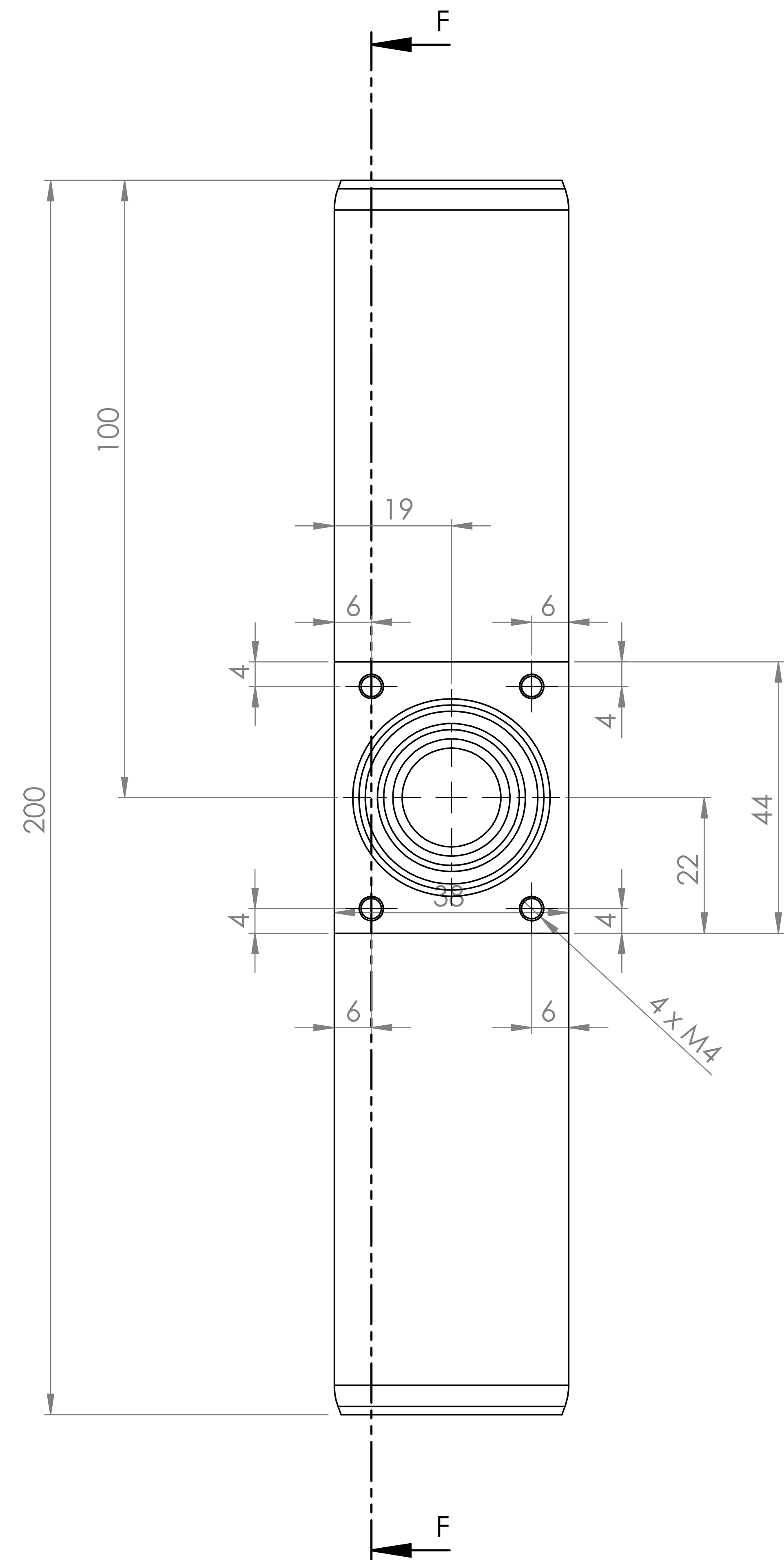

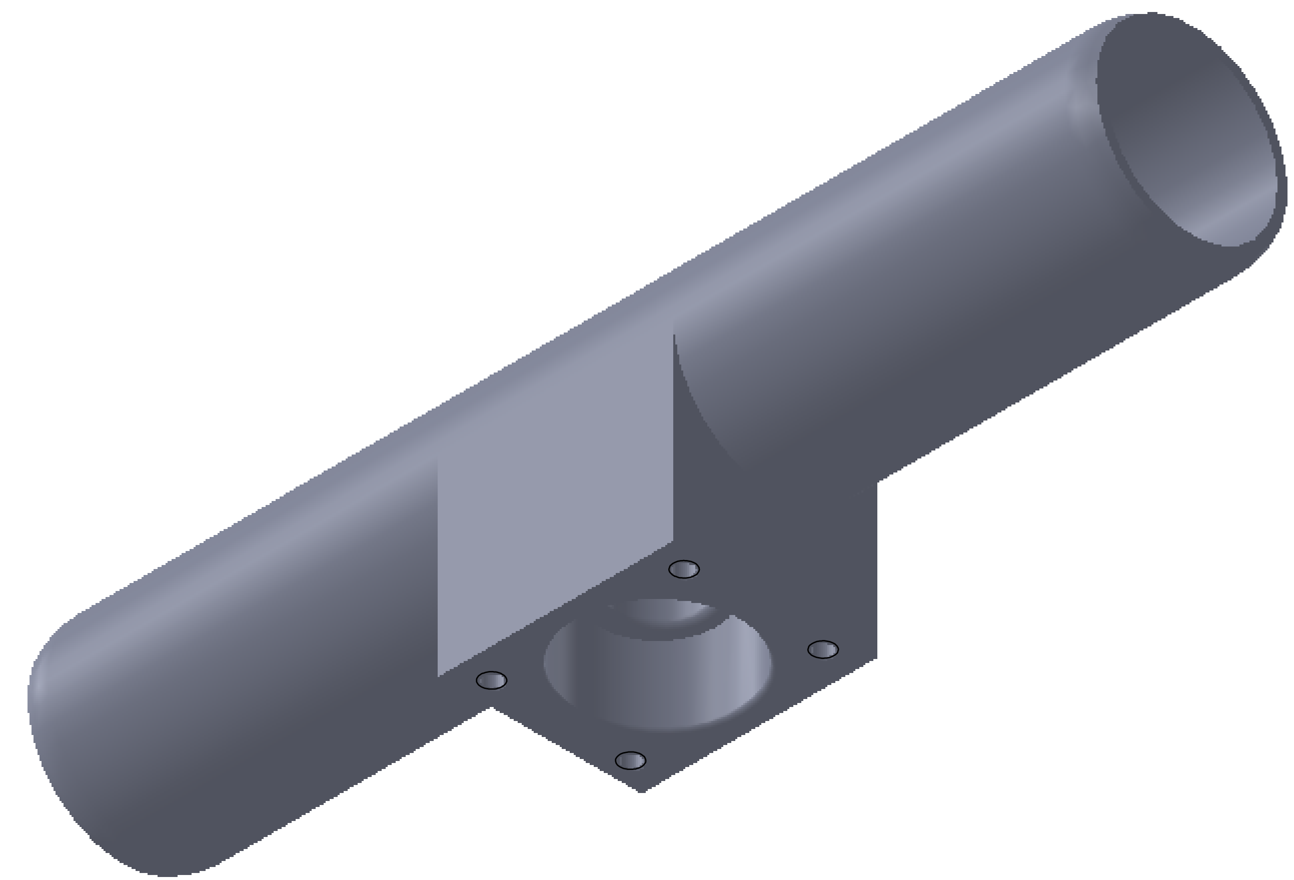

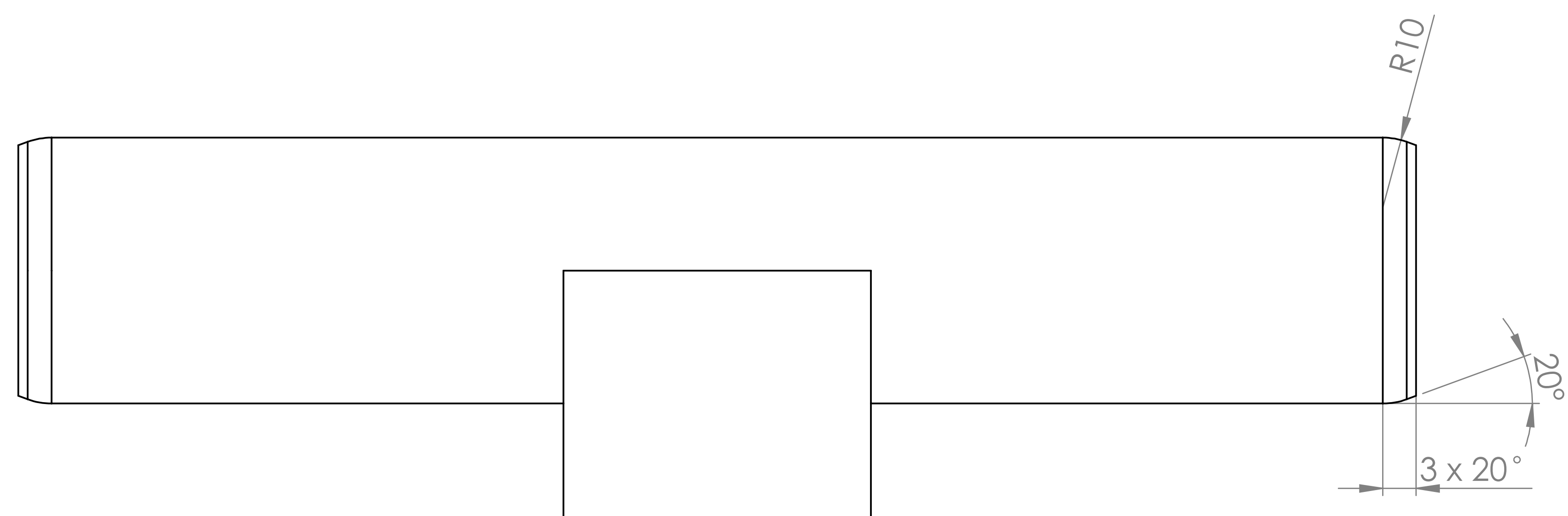

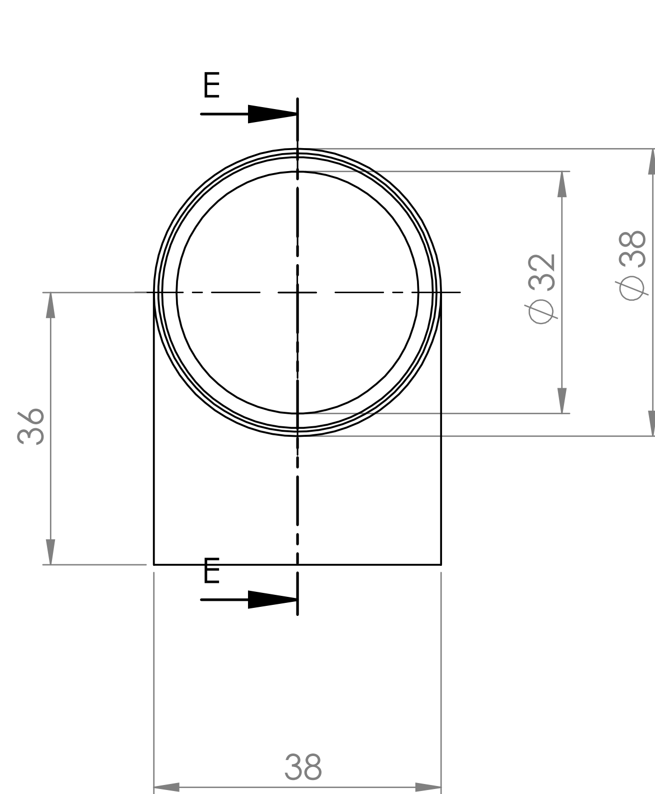

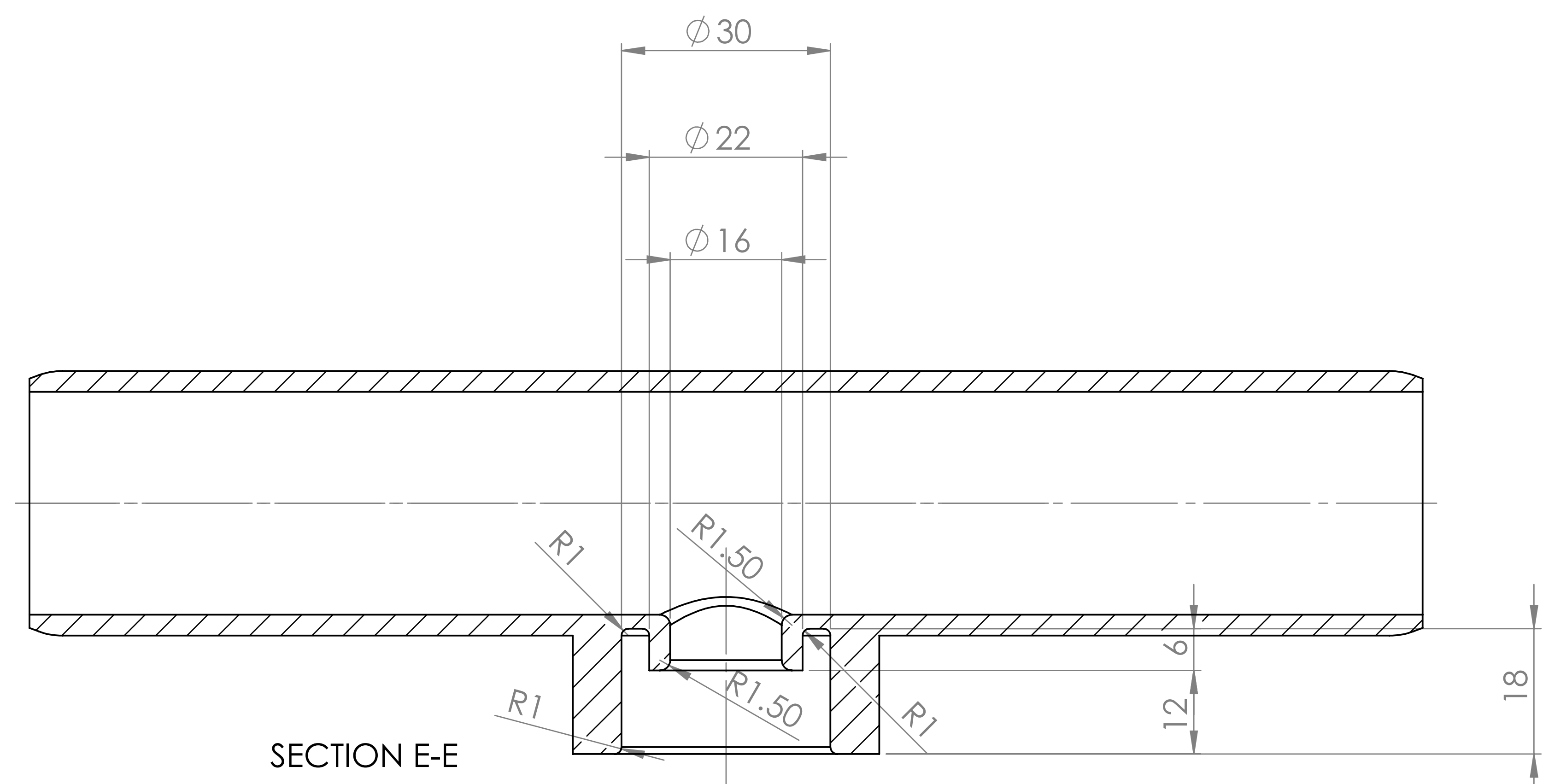

UNLESS OTHERWISE SPECIFIED: DIMENSIONS ARE IN MILLIMETERS SURFACE FINISH: TOLERANCES: LINEAR: ANGULAR:	FINISH:	DEBURR AND BREAK SHARP EDGES	DO NOT SCALE DRAWING	REVISION
			Stefano Soprani stefs@dtu.dk	
NAME / SIGNATURE / DATE			TITLE: Pipe section for sensor	
DRAWN				
CHK'D				
APPV'D				
MFG				
Q.A		MATERIAL: POM	DWG NO.	A2
		WEIGHT:	SCALE:1:1	SHEET 1 OF 1

SOLIDWORKS Student Edition.
For Academic Use Only.

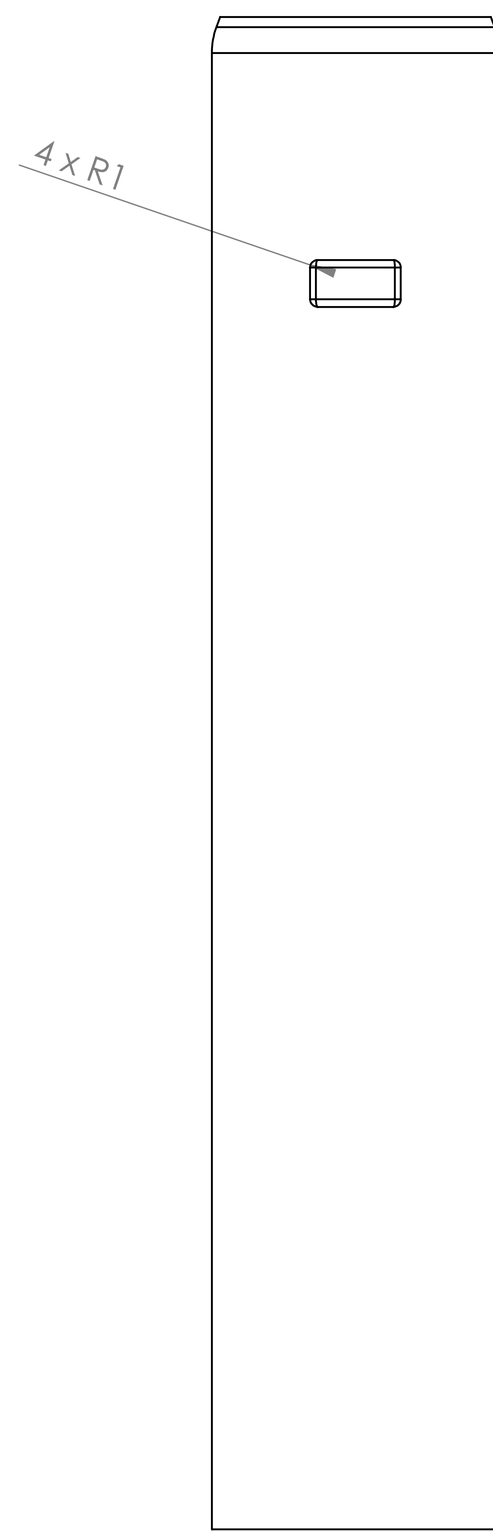

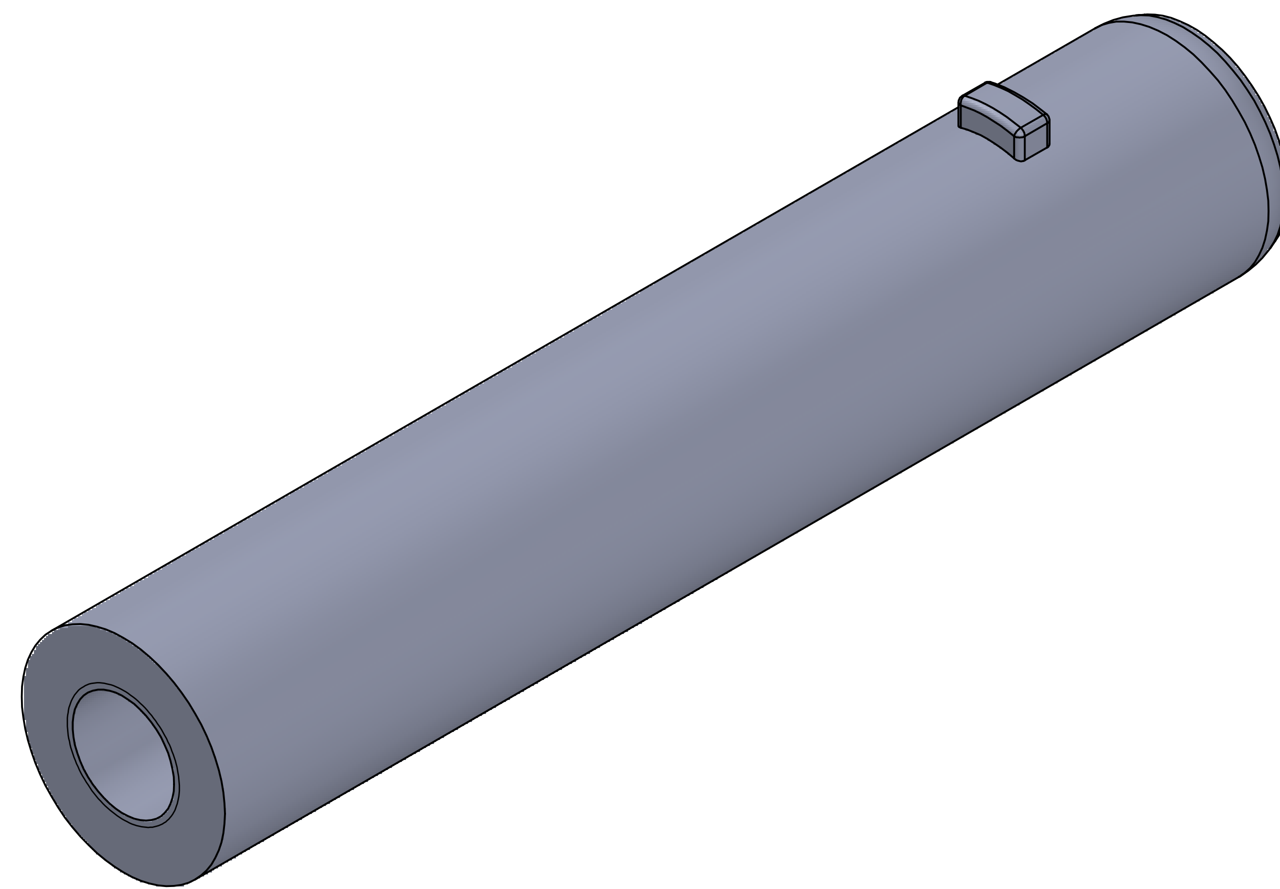

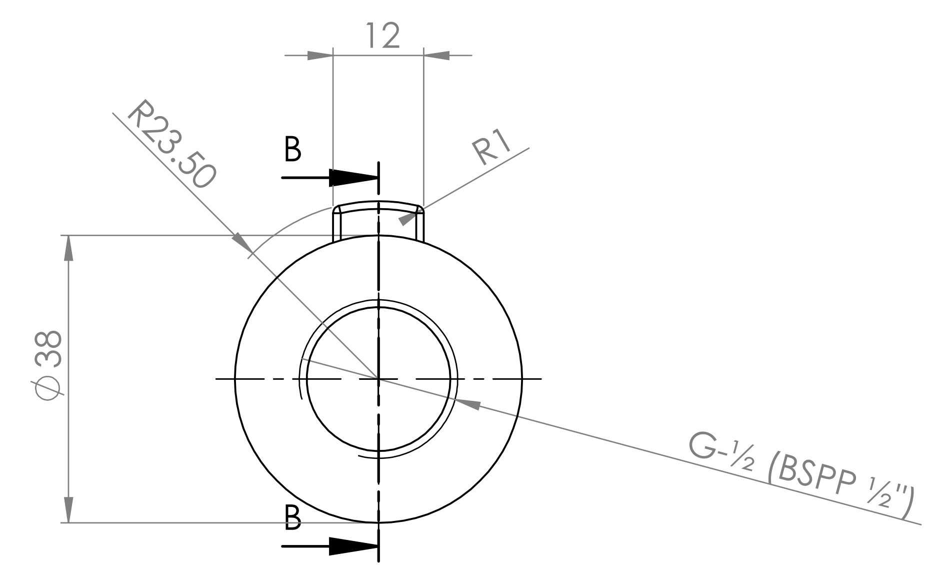

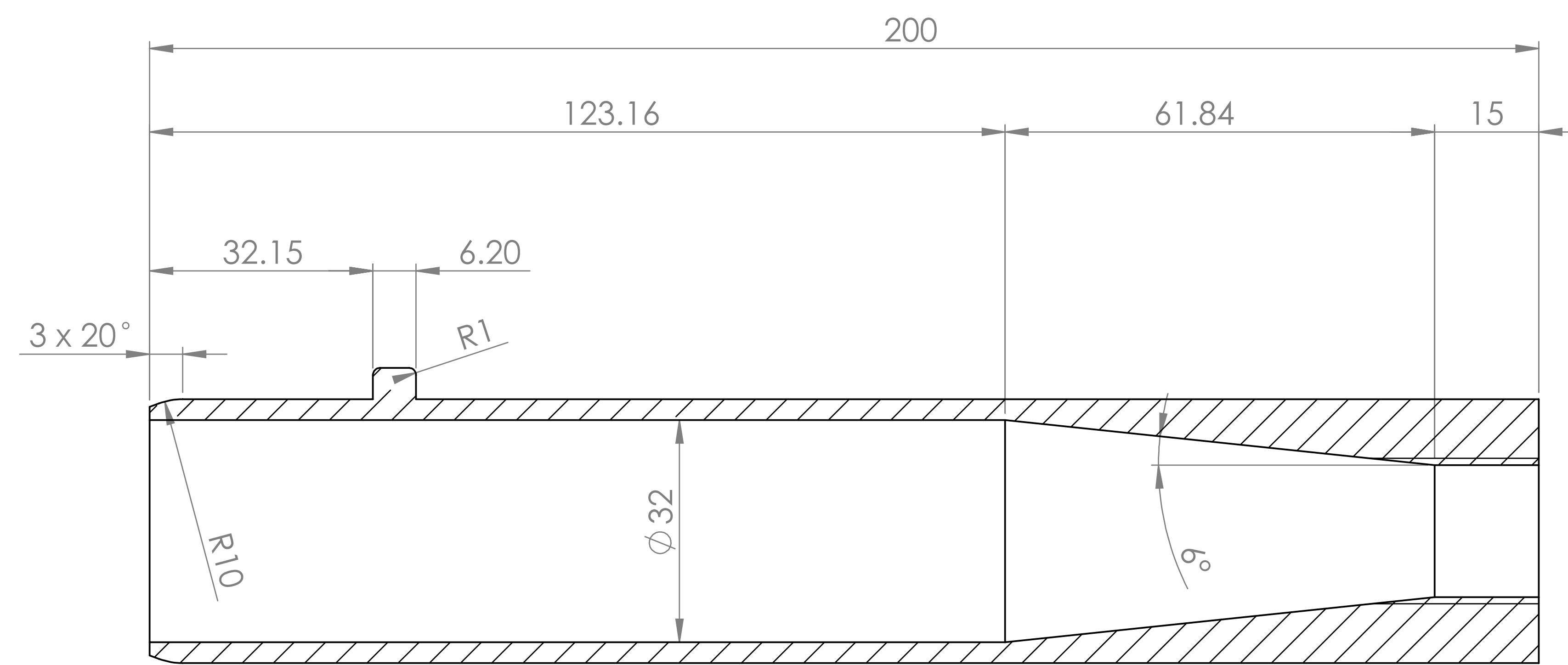

SECTION B-B

UNLESS OTHERWISE SPECIFIED: DIMENSIONS ARE IN MILLIMETERS SURFACE FINISH: TOLERANCES: LINEAR: ANGULAR:	FINISH:	DEBURR AND BREAK SHARP EDGES	DO NOT SCALE DRAWING	REVISION
			Stefano Soprani	stefs@dtu.dk
NAME / SIGNATURE / DATE			TITLE:	
DRAWN			Inlet-Outlet 1/2"	
CHK'D				
APPV'D				
MFG				
Q.A	MATERIAL: POM			A2
	WEIGHT:		SCALE:1:1	SHEET 1 OF 1

SOLIDWORKS Student Edition.
For Academic Use Only.

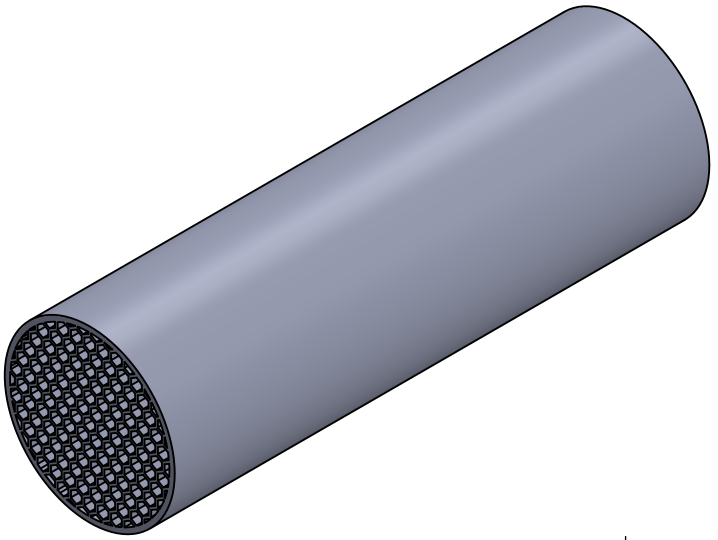

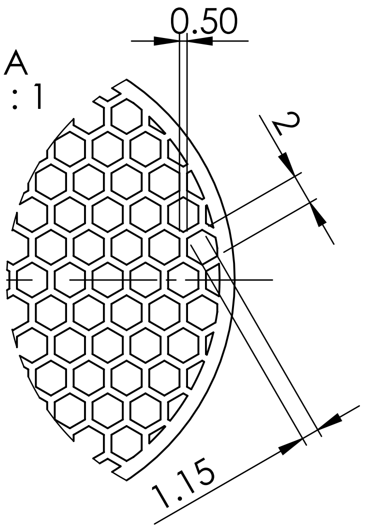

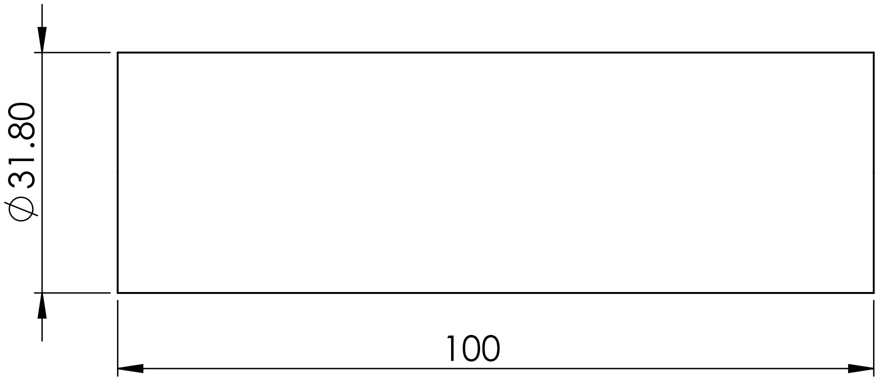

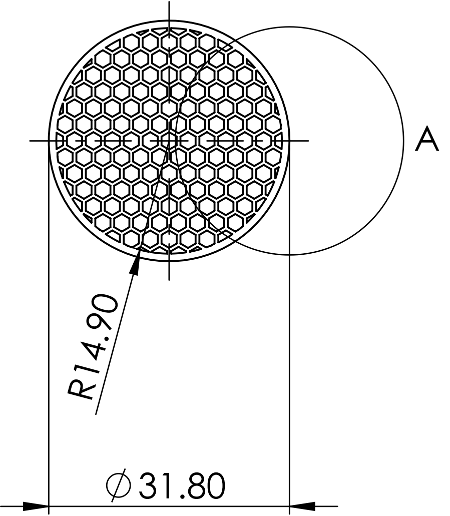

UNLESS OTHERWISE SPECIFIED: DIMENSIONS ARE IN MILLIMETERS SURFACE FINISH: TOLERANCES: LINEAR: ANGULAR:	FINISH:	DEBURR AND BREAK SHARP EDGES	DO NOT SCALE DRAWING	REVISION

	NAME	SIGNATURE	DATE	TITLE:
DRAWN				
CHK'D				
APPV'D				
MFG				
Q.A				

MATERIAL: PLA plastic

DWG NO. Flow straightener

A4

WEIGHT:

SCALE:1:2

SHEET 1 OF 1

SOLIDWORKS Student Edition.
For Academic Use Only.

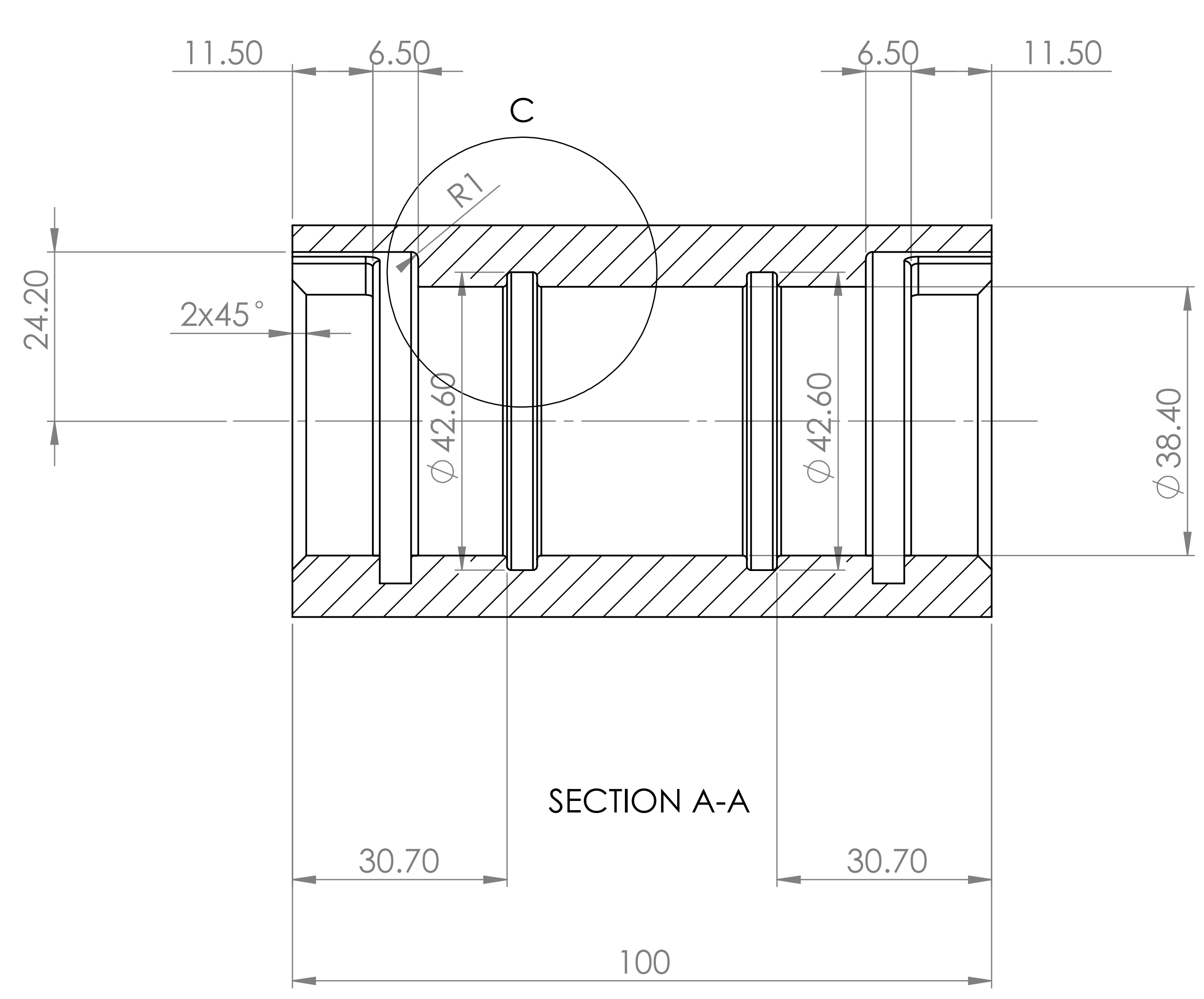

SECTION A-A

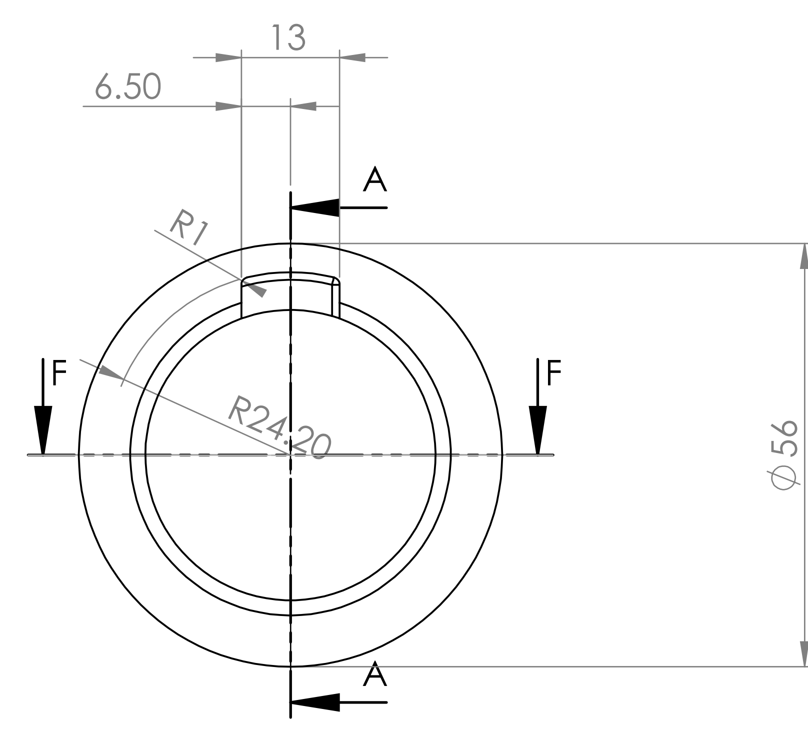

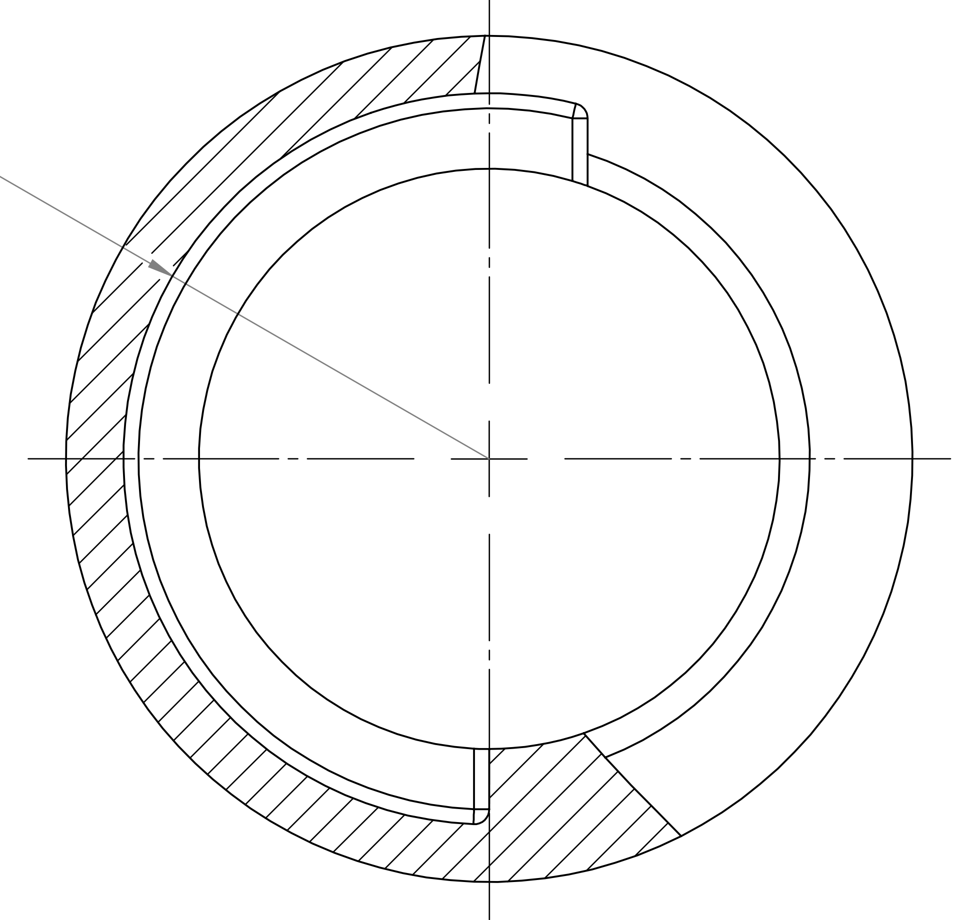

AUXILIARY VIEW
BROKEN-OUT VIEW OF THE FRONT SECTION
SCALE 2:1

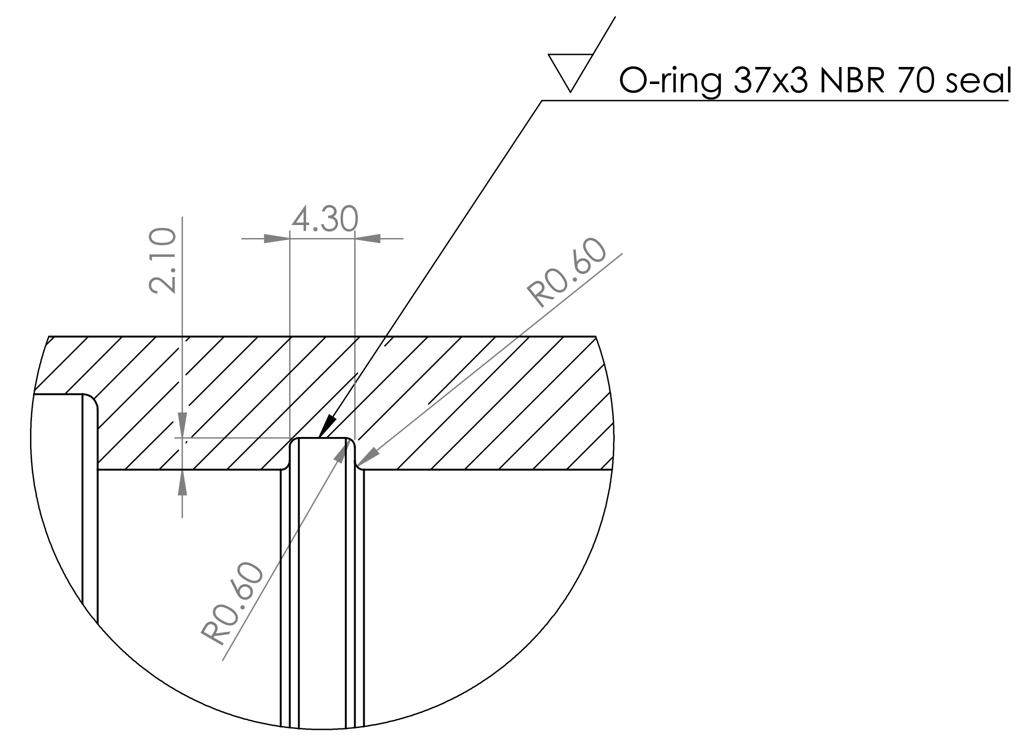

DETAIL C
SCALE 2 : 1

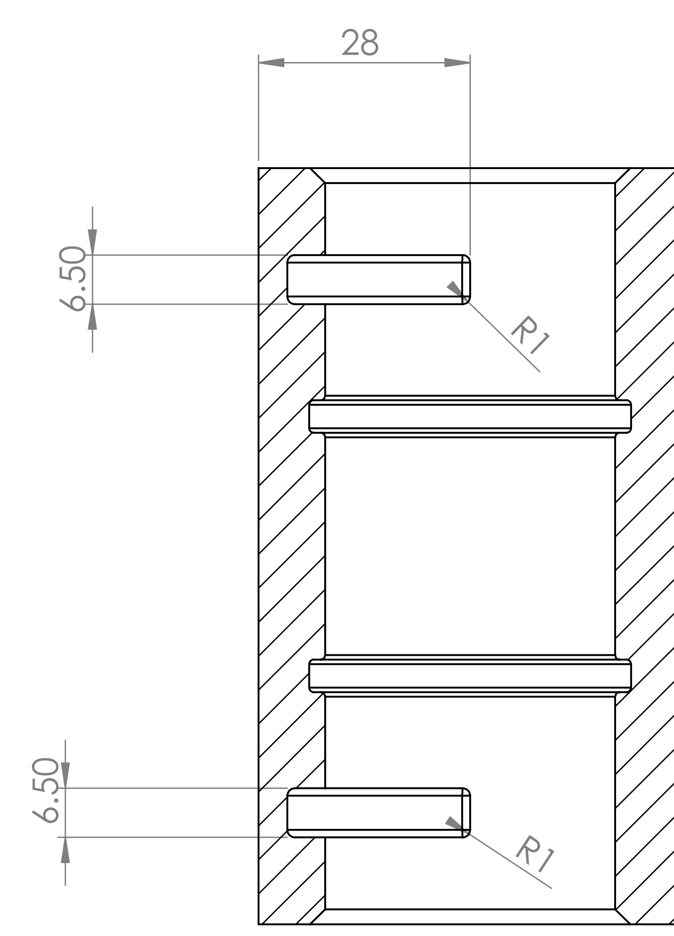

SECTION F-F

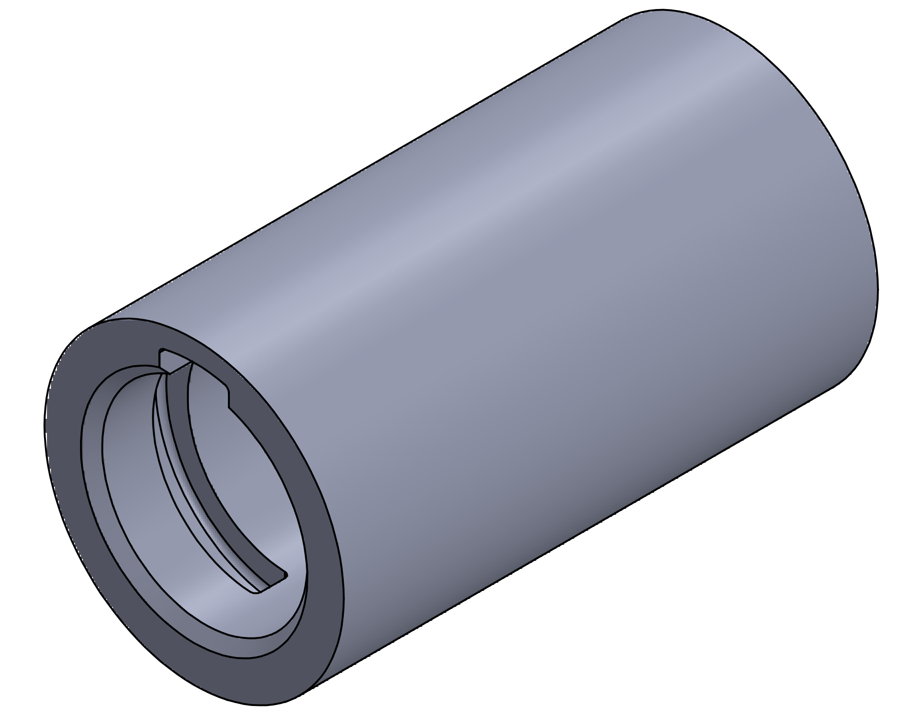

SOLIDWORKS Student Edition.
For Academic Use Only.

UNLESS OTHERWISE SPECIFIED: DIMENSIONS ARE IN MILLIMETERS SURFACE FINISH: TOLERANCES: LINEAR: ANGULAR:	FINISH:	DEBURR AND BREAK SHARP EDGES	DO NOT SCALE DRAWING	REVISION
NAME / SIGNATURE / DATE			Stefano Soprani	stefs@dtu.dk
DRAWN			TITLE: Coupling	
CHK'D				
APPV'D				
MFG				
Q.A	MATERIAL: POM		DWG NO.	A2
	WEIGHT:		SCALE:1:1	SHEET 1 OF 1